Ph.D. Program in Civil, Chemical and Environmental Engineering
Curriculum in Fluid Dynamics and Environmental Engineering

Department of Civil, Chemical and Environmental Engineering
Polytechnic School, University of Genoa, Italy.

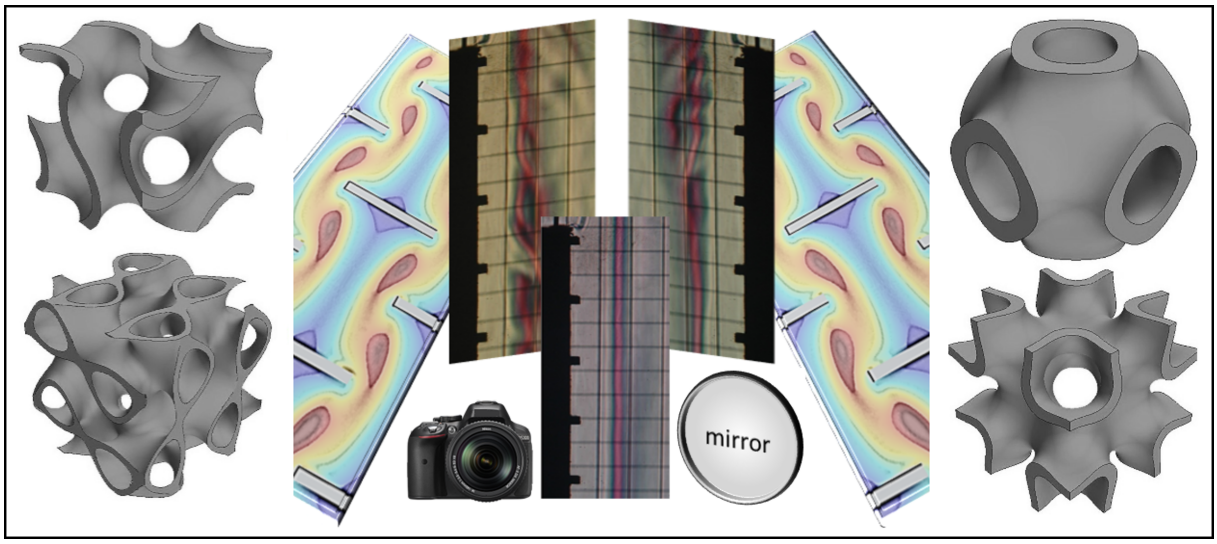

Buoyant and Forced Flows over Regularly Textured Surfaces and Porous Substrates

Essameldin Nabil Ahmed Kamal Abdo

BUOYANT AND FORCED FLOWS OVER REGULARLY TEXTURED SURFACES AND POROUS SUBSTRATES

BY

ESSAMELDIN NABIL AHMED KAMAL ABDO

Dissertation discussed in partial fulfillment of
the requirements for the Degree of

DOCTOR OF PHILOSOPHY

Civil, Chemical and Environmental Engineering
curriculum in Fluid Dynamics and Environmental Engineering,
Department of Civil, Chemical and Environmental Engineering, University of Genoa, Italy

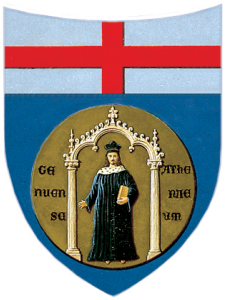

May, 2024

Advisers:
Prof. Alessandro Bottaro - Department of Civil, Chemical and Environmental Engineering (DICCA), University of Genoa
Prof. Giovanni Tanda - Department of Mechanical, Energy, Management and Transport Engineering (DIME), University of Genoa

External Reviewers:
Prof. Dario Ambrosini - Department of Industrial and Information Engineering and Economics, University of L'Aquila
Prof. Howard A. Stone - Department of Mechanical and Aerospace Engineering, Princeton University

Examination Committee:
Prof. Nicolas Mazellier - PRISME Laboratory, University of Orléans
Prof. Paola Causin - Department of Mathematics, University of Milan
Prof. Andrea Mazzino - Department of Civil, Chemical and Environmental Engineering (DICCA), University of Genoa

Ph.D. program in Civil, Chemical and Environmental Engineering
Curriculum in Fluid Dynamics and Environmental Engineering
Cycle XXXVI

Acknowledgements

Firstly, I would like to express my sincere gratitude to my supervisors, Prof. Alessandro Bottaro and Prof. Giovanni Tanda, for motivation, guidance, and continuous support. Secondly, I would like to extend thanks to all my teachers for the valuable courses and to Prof. Didier Lasseux (University of Bordeaux, France) and Prof. Francisco J. Valdés-Parada (Universidad Autónoma Metropolitana-Iztapalapa, Mexico) for several interesting discussions on the subject of upscaling. Finally, the financial support of the Italian Ministry of University and Research (program PRIN 2017, project 2017X7Z8S3 LUBRI-SMOOTH) and of the European Union Next Generation EU (PRIN PNRR 2022 grant, project code P2022CZ5KZ) is gratefully acknowledged.

To my late mother, dear father, and devoted wife

for love, patience, and support

ABSTRACT

The complex interaction between textured walls/substrates and a fluid is analyzed in different buoyant and forced flow problems. Experimental surveys on natural convection along rib-roughened vertical surfaces are conducted, in addition to numerical analyses of laminar buoyant flows over ribbed surfaces and of laminar/turbulent forced flows in channels with rough/permeable boundaries. The numerical work comprises (i) full feature-resolving simulations and (ii) homogenized ones that exploit effective boundary conditions to macroscopically mimic the phenomena, thus bypassing expensive numerical resolution of the fields near/within wall corrugations.

The theoretical/numerical work on buoyant flows along ribbed vertical surfaces focuses on the formulation and validation of high-order *effective* velocity and temperature boundary conditions at a fictitious plane interface next to the roughness elements. In the first experimental phase, the buoyant airflow over a heated vertical surface regularly roughened with wooden ribs of square cross section, either spanwise-elongated or truncated and arranged in a staggered pattern, is studied at relatively large Rayleigh numbers (Ra of order 10^8), and varying the rib height and pitch. The experiments utilize the schlieren method to visualize the thermal boundary layer and to estimate the local Nusselt number values along the vertical surface; also, miniature thermocouples are employed to measure the local air temperature near the wall. Exclusively for staggered ribs, heat transfer enhancement, sensitive to number of rib segments per row, is found, and the observations reveal the potential of truncated ribs to amplify thermal-field disturbances. The second phase of experiments is aimed at studying similar roughness geometries under conditions well within the laminar regime (Ra of order 10^7), which facilitates performing full/homogenized numerical simulations, to be validated against the experimental results. Both the continuous and the truncated rib patterns are found to degrade the convective heat transfer from the surface at such a low Rayleigh number.

In regard to the forced flow problems, first, the fully developed, laminar flow in a channel bounded by rough/porous walls is considered, and the Beavers-Joseph-Saffman condition for the slip velocity is revisited. The boundary condition used for the longitudinal velocity, available from the homogenization theory, applies not only to permeable but also to rough surfaces, including the case of separated flow. Moreover, the near-wall advection is incorporated into the analysis by means of an *Oseen's approximation*, and this widens the applicability range of the model considerably. Second, effective boundary conditions of the three velocity components are implemented to study turbulent channel flows over different porous substrates. The results demonstrate the possible drag-reducing effect of porous substrates with streamwise-preferential alignment of the solid inclusions, and show that the r.m.s. fluctuations of the transpiration velocity at the fictitious interface between the free-fluid region and the perturbed wall, $\tilde{V}_{rms}$, is a key control parameter of the roughness function, ΔU^+; further analysis reveals that $\tilde{V}_{rms}$ is strongly correlated to a single macroscopic quantity, Ψ, which comprises the upscaling coefficients of the model. Finally, a volume-averaging-based analysis of seepage in triply-periodic-minimal-surface-based porous structures is conducted, under conditions departing from Stokes'. An advection-sensitive "*effective*" permeability (rather than the merely geometry-dependent intrinsic permeability) in Darcy's law stems from upscaling, and can be evaluated by solving a closure problem through a *representative elementary volume* of the medium. It is found that advection can significantly reduce permeability, particularly at large porosities.

PREFACE

Different buoyancy-induced and forced flow problems over textured surfaces were tackled experimentally, mainly using schlieren imaging, and/or numerically through both the conventional fine-grained CFD simulations and the homogenization-based analysis; application of the latter treatment, which represents via upscaling a computationally cheaper numerical tool, is a major objective of the project. The thesis is based on the following published/submitted/ongoing papers on buoyant (**B**) and forced (**F**) flows, which include the main outputs of the project:

- **Paper B1:** AHMED, E.N., BOTTARO, A. & TANDA, G. 2022 A homogenization approach for buoyancy-induced flows over micro-textured vertical surfaces. *J. Fluid Mech.* **941**, A53.
- **Paper B2:** AHMED, E.N. 2023 Natural-convection heat transfer from regularly ribbed vertical surfaces: Homogenization-based simulations towards a correlation for the Nusselt number. *Numer. Heat Transfer A Appl.* **83** (9), 991–1013.
- **Paper B3:** AHMED, E.N., BOTTARO, A. & TANDA, G. 2024 Conjugate natural convection along regularly ribbed vertical surfaces: A homogenization-based study. *Numer. Heat Transfer A Appl.* **85** (9), 1331–1355.
- **Paper B4:** TANDA, G., AHMED, E.N. & BOTTARO, A. 2023 Natural convection heat transfer from a ribbed vertical plate: Effect of rib size, pitch, and truncation. *Exp. Therm. Fluid Sci.* **145**, 110898.
- **Paper B5:** TANDA, G., AHMED, E.N. & BOTTARO, A. (Submitted 2023) Experimental observations of the onset of unsteadiness for buoyant airflow along smooth and rough vertical isothermal walls. *Exp. Heat Transfer.*

  Paper B6: AHMED, E.N. & TANDA, G. 2024 An experimental and numerical study of laminar natural convection along vertical rib-roughened surfaces. *Intl J. Heat Mass Transfer.* **223**, 125227.
- **Paper F1:** AHMED, E.N. & BOTTARO, A. 2024 Laminar flow in a channel bounded by porous/rough walls: revisiting Beavers-Joseph-Saffman. *Eur. J. Mech. B Fluids* **103**, 269–283.
- **Paper F2:** AHMED, E.N., NAQVI, S.B., BUDA, L. & BOTTARO, A. 2022 A homogenization approach for turbulent channel flows over porous substrates: Formulation and implementation of effective boundary conditions. *Fluids* **7** (5), 178.
- **Paper F3:** AHMED, E.N. & BOTTARO, A. (Draft, 2024) Exploring the nexus among roughness function, apparent slip velocity and upscaling coefficients for turbulent flows over porous/textured walls. *To Be Submitted To J. Fluid Mech.*
- **Paper F4:** AHMED, E.N. & BOTTARO, A. 2023 Flow through porous metamaterials formed by TPMS-based unit cells: Effects of advection. *Eur. J. Mech. B Fluids* **100**, 202–207.

The presentation of the articles is preceded by an introduction to the subjects and problems considered, a chapter on the experimental procedure/tools and the numerical approaches, and a summary of the objectives and findings of each article.

It is worth pointing out that the research activities carried out during the Ph.D. period yielded, in addition, the following contributions (**not included in the thesis):**

- **Oral presentations at conferences/meetings (Presenting Author)**
  - AHMED, E.N., NAQVI, S.B. & BOTTARO, A. 2022 Turbulence over anisotropic porous substrates: A homogenization-based study. Presented at EDRFCM2022 / European Drag Reduction and Flow Control Meeting , Paris, France.
  - AHMED, E.N., BOTTARO, A. & TANDA, G. 2022 Natural convection over a vertical ribbed surface. Presented at EFMC14 / 14th European Fluid Mechanics Conference, Athens, Greece.
  - TANDA, G., AHMED, E.N. & BOTTARO, A. 2023 Experimental observations of the onset of unsteadiness for buoyant airflow along smooth and rough vertical isothermal walls. Presented at the 40th U.I.T. International Heat Transfer Conference, Assisi, Italy.
  - AHMED, E.N. & BOTTARO, A. 2023 Homogenization-based analytical solution for laminar flow problems in channels bounded by rough/permeable walls. Presented at EMI 2023 International Conference, Palermo, Italy.
  - AHMED, E.N. & BOTTARO, A. 2024 Turbulence over a microstructured wall. Presented at A Journey through Interfaces, Turbulence, and Moving Bodies in Fluids (A colloquium on the occasion of Jacques Magnaudet's 65th birthday), Toulouse, France.
- **Journal publication**
  - CAMPARDELLI, R., DE NEGRI ATANASIO, G., CAROTENUTO, C., GRIFFO, R., AHMED, E.N., CORRALES-GONZÁLEZ, M., WEI, J., TUJU, P.E., MAZZINO, A. & PRALITS, J.O. 2023 Rotor-stator emulsification in the turbulent inertial regime: Experiments toward a robust correlation for the droplet size. *Langmuir* **39** (50), 18518–18525[1].
- **Ongoing paper**
  - SEGALERBA, E., AHMED, E.N., PENNISI, M.V. & PRALITS, J.O. (Ongoing) Analytical modelling of conjugate heat transfer at moderate Reynolds number: From a plane channel to the human nose. *To Be Submitted To Appl. Math. Model.*

[1]This work was initiated during the Ph.D. course in Mathematical Modeling Camp held at the doctoral school of the Department of Civil, Chemical and Environmental Engineering, Genoa, Italy.

INDEX

INTRODUCTION

1.1. BUOYANT FLOWS ALONG RIBBED VERTICAL WALLS

Natural convection heat transfer from vertical ribbed surfaces is relevant to a wide range of applications. This includes electronic equipment cooling (Incropera, 1988), photovoltaic and thermal solar systems (Nghana *et al.*, 2022), passive solar heating and ventilation of buildings (Bohn & Anderson, 1984; Gilani *et al.*, 2017), heat removal in nuclear technology (Tzanos *et al.*, 1991), cooling garments (Yoshida, 2018; Nishikawa *et al.*, 2020), and many others. Compared with forced convection, a system that depends on the natural-convection heat transfer regime has lower cost, simpler design, less noise and vibrations, higher reliability, almost maintenance-free operations, and better ability for use in hostile environments under dust, moist air, etc. On the other hand, with the flow driven merely by the buoyancy force, the main problem facing the designers is the low heat transfer coefficient of these systems relative to those adopting active heat transfer mechanisms. As a consequence, it's widely accepted during the design process of systems with relatively high heat loads to depend on forced convection as the main cooling regime, and to employ natural convection as a supplementary or a backup system (Bhavnani & Bergles, 1990), whereas, for small/medium heat loads, the sufficiency of passive cooling should be investigated first before turning to more sophisticated cooling systems (Johnson, 1986).

The life and long-term reliability of electronic circuits can be considerably increased by keeping the operating temperature sufficiently below the maximum level allowed by the manufacturer (Nelson *et al.*, 1978; Genot, 1982; Johnson, 1986; Oktay *et al.*, 1986). Nevertheless, this has become practically challenging owing to the progressive miniaturization of electronic components, along with the reduction of operational execution time and the increase in power supply (Joshi *et al.*, 1989; Peterson & Ortega, 1990). Hence, optimization of the heat transfer performance of natural convection systems is essential to cope with higher heat generation rates per unit volume. Cooling systems of light-emitting diodes (LEDs) represent a typical application in which heat transfer enhancements are crucial. The main advantages of LEDs are their relatively long lifetime and high energy conversion efficiency; these devices are able to convert almost 40% of the supplied electric power to light while the rest (60%) is converted to heat (Narendran & Gu, 2005). Here, the critical point is the provision of efficient cooling to these units, otherwise the temperature increase can lead to dramatic deterioration in their energy conversion efficiency and life span (Ha & Graham, 2012). For such systems, promoting heat transfer by means of increasing the volume of the module is not appropriate as it comes at the expense of safety and cost. Therefore, an optimized design should be pursued for the cooling systems, that is, the design characterized by a low thermal resistance and an acceptable mass and volume (Park *et al.*, 2015).

Many experimental and numerical investigations have been carried out, seeking enhancement of the heat transfer performance of natural-convection systems through different techniques, including direct immersion into liquids (Park & Bergles, 1987; Joshi *et al.*, 1989; Tanda, 2017), controlling the spacing of plane heated channels under a variety of boundary conditions

(Azevedo & Sparrow, 1985; Webb & Hill, 1989), optimization of heat sink design (Park *et al.*, 2015) and, most related to the current project, adding surface alterations/extensions to vertical plates exposed to natural convection. The latter is an intuitively appealing solution in analogy to the well-established concept of heat transfer promotion by adding ribs/fins to surfaces exposed to forced convection (Bunker & Donnellan, 2003; Chyu *et al.*, 2007; Han *et al.*, 2012). However, studies on the effectiveness of adding surface alterations (ribs, interrupted fins, dimples, etc.) to vertical plates exposed to natural convection have not led yet to convincing guidelines, with some researchers reporting an improvement of up to 200% compared with the performance of plane vertical plates, and others who have found them useless or even of negative influence on the local and averaged heat transfer parameters (Bhavnani & Bergles, 1990). At first glance, the findings which have been reported so far appear contradictory (Bhavnani & Bergles, 1990), yet an in-depth analysis of the complex flow patterns over ribbed surfaces and their contrasting effects can provide insight into the plausible reasons for the differences between the reported trends, as outlined by Tanda (1997): (i) the presence of ribs may resist and partially block the natural convection stream, as buoyancy is the only driving force, and consequently reduce the heat transfer rate (*negative effect*); (ii) thermally inactive regions just upstream and downstream of each protrusion where hot recirculating vortices are present can lead to sharp drop in heat transfer at these locations (*negative effect*); (iii) ribs provide extra area for natural convection heat transfer provided that their materials are of high thermal conductivity (*positive effect*); (iv) surface roughness may anticipate turbulence and trigger it to occur at relatively low values of the Rayleigh number, which can favorably affect the characteristics of the natural convection heat transfer (*positive effect*). Thus, the study and optimization of heat transfer from corrugated/ribbed/finned surfaces have remained fertile fields for research.

A better understanding of the characteristics of buoyancy-driven flows (including the convective heat transfer performance as a main subject) along vertical heated surfaces in general, and rib-roughened ones in particular, is sought through the literature survey presented below. In Section 1.1.1., investigations on the map of transition from a purely laminar regime to turbulence are discussed first for the case of a smooth vertical surface exposed to natural convection; this is followed (in Section 1.1.2.) by mentioning some studies focusing on the consequent effects on the heat transfer from the plate. In Section 1.1.3., selected researches on the influence of adding surface perturbations to a vertical heated plate in terms of their potential to trigger an early transition to turbulence are presented. A detailed discussion on natural convection heat transfer characteristics over roughened/perturbed surfaces and channels is provided in Section 1.1.4., considering a wide range of studies dealing with different roughness shapes, dimensions, and thermal conductivity values.

1.1.1. Transition mechanism and criteria over a vertical smooth surface

Transition phenomena in buoyant boundary layers have been studied extensively from the past century to today. Linear stability theory as well as numerical calculations of the growth and nonlinear interaction of two-dimensional and transverse disturbances have been applied to explore the transition mechanism for a variety of natural convection flows and conditions (Dring & Gebhart, 1968; Gebhart, 1969; Audunson & Gebhart, 1976). Dring & Gebhart (1968) showed that

as a disturbance in the flow adjacent to a vertical surface is convected downstream, disturbance components amplify selectively and in a very narrow band of frequencies; further downstream, non-linear and three-dimensional effects become important (Mahajan & Gebhart, 1979). Since transitional and turbulent flow regimes can be pertinent to many practical situations, the criteria ruling the onset of transition in the buoyancy-driven flow along a heated vertical smooth surface are worth investigating, and this can help in the study of the more advanced case of a rough surface. First, some dimensionless control parameters are defined:

The Prandtl number:

$$Pr = \frac{\text{momentum diffusivity}}{\text{thermal diffusivity}} = \frac{\nu}{\alpha} = \frac{\mu\, c_p}{k_f}, \tag{1.1}$$

where ν, α, μ, c_p, and k_f denote , respectively, the kinematic viscosity, the thermal diffusivity, the dynamic viscosity, the specific heat, and the thermal conductivity, all characterizing the fluid under study.

The Grashof number based on local vertical position:

$$Gr_x = \frac{g\beta\,(\hat{T}_w - \hat{T}_\infty)\,\hat{x}^3}{\nu^2}, \tag{1.2}$$

Where g, β, $\hat{T}_w$, $\hat{T}_\infty$, and $\hat{x}$ denote, respectively, the gravitational acceleration, the thermal expansion coefficient of the fluid, the wall temperature, the ambient air temperature, and the vertical coordinate measured from the leading edge to the point of interest on the plate surface.

The Grashof number based on plate height:

$$Gr = \frac{g\beta\,(\hat{T}_w - \hat{T}_\infty)\,H^3}{\nu^2}, \tag{1.3}$$

Where H is the overall height of the plate.

The Rayleigh number based on local vertical position:

$$Ra_x = Gr_x \times Pr = \frac{g\beta\,(\hat{T}_w - \hat{T}_\infty)\,\hat{x}^3}{\alpha\,\nu}. \tag{1.4}$$

The Rayleigh number based on plate height:

$$Ra = Gr \times Pr = \frac{g\beta\,(\hat{T}_w - \hat{T}_\infty)\,H^3}{\alpha\,\nu}, \tag{1.5}$$

taking into account that the aforementioned definitions of the Grashof and the Rayleigh numbers are pertinent to a surface with uniform wall temperature ($\hat{T}_w$), while other definitions can be adopted for a surface exposed to a uniform heat flux.

Bejan & Lage (1990) showed that the Grashof number (and not the Rayleigh number) marks the transition in all fluids, with a value of order 10^9 at the beginning of transition (i.e., Rayleigh number of about 0.7×10^9 when air is the convective fluid), a criterion which is still assumed in heat transfer books (Bejan, 1993). Nevertheless, as indicated by Godaux & Gebhart (1974), the lack of a clear definition of transition in many relevant studies on natural convection has been a source of confusion and inconsistency in the literature, and the considerable disagreement between the reported values of the critical Grashof numbers in these investigations indicates the dependency of the experimental results on local conditions, the observation methods or other factors; this was highlighted by collecting and comparing data from different referential studies, for instance (Griffiths & Davis, 1922; Saunders, 1936, 1939; Warner & Arpaci, 1968; Cheesewright, 1968), showing the large spread of the reported values for the Grashof number at the onset of transition and at the beginning of the fully turbulent flow region. For instance, Cheesewright (1968), underlining the arbitrary nature of former attempts to specify the beginning and end of transition, indicated a Grashof number of 2×10^9 as the condition at which significant fluctuations first appear in the boundary layer, yet without significant changes in the mean temperature profiles or in the trend of heat transfer data; major changes in mean temperature profiles and heat transfer rates were found to appear at a Grashof number of 5×10^9 and up to 8×10^9; the amplitude of temperature fluctuations then decreased with the Grashof number from 8×10^9 to 2×10^{10}, while beyond the last threshold it remained approximately constant. Kato *et al.* (1968) analyzed and adapted some previous theories on natural convection over plane vertical surfaces and proposed a new criterion on the laminar to turbulent transition, that is, a critical value for the ratio between the potential energy gained due to buoyancy and the dissipated energy near the wall.

Godaux & Gebhart (1974) studied the route to turbulence in the water buoyant stream along a vertical smooth surface exposed to a uniform heat flux and reported important characteristics of the temperature field in the thermal transition region, including the behavior of the mean temperature profile, the growth rate of the thickness of the thermal boundary layer, and the amplitudes and predominant frequencies of the temperature disturbances. Their experiments revealed that the region of transition comprises a "*velocity transition*" sub-region and a "*thermal transition*" one. In detail, as illustrated in Fig. 1.1, the following stages are encountered in the route to turbulence: (i) disturbances from the surrounding medium interact with the initially laminar flow, become two dimensional, and as they are convected downstream they experience a strong filtering effect that amplifies only a narrow band of frequencies such that the disturbance energy becomes eventually concentrated in a single frequency; (ii) secondary mean motions arise which are associated with amplification of transverse disturbances and their interaction with the two dimensional ones; (iii) the first signs of turbulent disturbances takes place in the velocity field and alter the viscous boundary layer, yet these disturbances don't alter the mean temperature profile immediately; (iv) the onset of thermal transition is recorded further downstream, when the turbulent disturbances in the velocity field become strong enough to stimulate a process of turbulent thermal diffusion, and consequently the thickening rate of thermal boundary layer and the distribution of the mean temperature across it start to deviate from the laminar behavior; (v) a completely turbulent flow is developed by the end of thermal transition, and this is supposed to be followed by a region of adjustment of the turbulent parameters to the final form of the fully turbulent regime. Furthermore, Godaux and Gebhart indicated that the onset

of thermal transition can not be accurately correlated to the local Grashof number; instead, they proposed that for transition to occur at some elevation on the heated surface, the total amount of thermal energy convected from the surface to the boundary layer over the region from the leading edge to that elevation should reach some particular critical value.

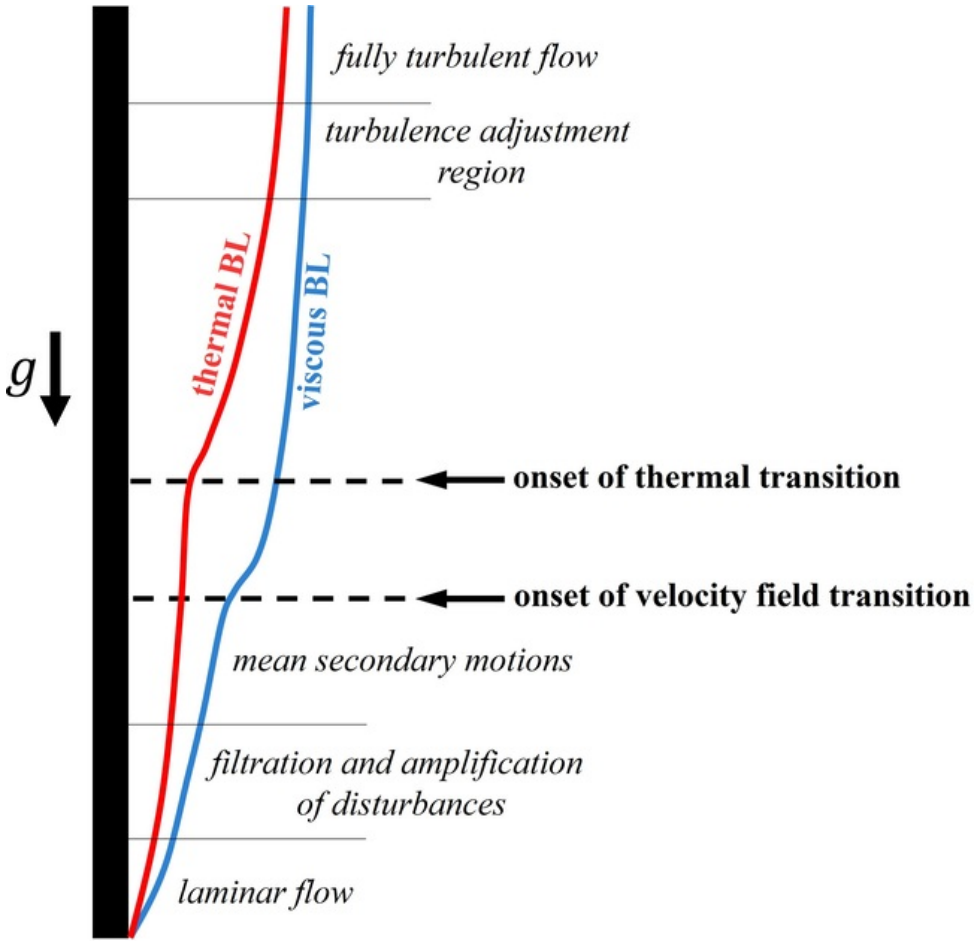

Figure 1.1: The route from a laminar regime to full turbulence in the buoyancy-driven water flow along a heated vertical surface, as described by Godaux & Gebhart (1974).

Finally, it should be noted that, regardless of the parameter assumed to assess the end of the laminar regime for the buoyant flow, discrepancies among findings by various researchers when air is used as convective fluid may be also ascribed to uncontrolled thermal gradients in the laboratory room which may trigger large-scale air currents, to the confinement configuration surrounding the heated plate, or to other factors (Cheesewright, 1968; Warner & Arpaci, 1968; Tsuji & Nagano, 1988).

1.1.2. Effects of transition on flow and heat transfer characteristics

The transition from a laminar regime to a turbulent one is always accompanied by enhancements of momentum and energy exchange between the hot fluid layers near the wall and the

far layers of lower temperatures. These actions lead to significant modifications in the velocity and temperature profiles across the viscous and the thermal boundary layers, respectively. Such modifications mainly appear in the form of higher wall-normal gradients of velocity and temperature near the heated surface, compared with the laminar flow case. The most favorable point here is that the majority of resistance to heat transfer now takes place across a thin layer near the wall instead of the whole boundary layer (Imbriale *et al.*, 2012), which results in a considerable enhancement of the heat transfer characteristics. A more friendly explanation for these events can be provided by comparing the classical Squire-Eckert theoretical predictions (refer to Lienhard & Lienhard (2019)) of the velocity and temperature profiles across the boundary layer for a laminar buoyant stream over a smooth vertical surface with the predictions by Eckert & Jackson (1950) for turbulent velocity and temperature profiles based on a combination between theoretical work and analysis of data from the literature; note that these studies considered fluids with values of $Pr \approx 1$ such that the viscous and thermal boundary layers are approximately identical in thickness.

Squire-Eckert predictions (laminar flow):

$$\frac{\hat{u}(\hat{x},\hat{y})}{\hat{u}_{max}(\hat{x})} = 6.75\,\frac{\hat{y}}{\hat{\delta}(\hat{x})}\left[1-\frac{\hat{y}}{\hat{\delta}(\hat{x})}\right]^2, \tag{1.6}$$

$$\Theta(\hat{x},\hat{y}) = \frac{\hat{T}(\hat{x},\hat{y})-\hat{T}_\infty}{\hat{T}_w-\hat{T}_\infty} = \left[1-\frac{\hat{y}}{\hat{\delta}(\hat{x})}\right]^2. \tag{1.7}$$

Eckert-Jackson predictions (turbulent flow):

$$\frac{\hat{u}(\hat{x},\hat{y})}{\hat{u}_{max}(\hat{x})} = 1.86\left[\frac{\hat{y}}{\hat{\delta}(\hat{x})}\right]^{\frac{1}{7}}\left[1-\frac{\hat{y}}{\hat{\delta}(\hat{x})}\right]^4, \tag{1.8}$$

$$\Theta(\hat{x},\hat{y}) = \frac{\hat{T}(\hat{x},\hat{y})-\hat{T}_\infty}{\hat{T}_w-\hat{T}_\infty} = 1-\left[\frac{\hat{y}}{\hat{\delta}(\hat{x})}\right]^{\frac{1}{7}}, \tag{1.9}$$

where $\hat{x}$, $\hat{y}$, $\hat{u}$, $\hat{u}_{max}$, $\hat{\delta}$, and Θ denote, respectively, the vertical distance measured from the leading edge, the horizontal coordinate, the streamwise component of the velocity (at the point of interest), the maximum velocity across the boundary layer (at the elevation of interest), the boundary layer thickness (at the elevation of interest), and the dimensionless temperature. The graphical representation of these equations is shown in Fig. 1.2. It's crystal clear that the velocity and temperature gradients near the wall are steeper, as expected, in the case of a turbulent flow regime; for instance, the velocity peaks ten times earlier than the laminar flow case.

To interpret the expected favorable effects of the transition to turbulence on the convective heat transfer characteristics, the following parameters of interest are defined first: the local heat transfer coefficient (h), the average heat transfer coefficient ($\overline{h}_D$) evaluated over the vertical surface area from the leading edge to some elevation D, the Nusselt numbers (Nu_x and Nu_D)

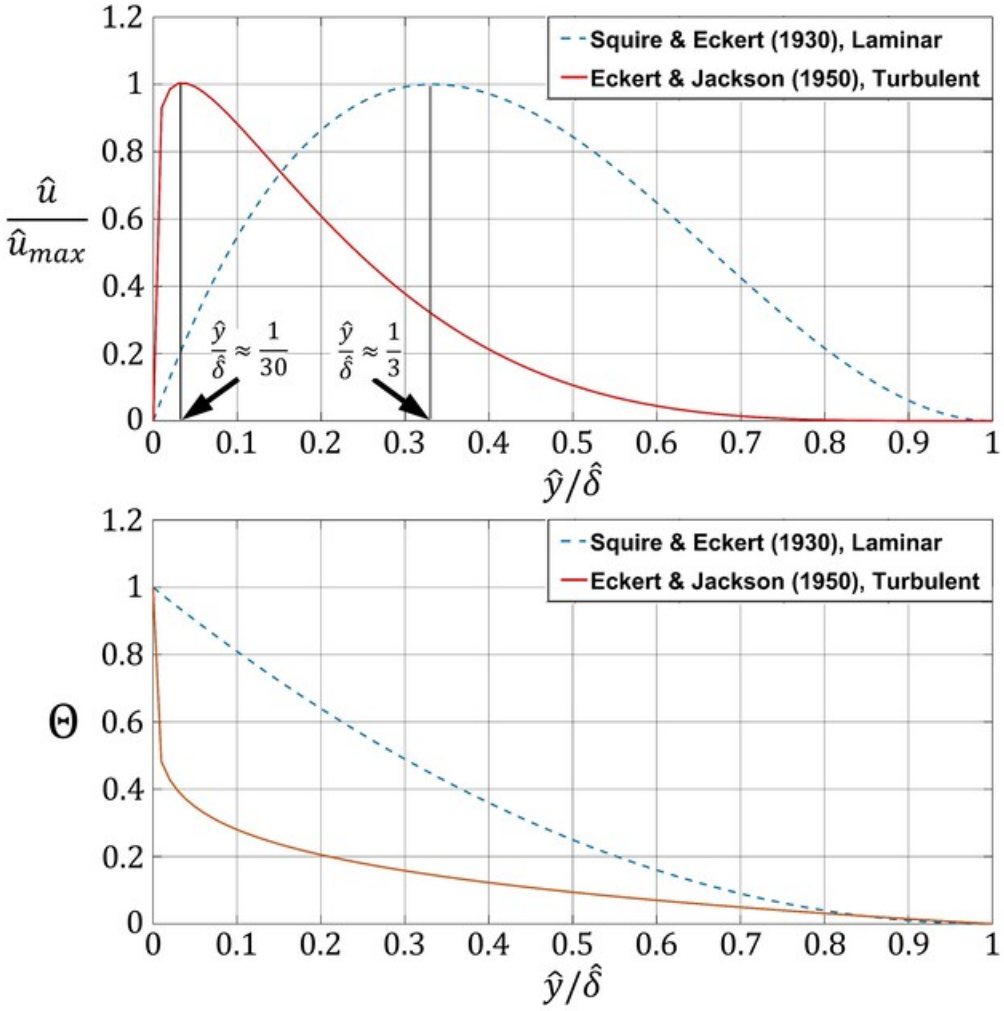

Figure 1.2: Graphical comparison between laminar and turbulent dimensionless velocity profiles (top) and laminar and turbulent dimensionless temperature profiles (bottom).

calculated based on the local heat transfer coefficient and either the vertical position of the point of interest $\hat{x}$ or the characteristic height D, respectively, and the average Nusselt number ($\overline{Nu}_D$). They are defined as follows:

$$h = -k_{f,w} \frac{(\partial \hat{T}/\partial \hat{y})_w}{\hat{T}_w - \hat{T}_\infty}, \tag{1.10}$$

$$\overline{h}_D = \frac{1}{D} \int_D h \, d\hat{x}, \tag{1.11}$$

$$Nu_x = \frac{h\,\hat{x}}{k_f}, \quad Nu_D = \frac{h\,D}{k_f}, \tag{1.12}$$

$$\overline{Nu}_D = \frac{1}{D} \int_D Nu_D \, d\hat{x}, \tag{1.13}$$

Table 1.1: Sample referential correlations of $\overline{Nu}$ under laminar and turbulent conditions. The last equation by Churchill & Chu (1975) can be used under laminar and turbulent flow conditions (all values of Ra) but their first equation is the preferred one in terms of accuracy under laminar flow conditions.

	References	Validity ranges	Correlations
Lam. flow	Squire-Eckert theory	$10^5 \lesssim Ra \lesssim 10^9$, Pr not too low	$\overline{Nu} = 0.678\, Ra^{0.25} \left(\frac{Pr}{0.952 + Pr}\right)^{0.25}$
	Eckert & Jackson (1950)	$10^5 \lesssim Ra \lesssim 10^9$, Pr close to 1, (ideally $Pr \approx 0.72$)	$\overline{Nu} = 0.555\, Ra^{0.25}$
	Le Fevre (1956)	$10^5 \lesssim Ra \lesssim 10^9$, $Pr = 0 \to \infty$	$\overline{Nu} = Ra^{0.25} \left(\frac{Pr}{2.435 + 4.884 Pr^{0.5} + 4.952 Pr}\right)^{0.25}$
	Churchill & Chu (1975)	$0 < Ra \lesssim 10^9$, $Pr = 0 \to \infty$	$\overline{Nu} = 0.68 + 0.67 Ra^{0.25} \left[1 + \left(\frac{0.492}{Pr}\right)^{\frac{9}{16}}\right]^{\frac{-4}{9}}$
Turb. flow	Eckert & Jackson (1950)	$Ra \gtrsim 10^9$, Pr close to 1, (ideally $Pr \approx 0.72$)	$\overline{Nu} = 0.021\, Ra^{0.4}$
	Churchill & Chu (1975)	$Ra \gtrsim 10^9$, $Pr = 0 \to \infty$	$\overline{Nu} = \left[0.825 + \frac{0.387 Ra^{\frac{1}{6}}}{\left[1 + \left(\frac{0.492}{Pr}\right)^{\frac{9}{16}}\right]^{\frac{8}{27}}}\right]^2$

with $k_{f,w}$ and k_f the values of the fluid thermal conductivity evaluated, respectively, at the wall ($\hat{y} = 0$) and at the film temperature ($\hat{T}_{film} = (\hat{T}_w + \hat{T}_\infty)/2$). Basically, the local Nusselt number (Nu_x) and the average Nusselt number ($\overline{Nu}_D$) can be expressed as functions of the Grashof number and the Prandtl number, for instance:

$$Nu_x = f_1\left(Gr_x,\, Pr\right), \quad \overline{Nu}_D = f_2\left(Gr_D,\, Pr\right) \tag{1.14}$$

Through the literature, it has been found that the independent variable in these equations mainly

takes the form $Gr \times Pr$, that is, the Rayleigh number. Based on this finding, most studies correlated the Nusselt number to the Rayleigh number, as the significant variable, and the Prandtl number, representing a secondary parameter (Lienhard & Lienhard, 2019):

$$Nu_x = F_1\left(Ra_x,\, Pr\right), \quad \overline{Nu}_D = F_2\left(Ra_D,\, Pr\right) \tag{1.15}$$

Experimental and theoretical studies have been conducted through the literature of natural convection heat transfer over vertical flat surfaces to explore the performance of the Nusselt number under laminar and turbulent flow conditions. Sample correlations for both cases are present in Table 1.1 with indications of their ranges of validity. A graphical comparison between the performance of the surface-averaged Nusselt number with the changes in the plate Rayleigh number under laminar versus turbulent conditions is presented in Fig. 1.3 based on correlations from the literature. As can be realized, the transition to turbulence leads to an enhancement in the heat transfer performance compared to the laminar flow case.

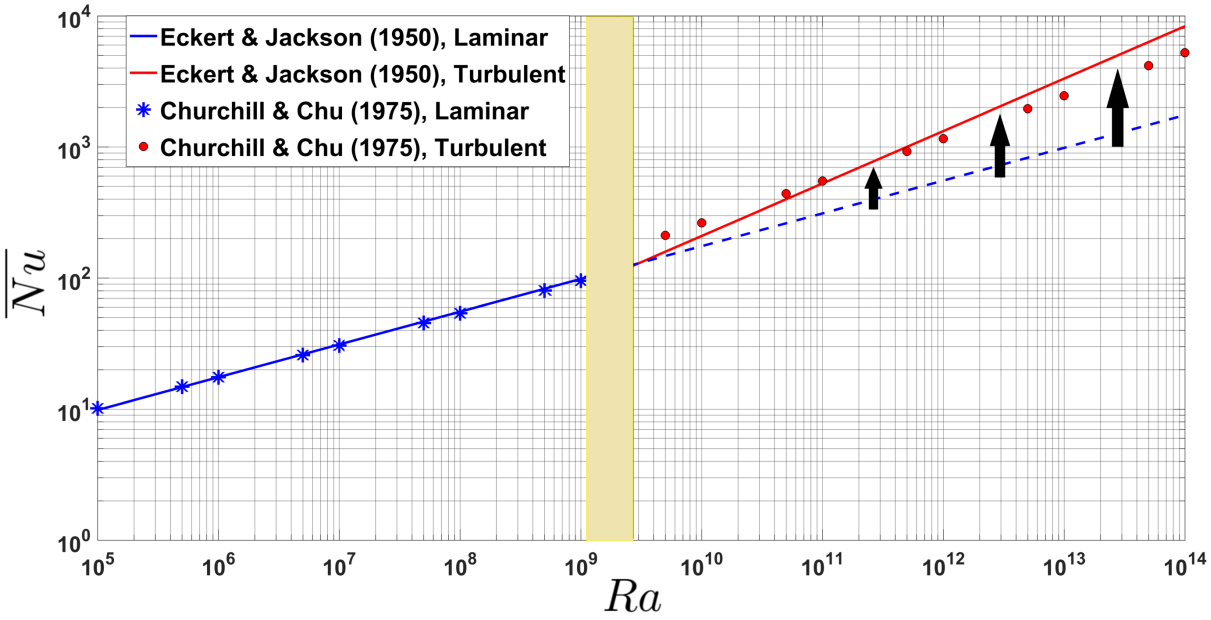

Figure 1.3: The behavior of $\overline{Nu}$ with Ra for laminar vs. turbulent conditions.

1.1.3. Turbulence anticipation by roughening the heated surface

The possibility of a premature transition to turbulence when roughness elements (e.g., ribs) are attached to the vertical heated surface exposed to the buoyancy-induced flow has been indicated in many references (Anderson & Bohn, 1986; Bhavnani & Bergles, 1991; Tanda, 1997, 2008; Yao, 2006; Imbriale *et al.*, 2012). However, on many occasions, the researchers mentioned this influence just as an introduction to their work, as a comment on relevant previous studies or as a conclusion that is not supported by sufficient measurements, and thus without a comprehensive analysis of the origin and consequences of this phenomenon. For instance, Tanda (1997,

2008) indicated that roughening a vertical heated surface can induce disturbances in the laminar buoyant stream and, hence, anticipate transition to turbulence (i.e. trigger it at a lower Grashof number compared with the smooth surface case). This statement was a mere justification of the importance of analyzing the complex effects of surface alterations on the heat transfer characteristics. Yao (2006) carried out numerical work on a vertical complex wavy surface, assuming laminar flow conditions. Nevertheless, it was mentioned that surface corrugations may lead to an early transition of the natural-convection boundary layer, leading to a further improvement of the heat transfer capability of the surface—a mechanism which wasn't studied in that paper. Imbriale *et al.* (2012) elucidated that the natural-convection flow can be early tripped to turbulence with the aid of strong boundary layer perturbations stimulated by surface disturbances such as surface obstructions (steps/coils/3D shapes), indentations (cavities/dimples), and roughness. However, no signs of transition were realized/captured in their experiments on different configurations of inclined and V-ribs.

Bhavnani & Bergles (1991) conducted experiments on the heat transfer performance over a vertical sinusoidal wavy surface with the aid of Mach-Zehnder interferometry optical technique. Visualizations revealed that, at a wave-amplitude-to-wave-length ratio of 0.3, the boundary layer becomes unstable at a Grashof number (based on the profile length) of around 2×10^7 which is one or two orders of magnitude lower than the critical value for the onset of transition on a plane vertical surface. In detail, flow instabilities appear to increase on each upward facing surface as a result of flow separation, whereas partial stabilization takes place later on the downward facing surface. This mechanism occurs in a periodic manner causing a gradual growth of instabilities under transition is supposed to be reached. However, Bhavnani and Bergles highlighted that the available observations/data were not sufficient to clearly prove that the visualized instabilities represent a true transition.

Anderson & Bohn (1986) investigated natural convection heat transfer through a water-filled cubical enclosure consisting of two opposite vertical sides with different thermal conditions (one heated and one cooled) while the other four sides were kept adiabatic. The heated vertical surface was either smooth or machine-roughened by a net of intersecting grooves, in order to study the effects of perturbing the surface on the onset of transition and on the heat transfer rate. Experimental observations using the *mirage* flow visualization technique revealed that transition was triggered at a vertical position which is lower by 5% than its corresponding location in the case of the flat surface; the consequent changes in the heat transfer behavior from the surface were monitored, and enhancements were reported for some cases.

1.1.4. Effects of surface alterations on natural convection heat transfer

This subsection presents a literature survey on the influence of disturbing vertical heated surfaces on the natural convection heat transfer, with focus on surface ribs and corrugations. In contrast to fins, ribs are by definition relatively small surface disturbances which affect the heat transfer rate from the surface mainly by altering the average heat transfer coefficient, while the increase in the heat transfer area is secondary. Therefore, attaching ribs rather than fins to the heated surface is advantageous in terms of minimizing the overall weight and size of the device, provided that the ribs are proved to be efficient in dissipating heat. There are situations where

roughness or obstacles are present naturally (or to perform functions related to the specific application, without paying primary attention to their impact on heat transfer) and others in which they are added intentionally to alter the buoyant-flow behavior and the heat transfer characteristics, for instance by producing physical disturbances in the laminar boundary layer which may stimulate an earlier transition to turbulence and, therefore, lead to an enhancement of the heat transfer performance. The former may be the case of electronic circuit boards, while passive solar systems and photovoltaic modules are examples of the latter. A proper understanding of the flow and thermal behaviors in these systems, in both cases, is essential for design optimization and/or operational restrictions.

From a conceptual point of view, when a heated vertical surface is periodically roughened, for instance with rib elements, a complex interaction takes place between the protrusions and the adjacent buoyancy-driven fluid layer, resulting in perturbation of the velocity and thermal fields in the vicinity of the wall, in a quasi-periodic manner, along with macroscopic development of the viscous and thermal boundary layers; accordingly, the distribution of the local heat transfer coefficient along the surface deviates both qualitatively and quantitatively from the corresponding distribution along a smooth surface. In particular, the local Nusselt number is significantly affected by mainstream separation and reattachment actions within the inter-rib regions, experiencing successive oscillations along the vertical surface (Bhavnani & Bergles, 1990; Tanda, 1997, 2017; Nishikawa *et al.*, 2020). The overall effect of surface roughening on the heat transfer rate can depend on many parameters including, for example, geometric properties of the protrusions, distribution and density of the roughness pattern, the Grashof number, the Prandtl number, and the flow regime. As widely discussed in the literature, ribs over a vertical surface may induce marked modification to the buoyant flow and, at the same time, add an extra heat transfer area (yet not as large as the area provided by fins). Although the increase in surface area is clearly beneficial to the heat transfer rate exchanged with the convective fluid, the effectiveness of roughness elements in enhancing the heat transfer coefficient is intriguingly controversial, with some studies indicating a slight increase (relative to the smooth surface) in limited circumstances (e.g., zigzag-shaped surfaces (Hærvig & Sørensen, 2020) and stepped surfaces (Bhavnani & Bergles, 1990)) and others finding a general reduction, as in the case of repeated spanwise-elongated ribs of square cross section (Bhavnani & Bergles, 1990; Tanda, 1997), due to the presence of stagnation zones just up- and downstream of the ribs, which result in local thickening of the thermal boundary layer. For some roughness geometries, the combined effect of the increase in surface area and the slight decrease of the heat transfer coefficient yields, eventually, an enhancement of the heat transfer rate (for example, complex wavy surfaces (Yao, 2006)). Further, provided that in the laminar flow regime the surface roughness elements have a limited influence (negative in most cases) on the local heat transfer coefficient (as indicated, for instance, by Fujii *et al.* (1973)), a perspective of heat transfer enhancement may be related to the chance of triggering the transition to turbulence at lower Rayleigh numbers relative to the smooth surface case.

The need to better understand the interaction between the surface microstructure and the buoyancy-driven flow has motivated many experimental and numerical investigations to assess the usefulness and the feasibility of adding different types of protrusions to the heated surfaces in terms of their effects on the flow regime, the heat transfer characteristics, and the mass of the cooling modules. Examples of some surface alterations/extensions, considered in previous

investigations, are displayed in Fig. 1.4, including periodic (wavy, rounded, zigzag) corrugations (Kishinami *et al.*, 1990; Bhavnani & Bergles, 1991; Yao, 2006; Hærvig & Sørensen, 2020), steps (Bhavnani & Bergles, 1990), two-dimensional ribs (Tanda, 1997; Cavazzuti & Corticelli, 2008), and different arrangements of fins (Guglielmini *et al.*, 1987; Ahmadi *et al.*, 2014; El Ghandouri *et al.*, 2020). Various experimental techniques have been adopted for mapping the thermal field to assess the detailed heat transfer performance. Two-dimensional and three-dimensional feature-resolving numerical simulations have also been demonstrated to be powerful tools for the acquisition of large amounts of data on thermal fields and flow regimes, particularly for complex configurations (Yao, 2006; Cavazzuti & Corticelli, 2008; Ahmadi *et al.*, 2014; Hærvig & Sørensen, 2020). Selected experimental/numerical studies from the literature, categorized based on the type of surface alteration, are discussed below in more detail.

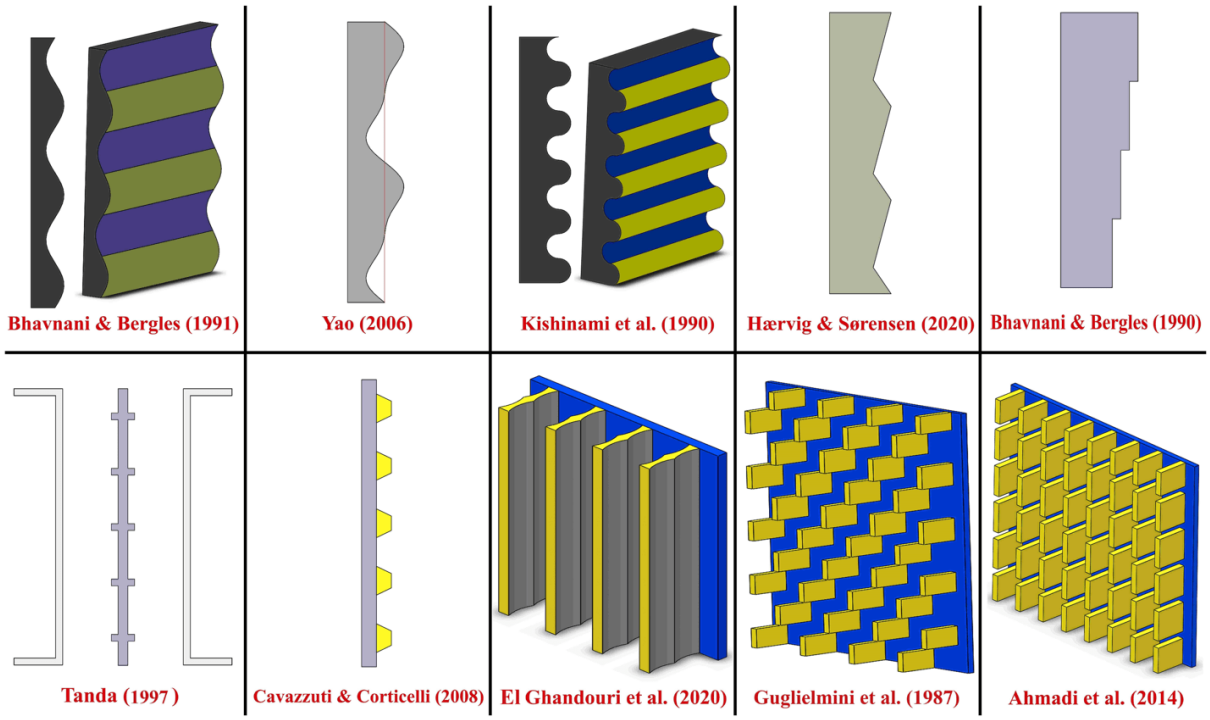

Figure 1.4: Schematic drawings of some surface alterations examined in the literature. The indicated geometries are (from top left to bottom right): sinusoidal waves (Bhavnani & Bergles, 1991), complex waves (Yao, 2006), convex-concave semi-circles (Kishinami *et al.*, 1990), zigzag shaping (Hærvig & Sørensen, 2020), steps (Bhavnani & Bergles, 1990); transverse square ribs (Tanda, 1997), transverse trapezoidal ribs (Cavazzuti & Corticelli, 2008), rippled vertical fins (El Ghandouri *et al.*, 2020), staggered arrangement of interrupted fins (Guglielmini *et al.*, 1987), in-line arrangement of interrupted fins (Ahmadi *et al.*, 2014).

- **Natural convection to air from vertical surfaces with transverse ribs**:

The advantages of depending on the natural convection regime for heat dissipation from a system have been detailed at the beginning of Section 1.1.. The simplest method is natural convection air-cooling by means of air circulation due to the buoyancy effect (Johnson, 1986)

stimulated by the temperature difference between the hot surface and the surrounding environment. One of the surface roughening methods which attracted the attention of many researchers through the past decades is to attach transverse (i.e., spanwise-elongated) ribs to the heated surface in the hope of enhancing the heat transfer to air.

Hung & Shiau (1988) studied natural convection in a vertical channel with one surface supplied with a uniform heat flux and roughened with a single transverse protrusion of a rectangular cross-section, while the opposite surface of the channel is smooth and is kept adiabatic. the experimental work included both quantitative temperature measurements in addition to flow regime visualization by means of smoke injection. The observations and measurements revealed that the presence of the protrusion (which is positioned in the mid-height of the heated surface) originated a downstream recirculation region followed by a turbulence zone, and thus the heat transfer characteristics from the plate surface there were of the turbulent type. Desrayaud & Fichera (2002) conducted two-dimensional numerical simulations to analyze the conjugate heat transfer through a channel of two isothermal sides with a protrusion of a rectangular cross-section attached to each of them. Only laminar flow regime was considered. The two protrusions were located symmetrically on the opposite sides, and their location was changed from one simulation to another, specifically, the bottom, the middle, and the top of the channel. Both adiabatic and thermally conductive ribs were considered, and the results showed that the latter are more favorable. It was found that the air mass flow rate always decreases with the increase of the rib distance from the channel leading edge. However, at high channel Rayleigh numbers, the average Nusselt number was the best when the ribs were positioned at the highest location.

Bhavnani & Bergles (1990) carried out experiments (with the aid of a Mach-Zehnder interferometer) on natural convection along an isothermal vertical surface with repeated transverse square ribs. They reported that attaching highly conducting ribs to the surface may decrease the overall heat transfer rate by more than 25%, whereas a lower deterioration, or even a slight enhancement, was detected with low-conductivity ribs since they interrupt the thickening of the thermal boundary layer, promoting the heat transfer process within the inter-rib regions of the baseplate. Tanda (1997) investigated natural convection heat transfer to air in a vertical channel with one side heated (isothermal) and rib-roughened with integrated square transverse elements of high thermal conductivity. The experimental work employed the schlieren optical technique to construct the temperature gradient field. It was concluded that the presence of ribs reduces the average Nusselt Nusselt number by about 28%, and a more pronounced deterioration (up to 44%) occurs in the case of a very low channel spacing-to-height ratio (typically below 0.1). The results by Tanda (2008) for the same configuration, but varying the number of ribs and using adiabatic ones, were not too different: adiabatic ribs decreased the average heat transfer coefficient of the vertical surface by up to 43%, and heat transfer enhancement was attained only locally, at a certain distance downstream of the rib, and not for very narrow channels. Small spacing between ribs was proved to be unfavorable as it hinders the process by which the fresh buoyant air is dragged towards the inter-rib region to wash it from the hot inactive recirculation zones. Cavazzuti & Corticelli (2008) numerically studied conjugate natural convection through a channel with one adiabatic surface and an opposite isothermal surface roughened with two-dimensional trapezoidal ribs; the ribbed channel cases examined were not found to outperform the smooth one, and recommendations were given to alleviate the deterioration, for example by using high-thermal-conductivity ribs with high lateral wall inclination. Nishikawa *et al.* (2020)

studied conjugate natural convection along a vertical surface with minuscule square ribs of low thermal conductivity, as a simplified representation of the yarns of a textile material. Intriguingly, a minor cooling effect was detected when the ribs were arranged at an adequate pitch, sufficient to allow the cool stream to be guided onto the base surface in the inter-rib regions.

- **Immersion of heated vertical ribbed surfaces into liquids**:

Despite the simplicity of natural convection air-cooling systems, their applicability is limited by the low heat transfer coefficient of air. Liquid cooling of micro-electronic components and packaged electronic modules has been receiving more attention due to its high heat removal capability and improved packaging and circuit density (Peterson & Ortega, 1990; Behnia & Dehghan, 1998). The cooling liquids for such applications must be highly dielectric, non-toxic, and thermally and chemically stable under the conditions of the operation. For these reasons, dielectric fluids, like the family of Fluorinerts, are used as cooling liquids instead of water (Behnia & Dehghan, 1998). However, only for experimental purposes, water may be used as a coolant.

Joshi *et al.* (1989) experimentally studied natural convection heat transfer to water from a free vertical surface with a single column of eight heated rectangular rib segments (of width less than the plate's). Besides temperature measurements, the flow was visualized with the aid of Helium-Neon Laser, and the inactive flow regions in the vicinity of each protrusion were recognized. The viscous boundary layer was found to be thinner with the increase of the heat flux. Wroblewski & Joshi (1994) conducted three-dimensional numerical simulations of the conjugate heat transfer for the case of a heated substrate-mounted chip in a box filled with Fluorinert (FC-75). They found that the ratio between the substrate and the fluid thermal conductivity coefficients significantly affects the maximum chip temperature. More recently, Abidi-Saad *et al.* (2016) carried out an experimental investigation on water natural convection in a vertical channel with an adiabatic protrusion on each side, while only a middle zone of one side is heated. Experiments employed thermocouples for temperature measurements and the particle-imaging velocimetry technique for acquiring the velocity field. Large-scale recirculation was detected during the transient analysis. By varying the location of the symmetrically positioned protrusions, they found that the most complex flow behavior is encountered in the case of the top-position ribs, with birth, merging, and disappearance of the vortices. Only the top-position ribs were able to enhance the average heat transfer coefficient, and this effect was attainable only for specific thermal and geometric conditions. Tanda (2017) performed experiments on water natural convection in a vertical channel with the heated side regularly roughened with five transverse, square-cross-sectioned ribs; the experimental data, recast in dimensionless form, were compared with those found in an earlier experimental survey on air natural convection (Tanda, 1997), and the local/average convective Nusselt numbers were found to be in excellent agreement at the same Rayleigh number and dimensionless geometric parameters, although the two fluid are different in terms of the Prandtl number.

- **Wall alteration by simple surface shaping (Steps, Zigzag-shaping, etc.)**:

Some researchers focused on the effects of modifying the heated surface by simple deflections and alterations. Interestingly, the results were favorable from the heat transfer point of view. Besides their investigation on adiabatic and thermally conductive square ribs, Bhavnani & Bergles (1990) studied within the same framework air natural convection from vertical heated surfaces with repeated steps. The experimental work revealed that, for the optimum height-to-pitch ratio of the steps, the convective heat transfer rate increases by about 23% compared to the flat surface. This finding was in contradiction to their negative results for the case of ribs. Hærvig & Sørensen (2020) examined and optimized natural convection heat transfer from zigzag-ribbed isothermal surfaces by performing a set of two-dimensional numerical simulations, varying the length, the pitch, and the height of the zigzag shape. Under the laminar flow assumption, it was concluded that, only if the proper dimensions are used, the zigzag-ribbed surfaces can promote the heat transfer characteristics. The increase in the average Nusselt number was up to 5%, which corresponded to an enhancement in the heat transfer rate of about 12% (taking into account the increase in surface area).

- **Natural convection heat transfer from wavy vertical surfaces**:

Kishinami *et al.* (1990) analyzed the heat transfer from a vertical surface corrugated with a pattern of convex/concave semi-circles attached to each other, examining the effects of changing the heating spot (either the convex region or the concave region). The experimental observations, with the aid of Mach-Zehnder interferometry, showed that vortex motion appears at the rear of the convex elements, consisting of two separate vortices rotating in opposite directions due to separation of the boundary layer and interaction of the main fluid stream with the vortex zone. Obviously, This makes the flow over the concave elements almost inactive, and consequently supplying heat to the concave elements (choosing them, instead of the convex ones, as the heating spots) results in a less effective operation from the heat transfer standpoint. Later, employing the same optical technique, Bhavnani & Bergles (1991) investigated natural convection heat transfer from a sinusoidal wavy vertical surface, varying the wave amplitude-to-length ratio. They reported that the heat transfer characteristics of the wavy surface differ considerably from the flat one only when the amplitude-to-wavelength ratio is relatively large; increasing this ratio yields a higher convective heat transfer rate in comparison with a flat surface having the same projected area, yet an adverse influence is clear when the comparison is made with a flat plate of an area equal to the typical surface area of the corrugated wall. In addition, boundary layer instabilities appeared at a Grashof number of 2×10^7 (local Gr, based on profile length) which is lower than the upper threshold of the laminar flow regime in the case of a flat vertical surface. Yao (2006) examined whether the above-mentioned enhancement in the heat transfer rate can be amplified by increasing the complexity of surface alteration in the hope of promoting the interaction between the boundary layer and the corrugations. This was done by studying a wavy surface formed by the sum of two sinusoidal waves (a fundamental one and its first harmonic), varying the amplitude of each wave independently. Thanks to the extra heat transfer area added by corrugating the vertical surface, it was found that the heat transfer rate may be doubled in comparison with a flat plate of the same projected area.

1.2. FORCED CHANNEL FLOWS OVER TEXTURED WALLS

The laminar/turbulent forced flow in a channel is crucially sensitive to the small-scale features of the rough/porous bounding walls. As the fluid passes near/within the surface corrugations, a complex, generally three-dimensional, hydrodynamic interaction takes place, which can significantly alter the flow behavior not only in the interfacial layer but also in the channel flow region fairly away from the boundary, as an extended effect on the macroscopic problem. With the significant progress in manufacturing and fabrication techniques, the study of the interaction between the microscale features of the surface (such as roughness, porosity, irregularity, compliance, superhydrophobicity, etc.) and the adjacent fluid flow has become more important for several applications. The numerical complexity of fully resolving the micro-details of the surface, especially when turbulent flows are studied via Direct Numerical Simulations (DNS) or even Large Eddy Simulations (LES), represents a challenge, and this can be a major hurdle when optimization of the surface (in terms of reducing skin-friction drag, promoting heat/mass transfer, etc.) is the ultimate goal. Therefore, the development of accurate macroscopic models for the fluid-wall interaction has become a very active field of research.

1.2.1. The slip velocity over rough/permeable boundaries

Starting with the literature on the laminar flow overlying a permeable substrate, one can realize that the low-Reynolds-number motion of an incompressible fluid in a plane channel bounded by a porous wall (which borders the duct, for instance, in $\hat{y} = 0$) has been a classical problem since the seminal experimental work by Beavers & Joseph (1967). They observed that the flow rate in the channel was larger in the presence of the porous layer than with a no-slip wall and hypothesized that the fluid could slip at some *Stokes–Darcy interface* with velocity

$$\hat{u}_{slip} = \frac{\sqrt{\hat{\mathcal{K}}}}{\alpha} \frac{\partial \hat{u}}{\partial \hat{y}}\bigg|_{\hat{y}\to 0^+} + \frac{\hat{\mathcal{K}}}{\mu}\,\mathcal{M}, \tag{1.16}$$

with the second term on the r.h.s. of Eq. (1.16) corresponding to Darcy's velocity; $\hat{\mathcal{K}}$ is a scalar measure of the permeability of the porous medium in its bulk, μ is the dynamic viscosity, and $\mathcal{M} = |\partial\hat{p}/\partial\hat{x}|$ denotes the magnitude of the macroscopic, streamwise pressure gradient. The dimensionless constant α was later observed to depend on the properties and the geometry of the permeable material near the dividing surface, on the local direction of the flow, on the Reynolds number and on the possible presence of structural non-uniformities at the surface of the porous medium, where the porosity is locally larger (Larson & Higdon, 1986; Sahraoui & Kaviany, 1992). Such non-uniformities are hardly avoidable in practice since solid inclusions cannot pack as tightly near the porous/free-fluid interface as they do in the bulk of the porous medium (Nield, 2009). Saffman (1971) gave a theoretical justification of the empirical condition by Beavers & Joseph (1967) by first applying ensemble averaging to the Stokes equation across the porous/free-fluid domain and then performing asymptotic matching at the two edges of the interface layer. A closer look at Saffman's development reveals that, upon retaining terms up to second order in the small parameter $\sqrt{\hat{\mathcal{K}}}$, the slip velocity is the same as in Eq. (1.16) except

for Darcy's term, which was found to be corrected by an order one dimensionless factor B, to become $(B\hat{\mathcal{K}}/\mu)\,\mathcal{M}$. The literature is rich of studies that sought to revisit/extend/generalize the Beavers-Joseph-Saffman (BJS) condition and/or investigate its limitations and deficiencies, e.g. Refs. (Neale & Nader, 1974; Vafai & Kim, 1990; Auriault, 2010; Eggenweiler & Rybak, 2020, 2021; Strohbeck *et al.*, 2023).

Some of the papers that followed the works by Beavers, Joseph and Saffman used upscaling theories to close the problem and identify the constant α (and, rarely, also B). Mikelić and colleagues (using asymptotic homogenization) and Whitaker and colleagues (using volume averaging) are among the major contributors, extensively cited in the recent review by Bottaro (2019). The asymptotic, multiscale homogenization approach is a theoretical framework through which the rapidly varying properties of the surface (the porous substrate in the present case) can be replaced by upscaled properties such as slip, interface permeability, etc. (Babuška, 1976; Bottaro, 2019), which contribute to the definition of *effective* boundary conditions at a fictitious plane interface next to the physical rough/porous boundaries wall; the macroscale behavior of the channel flow is then targeted, bypassing the need to fully resolve the motion between/in close vicinity of the solid protrusions/grains. This technique has been known and used by applied mathematicians for a long time, yet, in more recent years, it has been rediscovered and applied to a variety of physically relevant cases. The approach relies on the asymptotic expansion of the dependent variables in terms of a wisely-chosen small parameter whose existence is related to the presence of well-separated scales, for instance a microscopic length scale (ℓ) and a macroscopic length scale ($H >> \ell$), so that the parameter $\epsilon = \dfrac{\ell}{H} << 1$ can be defined, and the solution of the problem can be sought up to different orders of accuracy in terms of ϵ.

Although the classical first-order slip condition over a generic solid surface, proposed by Navier (1823), was based on empirical considerations concerning the near-wall flow behavior, recent studies adopting the homogenization technique have provided a robust method for the estimation of Navier's slip length, λ, without the need for any *ad hoc* correlation (Jiménez Bolaños & Vernescu, 2017). A tensorial generalization of the first-order Navier's slip condition over a micro-textured surface was given by Zampogna *et al.* (2019), with the slip tensor depending on the geometry of the roughness pattern. High-order effective boundary conditions were later derived by Bottaro & Naqvi (2020), for the flow over a rough surface, and by Sudhakar *et al.* (2021) and Naqvi & Bottaro (2021), for the flow over a porous bed. In view of the recent findings, a homogenization-based, second-order accurate, BJS-like condition for the streamwise slip velocity can be written as follows:

$$\hat{u}_{slip} = \hat{\lambda}\,\frac{\partial \hat{u}}{\partial \hat{y}}\bigg|_{\hat{y}\to 0^+} + \frac{\hat{\mathcal{K}}^{itf}}{\mu}\,\mathcal{M}; \tag{1.17}$$

the coefficients $\hat{\lambda}$, a *Navier slip length*, and $\hat{\mathcal{K}}^{itf}$, the *interface permeability*, are not simply proportional to $\sqrt{\hat{\mathcal{K}}}$ and $\hat{\mathcal{K}}$, and can be found by solving microscopic (*auxiliary*) problems in a representative unit cell, for any regular microscopic pattern. It should be highlighted that:

- The BJS-like condition (1.17) is valid for both permeable and rough, impermeable layers; in the latter case, $\hat{\mathcal{K}}$ vanishes, whilst $\hat{\lambda}$ and $\hat{\mathcal{K}}^{itf}$ do not.
- Computed values of $\hat{\lambda}$ and $\hat{\mathcal{K}}^{itf}$ are available in the literature for many rough (Lācis *et al.*,

2020; Bottaro & Naqvi, 2020; Sudhakar *et al.*, 2021) and porous (Lācis *et al.*, 2020; Sudhakar *et al.*, 2021; Naqvi & Bottaro, 2021) wall microstructures.

- If the microscopic pattern of the rough/permeable wall had a preferential orientation at an angle different from 0 or 90 degrees from the direction of the pressure gradient (here in $\hat{x}$), a near-wall transverse velocity component, $\hat{w}$, would appear (Stone *et al.*, 2004).

- Under turbulent flow conditions, it is necessary to define a three-directional effective velocity at the fictitious wall, even if the mean flow is one-directional. This is important since turbulent fluctuations along directions both tangent and normal to the fictitious interface considerably affect the behavior of the turbulent boundary layer and, therefore, the skin-friction drag (Orlandi *et al.*, 2006; Orlandi & Leonardi, 2006, 2008; Bottaro, 2019; Lācis *et al.*, 2020). Definition of the velocity vector at the virtual interface, valid up to second-order accuracy, is available in Ref. Naqvi & Bottaro (2021), and is discussed here in Section 2.2.2..

Moreover, when the flow regime in the interfacial layer departs considerably from the Stokes behavior, it becomes necessary to incorporate the effects of near-wall advection into the homogenization scheme, in order to extend the applicability range of the homogenization model. An Oseen-like linearization was proposed by Buda (2021) to try to partially take into account such effects when the microscopic problem is analyzed; accordingly, the boundary condition 1.17 is still valid, yet with macroscopic coefficients sensitive to a Reynolds number (pertinent to the near-wall motion), besides their original dependence on the micro-structural details of the boundary. However, should flow instabilities be present in the domain (e.g., at relatively high Reynolds numbers) in the form of vortex shedding next to the protrusions/grains or, eventually, transition to turbulence, homogenization would become a more complex undertaking. For instance, tackling near-wall advection with Oseen's linearization in the presence of such instabilities may be questionable, and a fully nonlinear model is probably needed; this could be achieved by the use of adjoint homogenization (Bottaro, 2019). In addition, when near-wall transient effects are significant, they should be considered in the upscaling framework, and sufficiently large microscopic unit cells must be identified (Agnaou *et al.*, 2016).

1.2.2. Turbulent flows in channels with textured/altered walls

The large skin-friction drag characterizing wall-bounded turbulent flows, as compared to laminar ones, represents a major challenge in engineering applications where efficiency and running costs of fluid transport systems are of interest. This has motivated several experimental and numerical studies aimed at a better understanding of the phenomenon of turbulence production and generation of Reynolds shear stress in such flows (Mansour *et al.*, 1988; Bernard *et al.*, 1993; Orlandi & Jiménez, 1994; Vreman & Kuerten, 2014); the coherent structures in the inner region of the wall layer and the *bursting* (ejection) and *sweep* (inrush) events related to such structures have been the object of intense research activities (Kline *et al.*, 1967; Cantwell, 1981; Jeong *et al.*, 1997; Guo *et al.*, 2010). The design of active or passive techniques for turbulent drag reduction requires in-depth understanding of the interacting mechanisms which contribute

to near-wall turbulence, in order for its effective control. The near-wall flow is characterized by a self-sustaining cycle responsible for the regeneration of turbulent fluctuations, owing to the dynamic interaction between longitudinal velocity streaks and quasi-streamwise vortices; this cycle is independent of the nature of the outer flow (Jiménez & Pinelli, 1999). Attenuating (or suppressing) any of the processes involved in this autonomous cycle can lead to a less disturbed flow field (or even to relaminarization) (Jiménez & Pinelli, 1999), a clear advantage when the objective of the control is skin-friction drag.

Many investigations have been conducted to optimize and assess the effectiveness and feasibility of active and passive drag reduction techniques, to favorably alter the structure of the turbulent boundary layer. Active techniques, involving energy input, have proved to yield significant drag reduction in wall-bounded turbulent flows. For instance, optimized uniform blowing of the fluid through a spanwise slot can produce a local drag reduction of 80% downstream of the slot (Kim *et al.*, 2003), while sufficiently high suction rates through a short porous flush-mounted strip can allow for local relaminarization of the turbulent boundary layer, resulting in a drag reduction of more than 50% (Antonia *et al.*, 1995). Counter-rotating large-scale streamwise vortices, externally initiated by a transverse array of longitudinal plasma actuators, can stabilize the streaks in the near-wall flow and attenuate the coherent structures, interrupting the turbulence regeneration cycle; a drag reduction of more than 25% can be achieved (Mahfoze & Laizet, 2017; Cheng *et al.*, 2021). Other studies focused on forcing wall-normal fluctuations (Kang & Choi, 2000) or in-plane wall oscillations (Choi, 2002; Wise & Ricco, 2014).

Passive drag reduction techniques have also been investigated extensively, along with remarkable advances in bio-inspired designs. Super-hydrophobic surfaces can reduce drag up to approximately 80% under optimal conditions, mainly due to the large effective slip of aqueous solutions on the walls (Rastegari & Akhavan, 2015). Riblets (longitudinal surface grooves) have proved to mitigate the velocity fluctuations near the wall, resulting in a more uniform flow field (Bechert & Bartenwerfer, 1989). The skin-friction drag over surfaces altered with riblets is crucially sensitive to their geometry and to the Reynolds number of the flow in their vicinity (characterized, for instance, by the lateral spacing of riblets measured in wall units, s^+) as found by many investigators (Walsh & Lindemann, 1984; Bechert *et al.*, 1997; El-Samni *et al.*, 2007; Gatti *et al.*, 2020; Endrikat *et al.*, 2021*a*,*b*; von Deyn *et al.*, 2022). Achieving drag reduction is thus contingent on the proper design of riblets for the specific operational conditions encountered. For example, the experiments by (Bechert *et al.*, 1997) on different configurations of riblets revealed that an optimized drag reduction of almost 10% can be attained, in particular with longitudinal blade ribs having depth and thickness equal to, respectively, 0.5 and 0.02 of the lateral rib spacing and with $s^+ \approx 17$. It should be noted that drag reduction breaks down at excessively large values of s^+; this is associated with the occurrence of inertial-flow mechanisms such as the Kelvin–Helmholtz instability (Garcia-Mayoral & Jimenez, 2011; Endrikat *et al.*, 2021*a*)

The ability of properly engineered permeable substrates to reduce skin-friction drag in turbulent channel flows, as a passive technique, has recently attracted much interest. Porous substrates are encountered in various natural and engineering applications, and have been a source of inspiration for many studies in which the effects of wall permeability on the behavior of the overlying turbulent boundary layer and the consequent reduction/increase in the skin-friction drag have been assessed. Several configurations of the porous substrate have been investigated,

with different values of the porosity (θ) and under different flow conditions. The diagonal components of the permeability tensor of the porous medium ($\hat{\mathcal{K}}_{xx}$, $\hat{\mathcal{K}}_{yy}$, $\hat{\mathcal{K}}_{zz}$) and the Navier-slip coefficients ($\hat{\lambda}_x$, $\hat{\lambda}_z$) at the dividing surface between the free-fluid region in the channel and the permeable layer are main parameters that have been widely tested in a number of investigations. In the following, $\hat{x}$, $\hat{y}$ and $\hat{z}$ denote, respectively, the streamwise, wall-normal and spanwise directions. The numerical work by Rosti *et al.* (2015) on turbulent channel flows over isotropic porous substrates ($\hat{\mathcal{K}}_{xx} = \hat{\mathcal{K}}_{yy} = \hat{\mathcal{K}}_{zz}$) has shown that even small values of the medium permeability can affect the response of the adjacent turbulent boundary layer: the disturbances were found to be intensified and the Reynolds stresses enhanced, with a consequent increase in skin-friction drag. This is in general agreement with the findings of earlier studies (Beavers *et al.*, 1970; Tilton & Cortelezzi, 2006, 2008). A similar behavior of disturbance intensification is observed when the porous substrates have preferential spanwise permeability. Wang *et al.* (2021) investigated the dynamic interaction between a turbulent channel flow and a porous bed made of spanwise-aligned cylinders, for which $\hat{\mathcal{K}}_{zz} > (\hat{\mathcal{K}}_{xx} = \hat{\mathcal{K}}_{yy})$. The structure of the *blowing* (upwelling) and *suction* (downwelling) events through the pores has been analyzed, particularly in terms of their role on the onset of the Kelvin-Helmholtz instability near the permeable wall. Other studies have focused on permeable walls potentially capable to yield turbulent drag reduction. Rosti *et al.* (2018) studied the turbulent flow over anisotropic porous beds characterized by equal values of the permeability in the streamwise and the spanwise directions, i.e., $\hat{\mathcal{K}}_{xx} = \hat{\mathcal{K}}_{zz} \neq \hat{\mathcal{K}}_{yy}$. They showed that a drag reduction of up to 20% can be achieved from walls of high in-plane permeability $(\hat{\mathcal{K}}_{xx} = \hat{\mathcal{K}}_{zz}) >> \hat{\mathcal{K}}_{yy}$, whereas the skin-friction drag may increase by the same amount for substrates of preferential wall-normal permeability $(\hat{\mathcal{K}}_{xx} = \hat{\mathcal{K}}_{zz}) << \hat{\mathcal{K}}_{yy}$. Among the different configurations considered in the literature, the use of porous substrates of preferential permeability along the streamwise direction, consisting, e.g., of longitudinal cylinders with $\hat{\mathcal{K}}_{xx} >> (\hat{\mathcal{K}}_{zz} = \hat{\mathcal{K}}_{yy})$, appears to provide the best results in terms of turbulent drag reduction. The drag reduction curves for this configuration are similar to those of riblets (Gómez-de Segura & García-Mayoral, 2019), and the theory behind the ability of such substrates to reduce skin-friction drag has been elaborated by Abderrahaman-Elena & García-Mayoral (2017). Conceptually, the drag reduction (DR) is proportional to the difference between the slip lengths along the streamwise and the spanwise directions, that is, $DR \approx \mu_0(\lambda_x^+ - \lambda_z^+)$ (Luchini *et al.*, 1991; Jiménez, 1994), which has been approximated by $\mu_0\,\xi\left(\sqrt{\mathcal{K}_{xx}^+} - \sqrt{\mathcal{K}_{zz}^+}\right)$ (Abderrahaman-Elena & García-Mayoral, 2017). All the macroscopic parameters are measured in wall units and this is indicated by the superscript '+'; the coefficient μ_0 is a function of the Reynolds number (Garcia-Mayoral & Jiménez, 2011), while the parameter ξ characterizes the inter-connectivity of the flow between the pores (Abderrahaman-Elena & García-Mayoral, 2017). The relation above in terms of the square root of the permeability components holds for substrates of relatively low wall-normal permeability; if $\mathcal{K}_{yy}^+$ exceeds some critical threshold, Kelvin-Helmholtz-like rollers are developed near the interface, and the drag reduction mechanism is adversely affected (Gómez-de Segura *et al.*, 2018). In addition to the several contributions discussed above, the reader is referred to the experimental/numerical investigations on turbulent flows over porous media of different configurations conducted by Suga's group (Suga *et al.*, 2013, 2018; Suga, 2016; Kuwata & Suga, 2017; Nishiyama *et al.*, 2020) and by Breugem *et al.* (2006), Liu & Prosperetti (2011), Manes *et al.* (2011), Chandesris *et al.* (2013), Esteban *et al.* (2022) and Wang *et al.* (2022).

1.3. SEEPAGE IN POROUS MEDIA BEYOND STOKES REGIME

1.3.1. Definitions, preliminaries and macroscale behavior

One of the aspects of this research project is to study the effect of advection on the steady, incompressible, Newtonian flow through a rigid, homogeneous porous medium formed by periodically arranged solid inclusions, as illustrated in Fig. 1.5).

The dimensional mass and momentum conservation equations governing the flow in the pores (here, σ and β indicate the solid and the fluid domains, respectively) are

$$\frac{\partial \hat{u}_i}{\partial \hat{x}_i} = 0 \quad \text{in } \beta, \tag{1.18}$$

$$\rho \hat{u}_j \frac{\partial \hat{u}_i}{\partial \hat{x}_j} = -\frac{\partial \hat{p}}{\partial \hat{x}_i} + \mu \frac{\partial^2 \hat{u}_i}{\partial \hat{x}_j^2} \quad \text{in } \beta, \tag{1.19}$$

with $\hat{u}_i$ the velocity, $\hat{p}$ the pressure, and ρ and μ the density and the dynamic viscosity of the fluid. In addition, the no-slip boundary condition is defined at the fluid-solid interface $\mathcal{A}_{\beta\sigma}$.

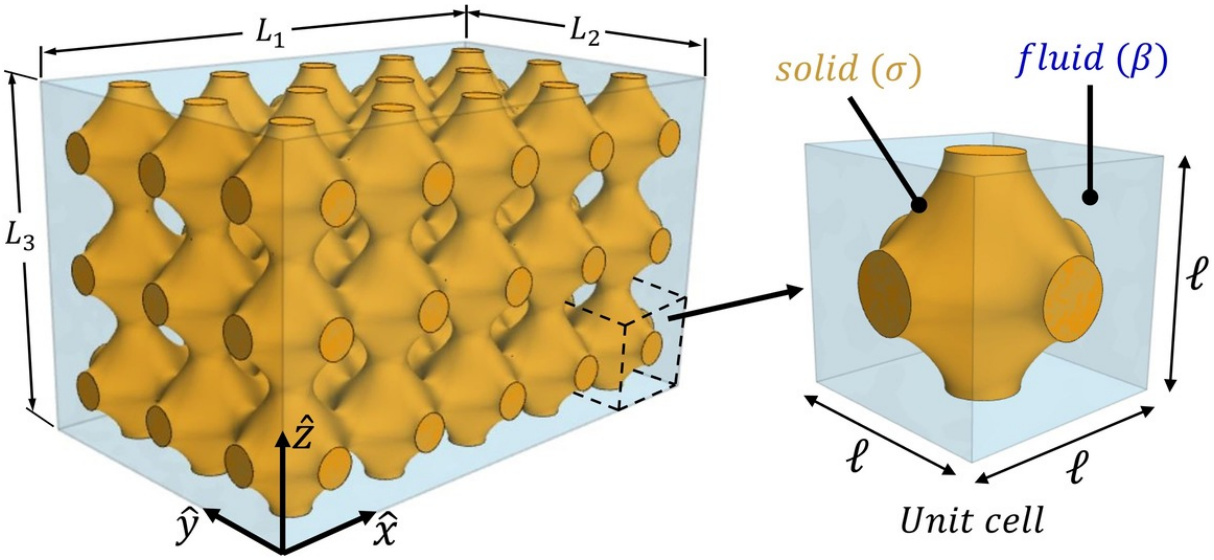

Figure 1.5: Sketch of the problem under study; right frame: a triply periodic unit cell.

Provided that the microscopic length scale ℓ (e.g., the pattern periodicity) is sufficiently smaller than the macroscopic length scale L characterizing the large-scale processes, the hierarchical problem is amenable to upscaling by applying, for instance, a volume-averaging approach. Two distinct dimensionless spatial variables are defined: a *fast* one, $x_i = \hat{x}_i/\ell$, related to field variations occurring at the small-scale level, and a *slow* one, $X_i = \hat{x}_i/L = \epsilon\, x_i$, with the small parameter $\epsilon = \ell/L \ll 1$. Given that the volume of the averaging domain is $V = V_\beta + V_\sigma$ (with the porosity $\theta = V_\beta/V$), the intrinsic average and the superficial average of any property

Γ, defined over the fluid domain, are respectively defined as

$$< \Gamma >^{\beta} = \frac{1}{V_\beta} \int_{\mathcal{V}_\beta} \Gamma \, dV, \quad < \Gamma >= \frac{1}{V} \int_{\mathcal{V}_\beta} \Gamma \, dV = \theta \, < \Gamma >^{\beta} . \tag{1.20}$$

The microscopic velocity scale, v_{ref}, is related to the magnitude of the external force driving the flow through the porous medium. In the present framework, the macroscopic pressure gradient, $\hat{\mathbf{M}}$, its magnitude, $\mathcal{M}$, and a unit vector along its direction, $\mathbf{e}^M$, are defined as follows:

$$\hat{M}_i = \frac{1}{L} \frac{\partial < \hat{p} >^{\beta}}{\partial X_i}, \qquad \mathcal{M} = \left|\left| \hat{\mathbf{M}} \right|\right|, \qquad e_i^M = \frac{\hat{M}_i}{\mathcal{M}}. \tag{1.21}$$

If viscous forces within the pores balance the external forcing, i.e. $\mu \frac{v_{ref}}{\ell^2} \sim \mathcal{M}$, the microscopic Reynolds number, $Re = \dfrac{\rho \, v_{ref} \, \ell}{\mu}$, might be written as

$$Re = \frac{\rho \mathcal{M} \ell^3}{\mu^2}. \tag{1.22}$$

- **Classical behavior in the limit** $Re \to 0$:

Under Stokes conditions, i.e. in the absence of inertial effects, the macroscale problem is simply governed by Darcy's law: the upscaled velocity vector is linked to the macroscopic pressure gradient , $\hat{\mathbf{M}}$, and the fluid viscosity, μ, via the definition of the *intrinsic* permeability tensor, $\hat{\mathbf{K}}$, as follows:

$$< \hat{u}_i > = -\frac{\hat{K}_{ij}}{\mu} \hat{M}_j, \tag{1.23}$$

and a dimensionless permeability, $K_{ij} = \hat{K}_{ij}/\ell^2$, can be introduced as

$$K_{ij} = < \mathcal{K}_{ij} > . \tag{1.24}$$

where $\mathcal{K}$ is a purely microscopic tensor (dependent on x_i only), available from the numerical solution of one *ad hoc* auxiliary system of equations defined on a *representative elementary volume* (REV). Such a problem, governing the spatial variations of the closure variables $\mathcal{K}_{ij}$ and f_j, is

$$\frac{\partial \mathcal{K}_{ij}}{\partial x_i} = 0 \qquad \text{in } \mathcal{V}_\beta, \tag{1.25}$$

$$-\frac{\partial f_j}{\partial x_i} + \frac{\partial^2 \mathcal{K}_{ij}}{\partial x_\ell^2} + \delta_{ij} = 0 \qquad \text{in } \mathcal{V}_\beta, \tag{1.26}$$

subject to

$$\mathcal{K}_{ij} = 0 \qquad \text{at } \mathcal{A}_{\beta\sigma}, \tag{1.27}$$

together with periodicity of the microscopic fields along x_1, x_2, and x_3. Additionally, since f_j appears in the closure problem in terms of its gradient only, we impose $< f_j >^{\beta} = 0$ as a necessary constraint for the problem to be well-posed. The above-mentioned closure problem renders the permeability, $\mathbf{K}$, intrinsic only to the micro-structural details of the porous medium

(including shape of grains, orientation of the inclusions with respect to the chosen axes, and porosity of the medium); this dependence has been widely investigated in the literature (refer to, for instance, Zampogna & Bottaro (2016); Bottaro (2019); Naqvi & Bottaro (2021); Ahmed *et al.* (2022*b*)).

- **Behavior beyond the Stokes regime**:

Beyond the limit $Re \to 0$, the macroscale behavior of the flow through a porous medium can be altered significantly by the presence of advection, which means that the validity of the classical Darcy's law with the intrinsic permeability $\mathbf{K}$ as a macroscopic coefficient becomes questionable; an extensive discussion on the effects of inertia is provided by Lasseux *et al.* (2011). However, according to the recent work by Valdés-Parada & Lasseux (2021*a*,*b*), a more versatile version of the Darcy's law in which the inertial effects are considered in the upscaling approach can be used: dependence of the average velocity on the macroscopic pressure gradient is properly described by a Darcy-like equation, with an effective (also termed *apparent*) permeability tensor, $\mathbf{H}$, strong function of the Reynolds number (Re) and the direction of the applied external forcing, unlike the intrinsic medium permeability $\mathbf{K}$ which is purely geometry-dependent. Such a generalized equation reads

$$< \hat{u}_i > = -\frac{\hat{H}_{ij}}{\mu}\,\hat{M}_j, \tag{1.28}$$

and a dimensionless effective permeability, $H_{ij} = \hat{H}_{ij}/\ell^2$, can be introduced as

$$H_{ij} = < \mathcal{H}_{ij} > . \tag{1.29}$$

A modified version of the closure problem (Eq. (1.25–1.27)) was derived by Valdés-Parada & Lasseux (2021*a*,*b*) in order to evaluate the purely microscopic tensor $\mathcal{H}$; it reads

$$\frac{\partial \mathcal{H}_{ij}}{\partial x_i} = 0 \qquad \text{in } \mathcal{V}_\beta, \tag{1.30}$$

$$-Re\,\mathcal{H}_{\ell q}\frac{\partial \mathcal{H}_{ij}}{\partial x_\ell}\,e_q^M = -\frac{\partial h_j}{\partial x_i} + \frac{\partial^2 \mathcal{H}_{ij}}{\partial x_\ell^2} + \delta_{ij} \qquad \text{in } \mathcal{V}_\beta, \tag{1.31}$$

subject to

$$\mathcal{H}_{ij} = 0 \qquad \text{at } \mathcal{A}_{\beta\sigma}. \tag{1.32}$$

Again, the microscopic fields are periodic along x_1, x_2, and x_3, and the constraint $< h_j >^\beta = 0$ is to be imposed.

It is worth highlighting that Eq. (1.28) can be mathematically recast into the so-called *Darcy-Forchheimer* equation, that is

$$< \hat{u}_i > = -\frac{\hat{K}_{ij}}{\mu}\,\hat{M}_j - F_{ij} < \hat{u}_j >, \tag{1.33}$$

with the Forchheimer correction tensor defined by $\mathbf{F} = \mathbf{K} \cdot \mathbf{H}^{-1} - \mathbf{I}$, as proposed by Whitaker (1996). Obviously, $\mathbf{H}$ becomes equal to K as $Re \to 0$, and therefore $\mathbf{F}$ vanishes, and Eq. (1.33) reduces to the classical Darcy's law (1.23).

In this project, the apparent permeability is evaluated for porous structures formed by different types of triply-periodic-minimal-surface-based unit cells, varying the porosity and the Reynolds number. For this reason, an introduction to the characteristics and applications of such media is presented in the following subsection.

1.3.2. Insights into TPMS-based porous metamaterials

Table 1.2: A list of selected recent publications on the properties of TPMS-based structures, with indication of the scope of each reference

Reference	Behaviors of interest			
	hydrodynamic	thermal	acoustic	mechanical
Bobbert *et al.* (2017)	✓			✓
Abou-Ali *et al.* (2019)				✓
Chen *et al.* (2019)				✓
Luo *et al.* (2020)	✓	✓		
Zhou *et al.* (2020)				✓
Yin *et al.* (2020)				✓
Ali *et al.* (2020)	✓			
Asbai-Ghoudan *et al.* (2021)	✓			
Lehder *et al.* (2021)				✓
Zeng & Wang (2022)	✓			
Zou *et al.* (2022)	✓			✓
Feng *et al.* (2022)	✓	✓		✓
Lin *et al.* (2022)			✓	
Li *et al.* (2022)	✓	✓		
Khalil *et al.* (2022)	✓	✓		
Rathore *et al.* (2023*a*)	✓			
Rathore *et al.* (2023*b*)	✓	✓		
Piatti (2023)	✓	✓		
Rezapourian *et al.* (2023)				✓
Zhao *et al.* (2023)			✓	✓
Gado *et al.* (2023)		✓		
Hawken *et al.* (2023)	✓			
Lu *et al.* (2023)			✓	

The design of metamaterials *(artificially engineered media with unique properties allowing them to offer novel functionalities, often unachievable by conventional materials)* based on triply periodic minimal surfaces TPMS *(periodic structures which locally minimize their area subject to specific boundary constraints)* is currently a very active field of research. TPMS-based structures are self-standing, highly interconnected, possibly of high porosity, lightweight, and manufacturable by 3D printing (Feng *et al.*, 2019; Asbai-Ghoudan *et al.*, 2021). The unique

topological, acoustic, hydrodynamic, thermal, and mechanical features they may exhibit render them multifunctional and promising for applications ranging from architectural structures (Feng *et al.*, 2019) to biomedical engineering (Bobbert *et al.*, 2017; Ali *et al.*, 2020) and to sound absorption (Yang *et al.*, 2020); the reader is referred to Table 1.2 in which some relevant references are listed.

The nodal coordinates that define a minimal surface can be described in many ways (Gandy *et al.*, 1999, 2001; Brakke, 1992; Yang *et al.*, 2010), yet the simplest and most used method approach is probably the level-set approximation equations (Al-Ketan *et al.*, 2020), from which different isosurfaces can be obtained corresponding to different isovalues of a level-set constant (indicated here as ψ_c); examples of these equations (for nine types of minimal surfaces) are provided in Table 1.3, while the isosurfaces obtained by setting ψ_c to 0 in each equation are correspondingly plotted in Fig. 1.6.

Table 1.3: Level-set approximation equations of some triply periodic minimal surfaces of interest. $(x', y', z') = 2\pi\,(x, y, z)$ with x,y, and z the dimensionless microscopic coordinates, defined by normalizing their dimensional counterparts by the pattern periodicity (ℓ, assumed here constant in the three directions), i.e. $(x, y, z) = \frac{1}{\ell}(\hat{x}, \hat{y}, \hat{z})$. For each equation, different isosurfaces are obtainable by varying the level-set constant ψ_c.

Surface	Formula
Schoen Gyroid	$cosx'siny' + cosy'sinz' + cosz'sinx' = \psi_c$
Schoen I-WP	$2\,(cosx'cosy' + cosy'cosz' + cosz'cosx')$ $-\,(cos2x' + cos2y' + cos2z') = \psi_c$
Schoen F-RD	$4\,cosx'cosy'cosz' - (cos2x'cos2y' + cos2y'cos2z' + cos2z'cos2x') = \psi_c$
Schwarz P	$cosx' + cosy' + cosz' = \psi_c$
Fischer-Koch S	$cos2x'siny'cosz' + cos2y'sinz'cosx' + cos2z'sinx'cosy' = \psi_c$
Fischer-Koch C(Y)	$-sinx'siny'sinz' + sin2x'siny' + sin2y'sinz' + sin2z'sinx'$ $-cosx'cosy'cosz' + sin2x'cosz' + sin2y'cosx' + sin2z'cosy' = \psi_c$
Lidinoid	$sin2x'cosy'sinz' + sin2y'cosz'sinx' + sin2z'cosx'siny'$ $-cos2x'cos2y' - cos2y'cos2z' - cos2z'cos2x' = \psi_c$
Split P	$1.1\,(sin2x'sinz'cosy' + sin2y'sinx'cosz' + sin2z'siny'cosx')$ $-0.2\,(cos2x'cos2y' + cos2y'cos2z' + cos2z'cos2x')$ $-0.4\,(cos2x' + cos2y' + cos2z') = \psi_c$
Neovius	$3\,(cosx' + cosy' + cosz') + 4\,cosx'cosy'cosz' = \psi_c$

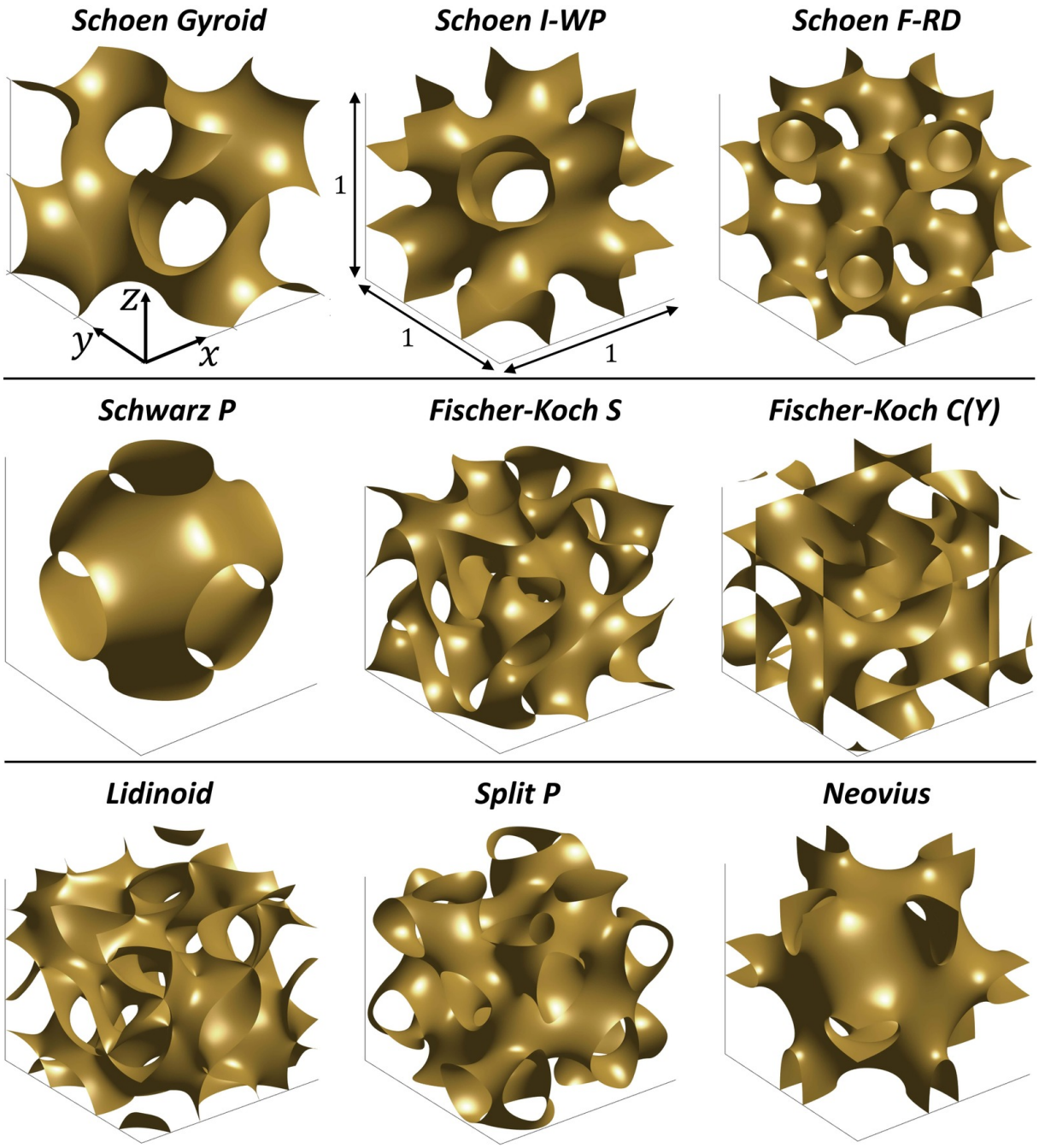

Figure 1.6: Graphical representation of some TPMSs based on the equations given in Table 1.3, with the level-set constant ψ_c set to *zero*. Unit cells are shown in the dimensionless microscopic coordinates.

The use of triply periodic minimal surfaces to form metamaterials exemplifies the integration between mathematics, applied physics, and manufacturing technology. TPMS-based patterns are commonly categorized, according to the region filled with the solid material, into network-based and sheet-based structures; for example, refer to (Kapfer *et al.*, 2011; Zhang *et al.*, 2018; Bonatti & Mohr, 2019; Zhou *et al.*, 2020): (i) in the network structure, the solid

material fills one sub-domain to form a skeleton with a one-side minimal surface which forms the solid/void interface; (ii) in the sheet structure, the solid material takes the form of a finite-thickness shell, obtained by inflation of the minimal surface, which detaches two void sub-spaces. The two designs are illustrated in Figs. 1.7 and 1.8, respectively, by taking the *Schwarz P*-based porous structures as an example. All the TPMS-based geometries presented in the thesis were modeled in MATLAB (Release 2021a) and exported in STL format (Rouhana, 2022, Sep. 4; Sven, 2023) to be available on request.

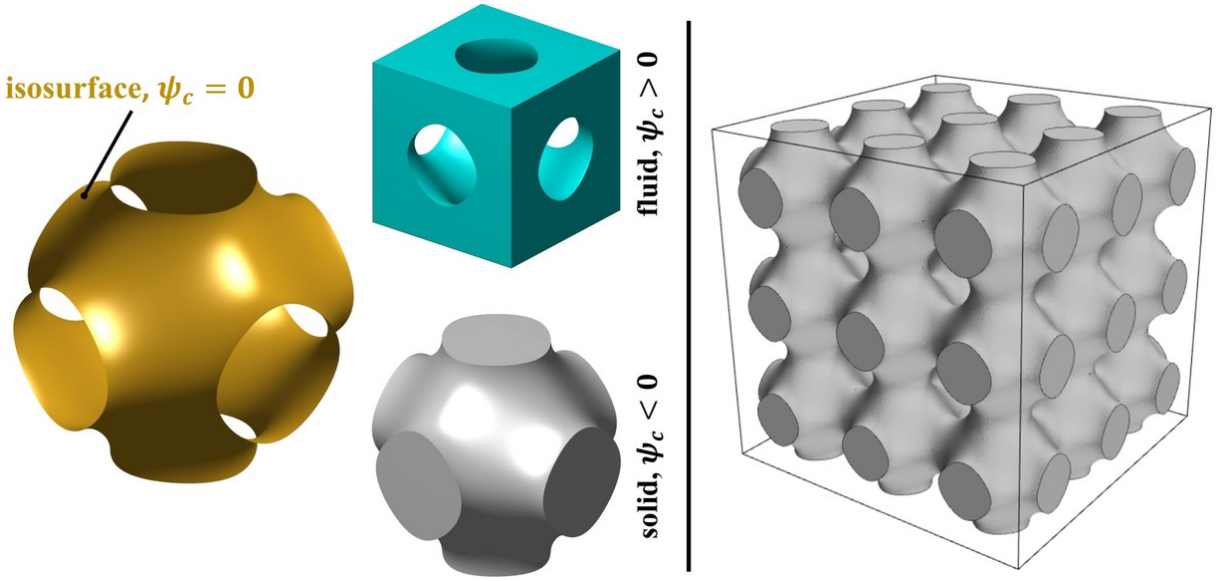

Figure 1.7: Formation of a network-based porous structure with a *Schwarz P* surface. An isosurface with $\psi_c = 0$ (as an example) is defined , and the region $\psi_c < 0$ is filled with the solid material.

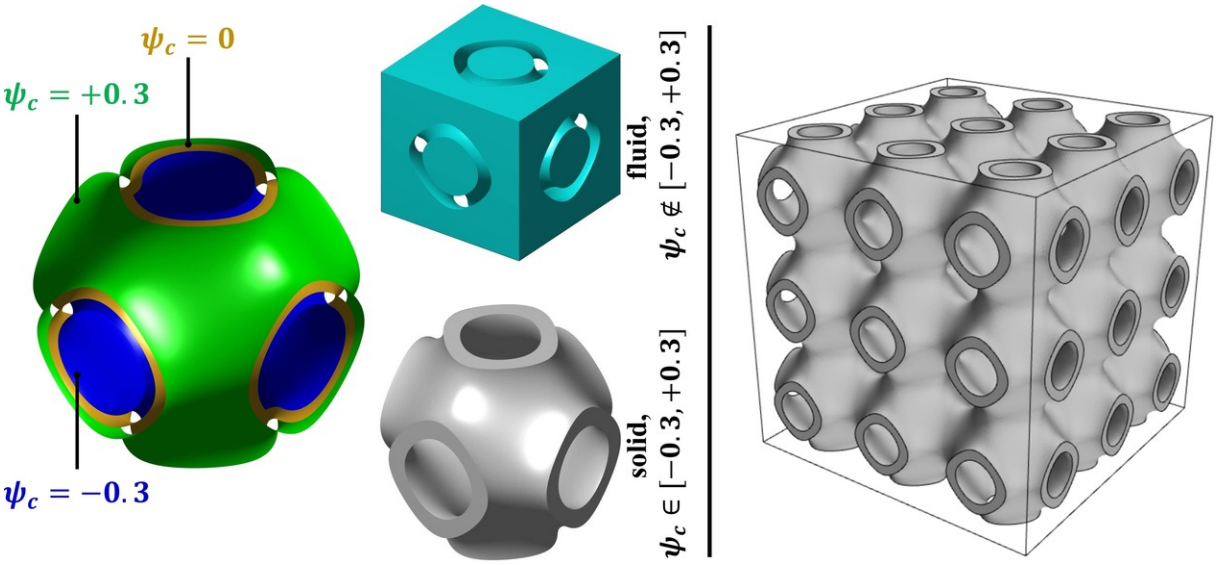

Figure 1.8: Formation of a sheet-based porous pattern with a *Schwarz P* surface. In this example, two isosurfaces with $\psi_c = \pm 0.3$ are defined, and the region in between is filled with the solid material.

In this project, focus will be on the hydrodynamics in sheet-based porous structures. From a mathematical point of view, one method to obtain a shell from any of the TPMSs in Table 1.3 is to assign two values of same magnitude and opposite signs (for instance $\pm s^*$) to the level-set parameter ψ_c such that the two correspondingly generated isosurfaces surround the region filled with the solid material (Zhou *et al.*, 2020). In this way, the porosity of the structure is controlled by the value of s^*. For example, sheet-based geometries of porosity $\theta = 0.8$ are shown in Fig. 1.9, with the values of s^* mentioned in the caption.

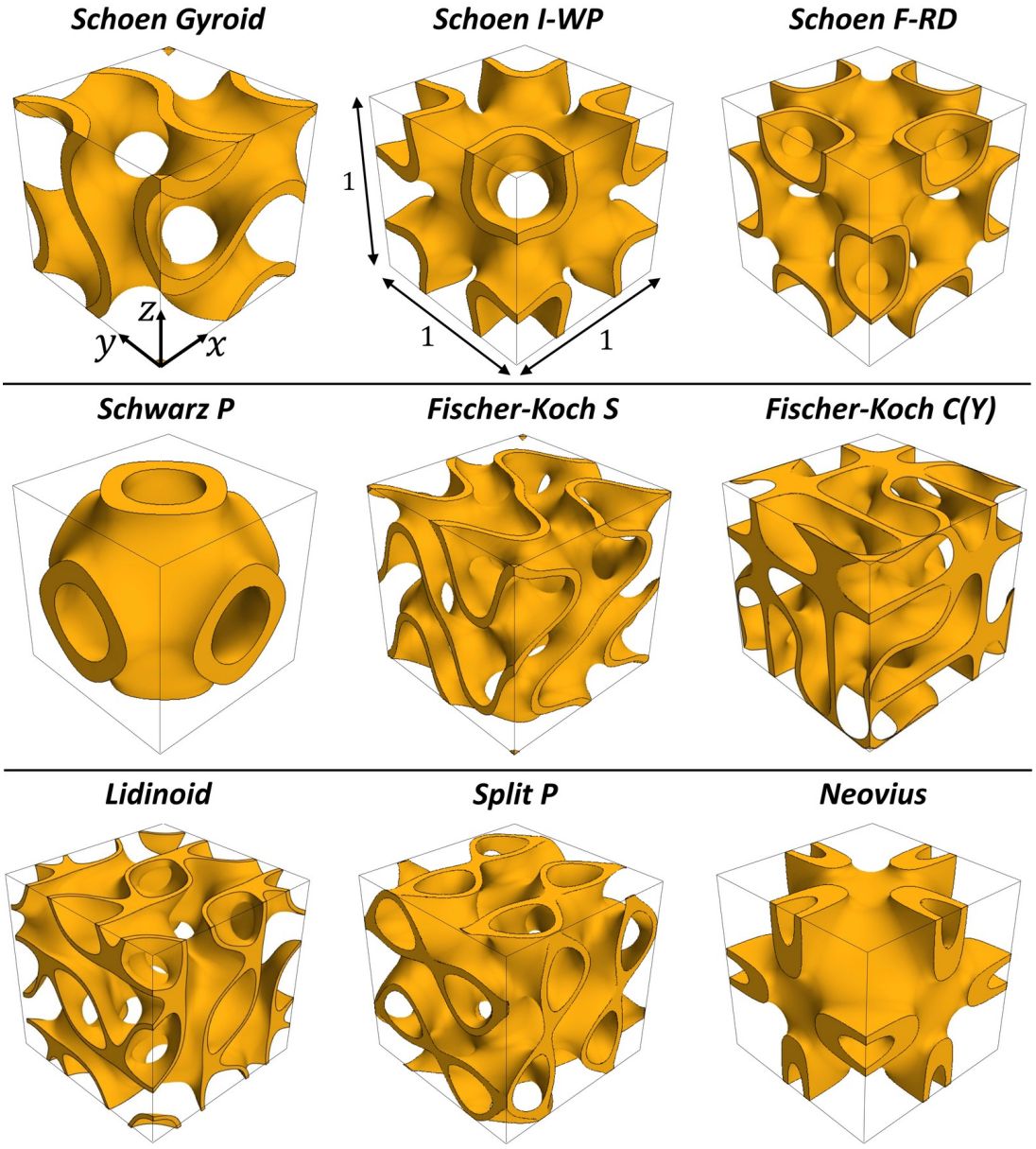

Figure 1.9: TPMS-based unit cells (sheet design) corresponding to the surfaces defined in Table 1.3. For each geometry, two isosurfaces corresponding to $\psi_c = \pm s^*$ were generated to surround the solid material, for the porosity to be equal to 0.8. For instance, *Schoen Gyroid*: $s^* \approx 0.32$; *Schoen I-WP*: $s^* \approx 0.78$; *Schoen F-RD*: $s^* \approx 0.48$; *Schwarz P*: $s^* \approx 0.35$.

Finally, it is useful to show, through the survey presented in Table 1.2, how active the research on sheet-based and network-based structures with a large variety of minimal surfaces has been during recent years.

Table 1.4: A list of selected references, published in the past few years, which investigate the behavior(s) of structures formed based on the TPMSs previously defined in Table 1.3.

Reference	Surface geometry								
	Schoen			*Schwarz*	*Fischer-Koch*		Others		
	Gyr.	*I-WP*	*F-RD*	*Primitive*	*S*	*C(Y)*	*Lidin.*	*Split P*	*Neov.*
Bobbert *et al.* (2017)	✓	✓		✓					
Abou-Ali *et al.* (2019)	✓	✓				✓			
Luo *et al.* (2020)	✓								
Zhou *et al.* (2020)	✓								
Yin *et al.* (2020)	✓	✓	✓	✓					
Asbai-Ghoudan *et al.* (2021)	✓			✓	✓				
Karakoç (2021)	✓	✓	✓	✓	✓		✓	✓	✓
Lehder *et al.* (2021)	✓			✓			✓	✓	✓
Zeng & Wang (2022)	✓	✓		✓					
Zou *et al.* (2022)	✓				✓				
Feng *et al.* (2022)	✓	✓	✓	✓					
Lin *et al.* (2022)	✓			✓					
Li *et al.* (2022)	✓			✓					
Khalil *et al.* (2022)	✓								
Rathore *et al.* (2023*a*)	✓	✓		✓					
Rathore *et al.* (2023*b*)	✓	✓		✓					
Piatti (2023)	✓						✓	✓	
Rezapourian *et al.* (2023)								✓	
Zhao *et al.* (2023)				✓					
Gado *et al.* (2023)	✓	✓		✓			✓		
Lu *et al.* (2023)	✓	✓	✓	✓	✓				✓

1.4. PROJECT ACTIVITIES

The research project includes several experimental and/or numerical studies on buoyant and forced flows over/through regularly textured walls and porous substrates, pertinent to the applications discussed in the previous sections. The outlines of the project are presented in Fig. 1.10, with indication of the published/submitted/ongoing papers related to each subject.

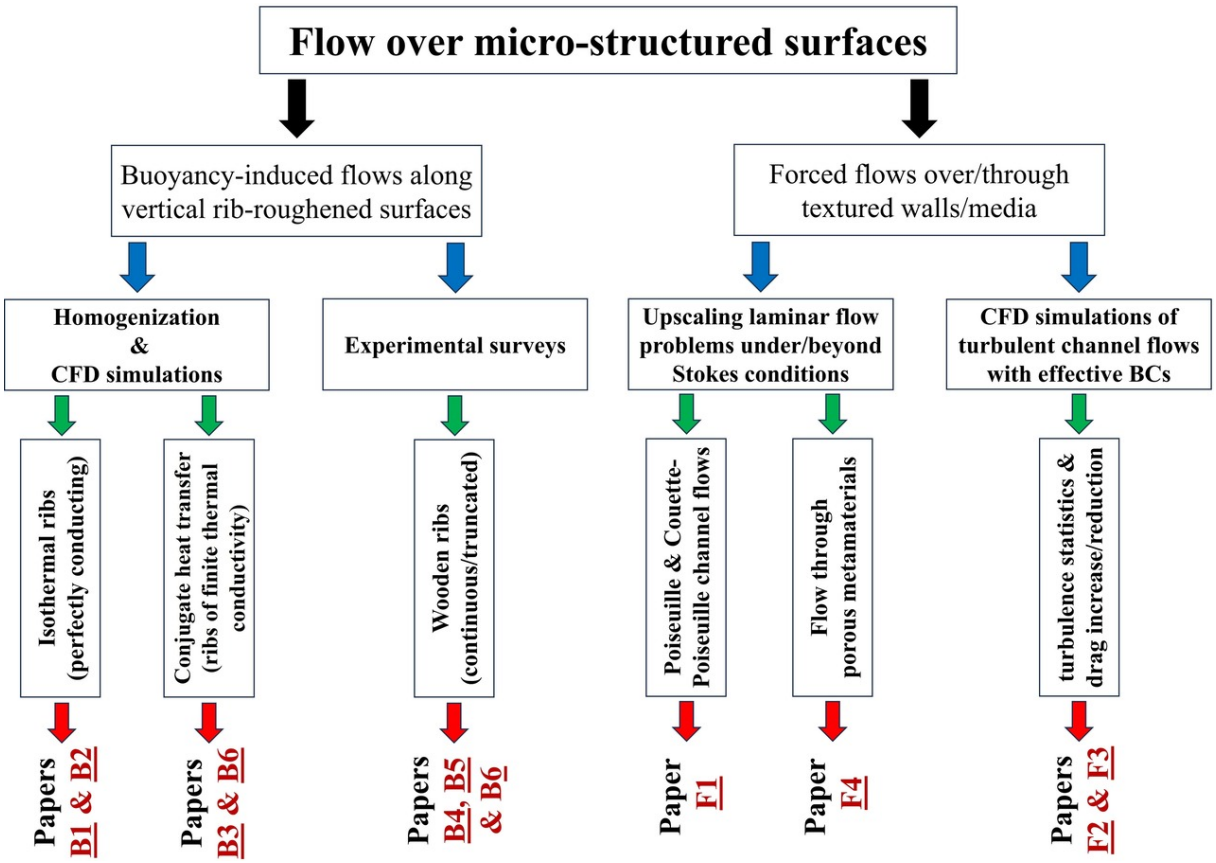

Figure 1.10: Aspects of the research project, with indication of the articles published/submitted/ongoing. **B1**: Ahmed *et al.* (2022*a*); **B2**: Ahmed (2023); **B3**: Ahmed *et al.* (2024); **B4**: Tanda *et al.* (2023); **B5**: Tanda *et al.* ((Submitted 2023)); **B6**: Ahmed & Tanda (2024); **F1**: Ahmed & Bottaro (2024); **F2**: Ahmed *et al.* (2022*b*); **F3**: Ahmed & Bottaro (Draft, 2024); **F4**: Ahmed & Bottaro (2023).

In brief, the numerical work on natural convection along periodically ribbed vertical surfaces includes formulation, implementation, validation, and making practical use of high-order *effective* velocity and temperature boundary conditions at a fictitious plane interface next to the roughness elements, beyond which the macroscale problem is to be numerically analyzed; these novel conditions were derived following a multiscale-homogenization approach, and are able to provide a computationally cheaper alternative to the standard full fine-grained simulations. This was performed, as a first step, for the case of perfectly conduction ribs (**Papers B1** and **B2**), while the model was later generalized to be applicable to rib elements of finite thermal conductivity, besides perfectly adiabatic/conducting ones, as described in **Paper B3**. With regard to the

relevant experimental surveys, in the first set of experiments (**Paper B4**), the buoyancy-driven airflow over a vertical surface of 0.5 m height, regularly roughened with spanwise-elongated wooden ribs of square cross section, was studied within a range of the plate Rayleigh number (Ra) extending from 3.4×10^8 to 4.6×10^8. The plate-height-to-rib-pitch ratio (H/ℓ) and the rib pitch-to-size ratio (ℓ/e) were varied. The experiments rely on the schlieren optical technique, through which the thermal boundary layer is visualized and the local Nusselt number distribution along the vertical surface is acquired. Later, the effectiveness of rib truncation in enhancing the heat transfer from the baseplate surface was explored (**Papers B4** and **B5**). Three staggered arrangements were considered, by varying the number of rib segments per row, and the thermal boundary layer was investigated by means of schlieren visualization and miniature thermocouple measurements, to detect any flow instabilities and the consequent influence on the heat transfer from the surface. The second phase (**Paper B6**) is aimed at studying, through a combined experimental-numerical framework, similar roughness geometries (continuous and truncated ribs) to those explored earlier, yet under conditions, well within the laminar regime ($Ra \approx 2 \times 10^7$), by using a plate with a shorter vertical length. The crux of the work is whether the imposition of a stable flow would maintain, for truncated ribs, superior heat transfer performance relative to the smooth plate, similar to that realized at higher Rayleigh numbers. Further, carrying out the study under the laminar flow regime facilitates performing numerical simulations of the conjugate heat transfer problem, and thus the experimental results can be used to validate the effective boundary conditions already derived.

In regard to the forced flow problems considered, the fully developed, steady, incompressible, laminar flow in a channel delimited by rough and/or permeable walls was considered at one stage of the project (**Paper F1**). The Beavers-Joseph-Saffman condition for the slip velocity was revisited; the boundary condition used instead (available from the homogenization approach) applies to both permeable and rough boundaries including the case of separated flow (Couette-Poiseuille motion with adverse pressure gradient). A closed-form solution of the Navier-Stokes equations was found for the flow in the channel, and was validated against fine-grained simulations for ordered/random textures. One of the most important issues addressed in this work was how to incorporate the near-wall advection into the upscaling procedure; an *Oseen's approximation* was employed to linearize the convective acceleration terms in the momentum conservation equations governing the microscale problem. Additionally, a more advanced analysis was conducted by implementing effective boundary conditions of the streamwise, the spanwise, and the wall-normal velocity components for the study of the turbulent flow in a channel bounded by a porous substrate consisting of an inline pattern of either longitudinal or transverse inclusions, with focus on monitoring and interpreting the drag-reducing or drag-increasing effects caused by these geometries, and on the sensitivity of the roughness function, ΔU^+, to the upscaled coefficients characterizing the wall (**Papers F2** and **F3**).

Finally, a volume-averaging approach was utilized to study laminar flow through triply-periodic-minimal-surface-based media, departing from the Stokes regime (**Paper F4**). A closure problem was solved through a microscopic unit cell to evaluate the effective permeability tensor $\mathbf{H}$ (advection-sensitive, different from the classical intrinsic permeability $\mathbf{K}$) for different types of TPMS-based porous structures, varying the porosity and the Reynolds number.

METHODS, APPROACHES AND TOOLS

The work conducted can be divided, according to the approach adopted, into the following activities: (i) experimental investigations of conjugate natural convection along rib-roughened vertical heated surfaces, mainly with the aid of the schlieren optical method; (ii) studies by homogenization theory and numerical simulations on buoyant flows along vertical ribbed surfaces and on forced flows in channels delimited by micro-textured boundaries; (iii) a volume-averaging-based analysis of seepage in porous media in the presence of advection. While the approach followed in the last activity has been described in sufficient detail in Section 1.3., it is useful to elaborate here on the experimental setup and procedure (first activity) and the homogenization-based treatment (second activity) which represent the backbone of the project.

2.1. EXPERIMENTAL SURVEYS (NATURAL CONVECTION)

This section provides essential information about the experiments conducted on buoyancy-driven air flows along regularly roughened surfaces, including description of the rib configurations examined, the test sections, the optical method used, and the measurements made. For a clearer understanding of the experimental setup, photos of the equipment and the tested plates are presented when necessary; the surveys were carried out at the Schlieren Lab in the Department of Mechanical, Energy, Management and Transport Engineering (DIME, University of Genoa). In-depth details about supplementary calculations and experimental uncertainty are not provided here, yet they are available in **Papers B4** and **B6** (refer to Chapter 4 for submitted/ongoing papers).

2.1.1. Description of ribbed plates and test sections

Experiments were performed on two different vertical plates, one at each stage of the project: the first test surface is a 500 mm-high and 5 mm-thick aluminum plate connected to a plane electrical heater and insulated on one side in order to convey as much heat flux as possible towards the side exposed to the ambient air, while the second plate has a height of 175 mm, and is made of two aluminum sheets with a plane heater sandwiched in between (overall thickness = 12 mm) such that, once the electric power is supplied to the heater, a symmetrical heat transfer on both sides of the plate is provided. Both plates have a spanwise length of 0.3 m.

The thickness of each plate was sufficient to promote, combined with the high thermal conductivity of aluminum, an efficient redistribution of heat by conduction within the plate and, therefore, to obtain a fairly uniform wall temperature. Several fine-gauge thermocouples, calibrated to ± 0.1 K, were embedded in the wall at different elevations to verify temperature uniformity and to provide the mean value of the wall temperature, assumed to be the mean of the individual readings. The wall-to-ambient air temperature difference was varied from 32 to 51 K

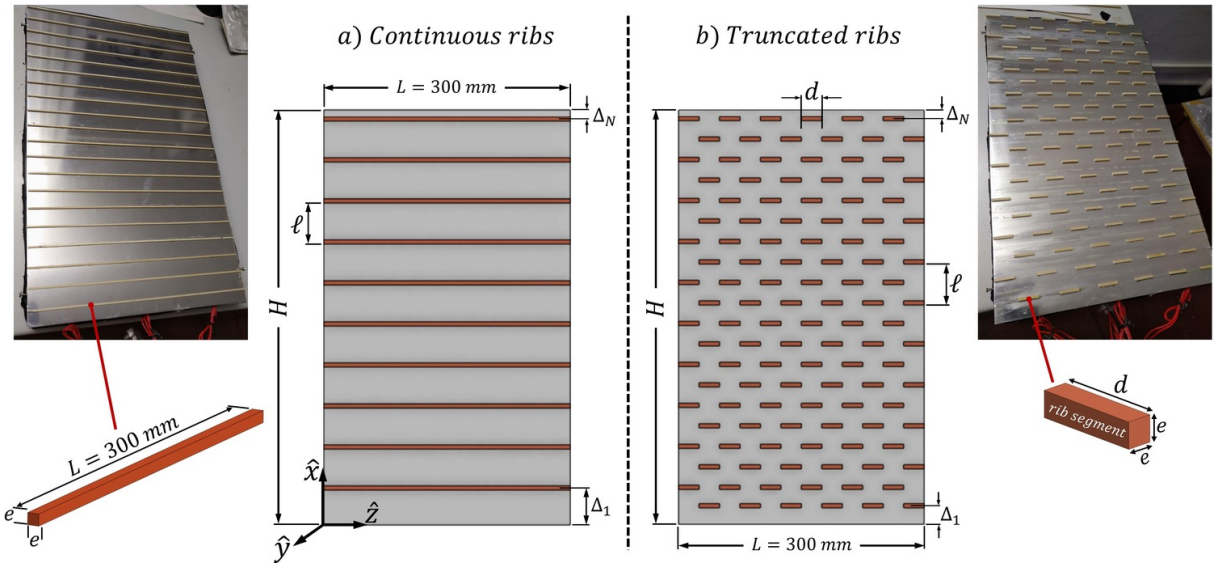

Figure 2.1: General description of the roughened heated surfaces under study, with indication of the main geometric parameters characterizing the patterns of continuous and truncated ribs.

for the plate of the larger height in order to span the range of the plate Rayleigh number from 3.4 to 4.9×10^8 (i.e. close to the upper threshold of the laminar regime over a corresponding smooth plate), whereas the temperature difference was set to 45 K in the case of the shorter plate and a Rayleigh number equal to 2×10^7 was obtained (well within the laminar flow range, which permits the use of the results to validate the numerical simulations discussed later).

Repeated ribs at pitch distance ℓ, having square cross-section ($e \times e$) and either spanwise-elongated (continuous ribs of length equal to the plate's) or cut into smaller segments and arranged in a staggered pattern (truncated ribs of length d) were attached to each of the two heated plates, as sketched in Fig. 2.1, in order to evaluate their effect on heat transfer performance. Ribs were made of wood due to the low cost and the ease of cutting and application; these advantages permit a systematic study of the effect of the main geometric parameters. Dimensions of the different rib configurations examined are detailed in Table 2.1. For the plate of larger height, three different sizes were considered for the continuous ribs, specifically $e = 2$, 3, and 5 mm, and for each size, the number of ribs deployed along the plate surface height was changed from one experiment to another ($N = 10$, 20, or 40), while additional tests were subsequently performed with 20 rows of truncated ribs having height $e = 3$ mm, varying the number of segments per row (three, six, or twelve). For the shorter plate, The rib size (for continuous/truncated elements) was 2 mm and the number of continuous ribs on each of the two symmetric vertical surfaces was varied from 5 to 25, while, in the case of truncated ribs, 11 rows were attached (again, with three, six, or twelve segments per row).

The two sets of experiments (i.e., with the two plates of different heights) allow investigation of: (i) the effect of continuous ribs on the local convective heat transfer performance along vertical heated plates, with the rib pitch-to-height ratio (ℓ/e) varied from 2.5 to 25 for the plate of height $H = 500$ mm (experiments at Ra of order 10^8) and from 3.5 to 20 for the plate of height $H = 175$ mm (experiments at Ra of order 10^7); (ii) the influence of truncation of the ribs into staggered segments on the local convective heat transfer from the plate, with focus on

the difference between their effect at relatively high Rayleigh numbers (Ra of order 10^8, close to the transitional regime) and at relatively low Rayleigh numbers (Ra of order 10^7, far below the upper threshold of the laminar regime); (iii) the overall convective heat transfer from the shorter plate when continuous or truncated ribs are attached, whose values are used to validate the homogenization-based numerical simulations as a major aim of the project.

Table 2.1: Values of the geometric parameters for the roughness patterns tested in the experimental work.

plate height	rib type	number of rows	number of truncated ribs per row	e (mm)	d (mm)	ℓ (mm)	Δ_1 (mm)	Δ_N (mm)
$H = 500$ mm	cont.	10	-	2	-	50	45	5
	cont.	20	-	2	-	25	20	5
	cont.	40	-	2	-	12.5	7.5	5
	cont.	10	-	3	-	50	45	5
	cont.	20	-	3	-	25	20	5
	cont.	40	-	3	-	12.5	7.5	5
	cont.	10	-	5	-	50	45	5
	cont.	20	-	5	-	25	20	5
	cont.	40	-	5	-	12.5	7.5	5
	trunc.	20	3	3	50	50	20	5
	trunc.	20	6	3	25	50	20	5
	trunc.	20	12	3	12.5	50	20	5
$H = 175$ mm	cont.	5	-	2	-	40	8	7
	cont.	9	-	2	-	20	8	7
	cont.	17	-	2	-	10	8	7
	cont.	6	-	2	-	32	8	7
	cont.	11	-	2	-	16	8	7
	cont.	21	-	2	-	8	8	7
	cont.	7	-	2	-	28	4	3
	cont.	13	-	2	-	14	4	3
	cont.	25	-	2	-	7	4	3
	trunc.	11	3	2	50	32	8	7
	trunc.	11	6	2	25	32	8	7
	trunc.	11	12	2	12.5	32	8	7

Figure 2.2 describes the test section and the confinement configuration used in the experimental survey on the shorter plate. Ambient air, at a temperature of 293 K, enters from the lower side of a shielding, whose function is to exclude possible air movements which are present in the laboratory room. For the same reason, at the top section of the shielding, the heated plate was delimited laterally by high-quality glasses (to permit optical access to the test section) and

frontally by two smooth and unheated vertical walls, located at distances equal to half the plate height. According to the previous study by Tanda (1997), a relatively large channel spacing-to-height ratio ($= 0.5$) is expected to have almost no influence on the heat transfer behavior along the plate relative to the case of an unconfined, isothermal, vertical plate. For the plate of larger

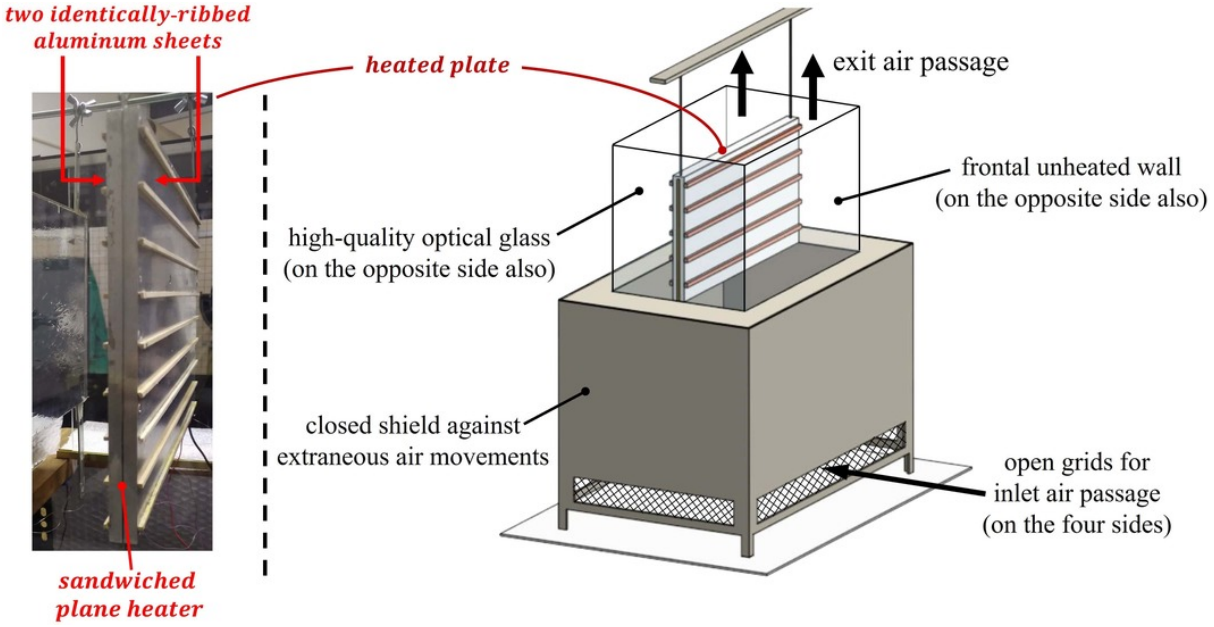

Figure 2.2: Illustration of the test section used for experiments on the 175 mm-high plate. The photo on the left shows the symmetrical design of the heated plate, with the sandwich principle.

height ($H = 500$ mm), much attention was directed to the role of the confinement configuration in the amplification/attenuation of thermal-field instabilities in the boundary layer adjacent to the smooth (unribbed) surface, when operating close to the expected range of transition; the four configurations examined are described and their effects are discussed in detail in **Paper B5**. Only one of these confinements was used in the survey on the larger-height plate in the presence of ribs, as explained in **Paper B4**.

2.1.2. Schlieren optical system

Optical methods are versatile tools for acquisition of qualitative information and quantitative measurements related to heat transfer and fluid flow phenomena since they allow a real-time analysis of the whole field of view covered by the employed instruments, with no intrusion on the physics/processes investigated (Hauf & Grigull, 1970; Merzkirch, 1974; Ambrosini & Tanda, 2006). The index-of-refraction techniques (such as interferometry and schlieren imaging), which are based on measuring the index of refraction, or its spatial derivative, of a medium and using this to obtain data about the thermal field of interest, are among the large variety of the optical methods currently employed in experimental surveys; the reader is encouraged to refer to the bibliography of publications devoted to optical methods, traced down by Ambrosini & Tanda (2006) in the form of a *didactic handbook*. Applicative examples of interferometry

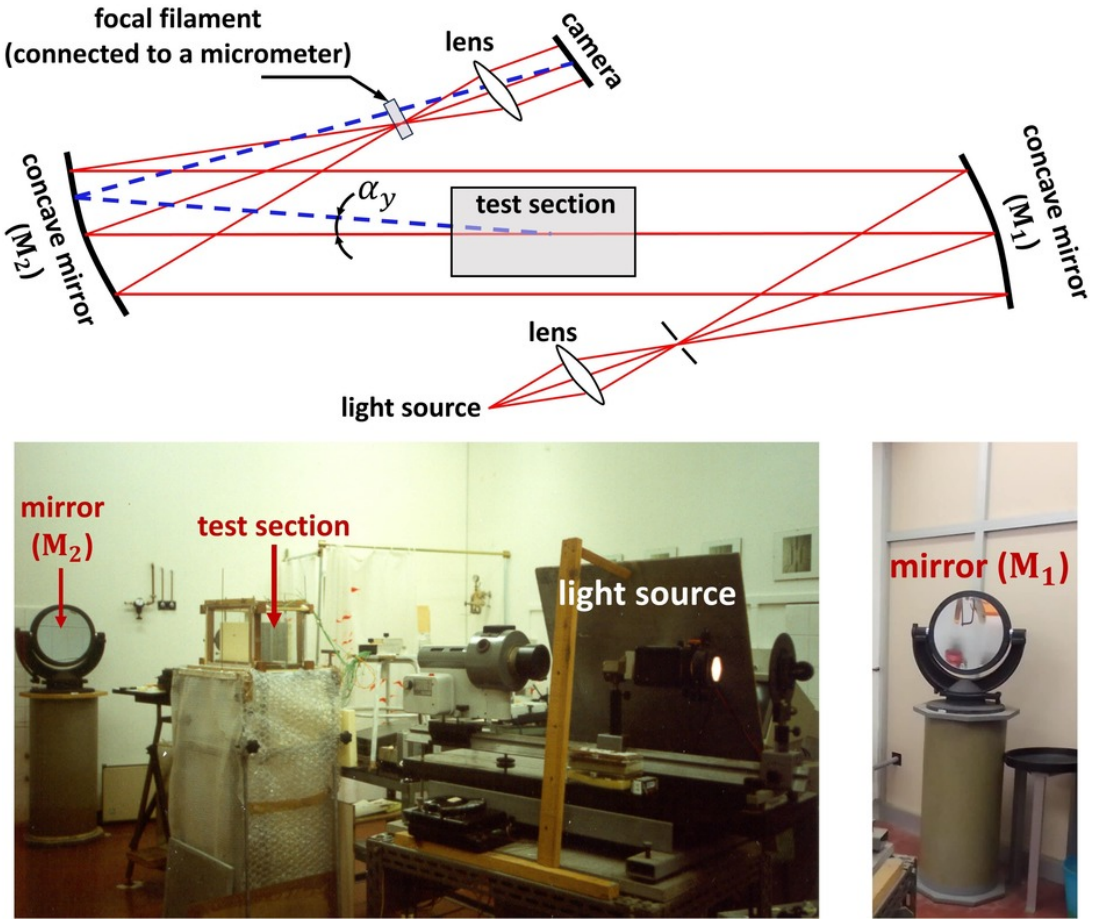

Figure 2.3: Description of the schlieren apparatus used. A schematic of the setup (plan view) is shown at the top: the concave mirrors M_1 and M_2 have a diameter of 0.38 m and a focal length of 1.9 m, and the distance between them is about 8 m.

and/or schlieren imaging are provided, for instance, in Refs. (Bhavnani & Bergles, 1990, 1991; Tanda, 1997; Kleine *et al.*, 2006; Ambrosini & Tanda, 2006; Hargather & Settles, 2012; Tanda *et al.*, 2014; Raffel, 2015; Jain *et al.*, 2016; Settles, 2018; Hampel *et al.*, 2019; Schulz *et al.*, 2020); the two methods are different in operation and optical instrumentation, despite being both based on the temperature dependence of the fluid refractive index, and they can be used in parallel to provide a more comprehensive description of the thermal phenomena via simultaneous visualization of the temperature distribution and the thermal-gradient pattern next to smooth and ribbed surfaces (Ambrosini & Tanda, 2006).

In the experimental part of this project, a schlieren optical setup (see Fig. 2.3) was employed to visualize the thermal boundary layer in the buoyant air stream adjacent to the smooth and the rib-roughened vertical heated surfaces, and to evaluate the local, natural convection heat transfer coefficient. An exhaustive description of the schlieren system used is given in Refs. (Tanda, 1993, 1997, 2008, 2017; Devia *et al.*, 1994; Tanda & Devia, 1998; Tanda *et al.*, 2014). Basically, it consists of a white light beam (composed of parallel rays) crossing the test section, a concave mirror (i.e., the schlieren mirror), which focuses the light onto its focal plane (i.e., the cut-off plane), a filter, and a camera to acquire a real image of the test section. As shown

in Fig. 2.4, when a focal filament (for instance, a thin dark strip or wire) is used as a filter, and no thermal gradients are present in the air crossed by the light beam, all light rays are intercepted by the filter when it is placed on the focus of mirror (and the image formed on the camera will be uniformly dark). When thermal gradients (in the $\hat{y}$-direction of Figs. 2.1 and 2.4) are present, individual light rays undergo angular deflections whose extent is related to the magnitude of the gradient; consequently, the corresponding spots appear bright in the camera, permitting a reliable visualization of the thermal boundary layer (more precisely of all air particles with a non-zero thermal gradient). The angular deflection α_y of a given light ray (i.e., passing through a given point of coordinates $\hat{x}$, $\hat{y}$) can be measured by moving the filter (connected to a micrometer) along the focal plane of the schlieren mirror until the point of interest appears colored by the same color adopted for the filter (violet). It can be demonstrated that the angular deflection α_y is given by the ratio between the filter displacement and the focal length of the mirror (since the angular deviation is small, $tan\,\alpha_y \approx \alpha_y$) (Goldstein, 1976).

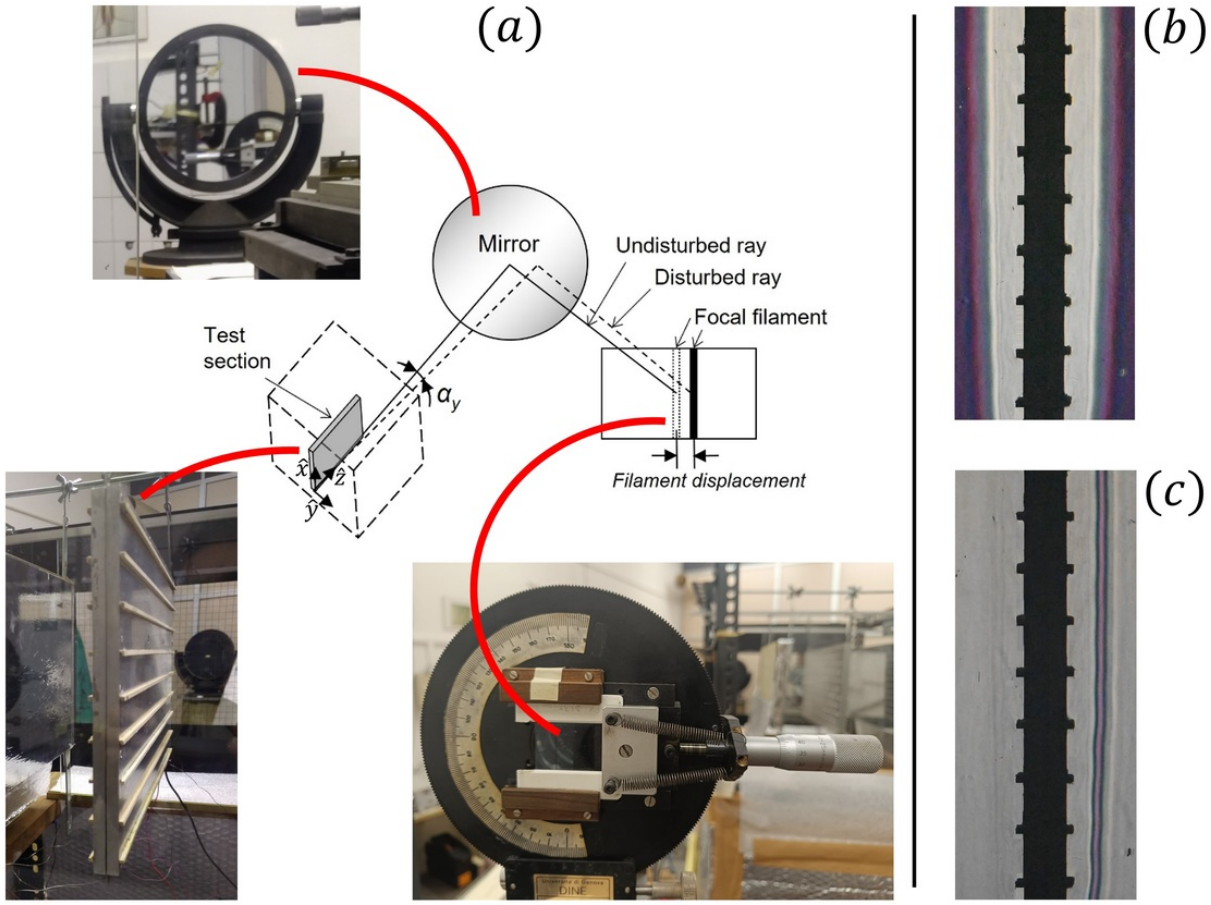

Figure 2.4: Illustration of the schlieren imaging method adopted. In panel (*a*), a simple sketch describing acquisition of light ray angular deflection is provided, besides typical photos of one of the test surfaces, the concave mirror, and the movable filter connected to a micrometer. The schlieren images presented show the optical field when the filament is positioned at the focus of schlieren mirror (frame *b*), and when it is displaced to intercept deflected light rays at a given angular deflection (frame *c*).

The local heat transfer coefficient at a point on the vertical baseplate surface is introduced, conventionally, as follows:

$$h = -k_{air,w} \frac{(\partial \hat{T}/\partial \hat{y})_w}{\hat{T}_w - \hat{T}_\infty}, \tag{2.1}$$

where $(\partial \hat{T}/\partial \hat{y})_w$ is the air temperature gradient in the wall-normal direction, $\hat{y}$, evaluated at the point of interest on the baseplate, and $k_{air,w}$ is the air thermal conductivity evaluated at the wall temperature. Due to the relation between the angular deflection of light and the thermal gradient in the fluid crossed, the heat transfer coefficient, h, can be directly calculated by measuring the deflection of light passing in the vicinity of the wall, using the following formula (refer to, for instance, Ref. (Tanda, 1997)):

$$h = \frac{k_{air,w}\, \alpha_{y,w}\, \hat{T}_w^2}{K(\hat{T}_w - \hat{T}_\infty)}, \tag{2.2}$$

where $\alpha_{y,w}$ is the angular deflection, along the $\hat{y}$-direction, of the light ray passing in the vicinity of the wall at the desired location, and K is a constant (equal to about 0.024 mK in these experiments) which depends on some air properties (Gladstone-Dale and ideal gas constants, index of refraction, pressure) and the length of the plate in the direction of light beam propagation ($\hat{z}$-coordinate in Fig. 2.4). Equation (2.2) provides values of the local heat transfer coefficient for a vertical surface, which depend on the thermal gradients in the $\hat{y}$-direction (whose effect is implicitly included via the consequent angular deflections $\alpha_{y,w}$). In this research, attention is focused on the vertical inter-rib regions of the plate; hence, the angular deviation along the $\hat{y}$-direction is the only optical data on which the heat transfer coefficient depends. In order to present the results in dimensionless form, the local Nusselt number was introduced as follows:

$$Nu = \frac{h\, H}{k_{air}}, \tag{2.3}$$

with k_{air} the thermal conductivity of air evaluated at the film temperature.

2.1.3. Exploration of 3D phenomena and thermal-field instabilities

As discussed earlier in Section 2.1.1., the experiments on the plate of larger height were conducted at Rayleigh numbers close to the reported values in the literature for the onset transition, and therefore it was important to monitor the temperature in the boundary layer to detect possible amplification of thermal-field disturbances when different confinement configurations are examined or when the ribs were attached to the plate surface, since an early transition to turbulence may be triggered. Even though the schlieren technique may exploit, in some circumstances, a tomographic treatment of optical data to get local temperature or heat transfer coefficient results for three-dimensional flows (Devia & Tanda, 2000), Eq. (2.2) assumes the thermal field to be two-dimensional, i.e., independent of the $\hat{z}$-coordinate; otherwise, it is still valid but the calculated heat transfer coefficient corresponds to the value averaged along the plate spanwise length L, that is the plate dimension along the $\hat{z}$-coordinate. This means that any three-dimensional feature of the flow emerging from the insertion of ribs can be observed only in a corresponding two-dimensional ($\hat{x}$-$\hat{y}$) domain with the results at each point averaged

over a line extending in $\hat{z}$. To partially overcome this issue, schlieren measurements were supplemented by the detection of air temperature fluctuations in the boundary layer by using a miniature thermocouple with an exposed junction, able to travel along the direction normal to the plate surface and to be located at any arbitrary position along the vertical and spanwise coordinates. A National Instrument acquisition unit (NI PXIe-1078 equipped with a NI TB-4353 module) was used to acquire the air temperature measurements at a frequency of 50 Hz.

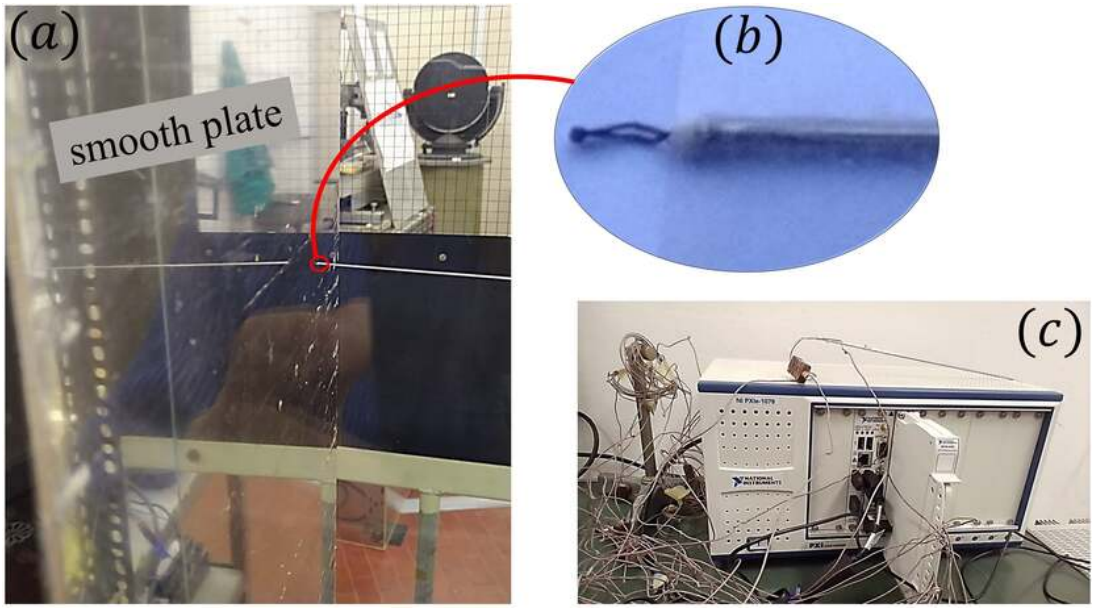

Figure 2.5: Photos of (a) the miniature thermocouple placed at a wall-normal distance of 4 mm from the heated surface, (b) the exposed junction of the thermocouple, and (c) the acquisition unit.

2.1.4. Energy balance calculations

The experiments conducted with the shorter plate included estimation of values of the average convective heat transfer coefficient over the roughened surface for the different rib configurations examined, which required extensive energy balance calculations in order to evaluate the portion of heat transferred from the ribbed "*main*" surfaces to the ambient air by convection ($q_{conv,m}$), i.e. by measuring the input electrical power to the plane heater (q_{el}) and subtracting the summation of the radiant heat transfer rate from the ribbed surfaces ($q_{rad,m}$) and the convective and radiant heat transfer rates from the unribbed "*side*" surfaces formed by the plate thickness ($q_{conv,s} + q_{rad,s}$), such that $q_{conv,m} = q_{el} - (q_{rad,m} + q_{conv,s} + q_{rad,s})$. Calculation of the radiant heat transfer rate from the ribbed surfaces ($q_{rad,m}$) was, in particular, a complex undertaking; this was tackled via an analytical scheme using a diffuse, gray-body network, which includes interactions between the heated plate (i.e., each side of the wooden ribs and the inter-rib aluminum surfaces) and the surrounding (i.e., the frontal unheated walls and the laboratory environment). More details about energy balance calculations are provided in **Paper B6**.

2.2. NUMERICAL ANALYSIS

The numerical work on buoyant and forced flow problems over textured walls/substrates comprises: (i) conventional fine-grained CFD simulations in which the typical geometric features of the physical surfaces, and consequently the detailed velocity and temperature (if considered) fields near the walls, are fully resolved; (ii) homogenization-based simulations which exploit effective boundary conditions, free of empirical parameters, to macroscopically mimic the phenomena, thus simplifying the numerical work by bypassing resolution of the fields through/between/in close vicinity of the grains or roughness elements. While the latter treatment is advantageous in terms of the mesh requirements and the numerical cost, and can be sufficient when the macroscale behavior of the flow is the main point of interest, the classical feature-resolving simulations provide an enhanced vision of the flow structure and patterns and a better understanding of the heat transfer characteristics, and their reliable results are used to validate the homogenization-based ones. All numerical simulations were run using Simcenter STAR-CCM+ finite-volume-based software. In this section, the outlines of the numerical analysis are explained, with focus on the effective boundary conditions derived and the definitions and behaviors of the upscaled coefficients involved.

2.2.1. Conjugate natural convection along a vertical ribbed surface

The physical problem is described in Fig. 2.6(a). The buoyancy-driven flow along a vertical surface of height H, periodically roughened with ribs of given geometry, distribution density, and thermal conductivity, is considered. Although the procedure followed in the analysis is quite general, focus in this work is on spanwise-elongated ribs ($\hat{z}$-invariant, two-dimensional) or truncated rib segments (three-dimensional), both of square cross section $e \times e$, in order to exploit the experimental results (refer to the geometries in Fig. 2.1) for the purpose of validation. The baseplate is assumed to be perfectly conducting and thus to remain isothermal at a temperature $\hat{T}_w$, higher than the ambient temperature ($\hat{T}_\infty$). After heat is supplied to the baseplate (e.g., by an electrical heater) for sufficient time, it is eventually balanced by the heat dissipated to air via natural convection, hence a time-independent value of $\hat{T}_w$ is reached and we can adopt a steady physical model to study the problem, provided that the flow regime remains laminar, which is the case in the experiments on the shorter plate ($H = 175$ mm, $Ra = \mathcal{O}(10^7)$) described in Section 2.1.1. whose results were used to validate the model. Assuming moderate variations in fluid density due to thermal gradient, one can apply the Boussinesq approximation with a linear temperature-density relationship so that the momentum conservation equation is linearly coupled with the energy equation, and the dimensional conservation equations in the fluid phase can be expressed as follows:

$$\frac{\partial \hat{u}_i}{\partial \hat{x}_i} = 0, \tag{2.4}$$

$$\rho\, \hat{u}_j \frac{\partial \hat{u}_i}{\partial \hat{x}_j} = -\frac{\partial (\hat{P} - \hat{P}_\infty)}{\partial \hat{x}_i} + \mu\, \frac{\partial^2 \hat{u}_i}{\partial \hat{x}_j^2} + \rho\beta(\hat{T} - \hat{T}_\infty) g\, \delta_{i1}, \tag{2.5}$$

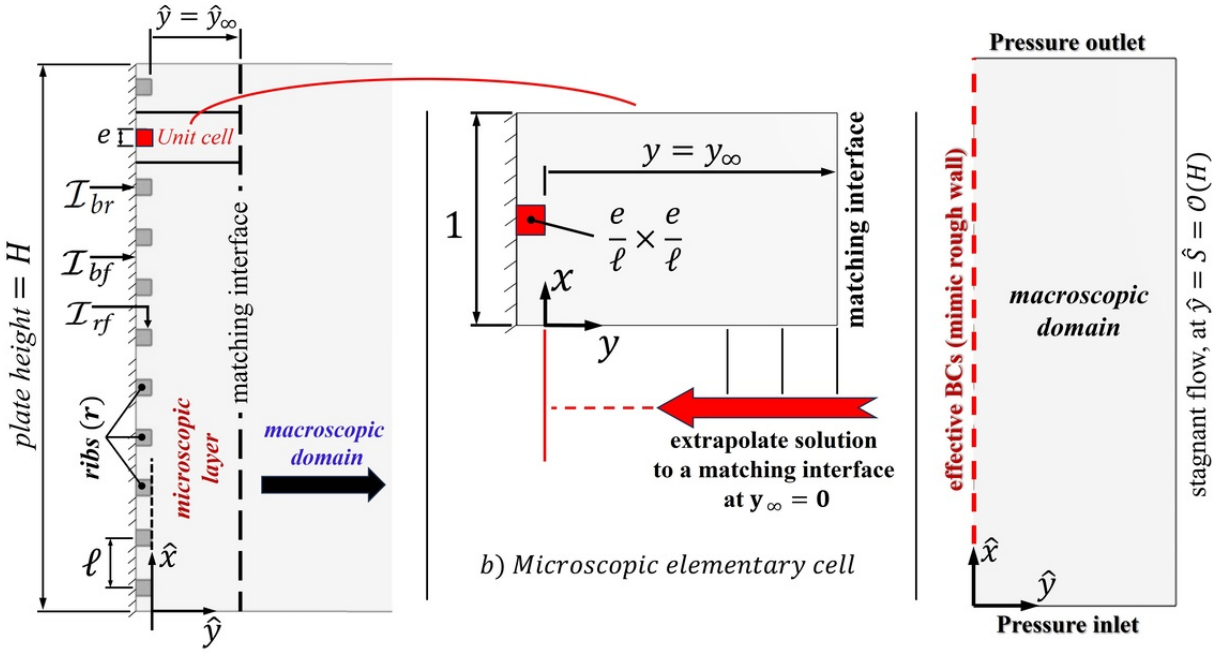

Figure 2.6: Numerical analysis of conjugate natural convection along a vertical rib-roughened surface: (*a*) sketch of the computational domain with a fully featured ribbed wall, indicating the microscopic and the macroscopic subdomains and the fictitious matching interface; (*b*) an elementary cell of the microscopic layer sketched in the dimensionless coordinates $x_i = \hat{x}_i/\ell$; (*c*) the computational domain for the macroscale problem.

$$\hat{u}_j \frac{\partial \hat{T}}{\partial \hat{x}_j} = \alpha \frac{\partial^2 \hat{T}}{\partial \hat{x}_j^2}, \tag{2.6}$$

where the velocity vector ($\hat{u}_i$), the temperature ($\hat{T}$) and the pressure ($\hat{P}$) are the dependent variables of interest, to be evaluated over space $\hat{x}_i$, and $\hat{P}_\infty$, g, and δ_{ij} are, respectively, the pressure in the stagnant region sufficiently far away from the wall, the magnitude of the gravitational acceleration, and the Kronecker delta function. The air density (ρ), dynamic viscosity (μ), thermal conductivity (k_{air}), and thermal diffusivity (α) are evaluated at the film temperature, that is $\hat{T}_{film} = (\hat{T}_w + \hat{T}_\infty)/2$, while the volumetric thermal expansion coefficient (β) is evaluated at the ambient temperature, as suggested by Raithby & Hollands (1985) and Tsuji & Nagano (1988). It is noteworthy that in the experiments on the shorter plate the baseplate wall temperature and the ambient temperature were, respectively, 338 and 293 K, so the criterion $\beta(\hat{T}_w - \hat{T}_\infty)$ is around 0.15, much smaller than 1; hence, the Boussinesq approximation adopted is assumed to be valid (Hærvig & Sørensen, 2020).

Steady thermal conduction takes place through the roughness elements; the temperature distribution in the ribs, $\hat{\mathcal{T}}(\hat{x}_i)$, is governed by the Laplace's equation

$$\frac{\partial^2 \hat{\mathcal{T}}}{\partial \hat{x}_j^2} = 0. \tag{2.7}$$

The temperature boundary conditions at the base-fluid interface ($\mathcal{I}_{bf}$), the base-rib interface

($\mathcal{I}_{br}$), and rib-fluid interface ($\mathcal{I}_{rf}$) are

$$\begin{cases} \hat{T} = \hat{T}_w & \text{at } \mathcal{I}_{bf}, \\ \hat{\mathcal{T}} = \hat{T}_w & \text{at } \mathcal{I}_{br}, \\ \hat{T} = \hat{\mathcal{T}}, \ \frac{\partial \hat{T}}{\partial \hat{n}} = \kappa \frac{\partial \hat{\mathcal{T}}}{\partial \hat{n}} & \text{at } \mathcal{I}_{rf}, \end{cases} \tag{2.8}$$

with $\kappa = \dfrac{k_{rib}}{k_{air}}$ the rib-to-fluid thermal conductivity ratio and $\hat{n}$ the dimensional distance in the direction normal to $\mathcal{I}_{rf}$ at any point. A No-slip velocity boundary condition is imposed at $\mathcal{I}_{rf}$ and $\mathcal{I}_{bf}$. In addition, uniform pressure boundary conditions are defined at the inlet ($\hat{x}_1 = 0$) and the outlet ($\hat{x}_1 = H$), satisfying an equilibrium with the hydrostatic pressure head, for the flow to be driven purely by the buoyant force. At the far boundary (located at $\hat{y} = \mathcal{O}(H)$), the boundary conditions $\dfrac{\partial \hat{T}}{\partial \hat{x}_2} = \dfrac{\partial \hat{u}_1}{\partial \hat{x}_2} = 0$ and $\hat{u}_2 = 0$ are smoothly attained.

It is important to highlight that at the early stages of this project the problem was studied considering the case of perfectly conducting ribs (i.e. $\kappa \to \infty$), for which the elements are theoretical isothermal and the temperature at the rib-fluid interface ($\mathcal{I}_{rf}$) is identical to the baseplate wall temperature ($\hat{T}_w$), in order to simplify the analysis by avoiding solution for the temperature distribution in the ribs. This condition can be approached in practice, for instance, with aluminum ribs (of high thermal conductivity) press-fit into the baseplate, as in (Bhavnani & Bergles, 1990), or machined integral with the surface, as in (Tanda, 1997), to avoid contact resistance. However, the analysis performed and the homogenization model constructed were later upgraded (**Paper B3**) where a general value of the thermal conductivity coefficient was set for the material of the ribs, which allows using the model to study natural convection over surfaces roughened with ribs of finite conductivity (e.g. wooden ribs like in the experiments), as well as perfectly-conductive or adiabatic ribs as the two limiting situations.

The presence of well-separated length scales, i.e. the microscopic scale ℓ characterizing periodicity of the roughness pattern and the macroscopic length scale H (the plate height), renders the problem amenable to upscaling via the multiscale homogenization approach; *effective* boundary conditions of the velocity vector and the temperature can be derived at fictitious plane interfaces, next to the physical rough boundary, to mimic the effects of small surface inhomogeneities on the macroscopic buoyant flow. As shown in Fig. 2.6(a), The whole flow domain is first decomposed into macroscopic and microscopic sub-domains, and a virtual matching interface at $\hat{y} = \hat{y}_\infty$ is defined where continuity of the velocity vector, the temperature, the traction vector, and the normal temperature gradient is applied. An asymptotic analysis is then conducted on the microscopic problems, which are accordingly reconstructed at different orders of the small parameters $\epsilon = \ell/H$. At each order, a generic solution of the problem considered is assumed, in which auxiliary, newly introduced, purely microscopic variables appear; systems of partial differential equations permit to numerically evaluate these variables (presented later) and to define the upscaled coefficients which enter directly the effective boundary conditions at the matching interface(s). In particular, it is convenient to eventually set $\hat{y}_\infty$ to 0 and, hence, to evaluate the macroscopic coefficients for a matching interface passing by the outer rims of the ribs. The homogenized boundary conditions, valid up to second-order in terms of ϵ, can be

formally expressed in the following dimensional form:

$$\hat{u}\big|_0 \approx \underbrace{\hat{\lambda}_x \left[\frac{\partial \hat{u}}{\partial \hat{y}} + \frac{\partial \hat{v}}{\partial \hat{x}}\right]_0 + \hat{\mathcal{K}}^{itf}_{xy} \frac{\beta\, g\, (\hat{T}_w - \hat{T}_\infty)}{\nu}}_{First-order} + \underbrace{\hat{\mathcal{K}}^{itf}_{xy} \frac{\partial}{\partial \hat{x}} \left[-\frac{(\hat{p} - \hat{p}_\infty)}{\mu} + 2\frac{\partial \hat{v}}{\partial \hat{y}}\right]_0 + \hat{\mathcal{B}}\, \frac{g\beta}{\nu} \left.\frac{\partial \hat{T}}{\partial \hat{y}}\right|_0}_{Second-order}, \tag{2.9}$$

$$\hat{v}\big|_0 \approx \underbrace{-\hat{\mathcal{K}}^{itf}_{xy} \frac{\partial}{\partial \hat{x}} \left[\frac{\partial \hat{u}}{\partial \hat{y}} + \frac{\partial \hat{v}}{\partial \hat{x}}\right]_0 - \hat{\mathcal{K}}^{itf}_{zy} \frac{\partial}{\partial \hat{z}} \left[\frac{\partial \hat{w}}{\partial \hat{y}} + \frac{\partial \hat{v}}{\partial \hat{z}}\right]_0}_{Second-order}, \tag{2.10}$$

$$\hat{w}\big|_0 \approx \underbrace{\hat{\lambda}_z \left[\frac{\partial \hat{w}}{\partial \hat{y}} + \frac{\partial \hat{v}}{\partial \hat{z}}\right]_0}_{First-order} + \underbrace{\hat{\mathcal{K}}^{itf}_{zy} \frac{\partial}{\partial \hat{z}} \left[-\frac{(\hat{p} - \hat{p}_\infty)}{\mu} + 2\frac{\partial \hat{v}}{\partial \hat{y}}\right]_0}_{Second-order}, \tag{2.11}$$

$$\hat{T}\big|_0 \approx \underbrace{\hat{T}_w}_{Zero-order} + \underbrace{\hat{\lambda}_\theta \left.\frac{\partial \hat{T}}{\partial \hat{y}}\right|_0}_{First-order}. \tag{2.12}$$

The classical Navier-slip condition for the streamwise and the spanwise velocity components is modified at second order by the gradient of the normal stress and the time-derivative of the shear stress. The streamwise slip velocity is additionally corrected by a buoyancy term at first order and a temperature-gradient term at second order. The normal velocity at the virtual surface appears only as a second-order transpiration condition. A Robin-like condition for the temperature is found, where the wall temperature is corrected with a temperature-gradient term representing thermal slip.

The dimensional groups of coefficients, i.e. the Navier-slip lengths in the streamwise and the spanwise directions and the thermal-slip coefficient (respectively, $\hat{\lambda}_x$, $\hat{\lambda}_z$ and $\hat{\lambda}_\theta$), the interface permeability coefficients ($\hat{\mathcal{K}}^{itf}_{xy}$ and $\hat{\mathcal{K}}^{itf}_{zy}$) and the velocity-flux sensitivity parameter ($\hat{\mathcal{B}}$) are homogeneous to, respectively, a length, a surface area and a volume, and correspond to the product of their dimensionless counterparts times, respectively, ℓ, ℓ^2 and ℓ^3, that is

$$\begin{cases} \hat{\lambda}_x = \ell\lambda_x, \quad \hat{\lambda}_z = \ell\lambda_z, \quad \hat{\lambda}_\theta = \ell\lambda_\theta, \\ \hat{\mathcal{K}}^{itf}_{xy} = \ell^2 \mathcal{K}^{itf}_{xy}, \quad \hat{\mathcal{K}}^{itf}_{zy} = \ell^2 \mathcal{K}^{itf}_{zy} \\ \hat{\mathcal{B}} = \ell^3 \mathcal{B}. \end{cases} \tag{2.13}$$

The dimensionless coefficients $\lambda_x, \lambda_z, \mathcal{K}^{itf}_{xy}$ and $\mathcal{K}^{itf}_{zy}$ are dependent merely on the geometric characteristics of the roughness pattern, for example the rib height-to-pitch ratio (e/ℓ) for transverse square ribs, while the dimensionless thermal-slip coefficient, λ_θ, and the parameter $\mathcal{B}$ also

depend on the rib-to-fluid thermal conductivity ratio, κ. In order to evaluate these coefficients, closure problems were derived (**Papers B1** and **B3**) and were solved over an elementary cell, representative of the microscopic domain, with the dimensions normalized by the microscopic length scale ℓ; the dimensionless coordinates $x_i = \hat{x}_i/\ell$ used to describe the closure fields are shown in Fig. 2.6(*b*). The auxiliary systems of interest are summarized below:

- **System I:** ***a Stokes problem towards*** λ_x

$$\begin{cases} \partial_i u^\dagger_{i1} = 0 \qquad \text{in the fluid domain,} \\ -\partial_i p^\dagger_1 + \partial^2_k u^\dagger_{i1} = 0 \qquad \text{in the fluid domain,} \\ u^\dagger_{i1} = 0 \qquad \text{at } \mathcal{I}_{\rm bf} \text{ and } \mathcal{I}_{\rm rf}, \\ -p^\dagger_1 \delta_{i2} + \partial_2 u^\dagger_{i1} + \partial_i u^\dagger_{21} = \delta_{i1} \qquad \text{at } y = y_\infty. \end{cases} \tag{2.14}$$

- **System II:** ***a Stokes problem towards*** λ_z

$$\begin{cases} \partial_i u^\dagger_{i3} = 0 \qquad \text{in the fluid domain,} \\ -\partial_i p^\dagger_3 + \partial^2_k u^\dagger_{i3} = 0 \qquad \text{in the fluid domain,} \\ u^\dagger_{i3} = 0 \qquad \text{at } \mathcal{I}_{\rm bf} \text{ and } \mathcal{I}_{\rm rf}, \\ -p^\dagger_3 \delta_{i2} + \partial_2 u^\dagger_{i3} + \partial_i u^\dagger_{23} = \delta_{i3} \qquad \text{at } y = y_\infty. \end{cases} \tag{2.15}$$

- **System III:** ***a Laplace problem towards*** λ_θ

$$\begin{cases} \partial^2_i \tilde{\theta} = 0 \qquad \text{in the fluid domain,} \\ \partial^2_i \tilde{\phi} = 0 \qquad \text{in the ribs,} \\ \tilde{\theta} = 0 \qquad \text{at } \mathcal{I}_{bf}, \\ \tilde{\phi} = 0 \qquad \text{at } \mathcal{I}_{br}, \\ \tilde{\theta} = \tilde{\phi}, \;\; \frac{\partial \tilde{\theta}}{\partial n} = \kappa \frac{\partial \tilde{\phi}}{\partial n} \qquad \text{at } \mathcal{I}_{rf}, \\ \partial_2 \tilde{\theta} = 1 \qquad \text{at } y = y_\infty. \end{cases} \tag{2.16}$$

- **System IV:** ***a Stokes problem towards*** $\mathcal{K}^{itf}_{xy}$

$$\begin{cases} \partial_i \dot{u}_{i12} = 0 \qquad \text{in the fluid domain,} \\ -\partial_i \dot{p}_{12} + \partial^2_q \dot{u}_{i12} = -\delta_{i1} \qquad \text{in the fluid domain,} \\ \dot{u}_{i12} = 0 \qquad \text{at } \mathcal{I}_{\rm bf} \text{ and } \mathcal{I}_{\rm rf}, \\ -\dot{p}_{12}\, \delta_{i2} + \partial_2 \dot{u}_{i12} + \partial_i \dot{u}_{212} = 0 \qquad \text{at } y = y_\infty. \end{cases} \tag{2.17}$$

- **System V:** ***a Stokes problem towards*** $\mathcal{K}_{zy}^{itf}$

$$\begin{cases} \partial_i \dot{u}_{i32} = 0 \qquad \text{in the fluid domain,} \\ -\partial_i \dot{p}_{32} + \partial_q^2 \dot{u}_{i32} = -\delta_{i3} \qquad \text{in the fluid domain,} \\ \dot{u}_{i32} = 0 \qquad \text{at } \mathcal{I}_{\text{bf}} \text{ and } \mathcal{I}_{\text{rf}}, \\ -\dot{p}_{32}\,\delta_{i2} + \partial_2 \dot{u}_{i32} + \partial_i \dot{u}_{232} = 0 \qquad \text{at } y = y_\infty. \end{cases} \tag{2.18}$$

- **System VI:** ***a Stokes problem towards*** $\mathcal{B}$

$$\begin{cases} \partial_i {u_i}' = 0 \qquad \text{in the fluid domain,} \\ -\partial_i p' + \partial_k^2 {u_i}' = -\tilde{\theta}\delta_{i1} \qquad \text{in the fluid domain,} \\ {u_i}' = 0 \qquad \text{at } \mathcal{I}_{\text{bf}} \text{ and } \mathcal{I}_{\text{rf}}, \\ -p'\,\delta_{i2} + \partial_2 {u_i}' + \partial_i {u_2}' = 0 \qquad \text{at } y = y_\infty, \end{cases} \tag{2.19}$$

with the operators $\partial_i = \dfrac{\partial}{\partial x_i}$ and $\partial_i^2 = \dfrac{\partial^2}{\partial x_i^2}$. These systems are subject to periodicity of the dependent variables in the x and z directions. The closure problems must be solved for a sufficiently large value of $y_\infty = \hat{y}_\infty/\ell$ such that the microscopic fields are homogeneous in x and z near the matching interface. By rerunning the simulations for a set of suitable values of y_∞ characterizing the matching plane (for example: $y_\infty = 8,\ 7,\ 6,\ 5,\ 4$) and evaluating the values of the closure variables at each matching plane, one can extrapolate the results to the fictitious matching interface of particular interest at $y_\infty = 0$, at which the effective boundary conditions are intended to be imposed. In particular, the macroscopic coefficients contributing to the effective conditions read

$$\begin{cases} \lambda_x = u_{11}^{\dagger}\Big|_{y=y_\infty=0}, \quad \lambda_z = u_{33}^{\dagger}\Big|_{y=y_\infty=0}, \quad \lambda_\theta = \tilde{\theta}\Big|_{y=y_\infty=0}, \\ \mathcal{K}_{xy}^{itf} = \dot{u}_{112}\Big|_{y=y_\infty=0}, \quad \mathcal{K}_{zy}^{itf} = \dot{u}_{332}\Big|_{y=y_\infty=0} \\ \mathcal{B} = u_1'\Big|_{y=y_\infty=0}. \end{cases} \tag{2.20}$$

It is worth mentioning that simpler and more accurate methods to evaluate the model coefficients are introduced in **Papers B1** and **B3**.

For transverse ribs of square cross section, as a representative examples, the trends of the merely geometry-dependent parameters $(\lambda_x, \lambda_z, \mathcal{K}_{xy}^{itf}, \mathcal{K}_{zy}^{itf})$ with variations in $\dfrac{e}{\ell}$ are displayed in Fig. 2.7(left). As λ_θ explicitly depends on κ, and $\mathcal{B}$ is implicitly dependent on it, it is useful to plot them against $\dfrac{e}{\ell}$ for different values of κ; cf. Fig. 2.7(right). The cases of adiabatic ribs and isothermal ribs are chosen as the two limiting situations, while the finite value $\kappa \approx 4$ is chosen as a representative case, corresponding to airflow over wooden ribs. For $\dfrac{e}{\ell} \to 0$, the surface tends to be flat and isothermal; thus, the thermal-slip coefficient $\lambda_\theta \to 0$. In general, the value of λ_θ increases with the decrease of κ at a given value of $\dfrac{e}{\ell}$, with the maximum λ_θ

corresponding to the case of adiabatic ribs. This effect becomes more pronounced for relatively large-sized ribs. For $\frac{e}{\ell} \to 1$, the surface becomes flat again as the inter-rib spaces vanish and the ribs become contiguous; the thermal-slip coefficient approaches zero for isothermal ribs and ∞ for adiabatic ribs.

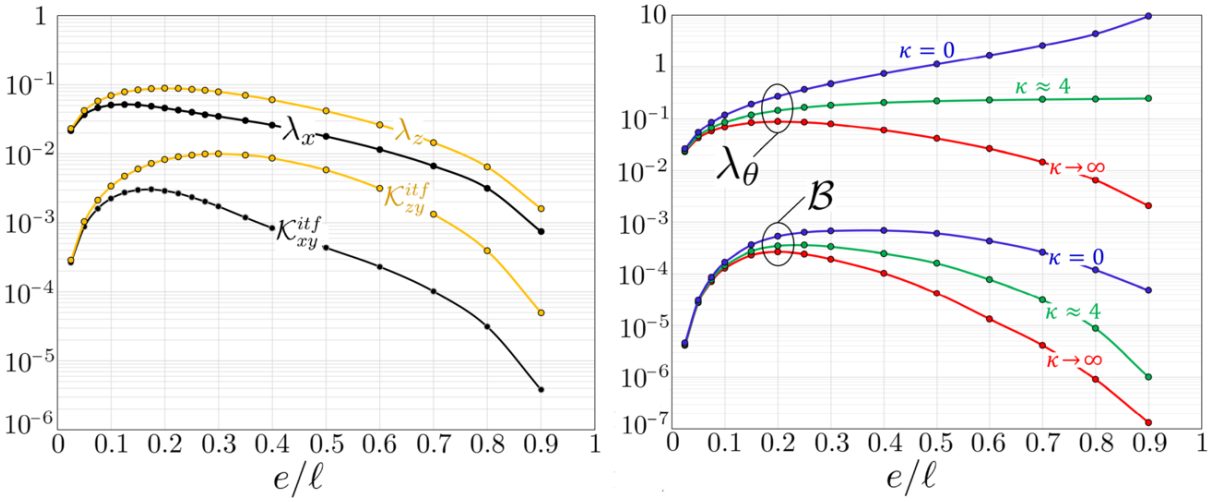

Figure 2.7: Dependence of the macroscopic coefficients on the height-to-pitch ratio e/ℓ of transverse square ribs. The thermal-slip coefficient λ_θ and the velocity-flux sensitivity parameter $\mathcal{B}$ are also dependent on the rib-to-fluid thermal conductivity ratio κ, as shown in the right frame.

Once the model coefficients are estimated for a given wall geometry and rib thermal conductivity, the effective boundary conditions can be implemented in the homogenization-based simulations which are concerned with the macroscale behavior of the fluid flow beyond the fictitious interface; the macroscopic fields targeted at each point in the domain should be equal (if accurately evaluated) to the running averages of the corresponding fully-featured ones resolved in the fine-grained simulations. Taking the case of a wall roughened with truncated ribs of pitch distances $\ell_x = \ell$ and $\ell_z = 2d$ (refer to Fig. 2.1(b)) as an example, one can define the upscaled fields at a point $\Phi : (\hat{x}_\phi, \hat{y}_\phi, \hat{z}_\phi)$, located in the fluid domain beyond the roughness layer (i.e., $\hat{y}_\phi > 0$), by averaging the corresponding fully featured fields over a rectangular $\hat{x} - \hat{z}$ region whose dimensions are $\ell_x \times \ell_z$ and whose center is the point Φ, that is

$$< T > \big|_{\hat{x}_\phi, \hat{y}_\phi, \hat{z}_\phi} = \frac{1}{\ell_x \times \ell_z} \int_{\hat{x}_\phi - \ell_x/2}^{\hat{x}_\phi + \ell_z/2} \int_{\hat{z}_\phi - \ell_z/2}^{\hat{z}_\phi + \ell_z/2} \hat{T}(\hat{x}, \hat{y}_\phi, \hat{z})\, d\hat{z}\, d\hat{x}, \tag{2.21}$$

and likewise for the velocity and pressure.

2.2.2. Forced flow over a textured wall/porous substrate

The incompressible, isothermal flow in a channel of height $2H$ bounded from the bottom and the top sides (subscripts b and t respectively) by rough/permeable walls, i.e. at $\hat{y}_b = 0$ and $\hat{y}_t = 0$, is analyzed; cf. Fig. 2.8(a). The dimensional mass and momentum conservation

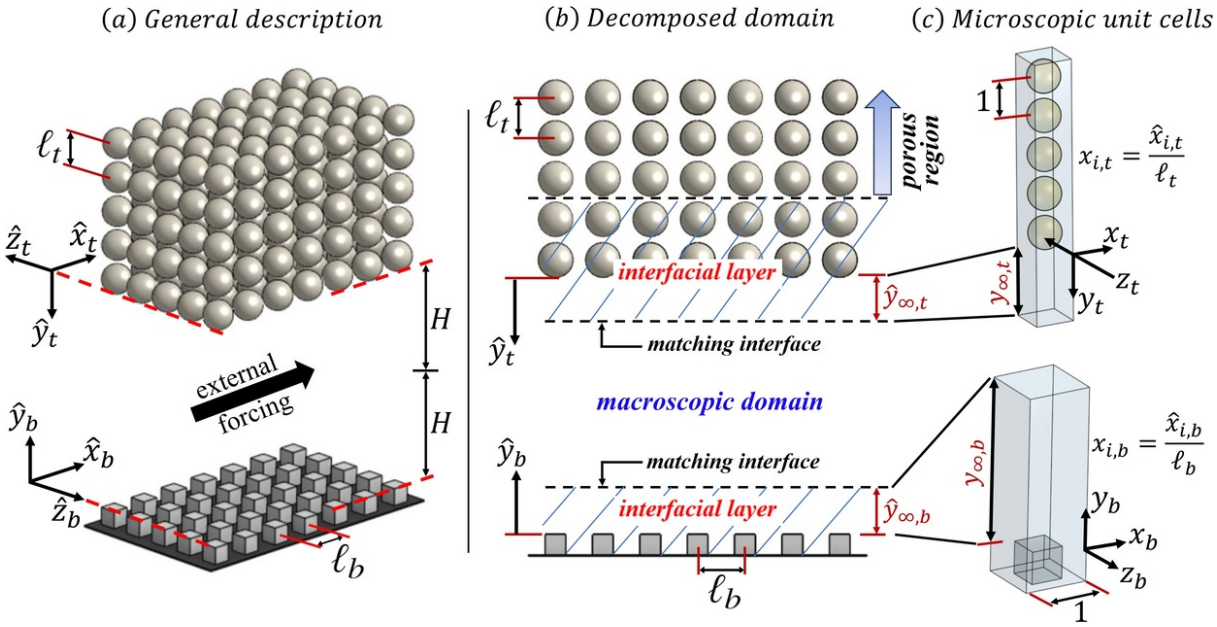

Figure 2.8: Analysis of forced flow in a channel delimited by porous/rough boundaries: (*a*) sketch of the hierarchical flow problem, with indication of the microscopic/macroscopic length scales; (*b*) description of domain decomposition; (*c*) doubly periodic elementary cells of the top and bottom microscopic domains, with their dimensions described in the dimensionless microscopic coordinates $x_{i,b(t)} = \hat{x}_{i,b(t)}/\ell_{b(t)}$.

equations governing the distribution of the velocity vector (whose components are denoted as $\hat{u}_1 = \hat{u}$, $\hat{u}_2 = \hat{v}$, $\hat{u}_3 = \hat{w}$) and the modified pressure $\hat{p}$ over space ($\hat{x}_{1,b(t)} = \hat{x}_{b(t)}$, $\hat{x}_{2,b(t)} = \hat{y}_{b(t)}$, $\hat{x}_{3,b(t)} = \hat{z}_{b(t)}$) are

$$\frac{\partial \hat{u}_i}{\partial \hat{x}_i} = 0, \quad \rho\left(\frac{\partial \hat{u}_i}{\partial \hat{t}} + \hat{u}_j \frac{\partial \hat{u}_i}{\partial \hat{x}_j}\right) = -\frac{\partial \hat{p}}{\partial \hat{x}_i} + \mu \frac{\partial^2 \hat{u}_i}{\partial \hat{x}_j^2}, \tag{2.22}$$

based on either of the two coordinate systems; ρ is the fluid density and μ is the dynamic viscosity. The channel flow is influenced by the presence of the micro-structured boundaries where a complex, generally three-dimensional interaction takes place as the fluid passes near/within the surface corrugations. Provided that the microscopic length scales ℓ_b and ℓ_t characterizing the bottom and top surfaces/substrates, respectively, are sufficiently smaller than the macroscopic length scale (chosen here as H, half the channel height) such that the small parameters $\epsilon_{b(t)} = \ell_{b(t)}/H \ll 1$ are defined, the asymptotic homogenization theory is applicable to the hierarchical problem under analysis, and *effective* boundary conditions of the velocity vector at virtual plane interfaces next to the physical rough/porous boundaries, i.e at $\hat{y}_b = \hat{y}_{\infty,b}$ and $\hat{y}_t = \hat{y}_{\infty,t}$, can be derived and imposed to simulate the macroscale behavior of the channel flow at a fraction of the cost of full feature-resolving simulations; refer to Fig. 2.8(*b*). As in Section 2.2.1., it is convenient to eventually set $\hat{y}_{\infty,b(t)}$ to 0 and, hence, to evaluate the macroscopic coefficients for matching interface(s) passing by the tips/crests/outer rims of the ribs (or the first row of inclusions). The homogenized boundary conditions, valid up to second-order in terms of $\epsilon_{b(t)}$, can be expressed in the following dimensional form (refer to **Paper F2** for derivation):

$$\hat{u}\big|_0 \approx \underbrace{\hat{\lambda}_x \left[\frac{\partial \hat{u}}{\partial \hat{y}} + \frac{\partial \hat{v}}{\partial \hat{x}}\right]_0}_{First-order} + \underbrace{\frac{\hat{\mathcal{K}}^{itf}_{xy}}{\mu}\frac{\partial}{\partial \hat{x}}\left[-\hat{p} + 2\mu\frac{\partial \hat{v}}{\partial \hat{y}}\right]_0}_{Second-order}, \tag{2.23}$$

$$\hat{v}\big|_0 \approx \underbrace{\frac{\hat{\mathcal{K}}_{yy}}{\mu}\frac{\partial}{\partial \hat{y}}\left[-\hat{p} + 2\mu\frac{\partial \hat{v}}{\partial \hat{y}}\right]_0 - \hat{\mathcal{K}}^{itf}_{xy}\frac{\partial}{\partial \hat{x}}\left[\frac{\partial \hat{u}}{\partial \hat{y}} + \frac{\partial \hat{v}}{\partial \hat{x}}\right]_0 - \hat{\mathcal{K}}^{itf}_{zy}\frac{\partial}{\partial \hat{z}}\left[\frac{\partial \hat{w}}{\partial \hat{y}} + \frac{\partial \hat{v}}{\partial \hat{z}}\right]_0}_{Second-order}, \tag{2.24}$$

$$\hat{w}\big|_0 \approx \underbrace{\hat{\lambda}_z \left[\frac{\partial \hat{w}}{\partial \hat{y}} + \frac{\partial \hat{v}}{\partial \hat{z}}\right]_0}_{First-order} + \underbrace{\frac{\hat{\mathcal{K}}^{itf}_{zy}}{\mu}\frac{\partial}{\partial \hat{z}}\left[-\hat{p} + 2\mu\frac{\partial \hat{v}}{\partial \hat{y}}\right]_0}_{Second-order}. \tag{2.25}$$

evaluated at the boundary of interest (either $\hat{y}_b = 0$ or $\hat{y}_t = 0$).

An in-depth look at these effective boundary conditions reveals that their structures are, in general, similar to those related to the case of a free flow along a rough surface, given in Section 2.2.1., except that (i) the two buoyancy-related terms in the expression for the slip velocity (2.9) are now, necessarily, absent in Eq. (2.23), and (ii) an additional term appears in the expression for the transpiration velocity (2.24) including the role of the medium permeability coefficient $\hat{\mathcal{K}}_{yy}$ associated with porous boundaries; if the boundary of interest is corrugated, yet not porous, the medium permeability vanishes while the interface permeabilities $\hat{\mathcal{K}}^{itf}_{xy}$ and $\hat{\mathcal{K}}^{itf}_{zy}$ do not. Again, the Navier-slip lengths in the streamwise and the spanwise directions $(\hat{\lambda}_{x,b(t)},\ \hat{\lambda}_{z,b(t)})$, and the interface and intrinsic permeability coefficients $(\hat{\mathcal{K}}^{itf}_{xy,b(t)},\ \hat{\mathcal{K}}^{itf}_{zy,b(t)},\ \hat{\mathcal{K}}_{yy,b(t)})$ are homogeneous to, respectively, a length and a surface area, and correspond to the product of their dimensionless counterparts times, respectively, $l_{b(t)}$ and $l^2_{b(t)}$. The same closure problems described by systems (2.14, 2.15, 2.17 and 2.18) should be solved over a microscopic elementary cell (like those sketched in Fig. 2.8(c)) to evaluate the dimensionless counterparts $\lambda_{x,b(t)}$, $\lambda_{z,b(t)}$, $\mathcal{K}^{itf}_{xy,b(t)}$ and $\mathcal{K}^{itf}_{zy,b(t)}$, respectively. For the medium permeability component $\mathcal{K}_{yy}$, a triply periodic unit cell of the porous region is considered, and the following closure system is solved over it, with the free index j set to 2:

$$\begin{cases} \partial_i \breve{u}_{ij} = 0, \\ -\partial_i \breve{p}_j + \partial^2_k \breve{u}_{ij} = -\delta_{ij}, \\ \breve{u}_{ij} = 0 \qquad \text{at } \mathcal{I}_{\beta\sigma}, \end{cases} \tag{2.26}$$

subject to periodicity of $\breve{u}_{ij}$ and $\breve{p}_j$ in x, y and z. $\mathcal{I}_{\beta\sigma}$ refers to the physical interface between the fluid phase (β) and the ribs/grains/solid walls (σ). Additionally, since $\breve{p}_j$ appears in the closure problem in terms of its gradient only, we impose $< \breve{p}_j >^\beta = 0$ (refer to the definition in Eq. (1.20)) as a necessary constraint for the problem to be well-posed. The $\breve{u}_{22}$ field is then superficially averaged over the volume of the unit cell to evaluate the coefficient $\mathcal{K}_{yy}$. Should the medium permeability components $\mathcal{K}_{xx}$ or $\mathcal{K}_{zz}$ be needed (although they do not contribute to the effective boundary conditions), system 2.26 is to be solved for j equal to 1 or 3, respectively,

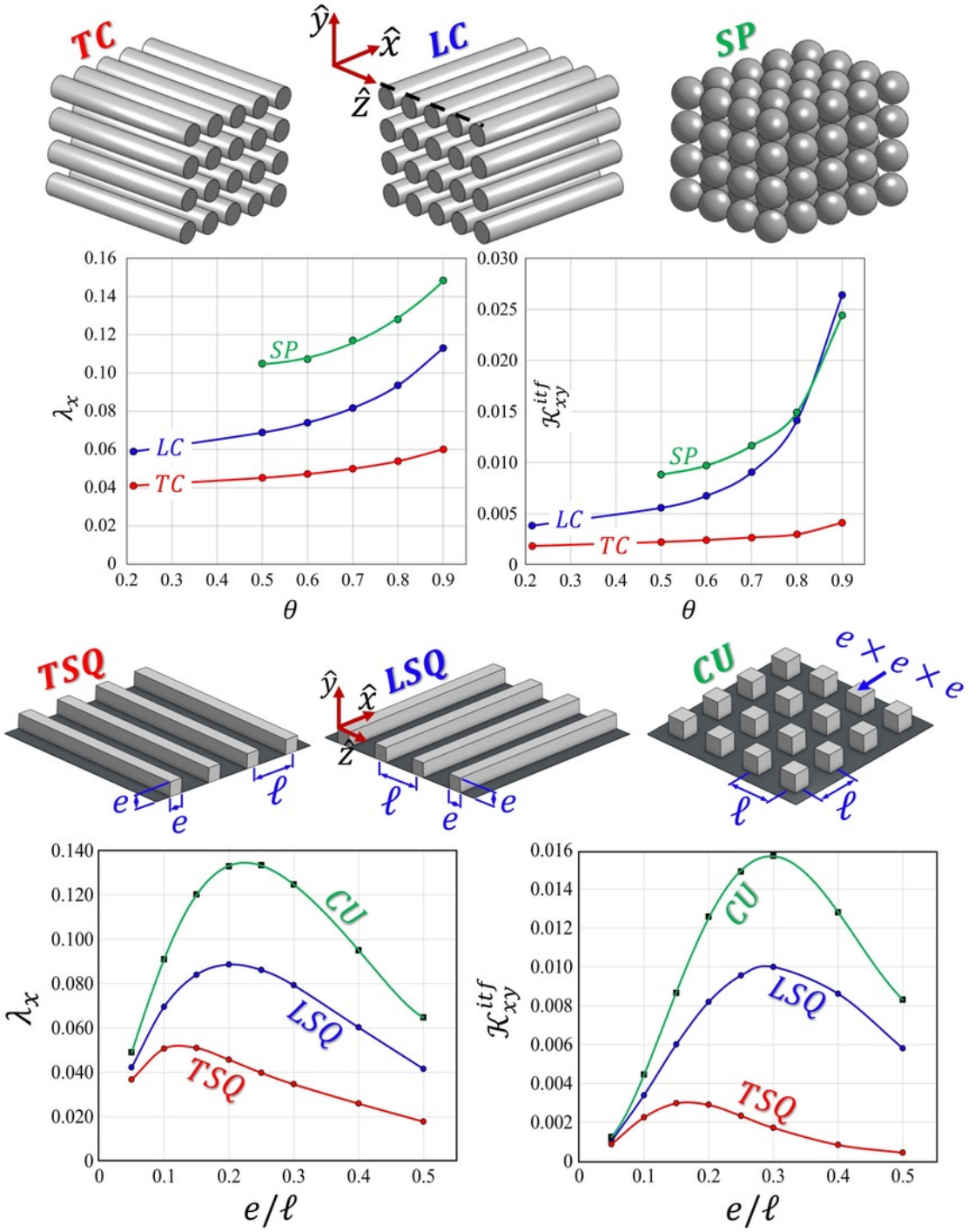

Figure 2.9: Dependence of the Navier-slip and the interface permeability coefficients (respectively, λ_x and $\mathcal{K}_{xy}^{itf}$) on the porosity, θ, of different permeable substrates (top) and the height-to-pitch ratio, e/ℓ, of different rough surfaces (bottom).

and the superficial averaging is to be applied considering, respectively, $\breve{u}_{11}$ or $\breve{u}_{33}$. Numerical values of the macroscopic coefficients entering the effective boundary conditions at the virtual

interface for selected wall micro-structures are plotted in Fig. 2.9, showing their behaviors with variations in the porosity (θ) for the different permeable beds and in the rib size-to-pitch ratio (e/ℓ) for the rough surfaces (the medium permeability values are not plotted here, but the reader can find them in **Paper F1**). For the case of longitudinal (respectively transverse) solid inclusions/ribs, values of the coefficients λ_z and $\mathcal{K}_{zy}^{itf}$ can be inferred, although they are not explicitly available in the figure, since they are equal to λ_x and $\mathcal{K}_{xy}^{itf}$ of the transverse (respectively longitudinal) case at the same value of θ or e/ℓ. When the cylindrical inclusions are elongated in the spanwise (z) or in the streamwise (x) direction. For isotropic patterns such as porous substrates made of ordered spherical grains or walls roughened with ordered cubes, it is clear that $\lambda_x = \lambda_z$ and $\mathcal{K}_{xy}^{itf} = \mathcal{K}_{zy}^{itf}$. For the rough walls considered, the macroscopic coefficients of interest exhibit non-monotonic relationships with the rib size-to-pitch ratio, where they all peak within the range $0.1 \lesssim e/\ell \lesssim 0.3$. This behavior is not unexpected, since the model coefficients vanish for cubic or longitudinal/transverse square ribs as e/ℓ tends to 0 or 1, when the smooth surface case is recovered.

- **The near-wall advection modeling**:

In the original structure of the homogenization model, inertial effects are absent from the problems at the two leading orders in ϵ, and the microscopic systems of equations are Stokes-like. Nevertheless, near-wall advection may contribute significantly to the problem at relatively large values of ϵ, limiting the validity range of the upscaling model adopted. It is, therefore, useful to apply an adjustment to the basic upscaling approach to include the influence of near-wall advection in a simplified way so that the effective boundary conditions (Eqs. (2.23) to (2.25)) hold at considerably large values of ϵ and/or the Reynolds number. The auxiliary systems used to evaluate the Navier-slip and the interface-permeability coefficients are to be reformulated to properly model the sensitivity of the microscopic fields, and therefore the model coefficients, to near-wall inertia, which essentially means that these parameters are dependent not only on the geometric characteristics of the boundary but also on the flow conditions. In this project, the general procedure outlined by Buda (2021) is followed, with some adjustment.

Accordingly, the convective acceleration terms in the momentum conservation equation governing the microscopic problem were linearized, by defining a constant, spatially invariant, dimensional velocity $\hat{u}_{\phi,i} = (\hat{u}_\phi, 0, 0)$ representative of the velocity level near the physical wall where the inertial effects may be significant as the fluid interacts with the protrusions/grains. Hence, the microscale problem is now governed by the following conservation equations:

$$\frac{\partial \hat{u}_i}{\partial \hat{x}_i} = 0, \quad \rho \hat{u}_{\phi,j} \frac{\partial \hat{u}_i}{\partial \hat{x}_j} = -\frac{\partial \hat{p}}{\partial \hat{x}_i} + \mu \frac{\partial^2 \hat{u}_i}{\partial \hat{x}_j^2}. \tag{2.27}$$

The microscopic Reynolds number, defined as $Re_\phi = \rho\, \hat{u}_\phi\, \ell/\mu$, is now assumed to be of $\mathcal{O}(1)$. A homogenization procedure similar, in principle, to the classical one was then followed by Buda (2021); the same effective boundary conditions (Eqs. (2.23)–(2.25)) were eventually attained, yet the closure problems based on which the macroscopic coefficients are calculated differ from those aforementioned in this Chapter. For example, the systems governing the fields

$u^\dagger_{i1}$ and $u^\dagger_{i3}$ (necessary to eventually evaluate λ_x and λ_z) now read, respectively:

$$\begin{cases} \partial_i u^\dagger_{i1} = 0, \\ -\partial_i p^\dagger_1 + \partial^2_k u^\dagger_{i1} = Re_\phi \, \partial_1 u^\dagger_{i1}, \\ u^\dagger_{i1} = 0 \qquad \text{at } \mathcal{I}_{\beta\sigma}, \\ -p^\dagger_1 \delta_{i2} + \partial_2 u^\dagger_{i1} + \partial_i u^\dagger_{21} = \delta_{i1} \qquad \text{at } y = y_\infty \end{cases} \tag{2.28}$$

and

$$\begin{cases} \partial_i u^\dagger_{i3} = 0, \\ -\partial_i p^\dagger_3 + \partial^2_k u^\dagger_{i3} = Re_\phi \, \partial_1 u^\dagger_{i3}, \\ u^\dagger_{i3} = 0 \qquad \text{at } \mathcal{I}_{\beta\sigma}, \\ -p^\dagger_3 \delta_{i2} + \partial_2 u^\dagger_{i3} + \partial_i u^\dagger_{23} = \delta_{i3} \qquad \text{at } y = y_\infty, \end{cases} \tag{2.29}$$

instead of systems (2.14) and (2.15). Attention is now drawn to the choice of the characteristic velocity $\hat{u}_\phi$, required for the definition of Re_ϕ which controls the auxiliary system. Buda (2021) adopted the simple assumption $\hat{u}_\phi = u_\tau$ (with u_τ corresponding to a shear velocity) was adopted, and thus $Re_\phi = \epsilon Re_\tau$ (with Re_τ corresponding to a shear-velocity Reynolds number, defined based on u_τ and the macroscopic length scale H). This assumption is, however, revisited in the present work; detailed description and validation on sample case studies are provided in **Paper F1**. The coefficients calculated based on this approach are indicated in this work as the *"Oseen-based"* coefficients, while those evaluated based on the original, advection-free system (2.14) are termed as the *"Stokes-based"* coefficients. Clearly, the Oseen-based system reduces to the Stokes-based one at $Re_\phi = 0$ for any surface texture. However, they are also identical at finite values of Re_ϕ for the special case of streamwise-elongated inclusions (for instance, walls modified with riblets or porous beds formed by longitudinal cylinders) since all the closure variables in the auxiliary systems become x_1-invariant, and therefore the terms $Re_\phi \, \partial_1 u^\dagger_{i1}$ and $Re_\phi \, \partial_1 u^\dagger_{i3}$.

SUMMARY OF PAPERS AND GENERAL CONCLUSIONS

In this chapter, the scope, objectives, and main findings of each of the journal articles published/submitted (or still in progress) through the research project are summarized. General conclusions of the work are presented at the end of the chapter.

Paper B1: AHMED, E.N., BOTTARO, A. & TANDA, G. 2022 A homogenization approach for buoyancy-induced flows over micro-textured vertical surfaces. *J. Fluid Mech.* **941**, A53.

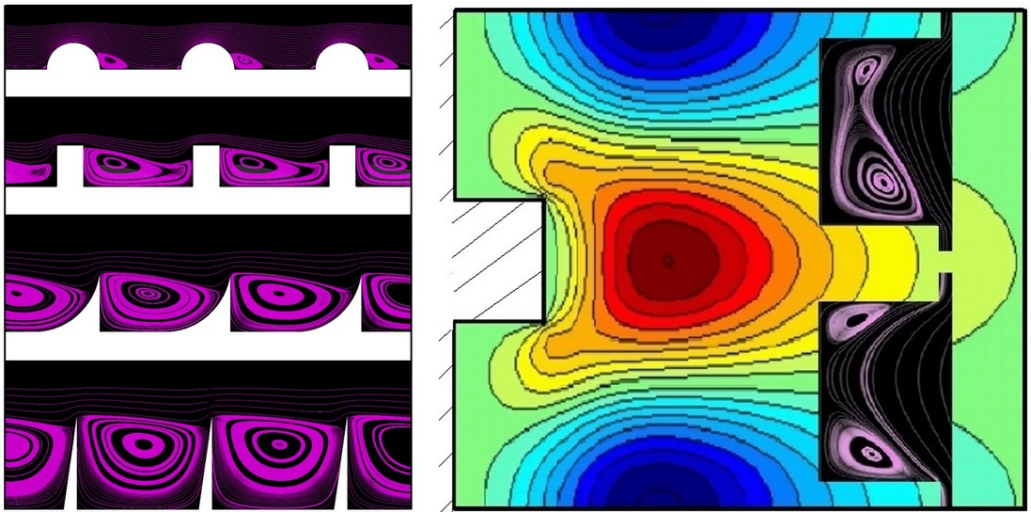

Scope	- Steady natural-convection flow over an isothermal vertical wall, periodically-roughened with spanwise-elongated ribs whose material is perfectly conducting.
Objectives	- Formulation, implementation and validation of upscaled *effective* boundary conditions at a smooth fictitious surface (next to the fully-featured physical one) to bypass the expensive numerical resolution of flow and temperature fields near and within wall corrugations.
Tools	- Multiscale homogenization theory. - CFD simulations.
Highlights	- High-order expressions of the upscaled velocity and temperature boundary conditions were formulated. - Closure problems, necessary to evaluate the macroscopic coefficients contributing to the effective boundary conditions, were derived and solved for sample surface microstructures. - The accuracy levels and the validity limit of the model were investigated under laminar flow conditions.

Paper B2: AHMED, E.N. 2023 Natural-convection heat transfer from regularly ribbed vertical surfaces: Homogenization-based simulations towards a correlation for the Nusselt number. *Numer. Heat Transfer A Appl.* **83** (9), 991–1013.

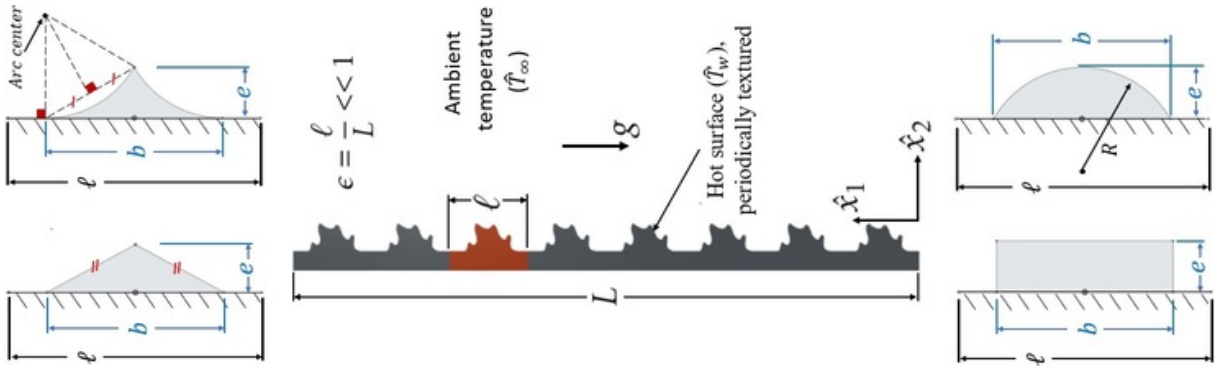

Scope	- Steady natural-convection heat transfer from periodically roughened vertical plates, with different rib geometries and densities of the roughness pattern.
Objectives	- To quantify the enhancement/deterioration of the natural-convection heat transfer rate when ribs are attached to the vertical heated surface. - To pursue a correlation between the Nusselt number and the parameters controlling heat transfer from the ribbed surface.
Tools	- Multiscale homogenization theory. - CFD simulations. - Response surface modeling/optimization. - Multiple-regression analysis.
Highlights	- A database of results describing the deviation of the Nusselt number, for different rib geometries and values of the Grashof number, relative to the reference value of a smooth isothermal wall was created. - It was proved that the presence of ribs generally has a negative effect on heat transfer from the surface. - The thermal-slip coefficient, as a single macroscopic control parameter, proved to imitate the dependence of the Nusselt number on surface micro-details under given pattern density and flow conditions. - A correlation coupling effects of the thermal-slip coefficient, the number of ribs, and the Grashof number on the Nusselt number was cast.

Paper B3: AHMED, E.N., BOTTARO, A. & TANDA, G. 2024 Conjugate natural convection along regularly ribbed vertical surfaces: A homogenization-based study. *Numer. Heat Transfer A Appl.* **85** (9), 1331–1355.

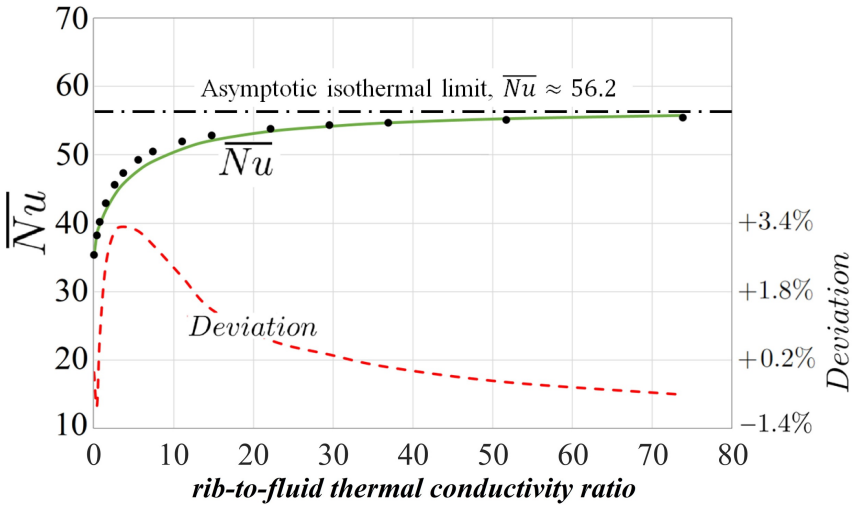

Scope	- Steady conjugate heat transfer problem combining natural convection over a regularly micro-textured vertical surface and the thermal conduction through the roughness elements.
Objectives	- Derivation, implementation and validation of a more versatile version of the effective boundary conditions (originally formulated in Paper 1) to account for thermal conduction through the micro-scale ribs and, therefore, the role of the ribs' thermal conductivity coefficient.
Tools	- Multiscale homogenization theory. - CFD simulations.
Highlights	- The temperature at the virtual boundary deviates from the uniform value at the baseplate, where the thermal slip is described via a temperature-gradient term with a coefficient that depends not only on the rib geometry but also on the rib-to-fluid thermal conductivity ratio. - Several case studies were investigated for the case of spanwise-elongated square ribs, varying the number of elements attached to the surface and the thermal conductivity ratio, and the validity of the model was confirmed. - The lower the thermal conductivity of the ribs, the more the overall convective heat transfer rate deteriorates. - Simplifying the analysis of low-thermal-conductivity elements by considering them adiabatic may be critical, as the heat transfer performance with wooden ribs (for instance) was found to be intermediate between the cases of isothermal and adiabatic ones.

Paper B4: TANDA, G., AHMED, E.N. & BOTTARO, A. 2023 Natural convection heat transfer from a ribbed vertical plate: Effect of rib size, pitch, and truncation. *Exp. Therm. Fluid Sci.* **145**, 110898.

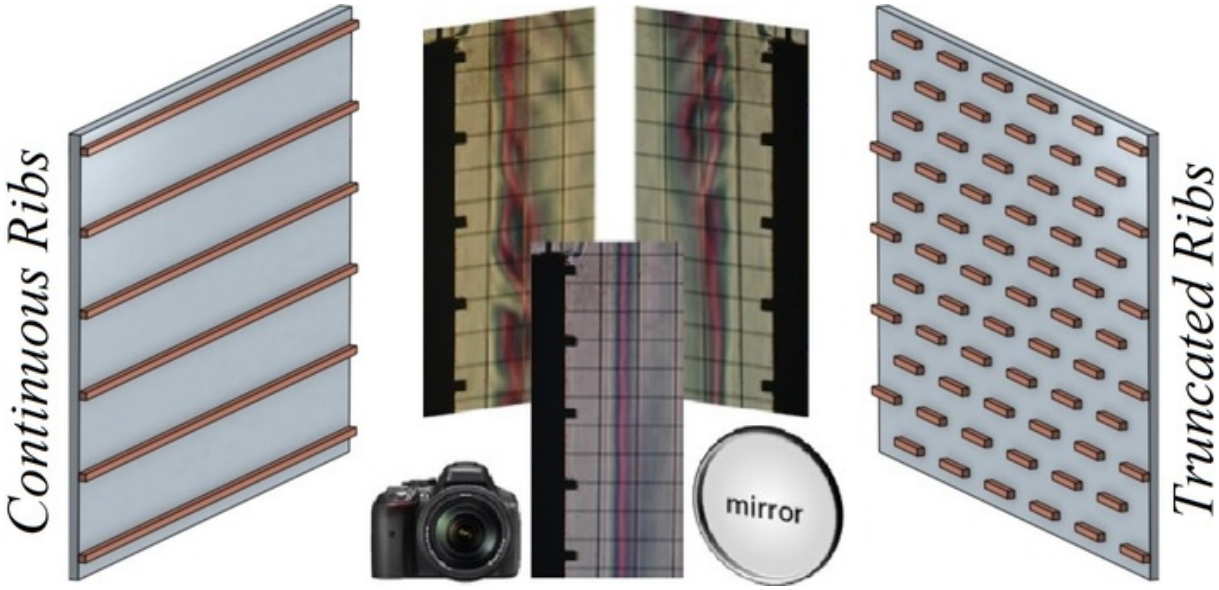

Scope	- Natural convection heat transfer from a vertical plate regularly ribbed with continuous/truncated wooden elements of square cross section, under conditions not far from the onset of the transitional regime and with air as the convective fluid.
Objectives	- Assessment of natural-convection heat transfer from a ribbed vertical plate, varying the size and pitch of spanwise-elongated ribs and considering effects of rib truncation into staggered segments. - Providing insight into the role of thermal-field disturbances close to turbulent transition.
Tools	- Schlieren imaging: for visualization of the thermal boundary layer and acquisition of the Nusselt number distribution. - Miniature thermocouple: for quantification of air temperature fluctuations in the boundary layer.
Highlights	- The presence of continuous ribs negatively affects the heat transfer performance within the range of variation of the parameters investigated. - When continuous ribs are replaced by truncated ones, significant heat transfer enhancements, relative to the smooth surface, were noticed, and an optimal length of the rib segments was found. - Truncated ribs of optimal length induce temperature fluctuations in the boundary layer much larger than those detected for the other configurations studied, a potential reason for their superior performance.

Paper B5: TANDA, G., AHMED, E.N. & BOTTARO, A. (Submitted 2023) Experimental observations of the onset of unsteadiness for buoyant airflow along smooth and rough vertical isothermal walls. *Exp. Heat Transfer.*

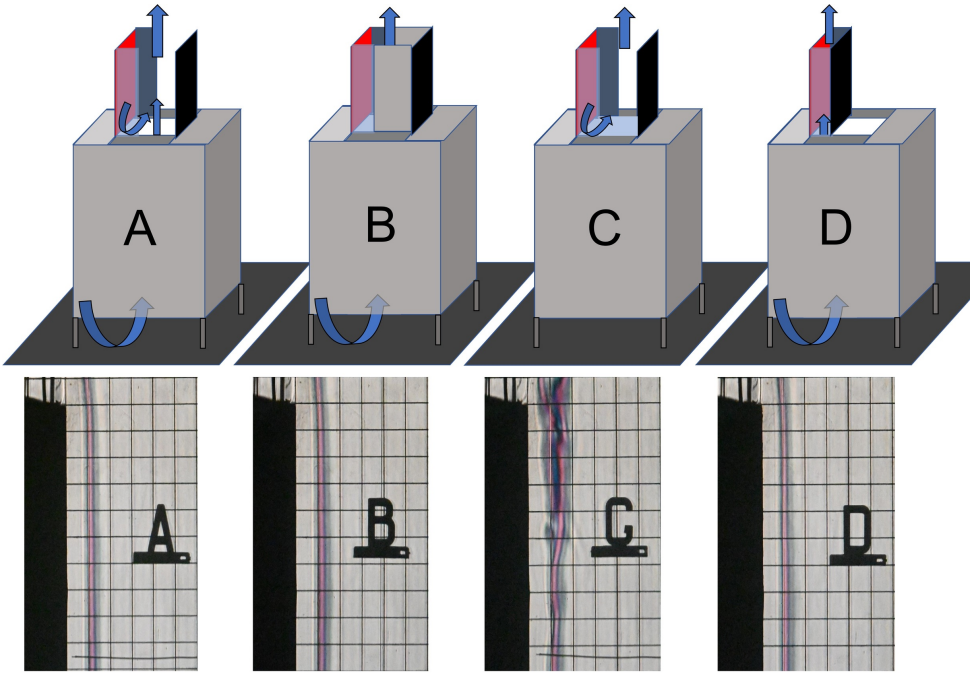

Scope	- Natural convection heat transfer from a vertical plate (smooth/ribbed) under conditions not far from the onset of the transitional regime, with air as the convective fluid.
Objectives	- Investigation of the thermal field in the buoyant airflow along an isothermal, smooth plate, with different enclosure configurations, at conditions close to the end of the laminar regime. - Analyzing the effect of the insertion of roughness elements (staggered rows of wooden segments) onto the vertical plate.
Tools	- Schlieren imaging: Visualization of the thermal boundary layer and acquisition of the Nusselt number distribution. - Miniature thermocouple: Quantification of air temperature fluctuations.
Highlights	- Natural-convection heat transfer results for the smooth plate significantly exceed laminar-flow-based theoretical predictions. - Low-frequency flow instabilities in the boundary layer, sensitive to the different configuration arrangements of the heated plate, were detected. - Temperature fluctuations in the boundary layer were strongly amplified when truncated ribs of optimal length were attached, and a consequent increase in the heat transfer coefficient was detected.

Paper B6: AHMED, E.N. & TANDA, G. 2024 An experimental and numerical study of laminar natural convection along vertical rib-roughened surfaces. *Intl J. Heat Mass Transfer.* **223**, 125227.

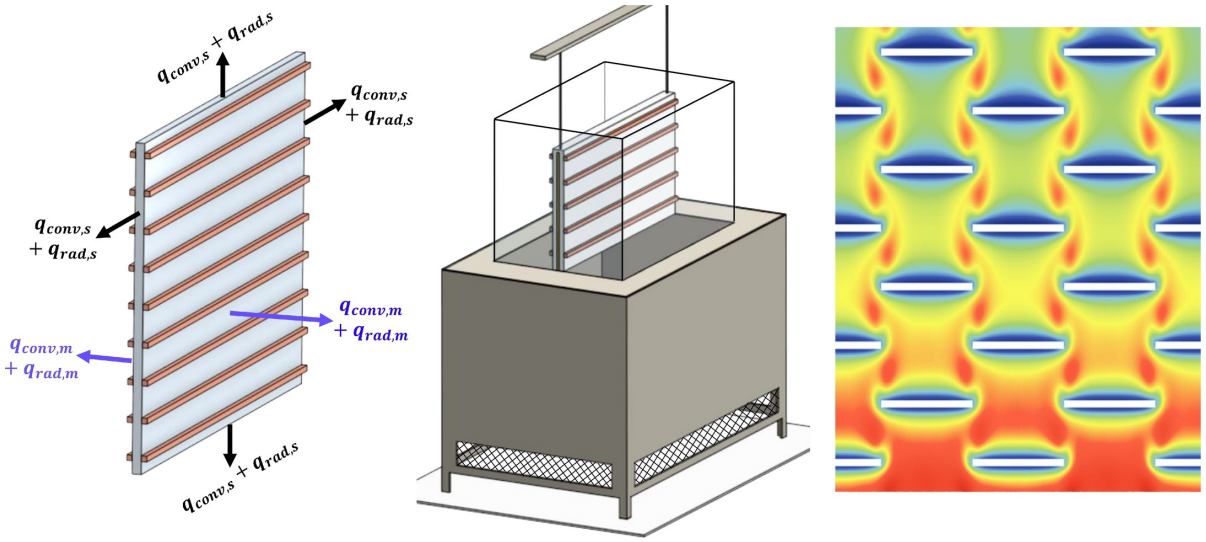

Scope	- Natural convection heat transfer to air from a vertical plate regularly ribbed with continuous/truncated wooden elements of square cross section, under conditions well within the laminar regime.
Objectives	- To investigate, through a combined experimental-numerical framework, whether the imposition of a stable flow would guarantee superior heat transfer performance, relative to the smooth plate, for the geometries which had been found beneficial for heat transfer coefficient enhancement close to the transitional regime in **Papers B4** and **B5** (e.g., truncated rib elements with a proper length). - Numerical model validation for the conjugate heat transfer problem.
Tools	- Schlieren imaging: for visualization of the thermal boundary layer and acquisition of the Nusselt number distribution. - Extensive energy balance calculations. - Multiscale homogenization theory & CFD simulations.
Highlights	- The continuous, ribs were generally found to degrade the local and overall convective heat transfer, with the deterioration becoming more pronounced when the ribs are densely packed on the surface. - Staggered truncated ribs failed to provide any local/overall enhancement to convective heat transfer. - The homogenization-based simulations led to heat transfer trends in line with those obtained by full simulations and experiments.

Paper F1: AHMED, E.N. & BOTTARO, A. 2024 Laminar flow in a channel bounded by porous/rough walls: revisiting Beavers-Joseph-Saffman. *Eur. J. Mech. B Fluids* **103**, 269–283.

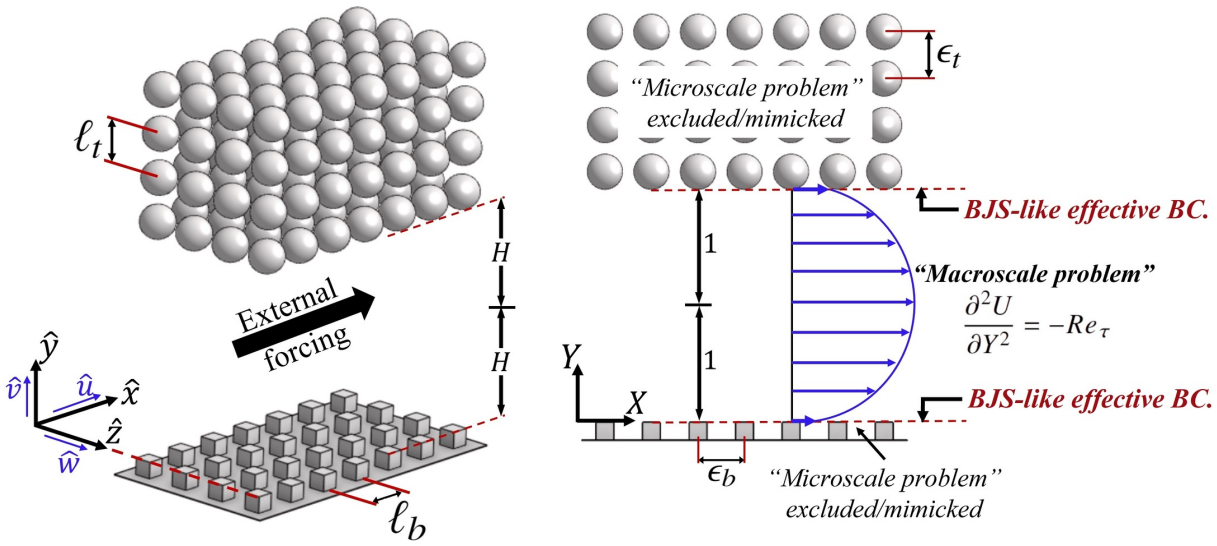

Scope	- Fully developed, incompressible, laminar Poiseuille and Couette-Poiseuille flows in a channel delimited by rough and/or permeable walls.
Objectives	- To revisit the Beavers-Joseph-Saffman condition for the slip velocity in view of the recent advances in the application of the homogenization theory, and to systematically pursue answers to critical questions regarding applicability of the effective boundary condition, especially (i) when the microscopic and macroscopic length scales are comparable, (ii) in the presence of near-wall backflow, and (iii) in the presence of sizeable near-wall advective effects.
Tools	- Multiscale homogenization theory & Oseen's approximation. - CFD simulations.
Highlights	- Analytical solutions of the Navier-Stokes equations were found for Poiseuille and combined Couette-Poiseuille flows in the channel, by defining effective velocity boundary conditions at virtual interfaces next to the physical walls. - The Stokes-based model used to identify the macroscopic coefficients in the effective boundary conditions is found to be reliable up to $\epsilon Re_\tau \approx 10$, with ϵ ratio of microscopic to macroscopic length scales and Re_τ the shear-velocity Reynolds number. - Above this threshold, the coefficients must account for advective effects: a new upscaling procedure, based on an *Oseen's approximation*, was proposed and validated, extending considerably beyond Stokes regime.

Paper F2: AHMED, E.N., NAQVI, S.B., BUDA, L. & BOTTARO, A. 2022 A homogenization approach for turbulent channel flows over porous substrates: Formulation and implementation of effective boundary conditions. *Fluids* **7** (5), 178.

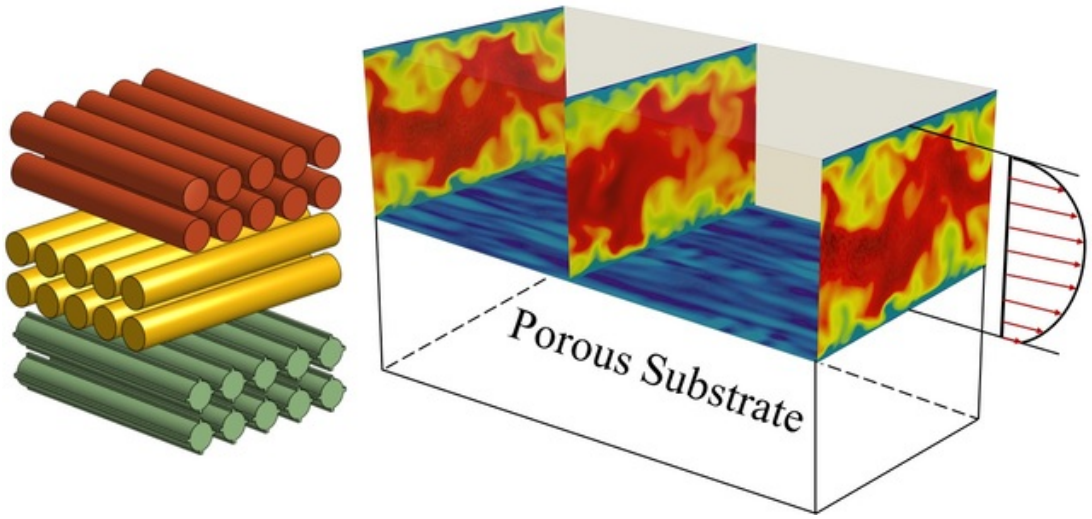

Scope	- Turbulent channel flows over transversely isotropic permeable beds of different microstructures, either spanwise- or streamwise-elongated.
Objectives	- To Formulate and implement effective boundary conditions for the three velocity components at a virtual plane interface next to the porous bed. - To monitor the behavior of the skin-friction drag coefficient for different porous boundaries and to interpret it by analyzing the turbulence statistics.
Tools	- Multiscale homogenization theory. - Direct Numerical Simulations (DNS).
Highlights	- Permeable substrates with preferential slip in the streamwise direction (e.g., beds consisting of longitudinal cylinders) are conditionally able to reduce skin-friction drag. - Permeable substrates with preferential slip in the spanwise direction (e.g., beds consisting of transverse cylinders) result in skin-friction drag increase. - The analysis of the turbulence statistics provides a meaningful picture of the levels of disturbances in the neighborhood of the permeable walls, which can be used to interpret the behaviors of the skin-friction drag coefficient.

Paper F3: AHMED, E.N. & BOTTARO, A. (Draft, 2024) Exploring the nexus among roughness function, apparent slip velocity and upscaling coefficients for turbulent flows over porous/textured walls. *To Be Submitted To J. Fluid Mech.*

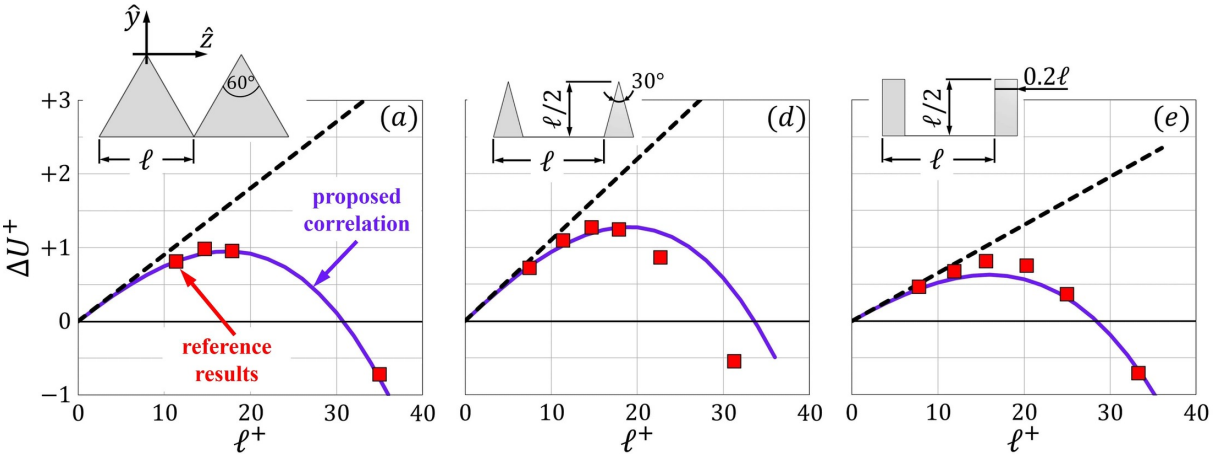

Scope	- The hydrodynamic interaction between a porous/rough boundary and a fluid, under turbulent flow conditions, with focus on the sensitivity of the roughness function, ΔU^+, to the upscaled coefficients for the wall.
Objectives	- To demonstrate that imposing *effective* velocity boundary conditions at a *virtual* plane boundary, next to the physical perturbed one, can efficiently simplify the direct numerical simulations (DNSs). - To pursue correlations to estimate ΔU^+ *a priori*, once the upscaled coefficients of the homogenization model (i.e., the Navier-slip coefficients and the interface/intrinsic permeabilities) are evaluated.
Tools	- Multiscale homogenization theory & Oseen's approximation. - Direct Numerical Simulations. - Regression analysis
Highlights	- Drag reduction is attainable exclusively over streamwise-aligned grains for ℓ^+ values (pitch distance in wall units) up to 20–30. - The drag increase over spanwise-aligned inclusions (or streamwise-aligned ones at excessive ℓ^+) is accompanied by enhanced turbulence levels, including intensified sweep and ejection events. - The r.m.s. fluctuations of the transpiration velocity at the virtual plane, $\tilde{V}_{rms}$, is a key control parameter of ΔU^+. - $\tilde{V}_{rms}$ is strongly correlated to a single macroscopic quantity, Ψ, which comprises the upscaling coefficients of the model. - Fitting relationships for ΔU^+ are proposed, and their applicability is confirmed against reference results.

Paper F4: AHMED, E.N. & BOTTARO, A. 2023 Flow through porous metamaterials formed by TPMS-based unit cells: Effects of advection. *Eur. J. Mech. B Fluids* **100**, 202–207.

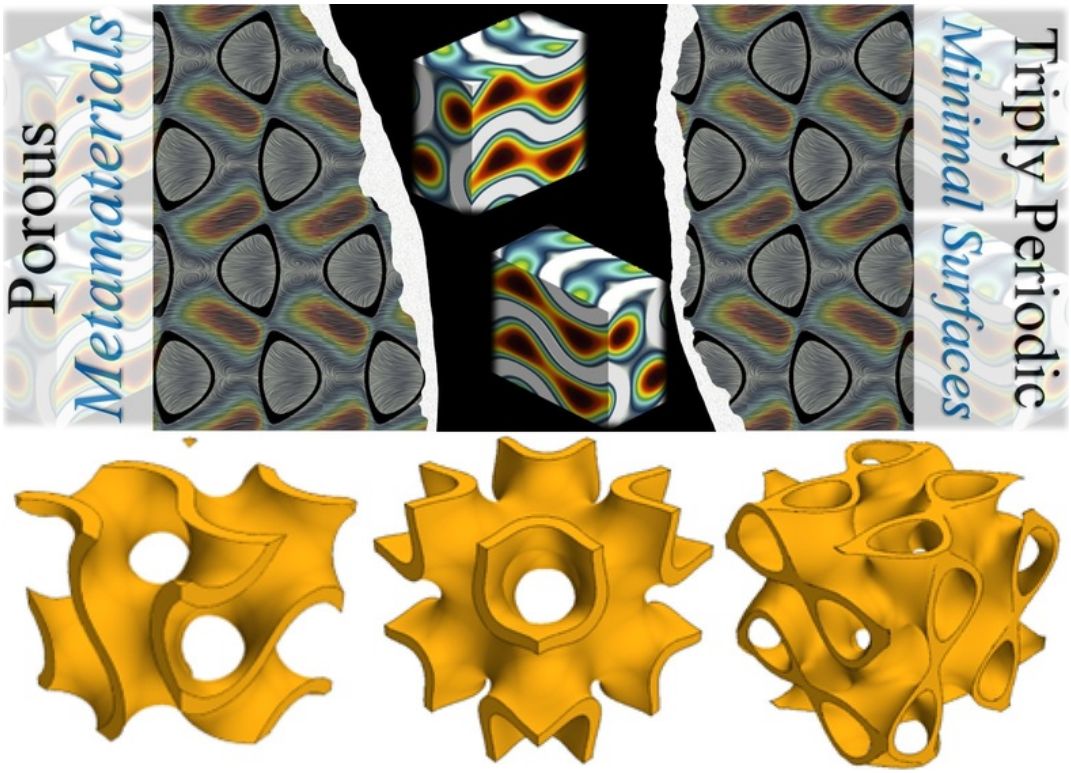

Scope	- Seepage in different triply-periodic-minimal-surface (TPMS)-based porous media beyond the linear, Stokes flow regime.
Objectives	- Employing upscaling to study the flow in TPMS-based porous structures, with focus on the effects of advection. - Investigation of the permeability of sample TPMS-based metamaterials.
Tools	- Volume-averaging-based upscaling method. - CFD simulations.
Highlights	- Effective (rather than intrinsic) permeability in Darcy's law stems from upscaling when advection is included in the model. - Effective permeability is strongly dependent on both the porosity and the Reynolds number; this was explored for six types of TPMS-based structures, namely *Gyroid*, *I-WP*, *Schwarz P*, *Split P*, *Fischer-Koch S*, and *Neovius*. - Advection can significantly reduce permeability, particularly at large porosity.

• General conclusions

Experimental surveys and numerical simulations were carried out to investigate the complex thermal/hydrodynamic interaction between a textured boundary and a fluid in different buoyancy-induced and forced flow problems.

One of the main contributions of the project is the implementation of the multiscale homogenization theory to derive effective boundary conditions of the velocity vector and the temperature at a fictitious plane interface next to a ribbed vertical wall exposed to natural-convection heat transfer. Expressions of the boundary conditions were provided up to second-order accuracy in a small parameter ϵ, ratio between the rib pitch and the plate height. Accordingly, the classical Navier-slip condition for the streamwise velocity component was modified at first order by a buoyancy term and at second order by the gradient of the normal stress besides a temperature-gradient term. A Robin-like condition for the temperature was found, where the wall temperature is corrected with a temperature-gradient term representing thermal slip; the thermal-slip coefficient, λ_θ, depends on both the geometric properties of the protrusions and the rib-to-fluid thermal conductivity ratio, κ. The effective boundary conditions were tested, mainly, on the case of natural convection of air along a heated vertical surface roughened with transverse square ribs, varying the small parameter ϵ, the rib pitch-to-height ratio, the Rayleigh number Ra, and κ. Upon validation against reference feature-resolving simulations, the accuracy levels and the applicability range of the homogenization-based treatment were estimated and it was proven to be an efficient tool to mimic the macroscopic flow behavior at a fraction of the numerical complexity/cost of the fine-grained numerical analysis. Further, conjugate natural convection (at $Ra = 2 \times 10^7$) along a vertical surface ribbed with wooden elements, either spanwise-elongated or truncated into staggered segments, was experimentally investigated via the schlieren optical method and extensive energy balance calculations, and the obtained trends/values of the local and the surface-averaged Nusselt numbers were employed to validate the numerical simulations (full/homogenized). For the considered range of the rib pitch-to-height ratio (from 3.5 to 20), the presence of transverse continuous ribs resulted, generally, in a convective heat transfer degradation, from both local and overall average perspectives, and even the staggered truncated elements failed to provide any local/overall enhancement. Another experimental survey was carried out considering similar rib configurations at larger Rayleigh numbers ($3.4 \times 10^8 - 4.6 \times 10^8$), close to the upper threshold of the laminar flow range in the case of a smooth surface; intriguingly, staggered arrangements resulted in significant heat transfer enhancements, relative to the smooth surface, throughout the majority (or the totality) of the inter-rib regions, which is likely related to either the more efficient redistribution of buoyant airflow within the laminar flow regime or to a premature transition to turbulence induced by rib truncation, as large-amplitude air temperature fluctuations suggest.

The forced flow in a channel delimited by porous/rough boundaries was studied, with focus on assessing/promoting the validity of the effective velocity boundary conditions for laminar (within and beyond the Stokes regime) and turbulent flows. The homogenization-based boundary condition used for the longitudinal velocity represents a more versatile version of the Beavers-Joseph-Saffman condition; it applies not only to permeable but also to rough surfaces, and it is free of any empirical parameters. The classical Stokes-based model used to identify

slip and interface permeability coefficients in the effective boundary conditions is found to be reliable and accurate up to $\epsilon Re_\tau \approx 10$, with ϵ here ratio of the textured pattern pitch distance to half the channel height and Re_τ the shear-velocity Reynolds number. Above this threshold, the coefficients must account for advective effects: a new upscaling procedure, based on an *Oseen's approximation*, is thus proposed and validated, extending considerably beyond the Stokes regime. A more advanced analysis was conducted by employing effective boundary conditions of the three velocity components to study turbulent channel flows with different porous substrates. The results, examined in terms of the mean velocity field and the turbulence statistics, showed that permeable substrates with streamwise-preferential slip, e.g., those designed with longitudinal cylinders, are able to reduce skin-friction drag, for ℓ^+ values (i.e., grains' pitch in wall units) up to 20–30. The drag increase over spanwise-aligned inclusions (or streamwise-aligned ones at excessive ℓ^+) is accompanied by enhanced turbulence levels, including intensified sweep and ejection events. The r.m.s. fluctuations of the transpiration velocity at the porous/free-fluid interface, $\tilde{V}_{rms}$, is a key control parameter of the roughness function , ΔU^+, and analysis shows that $\tilde{V}_{rms}$ is strongly correlated to a single macroscopic quantity, Ψ, which comprises the Navier-slip and interface/intrinsic permeability coefficients. Fitting relationships for ΔU^+ are proposed, and their applicability is confirmed against reference results considering turbulence over impermeable walls roughened with three-dimensional protrusions or different geometries of riblets.

Finally, an upscaling approach was employed to study the flow through TPMS-based porous media, with conditions departing from Stokes behavior. Dependence of the average velocity on the macroscopic pressure gradient was properly described by a Darcy-like equation, with an "*effective*" permeability, H, strong function of the Reynolds number of the flow through the pores, Re. A closure problem was solved through a *representative elementary volume* of the medium to evaluate H for six types of TPMS-based media, varying the porosity (θ) and Re. Inertial effects were found to be significant; for instance, the permeability is reduced by $15 - 50\%$ (according to the surface type) as Re increases from 0 to 50000, when $\theta = 0.98$. A porous material formed by *Gyroid* cells is the most permeable at low porosities ($\theta < 0.7$), almost independently of Re, for all tested structures. Above $\theta = 0.7$, the largest permeability is displayed by a *Schwarz P*-based metamaterial.

REFERENCES

ABDERRAHAMAN-ELENA, N. & GARCÍA-MAYORAL, R. 2017 Analysis of anisotropically permeable surfaces for turbulent drag reduction. *Phys. Rev. Fluids* **2** (11), 114609.

ABIDI-SAAD, A., POLIDORI, G., KADJA, M., BEAUMONT, F., POPA, C.-V. & KORICHI, A. 2016 Experimental investigation of natural convection in a vertical rib-roughened channel with asymmetric heating. *Mech. Res. Commun.* **76**, 1–10.

ABOU-ALI, A.M., AL-KETAN, O., ROWSHAN, R. & ABU AL-RUB, R. 2019 Mechanical response of 3D printed bending-dominated ligament-based triply periodic cellular polymeric solids. *J. Mater. Eng. Perform.* **28** (4), 2316–2326.

AGNAOU, M., LASSEUX, D. & AHMADI, A. 2016 From steady to unsteady laminar flow in model porous structures: An investigation of the first Hopf bifurcation. *Comput. Fluids* **136**, 67–82.

AHMADI, M., MOSTAFAVI, G. & BAHRAMI, M. 2014 Natural convection from rectangular interrupted fins. *Intl J. Therm. Sci.* **82**, 62–71.

AHMED, E.N. 2023 Natural-convection heat transfer from regularly ribbed vertical surfaces: Homogenization-based simulations towards a correlation for the Nusselt number. *Numer. Heat Transfer A Appl.* **83** (9), 991–1013.

AHMED, E.N. & BOTTARO, A. 2023 Flow through porous metamaterials formed by TPMS-based unit cells: Effects of advection. *Eur. J. Mech. B/Fluids* **100**, 202–207.

AHMED, E.N. & BOTTARO, A. 2024 Laminar flow in a channel bounded by porous/rough walls: Revisiting Beavers-Joseph-Saffman. *Eur. J. Mech. B Fluids* **103**, 269–283.

AHMED, E.N. & BOTTARO, A. Draft, 2024 Exploring the nexus among roughness function, apparent slip velocity and upscaling coefficients for turbulent flows over porous/textured walls. *To Be Submitted To J. Fluid Mech.* .

AHMED, E.N., BOTTARO, A. & TANDA, G. 2022*a* A homogenization approach for buoyancy-induced flows over micro-textured vertical surfaces. *J. Fluid Mech.* **941**, A53.

AHMED, E.N., BOTTARO, A. & TANDA, G. 2024 Conjugate natural convection along regularly ribbed vertical surfaces: A homogenization-based study. *Numer. Heat Transfer A Appl.* **85** (9), 1331–1355.

AHMED, E.N., NAQVI, S.B., BUDA, L. & BOTTARO, A. 2022*b* A homogenization approach for turbulent channel flows over porous substrates: Formulation and implementation of effective boundary conditions. *Fluids* **7** (5), 178.

AHMED, E.N. & TANDA, G. 2024 An experimental and numerical study of laminar natural convection along vertical rib-roughened surfaces. *Intl. J. Heat Mass Transfer* **223**, 125227.

AL-KETAN, O., LEE, D.-W., ROWSHAN, R. & ABU AL-RUB, R.K. 2020 Functionally graded and multi-morphology sheet TPMS lattices: Design, manufacturing, and mechanical properties. *J. Mech. Behav. Biomed. Mater.* **102**, 103520.

ALI, D., OZALP, M., BLANQUER, S.B.G. & ONEL, S. 2020 Permeability and fluid flow-induced wall shear stress in bone scaffolds with TPMS and lattice architectures: A CFD analysis. *Eur. J. Mech. B Fluids* **79**, 376–385.

AMBROSINI, D. & TANDA, G. 2006 Comparative measurements of natural convection heat transfer in channels by holographic interferometry and schlieren. *Eur. J. Phys.* **27** (1), 159–172.

ANDERSON, R. & BOHN, M. 1986 Heat transfer enhancement in natural convection enclosure flow. *ASME J. Heat Transfer* **108** (2), 330–336.

ANTONIA, R.A., ZHU, Y. & SOKOLOV, M. 1995 Effect of concentrated wall suction on a turbulent boundary layer. *Phys. Fluids* **7** (10), 2465–2474.

ASBAI-GHOUDAN, R., RUIZ DE GALARRETA, S. & RODRIGUEZ-FLOREZ, N. 2021 Analytical model for the prediction of permeability of triply periodic minimal surfaces. *J. Mech. Behav. Biomed. Mater.* **124**, 104804.

AUDUNSON, T. & GEBHART, B. 1976 Secondary mean motions arising in a buoyancy induced flow. *Intl J. Heat Mass Transfer* **19** (7), 737–750.

AURIAULT, J.-L. 2010 About the Beavers and Joseph boundary condition. *Transp. Porous Med.* **83** (2), 257–266.

AZEVEDO, L.F.A. & SPARROW, E.M. 1985 Natural convection in open-ended inclined channels. *ASME J. Heat Transfer* **107** (4), 893–901.

BABUŠKA, I. 1976 Homogenization and its application. Mathematical and computational problems, in: Hubbard, B. (Ed.), *Numerical Solution of Partial Differential Equations–III*, pp. 89–116. Academic Press .

BEAVERS, G.S. & JOSEPH, D.D. 1967 Boundary conditions at a naturally permeable wall. *J. Fluid Mech.* **30** (1), 197–207.

BEAVERS, G.S., SPARROW, E.M. & MAGNUSON, R.A. 1970 Experiments on coupled parallel flows in a channel and a bounding porous medium. *J. Basic Eng.* **92** (4), 843–848.

BECHERT, D.W. & BARTENWERFER, M. 1989 The viscous flow on surfaces with longitudinal ribs. *J. Fluid Mech.* **206**, 105–129.

BECHERT, D.W., BRUSE, M., HAGE, W., VAN DER HOEVEN, J.G.T. & HOPPE, G. 1997 Experiments on drag-reducing surfaces and their optimization with an adjustable geometry. *J. Fluid Mech.* **338**, 59–87.

BEHNIA, M. & DEHGHAN, A.A. 1998 A numerical study of natural convection immersion cooling of multiple heat sources parallel interacting open-top cavities. *Intl J. Heat Mass Transfer* **41** (4-5), 797–808.

BEJAN, A. 1993 *Heat Transfer*. New York, NY, USA: Wiley.

BEJAN, A. & LAGE, J.L. 1990 The Prandtl number effect on the transition in natural convection along a vertical surface. *ASME. J. Heat Transfer* **112** (3), 787–790.

BERNARD, P.S., THOMAS, J.M. & HANDLER, R.A. 1993 Vortex dynamics and the production of Reynolds stress. *J. Fluid Mech.* **253**, 385–419.

BHAVNANI, S.H. & BERGLES, A.E. 1990 Effect of surface geometry and orientation on laminar natural convection heat transfer from a vertical flat plate with transverse roughness elements. *Intl J. Heat Mass Transfer* **33** (5), 965–981.

BHAVNANI, S.H. & BERGLES, A.E. 1991 Natural convection heat transfer from sinusoidal wavy surfaces. *Wärme-Stoffübertrag.* **26** (6), 341–349.

BOBBERT, F.S.L., LIETAERT, K., EFTEKHARI, A.A., POURAN, B., AHMADI, S.M., WEINANS, H. & ZADPOOR, A.A. 2017 Additively manufactured metallic porous biomaterials based on minimal surfaces: A unique combination of topological, mechanical, and mass transport properties. *Acta Biomater.* **53**, 572–584.

BOHN, M. & ANDERSON, R. 1984 Heat-transfer enhancement in natural convection enclosure flow. *Solar Energy Research Institute,* Golden, CO, USA, Report No. SERI/TR–252-2103 .

BONATTI, C. & MOHR, D. 2019 Smooth-shell metamaterials of cubic symmetry: Anisotropic elasticity, yield strength and specific energy absorption. *Acta Mater.* **164**, 301–321.

BOTTARO, A. 2019 Flow over natural or engineered surfaces: an adjoint homogenization perspective. *J. Fluid Mech.* **877**, P1.

BOTTARO, A. & NAQVI, S.B. 2020 Effective boundary conditions at a rough wall: a high-order homogenization approach. *Meccanica* **55** (9), 1781–1800.

BRAKKE, K.A. 1992 The surface evolver. *Exp. Math.* **1** (2), 141–165.

BREUGEM, W.P., BOERSMA, B.J. & UITTENBOGAARD, R.E. 2006 The influence of wall permeability on turbulent channel flow. *J. Fluid Mech.* **562**, 35–72.

BUDA, L. 2021 Drag reduction over rough permeable surfaces: A homogenized-based approach. Master's Thesis in Physics, University of Genoa, Italy. Available at http://www.dicat.unige.it/bottaro/Presentation%20group/Thesis_Buda.pdf.

BUNKER, R.S. & DONNELLAN, K.F. 2003 Heat transfer and friction factors for flows inside circular tubes with concavity surfaces. *ASME J. Turbomach.* **125** (4), 665–672.

CANTWELL, B.J. 1981 Organized motion in turbulent flow. *Annu. Rev. Fluid Mech.* **13** (1), 457–515.

CAVAZZUTI, M. & CORTICELLI, M.A. 2008 Optimization of a buoyancy chimney with a heated ribbed wall. *Heat Mass Transfer* **44** (4), 421–435.

CHANDESRIS, M., D'HUEPPE, A., MATHIEU, B., JAMET, D. & GOYEAU, B. 2013 Direct numerical simulation of turbulent heat transfer in a fluid-porous domain. *Phys. Fluids* **25** (12), 125110.

CHEESEWRIGHT, R. 1968 Turbulent natural convection from a vertical plane surface. *ASME J. Heat Transfer* **90** (1), 1–6.

CHEN, Z., XIE, Y.M., WU, X., WANG, Z., LI, Q. & ZHOU, S. 2019 On hybrid cellular materials based on triply periodic minimal surfaces with extreme mechanical properties. *Mater. Des.* **183**, 108109.

CHENG, X.Q., WONG, C.W., HUSSAIN, F., SCHRÖDER, W. & ZHOU, Y. 2021 Flat plate drag reduction using plasma-generated streamwise vortices. *J. Fluid Mech.* **918**.

CHOI, K.S. 2002 Near-wall structure of turbulent boundary layer with spanwise-wall oscillation. *Phys. Fluids* **14** (7), 2530–2542.

CHURCHILL, S.W. & CHU, H.H.S. 1975 Correlating equations for laminar and turbulent free convection from a vertical plate. *Intl J. Heat Mass Transfer* **18** (11), 1323–1329.

CHYU, M.K., OLUYEDE, E.O. & MOON, H.-K. 2007 Heat transfer on convective surfaces with pin-fins mounted in inclined angles. *Turbo Expo: Power for Land, Sea, Air* **4**, 861–869.

DESRAYAUD, G. & FICHERA, A. 2002 Laminar natural convection in a vertical isothermal channel with symmetric surface-mounted rectangular ribs. *Intl J. Heat Fluid Flow* **23** (4), 519–529.

DEVIA, F., MILANO, G. & TANDA, G. 1994 Evaluation of thermal field in buoyancy-induced flows by a schlieren method. *Exp. Therm. Fluid Sci.* **8** (1), 1–9.

DEVIA, F. & TANDA, G. 2000 Investigation of natural convection heat transfer from a horizontal isothermal plate by schlieren tomography. *Heat Technol.* **18** (1), 41–46.

VON DEYN, L.H., GATTI, D. & FROHNAPFEL, B. 2022 From drag-reducing riblets to drag-increasing ridges. *J. Fluid Mech.* **951**, A16.

DRING, R.P. & GEBHART, B. 1968 A theoretical investigation of disturbance amplification in external laminar natural convection. *J. Fluid Mech.* **34** (3), 551–564.

ECKERT, E.R.G. & JACKSON, T.W. 1950 Analysis of turbulent free-convection boundary layer on flat plate. *NACA-TN-2207* .

EGGENWEILER, E. & RYBAK, I. 2020 Unsuitability of the Beavers–Joseph interface condition for filtration problems. *J. Fluid Mech.* **892**, A10.

EGGENWEILER, E. & RYBAK, I. 2021 Effective coupling conditions for arbitrary flows in Stokes–Darcy systems. *Multiscale Model. Simul.* **19** (2), 731–757.

EL GHANDOURI, I., EL MAAKOUL, A., SAADEDDINE, S. & MEZIANE, M. 2020 Design and numerical investigations of natural convection heat transfer of a new rippling fin shape. *Appl. Therm. Eng.* **178**, 115670.

EL-SAMNI, O.A., CHUN, H.H. & YOON, H.S. 2007 Drag reduction of turbulent flow over thin rectangular riblets. *Intl. J. Eng. Sci.* **45** (2–8), 436–454.

ENDRIKAT, S., MODESTI, D., GARCÍA-MAYORAL, R., HUTCHINS, N. & CHUNG, D. 2021*a* Influence of riblet shapes on the occurrence of Kelvin–Helmholtz rollers. *J. Fluid Mech.* **913**, A37.

ENDRIKAT, S., MODESTI, D., MACDONALD, M., GARCÍA-MAYORAL, R., HUTCHINS, N. & CHUNG, D. 2021*b* Direct numerical simulations of turbulent flow over various riblet shapes in minimal-span channels. *Flow Turbul. Combust.* **107** (1), 1–29.

ESTEBAN, L.B., RODRÍGUEZ-LÓPEZ, E., FERREIRA, M.A. & GANAPATHISUBRAMANI, B. 2022 Mean flow of turbulent boundary layers over porous substrates. *Phys. Rev. Fluid* **7** (9), 094603.

FENG, J., FU, J., SHANG, C., LIN, Z. & LI, B. 2019 Sandwich panel design and performance optimization based on triply periodic minimal surfaces. *Comput. Aided Des.* **115**, 307–322.

FENG, J., FU, J., YAO, X. & HE, Y. 2022 Triply periodic minimal surface (TPMS) porous structures: from multi-scale design, precise additive manufacturing to multidisciplinary applications. *Intl J. Extrem. Manuf.* **4** (2), 022001.

FUJII, T., FUJII, M. & TAKEUCHI, M. 1973 Influence of various surface roughness on the natural convection. *Intl J. Heat Mass Transfer* **16** (3), 629–636.

GADO, M.G., OOKAWARA, S. & HASSAN, H. 2023 Utilization of triply periodic minimal surfaces for performance enhancement of adsorption cooling systems: Computational fluid dynamics analysis. *Energy Convers. Manag.* **277**, 116657.

GANDY, P.J.F., BARDHAN, S., MACKAY, A.L. & KLINOWSKI, J. 2001 Nodal surface approximations to the P,G,D and I-WP triply periodic minimal surfaces. *Chem. Phys. Lett.* **336** (3), 187–195.

GANDY, P.J.F., CVIJOVIĆ, D., MACKAY, A.L. & KLINOWSKI, J. 1999 Exact computation of the triply periodic D ('diamond') minimal surface. *Chem. Phys. Lett.* **314** (5), 543–551.

GARCIA-MAYORAL, R. & JIMÉNEZ, J. 2011 Drag reduction by riblets. *Philos. Trans. Royal Soc. A* **369** (1940), 1412–1427.

GARCIA-MAYORAL, R. & JIMENEZ, J. 2011 Hydrodynamic stability and breakdown of the viscous regime over riblets. *J. Fluid Mech.* **678**, 317–347.

GATTI, D., VON DEYN, L., FOROOGHI, P. & FROHNAPFEL, B. 2020 Do riblets exhibit fully rough behaviour? *Exp. Fluids* **61** (3), 81.

GEBHART, B. 1969 Natural convection flow, instability, and transition. *ASME J. Heat Transfer* **91** (3), 293–309.

GENOT, M. 1982 Thermal architecture made with specific components, session PII: components manufacturing technologies pp. 377–803.

GILANI, S.E., AL-KAYIEM, H.H., WOLDEMICHEAL, D.E. & GILANI, S.I. 2017 Performance enhancement of free convective solar air heater by pin protrusions on the absorber. *Sol. Energy* **151**, 173–185.

GODAUX, F. & GEBHART, B. 1974 An experimental study of the transition of natural convection flow adjacent to a vertical surface. *Intl J. Heat Mass Transfer* **17** (1), 93–107.

GOLDSTEIN, R.J. 1976 Optical techniques for temperature measurement, in: Eckert, E.R.G. & Goldstein, R.J. (Eds.), *Measurements in Heat Transfer*, 2nd ed. Washington, WA, USA: Hemisphere Publishing Corporation (Chapter 5) .

GRIFFITHS, E. & DAVIS, A.H. 1922 The transmission of heat by radiation and convection. *Br. Food Investig. Board,* Spec. Report 9, DSIR, London .

GUGLIELMINI, G., NANNEI, E. & TANDA, G. 1987 Natural convection and radiation heat transfer from staggered vertical fins. *Intl J. Heat Mass Transfer* **30** (9), 1941–1948.

GUO, H., BORODULIN, V.I., KACHANOV, Y.S., PAN, C., WANG, J.J., LIAN, Q.X. & WANG, S.F. 2010 Nature of sweep and ejection events in transitional and turbulent boundary layers. *J. Turbul.* **11**, N34.

HA, M. & GRAHAM, S. 2012 Development of a thermal resistance model for chip-on-board packaging of high power LED arrays. *Microelectron. Reliab.* **52** (5), 836–844.

HÆRVIG, J. & SØRENSEN, H. 2020 Natural convective flow and heat transfer on unconfined isothermal zigzag-shaped ribbed vertical surfaces. *Intl Commun. Heat Mass Transfer* **119**, 104982.

HAMPEL, C., CROWDER, H. & DILLON, H. 2019 Study of laminar natural convection of an isothermal vertical plate using schlieren photography and numerical methods. *Heat Transfer Res.* **50** (6), 565–580.

HAN, J.-C., DUTTA, S. & EKKAD, S. 2012 *Gas Turbine Heat Transfer and Cooling Technology*. CRC Press.

HARGATHER, M.J. & SETTLES, G.S. 2012 A comparison of three quantitative schlieren techniques. *Opt. Lasers Eng.* **50** (1), 8–17.

HAUF, W. & GRIGULL, U. 1970 Optical methods in heat transfer, in: Hartnett, J.P. & Irvine, T.F. (Eds.), *Adavances in Heat Transfer*: Elsevier, **6,** pp. 133–366 .

HAWKEN, M.B., REID, S., CLARKE, D.A., WATSON, M., FEE, C.J. & HOLLAND, D.J. 2023 Characterization of pressure drop through Schwarz-Diamond triply periodic minimal surface porous media. *Chem. Eng. Sci.* **280**, 119039.

HUNG, Y.H. & SHIAU, W.M. 1988 Local steady-state natural convection heat transfer in vertical parallel plates with a two-dimensional rectangular rib. *Intl J. Heat Mass Transfer* **31** (6), 1279–1288.

IMBRIALE, M., PANELLI, M. & CARDONE, G. 2012 Heat transfer enhancement of natural convection with ribs. *Quant. InfraRed Thermogr. J.* **9** (1), 55–67.

INCROPERA, F.P. 1988 Convection heat transfer in electronic equipment cooling. *ASME J. Heat Transfer* **110** (4b), 1097–1111.

JAIN, D.S., RAO, S.S. & SRIVASTAVA, A. 2016 Rainbow schlieren deflectometry technique for nanofluid-based heat transfer measurements under natural convection regime. *Intl J. Heat Mass Transfer* **98**, 697–711.

JEONG, J., HUSSAIN, F., SCHOPPA, W. & KIM, J. 1997 Coherent structures near the wall in a turbulent channel flow. *J. Fluid Mech.* **332**, 185–214.

JIMÉNEZ, J. 1994 On the structure and control of near wall turbulence. *Phys. Fluids* **6** (2), 944–953.

JIMÉNEZ, J. & PINELLI, A. 1999 The autonomous cycle of near-wall turbulence. *J. Fluid Mech.* **389**, 335–359.

JIMÉNEZ BOLAÑOS, S. & VERNESCU, B. 2017 Derivation of the Navier slip and slip length for viscous flows over a rough boundary. *Phys. of Fluids* **29** (5), 057103.

JOHNSON, C.E. 1986 Evaluation of correlations for natural convection cooling of electronic equipment. *Heat Transfer Eng.* **7** (1-2), 36–45.

JOSHI, Y., WILLSON, T. & HAZARD, S.J., III 1989 An experimental study of natural convection from an array of heated protrusions on a vertical surface in water. *ASME J. Electron. Packag.* **111** (2), 121–128.

KANG, S. & CHOI, H. 2000 Active wall motions for skin-friction drag reduction. *Phys. Fluids* **12** (12), 3301–3304.

KAPFER, S.C., HYDE, S.T., MECKE, K., ARNS, C.H. & SCHRÖDER-TURK, G.E. 2011 Minimal surface scaffold designs for tissue engineering. *Biomaterials* **32** (29), 6875–6882.

KARAKOÇ, A. 2021 RegionTPMS—Region based triply periodic minimal surfaces (TPMS) for 3-D printed multiphase bone scaffolds with exact porosity values. *SoftwareX* **16**, 100835.

KATO, H., NISHIWAKI, N. & HIRATA, M. 1968 On the turbulent heat transfer by free convection from a vertical plate. *Intl J. Heat Mass Transfer* **11** (7), 1117–1125.

KHALIL, M., HASSAN ALI, M.I., KHAN, K.A. & ABU AL-RUB, R. 2022 Forced convection heat transfer in heat sinks with topologies based on triply periodic minimal surfaces. *Case Stud. Therm. Eng.* **38**, 102313.

KIM, J., KIM, K. & SUNG, H.J. 2003 Wall pressure fluctuations in a turbulent boundary layer after blowing or suction. *AIAA J.* **41** (9), 1697–1704.

KISHINAMI, K., SAITO, H. & TOKURA, I. 1990 An experimental study on natural convective heat transfer from a vertical wavy surface heated at convex/concave elements. *Exp. Therm. Fluid Sci.* **3** (3), 305–315.

KLEINE, H., GRÖNIG, H. & TAKAYAMA, K. 2006 Simultaneous shadow, schlieren and interferometric visualization of compressible flows. *Opt. Lasers Eng.* **44** (3–4), 170–189.

KLINE, S.J., REYNOLDS, W.C., SCHRAUB, F.A. & RUNSTADLER, P.W. 1967 The structure of turbulent boundary layers. *J. Fluid Mech.* **30** (4), 741–773.

KUWATA, Y. & SUGA, K. 2017 Direct numerical simulation of turbulence over anisotropic porous media. *J. Fluid Mech.* **831**, 41–71.

LĀCIS, U., SUDHAKAR, Y., PASCHE, S. & BAGHERI, S. 2020 Transfer of mass and momentum at rough and porous surfaces. *J. Fluid Mech.* **884**, A21.

LARSON, R.E. & HIGDON, J.J.L. 1986 Microscopic flow near the surface of two-dimensional porous media. Part 1. Axial flow. *J. Fluid Mech.* **166**, 449–472.

LASSEUX, D., ABBASIAN ARANI, A.A. & AHMADI, A. 2011 On the stationary macroscopic inertial effects for one phase flow in ordered and disordered porous media. *Phys. Fluids* **23** (7), 073103.

LE FEVRE, E.J. 1956 Laminar free convection from a vertical plane surface. In *the 9th Intl Congr. Appl. Mech.,* Brussels.

LEHDER, E.F., ASHCROFT, I.A., WILDMAN, R.D., RUIZ-CANTU, L.A. & MASKERY, I. 2021 A multiscale optimisation method for bone growth scaffolds based on triply periodic minimal surfaces. *Biomech. Model Mechanobiol.* **20** (6), 2085–209.

LI, W., LI, W. & YU, Z. 2022 Heat transfer enhancement of water-cooled triply periodic minimal surface heat exchangers. *Appl. Therm. Eng.* **217**, 119198.

LIENHARD, J.H., IV & LIENHARD, J.H., V 2019 *A Heat Transfer Textbook,* 5th ed. Cambridge, MA, USA: Phlogiston Press.

LIN, C., WEN, G., YIN, H., WANG, Z.-P., LIU, J. & XIE, Y. M. 2022 Revealing the sound insulation capacities of TPMS sandwich panels. *J. Sound Vib.* **540**, 117303.

LIU, Q. & PROSPERETTI, A. 2011 Pressure-driven flow in a channel with porous walls. *J. Fluid Mech.* **679**, 77–100.

LU, J.-Y., T., SILVA, F., ALZAABI, R.K., ABU AL-RUB & D.-W., LEE 2023 Insights into acoustic properties of seven selected triply periodic minimal surfaces-based structures: A numerical study. *J. Low Freq. Noise Vib. Act. Control* (online at https://doi.org/10.1177/146134842311909).

LUCHINI, P., MANZO, F. & POZZI, A. 1991 Resistance of a grooved surface to parallel flow and cross-flow. *J. Fluid Mech.* **228**, 87–109.

LUO, J.-W., CHEN, L., MIN, T., SHAN, F., KANG, Q. & TAO, W. 2020 Macroscopic transport properties of Gyroid structures based on pore-scale studies: Permeability, diffusivity and thermal conductivity. *Intl J. Heat Mass Transfer* **146**, 118837.

MAHAJAN, R.L. & GEBHART, B. 1979 An experimental determination of transition limits in a vertical natural convection flow adjacent to a surface. *J. Fluid Mech.* **91** (1), 131–154.

MAHFOZE, O. & LAIZET, S. 2017 Skin-friction drag reduction in a channel flow with streamwise-aligned plasma actuators. *Intl J. Heat Fluid Flow* **66**, 83–94.

MANES, C., POGGI, D. & RIDOLFI, L. 2011 Turbulent boundary layers over permeable walls: scaling and near-wall structure. *J. Fluid Mech.* **687**, 141–170.

MANSOUR, N.N., KIM, J. & MOIN, P. 1988 Reynolds-stress and dissipation-rate budgets in a turbulent channel flow. *J. Fluid Mech.* **194**, 15–44.

MERZKIRCH, W. 1974 *Flow Visualization*. Academic Press.

NAQVI, S.B. & BOTTARO, A. 2021 Interfacial conditions between a free-fluid region and a porous medium. *Intl J. Multiph. Flow* **141**, 103585.

NARENDRAN, N. & GU, Y. 2005 Life of LED-based white light sources. *IEEE/OSA J. Disp. Technol.* **1** (1), 167–170.

NAVIER, C. 1823 Mémoire sur les lois du mouvement des fluides. *Mém. Acad. R. Sci. Inst. France* **6**, 389–440.

NEALE, G. & NADER, W. 1974 Practical significance of Brinkman's extension of Darcy's law: Coupled parallel flows within a channel and a bounding porous medium. *Can. J. Chem. Eng.* **52** (4), 475–478.

NELSON, L., SEKHON, K. & FRITZ, J. 1978 Direct heat pipe cooling of semiconductor devices. In *the 3rd Int. Heat Pipe Conf.,* Palo Alto, California, USA. (doi: 10.2514/6.1978-450).

NGHANA, B., TARIKU, F. & BITSUAMLAK, G. 2022 Numerical assessment of the impact of transverse roughness ribs on the turbulent natural convection in a BIPV air channel. *Build. Environ.* **217**, 109093.

NIELD, D.A. 2009 The Beavers–Joseph boundary condition and related matters: A historical and critical note. *Transp. Porous Med.* **78** (3), 537–540.

NISHIKAWA, M., OTOMO, H., YOSHIDA, Y., DEGUCHI, J., TSUKAMOTO, M. & YAMAMOTO, T. 2020 The cooling mechanism of minuscule ribbed surfaces. *Sci. Rep.* **10** (1), 5635.

NISHIYAMA, Y., KUWATA, Y. & SUGA, K. 2020 Direct numerical simulation of turbulent heat transfer over fully resolved anisotropic porous structures. *Intl. J. Heat Fluid Flow* **81**, 108515.

OKTAY, S., HANNEMANN, R.J. & BAR-COHEN, A. 1986 High heat from a small package. *Mech. Eng.* **108** (3), 36–42.

ORLANDI, P. & JIMÉNEZ, J. 1994 On the generation of turbulent wall friction. *Phys. Fluids* **6** (2), 634–641.

ORLANDI, P. & LEONARDI, S. 2006 DNS of turbulent channel flows with two- and three-dimensional roughness. *J. Turbul.* **7**, N73.

ORLANDI, P. & LEONARDI, S. 2008 Direct numerical simulation of three-dimensional turbulent rough channels: parameterization and flow physics. *J. Fluid Mech.* **606**, 399–415.

ORLANDI, P., LEONARDI, S. & ANTONIA, R.A. 2006 Turbulent channel flow with either transverse or longitudinal roughness elements on one wall. *J. Fluid Mech.* **561**, 279–305.

PARK, K.-A. & BERGLES, A.E. 1987 Natural convection heat transfer characteristics of simulated microelectronic chips. *ASME J. Heat Transfer* **109** (1), 90–96.

PARK, S.-J., JANG, D., YOOK, S.-J. & LEE, K.-S. 2015 Optimization of a staggered pin-fin for a radial heat sink under free convection. *Intl J. Heat Mass Transfer* **87**, 184–188.

PETERSON, G.P. & ORTEGA, A. 1990 Thermal control of electronic equipment and devices. *Adv. Heat Transfer* **20**, 181–314.

PIATTI, C. 2023 Assessment of thermal-hydraulic performance of circular pipes equipped with Triply Periodic Minimal Surfaces. Master's Thesis in Energy and Nuclear Engineering, Polytechnic University of Turin, Italy .

RAFFEL, M. 2015 Background-oriented schlieren (BOS) techniques. *Exp. Fluids* **56** (3), 60.

RAITHBY, G.D. & HOLLANDS, K.G.T. 1985 Natural convection, in: Rohsenow, W.M., Hartnett, J.P. & Ganić, E.N. (Eds.), *Handbook of Heat Transfer Fundamentals*, 2nd ed. New York, NY, USA: McGraw Hill (Chapter 6). .

RASTEGARI, A. & AKHAVAN, R. 2015 On the mechanism of turbulent drag reduction with super-hydrophobic surfaces. *J. Fluid Mech.* **773**.

RATHORE, S.S., MEHTA, B., KUMAR, P. & ASFER, M. 2023*a* Flow characterization in triply periodic minimal surface (TPMS)-based porous geometries: Part 1—Hydrodynamics. *Transp. Porous Med.* **146** (3), 669–701.

RATHORE, S.S., MEHTA, B., KUMAR, P. & ASFER, M. 2023*b* Flow characterization in triply-periodic-minimal-surface (TPMS)-based porous geometries: Part 2—Heat transfer. *Transp. Porous Med.* (online at https://doi.org/10.1007/s11242-023-02036-x).

REZAPOURIAN, M., JASIUK, I., SAARNA, M. & HUSSAINOVA, I. 2023 Selective laser melted Ti6Al4V split-P TPMS lattices for bone tissue engineering. *Intl J. Mech. Sci.* **251**, 108353.

ROSTI, M.E., BRANDT, L. & PINELLI, A. 2018 Turbulent channel flow over an anisotropic porous wall–drag increase and reduction. *J. Fluid Mech.* **842**, 381–394.

ROSTI, M.E., CORTELEZZI, L. & QUADRIO, M. 2015 Direct numerical simulation of turbulent channel flow over porous walls. *J. Fluid Mech.* **784**, 396–442.

ROUHANA, R. 2022, Sep. 4 Generate gyroid structures using Matlab (Meshlab + FreeCAD conversion) [Video], YouTube. https://www.youtube.com/watch?v=uvCfVsFAcSw .

SAFFMAN, P.G. 1971 On the boundary condition at the surface of a porous medium. *Stud. Appl. Math.* **50** (2), 93–101.

SAHRAOUI, M. & KAVIANY, M. 1992 Slip and no-slip velocity boundary conditions at interface of porous, plain media. *Intl J. Heat Mass Transfer* **35** (4), 927–943.

SAUNDERS, O.A. 1936 The effect of pressure upon natural convection in air. *Proc. R. Soc.,* London 157A, 278 .

SAUNDERS, O.A. 1939 Natural convection in liquids. *Proc. R. Soc.,* London 172A, 55 .

SCHULZ, J.M., JUNNE, H., BÖHM, L. & KRAUME, M. 2020 Measuring local heat transfer by application of Rainbow Schlieren Deflectometry in case of different symmetric conditions. *Exp. Therm. Fluid Sci.* **110**, 109887.

GÓMEZ-DE SEGURA, G. & GARCÍA-MAYORAL, R. 2019 Turbulent drag reduction by anisotropic permeable substrates–analysis and direct numerical simulations. *J. Fluid Mech.* **875**, 124–172.

GÓMEZ-DE SEGURA, G., SHARMA, A. & GARCÍA-MAYORAL, R. 2018 Turbulent drag reduction using anisotropic permeable substrates. *Flow Turbul. Combust.* **100** (4), 995–1014.

SETTLES, G.S. 2018 Smartphone schlieren and shadowgraph imaging. *Opt. Lasers Eng.* **104**, 9–21.

STONE, H.A., STROOCK, A.D. & AJDARI, A. 2004 Engineering flows in small devices: Microfluidics towards a lab-on-a-chip. *Annu. Rev. Fluid Mech.* **36**, 381–411.

STROHBECK, P., EGGENWEILER, E. & RYBAK, I. 2023 A modification of the Beavers-Joseph condition for arbitrary flows to the fluid-porous interface. *Transp. Porous Med.* **147** (3), 605–628.

SUDHAKAR, Y., LĀCIS, U., PASCHE, S. & BAGHERI, S. 2021 Higher-order homogenized boundary conditions for flows over rough and porous surfaces. *Transp. Porous Med.* **136** (1), 1–42.

SUGA, K. 2016 Understanding and modelling turbulence over and inside porous media. *Flow Turbul. Combust.* **96** (3), 717–756.

SUGA, K., OKAZAKI, Y., HO, U. & KUWATA, Y. 2018 Anisotropic wall permeability effects on turbulent channel flows. *J. Fluid Mech.* **855**, 983–1016.

SUGA, K., TOMINAGA, S., MORI, M. & KANEDA, M. 2013 Turbulence characteristics in flows over solid and porous square ribs mounted on porous walls. *Flow Turbul. Combust.* **91** (1), 19–40.

SVEN 2023 stlwrite - write ASCII or Binary STL files. MATLAB Central File Exchange .

TANDA, G. 1993 Natural convection heat transfer from a staggered vertical plate array. *ASME J. Heat Transfer* **115** (4), 938–945.

TANDA, G. 1997 Natural convection heat transfer in vertical channels with and without transverse square ribs. *Intl J. Heat Mass Transfer* **40** (9), 2173–2185.

TANDA, G. 2008 Natural convective heat transfer in vertical channels with low-thermal-conductivity ribs. *Intl J. Heat Fluid Flow* **29** (5), 1319–1325.

TANDA, G. 2017 Experiments on natural convection in water-cooled ribbed channels with different aspect ratios. *Intl J. Heat Mass Transfer* **110**, 606–612.

TANDA, G., AHMED, E.N. & BOTTARO, A. 2023 Natural convection heat transfer from a ribbed vertical plate: Effect of rib size, pitch, and truncation. *Exp. Therm. Fluid Sci.* **145**, 110898.

TANDA, G., AHMED, E.N. & BOTTARO, A. (Submitted 2023) Experimental observations of the onset of unsteadiness for buoyant airflow along smooth and rough vertical isothermal walls. *Exp. Heat Transfer* .

TANDA, G. & DEVIA, F. 1998 Application of a schlieren technique to heat transfer measurements in free-convection. *Exp. Fluids* **24** (4), 285–290.

TANDA, G., FOSSA, M. & MISALE, M. 2014 Heat transfer measurements in water using a schlieren technique. *Intl J. Heat Mass Transfer* **71**, 451–458.

TILTON, N. & CORTELEZZI, L. 2006 The destabilizing effects of wall permeability in channel flows: A linear stability analysis. *Phys. Fluids* **18** (5), 051702.

TILTON, N. & CORTELEZZI, L. 2008 Linear stability analysis of pressure-driven flows in channels with porous walls. *J. Fluid Mech.* **604**, 411–445.

TSUJI, T. & NAGANO, Y. 1988 Characteristics of a turbulent natural convection boundary layer along a vertical flat plate. *Intl J. Heat Mass Transfer* **31** (8), 1723–1734.

TZANOS, C.P., TESSIER, J.H. & PEDERSEN, D.R. 1991 An optimization study for the reactor vessel auxiliary cooling system of a pool liquid-metal reactor. *Nucl. Technol.* **94** (1), 68–79.

VAFAI, K. & KIM, S.J. 1990 Fluid mechanics of the interface region between a porous medium and a fluid layer—an exact solution. *Intl J. Heat Fluid Flow* **11** (3), 254–256.

VALDÉS-PARADA, F.J. & LASSEUX, D. 2021*a* Flow near porous media boundaries including inertia and slip: A one-domain approach. *Phys. Fluids* **33** (7), 073612.

VALDÉS-PARADA, F.J. & LASSEUX, D. 2021*b* A novel one-domain approach for modeling flow in a fluid-porous system including inertia and slip effects. *Phys. Fluids* **33** (2), 022106.

VREMAN, A.W. & KUERTEN, J.G.M. 2014 Comparison of direct numerical simulation databases of turbulent channel flow at Re_τ= 180. *Phys. Fluids* **26** (1), 015102.

WALSH, M. & LINDEMANN, A. 1984 Optimization and application of riblets for turbulent drag reduction. In *the 22nd Aerosp. Sci. Meet.,* Reno, NV, USA. (doi: 10.2514/6.1984-347).

WANG, W., CHU, X., LOZANO-DURÁN, A., HELMIG, R. & WEIGAND, B. 2021 Information transfer between turbulent boundary layers and porous media. *J. Fluid Mech.* **920**, A21.

WANG, W., LOZANO-DURÁN, A., HELMIG, R. & CHU, X. 2022 Spatial and spectral characteristics of information flux between turbulent boundary layers and porous media. *J. Fluid Mech.* **949**, A16.

WARNER, C.Y. & ARPACI, V.S. 1968 An experimental investigation of turbulent natural convection in air at low pressure along a vertical heated flat plate. *Intl J. Heat Mass Transfer* **11** (3), 397–406.

WEBB, B.W. & HILL, D.P. 1989 High Rayleigh number laminar natural convection in an asymmetrically heated vertical channel. *ASME J. Heat Transfer* **111** (3), 649–656.

WHITAKER, S. 1996 The Forchheimer equation: A theoretical development. *Transp. Porous Media* **25** (1), 27–61.

WISE, D.J. & RICCO, P. 2014 Turbulent drag reduction through oscillating discs. *J. Fluid Mech.* **746**, 536–564.

WROBLEWSKI, D.E. & JOSHI, Y. 1994 Liquid immersion cooling of a subtrate-mounted protrusion in a three-dimensional enclosure: The effects of geometry and boundary conditions. *ASME J. Heat Transfer* **116** (1), 112–119.

YANG, S.-D., LEE, H.G. & KIM, J. 2010 A phase-field approach for minimizing the area of triply periodic surfaces with volume constraint. *Comput. Phys. Commun.* **181** (6), 1037–1046.

YANG, W., AN, J., CHUA, C.K. & ZHOU, K. 2020 Acoustic absorptions of multifunctional polymeric cellular structures based on triply periodic minimal surfaces fabricated by stereolithography. *Virtual Phys. Prototyp.* **15** (2), 242–249.

YAO, L.-S. 2006 Natural convection along a vertical complex wavy surface. *Intl J. Heat Mass Transfer* **49** (1-2), 281–286.

YIN, H., LIU, Z., DAI, J., WEN, G. & ZHANG, C. 2020 Crushing behavior and optimization of sheet-based 3D periodic cellular structures. *Compos. B. Eng.* **182**, 107565.

YOSHIDA, Y. 2018 Leg Product. *World Intellectual Patent Organization,* WO2018/070439 .

ZAMPOGNA, G.A. & BOTTARO, A . 2016 Fluid flow over and through a regular bundle of rigid fibres. *J. Fluid Mech.* **792**, 5–35.

ZAMPOGNA, G.A., MAGNAUDET, J. & BOTTARO, A. 2019 Generalized slip condition over rough surfaces. *J. Fluid Mech.* **858**, 407–436.

ZENG, C. & WANG, W. 2022 Modeling method for variable and isotropic permeability design of porous material based on TPMS lattices. *Tribol. Int.* **176**, 107913.

ZHANG, L., FEIH, S., DAYNES, S., CHANG, S., WANG, M.Y., WEI, J. & LU, W.F. 2018 Energy absorption characteristics of metallic triply periodic minimal surface sheet structures under compressive loading. *Addit. Manuf.* **23**, 505–515.

ZHAO, M., LI, Z. & CHUA, J.W. 2023 Enhanced energy-absorbing and sound-absorbing capability of functionally graded and helicoidal lattice structures with triply periodic minimal surfaces. *Intl J. Miner. Metall. Mater.* **30** (10), 1973–1985.

ZHOU, H., ZHAO, M., MA, Z., ZHANG, D.Z. & FU, G. 2020 Sheet and network based functionally graded lattice structures manufactured by selective laser melting: Design, mechanical properties, and simulation. *Intl J. Mech. Sci.* **175**, 105480.

ZOU, S., MU, Y., PAN, B., LI, G., SHAO, L., DU, J. & JIN, Y. 2022 Mechanical and biological properties of enhanced porous scaffolds based on triply periodic minimal surfaces. *Mater. Des.* **219**, 110803.

PUBLISHED/SUBMITTED/ONGOING PAPERS

PAPER B1

A homogenization approach for buoyancy-induced flows over micro-textured vertical surfaces [1,2]

Essam Nabil Ahmed[a], **Alessandro Bottaro**[a] and **Giovanni Tanda**[b]

[a] *DICCA, Università di Genova, via Montallegro 1, Genova, 16145, Italy*
[b] *DIME, Università di Genova, via Montallegro 1, Genova, 16145, Italy*

Asymptotic homogenization is employed to formulate upscaled *effective* boundary conditions at a smooth virtual surface for a natural-convection flow over a periodically-roughened vertical wall, to bypass the expensive numerical resolution of flow and temperature fields near and within wall corrugations. Microscale problems are found by expanding near-wall variables in terms of a small parameter ϵ, ratio between the microscopic and the macroscopic length scales. The expressions of the upscaled velocity and temperature boundary conditions are provided up to second-order accuracy in ϵ. The case of transverse square ribs is considered as a representative example. The classical Navier-slip condition for the streamwise and the spanwise velocity components is modified at second order by the gradient of the normal stress and the time-derivative of the shear stress. The streamwise slip velocity is additionally corrected by a buoyancy term at first order and a temperature-gradient term at second order. The normal velocity at the virtual surface appears only as a second-order transpiration condition. A Robin-like condition for the temperature is found, where the wall temperature is corrected with a temperature-gradient term representing thermal slip. The accuracy levels and the applicability range of the *effective* conditions to mimic the macroscopic flow behaviour are investigated under laminar flow conditions, in comparison to results of full feature-resolving simulations. A formal validity limit for the approximation is sought in terms of a single accuracy criterion (C) which combines the effects of the Grashof number and ribs' density. The introduced model is further tested on different rib geometries.

1 INTRODUCTION AND LITERATURE REVIEW

Natural convection over ribbed/finned surfaces is widely encountered in engineering applications, such as cooling of electronics and telecommunication devices, air solar collectors,

[1] Supplementary Material related to this manuscript is provided after the References.

[2] The Version of Record of this manuscript, together with the Supplementary Material, has been published and is available in: *Journal of Fluid Mechanics* **941** (2022) A53. https://doi.org/10.1017/jfm.2022.320

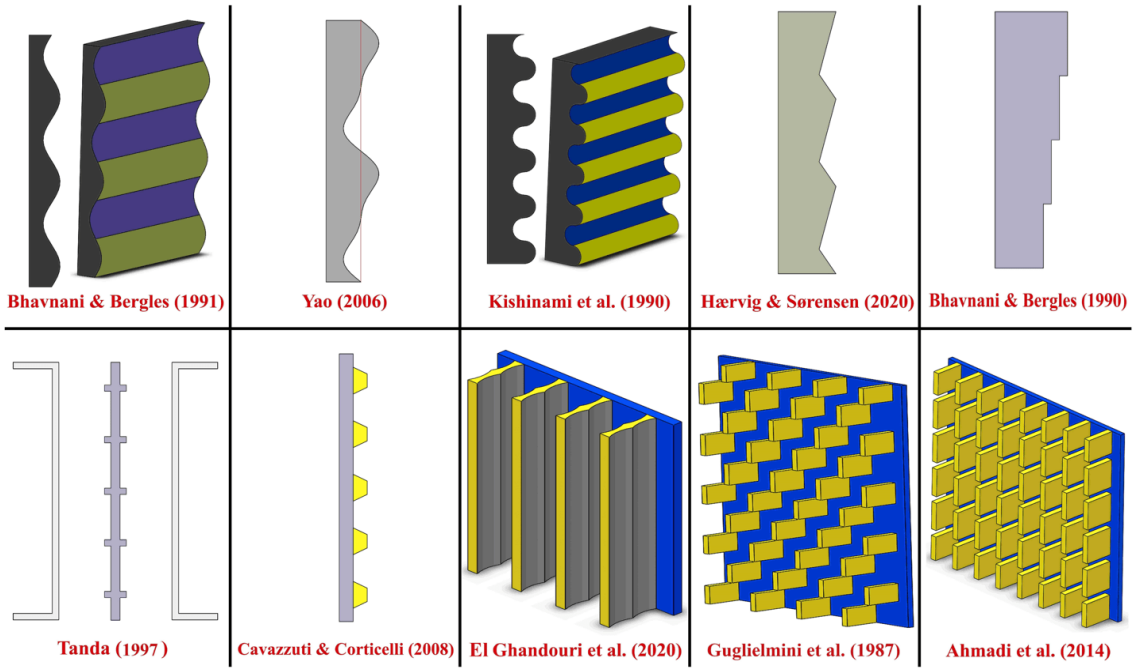

Figure 1: Schematic drawings of some surface alterations examined in the literature. The indicated geometries are (from top left to bottom right): sinusoidal waves (Bhavnani & Bergles, 1991), complex waves (Yao, 2006), convex-concave semi-circles (Kishinami *et al.*, 1990), zigzag shaping (Hærvig & Sørensen, 2020), steps (Bhavnani & Bergles, 1990); transverse square ribs (Tanda, 1997), transverse trapezoidal ribs (Cavazzuti & Corticelli, 2008), rippled vertical fins (El Ghandouri *et al.*, 2020), staggered arrangement of interrupted fins (Guglielmini *et al.*, 1987), in-line arrangement of interrupted fins (Ahmadi *et al.*, 2014).

and gas-cooled nuclear reactors. Compared with forced convection, a system that depends on the natural-convection heat transfer regime has lower initial and running costs, less noise and vibrations, higher reliability, almost maintenance-free operations, and better ability for use in hostile environments under dust, moist air, etc. On the other hand, the main problem facing designers is the low heat transfer coefficient of these systems. Due to the ever-growing trend of miniaturization of electronic components and the increase in power supply, higher heat generation rates per unit volume are encountered (Joshi *et al.*, 1989). This trend has stimulated many investigations to enhance natural-convection cooling systems so that they can be effective at handling operation requirements. One intuitively appealing solution to enhance the heat transfer performance of these systems is to apply some sort of alteration or disturbance on the heated surface(s) in analogy to the well-established concept of heat transfer promotion by adding ribs/fins to surfaces exposed to forced convection (Bunker & Donnellan, 2003; Chyu *et al.*, 2007; Han *et al.*, 2012). However, studies on the effectiveness of adding surface alterations (ribs, interrupted fins, dimples, etc.) to vertical plates exposed to natural convection have not led yet to convincing guidelines, with some researchers reporting an improvement of up to 200% compared to the performance of plane vertical plates, and others who have found them useless or even of negative influence to the local and averaged heat transfer parameters (Bhavnani & Bergles, 1990).

The need to better understand the interaction between the surface microstructure and the buoyancy-driven flow has motivated many experimental and numerical investigations to assess the usefulness and the feasibility of adding different types of protrusions to the heated surfaces in terms of their effects on the flow regime, the heat transfer characteristics, and the mass of the cooling modules. Examples of some surface alterations/extensions, considered in previous investigations, are displayed in Fig. 1, including periodic (wavy, rounded, zigzag) corrugations (Kishinami *et al.*, 1990; Bhavnani & Bergles, 1991; Yao, 2006; Hærvig & Sørensen, 2020), steps (Bhavnani & Bergles, 1990), two-dimensional ribs (Tanda, 1997; Cavazzuti & Corticelli, 2008), and different arrangements of fins (Guglielmini *et al.*, 1987; Ahmadi *et al.*, 2014; El Ghandouri *et al.*, 2020). Various experimental techniques have been adopted for mapping the thermal field to assess the detailed heat transfer performance. Two-dimensional and three-dimensional feature-resolving numerical simulations have also demonstrated to be powerful tools for the acquisition of large amounts of data on thermal fields and flow regimes, particularly for complex configurations (Yao, 2006; Cavazzuti & Corticelli, 2008; Ahmadi *et al.*, 2014; Hærvig & Sørensen, 2020).

Numerical work on flows over surfaces with complicated small-scale details including irregularities, roughness, porosity, etc. has been a challenge due to the high computational resources required to numerically discretize flow and temperature fields in the vicinity of the surface microstructures. In the present work, the multiscale homogenization approach is proposed to simplify the modelling of buoyancy-driven flows over periodically-roughened vertical surfaces, while maintaining an acceptable level of accuracy. Asymptotic homogenization is an approach which targets the study of the macroscale behaviour of a medium which contains microscopic details, by replacing the rapidly varying properties related to the heterogeneity of the medium by equivalent homogeneous macroscopic properties (Babuška, 1976). This technique can play a pivotal role when handling differential equations that govern physical problems with microscale fluctuations (Engquist & Souganidis, 2008) which are characterized by some sort of periodicity or pseudo-periodicity. These problems can be computationally simplified by first solving ad hoc auxiliary systems of equations in a microscopic domain to evaluate the necessary *upscaled* conditions by means of averaging. The approach relies on the asymptotic expansion of the dependent variables in terms of a wisely-chosen small parameter whose existence is related to the presence of well-separated scales, for instance a microscopic length scale (ℓ) and a macroscopic length scale ($L >> \ell$), so that the parameter $\epsilon = \frac{\ell}{L} << 1$ can be defined, and the solution of the problem can be sought up to different orders of accuracy in terms of ϵ.

Flow over micro-textured surfaces represents a typical homogenization problem. Jiménez Bolaños & Vernescu (2017) have derived the Navier-slip effective condition for the Stokes flow over a rough surface via homogenization theory as a first-order corrector term to the no-slip condition of a smooth surface. Zampogna *et al.* (2019*a*) have pursued a generalization of the classical first-order Navier-slip condition (Navier, 1823) over a rough surface by means of a third-order Navier-slip tensor. The homogenized model was pushed to second-order by Lācis *et al.* (2020) with the introduction of a transpiration

velocity, the normal velocity component at the fictitious interface, thus enhancing model predictions for a turbulent boundary layer over a rough surface. A further improvement has been added by Bottaro & Naqvi (2020) who sought a solution up to third-order accuracy. The range of applications subtended by homogenization theory is being continuously widened and enhancements to the basic formulation are ongoing. Zampogna *et al.* (2019*b*) have extended the theory to the study of the turbulent flow over compliant riblets, seeking reduction of the skin friction drag. *Adjoint* homogenization has been introduced by Bottaro (2019) as a method to take into account non-linear effects within the microscopic region.

The work presented in this paper is a novel implementation of the multiscale homogenization technique to study natural convection heat transfer over rough surfaces. The only previous contribution in this aspect was the work by Introïni *et al.* (2011) who applied the volume-averaging upscaling method to the study of the steady laminar buoyancy-driven flow over rough surfaces. However, their model suffered from some deficiencies that limit its applicability range. A critical assumption adopted by Introïni and collaborators was the neglect of buoyancy effects within the microscopic region, so that momentum and energy conservation equations are decoupled. This assumption, despite being mathematically advantageous, limits the model applicability to cases in which the Rayleigh number characterizing the microscopic problem (based on the microscopic length scale and the temperature difference across the microscopic region) is sufficiently small. To satisfy this condition, the bulk Rayleigh number must be lower than some threshold value, and the roughness elements must be confined within the thermal boundary layer. In practical situations, high values of the Rayleigh number are often encountered. Moreover, the model developed by Introïni *et al.* (2011) is only accurate to first-order in ϵ.

In this paper, asymptotic homogenization is used to formulate expressions for the macroscopic velocity and temperature effective conditions at a virtual interface separating the microscopic and the macroscopic sub-domains. Unlike Introïni *et al.* (2011), the Boussinesq approximation is employed for the buoyancy term in the microscopic momentum equation to be linearly coupled with the energy equation . The dependent parameters are expanded asymptotically in powers of the small parameter $\epsilon = \frac{pattern\ periodicity\ (\ell)}{plate\ length\ (L)}$. The effective conditions for velocity and temperature are all sought up to second-order accuracy. In the next section, the governing equations and the boundary conditions of the problem are outlined, and domain decomposition is explained. In Section 3, the microscopic region is considered where the asymptotic expansion of the dependent variables is defined, and the problem is reconstructed at different orders of ϵ. For each order, generic forms of the solutions are assumed and *auxiliary* differential systems are formulated. Then, the case of transverse square ribs is discussed in Section 4. The parameters of interest are determined via numerical solution of the auxiliary systems, and the effect of the matching surface location is considered. In Section 5, a parametric study seeking the effect of varying the rib size to the pitch distance ratio on the different coefficients is presented. In Section 6, the macroscale problem is considered by imposing the *upscaled* boundary conditions at a virtual vertical interface passing through the outer rims of the ribs; full feature-resolving simulations are also conducted to validate the predictions of

the model. In Section 7, the accuracy deterioration of the homogenized model is monitored with the increase of ϵ and/or the Grashof number, and the limit of validity of the approach is ascertained. Furthermore, the accuracy of the method is confirmed for different shapes of the roughness elements. In the concluding section, the main findings of the study are highlighted.

2 GOVERNING EQUATIONS AND DOMAIN DECOMPOSITION

2.1 The dimensional equations

As a major assumption, the changes in the density of the fluid are considered to only affect the buoyancy term in the momentum conservation equation. Under the Boussinesq approximation, the conservation equations in terms of the dimensional variables, space coordinates $\hat{x}_i$, time $\hat{t}$, pressure $\hat{P}$, velocity $\hat{u}_i$, and temperature $\hat{T}$, are expressed as follows:

$$\frac{\partial \hat{u}_i}{\partial \hat{x}_i} = 0, \tag{1-a}$$

$$\hat{\rho}_\infty \left(\frac{\partial \hat{u}_i}{\partial \hat{t}} + \hat{u}_j \frac{\partial \hat{u}_i}{\partial \hat{x}_j} \right) = -\frac{\partial (\hat{P} - \hat{P}_\infty)}{\partial \hat{x}_i} + \mu \frac{\partial^2 \hat{u}_i}{\partial \hat{x}_j^2} - \hat{\rho}_\infty \beta (\hat{T} - \hat{T}_\infty) g_i, \tag{1-b}$$

$$\frac{\partial \hat{T}}{\partial \hat{t}} + \hat{u}_j \frac{\partial \hat{T}}{\partial \hat{x}_j} = \alpha \frac{\partial^2 \hat{T}}{\partial \hat{x}_j^2}, \tag{1-c}$$

with $\hat{\rho}_\infty$, $\hat{P}_\infty$ and $\hat{T}_\infty$ the density, pressure and temperature in the stagnant flow region, sufficiently far away from the vertical wall. The parameters assumed constant in the equations above are the volumetric thermal expansion coefficient, β, the dynamic viscosity, $\mu = \hat{\rho}_\infty \nu$, with ν the kinematic viscosity, and the thermal diffusivity, α. With the axes as in Fig. 2, the volume force per unit mass has components $g_i = -g\,\delta_{i1}$ with g the acceleration of gravity and δ_{ij} the Kronecker index. The parameter controlling the thermal convection flow is the Rayleigh number Ra, defined as

$$Ra = \frac{g\beta(\hat{T}_w - \hat{T}_\infty)L^3}{\alpha\nu},$$

where the temperature of the wall, $\hat{T}_w$, is maintained constant, and the plate height, L, is the macroscopic length scale of the problem. We also define the Grashof number, $Gr = Ra/Pr$, with $Pr = \nu/\alpha$ the Prandtl number, a property of the fluid. Given the presence of two characteristic length scales, a macroscopic and a microscopic one, the latter related to the periodicity l of the microstructures present on the vertical surface, two problems will be set up. These two problems will be coupled at some distance from the wall, a distance that is asymptotically large when seen from the microscopic point of view and asymptotically small when seen from the macroscopic viewpoint.

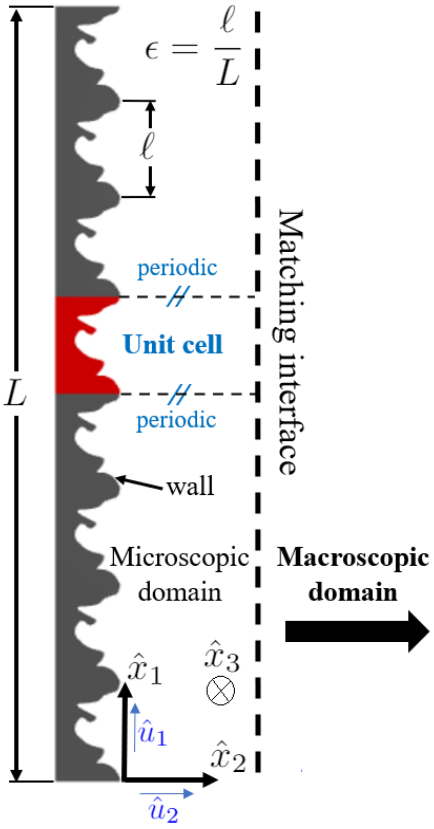

Figure 2: Sketch of a general vertical rough surface, periodically micro-patterned, with notations and indication of microscopic and macroscopic domains.

2.2 The macroscale problem

To set the proper scales of the macroscopic problem we consider the fact that the motion of the fluid is generated by the buoyancy force; if $\mathcal{U}$ is the characteristic velocity of the fluid, we can write

$$\frac{\hat{\rho}_\infty \mathcal{U}^2}{L} \sim \hat{\rho}_\infty \beta (\hat{T}_w - \hat{T}_\infty) g.$$

We thus define the velocity scale $\mathcal{U} = \sqrt{\beta(\hat{T}_w - \hat{T}_\infty) g L} = Gr^{1/2} \frac{\nu}{L}$ and normalize the velocity vector as:

$$U_i = \frac{\hat{u}_i}{\mathcal{U}}.$$

The other dimensionless variables are defined as follows:

$$X_i = \frac{\hat{x}_i}{L}, \qquad t = \frac{\hat{t}\mathcal{U}}{L}, \qquad P = \frac{\hat{P} - \hat{P}_\infty}{\hat{\rho}_\infty \mathcal{U}^2}, \qquad \Theta = \frac{\hat{T} - \hat{T}_\infty}{\hat{T}_w - \hat{T}_\infty},$$

for the balance equations to become:

$$\frac{\partial U_i}{\partial X_i} = 0, \tag{2-a}$$

$$\frac{\partial U_i}{\partial t} + U_j \frac{\partial U_i}{\partial X_j} = -\frac{\partial P}{\partial X_i} + \frac{1}{\sqrt{Gr}} \frac{\partial^2 U_i}{\partial X_j^2} + \Theta \delta_{i1}, \tag{2-b}$$

$$Pr\sqrt{Gr}\left(\frac{\partial \Theta}{\partial t} + U_j \frac{\partial \Theta}{\partial X_j}\right) = \frac{\partial^2 \Theta}{\partial X_j^2}. \tag{2-c}$$

These equations depend on only the macroscopic independent variables, t and X_i, and must be solved subject to matching conditions at $X_2 \to 0$, together with $\Theta = U_1 = 0$ and $\dfrac{\partial U_2}{\partial X_2} = 0$ for $X_2 \to \infty$.

2.3 The microscale problem

The near-wall problem differs from the previous one in that the microscopic velocity scale is taken to be $\epsilon\mathcal{U}$, with $\epsilon = \ell/L << 1$. Also, the pressure scale for the near-wall flow is the viscous pressure, i.e. $\mu\,(\epsilon\mathcal{U})/l$. Dimensionless variables in the microscopic domain are introduced as follows:

$$u_i = \frac{\hat{u}_i}{\epsilon\mathcal{U}}, \qquad x_i = \frac{\hat{x}_i}{l}, \qquad t = \frac{\hat{t}\,\mathcal{U}}{L}, \qquad p = \frac{(\hat{P} - \hat{P}_\infty)\,L}{\mu\,\mathcal{U}}, \qquad \theta = \frac{\hat{T} - \hat{T}_\infty}{\hat{T}_w - \hat{T}_\infty}.$$

The microscopic dimensionless equations are:

$$\frac{\partial u_i}{\partial x_i} = 0, \tag{3-a}$$

$$\epsilon\mathcal{R}_G\left(\frac{\partial u_i}{\partial t} + u_j \frac{\partial u_i}{\partial x_j}\right) = -\frac{\partial p}{\partial x_i} + \frac{\partial^2 u_i}{\partial x_j^2} + \mathcal{R}_G\,\theta\,\delta_{i1}, \tag{3-b}$$

$$\epsilon\mathcal{R}_G\,Pr\left(\frac{\partial \theta}{\partial t} + u_j \frac{\partial \theta}{\partial x_j}\right) = \frac{\partial^2 \theta}{\partial x_j^2}, \tag{3-c}$$

with the reduced Grashof number $\mathcal{R}_G$, defined by $\mathcal{R}_G = \epsilon\,\sqrt{Gr}$, assumed of order one. The microscale problem is bounded by the microstructured wall on one side; therefore, the following condition is imposed at this location.

$$u_i = 0, \quad \theta = 1 \qquad \text{for} \quad x_2 = y_w, \tag{3-d}$$

with $y_w = y_w\,(x_1, x_3)$ the micro-patterned wall. A *representative volume element* must be chosen, of unit length along x_1 and x_3 (cf. Fig. 2), and periodic conditions are enforced for all dependent variables along these directions. On account of the scalings adopted for inner (i.e., near-wall) and outer problems, the conditions for $x_2 \to \infty$ are:

$$-p\,\delta_{i2} + \left(\frac{\partial u_i}{\partial x_2} + \frac{\partial u_2}{\partial x_i}\right) = S_{i2}, \tag{3-e}$$

$$\frac{\partial \theta}{\partial x_2} = \epsilon\,\eta; \tag{3-f}$$

these amount to matching the components of the traction vector and of the heat flux between the two regions. For ease of notation in the equations above we have introduced the following definitions for the macroscopic dimensionless stresses in the streamwise, normal, and spanwise directions (respectively S_{12}, S_{22}, S_{32}) as well as the macroscopic dimensionless normal temperature gradient (η):

$$S_{i2} = -Gr^{1/2}\, P\, \delta_{i2} + \left(\frac{\partial U_i}{\partial X_2} + \frac{\partial U_2}{\partial X_i} \right),$$

$$\eta = \frac{\partial \Theta}{\partial X_2}.$$

Notice that both S_{i2} and η depend on only macroscopic variables; they represent the forcing of the outer flow on the near-wall state.

We still need to specify the asymptotic matching conditions which will eventually result in *effective boundary conditions* for the macroscopic problem, to be applied some distance from the microstructured wall. They are:

$$\lim_{X_2 \to 0} U_i = \lim_{x_2 \to \infty} \epsilon\, u_i, \tag{4-a}$$

$$\lim_{X_2 \to 0} \Theta = \lim_{x_2 \to \infty} \theta. \tag{4-b}$$

3 ASYMPTOTIC ANALYSIS OF THE MICROSCALE PROBLEM

3.1 Expansion of the inner variables

Asymptotic expansions in terms of the small parameter ϵ are introduced, and like-order terms are collected, leading to a hierarchy of problems. We impose:

$$u_i = u_i^{(0)} + \epsilon\, u_i^{(1)} + \epsilon^2\, u_i^{(2)} + ...,$$

and likewise for p and θ. Furthermore, using the chain rule, we replace in the microscopic equations the term $\dfrac{\partial}{\partial x_i}$ by $\dfrac{\partial}{\partial x_i} + \epsilon \dfrac{\partial}{\partial X_i}$. The asymptotic expressions are plugged into Eqs. (3-a to 3-f) governing the microscale problem.

3.2 Reconstruction of the problem at different orders

The problems at the asymptotic orders of interest are given below.

3.2.1 $\mathcal{O}(\epsilon^0)$ *problem*

$$\frac{\partial u_i^{(0)}}{\partial x_i} = 0, \tag{5-a}$$

$$-\frac{\partial p^{(0)}}{\partial x_i} + \frac{\partial^2 u_i^{(0)}}{\partial x_j^2} + \mathcal{R}_G\, \theta^{(0)}\, \delta_{i1} = 0, \tag{5-b}$$

$$\frac{\partial^2 \theta^{(0)}}{\partial x_j^2} = 0, \tag{5-c}$$

with boundary conditions

$$u_i^{(0)} = 0, \qquad \theta^{(0)} = 1 \qquad \text{at} \quad x_2 = y_w, \tag{5-d}$$

$$-p^{(0)}\, \delta_{i2} + \left(\frac{\partial u_i^{(0)}}{\partial x_2} + \frac{\partial u_2^{(0)}}{\partial x_i} \right) = S_{i2}, \qquad \frac{\partial \theta^{(0)}}{\partial x_2} = 0 \quad \text{for} \quad x_2 \to \infty. \tag{5-e}$$

A solution of this problem can be sought by separation of variables, on account of the linearity of the system, for the solution to take the form:

$$u_i^{(0)} = \breve{u}_{ik} S_{k2} + u_i^{\dagger} \mathcal{R}_G, \qquad p^{(0)} = \breve{p}_k S_{k2} + p^{\dagger} \mathcal{R}_G + P_0,$$

with $\breve{u}_{ik}$, $u_i^{\dagger}$, $\breve{p}_k$, and $p^{\dagger}$ tensors which depend on microscopic variables only, and P_0 an integration constant function only of X_j. After plugging the ansatz for the order zero solution into the balance equations, it becomes clear that uniqueness conditions are needed for $\breve{p}_k$ and $p^{\dagger}$, which appear in the system only through their gradients. We enforce the vanishing of the integrals of $\breve{p}_k$ and $p^{\dagger}$ over a cubic cell of unit side length positioned sufficiently far from the wall (nominally for $x_2 \to \infty$); this leads to the vanishing of P_0. It is also clear that we cannot stop the solution at this order, since the leading order temperature solution is simply $\theta^{(0)} = 1$, i.e. the effect of the microstructure appears in the temperature at the next ϵ-order.

The dynamic problem at $\mathcal{O}(\epsilon^0)$ yields the same equations for $\breve{u}_{ik}$ and $\breve{p}_k$ already given for the isothermal case by Bottaro & Naqvi (2020), so that we can anticipate that the first correction to the no-slip condition for the velocity will be a Navier-slip term. Such a leading-order problem reads:

$$\frac{\partial \breve{u}_{ik}}{\partial x_i} = 0, \tag{6-a}$$

$$-\frac{\partial \breve{p}_k}{\partial x_i} + \frac{\partial^2 \breve{u}_{ik}}{\partial x_j^2} = 0, \tag{6-b}$$

with

$$\breve{u}_{ik} = 0 \quad \text{at} \quad x_2 = y_w, \tag{6-c}$$

$$-\breve{p}_k\, \delta_{i2} + \left(\frac{\partial \breve{u}_{ik}}{\partial x_2} + \frac{\partial \breve{u}_{2k}}{\partial x_i} \right) = \delta_{ik} \quad \text{at} \quad x_2 \to \infty. \tag{6-d}$$

The † variables, which describe the effect of buoyancy on velocity and pressure fields, satisfy the steady system:

$$\frac{\partial u_i^\dagger}{\partial x_i} = 0, \tag{7-a}$$

$$-\frac{\partial p^\dagger}{\partial x_i} + \frac{\partial^2 u_i^\dagger}{\partial x_j^2} = -\delta_{i1}, \tag{7-b}$$

with

$$u_i^\dagger = 0 \quad \text{at} \quad x_2 = y_w, \tag{7-c}$$

$$-p^\dagger\,\delta_{i2} + \left(\frac{\partial u_i^\dagger}{\partial x_2} + \frac{\partial u_2^\dagger}{\partial x_i}\right) = 0 \quad \text{at} \quad x_2 \to \infty. \tag{7-d}$$

As it will be shown later on, the problems can be further simplified when x_3-elongated wall ribs are examined, as in the case of riblets (Bechert & Bartenwerfer, 1989; Luchini *et al.*, 1991).

3.2.2 $\mathcal{O}(\epsilon^1)$ *problem*

The equations at order ϵ are forced by the order one state, i.e.

$$\frac{\partial u_i^{(1)}}{\partial x_i} = -\frac{\partial u_i^{(0)}}{\partial X_i}, \tag{8-a}$$

$$-\frac{\partial p^{(1)}}{\partial x_i} + \frac{\partial^2 u_i^{(1)}}{\partial x_j^2} + \mathcal{R}_G\,\theta^{(1)}\,\delta_{i1} = \frac{\partial p^{(0)}}{\partial X_i} - 2\frac{\partial^2 u_i^{(0)}}{\partial x_j\,\partial X_j} + \mathcal{R}_G\left(\frac{\partial u_i^{(0)}}{\partial t} + u_j^{(0)}\frac{\partial u_i^{(0)}}{\partial x_j}\right), \tag{8-b}$$

$$\frac{\partial^2 \theta^{(1)}}{\partial x_j^2} = -2\frac{\partial^2 \theta^{(0)}}{\partial x_j\,\partial X_j} + \mathcal{R}_G\,Pr\left(\frac{\partial \theta^{(0)}}{\partial t} + u_j^{(0)}\frac{\partial \theta^{(0)}}{\partial x_j}\right), \tag{8-c}$$

with boundary conditions

$$u_i^{(1)} = \theta^{(1)} = 0 \quad \text{at} \quad x_2 = y_w, \tag{8-d}$$

$$-p^{(1)}\,\delta_{i2} + \left(\frac{\partial u_i^{(1)}}{\partial x_2} + \frac{\partial u_2^{(1)}}{\partial x_i}\right) = -\left(\frac{\partial u_i^{(0)}}{\partial X_2} + \frac{\partial u_2^{(0)}}{\partial X_i}\right) \quad \text{at} \quad x_2 \to \infty, \tag{8-e}$$

$$\frac{\partial \theta^{(1)}}{\partial x_2} = \eta - \frac{\partial \theta^{(0)}}{\partial X_2} \quad \text{at} \quad x_2 \to \infty. \tag{8-f}$$

We must now substitute the results for $u_i^{(0)}$, $p^{(0)}$, and $\theta^{(0)}$ into Eqs. (8-a to 8-f). As a first step, a solution for $\theta^{(1)}$ is to be sought from the energy equation and the corresponding boundary conditions. Specifically, these equations read:

$$\frac{\partial^2 \theta^{(1)}}{\partial x_i^2} = 0, \tag{9-a}$$

$$\theta^{(1)} = 0 \quad \text{at} \quad x_2 = y_w, \tag{9-b}$$

$$\frac{\partial \theta^{(1)}}{\partial x_2} = \eta \quad \text{at} \quad x_2 \to \infty. \tag{9-c}$$

Owing to linearity, the solution can be written as:

$$\theta^{(1)} = \tilde{\theta}(x_i)\ \eta(X_i) \tag{10}$$

The new microscopic field $\tilde{\theta}$ solves the system:

$$\frac{\partial^2 \tilde{\theta}}{\partial x_i^2} = 0, \tag{11-a}$$

$$\tilde{\theta} = 0 \quad \text{at} \quad x_2 = y_w, \tag{11-b}$$

$$\frac{\partial \tilde{\theta}}{\partial x_2} = 1 \quad \text{at} \quad x_2 \to \infty. \tag{11-c}$$

The equations governing the behaviour of $u_i^{(1)}$ and $p^{(1)}$ can be recast as follows:

$$\frac{\partial u_i^{(1)}}{\partial x_i} = -\breve{u}_{jk} \frac{\partial S_{k2}}{\partial X_j} \tag{12-a}$$

$$\begin{aligned} &-\frac{\partial p^{(1)}}{\partial x_i} + \frac{\partial^2 u_i^{(1)}}{\partial x_j^2} = \mathcal{R}_G^3 u_j^\dagger \frac{\partial u_i^\dagger}{\partial x_j} + \mathcal{R}_G^2 \left[\breve{u}_{jk} \frac{\partial u_i^\dagger}{\partial x_j} + u_j^\dagger \frac{\partial \breve{u}_{ik}}{\partial x_j} \right] S_{k2} \\ &+ \mathcal{R}_G \left[\breve{u}_{jk} \frac{\partial u_{i\ell}}{\partial x_j} \right] S_{k2} S_{\ell 2} + \mathcal{R}_G\, \breve{u}_{ik} \frac{\partial S_{k2}}{\partial t} - \mathcal{R}_G\, \eta\, \tilde{\theta}\, \delta_{i1} + \breve{p}_k \frac{\partial S_{k2}}{\partial X_i} - 2 \frac{\partial \breve{u}_{ik}}{\partial x_j} \frac{\partial S_{k2}}{\partial X_j}, \end{aligned} \tag{12-b}$$

with boundary conditions

$$u_i^{(1)} = 0 \quad \text{at} \quad x_2 = y_w, \tag{12-c}$$

$$\begin{aligned} &\frac{\partial u_1^{(1)}}{\partial x_2} + \frac{\partial u_2^{(1)}}{\partial x_1} = -\breve{u}_{1k} \frac{\partial S_{k2}}{\partial X_2} - \breve{u}_{2k} \frac{\partial S_{k2}}{\partial X_1}, \\ &-p^{(1)} + 2 \frac{\partial u_2^{(1)}}{\partial x_2} = -2 \breve{u}_{2k} \frac{\partial S_{k2}}{\partial X_2}, \\ &\frac{\partial u_3^{(1)}}{\partial x_2} + \frac{\partial u_2^{(1)}}{\partial x_3} = -\breve{u}_{3k} \frac{\partial S_{k2}}{\partial X_2} - \breve{u}_{2k} \frac{\partial S_{k2}}{\partial X_3} \quad \text{at} \quad x_2 \to \infty. \end{aligned} \tag{12-d}$$

Again, a generic form of the solution can sought, i.e.

$$\begin{aligned} u_i^{(1)} = {} & \dot{u}_{ijk} \left[\frac{\partial S_{k2}}{\partial X_j} \right] + \ddot{u}_{ik} \left[\mathcal{R}_G (S_{k2})^2 \right] + \ddot{u}_{i12} \left[\mathcal{R}_G S_{12} S_{22} \right] + \ddot{u}_{i13} \left[\mathcal{R}_G S_{12} S_{32} \right] \\ &+ \ddot{u}_{i23} \left[\mathcal{R}_G S_{22} S_{32} \right] + {u_i}' \left[\mathcal{R}_G\, \eta \right] + \overline{u}_{ik} \left[\mathcal{R}_G^2 S_{k2} \right] + u_i^{\ddagger} \left[\mathcal{R}_G^3 \right] + u_{ik}^t \left[\mathcal{R}_G \frac{\partial S_{k2}}{\partial t} \right], \end{aligned} \tag{13-a}$$

$$p^{(1)} = \dot{p}_{jk}\left[\frac{\partial S_{k2}}{\partial X_j}\right] + \ddot{p}_k\left[\mathcal{R}_G (S_{k2})^2\right] + \ddot{p}_{12}\left[\mathcal{R}_G S_{12} S_{22}\right] + \ddot{p}_{13}\left[\mathcal{R}_G S_{12} S_{32}\right]$$
$$+ \ddot{p}_{23}\left[\mathcal{R}_G S_{22} S_{32}\right] + p'\left[\mathcal{R}_G\,\eta\right] + \overline{p}_k\left[\mathcal{R}_G^2 S_{k2}\right] + p^{\ddagger}\left[\mathcal{R}_G^3\right] + p_k^t\left[\mathcal{R}_G \frac{\partial S_{k2}}{\partial t}\right]. \qquad \text{(13-b)}$$

Twenty-three decoupled systems of equations arise from substituting the preceding forms into Eqs. (12-a to 12-d). They are given in Appendix A.

3.2.3 *Taking the temperature condition to higher order*

Given that the macroscopic velocity at the matching surface is now available up to order ϵ^2 (cf. Eq. (4-a)), it is advisable to do the same with the temperature. Employing the values of the dependent variables at the earlier orders, the microscopic energy equation at $\mathcal{O}(\epsilon^2)$ now reads:

$$\frac{\partial^2 \theta^{(2)}}{\partial x_i^2} = Pr\mathcal{R}_G\left[\tilde{\theta}\,\frac{\partial \eta}{\partial t} + \breve{u}_{jk}\frac{\partial \tilde{\theta}}{\partial x_j}\eta\, S_{k2} + u_j^{\dagger}\frac{\partial \tilde{\theta}}{\partial x_j}\eta\,\mathcal{R}_G\right] - 2\frac{\partial \tilde{\theta}}{\partial x_j}\,\frac{\partial \eta}{\partial X_j}. \qquad \text{(14-a)}$$

The boundary conditions are:

$$\theta^{(2)} = 0 \qquad \text{at} \quad x_2 = y_w, \qquad \frac{\partial \theta^{(2)}}{\partial x_2} = -\tilde{\theta}\frac{\partial \eta}{\partial X_2} \qquad \text{at} \quad x_2 \to \infty. \qquad \text{(14-b)}$$

The following general form for the solution of $\theta^{(2)}$ may be assumed:

$$\theta^{(2)} = \theta_k^{!}\left[\frac{\partial \eta}{\partial X_k}\right] + \theta_k^{*}\left[Pr\mathcal{R}_G\,\eta S_{k2}\right] + \theta^{**}\left[Pr\mathcal{R}_G^2\,\eta\right] + \theta^{t}\left[Pr\,\mathcal{R}_G\frac{\partial \eta}{\partial t}\right]. \qquad (15)$$

Eight decoupled systems of equations stem from substituting the latter form into Eqs. (14-a and 14-b); they are provided in Appendix B.

4 THE CASE OF TRANSVERSE SQUARE RIBS

As an example of the implementation of the theory, the case of transverse square ribs is considered so that the auxiliary systems can be significantly simplified. In particular, because of invariance along x_3, all auxiliary problems simplify considerably (with derivatives $\partial/\partial x_3$ set to zero), and only two-dimensional Stokes-like (or Laplace-like, or Poisson-like) problems remain to be solved in the (x_1, x_2) plane, subject to periodic conditions along x_1. A sketch of the microscopic representative volume element is provided in Fig. 3. Some of the microscopic problems admit trivial solutions. For instance, it is easy to find that in the elementary cell it is $\breve{u}_{12} = \breve{u}_{22} = \breve{u}_{13} = \breve{u}_{23} = \breve{u}_{31} = \breve{u}_{32} = u_3^{\dagger} = 0$, plus $\breve{p}_2 = -1$ and $\breve{p}_3 = 0$. The systems which do not have a simple solution have been solved numerically by using the STAR-CCM+ multi-physics software (version 15.06.007-R8),

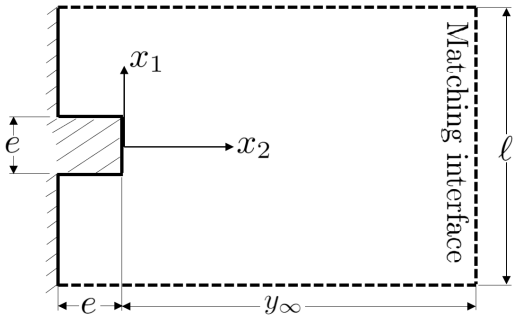

Figure 3: Sketch of a unit cell in the microscopic domain, indicating coordinates and geometric parameters.

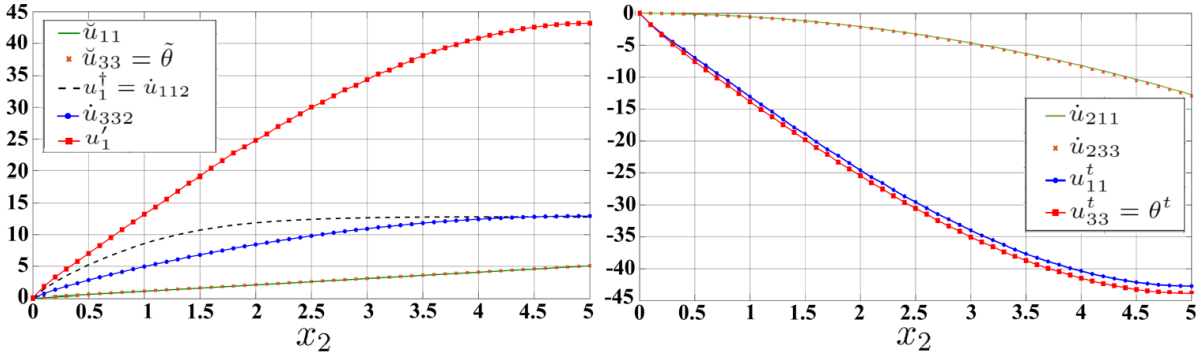

Figure 4: Behaviour of the parameters of interest along a line in the x_2-direction which goes through the middle of the rib ($x_1 = 0$ with reference to Fig. 3). The displayed numerical results are for the case $e/\ell = 0.25$ and $y_\infty = 5$.

by successfully refining the grid until fully grid-converged states are found, for varying dimensions of the cell along x_2. Detailed numerical results of the reduced auxiliary systems relative to the $\mathcal{O}(\epsilon^0)$, $\mathcal{O}(\epsilon^1)$ and $\mathcal{O}(\epsilon^2)$ problems are presented as *Supplementary Material*, for a rib size to periodicity ratio, e/l, equal to 0.25, and matching interface location positioned at $x_2 = y_\infty = 5$.

4.1 A synthesis of the microscopic results

The behaviours of the parameters of interest, those which contribute to the effective boundary conditions, are presented in Fig. 4, separating them into two groups according to their gradients in the x_2-direction (either positive or negative). At the matching interface ($x_2 = y_\infty = 5$), the variables contributing to the effective boundary conditions become independent of x_1 and take the following uniform values:

$$\breve{u}_{11} = 5.0396, \quad \breve{u}_{33} = \tilde{\theta} = 5.0861,$$

$$u_1^\dagger = \dot{u}_{112} = -\dot{u}_{211} = 12.7002, \quad \dot{u}_{332} = -\dot{u}_{233} = 12.9402,$$

$$u_1' = 43.0376, \quad u_{11}^t = -42.4485, \quad u_{33}^t = \theta^t = -43.8582.$$

4.2 Effects of varying the matching interface location

The effect of changing the matching surface distance, y_∞, on the values of the seven independent groups of effective parameters has been analyzed with the aid of successive numerical simulations, varying y_∞ from 2 to 6, as listed in Table 1.

Table 1: Microscopic results found at different values of y_∞ for square ribs with $e/\ell = 0.25$.

y_∞	$\breve{u}_{11}$	$\breve{u}_{33} = \tilde{\theta}$	$u_1^\dagger = \dot{u}_{112} = -\dot{u}_{211}$	$\dot{u}_{332} = -\dot{u}_{233}$	u_1'	u_{11}^t	$u_{33}^t = \theta^t$
2	2.0398	2.0861	2.0820	2.1818	2.8935	-2.8114	-3.0271
3	3.0397	3.0861	4.6213	4.7680	9.5340	-9.2334	-9.7986
4	4.0396	4.0861	8.1607	8.3541	21.8505	-21.5067	-22.7422
5	5.0396	5.0861	12.7002	12.9402	43.0376	-42.4485	-43.8582
6	6.0398	6.0861	18.2411	18.5264	74.2034	-72.2463	-75.1465
	Category (L) Linear relations		Category (Q) Quadratic relations		Category (C) Cubic relations		

An in-depth look into the table reveals that we have three categories of relations between the values of the microscopic parameters at the matching interface versus the location of the interface itself; specifically, linear, quadratic, and cubic relations. Fitting the results, we get the following expressions for the closure variables evaluated at y_∞:

$$\breve{u}_{11} = y_\infty + \lambda_x, \quad \breve{u}_{33} = \tilde{\theta} = y_\infty + \lambda_z,$$

$$u_1^\dagger = \dot{u}_{112} = -\dot{u}_{211} = \frac{y_\infty^2}{2} + \lambda_x y_\infty + m_{12}, \quad \dot{u}_{332} = -\dot{u}_{233} = \frac{y_\infty^2}{2} + \lambda_z y_\infty + m_{32},$$

$$u_1' = 2\left[\frac{y_\infty^3}{6} + m_{32}\, y_\infty^2 + \lambda_x\, y_\infty\right] + \mathcal{B}, \quad u_{11}^t = -2\left[\frac{y_\infty^3}{6} + m_{12}\, y_\infty^2 + \lambda_x\, y_\infty\right] + \mathcal{B}_{1t},$$

$$u_{33}^t = \theta^t = -2\left[\frac{y_\infty^3}{6} + \lambda_z\, \frac{y_\infty^2}{2} + m_{32}\, y_\infty\right] + \mathcal{B}_{3t}.$$

The dimensionless Navier-slip coefficients (λ_x, λ_z), surface permeability coefficients (m_{12}, m_{32}), velocity-flux sensitivity ($\mathcal{B}$), and time-fluctuations coefficients ($\mathcal{B}_{1t}$, $\mathcal{B}_{3t}$) are only dependent of the geometric parameters of the ribbed surface, e/ℓ in the case of square ribs. These coefficients can be calculated for any geometry of transverse ribs, once the microscopic numerical simulations are conducted with any suitable value of y_∞, and the results of the microscopic parameters at the matching interface are substituted in the fitting equations.

Simpler, accurate methods for the estimation of the coefficients of interest are proposed within the present framework. The Navier-slip coefficients can be calculated by

running the simulations of the leading-order systems, forced by S_{12} and S_{32}, with a suitable value of y_∞ to get, respectively, the fields of $\breve{u}_{11}$ and $\breve{u}_{33}$; thereafter, the values of λ_x and λ_z can be found by averaging the corresponding field on the plane $x_2 = 0$. It is interesting that these same fields can then be employed to estimate the values of m_{12} and m_{32}, making use of the numerical result pointed out by Bottaro & Naqvi (2020), i.e.

$$u_1^\dagger = \dot{u}_{112} = -\dot{u}_{211} = \int_{S_{\mathrm{cell}}} \breve{u}_{11}\,\mathrm{d}x_1\,\mathrm{d}x_2,$$
$$\dot{u}_{332} = -\dot{u}_{233} = \int_{S_{\mathrm{cell}}} \breve{u}_{33}\,\mathrm{d}x_1\,\mathrm{d}x_2,$$

with S_{cell} the surface of the representative near-wall cell. The following values of the coefficients eventually arise when $e/\ell = 0.25$:

$$\lambda_x = 0.03975, \quad \lambda_z = 0.08609, \quad m_{12} = 0.002332, \quad m_{32} = 0.009551,$$
$$\mathcal{B} = 0.0002399, \quad \mathcal{B}_{1t} = -0.0000839, \quad \mathcal{B}_{3t} = -0.0007794.$$

4.3 The formal expressions of the effective boundary conditions

The expressions of the microscopic dimensionless velocity components are now available up to $\mathcal{O}(\epsilon^1)$, while the microscopic dimensionless temperature (θ) is known up to $\mathcal{O}(\epsilon^2)$. The values of the preceding quantities can be linked to the corresponding dimensionless macroscopic parameters at the matching interface, based on the concept of continuity of velocity (Eq. (4-a)) and temperature (Eq. (4-b)). In particular, it is convenient to enforce the conditions on the outer rim of the ribs, which amounts to specifying $x_2 = \epsilon X_2 = 0$ in the matching relations (Eqs. (4-a, 4-b)), along with setting $y_\infty = 0$ in the fits of the microscopic parameters (given in Section 4.2) entering the effective boundary conditions. Eventually, we obtain:

$$U_1\big|_{X_2=0} = \epsilon\,[\lambda_x\,S_{12} + m_{12}\,\mathcal{R}_G]_{X_2=0} + \epsilon^2\left[m_{12}\,\frac{\partial S_{22}}{\partial X_1} + \mathcal{B}\,\mathcal{R}_G\frac{\partial \Theta}{\partial X_2} + \mathcal{B}_{1t}\mathcal{R}_G\frac{\partial S_{12}}{\partial t}\right]_{X_2=0} + \mathcal{O}(\epsilon^3), \tag{16-a}$$

$$U_2\big|_{X_2=0} = -\epsilon^2\left[m_{12}\,\frac{\partial S_{12}}{\partial X_1} + m_{32}\,\frac{\partial S_{32}}{\partial X_3}\right]_{X_2=0} + \mathcal{O}(\epsilon^3), \tag{16-b}$$

$$U_3\big|_{X_2=0} = \epsilon\,\lambda_z\,S_{32}\big|_{X_2=0} + \epsilon^2\left[m_{32}\,\frac{\partial S_{22}}{\partial X_3} + \mathcal{B}_{3t}\mathcal{R}_G\frac{\partial S_{32}}{\partial t}\right]_{X_2=0} + \mathcal{O}(\epsilon^3), \tag{16-c}$$

$$\Theta\big|_{X_2=0} = 1 + \epsilon\,\lambda_z\frac{\partial \Theta}{\partial X_2}\bigg|_{X_2=0} + \epsilon^2\,\mathcal{B}_{3t}\,\mathcal{R}_G\,Pr\,\frac{\partial^2\Theta}{\partial X_2\,\partial t}\bigg|_{X_2=0} + \mathcal{O}(\epsilon^3). \tag{16-d}$$

The no-slip conditions of the smooth surface are identically retrieved at $\mathcal{O}(\epsilon^0)$. The

effective conditions for velocity are similar to those given by Lācis *et al.* (2020) and Bottaro & Naqvi (2020) for flow over rough surfaces without heat transfer. Nevertheless, the presence of the buoyancy terms, proportional to $\mathcal{R}_G$ and $\mathcal{R}_G \frac{\partial \Theta}{\partial X_2}$ in the equation of the velocity component U_1, and of the time fluctuation terms in the equations of (U_1, U_3, Θ) should be highlighted. We emphasize that the presence of the buoyancy-related term is a first-order contribution to the effective condition for the streamwise velocity, $\hat{U}_1$, and is directly attributed to the assumption that the Grashof number is sufficiently large, i.e. $\epsilon \mathcal{R}_G = \epsilon^2 \sqrt{Gr}$ is of $\mathcal{O}(\epsilon^1)$, and not $\mathcal{O}(\epsilon^2)$.

In dimensional terms, the conditions on the plane $\hat{x}_2 = 0$ read

$$\begin{aligned}
\hat{u}_1\big|_{\hat{x}_2=0} \approx\ & \underbrace{\hat{\lambda}_x \left[\frac{\partial \hat{u}_1}{\partial \hat{x}_2} + \frac{\partial \hat{u}_2}{\partial \hat{x}_1}\right]_{\hat{x}_2=0} + \hat{m}_{12} \frac{\beta\, g\, (\hat{T}_w - \hat{T}_\infty)}{\nu}}_{First-order} \\
& + \underbrace{\hat{m}_{12} \left[\frac{\partial}{\partial \hat{x}_1}\left(-\frac{(\hat{p} - \hat{p}_\infty)}{\mu} + 2\frac{\partial \hat{u}_2}{\partial \hat{x}_2}\right)\right]_{\hat{x}_2=0} + \hat{\mathcal{B}} \frac{g\beta}{\nu} \frac{\partial \hat{T}}{\partial \hat{x}_2}\bigg|_{\hat{x}_2=0}}_{Second-order} \\
& + \underbrace{\hat{\mathcal{B}}_{1t} \frac{1}{\nu} \frac{\partial}{\partial \hat{t}} \left[\frac{\partial \hat{u}_1}{\partial \hat{x}_2} + \frac{\partial \hat{u}_2}{\partial \hat{x}_1}\right]_{\hat{x}_2=0}}_{Second-order}, \qquad \text{(17-a)}
\end{aligned}$$

$$\hat{u}_2\big|_{\hat{x}_2=0} \approx \underbrace{-\hat{m}_{12} \frac{\partial}{\partial \hat{x}_1} \left[\frac{\partial \hat{u}_1}{\partial \hat{x}_2} + \frac{\partial \hat{u}_2}{\partial \hat{x}_1}\right]_{\hat{x}_2=0} - \hat{m}_{32} \frac{\partial}{\partial \hat{x}_3} \left[\frac{\partial \hat{u}_3}{\partial \hat{x}_2} + \frac{\partial \hat{u}_2}{\partial \hat{x}_3}\right]_{\hat{x}_2=0}}_{Second-order}, \qquad \text{(17-b)}$$

$$\begin{aligned}
\hat{u}_3\big|_{\hat{x}_2=0} \approx\ & \underbrace{\hat{\lambda}_z \left[\frac{\partial \hat{u}_3}{\partial \hat{x}_2} + \frac{\partial \hat{u}_2}{\partial \hat{x}_3}\right]_{\hat{x}_2=0}}_{First-order} + \underbrace{\hat{m}_{32} \frac{\partial}{\partial \hat{x}_3} \left[-\frac{(\hat{p} - \hat{p}_\infty)}{\mu} + 2\frac{\partial \hat{u}_2}{\partial \hat{x}_2}\right]_{\hat{x}_2=0}}_{Second-order} \\
& + \underbrace{\hat{\mathcal{B}}_{3t} \frac{1}{\nu} \frac{\partial}{\partial \hat{t}} \left[\frac{\partial \hat{u}_3}{\partial \hat{x}_2} + \frac{\partial \hat{u}_2}{\partial \hat{x}_3}\right]_{\hat{x}_2=0}}_{Second-order}, \qquad \text{(17-c)}
\end{aligned}$$

$$\hat{T}\big|_{\hat{x}_2=0} \approx \underbrace{\hat{T}_w}_{Zero-order} + \underbrace{\hat{\lambda}_z \frac{\partial \hat{T}}{\partial \hat{x}_2}\bigg|_{\hat{x}_2=0}}_{First-order} + \underbrace{\hat{\mathcal{B}}_{3t} \frac{1}{\alpha} \frac{\partial^2 \hat{T}}{\partial \hat{x}_2\, \partial \hat{t}}\bigg|_{\hat{x}_2=0}}_{Second-order}. \qquad \text{(17-d)}$$

The dimensional groups of coefficients ($\hat{\lambda}_x$, $\hat{\lambda}_z$), ($\hat{m}_{12}$, $\hat{m}_{32}$) and ($\hat{\mathcal{B}}$, $\hat{\mathcal{B}}_{1t}$, $\hat{\mathcal{B}}_{3t}$) are homogeneous to, respectively, a length, a surface area and a volume, and correspond to the product of their dimensionless counterparts times, respectively, l, l^2 and l^3. The condi-

tions above represent the most important contribution of the present paper.

5 THE ROLE OF RIB HEIGHT TO PITCH DISTANCE RATIO: PARAMETRIC STUDY

From a practical point of view, it is advantageous to generate a database of the values of the seven dimensionless, geometry-dependent coefficients of interest, to cover a wide range of rib height to pitch distance ratios, e/l, in order to enable the direct use of the effective boundary conditions for the macroscopic problems. In this study, the ratio was varied within the range $0.025 \leq e/l \leq 0.8$. For each value of e/l, the procedure described in Section 4.2 for the accurate estimation of the coefficients was followed. The resulting database is presented in tabular form (Table 2) and graphically in Fig. 5. It is clear that all model coefficients peak, in magnitude, within the range $e/\ell = 0.1$ to 0.3, which implies significant velocity and thermal slip. All coefficients tend to zero as e tends to zero or approaches ℓ, for the effective boundary conditions at $x_2 = 0$ to become no-slip and isothermal wall.

Table 2: The upscaled coefficients of interest for different rib height to pitch distance ratios.

e/ℓ	$\boldsymbol{\lambda}_x$	$\boldsymbol{\lambda}_z$	$\boldsymbol{m}_{12}$	$\boldsymbol{m}_{32}$	$\boldsymbol{\mathcal{B}}$	$\boldsymbol{\mathcal{B}}_{1t}$	$\boldsymbol{\mathcal{B}}_{3t}$
0.025	0.02158	0.02296	0.000265	0.000286	0.0000041	-0.0000041	-0.0000046
0.050	0.03667	0.04215	0.000874	0.001037	0.0000270	-0.0000250	-0.0000320
0.075	0.04593	0.05757	0.001601	0.002120	0.0000710	-0.0000580	-0.0000920
0.100	0.05061	0.06949	0.002250	0.003384	0.0001280	-0.0000940	-0.0001850
0.125	0.05188	0.07822	0.002725	0.004716	0.0001855	-0.0001195	-0.0003000
0.150	0.05094	0.08400	0.002979	0.005999	0.0002290	-0.0001297	-0.0004237
0.175	0.04853	0.08738	0.003029	0.007184	0.0002550	-0.0001264	-0.0005449
0.200	0.04567	0.08859	0.002898	0.008188	0.0002651	-0.0001144	-0.0006477
0.225	0.04265	0.08803	0.002663	0.008976	0.0002578	-0.0000992	-0.0007269
0.250	0.03975	0.08609	0.002332	0.009551	0.0002399	-0.0000839	-0.0007794
0.275	0.03699	0.08302	0.002022	0.009892	0.0002171	-0.0000697	-0.0007982
0.300	0.03459	0.07921	0.001718	0.009987	0.0001912	-0.0000593	-0.0007870
0.350	0.03011	0.07011	0.001188	0.009600	0.0001430	-0.0000442	-0.0007011
0.400	0.02589	0.06023	0.000836	0.008612	0.0001024	-0.0000323	-0.0005671
0.500	0.01776	0.04155	0.000434	0.005803	0.0000417	-0.0000136	-0.0002944
0.600	0.01146	0.02624	0.000230	0.003128	0.0000132	-0.0000055	-0.0001188
0.700	0.00662	0.01453	0.000101	0.001326	0.0000041	-0.0000017	-0.0000364
0.800	0.00315	0.00642	0.000031	0.000391	0.0000009	-0.0000004	-0.0000072

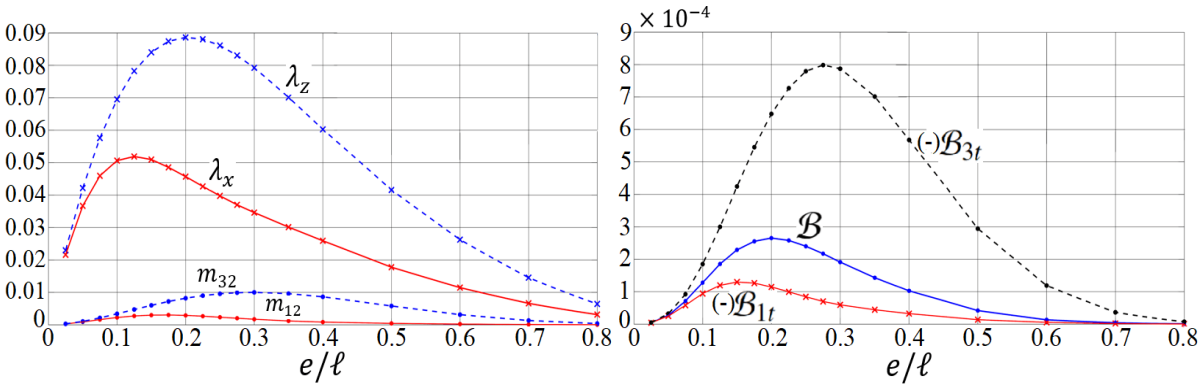

Figure 5: The behaviour of the upscaled coefficients of interest with the change of rib height to pitch distance ratio. The curves are fitted on the basis of kriging interpolation.

6 MACROSCALE BEHAVIOUR OF THE FLOW

In this section, attention is given to validation of the effective conditions obtained in Section 4, with the upscaled coefficients calculated for the case of square ribs. The macroscale problem is considered, with governing equations given in Section 2. Since the ribs are elongated in the transverse direction, and since only the case of laminar flow is considered, there is no need to resolve the spanwise direction; the problem can be simplified to its two-dimensional form in the (X_1, X_2) plane. In addition, steady-state solutions are targeted for validation purposes. Three types of simulations have been carried out: (i) natural convection over a vertical smooth surface; (ii) full feature-resolving natural convection over a vertical ribbed surface; (iii) homogenized problem with effective boundary conditions at a virtual wall. For each simulation, the computational domain, the boundary conditions, and the grid structure are explained in detail later in this section. As for the case of the microscopic problems, we have found it convenient to carry out the simulations with STAR-CCM+. The second-order upwind formulation has been adopted for the spatial discretization of all fields, with the calculation of the gradients based on a hybrid Gauss-least squares method. The SIMPLE scheme has been employed for the pressure-velocity coupling.

6.1 Isothermal vertical smooth surface case

A numerical calculation is first performed for a smooth isothermal surface at a plate Grashof number $Gr = 5.563 \times 10^8$ and a Prandtl number $Pr = 0.712$; this corresponds, for instance, to a buoyancy-driven air flow with $\hat{T}_\infty = 18\,^\circ C$, $\hat{T}_w = 58\,^\circ C$, $L = 0.5\,m$, and the fluid properties calculated at standard pressure and based on the film temperature $\hat{T}_f = \dfrac{\hat{T}_w + \hat{T}_\infty}{2}$. Different purposes are targeted from this step: (i) estimation of the adequacy of the computational domain; (ii) validation of the CFD numerical scheme and of the inlet/outlet boundary conditions by comparing the results with available databases

through the literature; (iii) the no-slip smooth surface case is equivalent to a homogenized simulation of the rough surface with zero-order effective conditions, so the results will help to monitor the accuracy enhancement when progressively higher-order approximations are used.

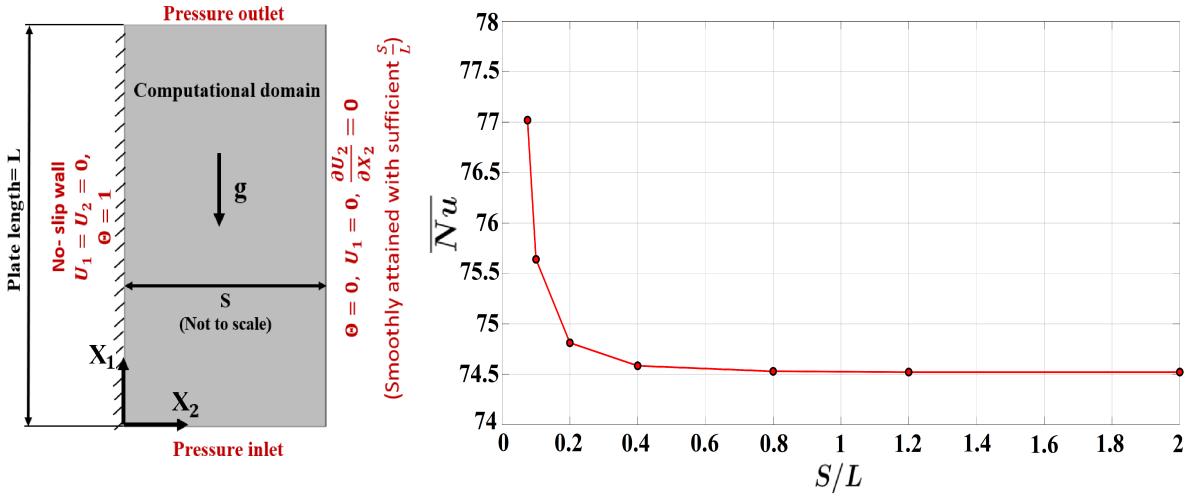

Figure 6: Computational domain with boundary conditions used for the numerical simulation of the natural convection over the isothermal vertical smooth plate ($X_2 = 0$). The right frame shows a graphical representation of the sensitivity of the solution to variations in the domain width. $Gr = 5.563 \times 10^8$, $Pr = 0.712$.

The computational domain and the boundary conditions are illustrated in Fig. 6. No-slip and constant temperature conditions are defined on the vertical wall; uniform pressure boundary conditions are imposed at the upper and the lower boundaries such that an equilibrium with the hydrostatic pressure head is satisfied. The width of the domain should be selected in such a way that the streamwise velocity smoothly vanishes at the far boundary at $X_2 = S$, with the normal gradients of horizontal velocity and temperature smoothly decreasing to zero[3]. This was checked by running the simulation with different values of the domain width, S, and monitoring a result of interest (the surface-averaged Nusselt number) until convergence was attained. The local Nusselt number (Nu) and its surface averaged counterpart ($\overline{Nu}$) are defined for the smooth surface by:

$$Nu = \frac{-L}{\hat{T}_w - \hat{T}_\infty} \frac{\partial \hat{T}}{\partial \hat{x}_2}\bigg|_{X_2=0} = -\frac{\partial \Theta}{\partial X_2}\bigg|_{X_2=0}, \tag{18-a}$$

$$\overline{Nu} = \int_0^1 -\frac{\partial \Theta}{\partial X_2}\bigg|_{X_2=0} dX_1. \tag{18-b}$$

As can be realized from Fig. 6 (right), a domain width $S = 0.8$ appears to be sufficient; however, a value of $S = 2$ was used throughout the work to ensure the absence of spurious reflections from the outer boundary when testing micro-structured walls and/or larger

[3]refer to **Paper B3** for accurate description of the condition imposed at the far boundary

values of Gr. The two-dimensional grid is described in detail in Appendix C; eventually, the extrapolated value of the average Nusselt number is estimated to be 75.055 based on the conducted mesh-dependency study, also illustrated in the appendix.

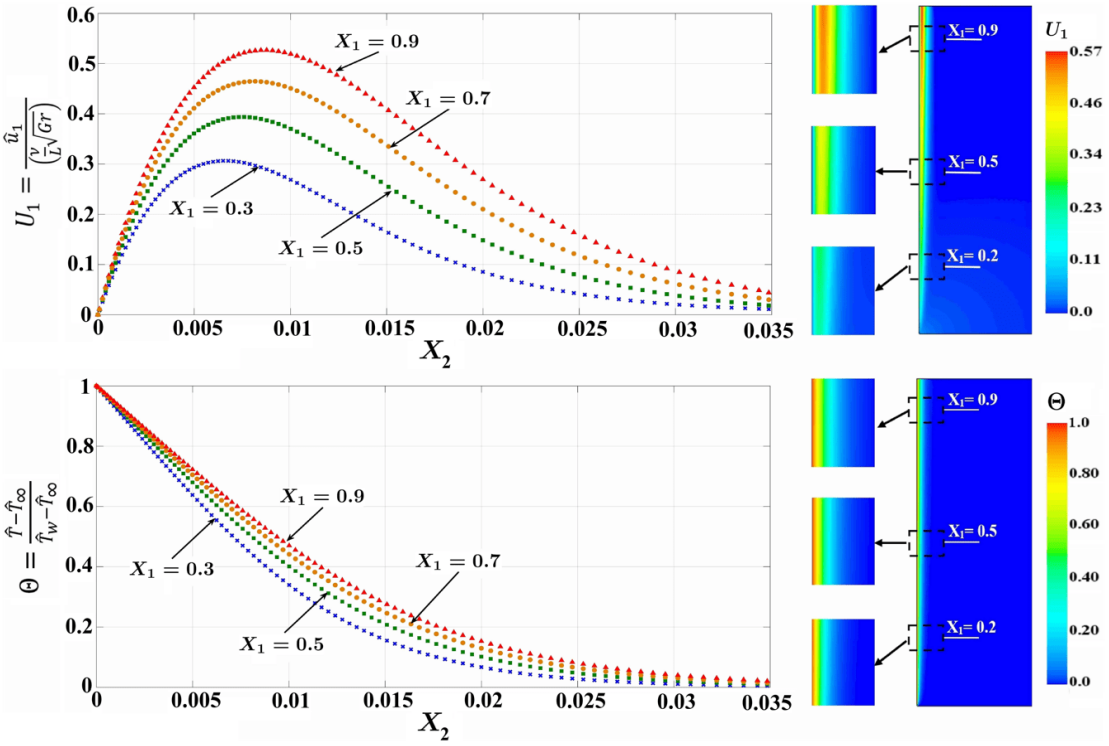

Figure 7: Smooth surface case: dimensionless velocity and temperature profiles across different normal sections distributed along the vertical plate. Contours representing the velocity and the thermal fields are also provided. $Gr = 5.563 \times 10^8$, $Pr = 0.712$.

The dimensionless temperature and streamwise velocity profiles are plotted across chosen normal sections distributed along the plate, as displayed in Fig. 7. The velocity and the temperature contours in the vicinity of the smooth wall are also shown, to highlight the development of the boundary layers. The peak of the velocity profile shifts away from the wall as X_1 increases, in qualitative agreement with the estimate of the classical Squire-Eckert theory (Lienhard & Lienhard, 2019) according to which the velocity peaks at almost $\frac{1}{3}$ of the boundary layer thickness. At the same time, the temperature gradient at the wall is reduced with X_1. The latter effect is responsible for the decrease of the local Nusselt number (Nu) along the plate, plotted in Fig. 8. The distribution of the local Nusselt number is in perfect agreement with the corresponding reference results by Ostrach (1953). An analysis of Ostrach's results reveals that the Nusselt number (Nu) is related to the vertical position (X_1) via the expression

$$\frac{X_1 Nu}{\left(\frac{Gr}{4}X_1^3\right)^{0.25}} = f_n(Pr). \tag{19}$$

At a Prandtl number of 0.712, the function $f_n(Pr)$ was estimated to be almost 0.504. Therefore, Eq. (19) can be recast as an explicit relation between Nu and X_1 at any fixed value of the Grashof number.

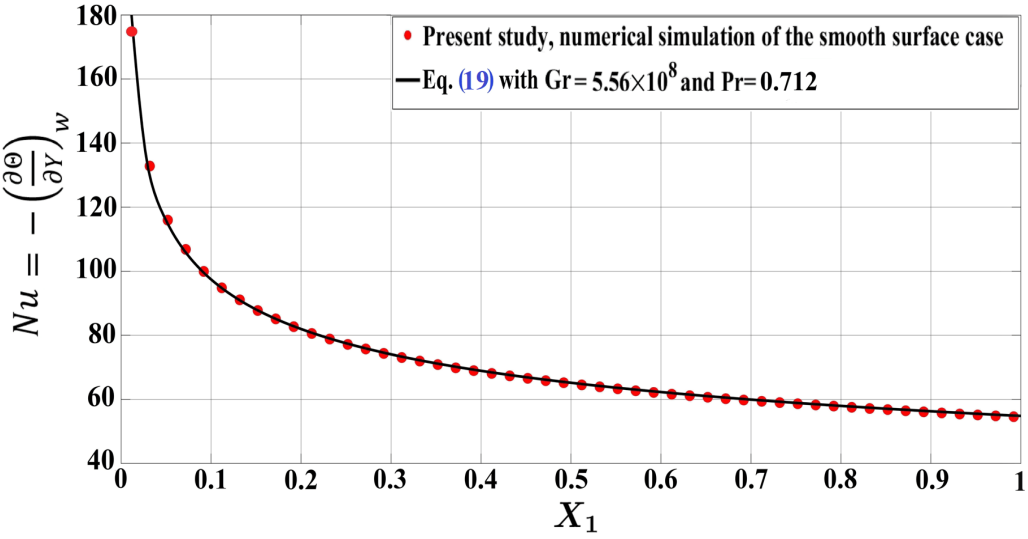

Figure 8: Smooth surface case: numerical prediction of the local Nusselt number distribution along the vertical plate, compared with the expected behaviour based on the similarity solution by Ostrach (1953).

6.2 The case of isothermal ribbed surface

A typical validation case is now considered. The developed asymptotic wall model is assumed to be reasonably accurate provided that ϵ is sufficiently small. In addition, limitations are imposed on the magnitude of the coefficient of the convective term in the normalized microscopic governing equations, $C = \epsilon^2 \sqrt{Gr} = \epsilon \mathcal{R}_G$, for convective effects to be absent in the leading-order problem but present at next order. For the basic validation case, we consider natural convection over an isothermal vertical plate with 168 transverse square ribs ($\epsilon = \frac{1}{168}$) with a pitch distance to rib height ratio $\frac{l}{e} = 3.75$. The problem is characterized by a plate Grashof number $Gr = 5.563 \times 10^8$ and a Prandtl number $Pr = 0.712$. With these parameters, the value of the coefficient C is 0.836. Results of the feature-resolving simulation and the homogenization-based calculations of the basic ribbed surface case are presented and compared.

6.2.1 *Feature-resolving simulation of the ribbed surface case*

The two-dimensional feature-resolving numerical simulation, where the details of the ribbed surface are captured by the grid, represents a necessary step for the validation of the homogenized model.

The computational domain is illustrated in Fig. 9, including the geometric details of the ribbed surface. The applied boundary conditions are the same as in the smooth surface case, taking into account that the no-slip velocity and temperature conditions are

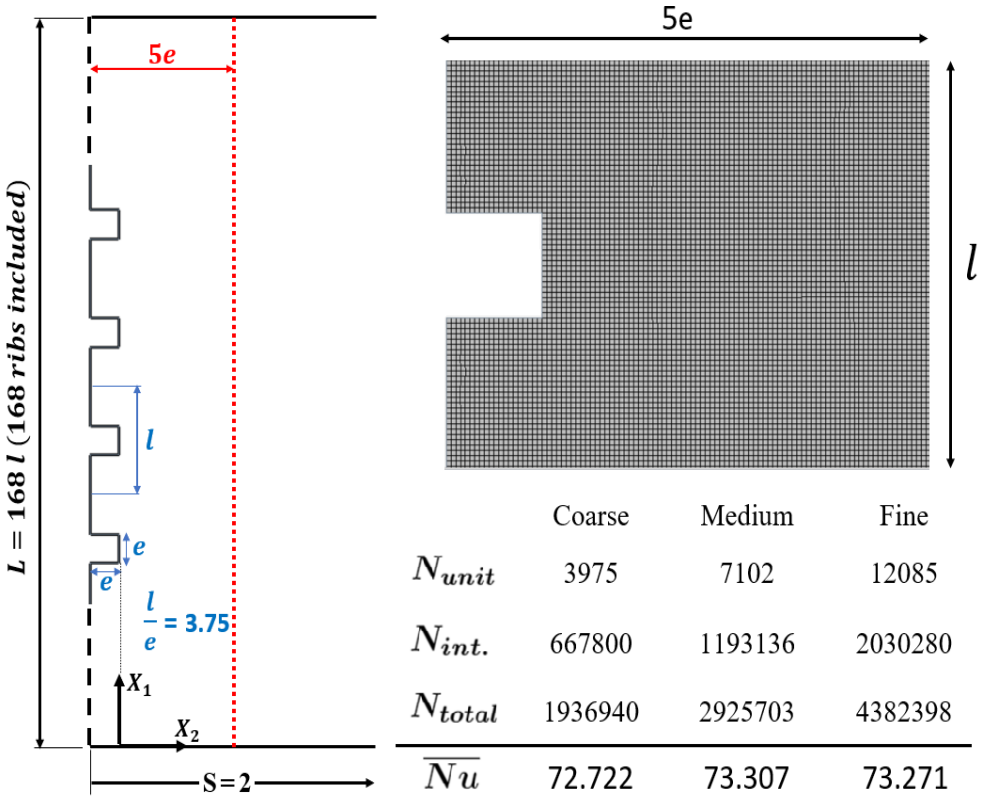

	Coarse	Medium	Fine
N_{unit}	3975	7102	12085
$N_{int.}$	667800	1193136	2030280
N_{total}	1936940	2925703	4382398
$\overline{Nu}$	72.722	73.307	73.271

Figure 9: Description of the computational domain and two-dimensional grid structure used for the feature-resolving numerical simulation. The grid is shown for one unit in the near-wall region (of thickness $5e$), defined for the highest mesh density. Indicated mesh parameters for different refinement levels are: N_{unit}: number of cells for a single unit in the near-wall region; $N_{int.}$: number of cells in the whole near-wall region of thickness $5e$; N_{total}: total number of cells in the computational domain.

now imposed on a patterned surface, not on a plain one. The two-dimensional grid near the ribs is also shown, and the different grid refinement levels are stated. A near-wall region of thickness $5e$ is defined where a high mesh density is employed to capture the flow dynamics in the vicinity of the perturbed surface; however, the gradual growth of the mesh guarantees that the whole field is fairly well resolved. The number of two-dimensional cells given in the figure illustrates clearly the high computational cost of the fully-featured simulation of the ribbed surface compared to requirements of the smooth surface case, described in Appendix C. The Nusselt number at any point on the ribbed surface is given by:

$$Nu = \frac{-L}{\hat{T}_w - \hat{T}_\infty} \times \left.\frac{\partial \hat{T}}{\partial \hat{n}}\right|_{wall} = -\left.\frac{\partial \Theta}{\partial n}\right|_{wall}, \tag{20-a}$$

where $\hat{n}$ denotes the dimensional distance in the surface-normal direction and $n = \dfrac{\hat{n}}{L}$. A dimensional surface distance $\hat{s}$ is defined in such a way that it goes along the ribbed surface capturing its details, i.e., $\hat{s}$ goes from 0 to $L + (2e \times N_{ribs})$ with $N_{ribs} = \dfrac{1}{\epsilon} = \dfrac{L}{\ell}$ the

number of ribs. Accordingly, the surface-averaged Nusselt number based on the projected area of the two-dimensional ribbed plate is defined as:

$$\overline{Nu} = \frac{1}{L}\int_0^{L+\frac{2e}{\epsilon}} -\frac{\partial\Theta}{\partial n}\bigg|_{wall} d\hat{s} = \int_0^{1+\frac{2e}{\ell}} -\frac{\partial\Theta}{\partial n}\bigg|_{wall} ds, \tag{20-b}$$

where $s = \dfrac{\hat{s}}{L}$, and the value of $\dfrac{e}{\ell}$ represents the rib height to the pitch distance ratio. The given expression for $\overline{Nu}$ takes into account the surface area increase, with respect to the baseplate area, due to the presence of ribs. For the considered values of parameters ($Gr = 5.563 \times 10^8$, $Pr = 0.712$, $\epsilon = \dfrac{1}{168}$, $\dfrac{l}{e} = 3.75$), the reported value of $\overline{Nu}$ was estimated based on Richardson's extrapolation of results for successively refined grids, and finally found to be 73.200 (compared with a value of 75.055 for a corresponding smooth surface case). This finding suggests that adding ribs to the vertical surface deteriorates the total heat transfer rate, for the geometric parameters and flow conditions under study.

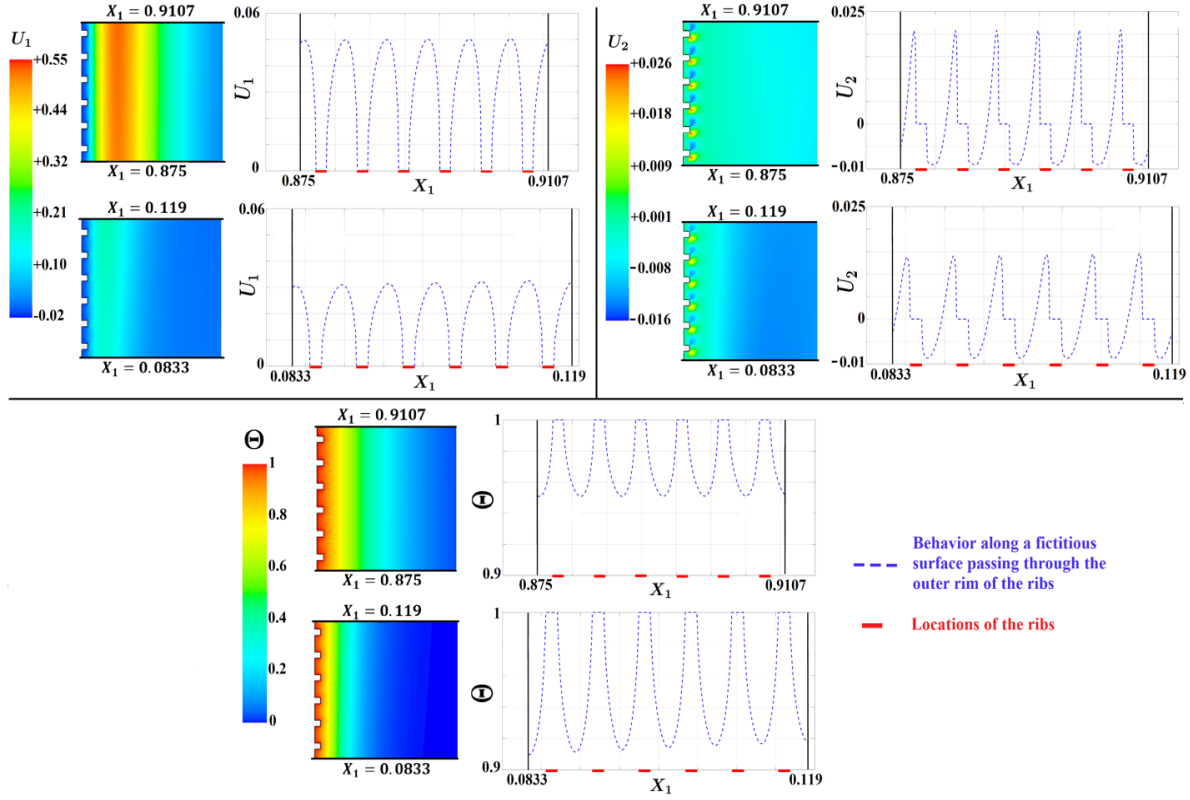

Figure 10: Feature-resolving simulation of the ribbed surface: detailed behaviours of (top left) streamwise velocity; (top right) normal velocity; (bottom) temperature. Results are plotted along the vertical plane passing through the outer rims of the ribs, through two specific ranges of X_1. The contours of the fields are also provided. $Gr_L = 5.563 \times 10^8$, $Pr = 0.712$.

The fully-featured simulation is described first to provide insight into the physics, before turning to the homogenized model. The patterns of the streamwise velocity, the normal velocity, and the temperature are plotted over two distant regions along the plane

surface tangent to the outer rims of the square ribs in order to show the behaviour of velocity and thermal fields near the leading edge and near the top of the plate, as displayed in Fig. 10. The fictitious surface at $X_2 = 0$ was specifically chosen for the plots as it represents the plane on which the effective conditions are imposed in the model simulations; therefore, monitoring the flow parameters along this surface is of interest. The contours of the velocity and the temperature near the wall are also shown so that details of the boundary layer can be captured. Velocity and temperature patterns are perturbed by the presence of the ribs and experience quasi-periodic behaviours along the vertical distance. By analyzing one unit of the distributions shown in the plots, it is evident that the no-slip velocity and temperature conditions are typically satisfied at the physical surface of the rib whereas deviations occur in the inter-rib fluid region. Proceeding along the vertical direction, the average levels of both the streamwise velocity and the temperature increase, which is qualitatively similar to the smooth surface case. The deflections of the streamlines, due to the flow interaction with the surface protrusions, are directly reflected in perturbation of the normal velocity where the successive negative and positive fluctuations represent, respectively, the inward and outward normal flow through the inter-rib region. The characteristics of the flow structure and the way in which the heat transfer from the surface is accordingly affected are shown in Fig. 11. The flow behaviour close to the ribbed surface is visualized with the aid of streamlines in two distant regions along the vertical direction, so that the development of the flow can be monitored. Two distinct flow regimes are observed, a *Separation-Reattachment-Separation* (SRS) regime and a *Full Separation* (FS) regime. For both patterns, the inter-rib region is characterized by the existence of two co-rotating vortices. At relatively low values of the local Grashof number $Gr_x = Gr\,X^3$, i.e., near the leading edge of the plate, the SRS flow regime is present where the low inertia of the mainstream allows the fluid to easily deflect in the normal direction and reattach to the surface of the baseplate, keeping the two eddies well-isolated. In contrast, sufficiently away from the leading edge, the *Full Separation* regime ensues as the increasing inertia of the accelerated stream hinders the normal deflection towards the baseplate, preventing the reattachment of the mainstream. As illustrated in the figure, the two vortices remain connected to each other via an outer belt-like stream that rotates in the same direction of both eddies, representing a separated entity that isolates the main flow from the baseplate in the inter-rib region.

The associated heat transfer behaviour is plotted in Fig. 11 in terms of detailed patterns of the local Nusselt number Nu. A quasi-periodic behaviour of the Nusselt number is observed while proceeding along the vertical plate, similarly to literature observations (Bhavnani & Bergles, 1990; Tanda, 1997, 2008, 2017; Nishikawa *et al.*, 2020). On a single-unit scale of analysis, it is evident that the heat transfer rate drastically drops just upstream and downstream of the square protrusion, a fact ascribed to the presence of the separation eddies that form a hot inactive zone in the vicinity of the rib where the thermal boundary layer thickening mitigates the heat transfer process. Conversely, the local Nusselt number peaks at some location within the inter-rib region as the mainstream reattaches to the surface of the baseplate. Even in the *Full Separation* regime, the inter-rib peak is experienced since the mainstream still approaches the surface (without reattaching). The major peak of the local Nusselt number is present on the outer rim

of the rib due to the considerable local thinning of the thermal boundary layer. From a macroscopic point of view, the average value of Nu decreases away from the leading edge along with the development of the thermal boundary layer.

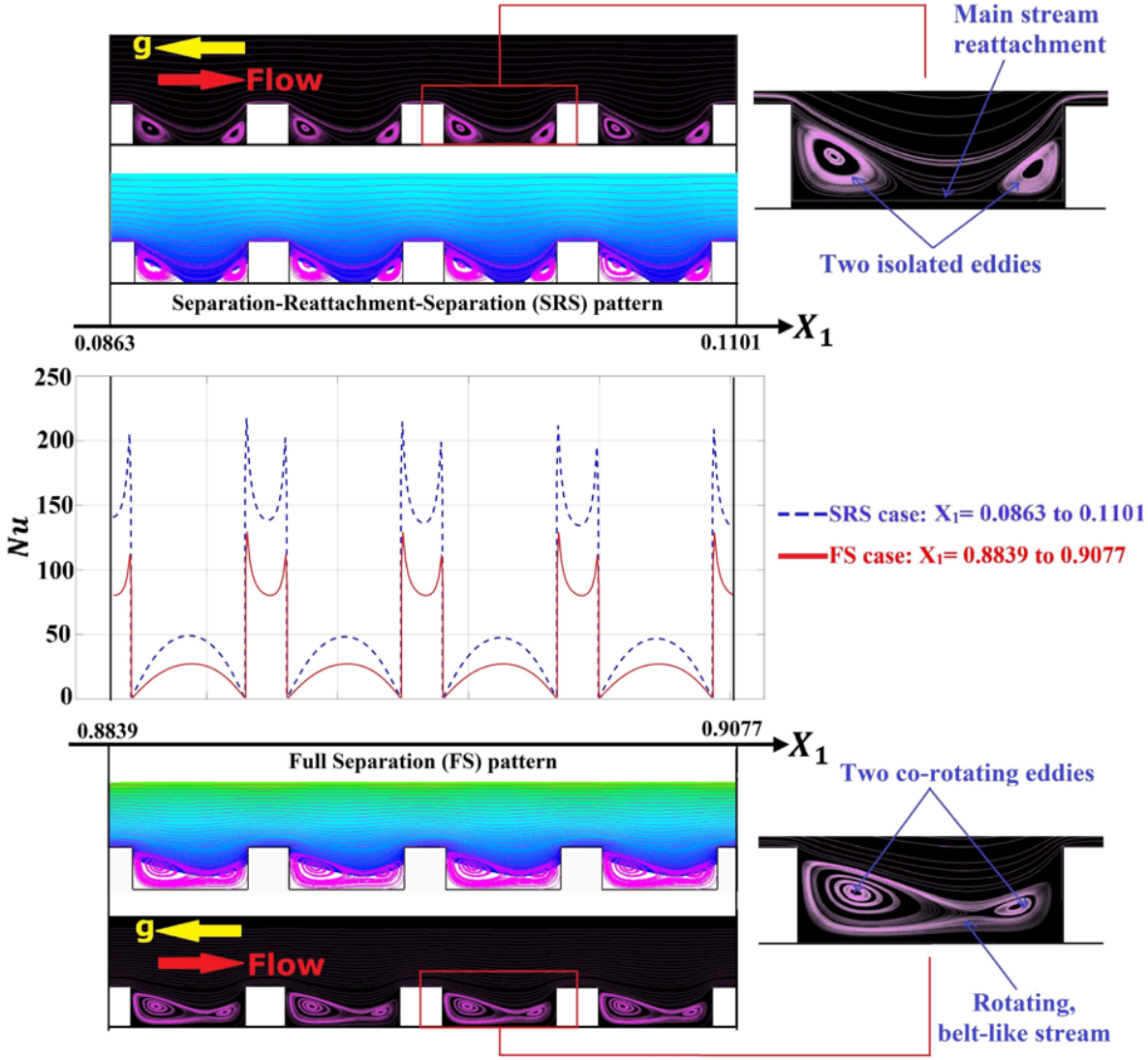

Figure 11: Feature-resolving simulation of the ribbed surface: Comparative description of the flow pattern and the behaviour of the Nusselt number through two distant regions: (top) near the leading edge; (bottom) near the end of the plate. The contours of U_1 are also shown; the colour map given in Fig. 10 is modified here so that the white portions within the grooves represent the regions with negative streamwise velocity, i.e., the back-flow regions. $\epsilon = \frac{1}{168}, \frac{l}{e} = 3.75$, $Gr = 5.563 \times 10^8$, $Pr = 0.712$.

6.3 The macroscopic homogenization-based simulations

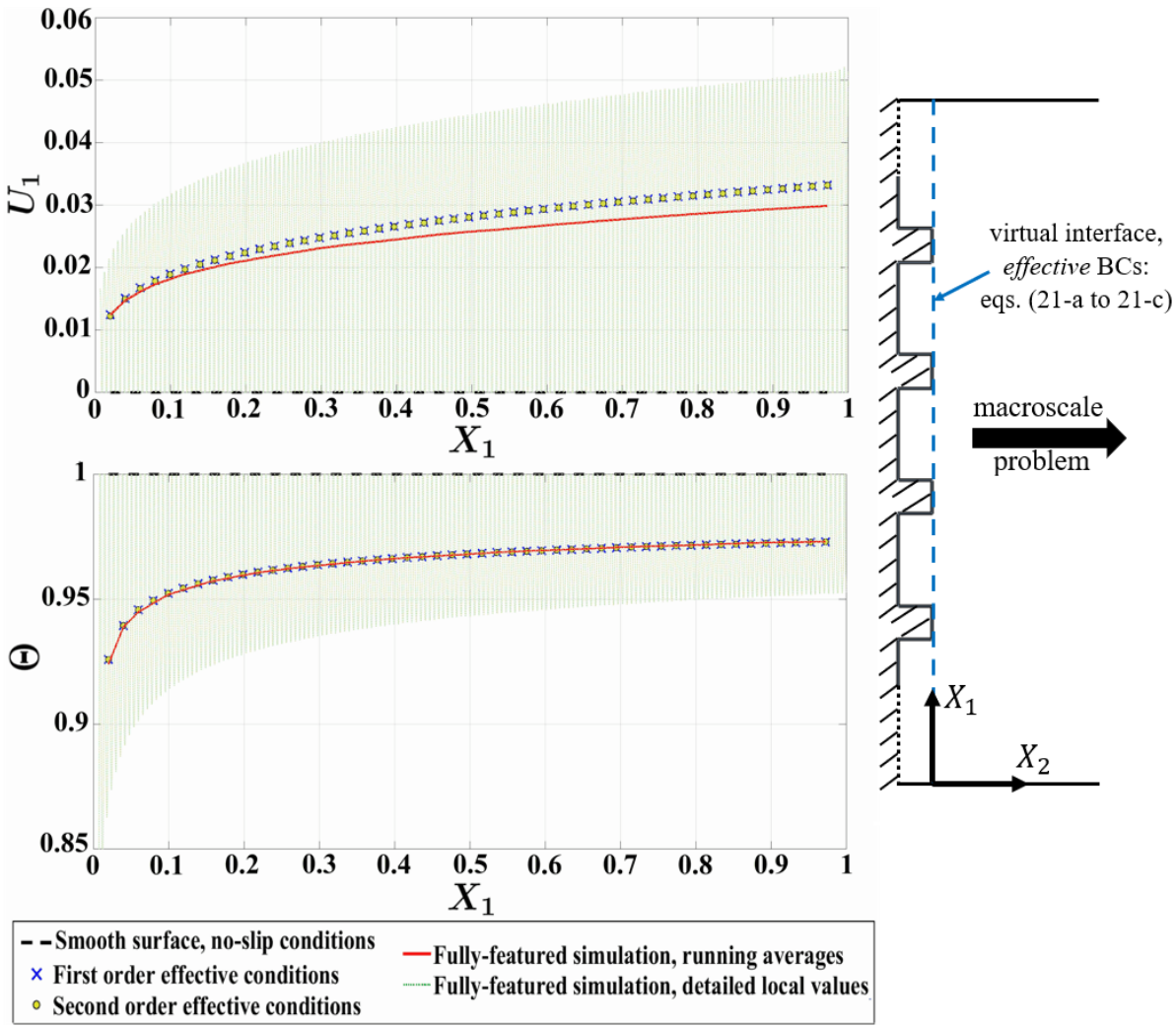

Figure 12: Effective boundary conditions for streamwise velocity and temperature in comparison to the running-average results of the feature-resolving simulation. $\epsilon = \frac{1}{168}, \frac{l}{e} = 3.75$, $Gr = 5.563 \times 10^8$, $Pr = 0.712$.

The effect of the surface microstructure on the behaviour of the buoyancy-driven stream is replaced here by the implementation of the homogenized effective boundary conditions on the plane at $X_2 = 0$ (refer to Fig. 12). As the present work targets the validation of the model on the steady-state solution of a two-dimensional laminar flow, the effective conditions can be simplified by neglecting the time-derivative terms and the gradients in the spanwise direction. The dimensionless conditions up to the second order in all

variables thus read:

$$U_1\big|_{X_2=0} = \epsilon\,[\lambda_x\,S_{12} + m_{12}\,\mathcal{R}_G]_{X_2=0} + \epsilon^2\left[m_{12}\,\frac{\partial S_{22}}{\partial X_1} + \mathcal{B}\,\mathcal{R}_G\frac{\partial \Theta}{\partial X_2}\right]_{X_2=0} + \mathcal{O}(\epsilon^3), \tag{21-a}$$

$$U_2\big|_{X_2=0} = -\epsilon^2\left[m_{12}\,\frac{\partial S_{12}}{\partial X_1}\right]_{X_2=0} + \mathcal{O}(\epsilon^3), \tag{21-b}$$

$$\Theta\big|_{X_2=0} = 1 + \epsilon\,\lambda_z\frac{\partial \Theta}{\partial X_2}\bigg|_{X_2=0} + \mathcal{O}(\epsilon^3), \tag{21-c}$$

Based on the parametric study presented in Section 5, at $\frac{l}{e} = 3.75$, the following values of the model coefficients are found:

$$\lambda_x = 0.03791, \qquad \lambda_z = 0.08404, \qquad m_{12} = 0.002125, \qquad \mathcal{B} = 0.0002247. \tag{22}$$

Since the ribbed surface is impermeable, the transpiration velocity is zero on average and its inclusion is not significant under laminar flow conditions; this was tested and confirmed in the present work.

The setup of the homogenization-based macroscopic simulations is similar to the setup of the smooth surface case with regard to the computational domain, the grid structure, the refinement levels and the boundary conditions except for replacing the no-slip velocity and temperature conditions by the effective conditions (Eqs. (21-a to 21-c)) on a virtual wall in $X_2 = 0$. It is comforting that the macroscopic simulations reach mesh-independence for grids which are more than 30 times coarser as compared to the fully-featured case, while providing accurate predictions of the surface-averaged Nusselt number (the metric being evaluated in the grid-dependence study). For the considered flow and geometric conditions ($Gr = 5.563 \times 10^8$, $Pr = 0.712$, $\epsilon = \frac{1}{168}$, $\frac{l}{e} = 3.75$), the converged values of $\overline{Nu}$ with first-order and second-order conditions are, respectively, 73.1667 and 73.1618. In comparison to the fully-featured result, the errors of the homogenized models are, respectively, -0.045% and -0.052%. It is worth restating that $\overline{Nu}$ of the smooth surface case is 2.54% larger than in the fully-featured ribbed case.

The results which can be achieved from the homogenized simulations illustrate the macroscopic behaviour of velocity and temperature fields; clearly, these results should be interpreted as spatially averaged values, whereas the detailed patterns near the wall are unavailable from the model simulations. For this purpose, the validation of the present approach is done by comparing the results of the macroscopic simulations with the running-average values of the fully-featured fields over streamwise distances equal to the periodicity of the pattern of the surface structure. For instance, the running-average value of the dimensionless velocity U_1 at an arbitrary point ($X_1 = a$, $X_2 = b$) is computed as:

$$< U_1 > \Big|_{X_1=a,X_2=b} = \frac{1}{\epsilon}\int_{a-\frac{\epsilon}{2}}^{a+\frac{\epsilon}{2}} U_1(X_1, b)\; dX_1. \tag{23}$$

The numerical predictions of U_1 and Θ resulting from the macroscopic simulations with the first-order accurate and the second-order accurate boundary conditions are extracted

at the fictitious boundary in $X_2 = 0$ to explicitly assess the accuracy of the expressions given in Eqs. (21-a to 21-c). The homogenized results are plotted in Fig. 12 in comparison with the corresponding running-average values of the feature-resolving simulation. It is clear that the present model can qualitatively predict the difference of the results from the no-slip values. The results show perfect agreement of the effective temperature estimates, apparently insensitive to the mild deviations observed for the predictions of the slip velocity. This fact may be attributed to the absence of strong non-linearities, i.e. the coupling between the velocity and the thermal fields is weak.

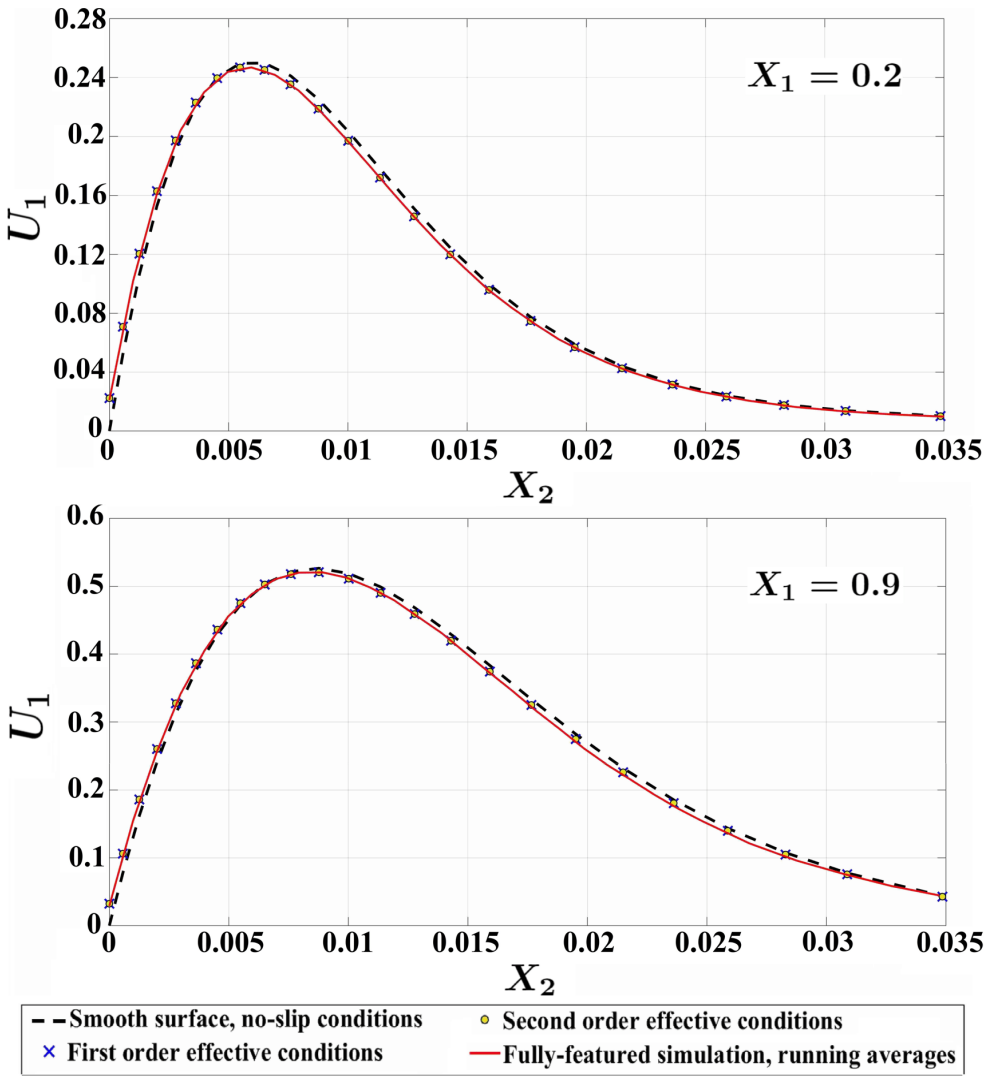

Figure 13: Homogenized-model predictions of the streamwise velocity profiles across two normal sections in comparison to the running-average results of the fully-featured simulation. $\epsilon = \frac{1}{168}, \frac{l}{e} = 3.75$, $Gr = 5.563 \times 10^8$, $Pr = 0.712$.

In order to show how the effect of the homogenized conditions propagates from the virtual wall to the flow domain, the profiles of streamwise velocity and temperature are

plotted across two normal sections and compared with the corresponding running-average profiles (Figs. 13 and 14).

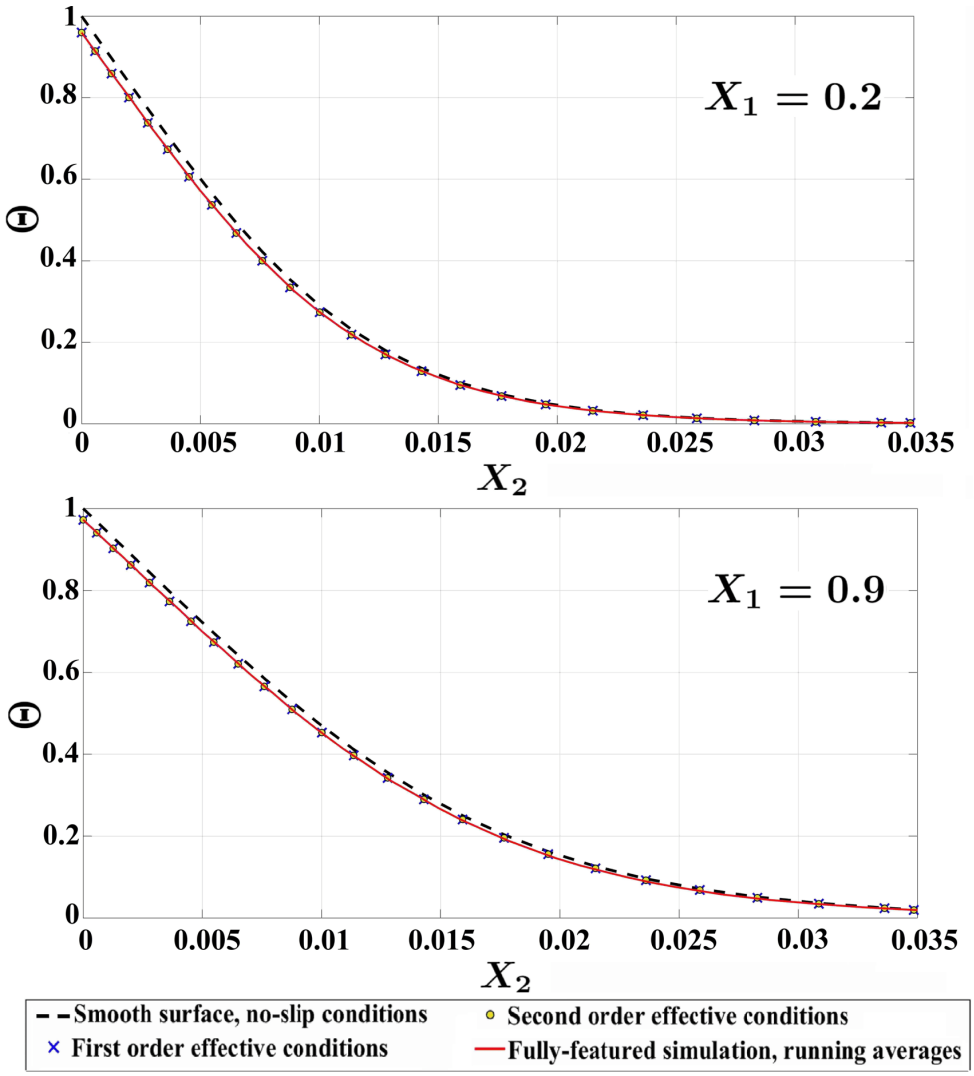

Figure 14: Validation of the homogenized-model results of the temperature profiles across two normal sections in comparison to the running-average results extracted from the fully-featured simulation. $\epsilon = \frac{1}{168}, \frac{l}{e} = 3.75$, $Gr = 5.563 \times 10^8$, $Pr = 0.712$.

It is noticeable that, in the present case, the effect of the surface inhomogeneities on the flow field is moderate. Another point is that the predictions based on first and second-order conditions are almost indistinguishable from one another to graphical accuracy, due to the very small value of ϵ. The normal gradients of Θ along the fictitious boundary, represented by the slopes at $X_2 = 0$ of the Θ profiles, were used to obtain the macroscopic behaviour of the Nusselt number along the plate (cf. Eq. (18-a)). The results are presented in comparison with the corresponding running-average values from the fully-featured simulation in Fig. 15. It can be realized that, under the present conditions, the ribs on the surface have a very mildly unfavorable effect on the heat transfer rate.

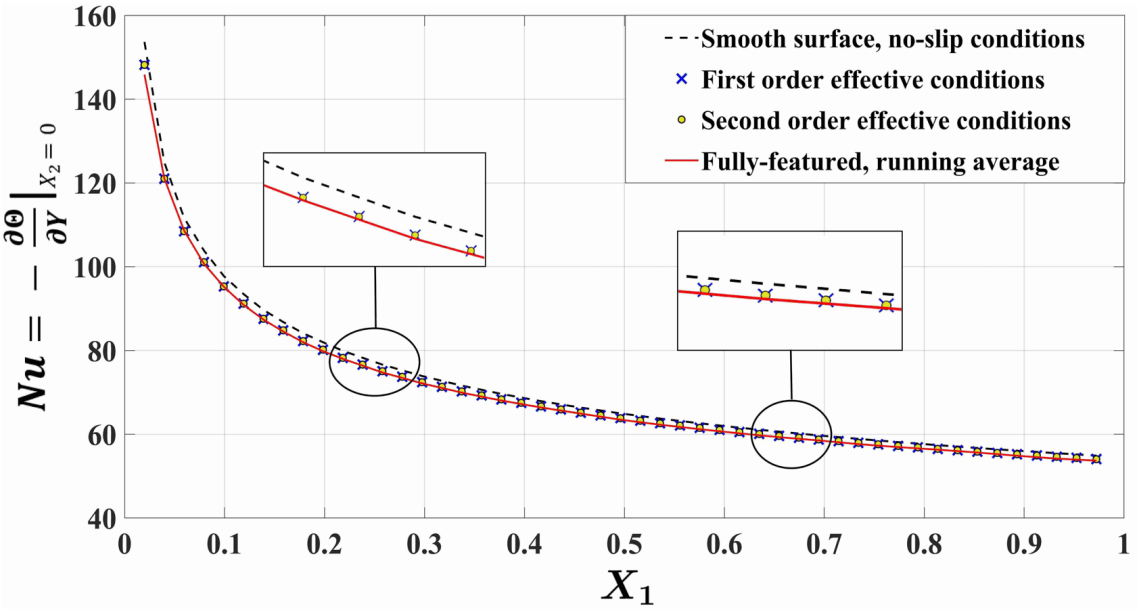

Figure 15: Homogenized model predictions of the Nusselt number in comparison to the running-average results of the feature-resolving simulation, based on the normal temperature gradient along the plane $X_2 = 0$. $\epsilon = \frac{1}{168}$, $\frac{l}{e} = 3.75$, $Gr = 5.563 \times 10^8$, $Pr = 0.712$.

It is very important to highlight that the present approach is only able to model the temperature-gradient-based heat transfer from the matching interface, while the convective contribution, resulting from the product of normal velocity and temperature, is not accounted for, since the fluctuations of the normal velocity cannot be resolved by the homogenized model under laminar flow conditions. The applicability of the model is, therefore, limited here to cases in which convective effects through the fictitious plane are negligible. This is assumed to be valid in the absence of strong non-linearities that may occur for large values of ϵ or in the presence of turbulence.

7 APPLICABILITY RANGE AND LIMIT OF VALIDITY OF THE MODEL

In this section, the results of several numerical simulations are presented to assess the deterioration of the accuracy of the proposed technique with the increase of the small parameter $\epsilon = \dfrac{\ell}{L} = \dfrac{1}{N_{ribs}}$ and the coefficient of the microscopic momentum-convective term $C = \epsilon^2 \sqrt{Gr} = \epsilon \mathcal{R}_G$.

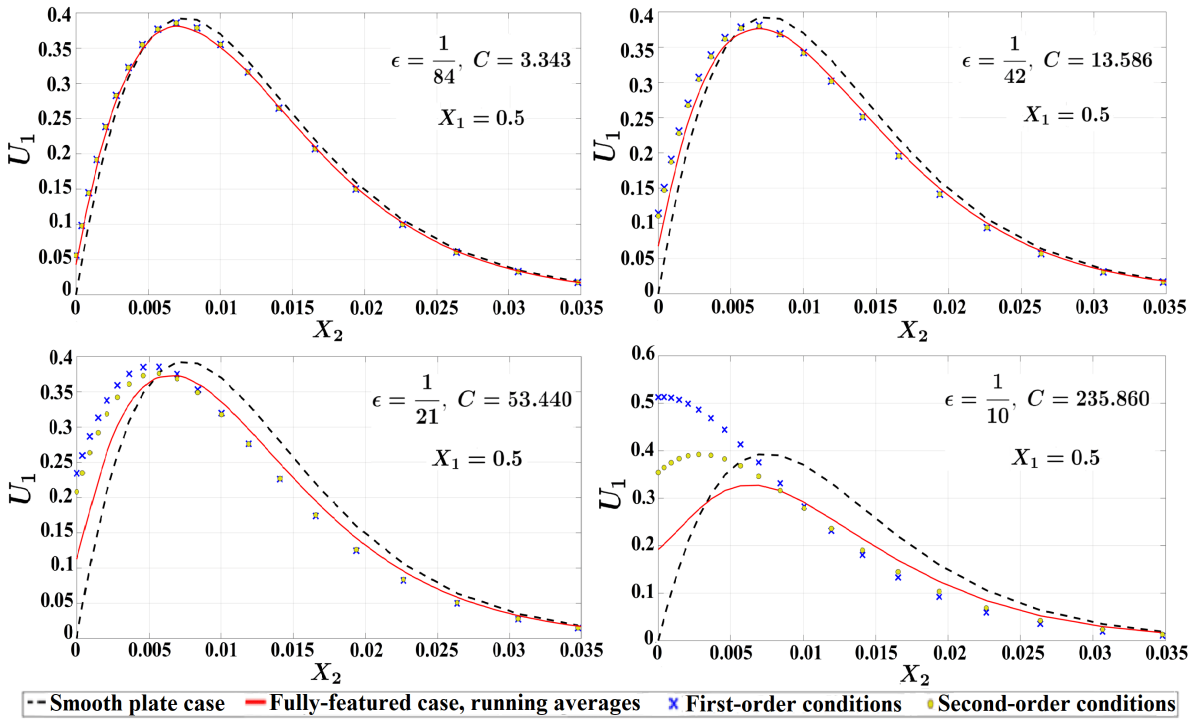

Figure 16: Predictions of the homogenized-model in comparison to the running-averages of the fully-featured results of the dimensionless streamwise velocity profiles at $X_1 = 0.5$ for different values of ϵ. $\frac{l}{e} = 3.75$, $Gr = 5.563 \times 10^8$, $Pr = 0.712$.

7.1 Effects of the increase in ϵ at a given Grashof number

The simulations of the macroscopic problem are now conducted for increasing values of the parameter ϵ in the effective boundary conditions (Eqs. (21-a to 21-c)), starting from $\epsilon = \frac{1}{84}$ up to $\epsilon = \frac{1}{10}$, at a constant value of the Grashof number ($Gr = 5.563 \times 10^8$) and for the values of the model coefficients at $\frac{\ell}{e} = 3.75$ (cf. Eq. (22)), in order to monitor the deterioration of the model with the increase of the controlling parameters ϵ and C. First, a validation database has been built by running the fully-featured simulations with the corresponding numbers of ribs (from 84 to 10). The running-average fields obtained from these simulations are presented in a comparative manner in Appendix E. The results of the macroscopic simulations with first-order and second-order accurate homogenized effective conditions are validated by comparing the streamwise velocity profiles and the temperature profiles across a normal section taken at $X_1 = 0.5$ with the corresponding running-average patterns from the fully-resolved numerical simulations, cf. Figs. 16 and 17. The purpose is to ascertain the validity range of the asymptotic model away from the conditions ($\epsilon = \frac{1}{168}, C = 0.836$) discussed in Section 6. In general, the predictions of the present approach concerning velocity and temperature fields are reliable below $\epsilon = \frac{1}{21}$ at the given Grashof number. It will be argued later that the reliability range becomes

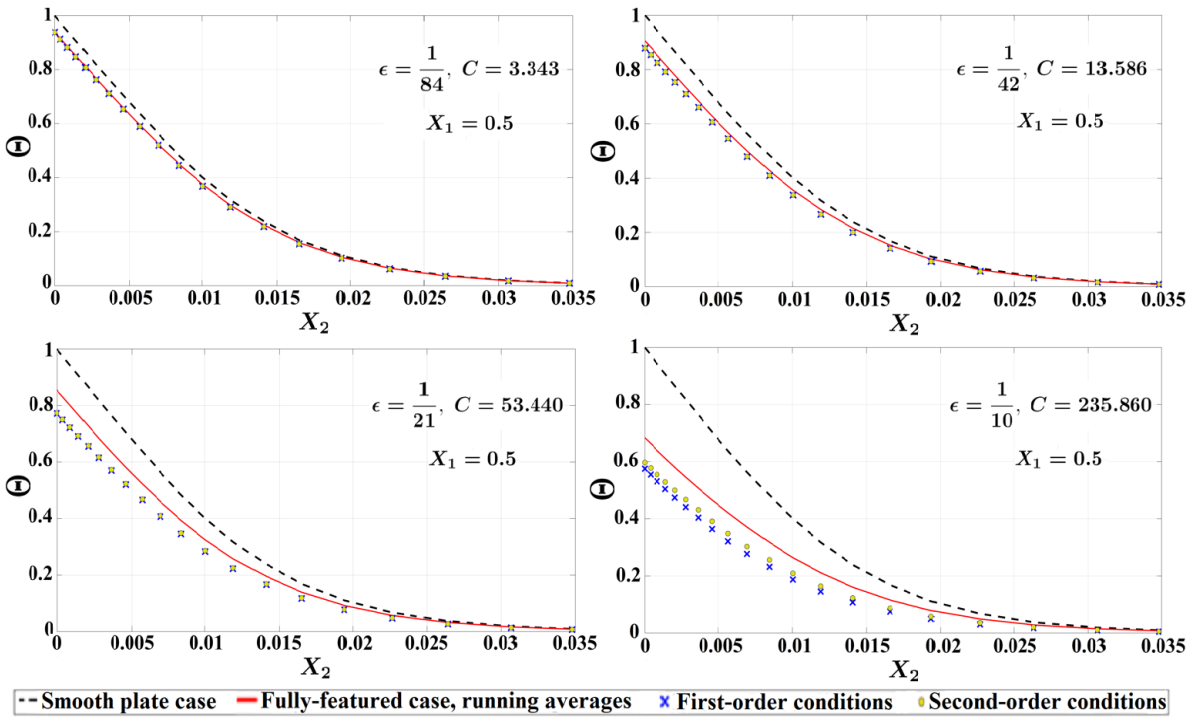

Figure 17: Predictions of the homogenized-model in comparison to the running-averages of the fully-featured results of the dimensionless temperature profiles at $X_1 = 0.5$ for different values of ϵ. $\frac{l}{e} = 3.75$, $Gr = 5.563 \times 10^8$, $Pr = 0.712$.

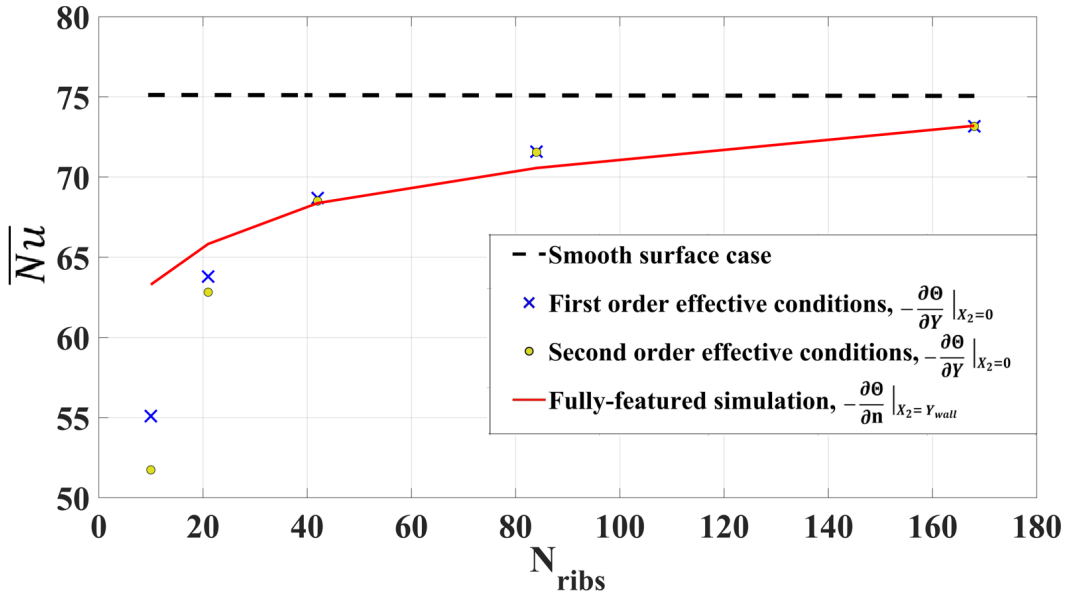

Figure 18: Effect of the number of the ribs ($N_{ribs} = \frac{1}{\epsilon}$) on the surface-averaged Nusselt number (corrected to account for the increase in surface area in the case of feature-resolving simulations of ribbed surfaces, cf. Eq. (20-b)). The parameters are $\frac{l}{e} = 3.75$, $Gr = 5.563 \times 10^8$, $Pr = 0.712$.

wider at lower values of the Grashof number. The accuracy of the temperature predictions is better than the velocity predictions, especially above the mentioned limit where the boundary conditions at second order are able to produce better results in comparison to the first-order conditions.

From the practical point of view, the most important factor is the surface-averaged Nusselt number. The behaviour of $\overline{Nu}$ with the increase of $N_{ribs} = \dfrac{1}{\epsilon}$ is shown in Fig. 18. Both fully-featured and homogenized-model results show a reduced heat transfer for the ribbed surface despite the increase in surface area (compared to smooth flat plate), for the values of parameters here considered. It is obvious that the level of accuracy of the model predictions is even better than that relative to velocity and temperature profiles. It is also noteworthy that improved predictions of $\overline{Nu}$ by shifting up to the second-order conditions are not systematically guaranteed.

Table 3: Error estimations of the homogenized model predictions for the velocity and temperature profiles at $X_1 = 0.5$ and surface-averaged Nusselt number. The fully-featured case is used as a reference. The deviations of the results of the smooth wall case compared to the rough case are also provided. In all cases: $\frac{l}{e} = 3.75$, $Gr = 5.563 \times 10^8$, $Pr = 0.712$.

		rms deviations of U_1 vs. X_2 profiles at X_1=0.5		
ϵ	**C**	**Smooth**	**First-order model**	**Second-order model**
$\frac{1}{168}$	0.835	15.877%	1.491%	1.465%
$\frac{1}{84}$	3.340	17.312%	5.643%	5.420%
$\frac{1}{42}$	13.371	19.397%	13.473%	12.304%
$\frac{1}{21}$	53.485	22.566%	25.475%	20.076%
$\frac{1}{10}$	235.860	31.660%	56.025%	30.069%
		rms deviations of Θ vs. X_2 profiles at X_1=0.5		
ϵ	**C**	**Smooth**	**First-order model**	**Second-order model**
$\frac{1}{168}$	0.835	3.044%	1.602%	1.617%
$\frac{1}{84}$	3.340	6.639%	1.909%	1.893%
$\frac{1}{42}$	13.371	11.689%	5.336%	5.220%
$\frac{1}{21}$	53.485	21.486%	12.781%	11.911%
$\frac{1}{10}$	235.860	49.687%	27.629%	19.887%
		relative error on $\overline{Nu}$		
ϵ	**C**	**Smooth**	**First-order model**	**Second-order model**
$\frac{1}{168}$	0.835	2.535%	-0.045%	-0.052%
$\frac{1}{84}$	3.340	6.363%	1.434%	1.397%
$\frac{1}{42}$	13.371	9.768%	0.459%	0.190%
$\frac{1}{21}$	53.485	14.015%	-3.080%	-4.569%
$\frac{1}{10}$	235.860	18.580%	-12.936%	-18.252%

The accuracy of the homogenization-based models is reported in a more quantitative manner in Table 3. For the velocity and temperature profiles shown in Figs. 16 and 17, root-mean-square (rms) deviations between the results of the macroscopic simulations and the results of the reference fully-featured simulations are defined. The rms deviations of the profiles are calculated over a normal distance between $X_2 = 0$ and $X_2 = 0.02$. For instance, the rms deviation of a modeled velocity profile (U_{mod} *vs.* X_2) relative to the corresponding fully-featured one (U_{FF} *vs.* X_2) is defined as

$$rms\ deviation = \sqrt{\frac{1}{0.02}\int_0^{0.02}\left(\frac{U_{mod} - U_{FF}}{U_{FF}}\right)^2 dX_2}. \tag{24}$$

The errors on the predictions of the surface-averaged Nusselt number relative to the fully-featured estimations are also shown in the table.

7.2 Effect of the Grashof number at a given ϵ

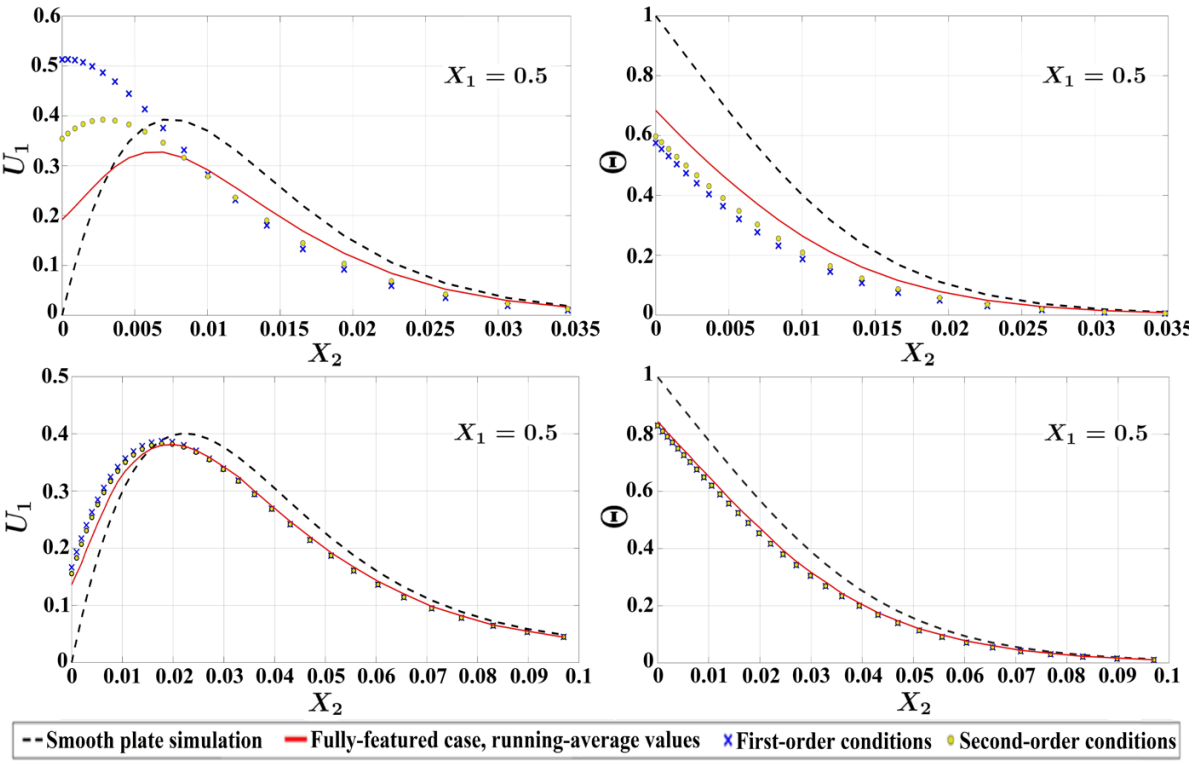

Figure 19: Predictions of the homogenized model in comparison to the fully-featured running-average results of the dimensionless streamwise velocity and temperature across a normal section at $X_1 = 0.5$, for two values of Gr: (top) $Gr = 5.563 \times 10^8$; (bottom) $Gr = 7.509 \times 10^6$. For both cases, $\epsilon = \frac{1}{10}$, $\frac{l}{e} = 3.75$, $Pr = 0.712$.

The observed deterioration of the predictions at relatively large values of ϵ is not explicitly related to the increase in ϵ; rather, it is due to the associated increase of the convective

coefficient $C = \epsilon^2 \sqrt{Gr}$ beyond a critical limit. In many circumstances (Bottaro, 2019; Lācis *et al.*, 2020; Bottaro & Naqvi, 2020), the theory has been validated for ϵ up to 0.2. Here, we set $\epsilon = 0.1$ and show that by reducing the Grashof number (and thus, C), the accuracy of the model improves. The macroscopic simulations are now set at a Grashof number of 7.509×10^6 (instead of 5.563×10^8), which results in a decrease of the convective coefficient C from 235.860 to 27.402. Fig. 19 demonstrates that even at first order, the effective conditions now provide a very good match with fully-featured simulation results. The same occurs for the temperature distribution along the virtual interface ($X_2 = 0$) and the behaviour of the local Nusselt number (Fig. 20).

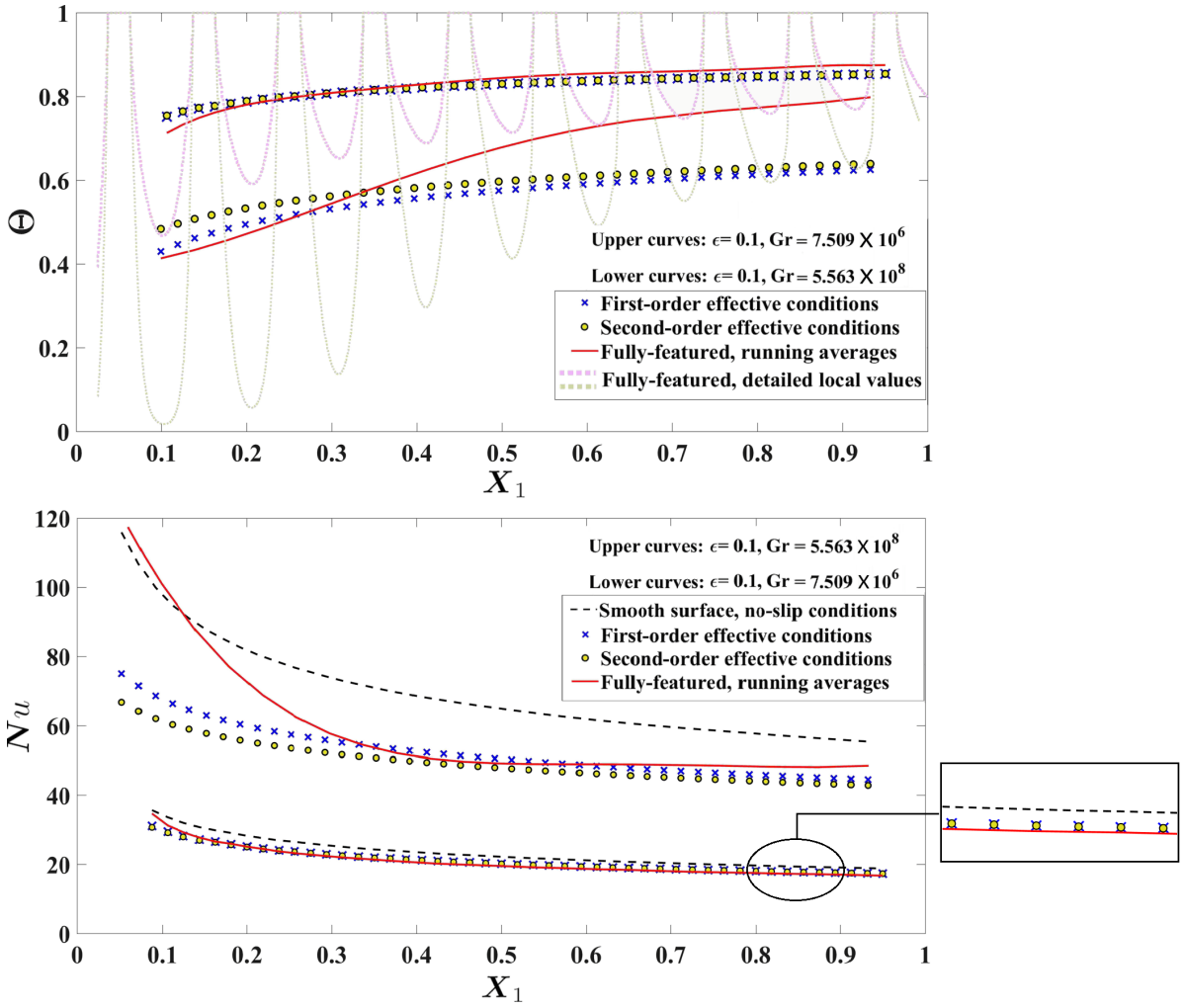

Figure 20: Predictions for: (top) the temperature distribution along the vertical fictitious surface ($X_2 = 0$); (bottom) the performance of the local Nusselt number. Patterns are given at two values of Gr. In both cases: $\epsilon = \frac{1}{10}$, $\frac{l}{e} = 3.75$, $Pr = 0.712$.

7.3 Limit of validity of the approximation

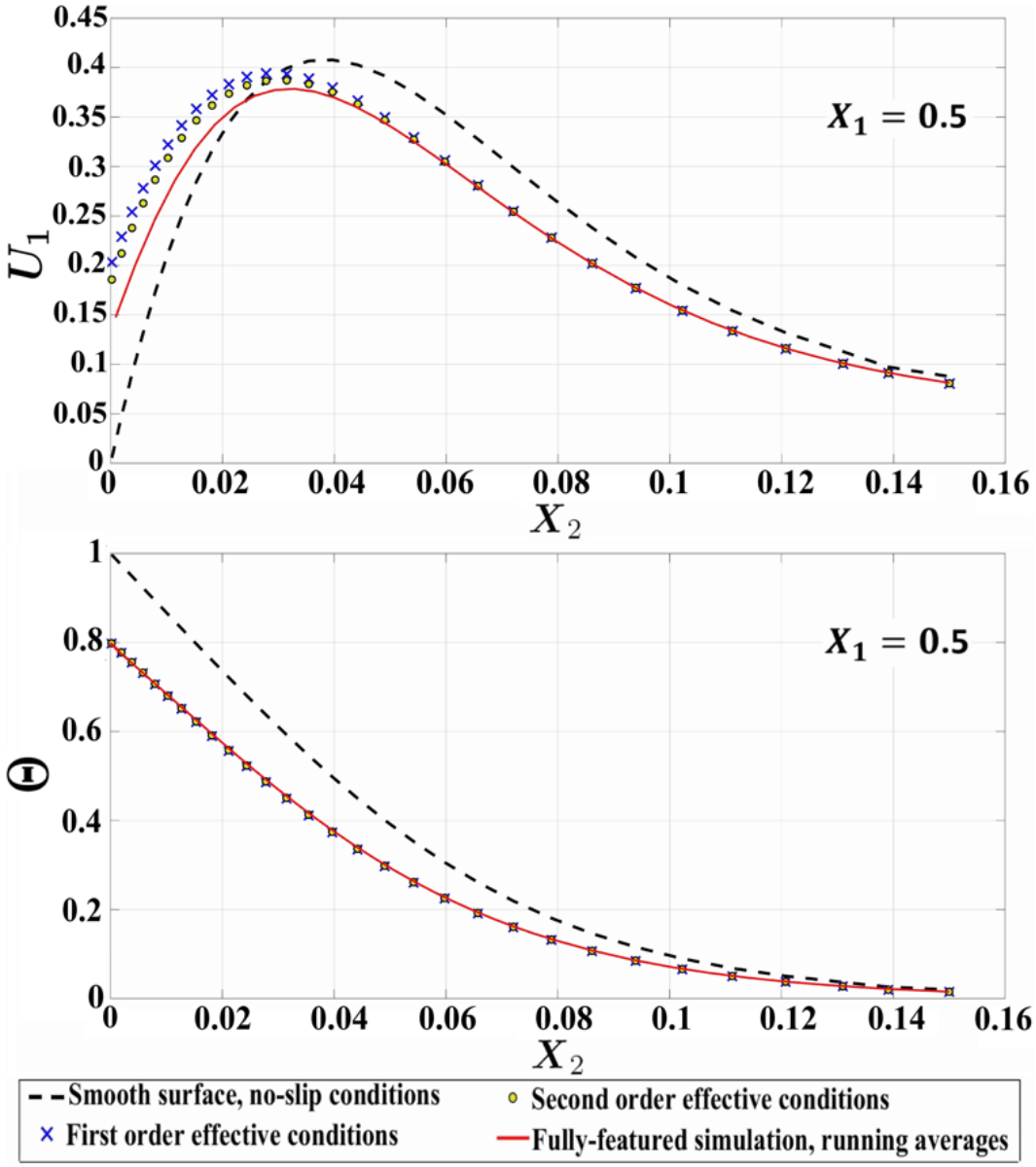

Figure 21: Predictions of the homogenized model in comparison to the fully-featured running-average results of the dimensionless temperature profiles at $X_1 = 0.5$. $\epsilon = 0.2$, $\frac{l}{e} = 3.75$, $Gr = 9.386 \times 10^5$, $Pr = 0.712$.

It has been argued in Section 7.2 that the accuracy of the proposed homogenization-based model may be linked to a single controlling parameter (C) that combines the effects of ϵ and Gr. Therefore, it is advantageous to define a limiting value of C below which the predictions of the presented model are assumed to be reliable. Based on analysis of the accuracy levels shown in Table 3, the critical value of C is expected to be around 40; below this value, rms deviations of the predicted velocity and temperature profiles are,

respectively, below 20% and 10%, and the absolute error on the predicted $\overline{Nu}$ is less than 4%. To validate this estimate, the simulation of the macroscopic problem has been carried out for the case of a vertical surface roughened with only five square ribs, i.e. $\epsilon = 0.2$ (relatively large), at $Gr = 9.386 \times 10^5$ so that the accuracy of the model at a value of $C = 38.752$ can be checked. The geometry of the ribs is characterized by a value of $\frac{\ell}{e} = 3.75$; the model coefficients given in Eq. (22) are used. The accuracy of the model is assessed through comparative analysis of velocity and temperature predictions across a normal section at $X_1 = 0.5$ (Fig. 21). Although the velocity predictions in the near-wall region are not perfect, especially with the first-order conditions, the temperature results are almost identical to the fully-featured running-average behaviour. From a practical point of view, the reliability of the thermal field predictions is sufficient to consider the model acceptable under the given condition, i.e. $C \lesssim 40$.

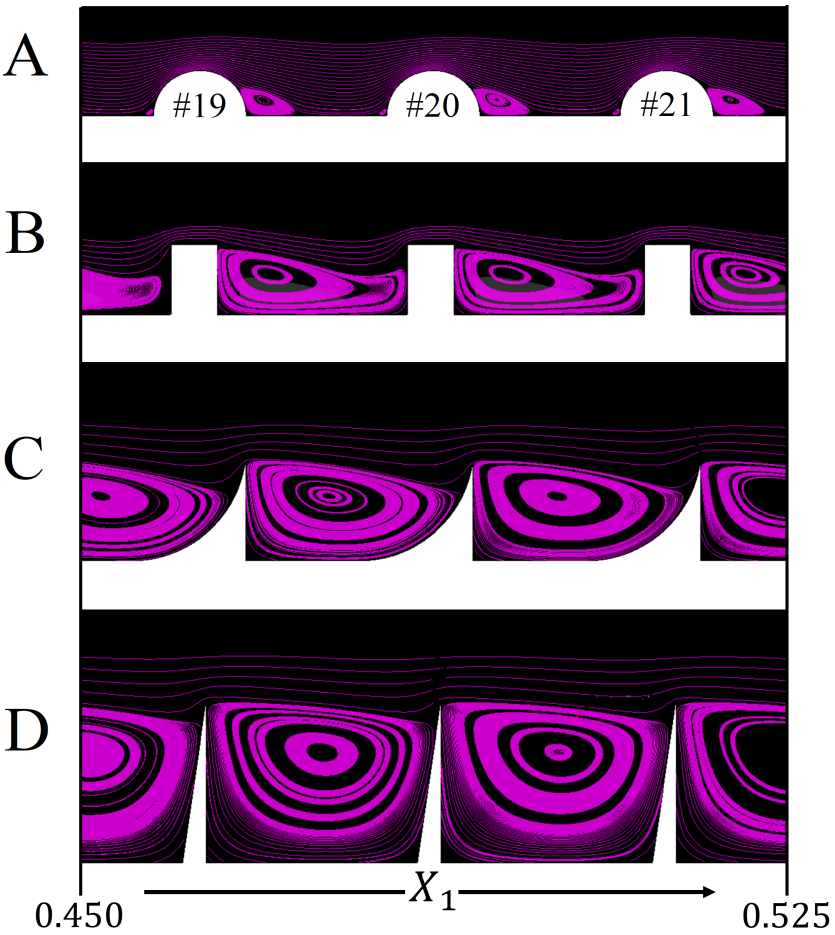

Figure 22: The different roughness patterns considered for model validation: (A) half circles with a diameter of 0.4ℓ; (B) rectangular ribs with a width of 0.2ℓ and a height of 0.3ℓ; (C) inward-curved ribs with a width of 0.5ℓ and a height of 0.45ℓ– circular curvature is tangential to baseplate; (D) right-angle triangles with a width of 0.1ℓ and a height of 0.7ℓ. The microscopic length scale, ℓ, indicates the pattern periodicity. Streamlines are displayed near and within the wall corrugations, for a specified range of X_1.

7.4 Model validation on different rib geometries

The robustness of the introduced model is further checked by employing the effective boundary conditions to study natural-convection heat transfer for different configurations of the roughness pattern, particularly, those shown in Fig. 22. Feature-resolving simulations and model calculations are conducted for the natural-convection flow over an isothermal vertical surface roughened with 40 ribs, at $Gr = 10^8$ and $Pr = 0.712$. Some complex flow structures within the inter-rib regions, captured by the full simulations, are displayed in the figure: these structures highlight the need of very well resolved (and expensive) simulations, highlighting the advantage of implementing equivalent, upscaled boundary conditions. In all cases examined the virtual wall is positioned on a plane passing through the tips/crests/outer rims of the ribs. It is noticeable that the *Full Separation* (FS) regime captured for blunt shapes (geometries B, C, D) differs qualitatively from that displayed in Fig. 11, with a single separation eddy between neighboring ribs, isolating the mainstream from the baseplate.

The model predictions of the surface-averaged Nusselt number ($\overline{Nu}$) are presented in Table 4; they are in good agreement with the corresponding results obtained from the full feature-resolving simulations, with a maximum deviation of less than 2.5% (detected for configuration A). For the flow conditions under investigation, all rib geometries considered reduce the heat transfer performance of the natural-convection system, with respect to smooth-wall case.

Table 4: Macroscopic coefficients and predictions of $\overline{Nu}$ for the studied rib geometries. the Nusselt number is calculated considering $\epsilon = \frac{1}{40}$, $Gr = 10^8$ and $Pr = 0.712$.

Geometry	λ_x	λ_z	m_{12}	$\mathcal{B}$	$\overline{Nu}$, first	$\overline{Nu}$, second	$\overline{Nu}$, resolving
A	0.0792	0.0890	0.0081	0.00029	48.587	48.530	47.480
B	0.0449	0.1040	0.0027	0.00035	45.769	45.711	45.470
C	0.0814	0.1938	0.0055	0.00168	42.565	42.353	42.313
D	0.0867	0.2117	0.0045	0.00132	41.718	41.560	41.852
Smooth	0	0	0	0	$\overline{Nu} = 49.544$		

8 CONCLUSIONS

A homogenization-based model is proposed for the study of the heat transfer by free convection over regularly micro-structured vertical surfaces. The approach provides a computationally cheap alternative to the standard feature-resolving simulations in the cases where the macroscopic behaviour of the flow is of interest, and it has been adopted in the past for the case of rough, micro-textured surfaces, in the absence of thermal effects. The procedure, eventually, yields parameters needed to enforce equivalent velocity and

temperature boundary conditions at a plane virtual surface, up to second order in terms of a small parameter ϵ, ratio of the pattern periodicity, ℓ, to the total plate length, L. Importantly, the effective boundary conditions derived here do not contain any empirical parameters.

As a typical implementation of the theory, the model is applied to the case of two-dimensional square ribs. The auxiliary systems are then reduced to either two-dimensional Stokes-like problems or Laplace-like or Poisson-like problems, which either admit trivial solutions or require a numerical solution in a periodic representative cell of the microscopic domain. The parameters contributing to the effective conditions belong to seven independent groups, i.e. the numerical solution of only seven auxiliary problems is sufficient to completely retrieve the effective conditions. The results are then extrapolated from distant matching surfaces to the plane passing through the outer edges of the ribs, beyond which the macroscopic simulation is intended to be performed. The most significant finding of the procedure is the proposed form of the effective boundary conditions. For the streamwise slip velocity, a buoyancy term acts as a corrector to the classical Navier-slip condition at first order, while pressure-gradient, temperature-gradient, and time-derivative terms appear at second order. A Robin boundary condition appears for the temperature effective condition, where a normal temperature gradient term, with a coefficient identical to Navier's spanwise slip coefficient, corrects the uniform wall temperature. The spanwise slip velocity and the transpiration velocity are also considered, to allow for example the usage of the model in turbulent flow cases where the spanwise and the normal velocity fluctuations are to be resolved in direct or large-eddy numerical simulations (Bottaro, 2019; Lācis *et al.*, 2020). A parametric study is conducted to investigate the effect of varying the rib size to pitch distance ratio on the values of the coefficients.

The efficiency of the proposed first- and second-order accurate conditions in modelling the effect of the surface microstructure on the macroscopic behaviour of the flow has been tested by comparing the obtained thermal and velocity fields with the corresponding results of full feature-resolving simulations at different values of ϵ and the Grashof number; the case of tiny square ribs is first considered for validation purposes, while other geometries are studied at a later stage for accuracy confirmation. All simulations have been conducted for laminar flow conditions at a constant Prandtl number equal to 0.712 (air). It is shown that the expensive mesh requirements for resolving complex inter-rib flow structures, associated with the *Separation-Reattachment-Separation* (SRS) regime at low values of Gr_x and the *Full Separation* (FS) regime at high values of Gr_x, can be significantly alleviated when the model is employed. A significant result is that the accuracy of the model can be linked to the single parameter $C = \epsilon^2 \sqrt{Gr}$ which measures the significance of the energy flux within the microscopic domain. A value of $C \approx 40$ is the critical limit below which the model is believed to yield acceptable predictions.

The dependence of the accuracy of the proposed model on a single parameter combining the effects of ϵ and Gr renders the approach applicable to large values of the Grashof number, provided that ϵ is sufficiently small, i.e. the number of ribs is ade-

quately large. The upscaling model described in this work represents a more versatile version of the effective conditions for natural convection over ribbed surfaces in comparison to the earlier model by Introïni *et al.* (2011) which neglected the buoyancy effect in the microscopic region and reported a single validity-limiting value of $Gr = 10^7$. In addition, the asymptotic homogenization method employed here represents a rigorous tool to formally advance in the order of accuracy. Second-order accurate boundary conditions are attained, which provides an enhancement to the validity range of Introïni's first-order approach.

This work opens up several perspectives, related for example to the accuracy and applicability limit of the model in the case of turbulent natural convection over ribbed surfaces. It would also be interesting to develop an optimization strategy to find optimal wall micro-patterns, able to maximize heat transfer from the surface. The procedure described can be easily extended to the case of weakly conducting or adiabatic corrugation elements. This will constitute the object of future investigations.

FUNDING

The financial support of the Italian Ministry of University and Research, program PRIN 2017, project 2017X7Z8S3 LUBRI-SMOOTH, is gratefully acknowledged.

Appendices

A AUXILIARY SYSTEMS FOR THE PROBLEM AT ORDER ϵ

The microscopic auxiliary systems at this order are arranged, according to the macroscopic forcing term, in the following groups:

Group (I): Forcing by the gradient of the outer stress (9 systems) $\dfrac{\partial S_{k2}}{\partial X_j}$

$$\frac{\partial \dot{u}_{ijk}}{\partial x_i} = -\breve{u}_{jk}, \qquad \frac{\partial^2 \dot{u}_{ijk}}{\partial x_\ell^2} - \frac{\partial \dot{p}_{jk}}{\partial x_i} = \breve{p}_k \delta_{ij} - 2\frac{\partial \breve{u}_{ik}}{\partial x_j}, \tag{25-a, b}$$

subject to

$$\dot{u}_{ijk} = 0 \quad \text{at } x_2 = y_w, \tag{25-c}$$

$$-\dot{p}_{jk}\,\delta_{i2} + \left(\frac{\partial \dot{u}_{ijk}}{\partial x_2} + \frac{\partial \dot{u}_{2jk}}{\partial x_i}\right) = -\left(\breve{u}_{ik}\,\delta_{j2} + \breve{u}_{2k}\,\delta_{ij}\right) \quad \text{at } x_2 \to \infty. \tag{25-d}$$

Group (II): Forcing by the square of outer stresses (3 systems) $\mathcal{R}_G(S_{k2})^2$

$$\frac{\partial \ddot{u}_{ik}}{\partial x_i} = 0, \qquad \frac{\partial^2 \ddot{u}_{ik}}{\partial x_\ell^2} - \frac{\partial \ddot{p}_k}{\partial x_i} = \breve{u}_{\ell k} \frac{\partial \breve{u}_{ik}}{\partial x_\ell}, \tag{26-a, b}$$

subject to

$$\ddot{u}_{ik} = 0 \quad \text{at } x_2 = y_w, \tag{26-c}$$

$$-\ddot{p}_k\,\delta_{i2} + \left(\frac{\partial \ddot{u}_{ik}}{\partial x_2} + \frac{\partial \ddot{u}_{2k}}{\partial x_i}\right) = 0 \quad \text{at } x_2 \to \infty. \tag{26-d}$$

Group (III): 3 systems: $\mathcal{R}_G S_{12} S_{22}$, $\mathcal{R}_G S_{12} S_{32}$, $\mathcal{R}_G S_{22} S_{32}$

(a) $\mathcal{R}_G S_{12} S_{22}$

$$\frac{\partial \ddot{u}_{i12}}{\partial x_i} = 0, \qquad \frac{\partial^2 \ddot{u}_{i12}}{\partial x_\ell^2} - \frac{\partial \ddot{p}_{12}}{\partial x_i} = \breve{u}_{\ell 1} \frac{\partial \breve{u}_{i2}}{\partial x_\ell} + \breve{u}_{\ell 2} \frac{\partial \breve{u}_{i1}}{\partial x_\ell}, \tag{27-a, b}$$

subject to

$$\ddot{u}_{i12} = 0 \quad \text{at } x_2 = y_w, \tag{27-c}$$

$$-\ddot{p}_{12}\,\delta_{i2} + \left(\frac{\partial \ddot{u}_{i12}}{\partial x_2} + \frac{\partial \ddot{u}_{212}}{\partial x_i}\right) = 0 \quad \text{at } x_2 \to \infty. \tag{27-d}$$

(b) $\mathcal{R}_G S_{12} S_{32}$

$$\frac{\partial \ddot{u}_{i13}}{\partial x_i} = 0, \qquad \frac{\partial^2 \ddot{u}_{i13}}{\partial x_\ell^2} - \frac{\partial \ddot{p}_{13}}{\partial x_i} = \breve{u}_{\ell 1} \frac{\partial \breve{u}_{i3}}{\partial x_\ell} + \breve{u}_{\ell 3} \frac{\partial \breve{u}_{i1}}{\partial x_\ell}, \tag{28-a, b}$$

subject to

$$\ddot{u}_{i13} = 0 \quad \text{at } x_2 = y_w, \tag{28-c}$$

$$-\ddot{p}_{13}\,\delta_{i2} + \left(\frac{\partial \ddot{u}_{i13}}{\partial x_2} + \frac{\partial \ddot{u}_{213}}{\partial x_i}\right) = 0 \quad \text{at } x_2 \to \infty. \tag{28-d}$$

(c) $\mathcal{R}_G S_{22} S_{32}$

$$\frac{\partial \ddot{u}_{i23}}{\partial x_i} = 0, \qquad \frac{\partial^2 \ddot{u}_{i23}}{\partial x_\ell^2} - \frac{\partial \ddot{p}_{23}}{\partial x_i} = \breve{u}_{\ell 2} \frac{\partial \breve{u}_{i3}}{\partial x_\ell} + \breve{u}_{\ell 3} \frac{\partial \breve{u}_{i2}}{\partial x_\ell}, \tag{29-a, b}$$

subject to

$$\ddot{u}_{i23} = 0 \quad \text{at } x_2 = y_w, \tag{29-c}$$

$$-\ddot{p}_{23}\,\delta_{i2} + \left(\frac{\partial \ddot{u}_{i23}}{\partial x_2} + \frac{\partial \ddot{u}_{223}}{\partial x_i}\right) = 0 \quad \text{at } x_2 \to \infty. \tag{29-d}$$

Group (IV): Coupling through the heat flux (1 system): $\mathcal{R}_G\,\eta$

$$\frac{\partial u_i{}'}{\partial x_i} = 0, \qquad \frac{\partial^2 u_i{}'}{\partial x_\ell^2} - \frac{\partial p'}{\partial x_i} = -\tilde{\theta}\delta_{i1}, \tag{30-a, b}$$

subject to

$$u_i{}' = 0 \quad \text{at } x_2 = y_w, \tag{30-c}$$

$$-p'\,\delta_{i2} + \left(\frac{\partial u_i{}'}{\partial x_2} + \frac{\partial u_2{}'}{\partial x_i}\right) = 0 \quad \text{at } x_2 \to \infty. \tag{30-d}$$

Group (V): Forcing by the outer stress (3 systems): $\mathcal{R}_G^2 S_{k2}$

$$\frac{\partial \overline{u}_{ik}}{\partial x_i} = 0, \qquad \frac{\partial^2 \overline{u}_{ik}}{\partial x_\ell^2} - \frac{\partial \overline{p}_k}{\partial x_i} = \breve{u}_{\ell k}\frac{\partial u_i^\dagger}{\partial x_\ell} + u_\ell^\dagger \frac{\partial \breve{u}_{ik}}{\partial x_\ell}, \tag{31-a, b}$$

subject to

$$\overline{u}_{ik} = 0 \quad \text{at } x_2 = y_w, \tag{31-c}$$

$$-\overline{p}_k\,\delta_{i2} + \left(\frac{\partial \overline{u}_{ik}}{\partial x_2} + \frac{\partial \overline{u}_{2k}}{\partial x_i}\right) = 0 \quad \text{at } x_2 \to \infty. \tag{31-d}$$

Group (VI): Forcing by a constant, buoyancy-related term (1 system): $\mathcal{R}_G^3$

$$\frac{\partial u_i^\ddagger}{\partial x_i} = 0, \qquad \frac{\partial^2 u_i^\ddagger}{\partial x_\ell^2} - \frac{\partial p^\ddagger}{\partial x_i} = u_\ell^\dagger \frac{\partial u_i^\dagger}{\partial x_\ell}, \tag{32-a, b}$$

subject to

$$u_i^\ddagger = 0 \quad \text{at } x_2 = y_w, \tag{32-c}$$

$$-p^\ddagger\,\delta_{i2} + \left(\frac{\partial u_i^\ddagger}{\partial x_2} + \frac{\partial u_2^\ddagger}{\partial x_i}\right) = 0 \quad \text{at } x_2 \to \infty. \tag{32-d}$$

Group (VII): Forcing by outer stress time fluctuation (3 systems): $\mathcal{R}_G \dfrac{\partial S_{k2}}{\partial t}$

$$\frac{\partial u_{ik}^t}{\partial x_i} = 0, \qquad \frac{\partial^2 u_{ik}^t}{\partial x_\ell^2} - \frac{\partial p_k^t}{\partial x_i} = \breve{u}_{ik}, \tag{33-a, b}$$

subject to

$$u_{ik}^t = 0 \quad \text{at } x_2 = y_w, \tag{33-c}$$

$$-p_k^t\,\delta_{i2} + \left(\frac{\partial u_{ik}^t}{\partial x_2} + \frac{\partial u_{2k}^t}{\partial x_i}\right) = 0 \quad \text{at } x_2 \to \infty. \tag{33-d}$$

B AUXILIARY SYSTEMS FOR THE TEMPERATURE AT ORDER ϵ^2

The eight microscopic auxiliary systems, defining the problem of the order ϵ^2 temperature, are arranged as follows:

Forcing by 2^{nd} derivative of the outer temperature (3 systems): $\dfrac{\partial \eta}{\partial X_k}$

$$\frac{\partial^2 \theta_k^!}{\partial x_i^2} = -2\frac{\partial \tilde{\theta}}{\partial x_k}, \tag{34-a}$$

subject to

$$\theta_k^! = 0 \quad \text{at } x_2 = y_w, \qquad \frac{\partial \theta_k^!}{\partial x_2} = -\tilde{\theta}\delta_{k2} \quad \text{at } x_2 \to \infty. \tag{34-b, c}$$

Coupling through the outer stress (3 systems): $Pr\mathcal{R}_G\,\eta S_{k2}$

$$\frac{\partial^2 \theta_k^*}{\partial x_i^2} = \breve{u}_{ik}\frac{\partial \tilde{\theta}}{\partial x_i}, \tag{35-a}$$

subject to

$$\theta_k^* = 0 \quad \text{at } x_2 = y_w, \qquad \frac{\partial \theta_k^*}{\partial x_2} = 0 \quad \text{at } x_2 \to \infty. \tag{35-b, c}$$

Forcing by the outer temperature gradient (1 system): $Pr\,\mathcal{R}_G^2\,\eta$

$$\frac{\partial^2 \theta^{**}}{\partial x_i^2} = u_i^\dagger \frac{\partial \tilde{\theta}}{\partial x_i}, \tag{36-a}$$

subject to

$$\theta^{**} = 0 \quad \text{at } x_2 = y_w, \qquad \frac{\partial \theta^{**}}{\partial x_2} = 0 \quad \text{at } x_2 \to \infty. \tag{36-b, c}$$

Forcing by time fluctuations of the outer heat flux (1 system): $Pr\,\mathcal{R}_G\dfrac{\partial \eta}{\partial t}$

$$\frac{\partial^2 \theta^t}{\partial x_i^2} = \tilde{\theta}, \tag{37-a}$$

subject to

$$\theta^t = 0 \quad \text{at } x_2 = y_w, \qquad \frac{\partial \theta^t}{\partial x_2} = 0 \quad \text{at } x_2 \to \infty. \tag{37-b, c}$$

C SMOOTH SURFACE CASE: SPECIFICATIONS OF THE TWO-DIMENSIONAL GRID

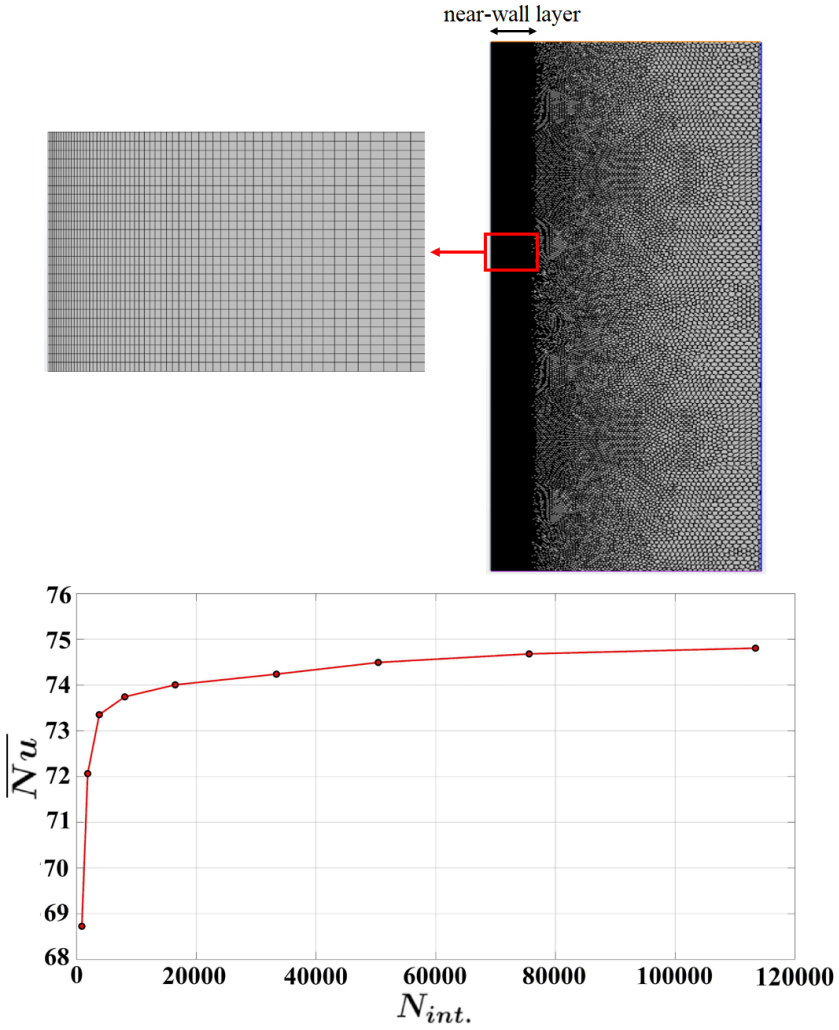

Figure 23: Description of the two-dimensional grid of the smooth plate case. A graphical representation of the solution dependence on the number of cells in the vicinity of the wall, $N_{int.}$, is provided in the bottom frame. Grid convergence is achieved for a number of cells in the near-wall layer above 10^5. $Gr = 5.563 \times 10^8$, $Pr = 0.712$.

The two-dimensional grid structure is shown in Fig. 23. Special care is devoted to the domain discretization near the wall. A *near-wall layer* is thus defined to include the viscous and the thermal boundary layers where the X_2-gradients of velocity and temperature are significant. A rough estimate of the thickness of the boundary layer may be obtained based on the classical Squire-Eckert theoretical prediction (Lienhard & Lienhard, 2019). Accordingly, the thickness of the boundary layers $\hat{\delta}$ (assuming $\hat{\delta}_{thermal} \approx \hat{\delta}_{viscous}$) can be calculated based on the vertical location along the plate ($\hat{x}_1$) and the local Grashof number (Gr_x) as follows:

$$\hat{\delta} = 3.936\,\hat{x}_1 \left[\frac{0.952 + Pr}{Gr_x\,Pr^2}\right]^{0.25}. \tag{38}$$

The maximum boundary layer thickness is reached at the end of the plate, with $\hat{x}_1 = L$ and $Gr_x = Gr = 5.563 \times 10^8$. From Eq. (38), the maximum boundary layer thickness is about $0.034L$. As shown in Fig. 23 (top), the thickness of the near-wall layer for the most refined mesh is taken equal to $0.06L$.

A grid-dependency study is carried out by successively refining the mesh near the surface, until the results of the surface-averaged Nusselt number converge, as shown in Fig. 23 (bottom). For all grids tested, the mesh growth rate in the wall-normal direction is 1.02, and the maximum cell aspect ratio is kept below 10 by refining the streamwise and the normal directions simultaneously. The reported value of the average Nusselt number is estimated to be 75.055 based on Richardson's extrapolation of the results on the two finest meshes.

D SMOOTH SURFACE CASE: FURTHER VALIDATION OF THE NUMERICAL RESULTS

The similarity solution by Ostrach (1953) provides a valuable database for the validation of the velocity and the temperature fields. According to Ostrach's model, the dimensionless streamwise velocity, $U_1^{Ost} = \dfrac{\hat{u}_1}{\frac{\nu}{\hat{x}_1}\sqrt{Gr_x}}$, and the dimensionless temperature, $\Theta = \dfrac{\hat{T} - \hat{T}_\infty}{\hat{T}_w - \hat{T}_\infty}$, are functions of a similarity parameter, $\eta = (\dfrac{Gr_x}{4})^{\frac{1}{4}}\,\dfrac{X_2}{X_1}$, for a given Prandtl number. A comparison between the present numerical results at different sections along the plate and the similarity solution is presented in Fig. 24. It is noticeable that the present results for both the velocity and the thermal fields are in good agreement with Ostrach's, especially at relatively low values of η, i.e., close to the wall. A similar conclusion was drawn when Ostrach compared the results of his model to experimental data from the literature, finding that the agreement was not perfect near the outer edge of the boundary layer. The slight deviation between the present results and Ostrach's solution away from the wall may be attributed to the fact that, unlike the present numerical setup, Ostrach's model considered a domain of infinite width, for the fields far

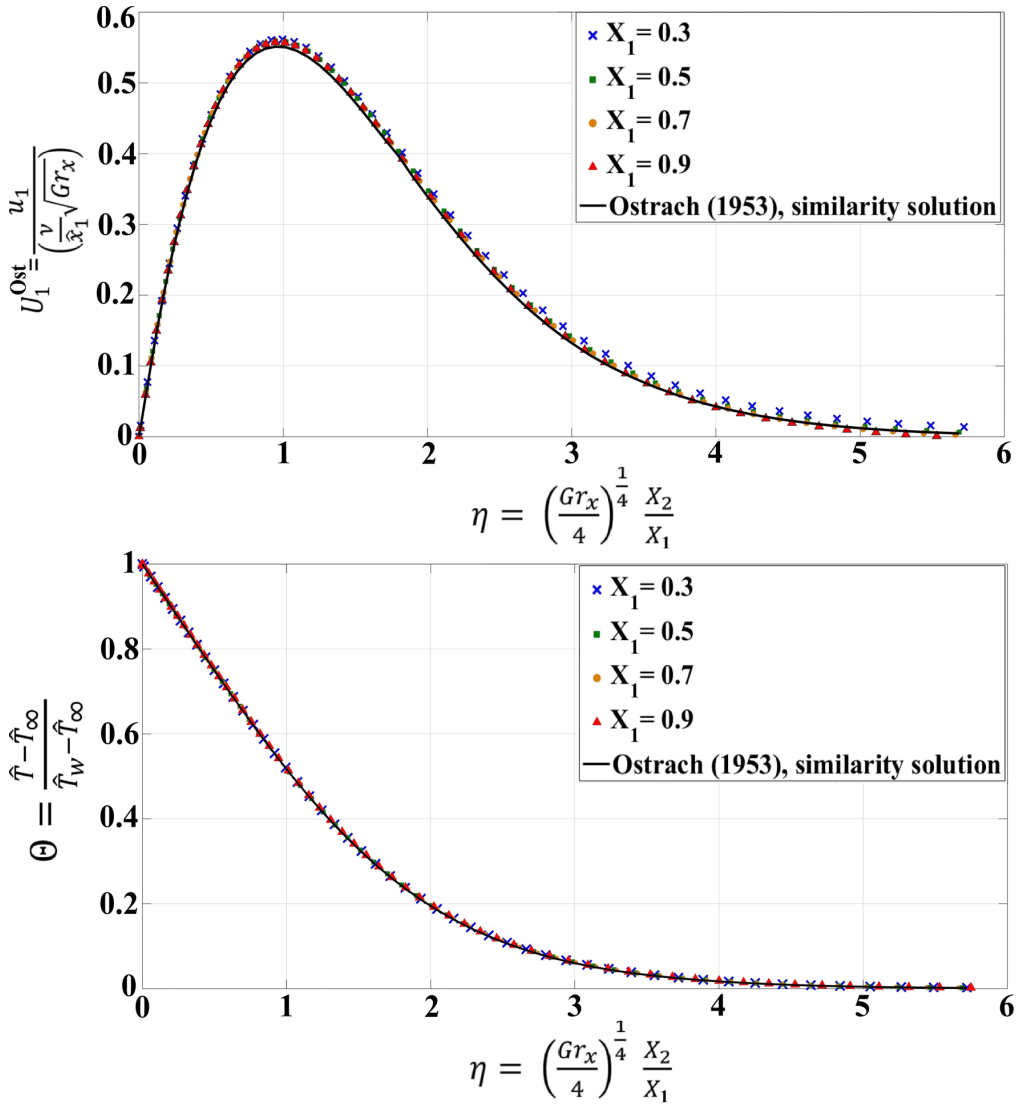

Figure 24: Smooth surface case: validation of the results of velocity and thermal fields with the reference similarity solution by Ostrach (1953) at $Pr = 0.712$.

from the plate to be unperturbed.

E FEATURE-RESOLVING SIMULATIONS OF THE RIBBED SURFACE AT DIFFERENT VALUES OF ϵ: COMPARATIVE DESCRIPTION OF RUNNING-AVERAGE FIELDS.

The running-average fields, obtained from different fully-featured simulations, along the vertical plane $X_2 = 0$ and across a normal section at the middle of the plate are presented in Fig. 25 in a comparative manner to get an idea about the effects of increasing ϵ on the flow characteristics. Note that the results of the corresponding smooth surface simulation

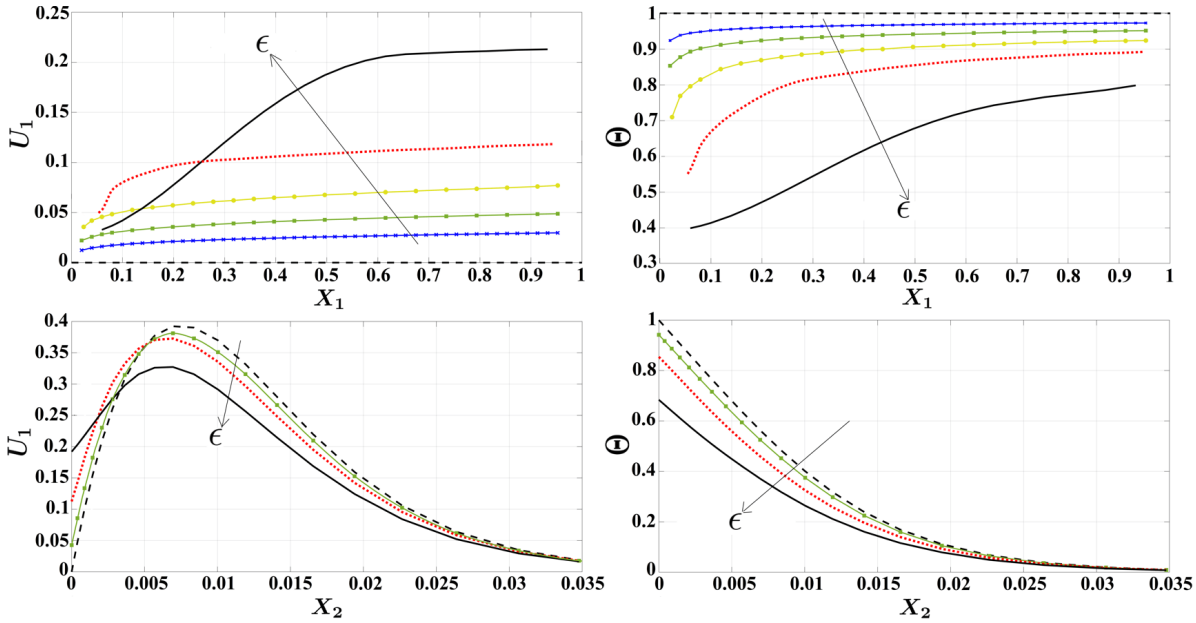

Figure 25: Fully-featured simulations with different values of ϵ: (top) running-averaged behaviours of the dimensionless streamwise velocity (left) and temperature (right) along the plane $X_2 = 0$; (bottom) running-averaged profiles of the dimensionless streamwise velocity (left) and temperature (right) across a normal section at $X_1 = 0.5$. Curves are: smooth surface (dashed black line), $\epsilon = \frac{1}{168}$ (blue line), $\epsilon = \frac{1}{84}$ (green line), $\epsilon = \frac{1}{42}$ (yellow line), $\epsilon = \frac{1}{21}$ (red dotted line), $\epsilon = \frac{1}{10}$ (solid black line). For all cases, $\frac{l}{e} = 3.75$, $Gr = 5.563 \times 10^8$, $Pr = 0.712$.

and the previously shown results of the case $\epsilon = \dfrac{1}{168}$ are included in the figure. The analysis of the velocity and the temperature distributions along the fictitious boundary (Fig. 25-(top)) reveals that the slip velocity (deviation from $U_1 = 0$) and the thermal slip (absolute deviation from $\Theta = 1$) increase with ϵ, which qualitatively agrees with the dependence given in Eqs. (21-a and 21-c). The magnitude of the normal temperature gradient at the wall decreases with ϵ, i.e. the heat transfer from the wall is reduced. It is also observed that the temperature level away from the surface is lower as ϵ increases, which in turn yields a reduction of the buoyancy term in the momentum equation, thus flattening the velocity peak.

REFERENCES

Ahmadi, M., Mostafavi, G. & Bahrami, M. 2014 Natural convection from rectangular interrupted fins. *Intl J. Therm. Sci.* **82**, 62–71.

Babuška, I. 1976 Homogenization and its application. Mathematical and computational problems, in: Hubbard, B. (Ed.), *Numerical Solution of Partial Differential Equations–III*, pp. 89–116. Academic Press .

Bechert, D.W. & Bartenwerfer, M. 1989 The viscous flow on surfaces with longitudinal ribs. *J. Fluid Mech.* **206**, 105–129.

Bhavnani, S.H. & Bergles, A.E. 1990 Effect of surface geometry and orientation on laminar natural convection heat transfer from a vertical flat plate with transverse roughness elements. *Intl J. Heat Mass Transfer* **33** (5), 965–981.

Bhavnani, S.H. & Bergles, A.E. 1991 Natural convection heat transfer from sinusoidal wavy surfaces. *Wärme-Stoffübertrag.* **26** (6), 341–349.

Bottaro, A. 2019 Flow over natural or engineered surfaces: an adjoint homogenization perspective. *J. Fluid Mech.* **877**, P1.

Bottaro, A. & Naqvi, S.B. 2020 Effective boundary conditions at a rough wall: a high-order homogenization approach. *Meccanica* **55** (9), 1781–1800.

Bunker, R.S. & Donnellan, K.F. 2003 Heat transfer and friction factors for flows inside circular tubes with concavity surfaces. *ASME J. Turbomach.* **125** (4), 665–672.

Cavazzuti, M. & Corticelli, M.A. 2008 Optimization of a buoyancy chimney with a heated ribbed wall. *Heat Mass Transfer* **44** (4), 421–435.

Chyu, M.K., Oluyede, E.O. & Moon, H.-K. 2007 Heat transfer on convective surfaces with pin-fins mounted in inclined angles. *Turbo Expo: Power for Land, Sea, and Air* **4**, 861–869.

El Ghandouri, I., El Maakoul, A., Saadeddine, S. & Meziane, M. 2020 Design and numerical investigations of natural convection heat transfer of a new rippling fin shape. *Appl. Therm. Eng.* **178**, 115670.

Engquist, B. & Souganidis, P.E. 2008 Asymptotic and numerical homogenization. *Acta Numer.* **17**, 147–190.

Guglielmini, G., Nannei, E. & Tanda, G. 1987 Natural convection and radiation heat transfer from staggered vertical fins. *Intl J. Heat Mass Transfer* **30** (9), 1941–1948.

Hærvig, J. & Sørensen, H. 2020 Natural convective flow and heat transfer on unconfined isothermal zigzag-shaped ribbed vertical surfaces. *Intl Commun. Heat Mass Transfer* **119**, 104982.

Han, J.-C., Dutta, S. & Ekkad, S. 2012 *Gas Turbine Heat Transfer and Cooling Technology*. CRC Press.

Introïni, C., Quintard, M. & Duval, F. 2011 Effective surface modeling for momentum and heat transfer over rough surfaces: Application to a natural convection problem. *Intl J. Heat Mass Transfer* **54** (15-16), 3622–3641.

Jiménez Bolaños, S. & Vernescu, B. 2017 Derivation of the Navier slip and slip length for viscous flows over a rough boundary. *Phys. of Fluids* **29** (5), 057103.

Joshi, Y., Willson, T. & Hazard, S.J., III 1989 An experimental study of natural convection from an array of heated protrusions on a vertical surface in water. *ASME J. Electron. Packag.* **111** (2), 121–128.

Kishinami, K., Saito, H. & Tokura, I. 1990 An experimental study on natural convective heat transfer from a vertical wavy surface heated at convex/concave elements. *Exp. Therm. Fluid Sci.* **3** (3), 305–315.

Lācis, U., Sudhakar, Y., Pasche, S. & Bagheri, S. 2020 Transfer of mass and momentum at rough and porous surfaces. *J. Fluid Mech.* **884**, A21.

Lienhard, J.H., IV & Lienhard, J.H., V 2019 *A Heat Transfer Textbook,* 5th ed. Cambridge, MA, USA: Phlogiston Press.

Luchini, P., Manzo, F. & Pozzi, A. 1991 Resistance of a grooved surface to parallel flow and cross-flow. *J. Fluid Mech.* **228**, 87–109.

Navier, C. 1823 Mémoire sur les lois du mouvement des fluides. *Mém. Acad. R. Sci. Inst. France* **6**, 389–440.

Nishikawa, M., Otomo, H., Yoshida, Y., Deguchi, J., Tsukamoto, M. & Yamamoto, T. 2020 The cooling mechanism of minuscule ribbed surfaces. *Sci. Rep.* **10** (1), 5635.

Ostrach, S. 1953 An analysis of laminar free-convection flow and heat transfer about a flat plate parallel to the direction of the generation body force. NACA Technical Report 1111 .

Tanda, G. 1997 Natural convection heat transfer in vertical channels with and without transverse square ribs. *Intl J. Heat Mass Transfer* **40** (9), 2173–2185.

Tanda, G. 2008 Natural convective heat transfer in vertical channels with low-thermal-conductivity ribs. *Intl J. Heat Fluid Flow* **29** (5), 1319–1325.

Tanda, G. 2017 Experiments on natural convection in water-cooled ribbed channels with different aspect ratios. *Intl J. Heat Mass Transfer* **110**, 606–612.

Yao, L.-S. 2006 Natural convection along a vertical complex wavy surface. *Intl J. Heat Mass Transfer* **49** (1-2), 281–286.

Zampogna, G.A., Magnaudet, J. & Bottaro, A. 2019*a* Generalized slip condition over rough surfaces. *J. Fluid Mech.* **858**, 407–436.

Zampogna, G.A., Naqvi, S.B., Magnaudet, J. & Bottaro, A. 2019*b* Compliant riblets: Problem formulation and effective macrostructural properties. *J. Fluids Struct.* **91**, 102708.

SUPPLEMENTARY MATERIAL

This part includes supplementary data related to the main article "A homogenization approach for buoyancy-induced flows over micro-textured vertical surfaces" by **Essam Nabil Ahmed**, **Alessandro Bottaro** and **Giovanni Tanda.**

S1 Numerical results of $\mathcal{O}(\epsilon^0)$ systems: $e/\ell = 0.25$, $y_\infty = 5$

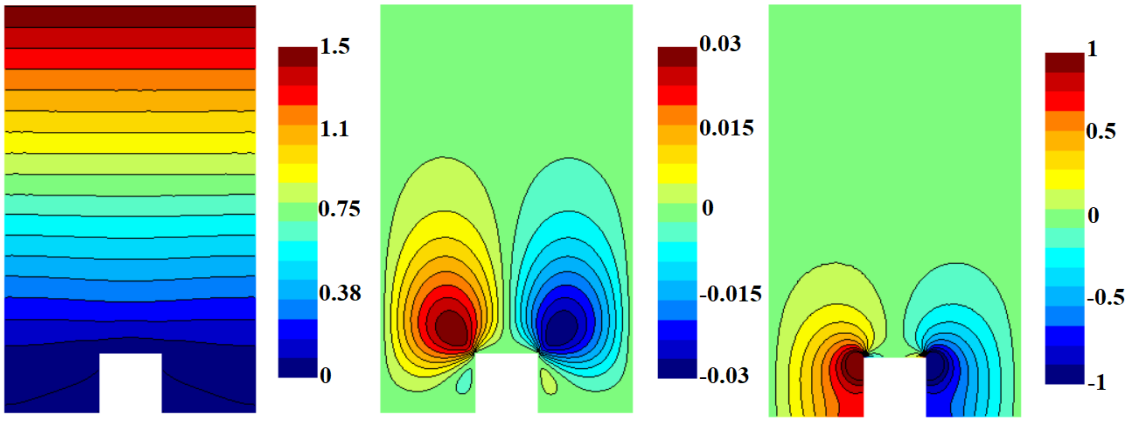

Figure S1: Numerical results in the proximity of the solid surface for: (left) $\breve{u}_{11}$; (center) $\breve{u}_{21}$; (right) $\breve{p}_1$.

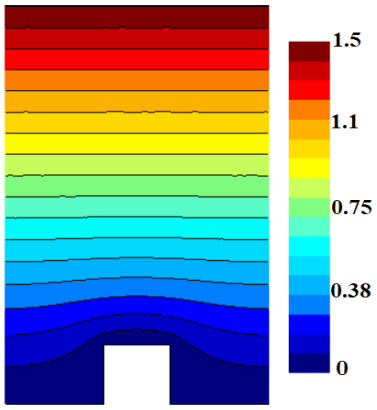

Figure S2: Numerical results for $\breve{u}_{33}$ in the proximity of the solid surface.

The systems S_{k2} represent the forcing of the leading-order problem by the three outer stresses (streamwise, normal, and spanwise). For the sub-system (S_{12}), the results of the Stokes problem ($\breve{u}_{11}$, $\breve{u}_{21}$, $\breve{p}_1$) near the rib are shown in Fig. S1. The only result of interest is $\breve{u}_{11}$ which increases monotonically with the coordinate x_2 until reaching a

value of 5.0396 at $x_2 = y_\infty = 5$. The result of the decoupled Laplace problem for the sub-system (S_{32}) is shown in Fig. S2. The value of $\breve{u}_{33}$ monotonically increases with x_2, reaching the value 5.0861 at the matching surface $x_2 = y_\infty = 5$. The system $\mathcal{R}_G$ represents the leading-order effect of the buoyancy force on the microscale problem. The results of the Stokes problem $(u_1^\dagger,\, u_2^\dagger,\, p^\dagger)$ in the vicinity of the rib are shown in Fig. S3. The only result of interest is $u_1^\dagger$ which monotonically increases at a slowing rate with the coordinate x_2, reaching a value of 12.7002 at $x_2 = y_\infty = 5$.

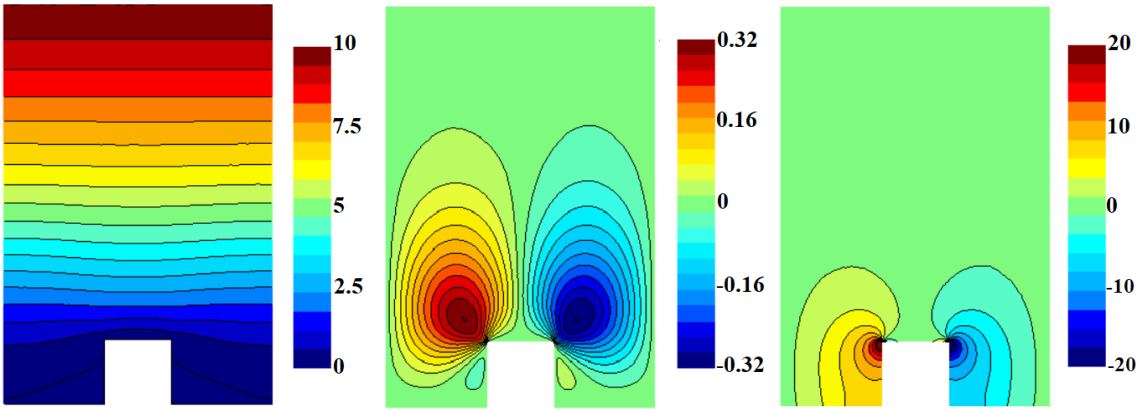

Figure S3: Numerical results in the proximity of the solid surface for: (left) $u_1^\dagger$; (center) $u_2^\dagger$; (right) $p^\dagger$.

S2 Numerical results of $\mathcal{O}(\epsilon^1)$ systems: $e/\ell = 0.25$, $y_\infty = 5$

For the temperature problem, the similarity between the Laplace system describing the microscopic parameter $\tilde{\theta}$ and that describing $\breve{u}_{33}$ allows for a solution of $\tilde{\theta}$ identical to that shown in Fig. S2. The velocity-related problems may be categorized as follows:

I- **Systems with trivial solutions**

The similarity between $\tilde{\theta}$ and $\breve{u}_{33}$, in addition to the already mentioned trivial solutions of many parameters in $\mathcal{O}(\epsilon^0)$ problem, simplifies and reduces different systems of equations in $\mathcal{O}(\epsilon^1)$ problem. The systems $\dfrac{\partial S_{22}}{\partial X_2}$, $\mathcal{R}_G^2 S_{22}$, $\mathcal{R}_G (S_{22})^2$, $\mathcal{R}_G (S_{32})^2$, $\mathcal{R}_G (S_{12} S_{22})$, $\mathcal{R}_G (S_{22} S_{32})$, and $\mathcal{R}_G \dfrac{\partial S_{22}}{\partial t}$ admit, respectively, the trivial solutions:

$$\frac{\partial S_{22}}{\partial X_2}: \quad \dot{u}_{122} = \dot{u}_{222} = \dot{u}_{322} = 0,\ \dot{p}_{22} = x_2 - y_\infty,$$

$$\mathcal{R}_G^2 S_{22}: \quad \overline{u}_{12} = \overline{u}_{22} = \overline{u}_{32} = \overline{p}_2 = 0,$$

$$\mathcal{R}_G (S_{22})^2: \quad \ddot{u}_{122} = \ddot{u}_{222} = \ddot{u}_{322} = \ddot{p}_{22} = 0,$$

$$
\begin{aligned}
\mathcal{R}_G(S_{32})^2: &\quad \ddot{u}_{133} = \ddot{u}_{233} = \ddot{u}_{333} = \ddot{p}_{33} = 0,\\
\mathcal{R}_G(S_{12}S_{22}): &\quad \ddot{u}_{112} = \ddot{u}_{212} = \ddot{u}_{312} = \ddot{p}_{12} = 0,\\
\mathcal{R}_G(S_{22}S_{32}): &\quad \ddot{u}_{123} = \ddot{u}_{223} = \ddot{u}_{323} = \ddot{p}_{23} = 0,\\
\mathcal{R}_G\frac{\partial S_{22}}{\partial t}: &\quad u^t_{12} = u^t_{22} = u^t_{32} = p^t_2 = 0.
\end{aligned}
$$

II- **Systems with all parameters vanishing away from the wall**

Poisson-like systems

The systems forced by $\frac{\partial S_{12}}{\partial X_3}$, $\frac{\partial S_{32}}{\partial X_1}$, $\mathcal{R}_G^2 S_{32}$, and $\mathcal{R}_G S_{12} S_{32}$ can be reduced to two-dimensional Poisson-like problems. The numerical solutions reveal that the values of the parameters $\dot{u}_{331}$, $\dot{u}_{313}$, $\overline{u}_{33}$, and $\ddot{u}_{313}$, respectively, vanish away from the ribbed wall, giving no contribution to the effective boundary conditions at the matching surface, as displayed in Fig. S4. The other parameters included in the above-mentioned four systems have zero values throughout the unit cell.

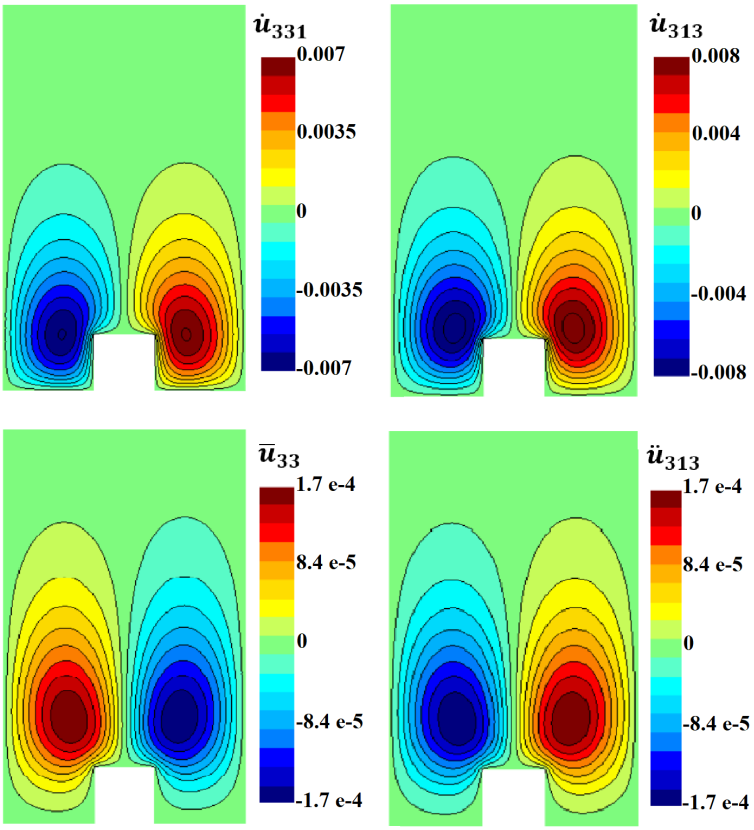

Figure S4: Numerical results of Poisson-like systems, in the $\mathcal{O}(\epsilon^1)$ problem, with no contribution to the effective boundary conditions.

Stokes-like systems

The systems forced by $\mathcal{R}_G^2 S_{12}$, $\mathcal{R}_G (S_{12})^2$, and $\mathcal{R}_G^3$ can be reduced to two-dimensional Stokes-like problems with the values of $\overline{u}_{31}$, $\ddot{u}_{311}$, and $u_3^{\ddagger}$ equal to zero throughout the unit cell. The non-trivial solutions of the Stokes-like problems show that all included parameters vanish away from the ribbed surface, as can be seen in figure S5.

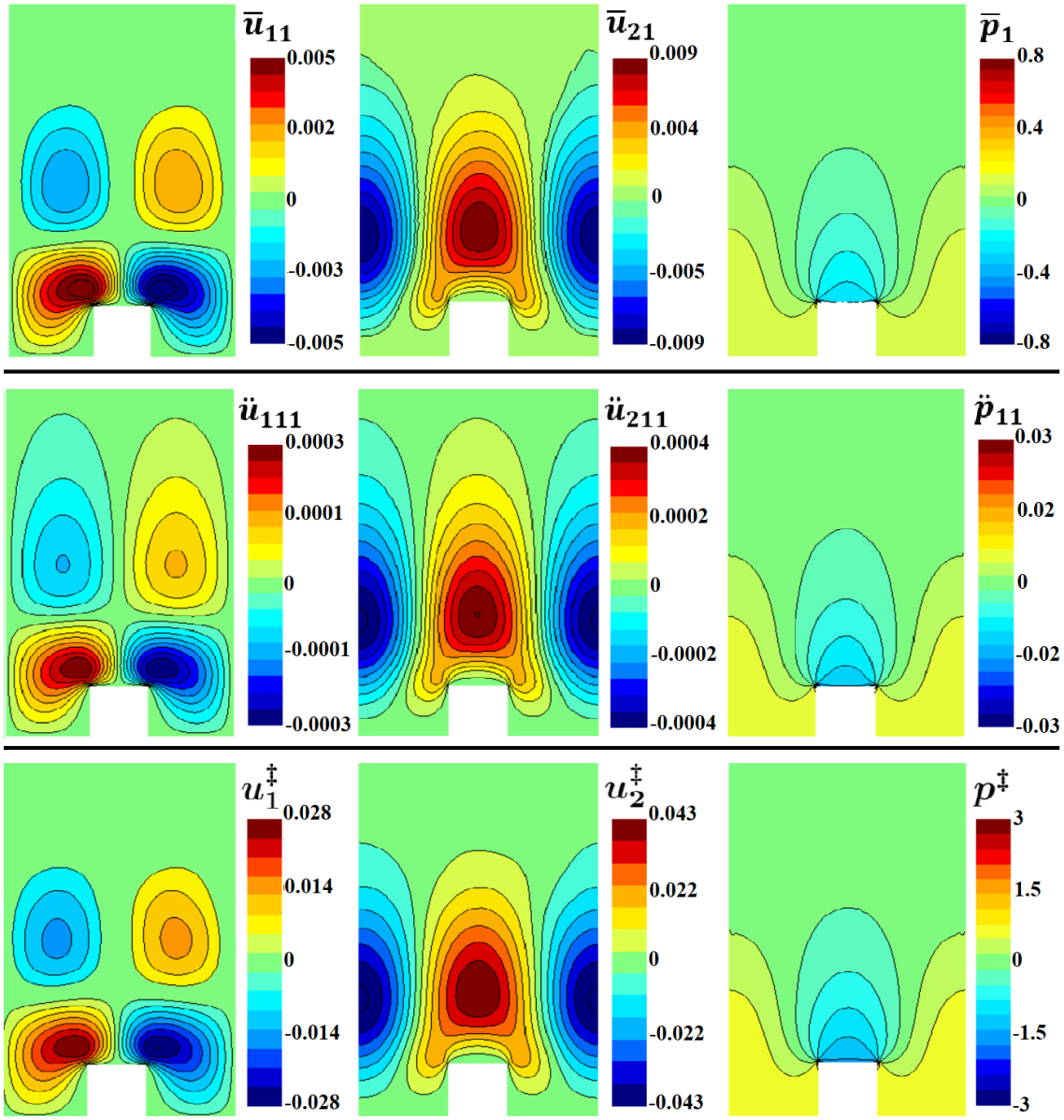

Figure S5: Numerical results of Stokes-like systems, in the $\mathcal{O}(\epsilon^1)$ problem, giving no contribution to the effective boundary conditions: (top) $\mathcal{R}_G^2 S_{12}$ system; (middle) $\mathcal{R}_G (S_{12})^2$ system; (bottom) $\mathcal{R}_G^3$ system.

III- **Systems with non-monotonic behavior along the y-direction**

The analysis of the systems forced by $\frac{\partial S_{12}}{\partial X_2}$ and $\frac{\partial S_{32}}{\partial X_2}$ shows non-monotonic quadratic behaviors of the parameters $\dot{u}_{121}$ and $\dot{u}_{323}$ along the x_2-direction, with vanishing values at the matching surface, as shown in Fig. S6. The other parameters included in the two systems have no contribution to the effective boundary conditions at the matching surface as they either monotonically vanish away from the rib ($\dot{u}_{221}$, $\dot{p}_{21}$) or have zero values throughout the whole unit cell ($\dot{u}_{321}$, $\dot{u}_{123}$, $\dot{u}_{223}$, $\dot{p}_{23}$).

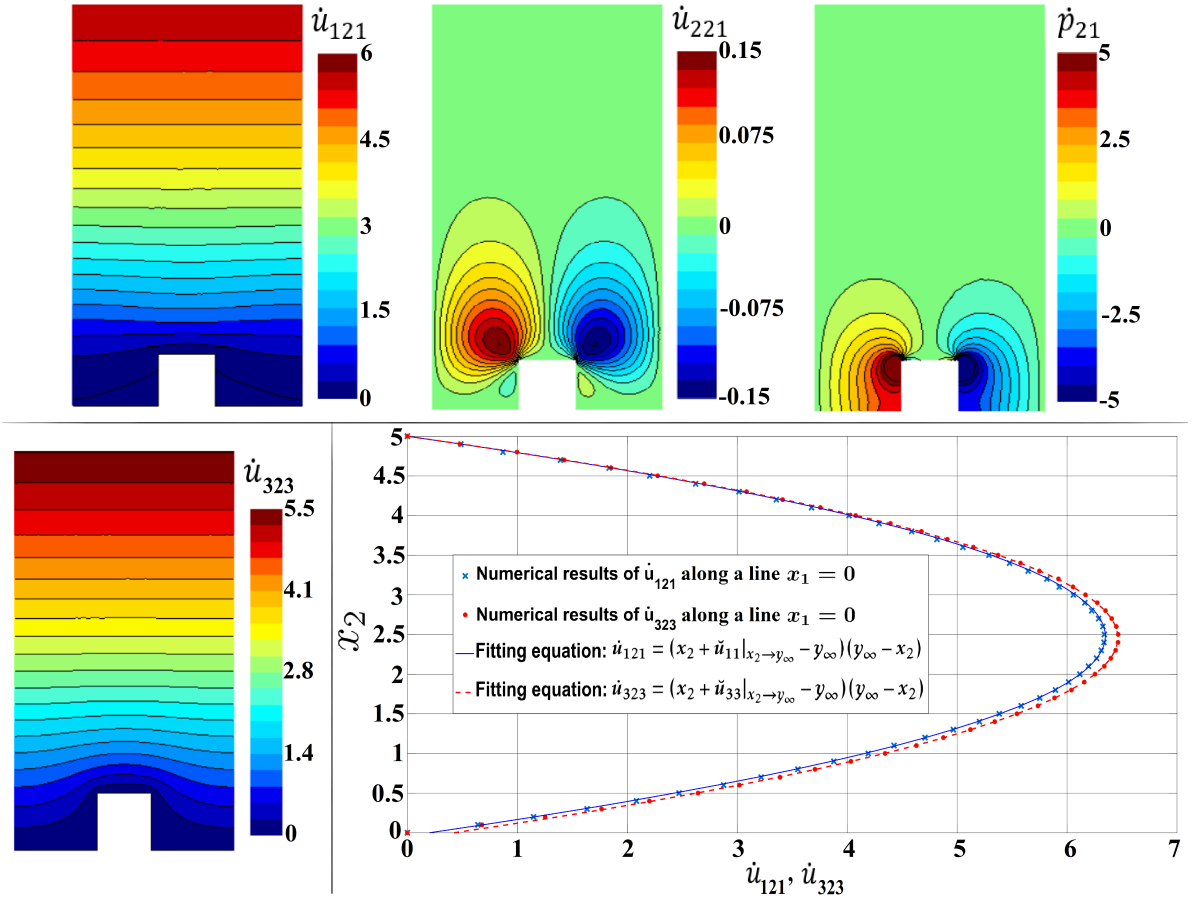

Figure S6: Systems with non-monotonic behavior: (top) $\frac{\partial S_{12}}{\partial X_2}$: the Stokes system; (bottom-left) $\frac{\partial S_{32}}{\partial X_2}$: the Laplace system; (bottom-right) graphical representations of the non-monotonic behaviors, with the quadratic fitting form by Bottaro & Naqvi (2020), admissible above $x_2 = 1$.

IV- **Systems with a monotonically-decreasing parameter of interest**

Poisson-like system

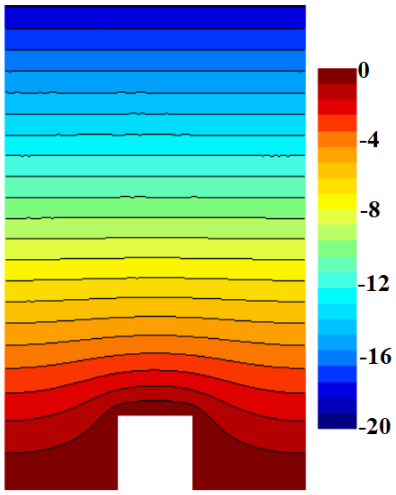

Figure S7: Contours of u^t_{33} in the vicinity of the wall.

The system forced by $\mathcal{R}_G \dfrac{\partial S_{32}}{\partial t}$ can be reduced to a two-dimensional Poisson-like problem in which the only value of interest is u^t_{33}. The contours of u^t_{33} in the vicinity of the rib are shown in Fig. S7. The value of this parameter experiences a monotonic decrease along the x_2-direction, reaching a value of about -43.8582 at $x_2 = y_\infty = 5$.

Stokes-like systems

The analysis of the systems forced by $\dfrac{\partial S_{12}}{\partial X_1}$, $\dfrac{\partial S_{32}}{\partial X_3}$, and $\mathcal{R}_G \dfrac{\partial S_{12}}{\partial t}$ shows that they become two-dimensional Stokes-like problems with vanishing values of $\dot{u}_{311}$, $\dot{u}_{333}$, and u^t_{31} throughout the unit cell. The numerical results of $\dot{u}_{211}$, $\dot{u}_{233}$, and u^t_{11} show monotonic decrease along x_2, reaching values of about -12.7002, -12.9402, and -42.4485 at the matching interface, respectively. The numerical results of the preceding systems in the vicinity of the rib are shown in Fig. S8.

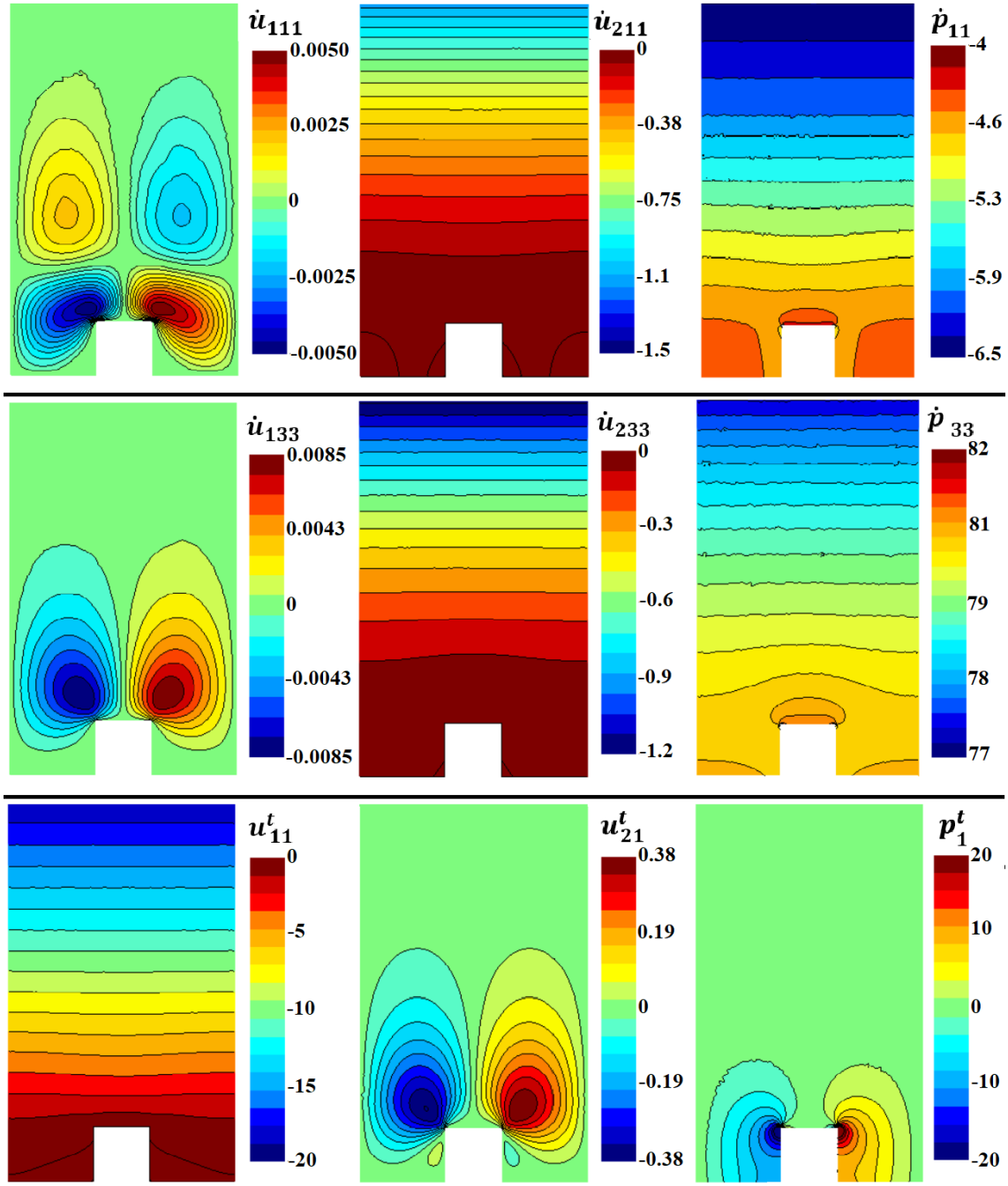

Figure S8: Numerical results of Stokes-like systems, in the $\mathcal{O}(\epsilon^1)$ problem, with parameters having monotonic decrease along the x_2-direction: (top) $\frac{\partial S_{12}}{\partial X_1}$ system; (middle) $\frac{\partial S_{32}}{\partial X_3}$ system; (bottom) $\mathcal{R}_G \frac{\partial S_{12}}{\partial t}$ system.

V- **Systems with a monotonically-increasing parameter of interest**

Poisson-like system

The system forced by $\dfrac{\partial S_{22}}{\partial X_3}$ can be reduced to two-dimensional Poisson-like problems in which the only value of interest is $\dot{u}_{332}$. The contours of $\dot{u}_{332}$ in the vicinity of the rib are shown in Fig. S9. The value of this parameter experiences a monotonic increase with x_2, reaching a value of about 12.9402 at $x_2 = y_\infty = 5$.

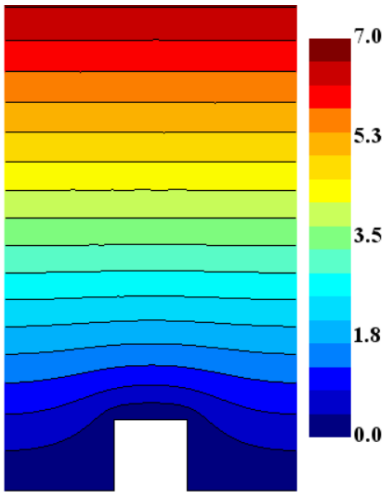

Figure S9: Contours of $\dot{u}_{332}$ in the vicinity of the wall.

Stokes-like systems

The analysis of the systems forced by $\dfrac{\partial S_{22}}{\partial X_1}$ and $\mathcal{R}_G\eta$ shows that they can be reduced to two-dimensional Stokes-like problems with the values of $\dot{u}_{312}$ and u'_3 equal to zero throughout the unit cell. The numerical results of $\dot{u}_{112}$ and u'_1 show monotonic increase with x_2, reaching values of about 12.7002 and 43.0376 at the matching interface, respectively. The numerical results of the preceding systems in the vicinity of the rib are shown in Fig. S10.

S3 Results of $\mathcal{O}(\epsilon^2)$ temperature systems: $e/\ell = 0.25$, $y_\infty = 5$

The systems $(\mathcal{R}_G\, Pr\, S_{22}\eta)$, $(\mathcal{R}_G\, Pr\, S_{32}\eta)$, and $(\dfrac{\partial \eta}{\partial X_3})$ admit, respectively, the trivial solutions $\theta^*_2 = \theta^*_3 = \theta^!_3 = 0$. For the other systems at this order, similarities are recognized with specific Laplace-like problems in $\mathcal{O}(\epsilon^1)$ problem. In particular, it is simple to see that:

$$\theta^!_1 = \dot{u}_{313}, \quad \theta^!_2 = \dot{u}_{323}, \quad \theta^{**} = \overline{u}_{33}, \quad \theta^t = u^t_{33}, \quad \theta^*_1 = \ddot{u}_{313}.$$

Therefore, the values of these microscopic temperature parameters at $x_2 = y_\infty = 5$ are:

$$\theta_1^! = \theta_2^! = \theta^{**} = \theta_1^* = 0, \quad \theta^t = -43.8582.$$

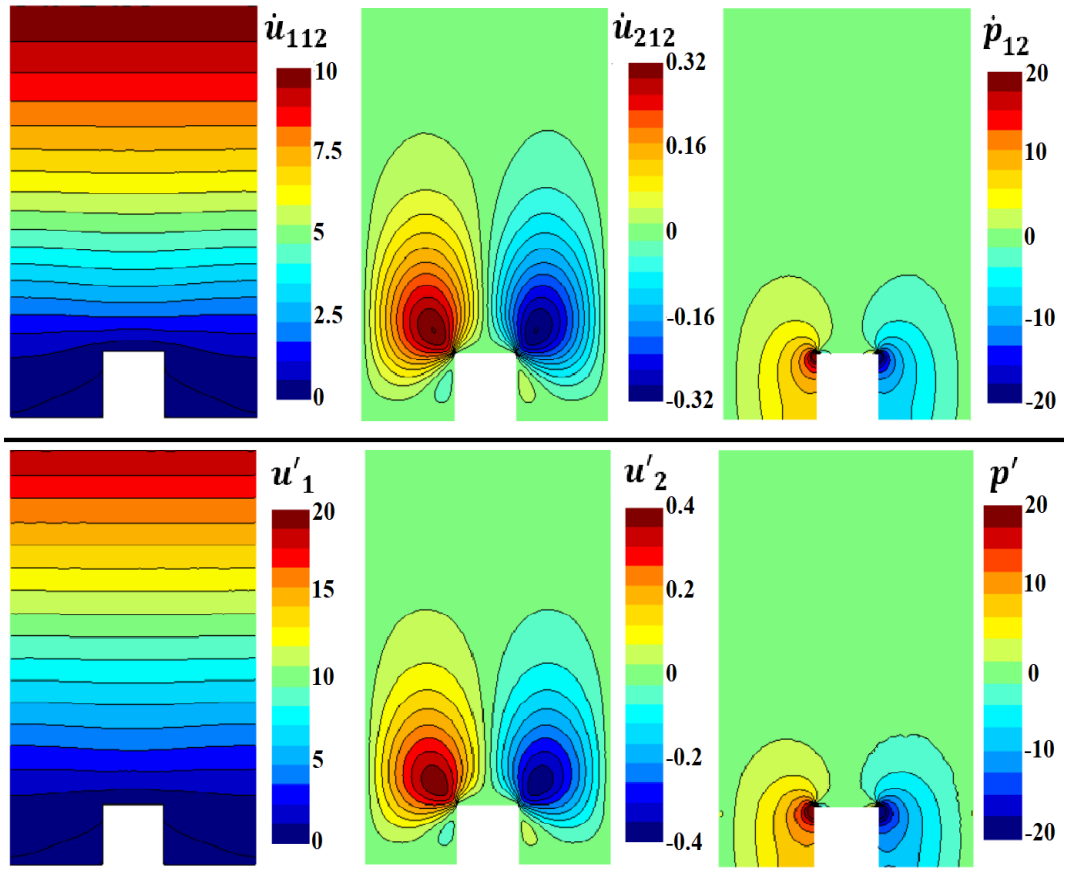

Figure S10: Numerical results of Stokes-like systems, in the $\mathcal{O}(\epsilon^1)$ problem, with parameters having monotonic decrease along the x_2-direction: (top) $\frac{\partial S_{22}}{\partial X_1}$ system; (bottom) $\mathcal{R}_G\eta$ system.

PAPER B2

Natural-convection heat transfer from regularly ribbed vertical surfaces: Homogenization-based simulations towards a correlation for the Nusselt number [1,2]

Essam Nabil Ahmed

DICCA, Università di Genova, via Montallegro 1, Genova, 16145, Italy

Free-convection heat transfer from vertical surfaces is widely encountered in engineering applications, yet the role played by surface alterations in the heat transfer process and their practical effectiveness are still points of confusion. In this work, buoyancy-driven flows over periodically ribbed vertical plates of different surface micro-textures are investigated, mainly based on an asymptotic homogenization model through which the expensive resolution of the velocity and thermal fields within the inter-rib regions is bypassed, by imposing equivalent *effective* boundary conditions at a virtual plane surface. Efficiency of the homogenized simulations in detecting macroscopic behavior of the Nusselt number is first assessed, compared with full feature-resolving simulations in which the effects of complex flow patterns, near and within wall corrugations, on the local Nusselt number are captured. Second, the validated model is used to construct a database of numerical results describing deviations of the average Nusselt number over different ribbed surfaces, relative to a corresponding smooth surface. Under the conditions investigated, it is found that surface roughening generally deteriorates heat transfer from vertical surfaces, with slight enhancement for geometries characterized by low thermal slip, for example, rectangular ribs of narrow inter-rib spaces. Finally, a multiple-regression analysis is conducted to formulate a correlation describing effects of the thermal-slip coefficient, the number of ribs, and the Grashof number on the surface-averaged Nusselt number; accuracy of the proposed correlation is attested via further validation. This paper aims to call attention of the heat transfer society to the ability of the homogenization approach to considerably alleviate the computational requirements for relevant simulations and, thus, to significantly accelerate parametric optimization studies.

[1]Supplementary Material related to this manuscript is provided after the References.

[2]The Version of Record of this manuscript, together with the Supplementary Material, has been published and is available in: *Numerical Heat Transfer, Part A: Applications* **83** (9) (2023) 991–1013. https://doi.org/10.1080/10407782.2023.2165993

1 INTRODUCTION AND LITERATURE REVIEW

Buoyancy-induced heat transfer is omnipresent in nature and in technological applications. Being simple in design, cost-effective, highly reliable and free of electromagnetic interference, natural-convection cooling has gained increasing importance in electronic systems handling low and medium heat loads (Johnson, 1986), or even as a pack-up or a supplementary regime in combination with forced convection in the case of high loads (Bhavnani & Bergles, 1990). The life and long-term reliability of electronic circuits can be considerably increased by keeping the operating temperature sufficiently below the maximum level allowed by the manufacturer (Genot, 1982; Johnson, 1986). Nevertheless, this has become practically challenging owing to the progressive miniaturization of electronic components, along with the reduction of operational execution time and the increase in power supply (Joshi *et al.*, 1989; Peterson & Ortega, 1990). Many experimental and numerical investigations have been carried out, seeking enhancement of the heat transfer performance of natural-convection systems through different techniques, including direct immersion into liquids (Park & Bergles, 1987; Joshi *et al.*, 1989; Tanda, 2017), controlling the spacing of plane heated channels under a variety of boundary conditions (Azevedo & Sparrow, 1985; Webb & Hill, 1989), optimization of heat sink design (Park *et al.*, 2015) and, most related to this paper, adding surface alterations/extensions to vertical plates exposed to natural convection, which is widely adopted in practical engineering applications such as air solar collectors and cooling of electronics.

In contrast to fins, ribs are by definition relatively small surface disturbances which affect the heat transfer rate from the surface mainly by altering the average heat transfer coefficient, while the increase in the heat transfer area is secondary. Therefore, attaching ribs rather than fins to the heated surface is advantageous in terms of minimizing the overall weight and size of the device, provided that the ribs are proved to be efficient in dissipating heat. This has motivated many experimental and numerical studies investigating the effectiveness of adding ribs, of different shapes and dimensions, to the heated surfaces (Bhavnani & Bergles, 1990; Tanda, 1997; Hærvig & Sørensen, 2020). Besides, ribs may be present naturally on the surface, like in the case of electronic components on a chip. Even the detection of adverse effects is important for naturally ribbed surfaces, so that the designer can take this into account while determining the maximum allowable power supply.

When a heated vertical surface is periodically roughened, complex interaction between surface micro-details and the adjacent buoyancy-driven fluid layer takes place, resulting in perturbation of the velocity and thermal fields in the vicinity of the wall, in a quasi-periodic manner, along with macroscopic development of the viscous and thermal boundary layers (cf. (Ahmed *et al.*, 2022)). Accordingly, the distribution of the local heat transfer coefficient along the surface deviates both qualitatively and quantitatively from the corresponding distribution along a smooth surface. In particular, the local Nusselt number is significantly affected by mainstream separation and reattachment actions within the inter-rib regions, experiencing successive oscillations along the vertical surface

(Bhavnani & Bergles, 1990; Tanda, 1997, 2017; Nishikawa *et al.*, 2020). The overall effect of surface roughening on the heat transfer rate depends on several parameters, including geometric properties of the protrusions, distribution and density of the roughness pattern, thermal properties of the ribs, the Grashof number, the Prandtl number, and the flow regime. However, strict guidelines describing the role of different control parameters are not explicitly available in the literature, a fact that can be deduced from the apparently contradictory findings of previous investigations, with some studies indicating enhancement of the heat transfer performance (Aydin, 1997; Hærvig & Sørensen, 2020), while negative effects of the ribs are reported in many other occasions (Tanda, 1997, 2008; Cavazzuti & Corticelli, 2008; Ahmed *et al.*, 2022).

In this paper, a homogenization-based numerical approach is employed to simulate the macroscale behavior of buoyancy-driven flows over isothermal vertical surfaces, with different periodic micro-patterns of transverse ribs, at a fraction of the cost of full feature-resolving simulations, allowing for generating a large database of numerical results describing the behavior of the average Nusselt number at different geometric and flow conditions, to be analyzed and optimized at a further step in a manner that provides a more mature understanding of complex effects of surface roughening on the heat transfer performance. The present work adopts the *effective* velocity and temperature boundary conditions constructed and validated by Ahmed *et al.* (2022), extending the scope of previous homogenization studies either not accounting for heat transfer from textured surfaces (cf. for example (Zampogna *et al.*, 2019; Bottaro & Naqvi, 2020)) or limited to low values of the Rayleigh number (Introïni *et al.*, 2011). In the next section, the physical problem is stated, the governing equations and effective boundary conditions are given, and the geometries under investigation are described in detail. In Section 3, selected cases are considered for simulation with both the feature-resolving approach and the homogenization model, for validation and clarification of the associated phenomena. The generated database of the Nusselt number values for different geometries and densities of patterns is analyzed in Section 4, for optimizing the heat transfer rate from the surface. The role of the thermal-slip coefficient is outlined in Section 5, and a comprehensive equation describing the Nusselt number dependence on the control parameters is formulated and validated. Important notes on the validity and limitations of the adopted physical model are highlighted in Section 6, besides a summary of the main findings of the study.

2 PROBLEM STATEMENT AND GOVERNING EQUATIONS

2.1 Outlines of the physical problem

The buoyancy-driven laminar flow over a periodically roughened vertical surface of height (L) and uniform wall temperature at the baseplate and the ribs' surfaces ($\hat{T}_w$), higher than

the ambient temperature ($\hat{T}_\infty$), is considered. Variations in fluid density due to thermal gradient are assumed moderate; the Boussinesq approximation with a linear temperature-density relationship applies (refer to (Desrayaud & Fichera, 2002; Cavazzuti & Corticelli, 2008; Hærvig & Sørensen, 2020)) so that a temperature-dependent term, representing the buoyancy effect, appears in the momentum conservation equation, allowing for numerical coupling with the energy equation. As a laminar flow is assumed, and since $\hat{T}_w$ and $\hat{T}_\infty$ are considered time-independent, a steady physical model is adopted here; refer to Section 6.1 for further details. In dimensional form, the conservation equations can be written in terms of space coordinates $\hat{x}_i$, velocity $\hat{u}_i$, pressure $\hat{P}$, and temperature $\hat{T}$ as follows:

$$\frac{\partial \hat{u}_i}{\partial \hat{x}_i} = 0, \tag{1-a}$$

$$\rho_\infty \hat{u}_j \frac{\partial \hat{u}_i}{\partial \hat{x}_j} = -\frac{\partial (\hat{P} - \hat{P}_\infty)}{\partial \hat{x}_i} + \mu \frac{\partial^2 \hat{u}_i}{\partial \hat{x}_j^2} + \rho_\infty \beta_\infty (\hat{T} - \hat{T}_\infty) g \, \delta_{i1}, \tag{1-b}$$

$$\hat{u}_j \frac{\partial \hat{T}}{\partial \hat{x}_j} = \alpha \frac{\partial^2 \hat{T}}{\partial \hat{x}_j^2}, \tag{1-c}$$

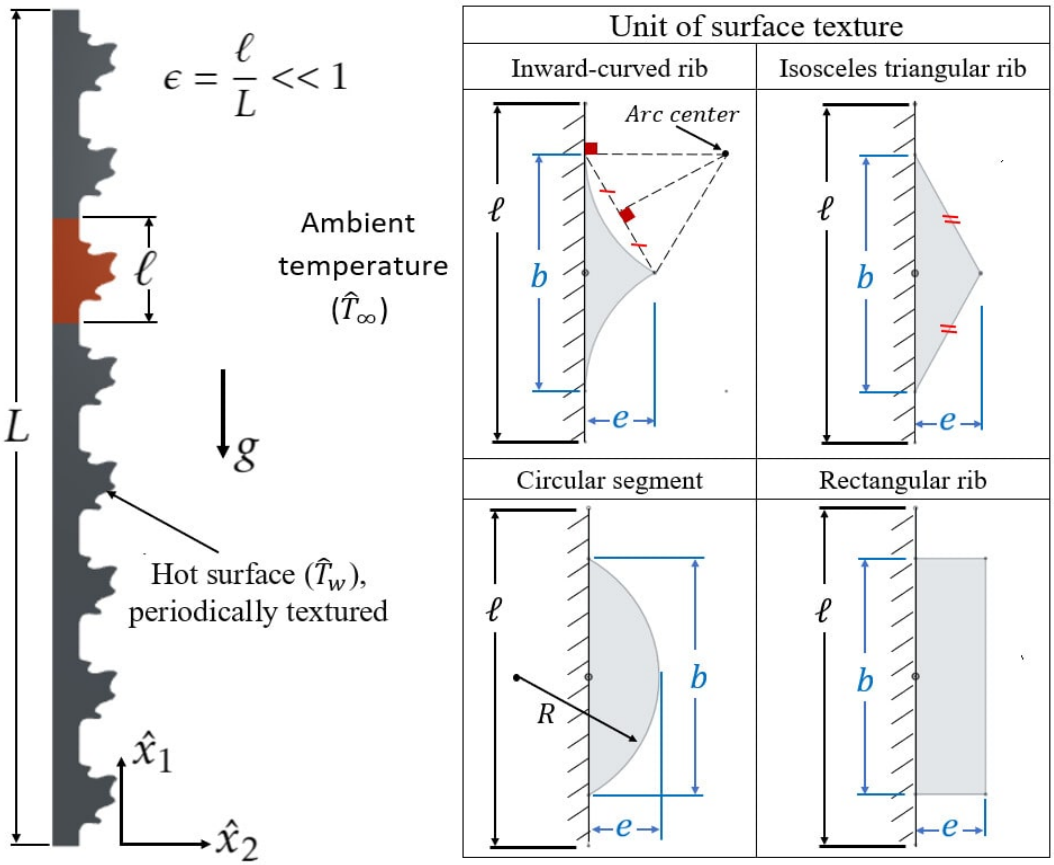

Figure 1: General description of the problem under study, with indication of the typical surface micro-textures investigated in the present analysis.

with ρ_∞, β_∞, $\hat{P}_\infty$ the density, the thermal expansion coefficient, and the pressure sufficiently away from the wall, g the gravitational acceleration, and δ_{i1} the Kronecker index (cf. Fig. 1 for definition of axes). The dynamic viscosity (μ) and the thermal diffusivity (α) are assumed constant; they are defined at the film temperature ($\hat{T}_f = \dfrac{\hat{T}_w + \hat{T}_\infty}{2}$). Additionally, the Prandtl number ($Pr = \dfrac{\mu}{\rho_\infty \alpha} = \dfrac{\nu}{\alpha}$) and the Grashof number ($Gr = \dfrac{g\beta_\infty(\hat{T}_w - \hat{T}_\infty)L^3}{\nu^2}$) are defined, as major parameters controlling natural-convection heat transfer from the surface.

2.2 Input variables and optimization objective

Maximization of the average Nusselt number ($\overline{Nu}$) over the roughened vertical surface is sought, as the objective of the optimization analysis. The local Nusselt number (Nu) at a point on the surface is defined as:

$$Nu = \frac{-L}{\hat{T}_w - \hat{T}_\infty} \times \left.\frac{\partial \hat{T}}{\partial \hat{n}}\right|_{wall}, \tag{2-a}$$

with $\hat{n}$ the dimensional distance in the profile-normal direction at the point of interest. The conventional definition of the average Nusselt number ($\overline{Nu}_{\text{conv}}$) relies on integrating the local Nusselt number over the rough surface and weighting by the total heat transfer area, which is essentially larger than the area of a smooth surface having the same height. Instead, an altered form of the average Nusselt number is defined and used throughout this paper, where the conventional form is corrected by the ribbed-to-smooth surface area ratio, that is $\overline{Nu} = \overline{Nu}_{\text{conv}} \times \dfrac{A_{\text{ribbed}}}{A_{\text{smooth}}}$, to directly indicate the overall deterioration/enhancement of the heat transfer rate in comparison with a corresponding smooth surface, taking into account the increase in surface area due to the presence of ribs; refer to (Hærvig & Sørensen, 2020). It can be easily proved that the latter definition of the average Nusselt number ($\overline{Nu}$) is equivalent to integrating the local Nusselt number over the rough surface and employing the projected (smooth) surface area as a weight, instead of the ribbed surface area. Accordingly, the average Nusselt number for the case of 2D ribs can be calculated as:

$$\overline{Nu} = \frac{1}{L}\int_0^{\hat{S}} Nu \, d\hat{s}, \tag{2-b}$$

with $\hat{s}$ dimensional distance along the ribbed profile and $\hat{S}$ the total profile length.

Four shapes of the roughness element are considered for investigation, specifically, inward-curved ribs with curves tangent to the base surface, isosceles triangular ribs, circular segments, and rectangular ribs (refer to Fig. 1). For all configurations, the geometry of an element, placed in a unit cell of length (ℓ), is characterized by the rib height (e) and width (b). In dimensionless form, the rib height to pitch distance ratio (e/ℓ) and the rib aspect ratio (b/e) are defined. The scope of the present study includes

only micro-patterned surfaces, i.e., the pattern periodicity (ℓ) is much smaller than the macroscopic length of the plate (L). This indicates that surfaces have a large number of ribs ($N_{ribs} = L/\ell$). The following constraints are set for the geometric variables:

$$0.05 \leq e/\ell \leq 0.25, \qquad 2 \leq b/e \leq 4, \qquad 20 \leq N_{ribs} \leq 160. \tag{3}$$

For all cases, laminar flow over the plate is considered with values of the Grashof number within the range $10^7 \leq Gr \leq 10^8$, and a constant value of the Prandtl number ($Pr = 0.712$).

2.3 Domain decomposition and homogenized model

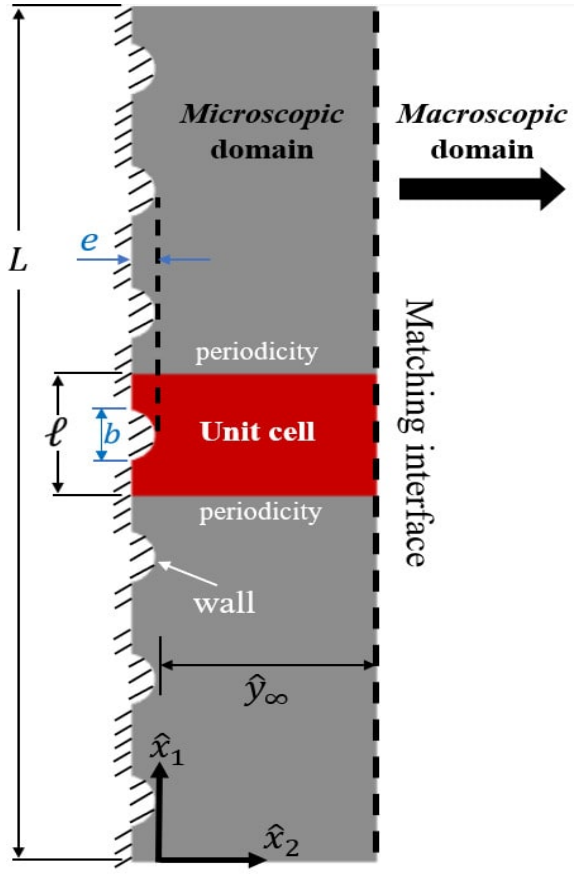

Figure 2: Sketch of the decomposed flow domain, highlighting a unit cell in the microscopic region and indicating the virtual interface between microscopic and macroscopic sub-domains.

Besides the basic feature-resolving numerical approach, that fully captures the surface details and their explicit effects on adjacent flow, the homogenization-based approach constructed and validated by Ahmed *et al.* (2022) is adopted within the present framework. Given the presence of well-separated length scales, that is, pattern periodicity

(ℓ) and plate length (L), the flow field is decomposed into two sub-domains (microscopic/macroscopic) of different characteristic parameters (Fig. 2). Information transfer takes place between the two sub-domains through a virtual matching interface, properly selected for coupling the two problems. The homogenization-based approach eventually seeks a solution to the macroscale problem by imposing upscaled *effective* velocity and temperature boundary conditions at the matching interface, to be constructed by manipulation of the microscale problem, taking advantage of its amenability to a solution via asymptotic expansions of variables.

In brief, the dimensionless conservation equations governing the macroscale problem read:

$$\frac{\partial U_i}{\partial X_i} = 0, \tag{4-a}$$

$$U_j \frac{\partial U_i}{\partial X_j} = -\frac{\partial P}{\partial X_i} + \frac{1}{\sqrt{Gr}} \frac{\partial^2 U_i}{\partial X_j^2} + \Theta \delta_{i1}, \tag{4-b}$$

$$Pr\sqrt{Gr} \left(U_j \frac{\partial \Theta}{\partial X_j} \right) = \frac{\partial^2 \Theta}{\partial X_j^2}, \tag{4-c}$$

where the macroscopic variables are defined as:

$$U_i = \frac{\hat{u}_i}{\mathcal{U}}, \qquad X_i = \frac{\hat{x}_i}{L}, \qquad P = \frac{\hat{P} - \hat{P}_\infty}{\rho_\infty \mathcal{U}^2}, \qquad \Theta = \frac{\hat{T} - \hat{T}_\infty}{\hat{T}_w - \hat{T}_\infty}, \tag{5}$$

using the velocity scale ($\mathcal{U} = \dfrac{\nu}{L}\sqrt{Gr}$).

Following the guidelines in (Ahmed *et al.*, 2022), effective boundary conditions can be imposed along the vertical plane passing through the crests/outer rims of the ribs ($X_2 = 0$). The first-order effective conditions, which proved to be efficient for predicting the Nusselt number, read:

$$U_1\big|_{X_2=0} = \epsilon \, [\lambda_x \, S_{12} + \, m_{12} \, \mathcal{R}_G]_{X_2=0} \, , \tag{6-a}$$

$$U_2\big|_{X_2=0} = 0, \tag{6-b}$$

$$\Theta\big|_{X_2=0} = 1 \, + \, \epsilon \, \lambda_z \frac{\partial \Theta}{\partial X_2}\bigg|_{X_2=0}, \tag{6-c}$$

with $\epsilon = \ell/L$ a small parameter characterizing the roughness pattern, $\mathcal{R}_G = \epsilon\sqrt{Gr}$ the reduced Grashof number, and S_{12} the macroscopic shear stress in streamwise direction, defined as:

$$S_{12} = \left(\frac{\partial U_1}{\partial X_2} + \frac{\partial U_2}{\partial X_1} \right). \tag{7}$$

The coefficients ($\lambda_z, \lambda_x, m_{12}$) appearing in the effective conditions are all dependent on the rib geometry, that is, rib type, e/ℓ and b/e. They are obtained by solving two-dimensional auxiliary systems of equations through a unit cell of the microscopic sub-domain, in particular, a Laplace-like system for λ_z and a Stokes-like system for λ_x and

m_{12}. The two systems are respectively defined in terms of ad hoc microscopic parameters $(\tilde{\theta},\, \breve{u}_{i1},\, \breve{p}_1)$ as follows (cf. (Ahmed *et al.*, 2022) for derivation):

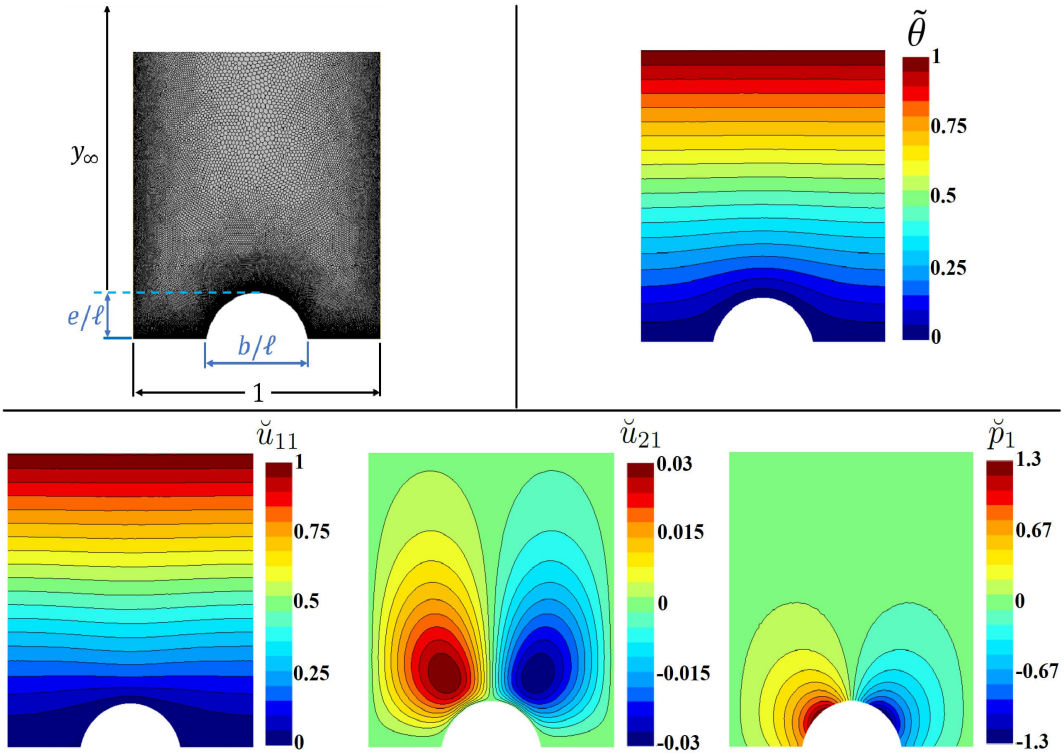

Figure 3: Numerical solutions of the auxiliary systems of interest over a unit cell in the microscopic domain, for a circular-segment rib with $e/\ell = 0.1663$ and $b/\ell = 0.4095$: (top left) discretized computational domain; (top right) Laplace problem (Eqs. (8-a to 8-c)); (bottom) Stokes problem (Eqs. (9-a to 9-d)). The matching interface is at $x_2 = y_\infty = 4$, while contours are displayed in vicinity of the wall.

I- Laplace-like problem

$$\frac{\partial^2 \tilde{\theta}}{\partial x_i^2} = 0, \tag{8-a}$$

with the boundary conditions

$$\tilde{\theta} = 0 \quad \text{at} \quad x_2 = y_w, \tag{8-b}$$

$$\frac{\partial \tilde{\theta}}{\partial x_2} = 1 \quad \text{at} \quad x_2 = y_\infty. \tag{8-c}$$

II- Stokes-like problem

$$\frac{\partial \breve{u}_{i1}}{\partial x_i} = 0, \tag{9-a}$$

$$-\frac{\partial \breve{p}_1}{\partial x_i} + \frac{\partial^2 \breve{u}_{i1}}{\partial x_j^2} = 0, \tag{9-b}$$

with the boundary conditions

$$\breve{u}_{i1} = 0 \quad \text{at} \quad x_2 = y_w, \tag{9-c}$$

$$-\breve{p}_1\,\delta_{i2} + \left(\frac{\partial \breve{u}_{i1}}{\partial x_2} + \frac{\partial \breve{u}_{21}}{\partial x_i}\right) = \delta_{i1} \quad \text{at} \quad x_2 = y_\infty, \tag{9-d}$$

with $x_i = \hat{x}_i/\ell$ the microscopic coordinates. Typical numerical solutions of the systems for the case of circular segment ($e/\ell = 0.1663$, $b/\ell = 0.4095$) are displayed in Fig. 3. The coefficients (λ_z, λ_x) are estimated by averaging the fields of ($\tilde{\theta}$, $\breve{u}_{11}$), respectively, at the plane $x_2 = 0$, while the coefficient (m_{12}) can be obtained by integrating the field of $\breve{u}_{11}$ over the area below the plane $x_2 = 0$.

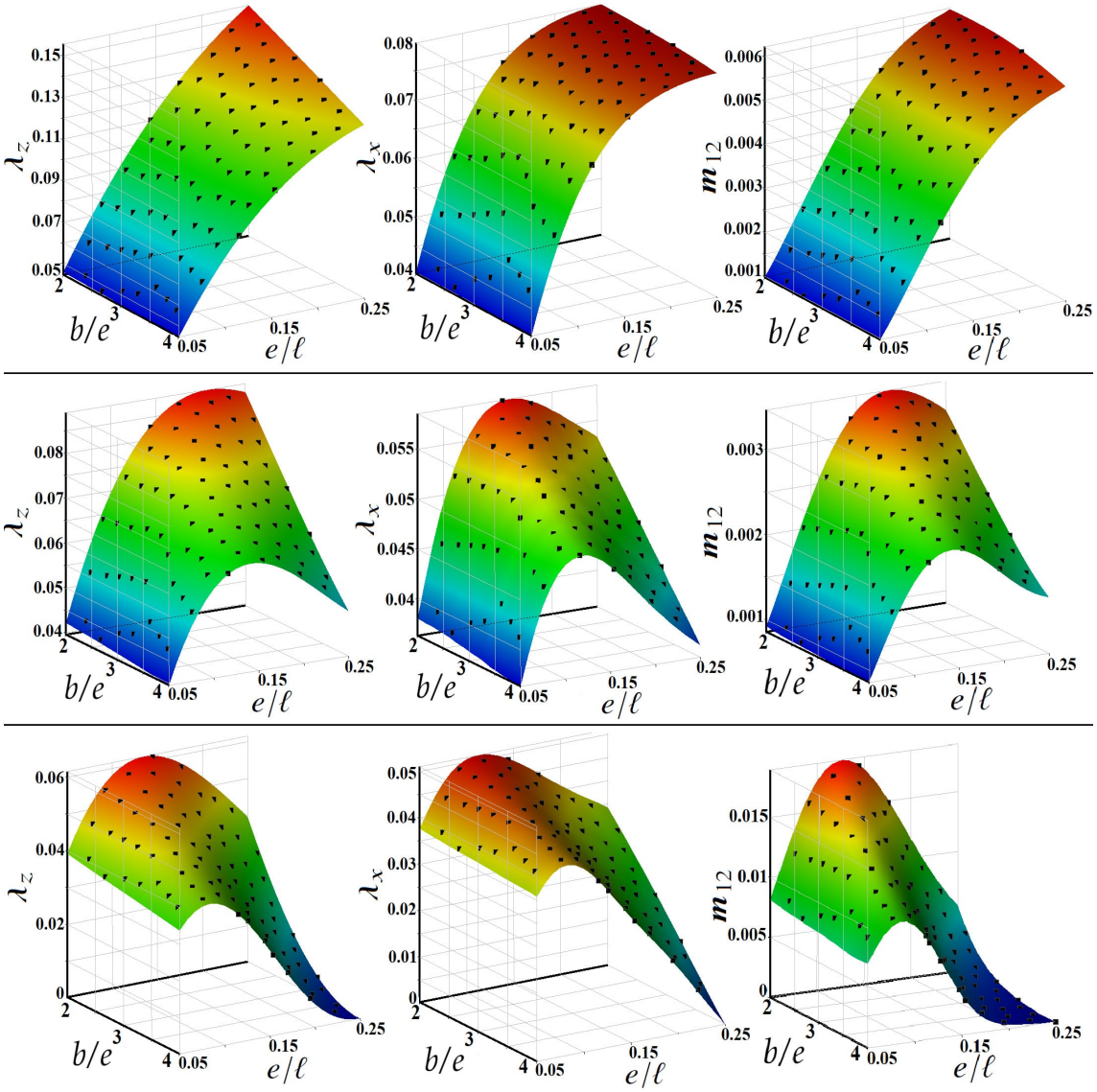

Figure 4: Response surfaces of the macroscopic parameters (λ_z,λ_x,m_{12}) as continuous functions of rib characteristic dimensions (e/ℓ, b/e), for different configurations: (top) inward-curved rib; (middle) circular segment; (bottom) rectangular rib. Typical design points, used to create the surrogate functions, are shown with black dots.

The numerical experiments were designed by defining eighty combinations of the geometric parameters (e/ℓ, b/e) for each rib type based on the Optimal-Space-Filling (OSF) algorithm that provides a more uniform extension to the Latin Hypercube Sampling (LHS) method (for more details, the reader is referred to (Ansys®, 2021 R1)). All numerical simulations were run using Simcenter STAR-CCM+ multiphysics software (versions 15.06.007-R8/16.02.009-R8). The values of the macroscopic coefficients ($\lambda_z, \lambda_x, m_{12}$) corresponding to all design points are listed in detail in the *Supplementary Material*. Response surfaces of the macroscopic coefficients, as surrogate functions of the geometric parameters, are shown in Fig. 4 for the different shapes. The Genetic Aggregation algorithm is employed for modeling the response surfaces for all rib types except the rectangular rib, for which the Non-Parametric Regression (NPR) technique is implemented to better handle the high non-linearities in behaviors, as can be realized from the figure. It is clear that, for a given shape, the trends of the three coefficients have some sort of dependence; this will be used in Section 5 to simplify the relationship between these coefficients and the Nusselt number.

3 FEATURE-RESOLVING SIMULATIONS AND MODEL VALIDATION

3.1 Setup of numerical simulations

In this section, three types of numerical simulations, with different targets and approaches, are discussed: (i) simulation of buoyancy-driven flow over a smooth flat plate, to provide a reference for the unperturbed velocity and temperature fields and the value of the Nusselt number relative to which the enhancement/deterioration of heat transfer due to surface roughening can be assessed; (ii) feature-resolving simulations of the flow over ribbed surfaces of different textures, to obtain the detailed perturbed fields and flow structures for a better understanding of the phenomena, and to provide accurate predictions of the Nusselt number for the chosen surfaces; (iii) homogenization-based simulations with first-order effective boundary conditions, to construct the macroscopic fields and the average Nusselt number ($\overline{Nu}$) for the different ribbed surface, to be validated by comparing results to the corresponding full feature-resolving simulations. Four cases of flow over ribbed surfaces are considered, that is, the four types of rib geometry shown in Fig. 1, with characteristic dimensions $e/\ell = 0.1663$ and $b/e = 2.4625$, are tested. For all cases, the number of ribs is 20 and the Grashof number is 10^8.

The two-dimensional computational domain is sketched in Fig. 5, with indication of the imposed boundary conditions. A domain width of $2L$ is selected, following the specifications by Ahmed *et al.* (2022), to ensure that the streamwise velocity smoothly vanishes at the far boundary. The uniform pressure values at the inlet and the outlet allow equilibrium with the hydrostatic pressure head in the stagnant flow region. No-slip velocity and uniform temperature boundary conditions are defined along the plane

$X_2 = 0$ for the smooth surface case, while the same conditions are to be imposed on the textured wall when feature-resolving simulations of the flow over ribbed plates are performed. As discussed in Section 2, the homogenization-based simulations requires the definition of the effective boundary conditions (Eqs. (6-a to 6-c)) at the plane $X_2 = 0$. For the geometric conditions under consideration, the following values of the macroscopic coefficients were numerically estimated:

$$inward-curved \quad \lambda_z = 0.1192, \quad \lambda_x = 0.0760, \quad m_{12} = 0.00497, \tag{10-a}$$

$$triangular \quad \lambda_z = 0.1047, \quad \lambda_x = 0.0731, \quad m_{12} = 0.00456, \tag{10-b}$$

$$circular\ segment \quad \lambda_z = 0.0814, \quad \lambda_x = 0.0554, \quad m_{12} = 0.00314, \tag{10-c}$$

$$rectangular \quad \lambda_z = 0.0481, \quad \lambda_x = 0.0404, \quad m_{12} = 0.00114. \tag{10-d}$$

Mesh structure and numerical methods are similar to those applied in (Ahmed *et al.*, 2022).

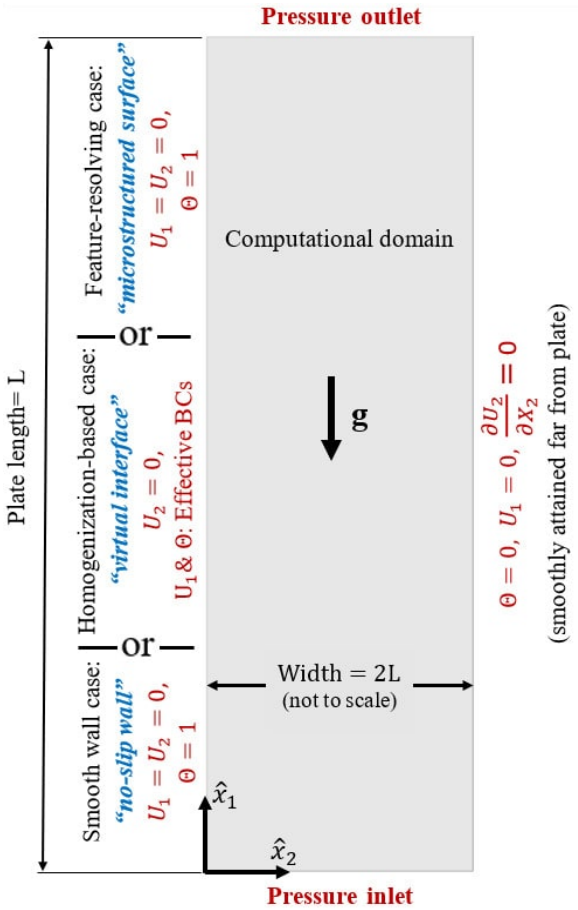

Figure 5: Computational domain and boundary conditions used for numerical simulation. Different categories of boundary conditions are indicated at the wall in accordance with the applied numerical approach, i.e., when ribbed plates are considered, the no-slip velocity and temperature boundary conditions are to be imposed over the real surface structure (feature-resolving approach) or to be replaced by effective boundary conditions at a virtual plane surface (homogenization-based approach).

3.2 Results and discussion

3.2.1 *Full feature-resolving simulations*

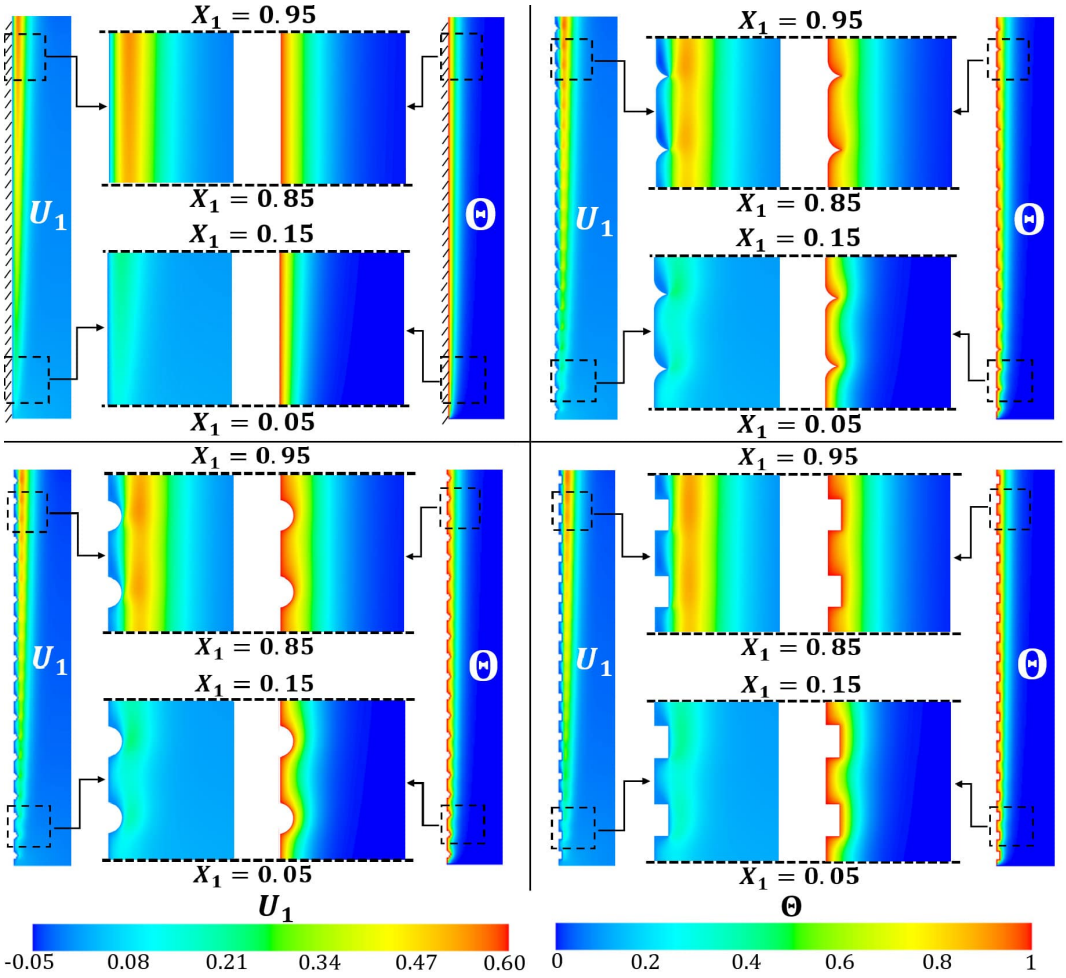

Figure 6: Contours of temperature and streamwise velocity close to the wall, displayed for different surface structures: (from top left to bottom right) smooth surface; inward-curved ribs; circular segments; rectangular rib. $N_{ribs} = 20$, $e/\ell = 0.1663$, $b/e = 2.4625$, $Gr = 10^8$, $Pr = 0.712$.

The velocity and temperature fields, characterizing the buoyancy-driven flow over the flat plate and the considered ribbed surfaces, are described in Fig. 6. The smooth development of the viscous and thermal boundary layers along the X_1-direction, adjacent to the flat wall, is disturbed by the presence of ribs in a quasi-oscillatory manner. Local increase of the streamwise velocity, accompanied by thermal boundary layer thinning, is realized near the tips/crests of ribs, implying local enhancement of the heat transfer performance. Conversely, the negative streamwise velocity values, clearly captured downstream of the ribs, are attributed to separation eddies where local thickening of the thermal boundary

layer is experienced. For a clearer vision, the typical flow patterns near the wall are displayed in Fig. 7, revealing complex structures in inter-rib regions where separation and reattachment of the mainstream take place. Proceeding along the plate, the local Grashof number, and the inertia of the flow, increase; consequently, the deflection of the accelerated stream towards the base surface is hindered, reattachment is delayed or even lost, and separation eddies become more pronounced. For the rib height and aspect ratio under consideration, it is noticeable that the recirculation eddies upstream of the ribs are too small to be well-captured by the displayed streamlines. Besides the flow patterns, the associated effects on the local behavior of the Nusselt number are presented in the figure. Enhancement of the heat transfer characteristics at tips of the ribs, and deterioration in the recirculation zones are quantified. A secondary peak of the local Nusselt number is detected where the flow approaches or reattaches to the base surface. The Nusselt number macroscopically decreases with the increase in X_1 due to development of the thermal boundary layer (compare levels at low and high local Grashof numbers).

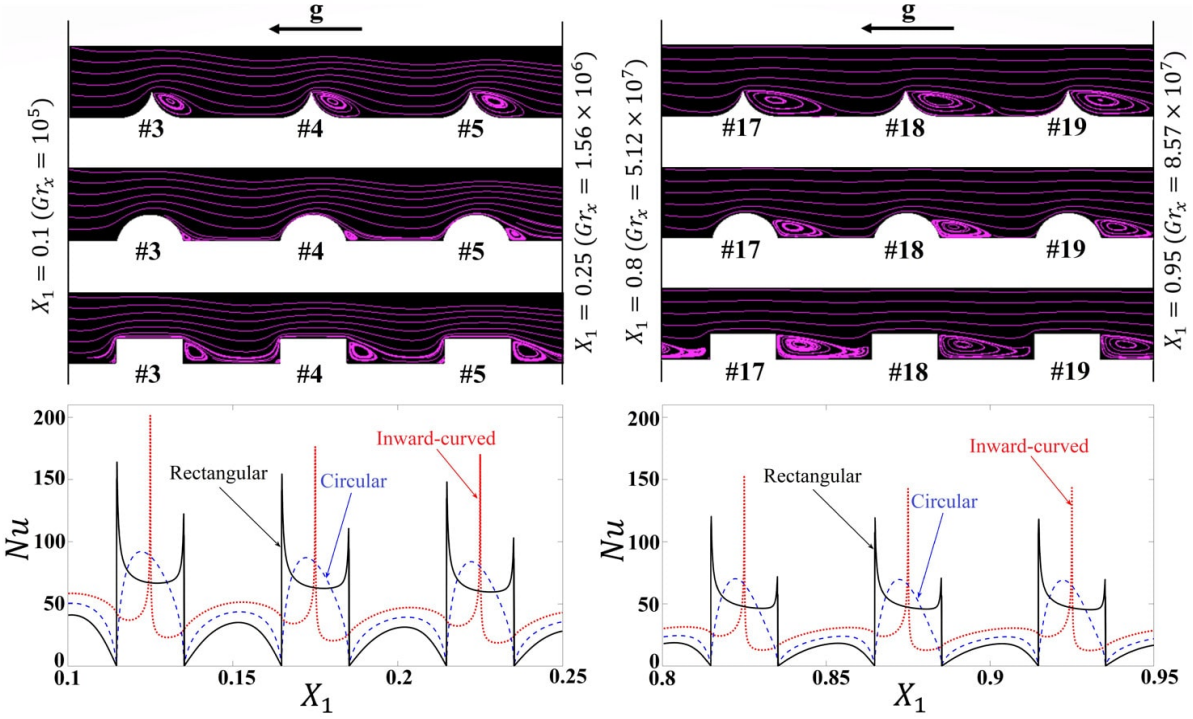

Figure 7: Feature-resolving simulations with different surface micro-textures: description of the flow structures in the vicinity of the wall and the corresponding behaviors of the local Nusselt number, displayed through two distant regions: (left) near the leading edge; (right) near the end of the plate. $N_{ribs} = 20$, $e/\ell = 0.1663$, $b/e = 2.4625$, $Gr = 10^8$, $Pr = 0.712$.

The distribution of the local Nusselt number ($Nu = \left.\dfrac{\partial \Theta}{\partial X_2}\right|_{X_2=0}$) along the flat plate is provided in Fig. 8. The numerical results are plotted together with the predictions of

Ostrach's similarity solution (Ostrach, 1953), that is:

$$\frac{X_1 Nu}{\left(\frac{Gr}{4} X_1^3\right)^{0.25}} = f_n(Pr). \tag{11-a}$$

At a Prandtl number of 0.712, the function $f_n(Pr)$ is about 0.504, and with a Grashof number of 10^8, Eq. (11-a) reads:

$$Nu \approx 35.638\, X_1^{-0.25}, \tag{11-b}$$

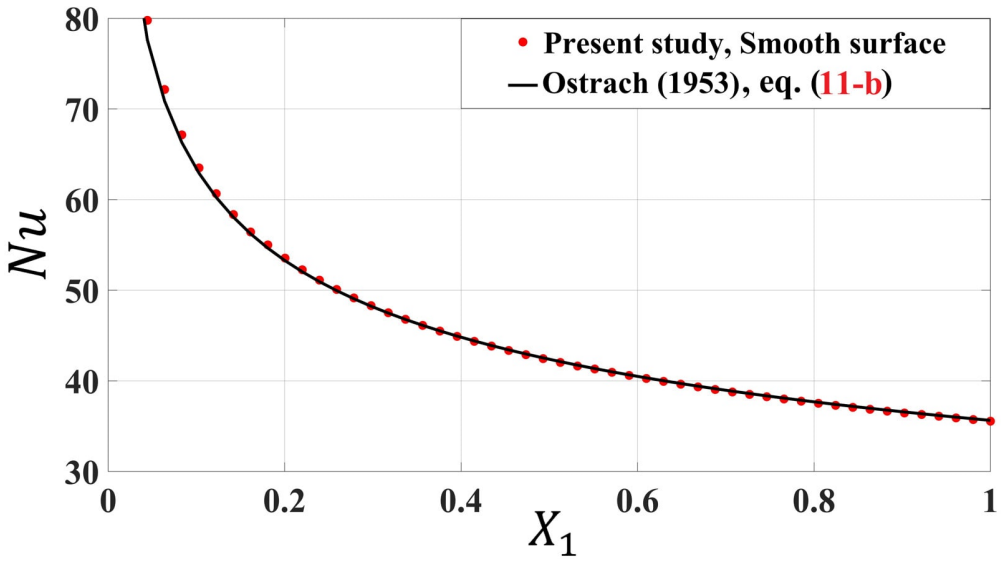

Figure 8: Numerical predictions of the local Nusselt number behavior along the vertical flat surface, in comparison with the expected values from the similarity solution by Ostrach (1953). $Gr = 10^8$, $Pr = 0.712$.

Further discussions on the critical assumptions behind the present physical model are presented in Section 6.1, with validation against reference experimental/numerical results from the literature.

3.2.2 *Validation of the homogenized model*

The homogenization-based numerical model, based on which the optimization analysis will be carried out later in Section 4, is validated here. Inherently, the model targets the macroscopic fields describing the natural-convection flow over the ribbed surface, instead of the detailed patterns of velocity and temperature. Therefore, validation of the model requires comparing its results with the running-average values of the fields resulting from corresponding feature-resolving simulations. For instance, the running-average value of

the dimensionless temperature (Θ) at an arbitrary point ($X_1 = a$, $X_2 = b$) is calculated as follows:

$$< \Theta > \Big|_{X_1=a, X_2=b} = \frac{1}{\epsilon} \int_{a-\frac{\epsilon}{2}}^{a+\frac{\epsilon}{2}} \Theta(X_1, b)\, dX_1. \tag{12}$$

The circular-segment rib is considered for validating the model predictions of the temperature field. As presented in Fig. 9 (top), the results of the model are plotted along the virtual interface ($X_2 = 0$), together with the running-average values of the fully-featured pattern, to explicitly assess accuracy of the temperature effective boundary condition (Eq. (6-c)). Reasonable agreement in predictions of the thermal slip is realized, i.e., deviation of macroscopic temperature at this virtual plane from its uniform value ($\Theta = 1$) over an isothermal smooth surface. In addition, the macroscopic temperature profile across a normal section taken at the middle of the plate ($X_1 = 0.5$) is plotted in Fig. 9 (bottom), showing perfect agreement with the running-average profile extracted from the feature-resolving simulation. The profile related to the smooth surface case is also displayed to indicate the deviations experienced when the plate is ribbed.

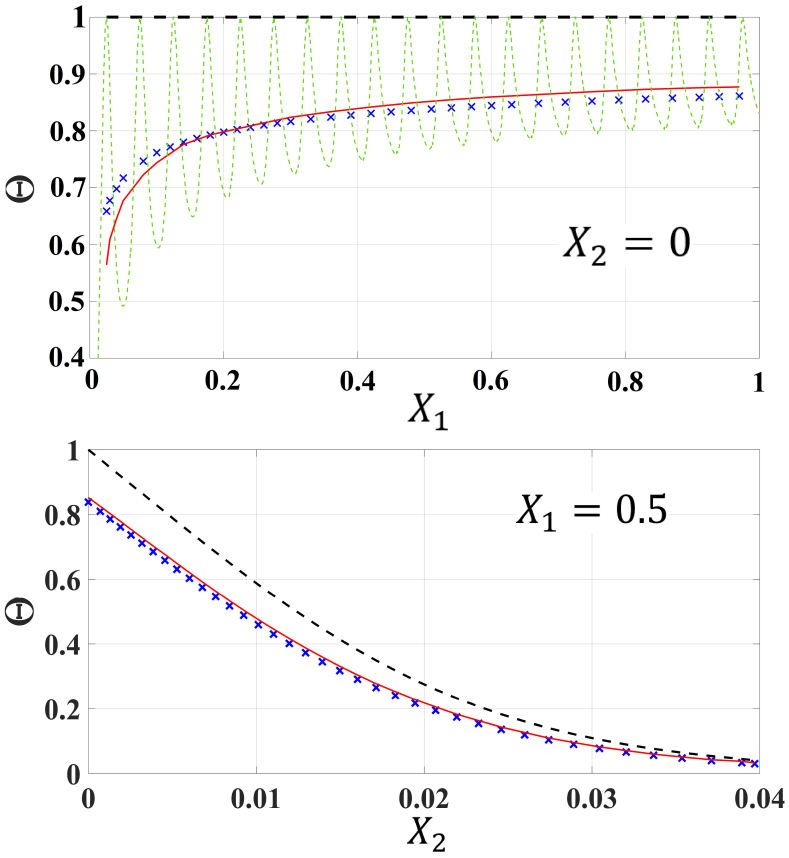

Figure 9: Temperature distribution for the case of circular-segment ribs, plotted: (top) along the vertical plane tangent to crests of ribs; (bottom) across a normal section at the middle of the plate. Predictions of the homogenized model (blue crosses) are compared with the running-average values based on the feature-resolving simulation (red solid lines), for validation. Typical temperature oscillations (green dotted line) and smooth surface results (black dashed lines) are also shown. $N_{ribs} = 20$, $e/\ell = 0.1663$, $b/e = 2.4625$, $Gr = 10^8$.

The main parameter of interest is the average Nusselt number ($\overline{Nu}$) over the ribbed plate, corrected with the projected area to directly indicate the total change in heat transfer rate relative to the smooth surface (Eq. (2-b)). The calculated values of $\overline{Nu}$ based on feature-resolving simulations of the flow over different ribbed surfaces are given in Table 1. The model predictions are also provided for the purpose of validation, those calculated based on the normal temperature gradient along the matching interface:

$$\overline{Nu} = \int_0^1 -\frac{\partial \Theta}{\partial X_2}\bigg|_{X_2=0} dX_1. \tag{13}$$

It is numerically advantageous to exclude the model predictions of the temperature gradient over the first pattern unit ($X = 0 \rightarrow \epsilon$), and to replace them in the integration with the corresponding values over a smooth isothermal plate; this can help to avoid numerical uncertainty associated with discretization of the effective temperature boundary condition near the domain inlet, in addition to the model error in this high-convection region (where higher-order effective conditions may be required). It is clear that, for the four cases given in the table, surface roughening negatively affects the heat transfer rate, with the maximum deterioration occurring for inward-curved ribs. Generally, the model predictions are consistent with the reference values of the feature-resolving simulations.

Table 1: Values of the surface-averaged Nusselt number ($\overline{Nu}$), predicted from homogenized simulations for different rib geometries, compared with results of the corresponding full feature-resolving simulations. $N_{ribs} = 20$, $e/\ell = 0.1663$, $b/e = 2.4625$, $Gr = 10^8$, $Pr = 0.712$.

Rib geometry	$\overline{Nu}$		
	Feature-resolving	Homogenization-based	Error
Inward-curved rib	44.414	44.917	+1.13%
Isosceles triangular rib	46.201	45.894	-0.66%
Circular segment	47.236	46.828	-0.86%
Rectangular rib	47.385	48.345	+2.03%
Smooth surface case	$\overline{Nu} = 49.544$		

4 OPTIMIZATION OF HEAT TRANSFER PERFORMANCE

The rate of heat transfer by natural convection from isothermal vertical surfaces, periodically roughened with transverse ribs of different shapes, characteristic dimensions and pattern densities (refer to Section 2.2 for typical constraints), is the objective of the optimization strategy. In this section, the study is carried out at a constant Grashof number (Gr) of 10^8; the effects of variations in the Grashof numbers are discussed later in Section 5. On account of its capability to alleviate the computational requirements of

full feature-resolving simulations, the homogenized model which has already been validated in Section 3.2.2 is employed to construct a database of numerical values showing the Nusselt number percentage deviation ($\mathcal{D}$) for different ribbed surfaces (refer to *Supplementary Material*). The deviation in the average Nusselt number is measured, taking the smooth surface case as a reference, that is:

$$\mathcal{D} = \frac{\overline{Nu}_{ribbed} - \overline{Nu}_{smooth}}{\overline{Nu}_{smooth}} \times 100(\%). \tag{14}$$

Again, as discussed at the beginning of Section 2.2, the average Nusselt number over rough surface is corrected (increased) by the ribbed-to-smooth surface area ratio such that ($\mathcal{D}$) directly indicates the total change in the heat transfer rate.

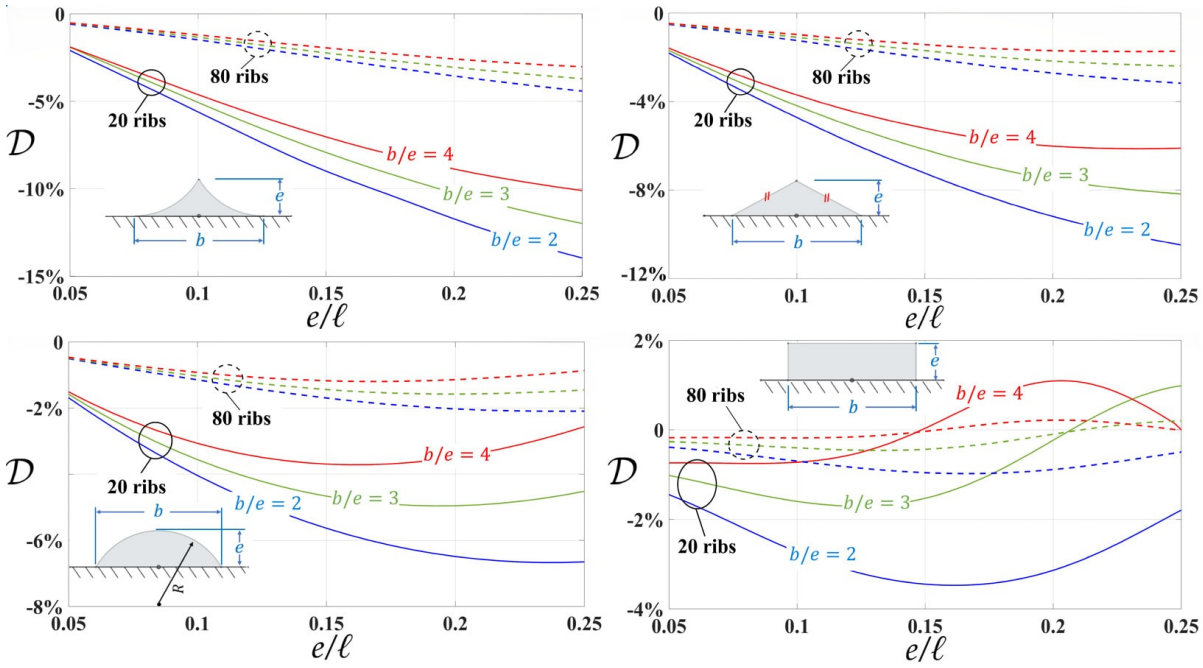

Figure 10: Nusselt number percentage deviation ($\mathcal{D}$) as surrogate function of rib characteristic dimensions for $N_{ribs} = 20$ and 80. Behaviors are plotted for the different types of protrusions included in the optimization study. Note that the full database, available in the *Supplementary Material* also includes results for $N_{ribs} = 40$ and 160. For all case, $Gr = 10^8$, $Pr = 0.712$.

Response surface modeling has been performed to obtain surrogate functions describing the behavior of the Nusselt number percentage deviation ($\mathcal{D}$) with variations in rib characteristic dimensions (e/ℓ, b/e) for different rib shapes and pattern densities (Fig. 10). The same meta-modeling algorithms previously chosen for the macroscopic parameters (Section 2.3) are adopted at this step, specifically the Non-Parametric Regression method for the rectangular rib and the Genetic Aggregation technique for other shapes. A comparative look at the levels of $\mathcal{D}$ for different rib types reveals that the deterioration in the heat transfer rate decreases by shifting from the blunt inward-curved rib to the more streamlined circular rib (passing by the triangular shape) owing to minimization of

surface areas exposed to unfavorable separation eddies (refer to typical flow structures in Fig. 7). The relatively favorable effect of increasing the rib aspect ratio (b/e) can be similarly justified. Under specific geometric conditions, the rectangular rib can exclusively promote the heat transfer rate from the surface compared with a smooth plate ($\mathcal{D} > 0$) thanks to its wide outer rim where the main enhancement of the local Nusselt number occurs (refer to distribution of the local Nusselt number in Fig. 7). It is obvious that, for given geometric parameters (e/ℓ, b/e), both deterioration and enhancement of the heat transfer rate become less pronounced by increasing the number of ribs on the vertical surface as the smooth surface case ($N_{ribs} \to \infty$, $\epsilon \to zero$) is gradually approached.

Based on the above-mentioned findings, special attention is given to surfaces roughened with twenty rectangular ribs for optimizing the heat transfer rate. For this case, the response surface of the Nusselt number percentage deviation ($\mathcal{D}$) is displayed in Fig. 11, as a continuous function of (e/ℓ, b/e). The rib dimensions corresponding to the maximum heat transfer rate were sought; the response surface was analyzed via the Non-Linear Programming by Quadratic Lagrangian (NLPQL) technique, a gradient-based algorithm that implements quasi-Newton methods (Ansys®, 2021 R1). A maximum increase in the heat transfer rate of about 1.17% has been attained with the geometric parameters $e/\ell = 0.214$ and $b/e = 3.741$. Overall, for shapes and ranges considered in the present study, ribs either deteriorate the natural-convection heat transfer performance of isothermal vertical surfaces or, at best, enhance it marginally.

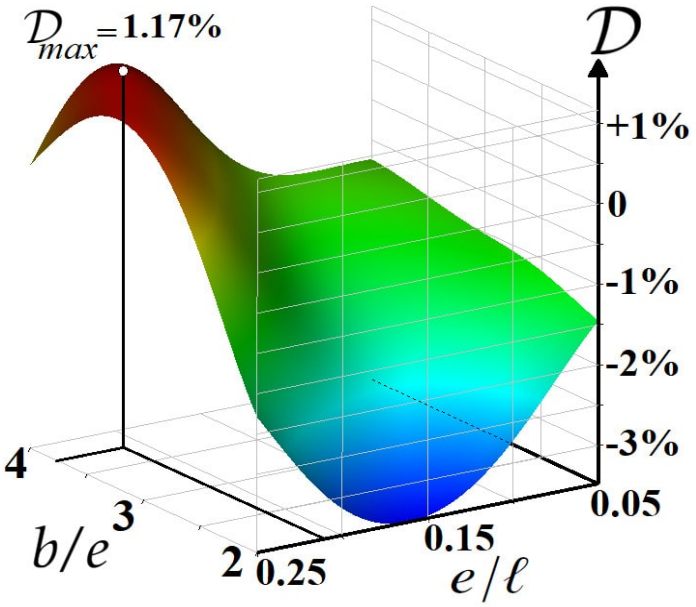

Figure 11: Response surface of the Nusselt number percentage deviation ($\mathcal{D}$), for the case of a wall roughened with 20 rectangular ribs, as a function of the rib characteristic dimensions. The optimum point is indicated.

5 ROLE OF THERMAL-SLIP COEFFICIENT AND PROPOSED CORRELATION

5.1 Role of thermal-slip coefficient (λ_z)

In the previous section, the effect of surface roughening on heat transfer performance has been analyzed with variations in rib shape, characteristic dimensions (e/ℓ, b/e), and the number of ribs on the surface (N_{ribs}). An alternative vision of the previous dependence is elucidated in this section. Revisiting the conservation equations (Eqs. (4-a to 4-c)) and the boundary conditions (Eqs. (6-a to 6-c)) governing the macroscale problem, it can be deduced that the thermal-slip coefficient (λ_z) together with the Navier's slip coefficient along the streamwise direction (λ_x) and the surface permeability coefficient (m_{12}) can macroscopically mimic the effects of rib geometry on the temperature and velocity fields of the buoyancy-driven flow. Accordingly, the Nusselt number percentage deviation ($\mathcal{D}$) can be expressed as follows:

$$\mathcal{D} = f_{n1}\left(\lambda_z,\, \lambda_x,\, m_{12},\, N_{ribs} = \frac{1}{\epsilon}, Gr\right). \tag{15}$$

In depth, Eq. (6-c) shows that the normal temperature gradient at the virtual interface ($\left(\frac{\partial \Theta}{\partial X_2}\right|_{X_2=0}$), controlling the Nusselt number, is explicitly related to the thermal-slip coefficient (λ_z). However, as the momentum and energy conservation equations (Eqs. (4-b and 4-c) are coupled in such a way that the temperature distribution is affected by the velocity field (and vice versa), implicit dependence of the Nusselt number on λ_x and m_{12} is present. It may be advantageous to investigate whether variations in secondary control parameters (λ_x, m_{12}) can be correlated to the behavior of the main parameter (λ_z), so that the function in Eq. (15) may be simplified. The values of the macroscopic parameters for different rib geometries, given in the *Supplementary Material*, are plotted together in Fig. 12; direct relationships between the secondary parameters and the thermal-slip coefficient (λ_z) are fairly described via 6^{th}-order polynomials. Consequently, Eq. (15) reduces to:

$$\mathcal{D} \approx f_{n2}\left(\lambda_z,\, N_{ribs}\,, Gr\right). \tag{16}$$

The dependence of $\mathcal{D}$ on the thermal-slip coefficient (λ_z) for different number of ribs (N_{ribs}) at a constant Grashof number ($Gr = 10^8$) is presented in Fig. 13, based on the numerical results given in the *Supplementary Material*. Inspection of the figure reveals that, in confirmation to accuracy of the simplified function (Eq. (16)), the Nusselt number percentage deviation ($\mathcal{D}$) is well correlated to λ_z for given values of N_{ribs} and Gr. A critical value of the thermal-slip coefficient, $\lambda_z)_{critical} \approx 0.025$, is indicated; favorable effects of surface roughening on the heat transfer performance of vertical plates are exclusively present below this limit. For both ranges of λ_z, the magnitude of the percentage deviation ($\mathcal{D}$) decreases when more ribs are present.

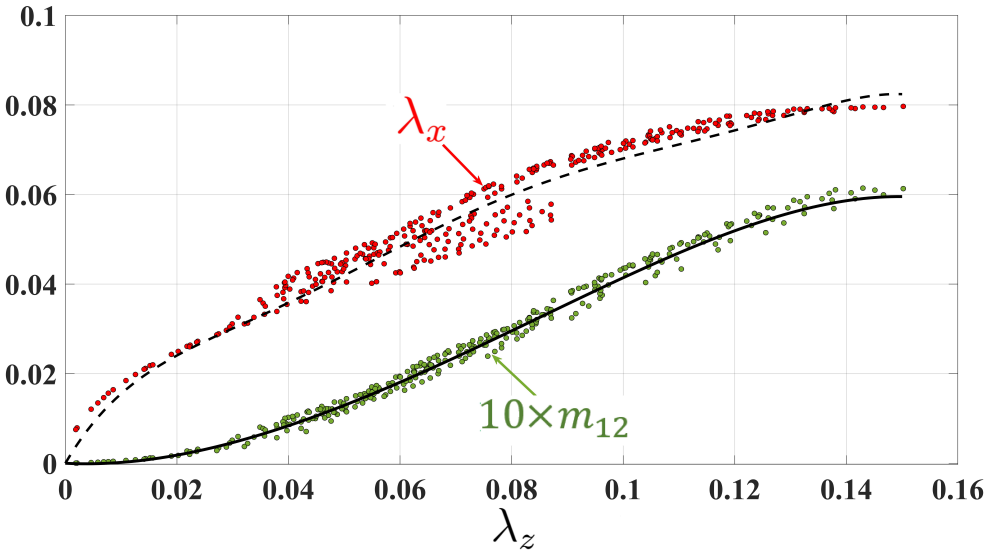

Figure 12: Values of Navier's slip coefficient in streamwise direction (λ_x) and surface permeability coefficient (m_{12}, multiplied by 10 for clarity), against the thermal-slip coefficient (λ_z). The plotted data are related to the different shapes and geometric parameters under investigation. Fitting curves are presented in the figure.

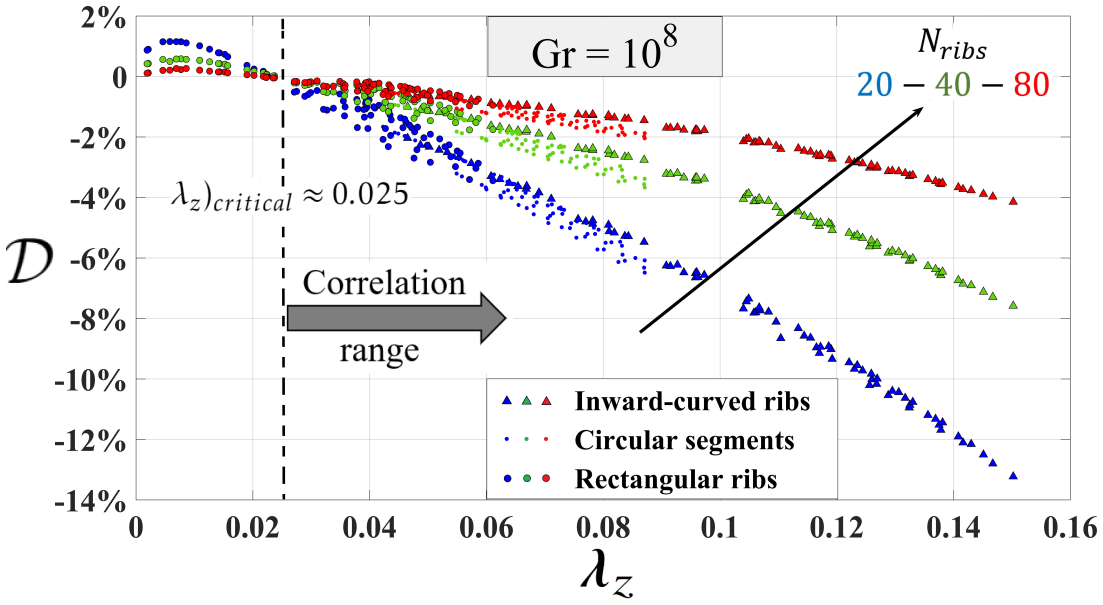

Figure 13: Dependence of the Nusselt number percentage deviation ($\mathcal{D}$) on the thermal-slip coefficient (λ_z) for different surface textures and number of ribs. $Gr = 10^8$, $Pr = 0.712$.

5.2 Correlation formulation and basic validation

In view of Eq. (16) and the available numerical results, a correlation describing the behavior of the Nusselt number percentage deviation is sought above the critical value of

λ_z, i.e., deterioration in the heat transfer performance due to surface ribbing is considered. The effects of variations in the Grashof number, previously unaccounted for in this paper, are analyzed first to be included in the formulation of the correlation at a further step. The values of ($\mathcal{D}$) for vertical surfaces with twenty ribs of different shapes and dimensions were calculated at three values of the Grashof number ($Gr = 10^7,\ 5 \times 10^7,\ 10^8$) based on macroscopic simulations (refer to the typical results in *Supplementary Material*); they are plotted against λ_z in Fig. 14. Notably, the deterioration in heat transfer rate is less considerable at lower values of the Grashof number. This may be attributed to the low level of inertia which allows the mainstream to easily reattach to the base surface so that the unfavorable separation eddies are minimized.

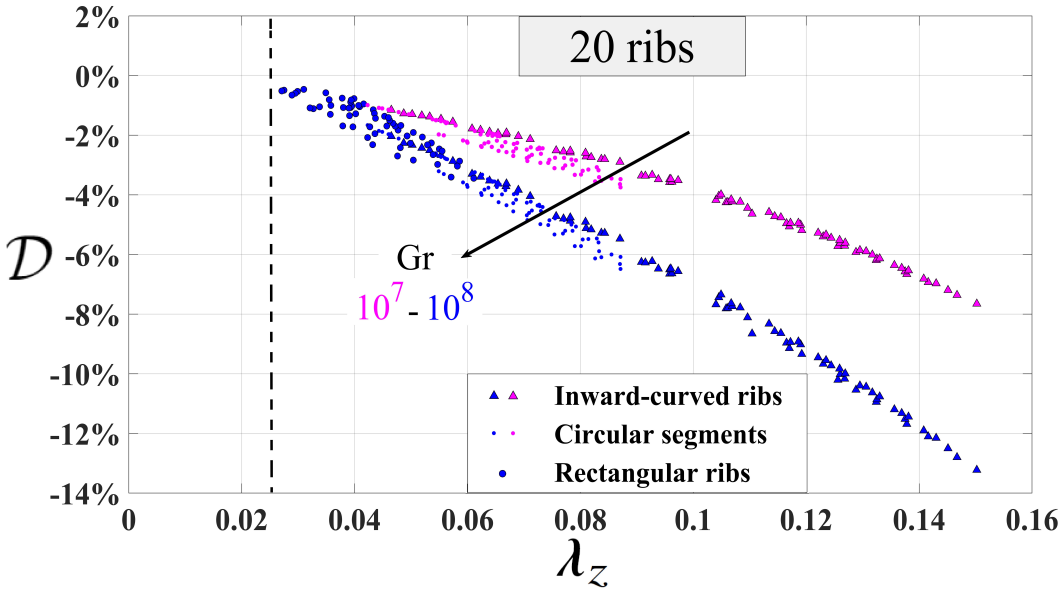

Figure 14: Behavior of the Nusselt number percentage deviation ($\mathcal{D}$) with variations of the thermal-slip coefficient (λ_z) for different surface textures, plotted at two values of the Grashof number. $N_{ribs} = 20$, $Pr = 0.712$.

Second, a multiple-regression analysis was performed to formulate a suitable correlation fitting the data given in the *Supplementary Material*, by implementing the Generalized Reduced Gradient (GRG) non-linear method. Eventually, the following form is proposed:

$$\mathcal{D} = (-1550 \ln Gr + 19740)\, \lambda_z^2\, N_{ribs}^{-0.85} \quad (\%), \tag{17-a}$$

valid at $Pr \approx 0.712$ (air), within the following ranges:

$$10^7 \leq Gr \leq 10^8, \qquad 0.025 \leq \lambda_z \leq 0.15, \qquad N_{ribs} \geq 20. \tag{17-b}$$

Predictions of the correlation are plotted in Fig. 15 against corresponding numerical values of $\mathcal{D}$, to give an idea about the fitting accuracy.

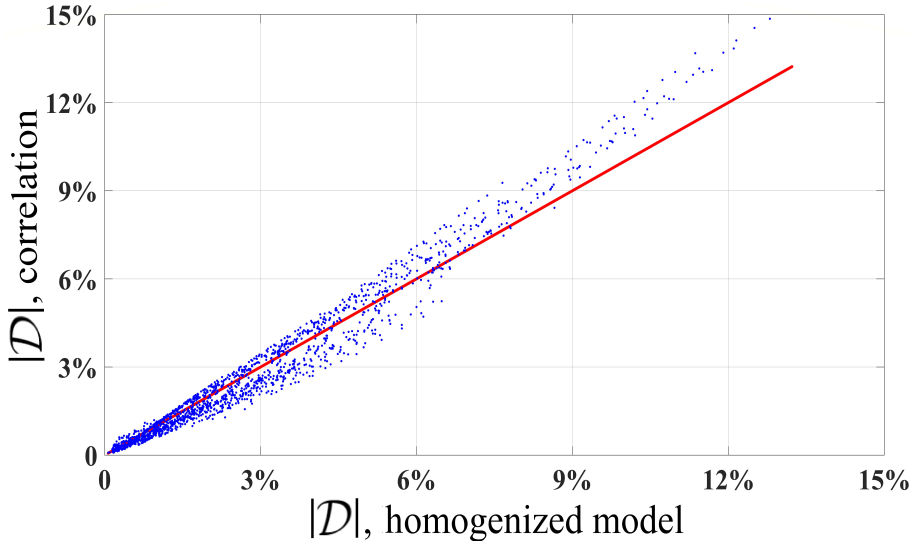

Figure 15: Correlation predictions of the Nusselt number percentage deviation ($\mathcal{D}$), against the corresponding reference database values.

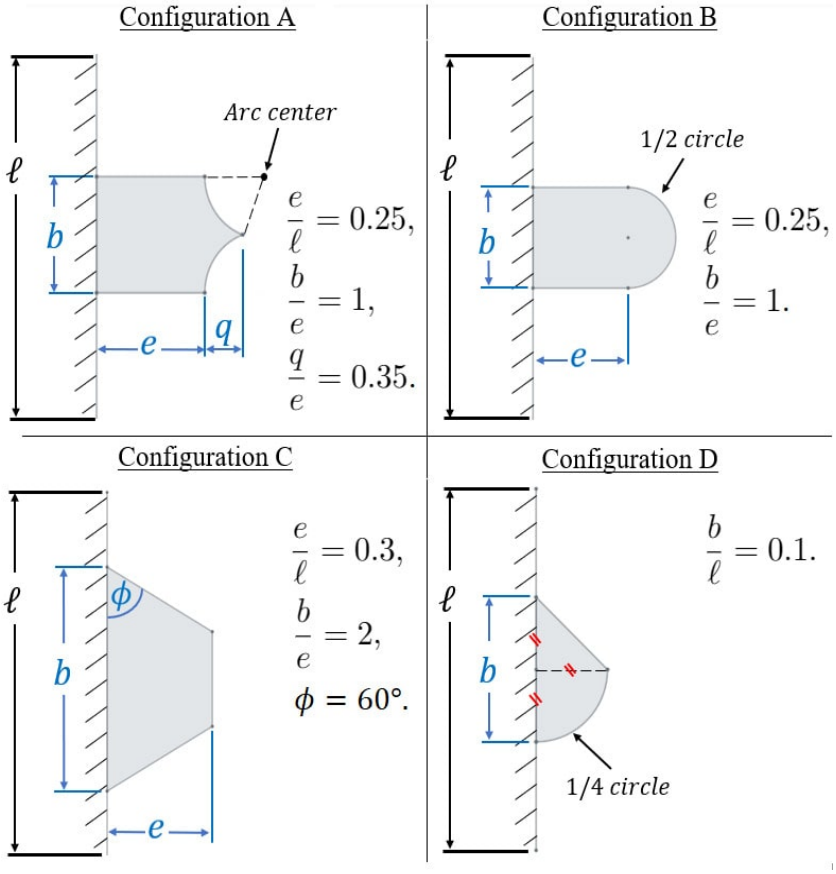

Figure 16: Sketch of rib geometries to be investigated by feature-resolving and homogenization-based numerical simulations, to validate the correlation predictions of the Nusselt number percentage deviation ($\mathcal{D}$).

To check the validity of the introduced correlation for handling rib shapes other than those based on which the correlation has been formulated, the configurations sketched in Fig. 16 were considered; the correlation predictions of the Nusselt number percentage deviation ($\mathcal{D}$) for different shapes, at $N_{ribs} = 20$ and $Gr = 10^8$, were compared with the results of macroscopic/feature-resolving simulations, and reasonable agreement was found (Table 2).

Table 2: Predictions of the Nusselt number percentage deviation ($\mathcal{D}$) for different rib geometries, based on the homogenized numerical model and the proposed correlation, in comparison with the values calculated from corresponding feature-resolving simulations. $N_{ribs} = 20$, $Gr = 10^8$, $Pr = 0.712$.

Configuration	Macroscopic parameters			$\mathcal{D}$		
	λ_z	λ_x	m_{12}	Feature-resolv.	Homog.	Correlation
A	0.1454	0.0778	0.00562	-13.69%	-13.16%	-14.60%
B	0.1238	0.0639	0.00410	-10.44%	-11.45%	-10.59%
C	0.0797	0.0384	0.00224	-6.74%	-7.46%	-4.39%
D	0.0434	0.0392	0.00093	-1.26%	-1.82%	-1.30%

With only the need to calculate λ_z by solving a two-dimensional Laplace system through a periodic unit cell of the microscopic domain, the present correlation is perfect for preliminary estimation of heat transfer deterioration over ribbed surfaces, before turning to computationally expensive feature-resolving simulations (if necessary). To elaborate this advantage, configuration **B** was considered for rough estimation of mesh requirements and elapsed wall-clock time for evaluating the Nusselt number percentage deviation ($\mathcal{D}$), via the three methods under discussion. To conduct the full simulation, a total mesh n_f^{tot} is used to resolve the features of the whole ribbed surface (with $N_{ribs} = 20$), and the fields through the full domain (cf. Fig. 5), where the conservation equations are discretized. In contrast, the proposed correlation (Eq. (17-a)) requires to consider only one representative volume element (cf. Figs. 2, 3), with a grid n_c^{tot}, to solve the Laplace system (Eqs. (8-a to 8-c)) for evaluating λ_z. The homogenization-based macroscale simulation requires, in addition, to solve the Stokes system (Eqs. (9-a to 9-d)) for evaluating the coefficients λ_x and m_{12}, so that the effective boundary conditions (Eqs. (6-a to 6-c)) are available to be imposed on a virtual smooth surface (cf. Fig. 5), beyond which the conservation equations (Eqs. (4-a to 4-c)) are numerically solved, using a grid n_h^{tot}. The mesh-dependency analysis in Fig. 17 (top) shows that, for a converged solution to be attained, the full simulation requires about one to two orders of magnitude more cells than the homogenization-based simulation and the correlation (to evaluate λ_z as a prerequisite). Interestingly, the wall-clock time (with six processors) elapsed to solve the Laplace system, so that λ_z is available to be plugged into the correlation, is five to six orders of magnitude less than the feature-resolving simulation, when mesh-independence is reached; cf. Fig. 17 (bottom). Note that the real time required for the homogenization-based simulation (t_h^{real}) includes calculation of the model coefficients and running the

macroscale simulation.

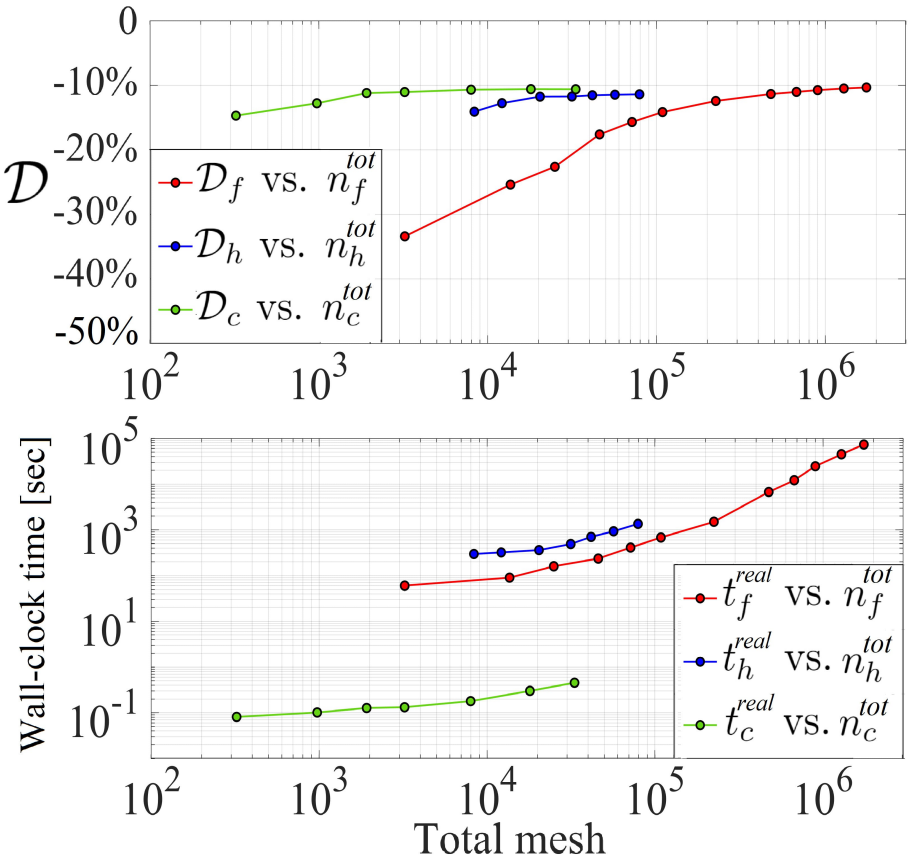

Figure 17: Total mesh (n^{tot}) and real-time (t^{real}) requirements for evaluating the Nusselt number percentage deviation ($\mathcal{D}$), for a vertical plate ribbed with twenty elements of geometry **B** (refer to Fig. 16, at $Gr = 10^8$ and $Pr = 0.712$. The subscripts f, h, c respectively indicate feature-resolving simulation, homogenization-based simulation and correlation (Eq. (17-a)).

6 COMMENTS ON PHYSICAL MODEL VALIDITY AND CONCLUDING REMARKS

6.1 Validity of the physical model

The validity of the physical assumptions adopted in the present work is to be properly assessed, to determine whether the obtained results reflect a true picture of what happens in practice. In particular, four critical assumptions are to be considered. First, the Boussinesq approximation is reliable under the constraint $\beta_\infty(\hat{T}_w - \hat{T}_\infty) << 1$ (cf. (Hærvig & Sørensen, 2020)), such that the density variations due to thermal gradient are significant only in the evaluation of the body force. This assumption, along with the linear temperature-density relationship, is numerically advantageous compared with using the

compressible form of the governing equations together with the ideal-Gas law. Second, the dynamic viscosity and the thermal diffusivity of the fluid are considered constant at the film temperature (cf. (Nishikawa *et al.*, 2020; Cavazzuti & Corticelli, 2008)). Third, laminar flow was assumed over the range $10^7 \leq Gr \leq 10^8$ ($7.12 \times 10^6 \leq Ra \leq 7.12 \times 10^7$ in terms of the Rayleigh number). A typical value of 10^9 has been reported/accepted by many investigators as the critical Rayleigh number (Bhavnani & Bergles, 1990); however, the criteria based on which the onset of transition is to be determined have been a source of confusion (Godaux & Gebhart, 1974). For instance, Godaux & Gebhart (1974) summarized observations from the literature on the value of the Grashof number at the onset of transition ($Gr_{trans.}$); accordingly, variations within the range $1.1 \times 10^8 \leq Gr_{trans.} \leq 10^{10}$ (which lies above the limit of the present study, $Gr = 10^8$) can be realized for air natural convection over an isothermal vertical smooth surface. Fourth, two-dimensional flow was assumed; this is reasonable only for the case of transverse ribs (uniform in the spanwise direction), attached to a sufficiently wide plate, over which the flow is laminar. The above-mentioned considerations/limitations necessitate further validation of the present model, mainly against reference experimental results.

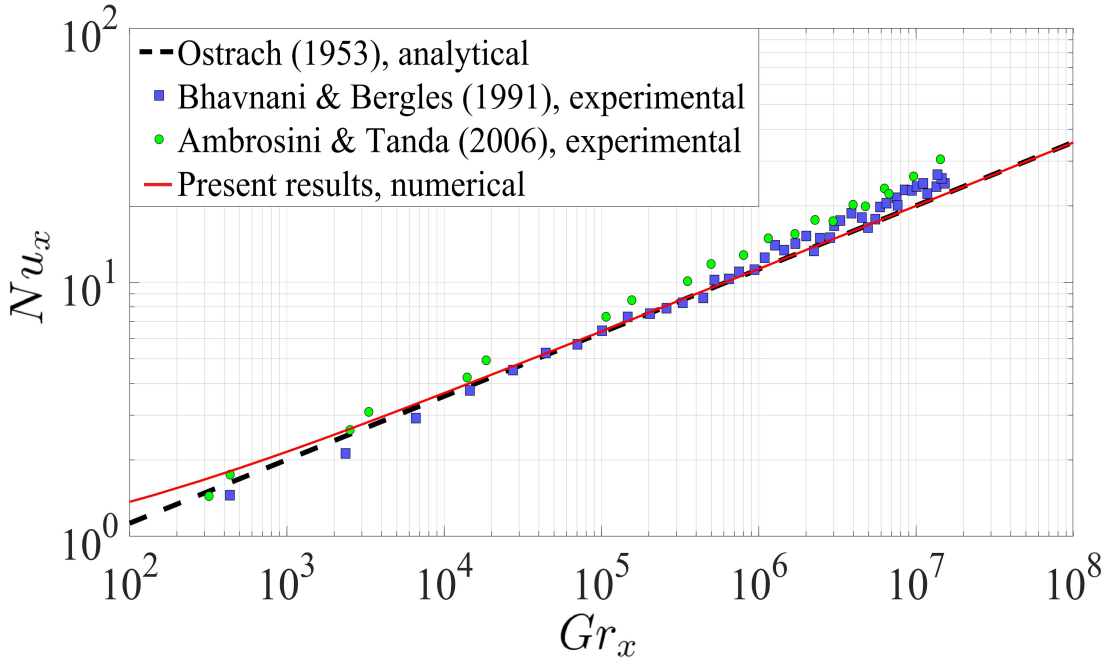

Figure 18: Dependence of (Nu_x) on the local Grashof number (Gr_x), at $Pr = 0.712$ (air).

The classical way for validation relies on plotting the behavior of the local Nusselt number (Nu_x) along the isothermal smooth surface as a function of the local Grashof number (Gr_x), as presented in Fig. 18 together with the experimental measurements in (Bhavnani & Bergles, 1991; Ambrosini & Tanda, 2006) and the Analytical solution by Ostrach (1953). It should be noted that Nu_x is defined based on the vertical position measured from the leading edge, while Nu, plotted in Fig. 8, was defined based on the total plate height (L); they are linked as $Nu_x = Nu\, X_1$. The local Grashof number (Gr_x)

may be calculated as $Gr_x = Gr\, X_1^3$, with Gr the plate Grashof number. At relatively low values of the local Grashof number, i.e. $Gr_x < 1000$, the present numerical results significantly deviate from Ostrach's solution, as the boundary-layer assumption used in developing the latter is invalid close to the leading edge of the plate, and applicable only for vertical distances sufficiently larger than the thickness of the boundary layer (Ostrach, 1953). Experimental difficulties related to building a perfectly sharp-edged test section may also affect the measurements close to the leading edge (Bhavnani & Bergles, 1991), resulting in deviations from the numerical values. At relatively large values of Gr_x, the present numerical results are identical to Ostrach's solution; however, the experimental results start to deviate, which may be attributed to periodic oscillations close to the trailing edge of the plate and extended effects of room-air turbulence, originally disturbing the outer edge of the boundary layer; refer to (Ostrach, 1953; Schmidt & Beckmann, 1930; Eckert & Soehngen, 1948).

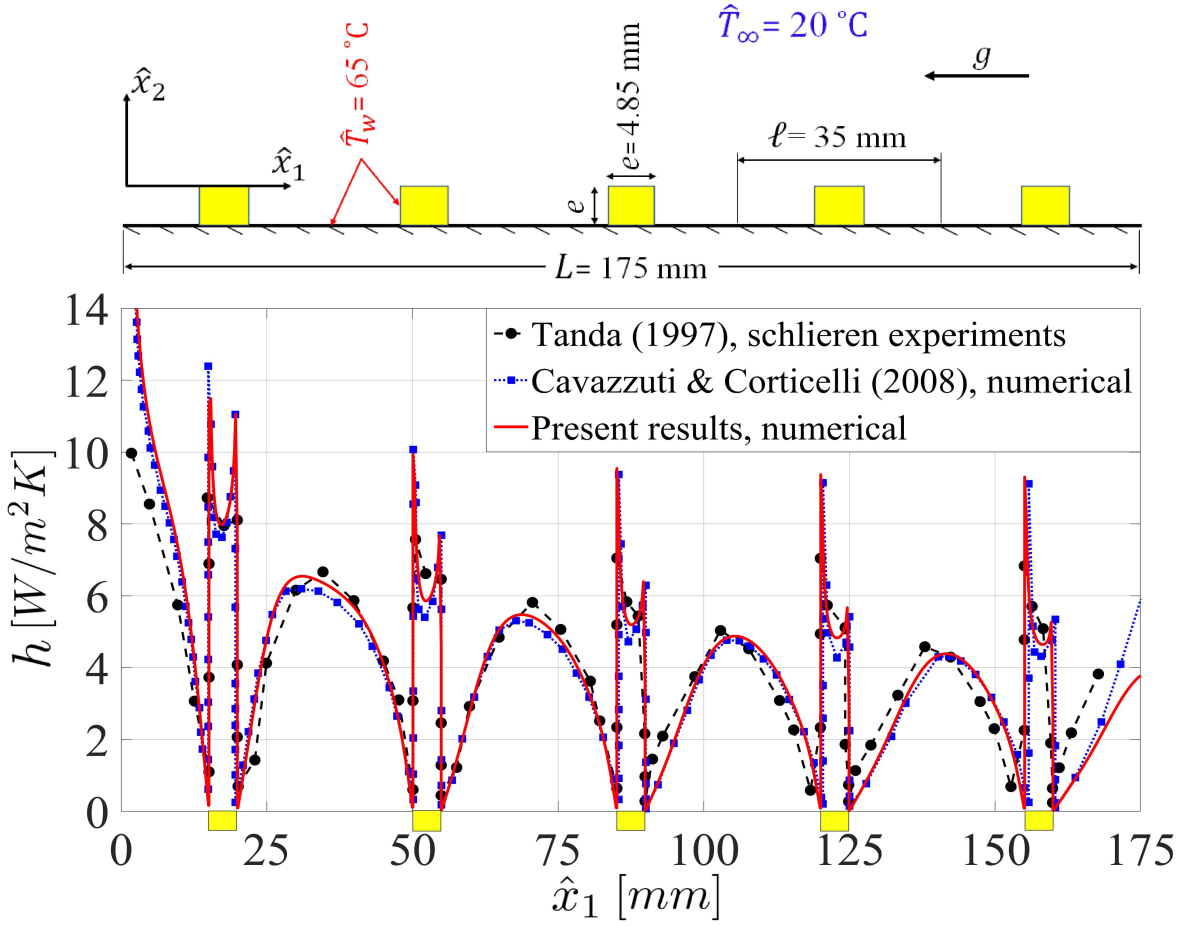

Figure 19: Distribution of the local heat transfer coefficient over ribbed surface, with the geometric and thermal conditions shown in the right frame.

Providing validation for results of the feature-resolving simulation over a ribbed surface is of much interest. The experimental measurements based on the schlieren technique

in (Tanda, 1997), with the largest channel aspect ratio, together with the numerical results (using *Fluent 6.2*) in (Cavazzuti & Corticelli, 2008), are used to validate the present fully-featured results of the local heat transfer coefficient (h) over a surface roughened with five square ribs, with the dimensions and thermal conditions shown in Fig. 19. With air as the moving fluid, this validation has been conducted at $Gr \approx 3 \times 10^7$, with the fluid properties calculated as discussed in Section 2.1. The results are in reasonable agreement over the edges of the ribs and also through the inter-rib regions. It is notable that a stable thermal boundary layer was optically captured in (Tanda, 1997), at the considered value of Gr, which justifies the agreement with the present laminar-flow model.

6.2 Conclusions

Natural-convection heat transfer over perturbed surfaces represents a major phenomenon in many engineering and natural processes. Whether the surface is naturally or intentionally roughened, it is vital to analyze the consequent deterioration/enhancement of heat transfer performance for efficiency assessment, design optimization, and determination of the maximum allowable heat load. In this paper, laminar buoyancy-driven flows ($10^7 \leq Gr \leq 10^8$) over isothermal vertical surfaces, intensively ribbed ($N_{ribs} > 20$) with elements of different shapes (inward-curved, triangular, circular, rectangular) and dimensions (height, aspect ratio, etc.) are numerically investigated at a constant Prandtl number ($Pr = 0.712$). Two numerical approaches, substantially different in scope and computational cost, were tested: (i) feature-resolving simulations with full capability of capturing the micro-structure details of the surface, revealing complex flow patterns including separation and reattachment of the mainstream from/to the baseplate in the inter-rib regions and local thinning and thickening of the thermal boundary layer, besides the associated effects on the local Nusselt number; (ii) homogenization-based simulations with effective boundary conditions, imposed at a virtual vertical plane passing by crests/outer rims of the ribs, to macroscopically mimic the behavior of the flow at a reduced level of mesh requirements and computational cost. For the selected cases, the values of the surface-averaged Nusselt number, based on the two approaches, were compared to validate the model.

Taking advantage of the ability of the validated model to accelerate numerical simulations, it was employed to create a database of results describing the deviation ($\mathcal{D}$) of the Nusselt number, for different rib geometries and values of the Grashof number, relative to the reference value of a smooth isothermal wall. A response surface optimization study was conducted, employing the Non-Linear Programming by Quadratic Lagrangian (NLPQL) technique. It is proved that the presence of ribs generally has a negative effect on heat transfer from the surface, reducing it by more than 10% for some cases, i.e., blunt inward-curved and triangular ribs of large depth. However, a marginal increase in the heat transfer rate has been realized for rectangular ribs of large aspect ratio (width to depth ratio). The maximum heat transfer enhancement, attained under the investigated conditions and ranges, is slightly above 1% and is related to the case of a vertical sur-

face ribbed with 20 rectangular elements characterized by an aspect ratio of 3.741 and a height to pitch distance ratio of 0.214, under natural convection with Grashof number equal to 10^8. It should be highlighted that this marginal improvement is difficult to be validated, as it clearly lies within the experimental uncertainty range (if experimental validation is sought), and even within the numerical uncertainty of the feature-resolving simulations. With the increase in the number of ribs, at a given aspect ratio, the positive/negative effects become mild, and the Nusselt number gradually approaches its value over a corresponding smooth surface.

A fundamentally novel view of the contribution of the surface micro-structure to heat transfer by natural convection from vertical surfaces is introduced; the thermal-slip coefficient (λ_z), as a single macroscopic control parameter, proved to imitate the inherent dependence of the Nusselt number on surface micro-details under given pattern density and flow conditions. Subsequently, a correlation coupling the effects of the thermal-slip coefficient (λ_z), the number of ribs (N_{ribs}), and the Grashof number (Gr) on the projected-area-based Nusselt number ($\overline{Nu}$) was cast based on the available database. The proposed correlation was tested on selected geometries and the results are comparable to those obtained from feature-resolving/homogenized simulations. Accordingly, the correlation is expected to provide a reasonable preliminary estimation of the Nusselt number at an interestingly low computational cost.

REFERENCES

Ahmed, E.N., Bottaro, A. & Tanda, G. 2022 A homogenization approach for buoyancy-induced flows over micro-textured vertical surfaces. *J. Fluid Mech.* **941**, A53.

Ambrosini, D. & Tanda, G. 2006 Comparative measurements of natural convection heat transfer in channels by holographic interferometry and schlieren. *Eur. J. Phys.* **27** (1), 159–172.

Ansys® 2021 R1 Ansys workbench user's guide .

Aydin, M. 1997 Dependence of the natural convection over a vertical flat plate in the presence of the ribs. *Intl Commun. Heat Mass Transfer* **24** (4), 521–531.

Azevedo, L.F.A. & Sparrow, E.M. 1985 Natural convection in open-ended inclined channels. *ASME J. Heat Transfer* **107** (4), 893–901.

Bhavnani, S.H. & Bergles, A.E. 1990 Effect of surface geometry and orientation on laminar natural convection heat transfer from a vertical flat plate with transverse roughness elements. *Intl J. Heat Mass Transfer* **33** (5), 965–981.

Bhavnani, S.H. & Bergles, A.E. 1991 Natural convection heat transfer from sinusoidal wavy surfaces. *Wärme-Stoffübertrag.* **26** (6), 341–349.

Bottaro, A. & Naqvi, S.B. 2020 Effective boundary conditions at a rough wall: a high-order homogenization approach. *Meccanica* **55** (9), 1781–1800.

Cavazzuti, M. & Corticelli, M.A. 2008 Optimization of a buoyancy chimney with a heated ribbed wall. *Heat Mass Transfer* **44** (4), 421–435.

Desrayaud, G. & Fichera, A. 2002 Laminar natural convection in a vertical isothermal channel with symmetric surface-mounted rectangular ribs. *Intl J. Heat Fluid Flow* **23** (4), 519–529.

Eckert, E.R.G. & Soehngen, E.E. 1948 Studies on heat transfer in laminar free convection with the Zehnder-Mach interferometer. *Air Material Command,* Dayton, Ohio (Tech. Rep. 5747, ATI-44580).

Genot, M. 1982 Thermal architecture made with specific components, session PII: components manufacturing technologies pp. 377–803.

Godaux, F. & Gebhart, B. 1974 An experimental study of the transition of natural convection flow adjacent to a vertical surface. *Intl J. Heat Mass Transfer* **17** (1), 93–107.

Hærvig, J. & Sørensen, H. 2020 Natural convective flow and heat transfer on unconfined isothermal zigzag-shaped ribbed vertical surfaces. *Intl Commun. Heat Mass Transfer* **119**, 104982.

Introïni, C., Quintard, M. & Duval, F. 2011 Effective surface modeling for momentum and heat transfer over rough surfaces: Application to a natural convection problem. *Intl J. Heat Mass Transfer* **54** (15-16), 3622–3641.

Johnson, C.E. 1986 Evaluation of correlations for natural convection cooling of electronic equipment. *Heat Transfer Eng.* **7** (1-2), 36–45.

Joshi, Y., Willson, T. & Hazard, S.J., III 1989 An experimental study of natural convection from an array of heated protrusions on a vertical surface in water. *ASME J. Electron. Packag.* **111** (2), 121–128.

Nishikawa, M., Otomo, H., Yoshida, Y., Deguchi, J., Tsukamoto, M. & Yamamoto, T. 2020 The cooling mechanism of minuscule ribbed surfaces. *Sci. Rep.* **10** (1), 5635.

Ostrach, S. 1953 An analysis of laminar free-convection flow and heat transfer about a flat plate parallel to the direction of the generation body force. NACA Technical Report 1111 .

Park, K.-A. & Bergles, A.E. 1987 Natural convection heat transfer characteristics of simulated microelectronic chips. *ASME J. Heat Transfer* **109** (1), 90–96.

Park, S.-J., Jang, D., Yook, S.-J. & Lee, K.-S. 2015 Optimization of a staggered pin-fin for a radial heat sink under free convection. *Intl J. Heat Mass Transfer* **87**, 184–188.

Peterson, G.P. & Ortega, A. 1990 Thermal control of electronic equipment and devices. *Adv. Heat Transfer* **20**, 181–314.

Schmidt, E. & Beckmann, W. 1930 Das temperatur-und geschwindigkeitsfeld vor einer wärme abgebenden senkrechten platte bei natürlicher konvektion. *Tech. Mech. Thermodyn.* **1** (11), 391–406.

Tanda, G. 1997 Natural convection heat transfer in vertical channels with and without transverse square ribs. *Intl J. Heat Mass Transfer* **40** (9), 2173–2185.

Tanda, G. 2008 Natural convective heat transfer in vertical channels with low-thermal-conductivity ribs. *Intl J. Heat Fluid Flow* **29** (5), 1319–1325.

Tanda, G. 2017 Experiments on natural convection in water-cooled ribbed channels with different aspect ratios. *Intl J. Heat Mass Transfer* **110**, 606–612.

Webb, B.W. & Hill, D.P. 1989 High Rayleigh number laminar natural convection in an asymmetrically heated vertical channel. *ASME J. Heat Transfer* **111** (3), 649–656.

Zampogna, G.A., Magnaudet, J. & Bottaro, A. 2019 Generalized slip condition over rough surfaces. *J. Fluid Mech.* **858**, 407–436.

SUPPLEMENTARY MATERIAL

This part includes supplementary data related to the main article "Natural-convection heat transfer from regularly ribbed vertical surfaces: Homogenization-based simulations towards a correlation for the Nusselt number" by **Essam Nabil Ahmed.**

For the different rib geometries shown in Fig. 1 (of the main article), values of the corresponding percentage increase in the heat transfer area (relative to a smooth surface) are given below in Table S1. The macroscopic coefficients for the different rib shapes and dimensions, and the consequent values of the Nusselt number percentage deviation ($\mathcal{D}$) with different densities of the roughness pattern, at $Gr = 10^8$ and $Pr = 0.712$, are listed in Tables S2 to S5. The effects of varying the Grashof number on the Nusselt number percentage deviation ($\mathcal{D}$) is shown in Table S6, only for the case of 20 ribs.

Table S1: Percentage increase in the heat transfer area ($\Delta A\%$) due to surface roughening, evaluated for the four rib types under consideration varying the characteristic dimensions (e/ℓ and b/e).

Dimensions		$\Delta A\%$			
e/ℓ	b/e	inward-curved	isosceles triangular	circular segment	rectangular
0.0513	2.6625	4.66%	3.42%	4.66%	10.25%
0.0538	2.3375	5.44%	3.97%	5.44%	10.75%
0.0563	2.9375	4.71%	3.47%	4.71%	11.25%
0.0588	3.1625	4.61%	3.40%	4.61%	11.75%
0.0613	3.7875	4.10%	3.04%	4.10%	12.25%
0.0638	3.5875	4.48%	3.31%	4.48%	12.75%
0.0663	3.3625	4.93%	3.64%	4.93%	13.25%
0.0688	2.1625	7.39%	5.38%	7.39%	13.75%
0.0713	2.4375	6.97%	5.10%	6.97%	14.25%
0.0738	2.6375	6.76%	4.96%	6.76%	14.75%
0.0763	2.8375	6.57%	4.83%	6.57%	15.25%
0.0788	3.0625	6.36%	4.69%	6.36%	15.75%
0.0813	3.9125	5.28%	3.91%	5.28%	16.25%
0.0838	3.6875	5.74%	4.25%	5.74%	16.75%
0.0863	3.4625	6.25%	4.62%	6.25%	17.25%
0.0888	2.0625	9.90%	7.19%	9.90%	17.75%
0.0913	2.2875	9.39%	6.85%	9.39%	18.25%
0.0938	2.5125	8.95%	6.55%	8.95%	18.75%
0.0963	3.1875	7.51%	5.54%	7.51%	19.25%
0.0988	2.7375	8.78%	6.45%	8.78%	19.75%
0.1013	2.9625	8.41%	6.20%	8.41%	20.25%
0.1038	3.8125	6.90%	5.11%	6.90%	20.75%
0.1063	3.3875	7.85%	5.80%	7.85%	21.25%
0.1088	3.6125	7.59%	5.62%	7.59%	21.75%
0.1113	2.1125	12.18%	8.86%	12.18%	22.25%
0.1138	2.3625	11.41%	8.34%	11.41%	22.75%
0.1163	3.9875	7.42%	5.50%	7.42%	23.25%
0.1188	2.5625	11.15%	8.17%	11.15%	23.75%
0.1213	3.2125	9.39%	6.93%	9.39%	24.25%
0.1238	2.7875	10.83%	7.96%	10.83%	24.75%
0.1263	3.0125	10.34%	7.62%	10.34%	25.25%
0.1288	3.4375	9.39%	6.95%	9.39%	25.75%
0.1313	3.6375	9.10%	6.74%	9.10%	26.25%
0.1338	2.1875	14.26%	10.39%	14.26%	26.75%
0.1363	3.8375	9.01%	6.67%	9.01%	27.25%
0.1388	2.4125	13.68%	10.01%	13.68%	27.75%
0.1413	2.6125	13.05%	9.57%	13.05%	28.25%
0.1438	2.0125	16.33%	11.86%	16.33%	28.75%

0.1463	3.3375	10.95%	8.09%	10.95%	29.25%
0.1488	3.1125	11.84%	8.73%	11.84%	29.75%
0.1513	2.8875	12.85%	9.45%	12.85%	30.25%
0.1538	3.5375	10.94%	8.09%	10.94%	30.75%
0.1563	3.9625	10.03%	7.44%	10.03%	31.25%
0.1588	2.2375	16.62%	12.12%	16.62%	31.75%
0.1613	3.7375	10.92%	8.09%	10.92%	32.25%
0.1638	2.6875	14.78%	10.85%	14.78%	32.75%
0.1663	2.4625	16.12%	11.80%	16.12%	33.25%
0.1688	3.2875	12.81%	9.46%	12.81%	33.75%
0.1713	3.0375	13.93%	10.26%	13.93%	34.25%
0.1738	2.0375	19.56%	14.21%	19.56%	34.75%
0.1763	3.5125	12.62%	9.33%	12.62%	35.25%
0.1788	3.8625	11.75%	8.71%	11.75%	35.75%
0.1813	2.8125	15.74%	11.57%	15.74%	36.25%
0.1838	2.2125	19.41%	14.15%	19.41%	36.75%
0.1863	2.5875	17.35%	12.72%	17.35%	37.25%
0.1888	3.2375	14.52%	10.72%	14.52%	37.75%
0.1913	3.6625	13.19%	9.76%	13.19%	38.25%
0.1938	2.9875	15.98%	11.77%	15.98%	38.75%
0.1963	2.3875	19.52%	14.27%	19.52%	39.25%
0.1988	3.9375	12.83%	9.52%	12.83%	39.75%
0.2013	3.4125	14.78%	10.93%	14.78%	40.25%
0.2038	2.1375	22.11%	16.09%	22.11%	40.75%
0.2063	2.7625	18.19%	13.36%	18.19%	41.25%
0.2088	3.1375	16.51%	12.18%	16.51%	41.75%
0.2113	3.7625	14.22%	10.53%	14.22%	42.25%
0.2138	2.5375	20.23%	14.82%	20.23%	42.75%
0.2163	3.5625	15.28%	11.31%	15.28%	43.25%
0.2188	2.3125	22.32%	16.29%	22.32%	43.75%
0.2213	2.9125	18.65%	13.73%	18.65%	44.25%
0.2238	3.3125	16.87%	12.46%	16.87%	44.75%
0.2263	2.0875	25.00%	18.18%	25.00%	45.25%
0.2288	3.8875	14.94%	11.08%	14.94%	45.75%
0.2313	2.7125	20.71%	15.21%	20.71%	46.25%
0.2338	3.0875	18.74%	13.82%	18.74%	46.75%
0.2363	2.4875	22.73%	16.64%	22.73%	47.25%
0.2388	3.4875	17.20%	12.72%	17.20%	47.75%
0.2413	3.7125	16.43%	12.17%	16.43%	48.25%
0.2438	2.2625	25.30%	18.46%	25.30%	48.75%
0.2463	2.8625	21.07%	15.50%	21.07%	49.25%
0.2488	3.2625	19.01%	14.04%	19.01%	49.75%

Table S2: Inward-curved ribs. Values of the Nusselt number percentage deviation ($\mathcal{D}$), relative to a smooth surface at $Gr = 10^8$ and $Pr = 0.712$, are listed for different dimensions and densities of the roughness pattern, where the average Nusselt number over a rough surface is corrected (increased) by the ribbed-to-smooth area ratio such that ($\mathcal{D}$) directly indicates the total change in the heat transfer rate.

Dimensions		Macroscopic coefficients			$\mathcal{D}$			
e/ℓ	b/e	λ_z	λ_x	m_{12}	20 ribs	40 ribs	80 ribs	160 ribs
0.0513	2.6625	0.0465	0.0415	0.00101	-2.04%	-1.00%	-0.57%	-0.38%
0.0538	2.3375	0.0487	0.0427	0.00109	-2.27%	-1.12%	-0.63%	-0.42%
0.0563	2.9375	0.0502	0.0441	0.00118	-2.33%	-1.14%	-0.64%	-0.42%
0.0588	3.1625	0.0519	0.0456	0.00126	-2.43%	-1.19%	-0.66%	-0.43%
0.0613	3.7875	0.0533	0.0467	0.00135	-2.51%	-1.22%	-0.68%	-0.44%
0.0638	3.5875	0.0553	0.0481	0.00143	-2.67%	-1.30%	-0.71%	-0.46%
0.0663	3.3625	0.0574	0.0494	0.00153	-2.87%	-1.40%	-0.76%	-0.48%
0.0688	2.1625	0.0608	0.0508	0.00163	-3.30%	-1.63%	-0.88%	-0.54%
0.0713	2.4375	0.0623	0.0519	0.00172	-3.40%	-1.68%	-0.91%	-0.55%
0.0738	2.6375	0.0639	0.0530	0.00182	-3.52%	-1.74%	-0.94%	-0.57%
0.0763	2.8375	0.0654	0.0542	0.00190	-3.63%	-1.79%	-0.96%	-0.58%
0.0788	3.0625	0.0668	0.0553	0.00200	-3.72%	-1.83%	-0.98%	-0.59%
0.0813	3.9125	0.0669	0.0561	0.00207	-3.62%	-1.77%	-0.94%	-0.57%
0.0838	3.6875	0.0690	0.0570	0.00219	-3.84%	-1.89%	-1.01%	-0.60%
0.0863	3.4625	0.0711	0.0584	0.00227	-4.05%	-1.99%	-1.05%	-0.63%
0.0888	2.0625	0.0757	0.0594	0.00239	-4.72%	-2.37%	-1.25%	-0.73%
0.0913	2.2875	0.0770	0.0603	0.00250	-4.80%	-2.41%	-1.28%	-0.74%
0.0938	2.5125	0.0782	0.0613	0.00258	-4.87%	-2.44%	-1.28%	-0.74%
0.0963	3.1875	0.0782	0.0618	0.00267	-4.76%	-2.38%	-1.25%	-0.72%
0.0988	2.7375	0.0810	0.0628	0.00278	-5.12%	-2.57%	-1.35%	-0.78%
0.1013	2.9625	0.0819	0.0637	0.00285	-5.16%	-2.59%	-1.36%	-0.78%
0.1038	3.8125	0.0809	0.0641	0.00291	-4.91%	-2.45%	-1.28%	-0.74%
0.1063	3.3875	0.0837	0.0649	0.00302	-5.28%	-2.66%	-1.40%	-0.80%
0.1088	3.6125	0.0843	0.0655	0.00312	-5.28%	-2.66%	-1.40%	-0.80%
0.1113	2.1125	0.0908	0.0666	0.00324	-6.25%	-3.22%	-1.70%	-0.96%
0.1138	2.3625	0.0915	0.0672	0.00334	-6.27%	-3.23%	-1.70%	-0.96%
0.1163	3.9875	0.0870	0.0673	0.00333	-5.47%	-2.76%	-1.45%	-0.83%
0.1188	2.5625	0.0938	0.0685	0.00351	-6.48%	-3.34%	-1.76%	-0.99%
0.1213	3.2125	0.0927	0.0687	0.00357	-6.23%	-3.20%	-1.69%	-0.95%
0.1238	2.7875	0.0958	0.0695	0.00368	-6.65%	-3.44%	-1.82%	-1.02%
0.1263	3.0125	0.0962	0.0700	0.00376	-6.64%	-3.44%	-1.81%	-1.02%
0.1288	3.4375	0.0958	0.0706	0.00379	-6.50%	-3.35%	-1.76%	-0.99%
0.1313	3.6375	0.0960	0.0706	0.00386	-6.47%	-3.34%	-1.76%	-0.99%
0.1338	2.1875	0.1040	0.0717	0.00404	-7.67%	-4.05%	-2.15%	-1.19%
0.1363	3.8375	0.0973	0.0716	0.00398	-6.56%	-3.38%	-1.77%	-0.99%
0.1388	2.4125	0.1058	0.0725	0.00419	-7.81%	-4.13%	-2.19%	-1.21%

0.1413	2.6125	0.1061	0.0729	0.00426	-7.80%	-4.12%	-2.18%	-1.21%
0.1438	2.0125	0.1104	0.0733	0.00434	-8.65%	-4.52%	-2.40%	-1.32%
0.1463	3.3375	0.1045	0.0733	0.00438	-7.44%	-3.91%	-2.07%	-1.15%
0.1488	3.1125	0.1069	0.0738	0.00449	-7.74%	-4.10%	-2.18%	-1.21%
0.1513	2.8875	0.1096	0.0743	0.00456	-8.11%	-4.32%	-2.30%	-1.27%
0.1538	3.5375	0.1067	0.0744	0.00453	-7.64%	-4.03%	-2.14%	-1.19%
0.1563	3.9625	0.1049	0.0742	0.00454	-7.34%	-3.86%	-2.05%	-1.14%
0.1588	2.2375	0.1170	0.0754	0.00476	-9.14%	-4.95%	-2.64%	-1.45%
0.1613	3.7375	0.1083	0.0751	0.00467	-7.78%	-4.12%	-2.19%	-1.21%
0.1638	2.6875	0.1165	0.0759	0.00489	-8.96%	-4.84%	-2.59%	-1.42%
0.1663	2.4625	0.1192	0.0760	0.00497	-9.34%	-5.08%	-2.72%	-1.50%
0.1688	3.2875	0.1144	0.0761	0.00494	-8.57%	-4.61%	-2.46%	-1.36%
0.1713	3.0375	0.1172	0.0766	0.00505	-8.94%	-4.83%	-2.58%	-1.42%
0.1738	2.0375	0.1256	0.0768	0.00515	-10.21%	-5.62%	-3.02%	-1.65%
0.1763	3.5125	0.1155	0.0766	0.00507	-8.64%	-4.66%	-2.49%	-1.37%
0.1788	3.8625	0.1134	0.0763	0.00505	-8.32%	-4.47%	-2.38%	-1.31%
0.1813	2.8125	0.1230	0.0772	0.00531	-9.67%	-5.30%	-2.84%	-1.56%
0.1838	2.2125	0.1288	0.0777	0.00537	-10.54%	-5.83%	-3.14%	-1.71%
0.1863	2.5875	0.1268	0.0777	0.00545	-10.17%	-5.61%	-3.02%	-1.66%
0.1888	3.2375	0.1221	0.0776	0.00541	-9.45%	-5.17%	-2.78%	-1.53%
0.1913	3.6625	0.1190	0.0775	0.00531	-9.02%	-4.89%	-2.62%	-1.44%
0.1938	2.9875	0.1260	0.0780	0.00548	-10.01%	-5.51%	-2.97%	-1.63%
0.1963	2.3875	0.1324	0.0783	0.00558	-10.95%	-6.10%	-3.29%	-1.80%
0.1988	3.9375	0.1186	0.0775	0.00535	-8.92%	-4.84%	-2.59%	-1.43%
0.2013	3.4125	0.1244	0.0781	0.00554	-9.72%	-5.34%	-2.88%	-1.58%
0.2038	2.1375	0.1378	0.0785	0.00569	-11.69%	-6.57%	-3.56%	-1.95%
0.2063	2.7625	0.1325	0.0785	0.00572	-10.86%	-6.06%	-3.28%	-1.80%
0.2088	3.1375	0.1295	0.0786	0.00570	-10.40%	-5.77%	-3.12%	-1.71%
0.2113	3.7625	0.1235	0.0782	0.00558	-9.55%	-5.24%	-2.82%	-1.55%
0.2138	2.5375	0.1375	0.0788	0.00587	-11.52%	-6.49%	-3.53%	-1.93%
0.2163	3.5625	0.1269	0.0786	0.00570	-9.99%	-5.52%	-2.98%	-1.64%
0.2188	2.3125	0.1416	0.0792	0.00591	-12.10%	-6.85%	-3.73%	-2.03%
0.2213	2.9125	0.1356	0.0792	0.00591	-11.20%	-6.28%	-3.40%	-1.86%
0.2238	3.3125	0.1317	0.0790	0.00584	-10.63%	-5.92%	-3.20%	-1.75%
0.2263	2.0875	0.1467	0.0794	0.00599	-12.80%	-7.29%	-3.97%	-2.16%
0.2288	3.8875	0.1259	0.0785	0.00571	-9.83%	-5.42%	-2.92%	-1.60%
0.2313	2.7125	0.1408	0.0794	0.00604	-11.90%	-6.74%	-3.67%	-2.00%
0.2338	3.0875	0.1369	0.0792	0.00603	-11.32%	-6.37%	-3.46%	-1.89%
0.2363	2.4875	0.1451	0.0795	0.00610	-12.50%	-7.12%	-3.88%	-2.12%
0.2388	3.4875	0.1330	0.0792	0.00595	-10.76%	-6.02%	-3.26%	-1.79%
0.2413	3.7125	0.1306	0.0791	0.00587	-10.44%	-5.80%	-3.14%	-1.72%
0.2438	2.2625	0.1502	0.0797	0.00613	-13.22%	-7.58%	-4.15%	-2.26%
0.2463	2.8625	0.1430	0.0796	0.00614	-12.15%	-6.90%	-3.77%	-2.06%
0.2488	3.2625	0.1381	0.0794	0.00611	-11.44%	-6.46%	-3.51%	-1.92%

Table S3: Isosceles triangular ribs. Values of the Nusselt number percentage deviation ($\mathcal{D}$), relative to a smooth surface at $Gr = 10^8$ and $Pr = 0.712$, are listed for different dimensions and densities of the roughness pattern, where the average Nusselt number over a rough surface is corrected (increased) by the ribbed-to-smooth area ratio such that ($\mathcal{D}$) directly indicates the total change in the heat transfer rate.

Dimensions		Macroscopic coefficients			$\mathcal{D}$			
e/ℓ	b/e	λ_z	λ_x	m_{12}	20 ribs	40 ribs	80 ribs	160 ribs
0.0513	2.6625	0.0448	0.0411	0.00100	-1.78%	-0.86%	-0.50%	-0.35%
0.0538	2.3375	0.0472	0.0426	0.00107	-2.00%	-0.97%	-0.55%	-0.37%
0.0563	2.9375	0.0483	0.0435	0.00114	-2.05%	-0.99%	-0.56%	-0.38%
0.0588	3.1625	0.0496	0.0448	0.00122	-2.10%	-1.01%	-0.57%	-0.38%
0.0613	3.7875	0.0503	0.0453	0.00128	-2.13%	-1.03%	-0.58%	-0.39%
0.0638	3.5875	0.0523	0.0463	0.00138	-2.33%	-1.14%	-0.64%	-0.42%
0.0663	3.3625	0.0543	0.0480	0.00148	-2.46%	-1.19%	-0.66%	-0.43%
0.0688	2.1625	0.0583	0.0504	0.00160	-2.88%	-1.40%	-0.76%	-0.48%
0.0713	2.4375	0.0594	0.0513	0.00168	-2.94%	-1.42%	-0.77%	-0.49%
0.0738	2.6375	0.0606	0.0523	0.00177	-3.02%	-1.46%	-0.79%	-0.50%
0.0763	2.8375	0.0618	0.0529	0.00185	-3.11%	-1.52%	-0.82%	-0.51%
0.0788	3.0625	0.0628	0.0539	0.00191	-3.16%	-1.53%	-0.83%	-0.51%
0.0813	3.9125	0.0618	0.0536	0.00193	-2.99%	-1.45%	-0.79%	-0.49%
0.0838	3.6875	0.0637	0.0547	0.00202	-3.18%	-1.54%	-0.83%	-0.52%
0.0863	3.4625	0.0659	0.0560	0.00213	-3.39%	-1.65%	-0.89%	-0.54%
0.0888	2.0625	0.0717	0.0587	0.00234	-4.07%	-2.01%	-1.07%	-0.63%
0.0913	2.2875	0.0725	0.0594	0.00243	-4.10%	-2.03%	-1.08%	-0.64%
0.0938	2.5125	0.0732	0.0601	0.00249	-4.11%	-2.02%	-1.06%	-0.63%
0.0963	3.1875	0.0720	0.0598	0.00249	-3.92%	-1.92%	-1.01%	-0.60%
0.0988	2.7375	0.0751	0.0613	0.00264	-4.26%	-2.10%	-1.11%	-0.65%
0.1013	2.9625	0.0754	0.0616	0.00270	-4.25%	-2.10%	-1.11%	-0.65%
0.1038	3.8125	0.0728	0.0603	0.00263	-3.93%	-1.93%	-1.03%	-0.61%
0.1063	3.3875	0.0759	0.0618	0.00277	-4.28%	-2.12%	-1.12%	-0.66%
0.1088	3.6125	0.0759	0.0619	0.00280	-4.24%	-2.10%	-1.11%	-0.66%
0.1113	2.1125	0.0844	0.0655	0.00316	-5.27%	-2.66%	-1.40%	-0.80%
0.1138	2.3625	0.0845	0.0659	0.00321	-5.22%	-2.63%	-1.38%	-0.79%
0.1163	3.9875	0.0767	0.0623	0.00292	-4.28%	-2.14%	-1.14%	-0.67%
0.1188	2.5625	0.0858	0.0666	0.00332	-5.33%	-2.69%	-1.42%	-0.81%
0.1213	3.2125	0.0832	0.0656	0.00325	-4.97%	-2.50%	-1.32%	-0.76%
0.1238	2.7875	0.0868	0.0670	0.00344	-5.38%	-2.74%	-1.45%	-0.83%
0.1263	3.0125	0.0864	0.0670	0.00345	-5.30%	-2.69%	-1.42%	-0.82%
0.1288	3.4375	0.0845	0.0663	0.00337	-5.07%	-2.56%	-1.36%	-0.78%
0.1313	3.6375	0.0839	0.0659	0.00337	-5.00%	-2.53%	-1.34%	-0.78%
0.1338	2.1875	0.0949	0.0702	0.00387	-6.31%	-3.26%	-1.73%	-0.97%
0.1363	3.8375	0.0839	0.0657	0.00341	-4.98%	-2.53%	-1.34%	-0.77%
0.1388	2.4125	0.0955	0.0703	0.00395	-6.34%	-3.28%	-1.73%	-0.97%

0.1413	2.6125	0.0949	0.0703	0.00397	-6.23%	-3.22%	-1.70%	-0.96%
0.1438	2.0125	0.1005	0.0720	0.00420	-6.94%	-3.63%	-1.92%	-1.07%
0.1463	3.3375	0.0907	0.0687	0.00380	-5.71%	-2.94%	-1.56%	-0.89%
0.1488	3.1125	0.0934	0.0697	0.00395	-6.01%	-3.11%	-1.65%	-0.94%
0.1513	2.8875	0.0961	0.0708	0.00410	-6.32%	-3.28%	-1.74%	-0.98%
0.1538	3.5375	0.0909	0.0685	0.00386	-5.72%	-2.95%	-1.57%	-0.90%
0.1563	3.9625	0.0875	0.0666	0.00364	-5.40%	-2.79%	-1.49%	-0.85%
0.1588	2.2375	0.1044	0.0731	0.00448	-7.37%	-3.90%	-2.08%	-1.16%
0.1613	3.7375	0.0906	0.0679	0.00384	-5.72%	-2.97%	-1.59%	-0.91%
0.1638	2.6875	0.1017	0.0721	0.00441	-7.01%	-3.71%	-1.98%	-1.11%
0.1663	2.4625	0.1047	0.0731	0.00456	-7.37%	-3.91%	-2.09%	-1.17%
0.1688	3.2875	0.0968	0.0703	0.00419	-6.41%	-3.37%	-1.80%	-1.02%
0.1713	3.0375	0.1000	0.0714	0.00435	-6.80%	-3.59%	-1.92%	-1.08%
0.1738	2.0375	0.1116	0.0748	0.00488	-8.20%	-4.41%	-2.36%	-1.31%
0.1763	3.5125	0.0957	0.0693	0.00413	-6.31%	-3.33%	-1.78%	-1.01%
0.1788	3.8625	0.0920	0.0676	0.00391	-5.93%	-3.11%	-1.66%	-0.94%
0.1813	2.8125	0.1049	0.0725	0.00460	-7.39%	-3.95%	-2.11%	-1.18%
0.1838	2.2125	0.1126	0.0748	0.00495	-8.33%	-4.50%	-2.41%	-1.33%
0.1863	2.5875	0.1088	0.0738	0.00482	-7.83%	-4.20%	-2.25%	-1.25%
0.1888	3.2375	0.1011	0.0712	0.00442	-6.94%	-3.69%	-1.97%	-1.11%
0.1913	3.6625	0.0959	0.0691	0.00412	-6.39%	-3.37%	-1.81%	-1.02%
0.1938	2.9875	0.1052	0.0722	0.00463	-7.43%	-3.98%	-2.14%	-1.19%
0.1963	2.3875	0.1137	0.0748	0.00504	-8.44%	-4.58%	-2.46%	-1.37%
0.1988	3.9375	0.0929	0.0675	0.00393	-6.09%	-3.21%	-1.72%	-0.98%
0.2013	3.4125	0.1004	0.0704	0.00436	-6.91%	-3.69%	-1.98%	-1.11%
0.2038	2.1375	0.1189	0.0758	0.00528	-9.09%	-4.98%	-2.69%	-1.48%
0.2063	2.7625	0.1104	0.0740	0.00493	-8.02%	-4.34%	-2.33%	-1.30%
0.2088	3.1375	0.1053	0.0722	0.00467	-7.42%	-3.99%	-2.15%	-1.20%
0.2113	3.7625	0.0962	0.0688	0.00412	-6.44%	-3.41%	-1.83%	-1.04%
0.2138	2.5375	0.1150	0.0747	0.00514	-8.61%	-4.70%	-2.54%	-1.41%
0.2163	3.5625	0.0995	0.0700	0.00431	-6.81%	-3.63%	-1.95%	-1.10%
0.2188	2.3125	0.1194	0.0757	0.00534	-9.14%	-5.03%	-2.72%	-1.50%
0.2213	2.9125	0.1102	0.0736	0.00490	-8.01%	-4.33%	-2.33%	-1.29%
0.2238	3.3125	0.1039	0.0715	0.00456	-7.30%	-3.91%	-2.10%	-1.17%
0.2263	2.0875	0.1244	0.0768	0.00554	-9.76%	-5.40%	-2.92%	-1.60%
0.2288	3.8875	0.0949	0.0683	0.00404	-6.30%	-3.33%	-1.79%	-1.01%
0.2313	2.7125	0.1146	0.0742	0.00511	-8.59%	-4.70%	-2.53%	-1.40%
0.2338	3.0875	0.1084	0.0727	0.00479	-7.84%	-4.24%	-2.28%	-1.27%
0.2363	2.4875	0.1191	0.0754	0.00532	-9.13%	-5.02%	-2.71%	-1.50%
0.2388	3.4875	0.1017	0.0706	0.00442	-7.08%	-3.79%	-2.04%	-1.14%
0.2413	3.7125	0.0979	0.0694	0.00421	-6.64%	-3.53%	-1.90%	-1.07%
0.2438	2.2625	0.1242	0.0765	0.00550	-9.77%	-5.41%	-2.93%	-1.61%
0.2463	2.8625	0.1134	0.0741	0.00503	-8.45%	-4.61%	-2.48%	-1.38%
0.2488	3.2625	0.1061	0.0720	0.00466	-7.59%	-4.09%	-2.20%	-1.23%

Table S4: Circular segments. Values of the Nusselt number percentage deviation ($\mathcal{D}$), relative to a smooth surface at $Gr = 10^8$ and $Pr = 0.712$, are listed for different dimensions and densities of the roughness pattern, where the average Nusselt number over a rough surface is corrected (increased) by the ribbed-to-smooth area ratio such that ($\mathcal{D}$) directly indicates the total change in the heat transfer rate.

Dimensions		Macroscopic coefficients			$\mathcal{D}$			
e/ℓ	b/e	λ_z	λ_x	m_{12}	20 ribs	40 ribs	80 ribs	160 ribs
0.0513	2.6625	0.0423	0.0383	0.00092	-1.66%	-0.84%	-0.50%	-0.35%
0.0538	2.3375	0.0443	0.0395	0.00100	-1.86%	-0.94%	-0.55%	-0.38%
0.0563	2.9375	0.0449	0.0399	0.00105	-1.89%	-0.96%	-0.56%	-0.39%
0.0588	3.1625	0.0460	0.0406	0.00111	-1.97%	-1.00%	-0.59%	-0.40%
0.0613	3.7875	0.0461	0.0406	0.00114	-1.97%	-1.01%	-0.59%	-0.40%
0.0638	3.5875	0.0478	0.0416	0.00121	-2.11%	-1.08%	-0.63%	-0.42%
0.0663	3.3625	0.0496	0.0428	0.00129	-2.27%	-1.16%	-0.67%	-0.44%
0.0688	2.1625	0.0538	0.0457	0.00144	-2.62%	-1.33%	-0.75%	-0.48%
0.0713	2.4375	0.0545	0.0462	0.00150	-2.66%	-1.35%	-0.76%	-0.49%
0.0738	2.6375	0.0553	0.0467	0.00155	-2.73%	-1.39%	-0.78%	-0.50%
0.0763	2.8375	0.0560	0.0470	0.00160	-2.77%	-1.41%	-0.80%	-0.51%
0.0788	3.0625	0.0564	0.0472	0.00165	-2.80%	-1.44%	-0.81%	-0.51%
0.0813	3.9125	0.0544	0.0457	0.00161	-2.61%	-1.35%	-0.77%	-0.50%
0.0838	3.6875	0.0562	0.0465	0.00169	-2.80%	-1.46%	-0.83%	-0.52%
0.0863	3.4625	0.0579	0.0476	0.00178	-2.95%	-1.54%	-0.87%	-0.54%
0.0888	2.0625	0.0644	0.0519	0.00204	-3.55%	-1.82%	-1.00%	-0.61%
0.0913	2.2875	0.0647	0.0520	0.00208	-3.55%	-1.83%	-1.01%	-0.62%
0.0938	2.5125	0.0648	0.0519	0.00211	-3.55%	-1.83%	-1.01%	-0.61%
0.0963	3.1875	0.0626	0.0505	0.00205	-3.32%	-1.73%	-0.96%	-0.59%
0.0988	2.7375	0.0657	0.0519	0.00219	-3.65%	-1.90%	-1.05%	-0.64%
0.1013	2.9625	0.0653	0.0516	0.00221	-3.61%	-1.89%	-1.05%	-0.64%
0.1038	3.8125	0.0613	0.0489	0.00205	-3.24%	-1.72%	-0.97%	-0.60%
0.1063	3.3875	0.0644	0.0504	0.00219	-3.56%	-1.89%	-1.06%	-0.64%
0.1088	3.6125	0.0636	0.0497	0.00218	-3.48%	-1.86%	-1.04%	-0.64%
0.1113	2.1125	0.0733	0.0557	0.00261	-4.41%	-2.32%	-1.27%	-0.75%
0.1138	2.3625	0.0727	0.0553	0.00261	-4.33%	-2.29%	-1.26%	-0.75%
0.1163	3.9875	0.0623	0.0485	0.00216	-3.38%	-1.83%	-1.04%	-0.64%
0.1188	2.5625	0.0728	0.0547	0.00263	-4.38%	-2.33%	-1.29%	-0.76%
0.1213	3.2125	0.0688	0.0524	0.00248	-3.96%	-2.13%	-1.19%	-0.71%
0.1238	2.7875	0.0724	0.0541	0.00265	-4.36%	-2.34%	-1.30%	-0.77%
0.1263	3.0125	0.0712	0.0533	0.00261	-4.23%	-2.28%	-1.27%	-0.76%
0.1288	3.4375	0.0682	0.0511	0.00246	-3.98%	-2.16%	-1.22%	-0.73%
0.1313	3.6375	0.0667	0.0500	0.00241	-3.84%	-2.10%	-1.19%	-0.72%
0.1338	2.1875	0.0792	0.0572	0.00300	-5.06%	-2.73%	-1.51%	-0.88%
0.1363	3.8375	0.0652	0.0488	0.00233	-3.74%	-2.05%	-1.16%	-0.70%
0.1388	2.4125	0.0784	0.0562	0.00298	-5.00%	-2.71%	-1.50%	-0.87%

0.1413	2.6125	0.0771	0.0555	0.00294	-4.85%	-2.64%	-1.46%	-0.85%
0.1438	2.0125	0.0829	0.0585	0.00321	-5.46%	-2.96%	-1.63%	-0.94%
0.1463	3.3375	0.0705	0.0513	0.00262	-4.26%	-2.35%	-1.32%	-0.79%
0.1488	3.1125	0.0730	0.0523	0.00273	-4.54%	-2.51%	-1.41%	-0.83%
0.1513	2.8875	0.0755	0.0535	0.00286	-4.79%	-2.64%	-1.48%	-0.87%
0.1538	3.5375	0.0686	0.0495	0.00251	-4.16%	-2.31%	-1.31%	-0.78%
0.1563	3.9625	0.0637	0.0465	0.00224	-3.76%	-2.11%	-1.20%	-0.73%
0.1588	2.2375	0.0832	0.0570	0.00324	-5.60%	-3.09%	-1.71%	-0.99%
0.1613	3.7375	0.0661	0.0477	0.00237	-3.99%	-2.23%	-1.27%	-0.76%
0.1638	2.6875	0.0786	0.0541	0.00299	-5.21%	-2.89%	-1.61%	-0.94%
0.1663	2.4625	0.0814	0.0554	0.00314	-5.48%	-3.04%	-1.69%	-0.98%
0.1688	3.2875	0.0714	0.0501	0.00262	-4.52%	-2.53%	-1.43%	-0.85%
0.1713	3.0375	0.0745	0.0514	0.00278	-4.85%	-2.71%	-1.53%	-0.90%
0.1738	2.0375	0.0871	0.0578	0.00343	-6.08%	-3.38%	-1.87%	-1.07%
0.1763	3.5125	0.0681	0.0478	0.00243	-4.28%	-2.41%	-1.37%	-0.82%
0.1788	3.8625	0.0630	0.0450	0.00216	-3.82%	-2.15%	-1.23%	-0.74%
0.1813	2.8125	0.0773	0.0521	0.00290	-5.20%	-2.92%	-1.64%	-0.95%
0.1838	2.2125	0.0855	0.0562	0.00332	-6.00%	-3.35%	-1.86%	-1.07%
0.1863	2.5875	0.0804	0.0537	0.00307	-5.50%	-3.08%	-1.72%	-1.00%
0.1888	3.2375	0.0709	0.0488	0.00255	-4.61%	-2.59%	-1.46%	-0.86%
0.1913	3.6625	0.0643	0.0454	0.00220	-4.01%	-2.26%	-1.29%	-0.78%
0.1938	2.9875	0.0743	0.0498	0.00269	-5.01%	-2.83%	-1.59%	-0.93%
0.1963	2.3875	0.0833	0.0542	0.00316	-5.89%	-3.31%	-1.85%	-1.06%
0.1988	3.9375	0.0592	0.0425	0.00192	-3.58%	-2.03%	-1.17%	-0.71%
0.2013	3.4125	0.0669	0.0460	0.00229	-4.35%	-2.46%	-1.40%	-0.83%
0.2038	2.1375	0.0870	0.0554	0.00333	-6.32%	-3.56%	-1.99%	-1.14%
0.2063	2.7625	0.0769	0.0509	0.00282	-5.30%	-2.99%	-1.68%	-0.98%
0.2088	3.1375	0.0705	0.0478	0.00248	-4.68%	-2.65%	-1.50%	-0.88%
0.2113	3.7625	0.0599	0.0428	0.00194	-3.67%	-2.08%	-1.19%	-0.73%
0.2138	2.5375	0.0801	0.0517	0.00293	-5.72%	-3.23%	-1.81%	-1.05%
0.2163	3.5625	0.0624	0.0438	0.00205	-3.94%	-2.23%	-1.28%	-0.77%
0.2188	2.3125	0.0837	0.0531	0.00310	-6.09%	-3.45%	-1.93%	-1.11%
0.2213	2.9125	0.0729	0.0485	0.00256	-4.98%	-2.81%	-1.58%	-0.92%
0.2238	3.3125	0.0655	0.0452	0.00220	-4.25%	-2.40%	-1.36%	-0.81%
0.2263	2.0875	0.0871	0.0543	0.00324	-6.48%	-3.67%	-2.04%	-1.16%
0.2288	3.8875	0.0549	0.0402	0.00170	-3.21%	-1.82%	-1.06%	-0.65%
0.2313	2.7125	0.0754	0.0490	0.00264	-5.33%	-3.02%	-1.70%	-0.98%
0.2338	3.0875	0.0681	0.0461	0.00230	-4.55%	-2.57%	-1.46%	-0.86%
0.2363	2.4875	0.0790	0.0505	0.00280	-5.72%	-3.24%	-1.81%	-1.05%
0.2388	3.4875	0.0600	0.0425	0.00193	-3.73%	-2.11%	-1.21%	-0.74%
0.2413	3.7125	0.0558	0.0405	0.00173	-3.30%	-1.87%	-1.09%	-0.67%
0.2438	2.2625	0.0826	0.0517	0.00295	-6.13%	-3.47%	-1.94%	-1.11%
0.2463	2.8625	0.0706	0.0470	0.00239	-4.85%	-2.74%	-1.55%	-0.91%
0.2488	3.2625	0.0625	0.0435	0.00203	-4.00%	-2.27%	-1.30%	-0.78%

Table S5: Rectangular ribs. Values of the Nusselt number percentage deviation ($\mathcal{D}$), relative to a smooth surface at $Gr = 10^8$ and $Pr = 0.712$, are listed for different dimensions and densities of the roughness pattern, where the average Nusselt number over a rough surface is corrected (increased) by the ribbed-to-smooth area ratio such that ($\mathcal{D}$) directly indicates the total change in the heat transfer rate.

Dimensions		Macroscopic coefficients			$\mathcal{D}$			
e/ℓ	b/e	λ_z	λ_x	m_{12}	20 ribs	40 ribs	80 ribs	160 ribs
0.0513	2.6625	0.0380	0.0375	0.00079	-1.07%	-0.47%	-0.28%	-0.22%
0.0538	2.3375	0.0402	0.0389	0.00087	-1.28%	-0.58%	-0.34%	-0.25%
0.0563	2.9375	0.0393	0.0392	0.00087	-1.07%	-0.46%	-0.27%	-0.22%
0.0588	3.1625	0.0395	0.0397	0.00090	-1.02%	-0.43%	-0.25%	-0.21%
0.0613	3.7875	0.0378	0.0394	0.00086	-0.76%	-0.28%	-0.18%	-0.17%
0.0638	3.5875	0.0393	0.0403	0.00092	-0.89%	-0.35%	-0.21%	-0.19%
0.0663	3.3625	0.0409	0.0413	0.00098	-1.04%	-0.43%	-0.25%	-0.21%
0.0688	2.1625	0.0477	0.0445	0.00121	-1.83%	-0.84%	-0.46%	-0.31%
0.0713	2.4375	0.0472	0.0447	0.00122	-1.70%	-0.76%	-0.42%	-0.29%
0.0738	2.6375	0.0468	0.0449	0.00122	-1.60%	-0.71%	-0.39%	-0.28%
0.0763	2.8375	0.0462	0.0449	0.00122	-1.50%	-0.65%	-0.36%	-0.26%
0.0788	3.0625	0.0453	0.0446	0.00120	-1.37%	-0.58%	-0.32%	-0.24%
0.0813	3.9125	0.0399	0.0417	0.00102	-0.77%	-0.28%	-0.18%	-0.17%
0.0838	3.6875	0.0416	0.0426	0.00108	-0.95%	-0.37%	-0.22%	-0.19%
0.0863	3.4625	0.0433	0.0435	0.00115	-1.15%	-0.47%	-0.27%	-0.22%
0.0888	2.0625	0.0550	0.0492	0.00159	-2.46%	-1.16%	-0.62%	-0.39%
0.0913	2.2875	0.0536	0.0488	0.00155	-2.26%	-1.05%	-0.56%	-0.37%
0.0938	2.5125	0.0520	0.0480	0.00151	-2.06%	-0.94%	-0.50%	-0.33%
0.0963	3.1875	0.0460	0.0448	0.00127	-1.41%	-0.61%	-0.34%	-0.25%
0.0988	2.7375	0.0504	0.0469	0.00144	-1.91%	-0.87%	-0.47%	-0.32%
0.1013	2.9625	0.0482	0.0458	0.00137	-1.67%	-0.75%	-0.42%	-0.29%
0.1038	3.8125	0.0394	0.0405	0.00100	-0.82%	-0.33%	-0.20%	-0.18%
0.1063	3.3875	0.0435	0.0425	0.00116	-1.27%	-0.56%	-0.33%	-0.25%
0.1088	3.6125	0.0407	0.0409	0.00105	-1.00%	-0.43%	-0.26%	-0.21%
0.1113	2.1125	0.0586	0.0504	0.00180	-2.87%	-1.39%	-0.75%	-0.46%
0.1138	2.3625	0.0555	0.0489	0.00167	-2.53%	-1.22%	-0.66%	-0.41%
0.1163	3.9875	0.0349	0.0365	0.00081	-0.58%	-0.23%	-0.16%	-0.17%
0.1188	2.5625	0.0529	0.0469	0.00153	-2.32%	-1.12%	-0.61%	-0.39%
0.1213	3.2125	0.0437	0.0416	0.00114	-1.43%	-0.67%	-0.38%	-0.28%
0.1238	2.7875	0.0493	0.0445	0.00137	-2.03%	-0.98%	-0.55%	-0.36%
0.1263	3.0125	0.0457	0.0423	0.00121	-1.69%	-0.81%	-0.46%	-0.32%
0.1288	3.4375	0.0390	0.0382	0.00093	-1.09%	-0.50%	-0.31%	-0.24%
0.1313	3.6375	0.0355	0.0357	0.00078	-0.81%	-0.36%	-0.24%	-0.21%
0.1338	2.1875	0.0582	0.0484	0.00173	-3.04%	-1.52%	-0.83%	-0.50%
0.1363	3.8375	0.0310	0.0326	0.00060	-0.46%	-0.19%	-0.15%	-0.16%
0.1388	2.4125	0.0539	0.0456	0.00151	-2.65%	-1.32%	-0.73%	-0.45%

0.1413	2.6125	0.0499	0.0434	0.00134	-2.27%	-1.13%	-0.62%	-0.40%
0.1438	2.0125	0.0611	0.0489	0.00183	-3.44%	-1.75%	-0.95%	-0.57%
0.1463	3.3375	0.0358	0.0351	0.00074	-1.00%	-0.47%	-0.29%	-0.23%
0.1488	3.1125	0.0391	0.0367	0.00085	-1.35%	-0.65%	-0.39%	-0.28%
0.1513	2.8875	0.0427	0.0385	0.00099	-1.72%	-0.85%	-0.49%	-0.33%
0.1538	3.5375	0.0299	0.0311	0.00051	-0.53%	-0.24%	-0.18%	-0.18%
0.1563	3.9625	0.0218	0.0261	0.00027	+0.17%	+0.12%	0.00%	-0.09%
0.1588	2.2375	0.0547	0.0444	0.00147	-2.98%	-1.53%	-0.84%	-0.51%
0.1613	3.7375	0.0237	0.0272	0.00031	-0.02%	+0.02%	-0.05%	-0.11%
0.1638	2.6875	0.0436	0.0381	0.00097	-1.95%	-0.98%	-0.56%	-0.37%
0.1663	2.4625	0.0481	0.0404	0.00114	-2.42%	-1.23%	-0.69%	-0.44%
0.1688	3.2875	0.0295	0.0304	0.00045	-0.59%	-0.27%	-0.19%	-0.19%
0.1713	3.0375	0.0338	0.0326	0.00059	-1.05%	-0.51%	-0.32%	-0.25%
0.1738	2.0375	0.0571	0.0445	0.00149	-3.41%	-1.77%	-0.97%	-0.58%
0.1763	3.5125	0.0224	0.0264	0.00026	+0.07%	+0.07%	-0.02%	-0.10%
0.1788	3.8625	0.0152	0.0218	0.00012	+0.73%	+0.40%	+0.15%	-0.01%
0.1813	2.8125	0.0357	0.0333	0.00061	-1.30%	-0.64%	-0.38%	-0.28%
0.1838	2.2125	0.0504	0.0405	0.00115	-2.84%	-1.46%	-0.81%	-0.49%
0.1863	2.5875	0.0397	0.0355	0.00073	-1.72%	-0.85%	-0.49%	-0.33%
0.1888	3.2375	0.0235	0.0270	0.00026	-0.05%	+0.02%	-0.05%	-0.11%
0.1913	3.6625	0.0143	0.0212	0.00010	+0.78%	+0.42%	+0.15%	-0.01%
0.1938	2.9875	0.0275	0.0289	0.00034	-0.49%	-0.21%	-0.17%	-0.17%
0.1963	2.3875	0.0423	0.0362	0.00078	-2.08%	-1.05%	-0.60%	-0.39%
0.1988	3.9375	0.0077	0.0157	0.00004	+1.15%	+0.58%	+0.23%	+0.09%
0.2013	3.4125	0.0157	0.0220	0.00012	+0.65%	+0.36%	+0.12%	+0.06%
0.2038	2.1375	0.0476	0.0385	0.00094	-2.70%	-1.38%	-0.77%	-0.40%
0.2063	2.7625	0.0289	0.0297	0.00036	-0.66%	-0.29%	-0.20%	-0.10%
0.2088	3.1375	0.0190	0.0243	0.00016	+0.37%	+0.23%	+0.06%	+0.03%
0.2113	3.7625	0.0069	0.0147	0.00003	+1.15%	+0.58%	+0.26%	+0.08%
0.2138	2.5375	0.0327	0.0313	0.00044	-1.11%	-0.53%	-0.33%	-0.17%
0.2163	3.5625	0.0086	0.0164	0.00004	+1.11%	-0.57%	-0.26%	-0.09%
0.2188	2.3125	0.0379	0.0339	0.00057	-1.69%	-0.83%	-0.48%	-0.24%
0.2213	2.9125	0.0202	0.0250	0.00018	+0.24%	+0.17%	+0.03%	-0.06%
0.2238	3.3125	0.0109	0.0185	0.00006	+1.01%	+0.53%	+0.21%	+0.10%
0.2263	2.0875	0.0432	0.0361	0.00071	-2.32%	-1.17%	-0.65%	-0.29%
0.2288	3.8875	0.0021	0.0079	0.00001	+0.90%	+0.43%	+0.12%	-0.03%
0.2313	2.7125	0.0223	0.0260	0.00020	0.00%	+0.05%	-0.04%	-0.01%
0.2338	3.0875	0.0126	0.0198	0.00008	+0.90%	+0.49%	+0.18%	+0.09%
0.2363	2.4875	0.0271	0.0287	0.00028	-0.52%	-0.21%	-0.17%	-0.07%
0.2388	3.4875	0.0046	0.0121	0.00002	+1.15%	+0.56%	+0.20%	+0.01%
0.2413	3.7125	0.0019	0.0075	0.00000	+0.87%	+0.42%	+0.11%	-0.04%
0.2438	2.2625	0.0321	0.0311	0.00037	-1.09%	-0.50%	-0.31%	-0.15%
0.2463	2.8625	0.0141	0.0210	0.00009	+0.78%	+0.43%	+0.15%	+0.08%
0.2488	3.2625	0.0058	0.0135	0.00002	+1.15%	+0.50%	+0.21%	+0.01%

Table S6: The Nusselt number percentage deviation ($\mathcal{D}$) for surfaces ribbed with 20 protrusions of different geometries, at $Gr = 10^7$ and $Gr = 5 \times 10^7$.

Dimensions		$\mathcal{D}$ = % Deviation in $\overline{Nu}$ (from smooth surface value)					
e/l	b/e	Inward-curved		Triangular		Circular	
		Gr=10^7	Gr=5x10^7	Gr=10^7	Gr=5x10^7	Gr=10^7	Gr=5x10^7
0.0513	2.6625	-1.15%	-1.65%	-1.02%	-1.43%	-0.99%	-1.35%
0.0538	2.3375	-1.27%	-1.83%	-1.12%	-1.60%	-1.08%	-1.50%
0.0563	2.9375	-1.30%	-1.88%	-1.15%	-1.65%	-1.10%	-1.54%
0.0588	3.1625	-1.34%	-1.96%	-1.17%	-1.69%	-1.15%	-1.60%
0.0613	3.7875	-1.38%	-2.03%	-1.19%	-1.72%	-1.15%	-1.61%
0.0638	3.5875	-1.46%	-2.16%	-1.30%	-1.89%	-1.23%	-1.73%
0.0663	3.3625	-1.55%	-2.33%	-1.35%	-1.99%	-1.30%	-1.86%
0.0688	2.1625	-1.78%	-2.69%	-1.56%	-2.33%	-1.47%	-2.14%
0.0713	2.4375	-1.82%	-2.77%	-1.58%	-2.39%	-1.49%	-2.18%
0.0738	2.6375	-1.89%	-2.88%	-1.62%	-2.46%	-1.53%	-2.24%
0.0763	2.8375	-1.94%	-2.97%	-1.67%	-2.54%	-1.56%	-2.28%
0.0788	3.0625	-1.97%	-3.04%	-1.69%	-2.58%	-1.58%	-2.31%
0.0813	3.9125	-1.92%	-2.96%	-1.60%	-2.44%	-1.50%	-2.17%
0.0838	3.6875	-2.04%	-3.14%	-1.70%	-2.59%	-1.60%	-2.31%
0.0863	3.4625	-2.14%	-3.32%	-1.81%	-2.77%	-1.67%	-2.44%
0.0888	2.0625	-2.51%	-3.88%	-2.16%	-3.33%	-1.95%	-2.92%
0.0913	2.2875	-2.55%	-3.96%	-2.18%	-3.37%	-1.97%	-2.95%
0.0938	2.5125	-2.58%	-4.02%	-2.17%	-3.38%	-1.98%	-2.95%
0.0963	3.1875	-2.52%	-3.93%	-2.07%	-3.22%	-1.87%	-2.77%
0.0988	2.7375	-2.72%	-4.22%	-2.25%	-3.50%	-2.04%	-3.03%
0.1013	2.9625	-2.74%	-4.27%	-2.25%	-3.50%	-2.03%	-3.01%
0.1038	3.8125	-2.59%	-4.05%	-2.09%	-3.24%	-1.86%	-2.72%
0.1063	3.3875	-2.80%	-4.37%	-2.27%	-3.52%	-2.02%	-2.97%
0.1088	3.6125	-2.81%	-4.38%	-2.25%	-3.50%	-1.99%	-2.92%
0.1113	2.1125	-3.36%	-5.20%	-2.80%	-4.35%	-2.44%	-3.66%
0.1138	2.3625	-3.36%	-5.23%	-2.77%	-4.33%	-2.42%	-3.63%
0.1163	3.9875	-2.90%	-4.55%	-2.28%	-3.56%	-1.97%	-2.88%
0.1188	2.5625	-3.48%	-5.40%	-2.84%	-4.40%	-2.45%	-3.65%
0.1213	3.2125	-3.33%	-5.20%	-2.65%	-4.13%	-2.26%	-3.34%
0.1238	2.7875	-3.58%	-5.55%	-2.88%	-4.47%	-2.46%	-3.66%
0.1263	3.0125	-3.57%	-5.55%	-2.83%	-4.41%	-2.41%	-3.56%
0.1288	3.4375	-3.48%	-5.43%	-2.71%	-4.22%	-2.29%	-3.37%
0.1313	3.6375	-3.47%	-5.41%	-2.67%	-4.16%	-2.23%	-3.25%
0.1338	2.1875	-4.18%	-6.44%	-3.40%	-5.26%	-2.84%	-4.23%
0.1363	3.8375	-3.51%	-5.49%	-2.66%	-4.14%	-2.18%	-3.16%
0.1388	2.4125	-4.25%	-6.56%	-3.41%	-5.28%	-2.82%	-4.18%
0.1413	2.6125	-4.25%	-6.56%	-3.36%	-5.21%	-2.76%	-4.10%
0.1438	2.0125	-4.64%	-7.12%	-3.76%	-5.81%	-3.08%	-4.60%

0.1463	3.3375	-4.04%	-6.25%	-3.08%	-4.80%	-2.48%	-3.65%
0.1488	3.1125	-4.22%	-6.51%	-3.25%	-5.03%	-2.62%	-3.84%
0.1513	2.8875	-4.44%	-6.84%	-3.42%	-5.29%	-2.76%	-4.05%
0.1538	3.5375	-4.16%	-6.43%	-3.09%	-4.80%	-2.44%	-3.55%
0.1563	3.9625	-3.99%	-6.18%	-2.92%	-4.52%	-2.24%	-3.21%
0.1588	2.2375	-5.06%	-7.73%	-4.03%	-6.17%	-3.18%	-4.69%
0.1613	3.7375	-4.23%	-6.56%	-3.11%	-4.82%	-2.37%	-3.44%
0.1638	2.6875	-4.96%	-7.58%	-3.83%	-5.88%	-2.99%	-4.39%
0.1663	2.4625	-5.19%	-7.92%	-4.04%	-6.21%	-3.15%	-4.65%
0.1688	3.2875	-4.72%	-7.26%	-3.50%	-5.40%	-2.66%	-3.88%
0.1713	3.0375	-4.94%	-7.57%	-3.72%	-5.72%	-2.83%	-4.12%
0.1738	2.0375	-5.72%	-8.67%	-4.53%	-6.92%	-3.47%	-5.14%
0.1763	3.5125	-4.76%	-7.32%	-3.46%	-5.34%	-2.55%	-3.69%
0.1788	3.8625	-4.58%	-7.04%	-3.24%	-4.98%	-2.28%	-3.25%
0.1813	2.8125	-5.40%	-8.21%	-4.07%	-6.22%	-3.01%	-4.39%
0.1838	2.2125	-5.92%	-8.97%	-4.61%	-7.05%	-3.45%	-5.09%
0.1863	2.5875	-5.71%	-8.66%	-4.32%	-6.63%	-3.20%	-4.69%
0.1888	3.2375	-5.27%	-8.04%	-3.81%	-5.86%	-2.72%	-3.95%
0.1913	3.6625	-5.00%	-7.66%	-3.50%	-5.39%	-2.39%	-3.43%
0.1938	2.9875	-5.61%	-8.52%	-4.10%	-6.26%	-2.93%	-4.24%
0.1963	2.3875	-6.19%	-9.34%	-4.70%	-7.15%	-3.41%	-5.00%
0.1988	3.9375	-4.94%	-7.58%	-3.34%	-5.16%	-2.18%	-3.12%
0.2013	3.4125	-5.44%	-8.27%	-3.81%	-5.82%	-2.57%	-3.68%
0.2038	2.1375	-6.66%	-9.99%	-5.09%	-7.70%	-3.64%	-5.34%
0.2063	2.7625	-6.14%	-9.28%	-4.45%	-6.81%	-3.11%	-4.54%
0.2088	3.1375	-5.86%	-8.87%	-4.11%	-6.29%	-2.77%	-4.01%
0.2113	3.7625	-5.34%	-8.13%	-3.54%	-5.44%	-2.21%	-3.15%
0.2138	2.5375	-6.57%	-9.85%	-4.81%	-7.29%	-3.32%	-4.82%
0.2163	3.5625	-5.61%	-8.53%	-3.75%	-5.77%	-2.37%	-3.40%
0.2188	2.3125	-6.93%	-10.37%	-5.13%	-7.75%	-3.53%	-5.14%
0.2213	2.9125	-6.36%	-9.58%	-4.44%	-6.79%	-2.93%	-4.24%
0.2238	3.3125	-6.01%	-9.08%	-4.03%	-6.18%	-2.53%	-3.63%
0.2263	2.0875	-7.36%	-10.98%	-5.50%	-8.29%	-3.75%	-5.48%
0.2288	3.8875	-5.52%	-8.39%	-3.46%	-5.36%	-1.97%	-2.82%
0.2313	2.7125	-6.81%	-10.20%	-4.80%	-7.27%	-3.10%	-4.49%
0.2338	3.0875	-6.46%	-9.70%	-4.35%	-6.65%	-2.70%	-3.89%
0.2363	2.4875	-7.20%	-10.73%	-5.13%	-7.76%	-3.33%	-4.85%
0.2388	3.4875	-6.13%	-9.21%	-3.91%	-6.01%	-2.25%	-3.22%
0.2413	3.7125	-5.90%	-8.92%	-3.66%	-5.61%	-2.00%	-2.82%
0.2438	2.2625	-7.65%	-11.36%	-5.51%	-8.30%	-3.55%	-5.16%
0.2463	2.8625	-6.97%	-10.44%	-4.72%	-7.19%	-2.86%	-4.15%
0.2488	3.2625	-6.53%	-9.81%	-4.21%	-6.44%	-2.39%	-3.42%

PAPER B3

Conjugate natural convection along regularly ribbed vertical surfaces: A homogenization-based study [1,2]

Essam Nabil Ahmed[a], **Alessandro Bottaro**[a] and **Giovanni Tanda**[b]

[a] *DICCA, Università di Genova, via Montallegro 1, Genova, 16145, Italy*
[b] *DIME, Università di Genova, via Montallegro 1, Genova, 16145, Italy*

Natural convection heat transfer from periodically ribbed vertical surfaces is targeted for upscaling, incorporating the analysis of thermal conduction through the micro-scale ribs. Asymptotic homogenization theory is employed, considering the steady conjugate heat transfer problem, to formulate second-order accurate *effective* conditions for velocity and temperature at a fictitious plane surface, beyond which the macroscale behavior of the flow is computed. This allows to avoid the numerically expensive resolution of fields within and through the micro-structured corrugations. For the streamwise velocity component, the no-slip boundary condition is corrected at first order (in terms of a small parameter ϵ, ratio of microscopic to macroscopic length scales) by the classical Navier-slip condition plus a buoyancy term, while the gradient of the normal stress appears at second order together with a temperature-gradient term. The temperature at the virtual boundary deviates from the uniform value at the baseplate; the thermal slip is described via a first-order temperature-gradient term with a coefficient depending on rib geometry and thermal conductivity. Different case studies are conducted on the case of transverse square ribs, varying the density of the pattern and the rib-to-fluid thermal conductivity ratio, to provide extensive validation of the model against full feature-resolving simulations. Beyond the validation phase, a better understanding of the effects of different parameters on the heat transfer performance is pursued. The presence of ribs is found to decrease the overall heat transfer rate from the surface, and this deterioration is only partially alleviated by raising the thermal conductivity of the ribs. Increasing the number of conducting ribs on the hot surface has a complex, non-monotonic effect on the heat transfer rate, unlike the case of adiabatic ribs where the average Nusselt number decays monotonically. The performance of low-thermal-conductivity elements (e.g. wooden ribs) may considerably differ from that of perfectly-adiabatic ones.

[1] Supplementary Material related to this manuscript is provided after the References.

[2] The Version of Record of this manuscript, together with the Supplementary Material, has been published and is available in: *Numerical Heat Transfer, Part A: Applications* **85** (9) (2024) 1331–1355. https://doi.org/10.1080/10407782.2023.2202347

1 INTRODUCTION AND LITERATURE REVIEW

Natural convection is a simple, reliable, cost-effective heat transfer regime, with almost maintenance-free operation and easily employable in hostile environments under dust, moist air, etc. With the flow driven merely by the buoyancy force, the main problem facing the designers is the low heat transfer coefficient of these systems, relative to those adopting active heat transfer mechanisms. Optimization of the heat transfer performance of natural convection systems is essential, to cope with the trend of manufacturing compact devices with high input power, resulting in higher heat generation rates per unit volume (Joshi *et al.*, 1989; Peterson & Ortega, 1990) which should be effectively dissipated; the life and reliability of electronic systems may be severely affected by the increase in the operating temperature of a single component over the permissible limit (Nelson *et al.*, 1978).

The literature on natural convection is rich of experimental and numerical studies investigating the effectiveness of adding surface alterations to vertical plates, as a potential method to promote the convective heat transfer performance. At first glance, the findings which have been reported so far appear contradictory in terms of the overall effect on the heat transfer rate (Bhavnani & Bergles, 1990). However, in-depth analysis of the complex flow patterns over ribbed surfaces and their contrasting effects can provide insight into the plausible reasons for the differences between the reported trends, as outlined by Tanda (1997). Thus, the study and optimization of heat transfer from corrugated/ribbed/finned surfaces have remained fertile fields for research; the major findings of some relevant studies are summarized in the following. Bhavnani & Bergles (1990) carried out experiments on natural convection along an isothermal vertical surface with repeated transverse square ribs. They reported that attaching highly conducting ribs to the surface may decrease the overall heat transfer rate by more than 25%, whereas a lower deterioration, or even an enhancement, was detected with low-conductivity ribs since they interrupt the thickening of the thermal boundary layer, promoting the heat transfer process within the inter-rib regions of the baseplate. The experiments by Tanda (2008) on natural convection through a vertical channel with wooden square ribs attached to the hot surface revealed similar local enhancements of the heat transfer coefficient compared with the earlier measurements by Tanda (1997) using aluminum ribs, provided that the channel aspect ratio was sufficiently large. Cavazzuti & Corticelli (2008) numerically investigated conjugate natural convection through a channel with one adiabatic surface and an opposite isothermal surface roughened with trapezoidal ribs; the ribbed channel cases examined were not found to outperform the smooth one, and recommendations were given to alleviate the deterioration. The numerical study by Yao (2006) on natural convection along isothermal, wavy plates showed that, despite the decrease experienced in the surface-averaged heat transfer coefficient, the overall heat transfer rate was enhanced (compared with a flat surface) thanks to the increase in the surface area. Hærvig & Sørensen (2020) simulated the effect of adding zigzag alterations to a vertical surface exposed to free convection, and found that these surface perturbations can enhance the heat transfer rate by about 12% under optimal conditions. Nishikawa *et al.* (2020) stud-

ied conjugate natural convection along a vertical surface with minuscule square ribs of low thermal conductivity, as a simplified representation of the yarns of a textile material. Intriguingly, a minor cooling effect was detected when the minuscule ribs were arranged at an adequate pitch, sufficient to allow the cool stream to be guided onto the base surface in the inter-rib regions. Zhou *et al.* (2022) investigated the effectiveness of attaching an array of vortex generators to the rear surface of a photovoltaic module exposed to free convection, as an economical cooling method. According to their experiments and simulations, the resulting change in the operating temperature is sensitive not only to the material thermal conductivity but also to the aerodynamic shape and spacing of the protrusions, which affect the formation of vortices and, therefore, the favorable mixing in the boundary layer. The reader is also encouraged to refer to studies on natural convection heat transfer from vertical surfaces with rippled vertical fins (El Ghandouri *et al.*, 2020), W-type fin arrays (Zhang *et al.*, 2020), and in-line/staggered arrangements of interrupted fins (Guglielmini *et al.*, 1987; Ahmadi *et al.*, 2014).

The present study is a part of an ongoing project in which different geometric and thermal conditions affecting natural convection heat transfer from ribbed vertical surfaces are extensively investigated via theoretical and numerical analyses (Ahmed *et al.*, 2022; Ahmed, 2023) and experimental surveys. In our endeavor, we employ asymptotic homogenization to analyze buoyancy-induced flows over periodically roughened vertical surfaces with conjugate heat transfer; i.e., the conductive heat transfer through the ribs and the convective heat transfer from the ribs to the flowing fluid are both considered in the homogenization procedure. The expensive numerical resolution of the velocity and thermal fields within surface corrugations, and the resolution of the temperature distribution through the ribs, are replaced by the use of effective boundary conditions, to be enforced at a virtual smooth wall. The model is formulated proceeding along the lines of Ahmed *et al.* (2022); however, a general value of the thermal conductivity coefficient is set here for the material of the ribs, which allows for employing the model to study natural convection over surfaces roughened with ribs of finite conductivity, as well as perfectly-conductive or adiabatic ribs as the two limiting situations. For instance, this is beneficial for the numerical study of natural convection along vertical surfaces with wooden/low-thermal-conductivity roughness elements (like those considered by Bhavnani & Bergles (1990), Tanda (2008) and Nishikawa *et al.* (2020)), to highlight the differences from the theoretical performance of perfectly-adiabatic ribs. In the next section, the physical problem is described, the governing equations are given, and formal expressions of the effective boundary conditions are derived. In Section 3, the model coefficients are estimated for the case of two-dimensional ribs of square cross-section, varying the rib size to pitch distance ratio and the thermal conductivity. The macroscale problem is then considered in Section 4, and the homogenization-based model is validated against standard, feature-resolving simulations under different geometric and thermal conditions; furthermore, the trends of the heat transfer performance are discussed and physical interpretations are provided. Summarizing remarks are presented in Section 5.

2 PROBLEM STATEMENT AND UPSCALING PROCEDURE

2.1 The dimensional governing equations

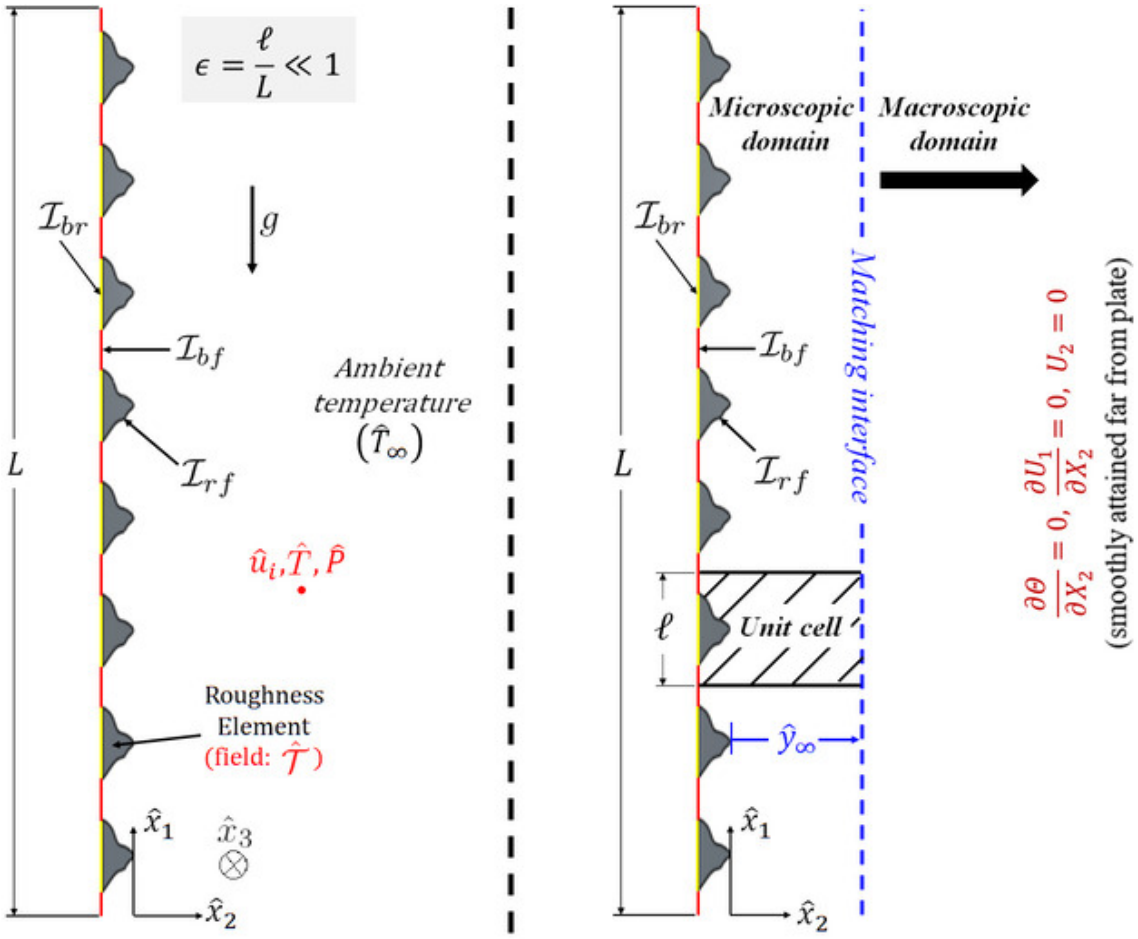

Figure 1: Sketches showing: (left) a general description of the conjugate heat transfer problem under study, with indication of the base-fluid interface ($\mathcal{I}_{bf}$), the base-rib interface ($\mathcal{I}_{br}$) and the rib-fluid interface ($\mathcal{I}_{rf}$); (right) the decomposed flow domain, with indication of a generic matching interface between the microscopic and the macroscopic regions.

The physical problem is described in Fig. 1(left). The buoyancy-induced flow over a vertical surface of height L, periodically ribbed with roughness elements of given geometry, distribution density and thermal conductivity, is considered. The baseplate is assumed to be perfectly conducting and thus to remain isothermal at a temperature $\hat{T}_b$, higher than the ambient temperature ($\hat{T}_\infty$). After heat is supplied to the baseplate (e.g., by an electrical heater) for sufficient time, it is eventually balanced by the heat dissipated to air via natural convection, hence a time-independent value of $\hat{T}_b$ is reached and we can adopt a steady physical model to study the problem, provided that the flow regime remains

laminar. At any point in the fluid phase, the velocity vector ($\hat{u}_i$), the temperature ($\hat{T}$) and the pressure ($\hat{P}$) are the dependent variables of interest, to be evaluated over space $\hat{x}_i$. Assuming moderate variations in fluid density due to thermal gradient, one can apply the Boussinesq approximation with a linear temperature-density relationship so that the momentum conservation equation is linearly coupled with the energy equation. The dimensional conservation equations in the fluid phase are written as follows:

$$\frac{\partial \hat{u}_i}{\partial \hat{x}_i} = 0, \tag{1-a}$$

$$\rho\, \hat{u}_j \frac{\partial \hat{u}_i}{\partial \hat{x}_j} = -\frac{\partial (\hat{P} - \hat{P}_\infty)}{\partial \hat{x}_i} + \mu\, \frac{\partial^2 \hat{u}_i}{\partial \hat{x}_j^2} + \rho\beta(\hat{T} - \hat{T}_\infty) g\, \delta_{i1}, \tag{1-b}$$

$$\hat{u}_j \frac{\partial \hat{T}}{\partial \hat{x}_j} = \alpha \frac{\partial^2 \hat{T}}{\partial \hat{x}_j^2}, \tag{1-c}$$

with $\hat{P}_\infty$, g and δ_{ij} the pressure sufficiently far away from the wall, the magnitude of the gravitational acceleration and the Kronecker delta. The fluid properties, i.e. the density ρ, the dynamic viscosity μ, the thermal diffusivity α and the thermal expansion coefficient β are assumed constant in $\hat{x}_i$. Additionally, it is useful to define the Prandtl number ($Pr = \dfrac{\mu}{\rho\,\alpha} = \dfrac{\nu}{\alpha}$) and the Grashof number ($Gr = \dfrac{g\beta(\hat{T}_b - \hat{T}_\infty)L^3}{\nu^2}$), which control the problem.

Moving to the solid phase, thermal conduction in the roughness elements is also assumed to be steady, so that only the spatial variations of the temperature ($\hat{\mathcal{T}}$) are considered. The thermal conduction is thus governed by Laplace's equation:

$$\frac{\partial^2 \hat{\mathcal{T}}}{\partial \hat{x}_j^2} = 0. \tag{1-d}$$

At the base/fluid interface, the fluid temperature and velocity read

$$\hat{T} = \hat{T}_b, \quad \hat{u}_i = 0 \quad at\ \mathcal{I}_{bf}. \tag{1-e}$$

Neglecting the thermal resistance between the base and the rib, we may assume that

$$\hat{\mathcal{T}} = \hat{T}_b \quad at\ \mathcal{I}_{br}. \tag{1-f}$$

At the rib/fluid interface, the no-slip condition $\hat{u}_i = 0$ is imposed. Since it is essential to describe the thermal interaction in terms of the continuity of temperature and heat flux, we impose

$$\hat{T} = \hat{\mathcal{T}}, \qquad \frac{\partial \hat{T}}{\partial \hat{n}} = \kappa\, \frac{\partial \hat{\mathcal{T}}}{\partial \hat{n}} \quad at\ \mathcal{I}_{rf}, \tag{1-g}$$

with κ the rib-to-fluid thermal conductivity ratio ($\kappa = \dfrac{k_r}{k_f}$; the fluid thermal conductivity k_f is assumed spatially constant) and $\hat{n}$ the dimensional distance along the direction normal to the rib/fluid interface at any point.

2.2 Domain decomposition

Given that the periodicity of the roughness pattern (ℓ) and the plate height (L) are well-separated length scales, i.e. $\ell << L$, we seek upscaling of the problem starting by decomposing the flow domain into two sub-regions (microscopic/macroscopic); cf. Fig. 1(right). The two newly defined problems are coupled at a matching interface whose distance from the vertical surface is to be properly specified.

2.2.1 *The macroscopic problem*

Characteristic scales are now sought for the macroscopic problem. Since the flow is driven by buoyancy, we anticipate that the inertial force (per unit volume) is of the same order of magnitude as the Boussinesq term. The characteristic velocity, $\mathcal{U}$, is therefore defined as $\mathcal{U} = \sqrt{\beta(\hat{T}_b - \hat{T}_\infty)gL} = \frac{\nu}{L}\sqrt{Gr}$, and the normalized velocity vector is $U_i = \frac{\hat{u}_i}{\mathcal{U}}$. The other dimensionless variables are defined as follows:

$$X_i = \frac{\hat{x}_i}{L}, \qquad P = \frac{\hat{P} - \hat{P}_\infty}{\rho \mathcal{U}^2}, \qquad \Theta = \frac{\hat{T} - \hat{T}_\infty}{\hat{T}_b - \hat{T}_\infty}$$

Accordingly, the dimensionless equations governing the macroscopic problem read

$$\frac{\partial U_i}{\partial X_i} = 0, \tag{2-a}$$

$$U_j \frac{\partial U_i}{\partial X_j} = -\frac{\partial P}{\partial X_i} + \frac{1}{\sqrt{Gr}} \frac{\partial^2 U_i}{\partial X_j^2} + \Theta \delta_{i1}, \tag{2-b}$$

$$Pr\sqrt{Gr}\left(U_j \frac{\partial \Theta}{\partial X_j}\right) = \frac{\partial^2 \Theta}{\partial X_j^2}, \tag{2-c}$$

subject to matching conditions (defined later) at $X_2 \to 0$, while the conditions $\frac{\partial \Theta}{\partial X_2} = \frac{\partial U_1}{\partial X_2} = 0$ and $U_2 = 0$ are expected to be smoothly satisfied far away from the wall, i.e. for $X_2 \to \infty$.

2.2.2 *The microscopic problem*

The scale $\epsilon \mathcal{U}$ is chosen for the velocity in the microscopic region, with the small parameter ϵ defined as $\epsilon = \ell/L << 1$. This choice stems from matching the shear stress at the interface between microscopic and macroscopic domains (Ahmed *et al.*, 2022). The following normalization is used

$$u_i = \frac{\hat{u}_i}{\epsilon \mathcal{U}}, \qquad x_i = \frac{\hat{x}_i}{l}, \qquad p = \frac{(\hat{P} - \hat{P}_\infty)\, L}{\mu \mathcal{U}}, \qquad \theta = \frac{\hat{T} - \hat{T}_\infty}{\hat{T}_b - \hat{T}_\infty} \qquad \phi = \frac{\hat{\mathcal{T}} - \hat{T}_\infty}{\hat{T}_b - \hat{T}_\infty},$$

for the microscopic equations in the fluid phase to read

$$\frac{\partial u_i}{\partial x_i} = 0, \tag{3-a}$$

$$\epsilon \mathcal{R}_G \left(u_j \frac{\partial u_i}{\partial x_j} \right) = -\frac{\partial p}{\partial x_i} + \frac{\partial^2 u_i}{\partial x_j^2} + \mathcal{R}_G \, \theta \, \delta_{i1}, \tag{3-b}$$

$$\epsilon \mathcal{R}_G \, Pr \left(u_j \frac{\partial \theta}{\partial x_j} \right) = \frac{\partial^2 \theta}{\partial x_j^2}, \tag{3-c}$$

with $\mathcal{R}_G = \epsilon \sqrt{Gr}$ the *reduced* Grashof number, assumed to be of order one as the model is intended applicable at relatively large values of Gr. Steady thermal conduction within the ribs is governed by the following dimensionless equation:

$$\frac{\partial^2 \phi}{\partial x_j^2} = 0. \tag{3-d}$$

The following boundary conditions are imposed at the interfaces ($\mathcal{I}_{bf}, \mathcal{I}_{br}, \mathcal{I}_{rf}$):

$$\theta = 1, \quad u_i = 0 \quad at \;\; \mathcal{I}_{bf}, \qquad \phi = 1 \quad at \;\; \mathcal{I}_{br}, \tag{3-e,f}$$

$$\theta = \phi, \qquad \frac{\partial \theta}{\partial n} = \kappa \, \frac{\partial \phi}{\partial n}, \qquad u_i = 0 \quad at \;\; \mathcal{I}_{rf}, \tag{3-g}$$

with $n = \dfrac{\hat{n}}{\ell}$.

Matching the traction vector and the heat flux between the microscopic and the macroscopic sub-regions, considering the scales adopted for each, the conditions for $x_2 \to \infty$ can be recast as follows:

$$-p \, \delta_{i2} + \left(\frac{\partial u_i}{\partial x_2} + \frac{\partial u_2}{\partial x_i} \right) = S_{i2}, \qquad \frac{\partial \theta}{\partial x_2} = \epsilon \, \eta, \tag{3-h}$$

with S_{12}, S_{22} and S_{32} the macroscopic dimensionless stresses in the streamwise, normal and spanwise directions, and η the macroscopic dimensionless normal temperature gradient, i.e.

$$S_{i2} = -Gr^{1/2} \, P \, \delta_{i2} + \left(\frac{\partial U_i}{\partial X_2} + \frac{\partial U_2}{\partial X_i} \right), \qquad \eta = \frac{\partial \Theta}{\partial X_2}.$$

Since the *effective boundary conditions* are sought in terms of the macroscopic velocity vector and temperature at the matching interface, coupling with the microscopic problem is required, i.e.

$$\lim_{X_2 \to 0} U_i = \lim_{x_2 \to \infty} \epsilon \, u_i, \qquad \lim_{X_2 \to 0} \Theta = \lim_{x_2 \to \infty} \theta. \tag{4}$$

2.3 Asymptotic treatment of the microscopic problem

The microscopic dependent variables are asymptotically expanded in terms of ϵ, for the microscopic problem to be later reconstructed at the different orders; we impose

$$u_i = u_i^{(0)} + \epsilon\, u_i^{(1)} + \epsilon^2\, u_i^{(2)} + ...,$$

and similarly for p, θ and ϕ. Generally, the variables in the expansions are dependent on both x_i and X_i. These expressions are then substituted into eqs. (3-a to 3-h), together with replacing the derivative $\dfrac{\partial}{\partial x_i}$ by $\dfrac{\partial}{\partial x_i} + \epsilon \dfrac{\partial}{\partial X_i}$ as by the chain rule.

2.3.1 $\mathcal{O}(\epsilon^0)$ *problem*

The leading-order problem in the fluid phase reads

$$\frac{\partial u_i^{(0)}}{\partial x_i} = 0, \qquad -\frac{\partial p^{(0)}}{\partial x_i} + \frac{\partial^2 u_i^{(0)}}{\partial x_j^2} + \mathcal{R}_G\, \theta^{(0)}\, \delta_{i1} = 0, \qquad \frac{\partial^2 \theta^{(0)}}{\partial x_j^2} = 0, \tag{5-a,b,c}$$

while in the roughness elements, we have

$$\frac{\partial^2 \phi^{(0)}}{\partial x_j^2} = 0, \tag{5-d}$$

with the boundary conditions

$$\theta^{(0)} = 1, \quad u_i^{(0)} = 0 \quad at\ \mathcal{I}_{bf}, \qquad \phi^{(0)} = 1 \quad at\ \mathcal{I}_{br}, \tag{5-e,f}$$

$$\theta^{(0)} = \phi^{(0)}, \qquad \frac{\partial \theta^{(0)}}{\partial n} = \kappa\, \frac{\partial \phi^{(0)}}{\partial n}, \qquad u_i^{(0)} = 0 \quad at\ \mathcal{I}_{rf}, \tag{5-g}$$

$$-p^{(0)}\, \delta_{i2} + \left(\frac{\partial u_i^{(0)}}{\partial x_2} + \frac{\partial u_2^{(0)}}{\partial x_i} \right) = S_{i2} \quad \text{for} \quad x_2 \to \infty, \tag{5-h}$$

$$\frac{\partial \theta^{(0)}}{\partial x_2} = 0 \quad \text{for} \quad x_2 \to \infty. \tag{5-i}$$

Trivial solution exists for the thermal problem, i.e.

$$\theta^{(0)} = 1 \quad \text{(over the fluid phase)}, \qquad \phi^{(0)} = 1 \quad \text{(over the solid phase)}.$$

Taking advantage of the linearity of the dynamic problem, a generic solution can be sought via separation of variables, that is

$$u_i^{(0)} = \breve{u}_{ik} S_{k2} + u_i^{\dagger} \mathcal{R}_G, \qquad p^{(0)} = \breve{p}_k S_{k2} + p^{\dagger} \mathcal{R}_G,$$

where $\breve{u}_{ik}$, $u_i^{\dagger}$, $\breve{p}_k$ and $p^{\dagger}$ are purely microscopic variables, described over x_i only. The auxiliary problem governing $\breve{u}_{ik}$ and $\breve{p}_k$ reads

$$\frac{\partial \breve{u}_{ik}}{\partial x_i} = 0, \qquad -\frac{\partial \breve{p}_k}{\partial x_i} + \frac{\partial^2 \breve{u}_{ik}}{\partial x_j^2} = 0, \tag{6-a,b}$$

with

$$\breve{u}_{ik} = 0 \quad \text{at} \quad \mathcal{I}_{bf} \quad \text{and} \quad \mathcal{I}_{rf}, \qquad -\breve{p}_k\,\delta_{i2} + \left(\frac{\partial \breve{u}_{ik}}{\partial x_2} + \frac{\partial \breve{u}_{2k}}{\partial x_i}\right) = \delta_{ik} \quad \text{at} \quad x_2 \to \infty. \quad \text{(6-c,d)}$$

The buoyant effect in the microscopic layer is described via the † variables satisfying

$$\frac{\partial u_i^\dagger}{\partial x_i} = 0, \qquad -\frac{\partial p^\dagger}{\partial x_i} + \frac{\partial^2 u_i^\dagger}{\partial x_j^2} = -\delta_{i1}, \qquad \text{(7-a,b)}$$

with

$$u_i^\dagger = 0 \quad \text{at} \quad \mathcal{I}_{bf} \quad \text{and} \quad \mathcal{I}_{rf}, \qquad -p^\dagger\,\delta_{i2} + \left(\frac{\partial u_i^\dagger}{\partial x_2} + \frac{\partial u_2^\dagger}{\partial x_i}\right) = 0 \quad \text{at} \quad x_2 \to \infty. \quad \text{(7-c,d)}$$

All auxiliary systems should be solved over a representative volume element (cf. Fig. 1(right)), enforcing periodicity of the microscopic variables along x_1 and x_3.

2.3.2 $\mathcal{O}(\epsilon^1)$ *problem*

As the leading-order problem has revealed that $\theta^{(0)}$ and $\phi^{(0)}$ are constant fields, the thermal problem in the fluid and the solid phases at order ϵ can be written as follows[3]:

$$\text{Fluid phase}: \frac{\partial^2 \theta^{(1)}}{\partial x_j^2} = 0, \qquad \text{solid phase}: \frac{\partial^2 \phi^{(1)}}{\partial x_j^2} = 0, \qquad \text{(8-a,b)}$$

$$\theta^{(1)} = 0 \quad at\ \mathcal{I}_{bf}, \qquad \phi^{(1)} = 0 \quad at\ \mathcal{I}_{br}, \qquad \text{(8-c,d)}$$

$$\theta^{(1)} = \phi^{(1)}, \qquad \frac{\partial \theta^{(1)}}{\partial n} = \kappa\,\frac{\partial \phi^{(1)}}{\partial n} \quad at\ \mathcal{I}_{rf}, \qquad \text{(8-e)}$$

$$\frac{\partial \theta^{(1)}}{\partial x_2} = \eta \quad \text{for} \quad x_2 \to \infty. \qquad \text{(8-f)}$$

Thanks to linearity, a generic solution can be assumed in the form

$$\theta^{(1)} = \tilde{\theta}(x_i)\ \eta(X_i), \qquad \phi^{(1)} = \tilde{\phi}(x_i)\ \eta(X_i).$$

The new purely microscopic fields, $\tilde{\theta}$ and $\tilde{\phi}$, solve the following Laplace equations:

$$\text{fluid phase}: \frac{\partial^2 \tilde{\theta}}{\partial x_j^2} = 0, \qquad \text{solid phase}: \frac{\partial^2 \tilde{\phi}}{\partial x_j^2} = 0, \qquad \text{(9-a,b)}$$

with boundary conditions

$$\tilde{\theta} = 0 \quad at\ \mathcal{I}_{bf}, \qquad \tilde{\phi} = 0 \quad at\ \mathcal{I}_{br}, \qquad \tilde{\theta} = \tilde{\phi} \quad \text{and} \quad \frac{\partial \tilde{\theta}}{\partial n} = \kappa\,\frac{\partial \tilde{\phi}}{\partial n} \quad at\ \mathcal{I}_{rf}, \qquad \text{(9-c,d,e)}$$

$$\frac{\partial \tilde{\theta}}{\partial x_2} = 1 \quad \text{for} \quad x_2 \to \infty, \qquad \text{(9-f)}$$

[3]Corrections, written in red, are made to Eqs. (8-f) and (9-f) since they have typos in the published version.

Considering the dynamic problem, we have

$$\frac{\partial u_i^{(1)}}{\partial x_i} = -\frac{\partial u_i^{(0)}}{\partial X_i}, \tag{10-a}$$

$$-\frac{\partial p^{(1)}}{\partial x_i} + \frac{\partial^2 u_i^{(1)}}{\partial x_j^2} + \mathcal{R}_G\,\theta^{(1)}\,\delta_{i1} = \frac{\partial p^{(0)}}{\partial X_i} - 2\frac{\partial^2 u_i^{(0)}}{\partial x_j\,\partial X_j} + \mathcal{R}_G\,u_j^{(0)}\frac{\partial u_i^{(0)}}{\partial x_j}, \tag{10-b}$$

$$u^{(1)} = 0 \qquad at\ \ \mathcal{I}_{bf}\ \text{ and }\ \mathcal{I}_{rf}, \tag{10-c}$$

$$-p^{(1)}\,\delta_{i2} + \left(\frac{\partial u_i^{(1)}}{\partial x_2} + \frac{\partial u_2^{(1)}}{\partial x_i}\right) = -\left(\frac{\partial u_i^{(0)}}{\partial X_2} + \frac{\partial u_2^{(0)}}{\partial X_i}\right) \quad \text{at} \quad x_2 \to \infty. \tag{10-d}$$

The expressions of $u_i^{(0)}$ and $p^{(0)}$ must now be substituted into the preceding equations; the behavior of $u_i^{(1)}$ and $p^{(1)}$ is thus described by

$$\frac{\partial u_i^{(1)}}{\partial x_i} = -\breve{u}_{jk}\frac{\partial S_{k2}}{\partial X_j}, \tag{11-a}$$

$$-\frac{\partial p^{(1)}}{\partial x_i} + \frac{\partial^2 u_i^{(1)}}{\partial x_j^2} = \mathcal{R}_G^3 u_j^\dagger \frac{\partial u_i^\dagger}{\partial x_j} + \mathcal{R}_G^2\left[\breve{u}_{jk}\frac{\partial u_i^\dagger}{\partial x_j} + u_j^\dagger\frac{\partial \breve{u}_{ik}}{\partial x_j}\right] S_{k2} + \mathcal{R}_G\left[\breve{u}_{jk}\frac{\partial u_{i\ell}}{\partial x_j}\right] S_{k2}S_{\ell 2}$$
$$-\mathcal{R}_G\,\eta\,\tilde{\theta}\,\delta_{i1} + \breve{p}_k\frac{\partial S_{k2}}{\partial X_i} - 2\frac{\partial \breve{u}_{ik}}{\partial x_j}\frac{\partial S_{k2}}{\partial X_j}, \tag{11-b}$$

subject to

$$u^{(1)} = 0 \qquad at\ \ \mathcal{I}_{bf}\ \text{ and }\ \mathcal{I}_{rf}, \tag{11-c}$$

and

$$-p^{(1)}\delta_{i2} + \frac{\partial u_i^{(1)}}{\partial x_2} + \frac{\partial u_2^{(1)}}{\partial x_i} = -\breve{u}_{ik}\frac{\partial S_{k2}}{\partial X_2} - \breve{u}_{2k}\frac{\partial S_{k2}}{\partial X_i} \quad \text{at} \quad x_2 \to \infty. \tag{11-d}$$

Again, a solution is sought in a form that takes advantage of the forcing terms, i.e.:

$$u_i^{(1)} = \dot{u}_{ijk}\left[\frac{\partial S_{k2}}{\partial X_j}\right] + \ddot{u}_{ik}\left[\mathcal{R}_G(S_{k2})^2\right] + \ddot{u}_{i12}\left[\mathcal{R}_G S_{12}S_{22}\right] + \ddot{u}_{i13}\left[\mathcal{R}_G S_{12}S_{32}\right] + \ddot{u}_{i23}\left[\mathcal{R}_G S_{22}S_{32}\right]$$
$$+ u_i{}'\left[\mathcal{R}_G\,\eta\right] + \overline{u}_{ik}\left[\mathcal{R}_G^2 S_{k2}\right] + u_i^\ddagger\left[\mathcal{R}_G^3\right],$$

and likewise for $p^{(1)}$. The decoupled systems of equations arising from substituting the generic forms above into eqs. (11-a to 11-d) are similar to those given in (Ahmed *et al.*, 2022).

Revisiting eq. (4), the macroscopic velocity and temperature at the matching interface are now available up to $\mathcal{O}(\epsilon^2)$ and $\mathcal{O}(\epsilon^1)$, respectively. However, following the same lines of Ahmed *et al.* (2022), we can find that taking the temperature to $\mathcal{O}(\epsilon^2)$ under steady conditions leads to microscopic parameters which vanish at the matching interface and thus do not contribute to the effective temperature boundary condition.

3 EVALUATION OF THE CLOSURE PARAMETERS: PARAMETRIC STUDY

3.1 The parameters of interest

We are only interested here in the closure parameters that contribute to the effective velocity and temperature boundary conditions at the matching interface ($x_2 = y_\infty$). Fortunately, many of the auxiliary systems defined in Section 2.3 yield microscopic variables that vanish at the matching plane. Following the procedure by Ahmed *et al.* (2022), we specify the following parameters of interest: $\breve{u}_{11}$, $\breve{u}_{33}$, $u_1^\dagger$, $\tilde{\theta}$, $\dot{u}_{112}$, $\dot{u}_{211}$, $\dot{u}_{332}$, $\dot{u}_{233}$ and u_1'. The distributions of these variables are to be sought by numerically solving the corresponding auxiliary problems through a representative periodic unit cell in the microscopic domain, bounded by the solid/solid and solid/fluid interfaces from one side and by the matching interface on the other. The outer boundary of the microscopic problems should be located far enough away from the physical surface for the fields to become uniform in x_1 and x_3. The following step is to vary the location of the matching interface and to accordingly estimate the values of the closure variables at the outer x_2-edge of the domain. For convenience, the values of the closure variables computed at different y_∞ are later extrapolated to a virtual matching plane chosen to go through the tips of the ribs, at $x_2 = 0$; cf. Fig. 1(right). At this specific location, the model coefficients may be defined as follows, taking advantage of the equalities found in (Ahmed *et al.*, 2022):

$$\breve{u}_{11}\big|_{x_2=0} = \lambda_x, \qquad \breve{u}_{33}\big|_{x_2=0} = \lambda_z, \qquad \tilde{\theta}\big|_{x_2=0} = \lambda_\theta,$$

$$u_1^\dagger\big|_{x_2=0} = \dot{u}_{112}\big|_{x_2=0} = -\dot{u}_{211}\big|_{x_2=0} = m_{12}, \quad \dot{u}_{332}\big|_{x_2=0} = -\dot{u}_{233}\big|_{x_2=0} = m_{32}, \quad u_1'\big|_{x_2=0} = \mathcal{B}.$$

The Navier-slip coefficients (λ_x, λ_z) and surface permeability coefficients (m_{12}, m_{32}) are only dependent on the geometric parameters of the ribbed surface, while the thermal-slip coefficient (λ_θ) and the velocity-flux sensitivity ($\mathcal{B}$) depend also on the rib-to-fluid thermal conductivity ratio (κ), which is the novel contribution of the present work. If the ribs were assumed to be perfectly conducting the thermal-slip coefficient would be identical to λ_z (Ahmed *et al.*, 2022). One of the main contributions of the present work consists in the following set of second-order macroscopic boundary conditions:

$$U_1\big|_{X_2=0} = \epsilon\,[\lambda_x\, S_{12} + m_{12}\,\mathcal{R}_G]_{X_2=0} + \epsilon^2 \left[m_{12}\,\frac{\partial S_{22}}{\partial X_1} + \mathcal{B}\,\mathcal{R}_G \frac{\partial \Theta}{\partial X_2}\right]_{X_2=0} + \mathcal{O}(\epsilon^3), \quad \text{(12-a)}$$

$$U_2\big|_{X_2=0} = -\epsilon^2 \left[m_{12}\,\frac{\partial S_{12}}{\partial X_1} + m_{32}\,\frac{\partial S_{32}}{\partial X_3}\right]_{X_2=0} + \mathcal{O}(\epsilon^3), \quad \text{(12-b)}$$

$$U_3\big|_{X_2=0} = \epsilon\,\lambda_z\, S_{32}\big|_{X_2=0} + \epsilon^2 \left[m_{32}\,\frac{\partial S_{22}}{\partial X_3}\right]_{X_2=0} + \mathcal{O}(\epsilon^3), \quad \text{(12-b)}$$

$$\Theta\big|_{X_2=0} = 1 + \epsilon\,\lambda_\theta \frac{\partial \Theta}{\partial X_2}\bigg|_{X_2=0} + \mathcal{O}(\epsilon^3). \quad \text{(12-d)}$$

3.2 The case of transverse square ribs

In this work, the case of transverse (x_3-elongated) ribs of square cross-section is considered so that the auxiliary systems can be considerably simplified, with the derivatives $\partial/\partial x_3$ set to zero. Only two-dimensional (x_1, x_2) Stokes-/Laplace-/Poisson-like problems are to be solved, enforcing periodicity along x_1. A microscopic representative unit cell is sketched in Fig. 2.

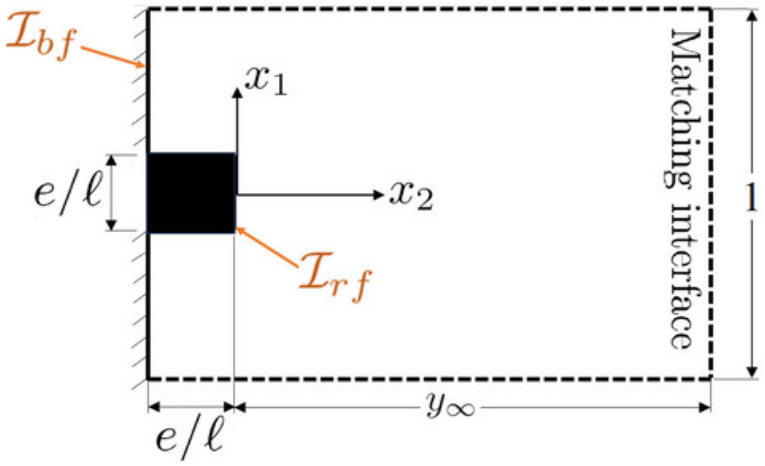

Figure 2: A representative microscopic unit cell for the case of two-dimensional square ribs, with the geometric parameters indicated.

The numerical results of sample auxiliary systems, with the matching interface located at $x_2 = y_\infty = 5$, are presented as *Supplementary Material*. The behaviors of the model coefficients, resulting from extrapolation to $x_2 = 0$, are then sought. The trends of the merely geometry-dependent parameters $(\lambda_x, \lambda_z, m_{12}, m_{32})$ with variations in $\frac{e}{\ell}$, displayed in Fig. 3(left), are identical to those in (Ahmed *et al.*, 2022). As λ_θ explicitly depends on κ, and $\mathcal{B}$ is implicitly dependent on it, it is useful to plot them against $\frac{e}{\ell}$ for different values of κ; cf. Fig. 3(right). The cases of adiabatic ribs and isothermal ribs are chosen as the two limiting situations, while the finite value $\kappa \approx 4$ is chosen as a representative case, corresponding to airflow over wooden ribs. For $\frac{e}{\ell} \to 0$, the surface tends to be flat and isothermal; thus, the thermal-slip coefficient $\lambda_\theta \to 0$. In general, the value of λ_θ increases with the decrease of κ at a given value of $\frac{e}{\ell}$, with the maximum λ_θ corresponding to the case of adiabatic ribs. This effect becomes more pronounced for relatively large-sized ribs. For $\frac{e}{\ell} \to 1$, the surface becomes flat again as the inter-rib spaces vanish and the ribs become contiguous; the thermal-slip coefficient approaches zero for isothermal ribs and ∞ for adiabatic ribs.

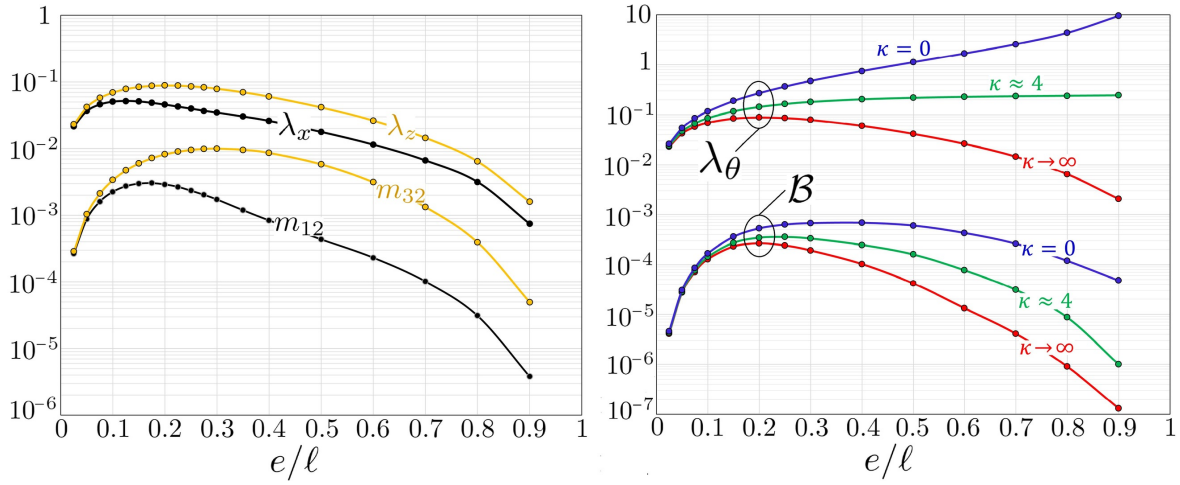

Figure 3: Dependence of the upscaled model coefficients on the aspect ratio $\frac{e}{\ell}$.

4 MODEL VALIDATION ON DIFFERENT CASE STUDIES

4.1 Overview of the conditions considered and numerical procedure

The effective boundary conditions formulated in the previous section are to be validated here for the laminar, steady buoyancy-driven flow over transverse square ribs. Different case studies are analyzed at a Prandtl number of 0.712 (air) and a plate Grashof number of about 2.78×10^8 (this corresponds, for instance, to a vertical surface of 0.4 m height with a baseplate temperature roughly $40\,°C$ above the ambient temperature), considering changes in thermal conductivity and size of the ribs.

The indicated conditions raise concerns about the validity of the physical model adopted, in particular the Boussinesq approximation and the laminar-flow assumption. First, the Boussinesq approximation is applicable provided that $\beta(\hat{T}_b - \hat{T}_\infty) << 1$ (cf. (Hærvig & Sørensen, 2020)), and this applies here since, for example, if $\hat{T}_b - \hat{T}_\infty = 40\,°C$ and $\beta(\text{air}) \approx 0.0034\ K^{-1}$, the value of $\beta(\hat{T}_b - \hat{T}_\infty)$ is equal to 0.136. Second, steady natural convection is considered at a plate Rayleigh number ($Ra = Gr \times Pr$) of about 2×10^8. A critical value of $Gr = 10^9$ is typically indicated in the literature for turbulent transition over a vertical smooth surface (Bejan & Lage, 1990; Bejan, 1993); this corresponds to $Ra \approx 7 \times 10^8$ with air as the convective fluid. Since the upper threshold of the laminar flow range may differ when the surface is ribbed, an experimental campaign has been carried out to investigate this issue (Tanda *et al.*, 2023), employing the schlieren imaging technique to study natural convection from a vertical surface ribbed with continuous transverse elements of square cross-section, varying rib size and pitch, at values of the plate Rayleigh number up to about 5×10^8. Interestingly, a steady thermal boundary layer has been optically captured, and this was confirmed via measurements of the time history of temperature at different normal distances from the wall, where the intensity

of air temperature fluctuations in the boundary layer has been found to be far below the ranges reported in the literature for the onset of transitional effects (cf. (Tsuji & Nagano, 1988)). Furthermore, a discussion on the effects of external disturbances, present in practice, on the heat transfer performance is provided in (Tanda *et al.*, 2023).

The dimensionless equations governing the macroscale problem, i.e. eqs. (2-a to 2-c), are solved beyond the fictitious surface passing through the outer rims of the ribs. The effective boundary conditions at $X_2 = 0$, i.e. eqs. (12-a to 12-d), can be further simplified as validation of the model is targeted at the steady-state solution of a two-dimensional laminar flow; the gradients in the spanwise direction can thus be neglected. In addition, since the ribbed surface is impermeable, the local transpiration velocity (U_2 at $X_2 = 0$) is zero on average and its inclusion has been found to be irrelevant under laminar flow conditions. Eventually, the effective boundary conditions simplify to the slip velocity in the streamwise direction $U_1\big|_{X_2=0}$ and the effective temperature $\Theta\big|_{X_2=0}$.

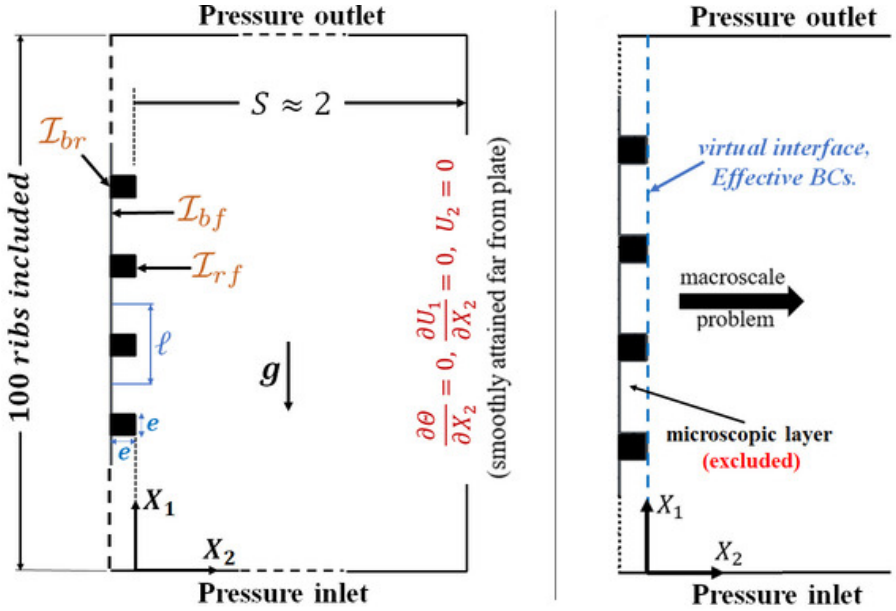

Figure 4: General description of the computational domain and the boundary conditions used for (left) feature-resolving simulations and (right) homogenization-based simulations.

The validation of the homogenization-based model requires conducting reliable feature-resolving simulations, in which the full domain is considered and the velocity and thermal fields within the inter-rib regions are fully resolved; cf. Fig. 4 for a clearer view of the differences between the two categories of numerical simulations. The fully-resolved fields can contribute to our understanding of the associated phenomena; nevertheless, they cannot be used directly to validate the results of the homogenized model. For this purpose, the running averages of the full simulation results should be defined. For instance, the running-average value of the dimensionless temperature (Θ) at the arbitrary point

$X_1 = a$, $X_2 = b$ is calculated as follows:

$$< \Theta > \Big|_{X_1=a, X_2=b} = \frac{1}{\epsilon} \int_{a-\frac{\epsilon}{2}}^{a+\frac{\epsilon}{2}} \Theta(X_1, b)\, dX_1. \tag{13}$$

For each one of the cases studied, the local results of the full simulations will be first described, and the running-average fields will then be used to validate the homogenization-based solutions.

The mesh was generated using quadrilateral cells, where structured layers were created in the vicinity of the rough surface (or, in macroscopic simulations, the matching interface). To get a preliminary estimation of the maximum thickness of the thermal boundary layer ($\hat{\delta}_{max}$), i.e. the thickness reached at $\hat{x}_1 = L$, the classical Squire-Eckert theoretical prediction (refer to (Lienhard & Lienhard, 2019)) was used, that is

$$\hat{\delta}_{max} = 3.936\, L \left[\frac{0.952 + Pr}{Gr\, Pr^2}\right]^{0.25} \approx 0.04L. \tag{14}$$

Accordingly, to ensure that the boundary layer is well resolved, a near-wall region of interest for mesh refinement, of thickness $\approx 0.08L$, was specified. In addition, attention should be focused on the region near the inlet of the domain, where the thickness of the thermal boundary layer approaches zero as $X_1 \to 0$ and the local heat transfer coefficient tends to ∞. To handle this issue, avoiding extra refinement of the mesh near the inlet, a correlation proposed by Churchill & Chu (1975), and assumed to be valid over the full laminar-flow range, was employed to calculate the average Nusselt number over the range $0 \leq X_1 \leq (\frac{d}{L} = 0.001)$, i.e. in the neighborhood of the leading edge of the flat plate, as follows:

$$\overline{Nu}_d = 0.68 + 0.67\,(Gr_d\, Pr)^{0.25} \left[1 + \left(\frac{0.492}{Pr}\right)^{\frac{9}{16}}\right]^{\frac{-4}{9}}, \tag{15}$$

where $\overline{Nu}_d = \dfrac{\overline{h}_d\,(\text{average heat transf. coeff.}) \times d}{k_f}$. With $Gr_d = Gr \times \left(\dfrac{d}{L}\right)^3 = 0.278$ and $Pr = 0.712$, we obtain $\overline{Nu}_d \approx 1.023$. The value of d should be much smaller than the distance from the leading edge to the first rib. For more information about the grid structure and the mesh-dependence levels for the macroscopic and the feature-resolving simulations, the reader is referred to (Ahmed *et al.*, 2022). However, in the current work, an additional complexity appears because of thermal conduction through the roughness elements, so that the solid domain is also discretized, increasing the total mesh requirements for the full feature-resolving simulations. For example, 35×35 square cells (finest mesh) were used to discretize each rib in the cases discussed in Section 4.3, where the number of ribs was $N_{ribs} = 20$ and $\dfrac{e}{\ell} = 0.25$.

In all simulations, the finite volume method was applied to discretize the two-dimensional transport equations, using Simcenter STAR-CCM+ multiphysics software (version 16.02.009-R8). The numerical procedure is similar to that employed in (Ahmed

et al., 2022), except for the spatial discretization which has been upgraded via the hybrid MUSCL 3rd-order/central-differencing scheme (refer to (Van Leer, 1979; Van Leer & Nishikawa, 2021)). The hybrid Gauss–least squares method was used for the computation of gradients, with the Venkatakrishnan gradient limiter activated (refer to (Venkatakrishnan, 1993)). The pressure-velocity coupling was based on the SIMPLE scheme. The average Nusselt number ($\overline{Nu}$) was monitored and used as the convergence criterion. Throughout this paper, the average Nusselt number is evaluated by integrating the local Nusselt number (Nu) over the area of the surface of interest, while the projected surface area (area of a flat surface of same height) is used as weight such that the changes in $\overline{Nu}$ directly reflect the adverse/favorable trends of the heat transfer rate (Hærvig & Sørensen, 2020; Ahmed *et al.*, 2022); the expressions of Nu and $\overline{Nu}$ over a vertical surface of height L roughened with two-dimensional square ribs of size e and pitch ℓ are

$$Nu = \frac{-L}{\hat{T}_b - \hat{T}_\infty} \times \left.\frac{\partial \hat{T}}{\partial \hat{n}}\right|_{wall} = -\left.\frac{\partial \Theta}{\partial n}\right|_{wall}, \tag{16-a}$$

$$\overline{Nu} = \frac{1}{L}\int_0^{L+\frac{2e}{\epsilon}} -\left.\frac{\partial \Theta}{\partial n}\right|_{wall} d\hat{s} = \int_0^{1+\frac{2e}{\ell}} -\left.\frac{\partial \Theta}{\partial n}\right|_{wall} ds, \tag{16-b}$$

where $s = \dfrac{\hat{s}}{L}$, with $\hat{s}$ a dimensional distance that goes along the ribbed surface capturing its details (as opposed to the vertical distance $\hat{x}_1$). On the other hand, Nu and $\overline{Nu}$ over the vertical virtual interface (for the simulations employing the *effective* conditions) are simply evaluated as

$$Nu = -\left.\frac{\partial \Theta}{\partial X_2}\right|_{X_2=0}, \qquad \overline{Nu} = \int_0^1 -\left.\frac{\partial \Theta}{\partial X_2}\right|_{X_2=0} dX_1. \tag{17-a,b}$$

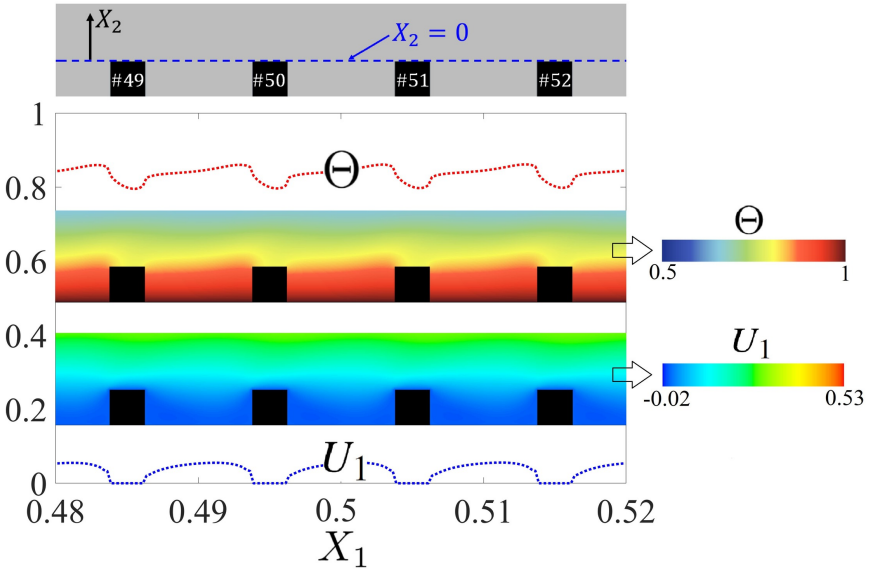

Figure 5: Fully-resolved contours of Θ and U_1 next to the wall for four adiabatic ribs placed halfway through the plate, with plots of the typical values at the virtual interface ($X_2 = 0$); $\epsilon = \dfrac{1}{100}$ and $\dfrac{e}{\ell} = 0.25$.

4.2 The basic validation case

In pursuit of basic validation of the theory, it is wise to consider the two limiting values of the thermal conductivity ratio, κ, i.e. $\kappa = 0$ (adiabatic ribs) and $\kappa \to \infty$ (isothermal ribs). Since the model is validated in detail for isothermal ribs in (Ahmed *et al.*, 2022), our basic validation here will be limited to the case of adiabatic ribs. Moreover, we start by analyzing an intensively ribbed surface ($N_{ribs} = 100$), to ensure that the value of the parameter $\epsilon = \dfrac{1}{N_{ribs}}$ is sufficiently small, and the model is therefore applied within its validity range. The reader is referred to (Ahmed *et al.*, 2022), in which a parameter $C = \epsilon^2\sqrt{Gr}$ was identified as a reliable accuracy indicator, with the homogenized model yielding acceptable results for $C \lesssim 40$. Given that the Grashof number is here equal to 2.78×10^8, we have a value of $C \approx 1.67$, well within the range of applicability of the model. In addition, a value of 0.25 is specified for the rib size-to-pitch ratio $(\dfrac{e}{\ell})$.

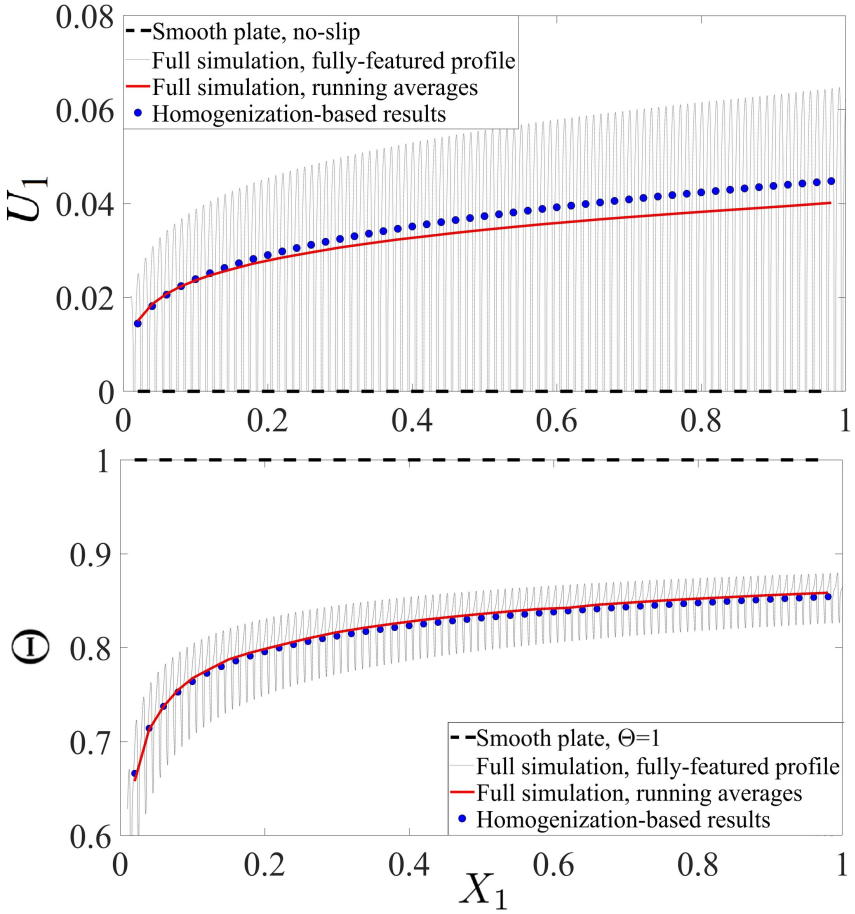

Figure 6: Numerical results of the effective boundary conditions for U_1 and Θ, against the corresponding running-average values extracted from the full feature-resolving simulation. The fully-resolved local values of the fields are also shown in the background. Same conditions and parameters as Fig. 5.

Distributions of the thermal and velocity fields in vicinity of the ribbed wall are displayed in Fig. 5. The role of adiabatic ribs in interrupting the development of the thermal boundary layer can be noticed, in terms of the temperature drop experienced at the outer rims. The fully-featured patterns of U_1 and Θ along the plane at $X_2 = 0$ are presented in Fig. 6. The running-average values of these fields can be directly used to validate the homogenization-based results of the effective velocity and temperature boundary conditions as shown in the figure; reasonably good agreement can be observed, particularly for the temperature (Θ).

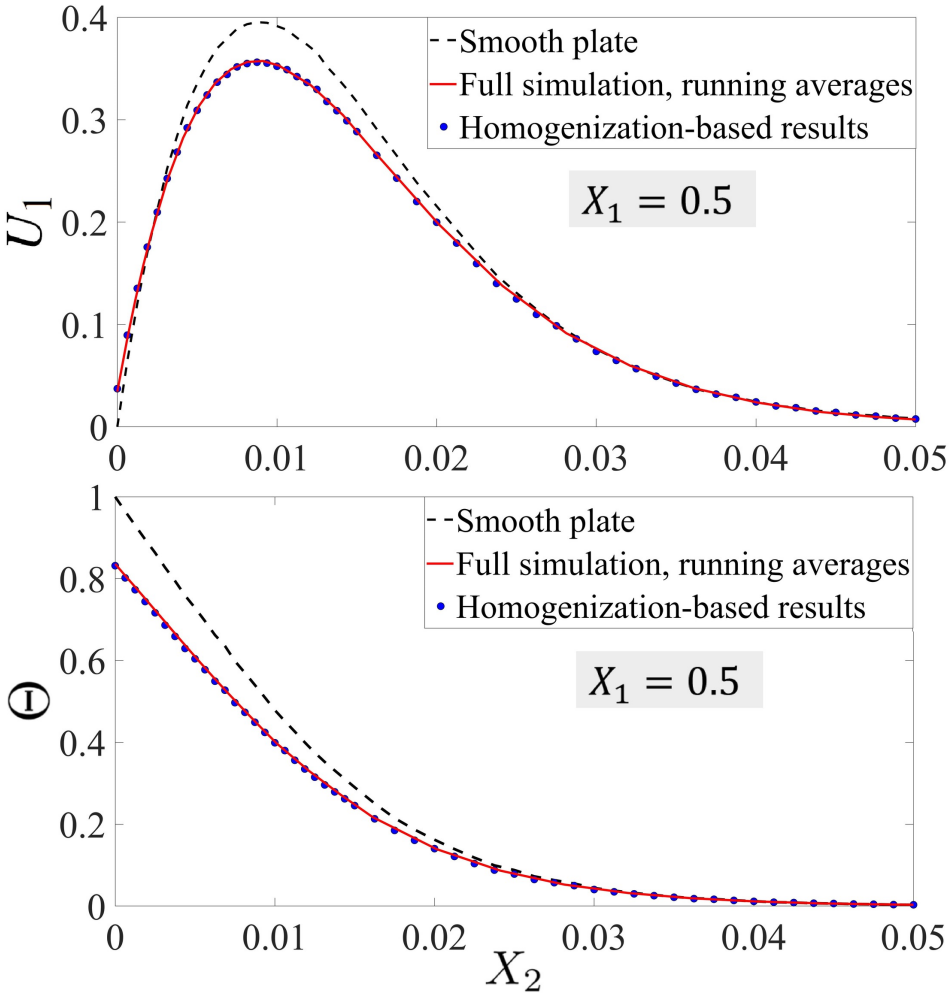

Figure 7: Homogenization-based predictions for the profiles of U_1 and Θ across a section at $X_1 = 0.5$, validated against the running-average results of the feature-resolving simulation. Adiabatic ribs are considered, with $\epsilon = \frac{1}{100}$ and $\frac{e}{\ell} = 0.25$.

It is also important to assess the accuracy of the model predictions for the behavior of the velocity and thermal boundary layers. For this purpose, the model results of the profiles of U_1 and Θ across a section at the middle of the plate are compared in Fig. 7 with the corresponding running-average results of the full simulation. It can be noticed

that the results are quantitatively in perfect agreement. It is worth noting that, since the adiabatic ribs attenuate the temperature increase over the plate (and consequently the buoyant force), the peak velocity is lower than in the case of an isothermal flat surface.

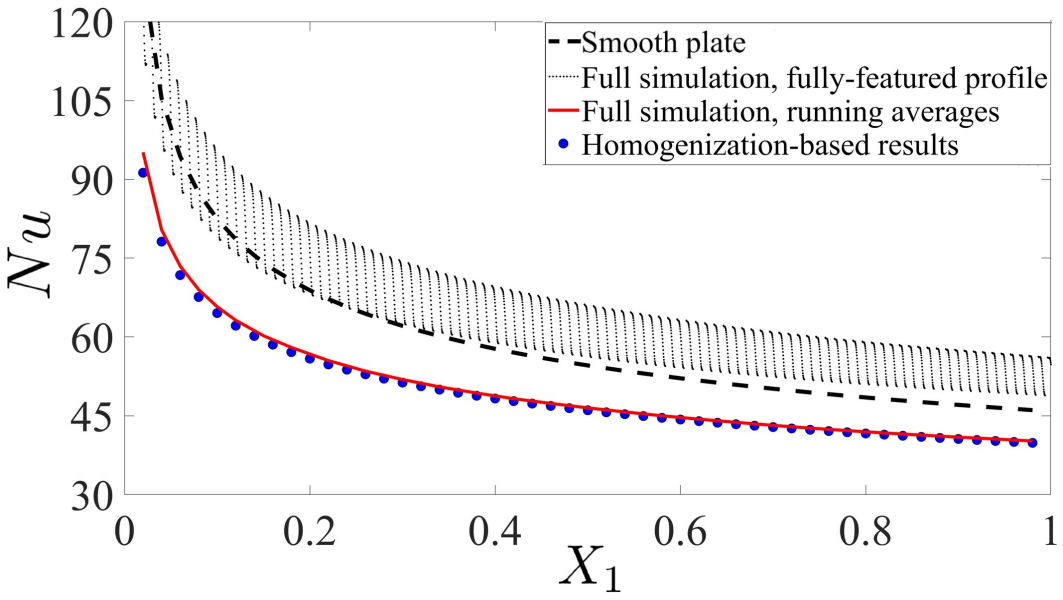

Figure 8: Homogenized model predictions for the Nusselt number, plotted together with the running-average results of the feature-resolving simulation, for validation. Adiabatic ribs are considered, with $\epsilon = \frac{1}{100}$ and $\frac{e}{\ell} = 0.25$. The corresponding distribution of Nu along a smooth isothermal surface is also displayed.

Analyzing the model results of the temperature profiles across different normal sections along the plate, we can state that the normal temperature gradients at $X_2 = 0$, i.e. $\frac{\partial \Theta}{\partial X_2}\big|_{X_2=0}$, directly indicate the model prediction of the macroscopic Nusselt number distribution along the plate. On the other hand, the fully-featured results of the Nusselt number, those directly obtained from the feature-resolving simulation, are calculated based on the temperature gradient in the direction normal to the physical surface at each point on the baseplate and on the rims of the square ribs; the running-average behavior should be therefore evaluated to validate the model results (cf. Fig. 8). One should take into account that the evaluation of the running-average Nusselt number is done in a similar way to eq. (13), yet the local values of the Nusselt number are to be integrated along the physical surface in a unit cell. Furthermore, the average Nusselt number (based on the projected area), $\overline{Nu}$, was calculated. It is noticeable that the deviation of the predicted value from the model ($\overline{Nu} = 52.28$) from the result of the full simulation ($\overline{Nu} = 52.68$) is less than 1%. Both are below the corresponding value for the case of an isothermal flat surface ($\overline{Nu} = 63.24$).

4.3 Role of the ribs' thermal conductivity

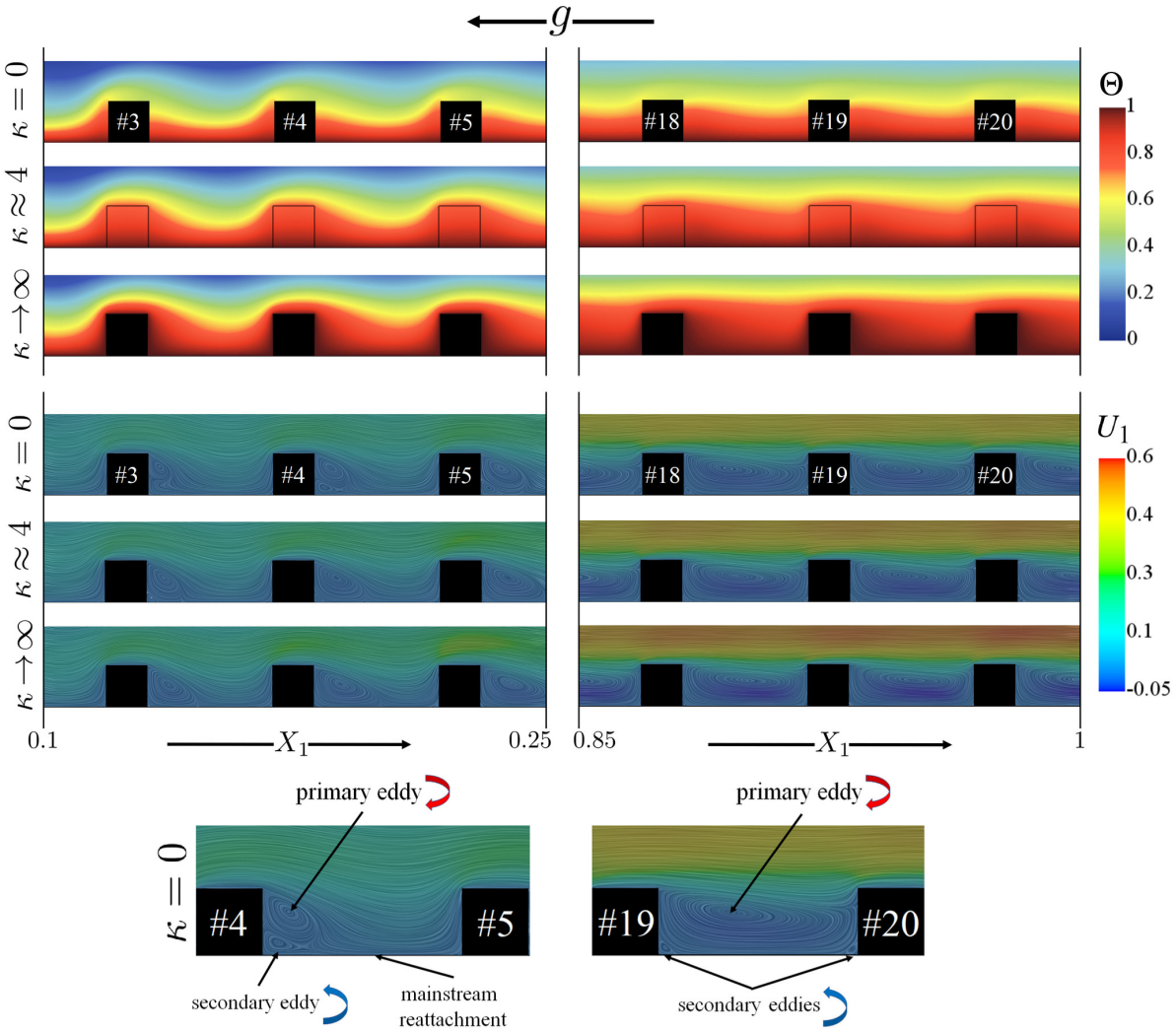

Figure 9: Contours of the dimensionless temperature (Θ) and streamwise velocity (U_1) adjacent to the rough surface, displayed through two specific portions of the plate: (left) $X_1 = 0.1$ to 0.25; (right) $X_1 = 0.85$ to 1. Three distinct values of the rib-to-fluid thermal conductivity ratio are considered. Close-ups of the flow structures within two distant inter-rib regions, for the case of adiabatic ribs, are shown in the bottom frame. For all cases, it is $\epsilon = \frac{1}{20}$ and $\frac{e}{\ell} = 0.25$.

We now discuss the effects of the rib-to-fluid thermal conductivity ratio (κ) on the characteristics of the buoyancy-driven flow and the heat transfer phenomena. Three distinct situations are considered for analysis via both the feature-resolving simulations and the homogenization-based model, specifically the case of adiabatic ribs ($\kappa = 0$), isothermal ribs ($\kappa \to \infty$), and ribs of finite thermal conductivity ($\kappa \approx 4$). The latter represents a situation that is frequently encountered in experiments, where wooden roughness elements (with $k_r \approx 0.1\,W/mK$) are used and the flowing fluid is air (with

$k_f \approx 0.025 - 0.028\,W/mK$). We consider a roughness pattern consisting of 20 square ribs, i.e. $\epsilon = \dfrac{1}{N_{ribs}} = \dfrac{1}{20}$, with $\dfrac{e}{\ell} = 0.25$ and with the flow conditions described by $Pr = 0.712$ and $Gr \approx 2.78 \times 10^8$.

4.3.1 *The feature-resolving cases*

As a starting point, results of the full feature-resolving simulations are presented and discussed. Contours of the temperature Θ and the streamwise velocity U_1 are displayed in Fig. 9, with the aid of streamlines to detect the complex flow structures within the inter-rib regions. This provides a clear view of the expensive mesh requirements of the full simulations and thus highlights the advantages of employing the homogenized model. The fields are displayed in the figure close to the leading edge ($X_1 = 0.1$ to 0.25) and near the end of the plate ($X_1 = 0.85$ to 1), to indicate the development of the thermal and the viscous boundary layers along the vertical direction and the associated variations in flow patterns within the corrugations. Proceeding along the plate, we can realize that the mainstream reattachment to the baseplate is gradually delayed and eventually lost, with a large, primary eddy separating the mainstream from the baseplate. Secondary eddies are also resolved in the figure. In-depth inspection of Fig. 9 reveals that the development of the thermal boundary layer is significantly interrupted when ribs of low thermal conductivity (or adiabatic ribs) are used, and therefore the temperature levels in the adjacent fluid layers are lower compared to the case of isothermal ribs. This effect becomes more pronounced as we proceed along the plate (far from the leading edge). The patterns of the temperature and the streamwise velocity along the fictitious interface at $X_2 = 0$ are plotted in Fig. 10 (top). Exclusively for isothermal ribs, the temperature at the outer rims of the square elements is equal to the baseplate temperature ($\Theta = 1$). The level of the streamwise velocity is adversely affected by the decrease of the thermal conductivity of the ribs, as the buoyancy force is limited.

The consequent effects of the thermal conductivity variations on the distribution of the local Nusselt number along the ribbed surface are illustrated in Fig. 10 (bottom). The Nusselt number experiences a quasi-periodic behavior while proceeding along the vertical plate (for the three cases considered), which agrees with the findings by Tanda (1997) and Nishikawa *et al.* (2020) with highly-conducting ribs and by Tanda (2008) and Nishikawa *et al.* (2020) with poorly-conducting ribs. It is evident that the interruption of the thermal boundary layer development over adiabatic, or low-conductivity, ribs enhances the heat transfer performance of the isothermal baseplate in the inter-rib regions, consistent with the results reported in (Bhavnani & Bergles, 1990; Tanda, 2008). Conversely, the heat transfer from the outer rims of the ribs plays a significant role in the case of isothermal elements ($\kappa \to \infty$), while this contribution is reduced as κ decreases, until $\kappa = 0$ is reached where no heat transfer takes place from the surfaces of the adiabatic ribs. It is shown later that, on average, the highly conducting ribs outperform the low-conductivity ones (contrary to (Bhavnani & Bergles, 1990)), which implies that the latter contribution (heat transfer from ribs) is dominant.

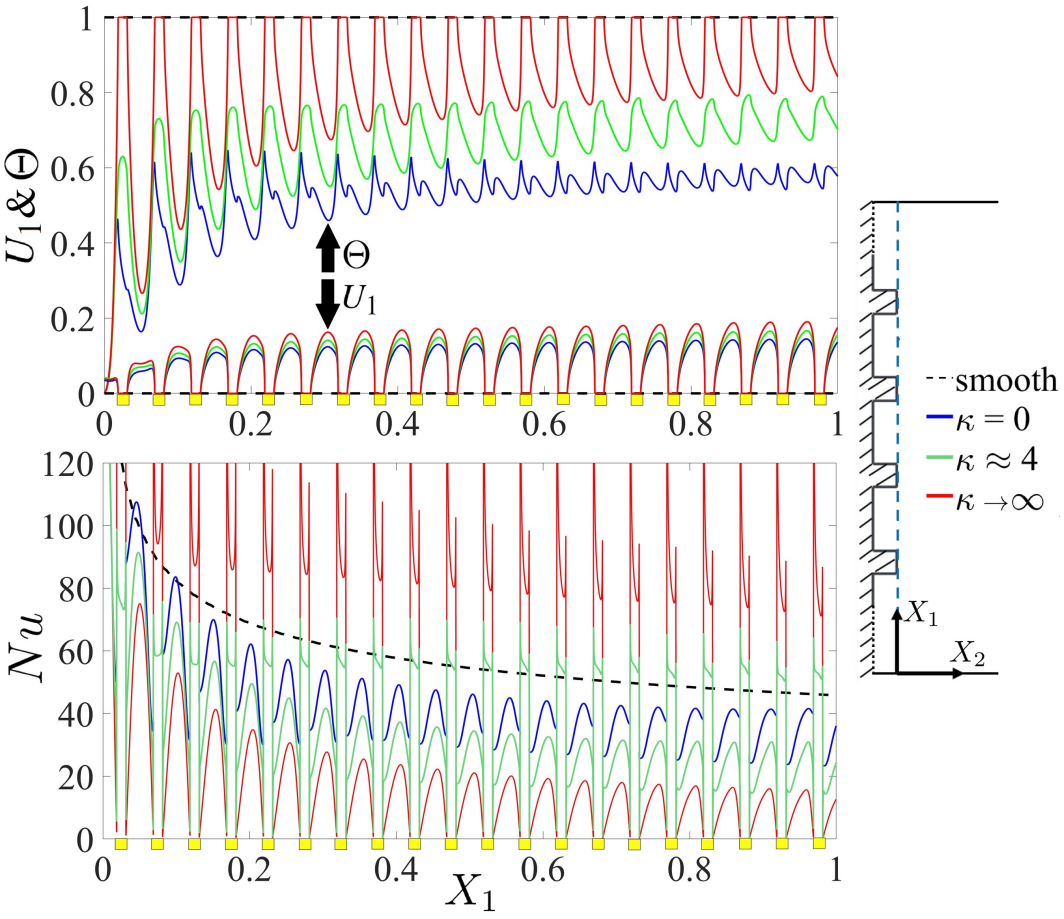

Figure 10: Fully-featured results of U_1 and Θ along a virtual plane at $X_2 = 0$ (top) and patterns of the local Nusselt number (bottom), extracted from full simulations at three values of κ, with $\epsilon = \frac{1}{20}$ and $\frac{e}{\ell} = 0.25$. The yellow elements below the horizontal axis indicate the locations of the ribs.

4.3.2 *Validation of the model results*

Predictions of the homogenization-based simulations are now compared with the corresponding running-average results of the feature-resolving simulations, for accuracy estimation and assessment of possible weak points in the model. It is anticipated that the model is tested here close to its expected limit of applicability (cf. (Ahmed *et al.*, 2022)) as $C = \epsilon^2\sqrt{Gr}$ is now equal to 41.6, close to the threshold ($C \approx 40$).

The running-average distributions of the Nusselt number (calculated based on the fully-resolved patterns given in Fig. 10 (bottom)) are plotted against X_1 in Fig. 11. The heat transfer performance of the ribbed surfaces is lower than the performance of an isothermal smooth surface; surface roughening deteriorates heat transfer under the present conditions. The deterioration becomes more pronounced with the decrease of the ribs' thermal conductivity. Considering the model results of the macroscopic distribution

of the Nusselt numbers, we observe that they fit well with the reference running-average values beyond some distance from the leading edge of the plate; deviations along almost the first 20% of the plate length are significant. In order to alleviate this problem, a length, indicated here as the compensation distance (X_c), is specified near the leading edge, where the model results of the Nusselt number are to be excluded and replaced by the corresponding results over an isothermal flat surface when evaluating the average Nusselt number ($\overline{Nu}$) over the plate. This distance is chosen here such that the compensation region extends over the first two pitch distances ($X_c = 2\epsilon$) if the rib size is negligible, while it should be gradually decreased with the increase of the rib size as the contribution of the ribs to the physical phenomenon acquires prominence. Given that A_r is the surface area of the ribs and A_t is the total surface area (including the ribs and the baseplate portions in the inter-rib regions), the following expression of X_c is proposed:

$$X_c = 2\epsilon \left(1 - \frac{A_r}{A_t}\right) \tag{18}$$

For the case of transverse square ribs of size e and pitch ℓ, the previous equation reads:

$$X_c = 2\epsilon \left(1 - \frac{3e}{\ell + 2e}\right) = 2\epsilon \left(1 - \frac{3}{\ell/e + 2}\right). \tag{19}$$

For $\ell/e = 4$, the compensation distance is equal to ϵ (the first pitch distance). The hypothesis stated here contributes to the calculations of $\overline{Nu}$ throughout this paper (including results in Section 4.2); accordingly, the resulting values of $\overline{Nu}$ are indicated as the *corrected* homogenized-model predictions, while the *uncorrected*, pure results of the model are presented occasionally for comparison.

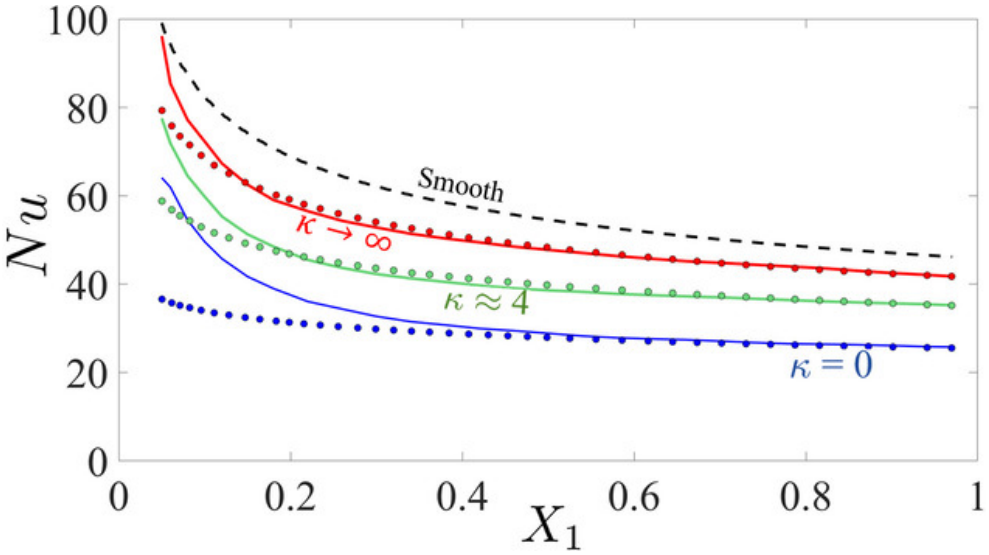

Figure 11: Distributions of the Nusselt number along the plate for different values of κ, with $\epsilon = \frac{1}{20}$ and $\frac{e}{\ell} = 0.25$. Predictions of the homogenized model (filled circles) are validated against running-average results of full simulations (solid lines). The corresponding behavior along a smooth surface is also given (dashed black line).

The effect of the thermal conductivity ratio κ on the average Nusselt number ($\overline{Nu}$) is graphically displayed in Fig. 12. Predictions of the homogenized model are interestingly consistent with results of the full simulations, with the maximum deviation below 3.4%. The average Nusselt number for the case of isothermal ribs ($\kappa \to \infty$) is 56.22 based on the homogenized model, and 56.00 based on the full simulation. This value declines gradually with the decrease of κ until reaching the case of adiabatic ribs $\kappa = 0$, in which the heat transfer takes place only through the inter-rib regions ($\overline{Nu} \approx 35.4$). As ribs are, by definition, of small size relative to the plate height, thermal conduction across them is of significance even for relatively low values of the thermal conductivity coefficient. It can be realized that the average Nusselt number for values of $\kappa \gtrsim 30$ is very close to its value for the isothermal case. With air as the moving fluid, this range corresponds to ribs' thermal conductivity $k_r \gtrsim 0.8\,W/mK$, which can be easily satisfied in practice (for instance, aluminum ribs are of thermal conductivity far beyond this threshold, especially when they are press-fit into the baseplate, as in (Bhavnani & Bergles, 1990), or machined integral with the surface, as in (Tanda, 1997), to avoid contact resistance). Even for wooden ribs ($\kappa \approx 4$), the average Nusselt number is about 47, which is intermediate between the values for adiabatic and isothermal ribs; this implies that it is difficult to experimentally approach the adiabatic limit, and that modeling wooden ribs (or low-conductivity ribs in general) as adiabatic elements in numerical simulations may lead to questionable results.

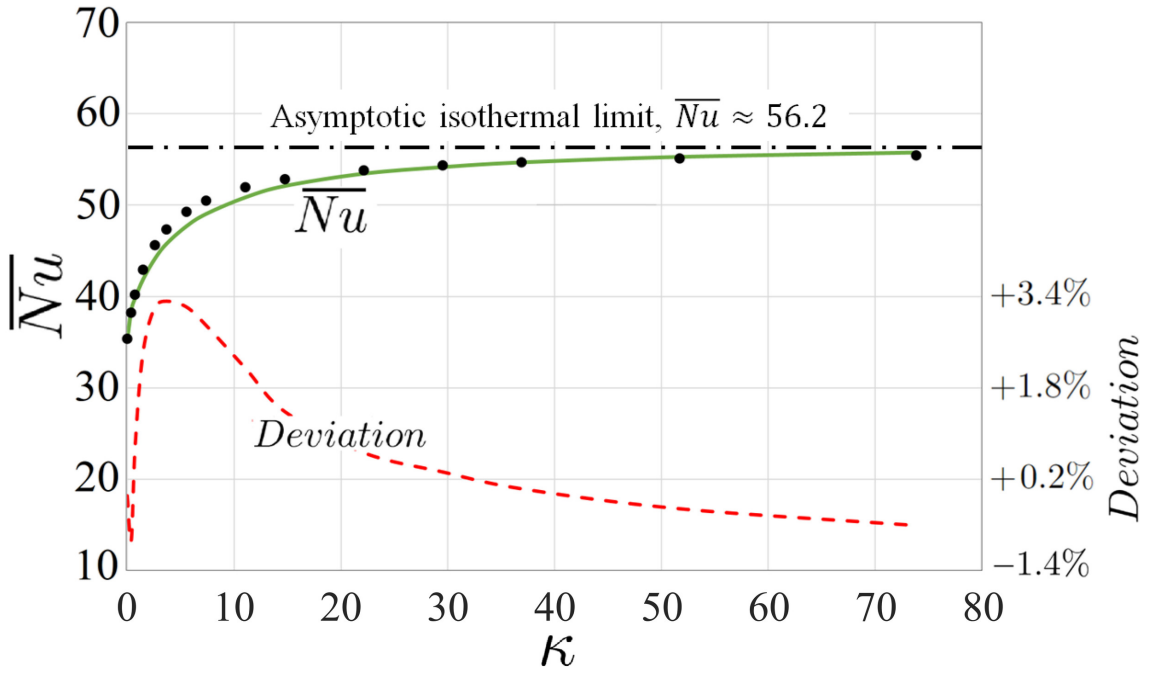

Figure 12: Effect of the rib-to-fluid thermal conductivity ratio (κ) on the average Nusselt number, based on the *corrected* homogenized-model results (filled circles) and the feature-resolving simulations (solid line). Percentage errors in the model results are plotted using dashed red line. The conditions under study are $\epsilon = \frac{1}{20}$, $\frac{e}{\ell} = 0.25$, $Gr \approx 2.78 \times 10^8$ and $Pr \approx 0.712$.

For a clearer view of the significance of correcting the model predictions for $\overline{Nu}$, based on eq. (19), the *uncorrected* homogenized-model results and their percentage deviations from the reference results of the full feature-resolving simulations are given in Table 1; the errors in the pure predictions of the model are considerably large at relatively low values of κ. For replication of the macroscopic simulations, typical values of the model coefficients (λ_θ, $\mathcal{B}$), corresponding to $\frac{e}{\ell} = 0.25$ and the specific considered values of κ, are also presented in the table. Being dependent only on $\frac{e}{\ell}$, the coefficients λ_x and m_{12} are constant regardless of variations in κ; their values (cf. Fig. 3) are 0.0398 and 0.0023, respectively.

Table 1: Comparison between the *corrected* and the *uncorrected* homogenized-model predictions for the average Nusselt number at different values of κ. Percentage deviations in the predictions are estimated relative to the reference results of the feature-resolving simulations.

$\kappa = \frac{k_r}{k_f}$	Macroscopic coefficients		Full sim.	Model, *corrected*		Model, *uncorrected*	
	λ_θ	$\mathcal{B}$	$\overline{Nu}$	$\overline{Nu}$	% error	$\overline{Nu}$	% error
0	0.3657	0.00063	35.39	35.36	-0.09%	29.08	-17.84%
0.369	0.3043	0.00056	38.55	38.22	-0.88%	32.24	-16.39%
0.739	0.2685	0.00051	39.86	40.17	0.77%	34.41	-13.67%
1.477	0.2252	0.00046	41.90	42.91	2.42%	37.49	-10.53%
2.585	0.1895	0.00041	44.15	45.56	3.21%	40.49	-8.27%
3.693	0.1686	0.00038	45.80	47.31	3.32%	42.49	-7.21%
5.540	0.1479	0.00035	47.69	49.22	3.22%	44.69	-6.29%
7.387	0.1356	0.00033	49.03	50.45	2.89%	46.11	-5.94%
11.080	0.1215	0.00031	50.84	51.93	2.14%	47.85	-5.88%
14.773	0.1137	0.00029	52.08	52.80	1.38%	48.88	-6.16%
22.160	0.1053	0.00028	53.43	53.78	0.66%	50.04	-6.34%
29.546	0.1009	0.00028	54.14	54.32	0.33%	50.67	-6.40%
36.933	0.0981	0.00027	54.65	54.67	0.03%	51.10	-6.51%
51.706	0.0949	0.00026	55.25	55.08	-0.32%	51.58	-6.64%
73.866	0.0924	0.00026	55.73	55.39	-0.61%	51.96	-6.76%
∞	0.0861	0.00024	56.00	56.22	0.40%	52.97	-5.41%

4.4 Considerations on the density of the roughness pattern

The aim of this section is to investigate how the behavior of the buoyancy-driven flow and the Nusselt number are affected when the density of the roughness pattern is varied, i.e. the number of ribs attached to the surface is changed. We consider here buoyancy-

induced flows ($Gr \approx 2.78 \times 10^8$ and $Pr \approx 0.712$) over a vertical plate roughened with two-dimensional square elements which are either perfectly conducting ($\kappa \to \infty$), perfectly adiabatic ($\kappa = 0$), or of low thermal conductivity ($\kappa = 4$). The rib size to plate height ratio is fixed ($\frac{e}{L} = \frac{1}{80}$). The maximum possible number of ribs to be attached to the surface corresponds to the case in which the roughness elements become contiguous; at this point the pitch distance (ℓ) becomes equal to the rib size (e) such that $\frac{e}{L} = \frac{\ell}{L} = \epsilon = \frac{1}{80}$, hence, the maximum value of N_{ribs} is 80. Sample results of the full feature-resolving simulations will be displayed first before moving to validation of the homogenized predictions.

4.4.1 *Results of the feature-resolving simulations*

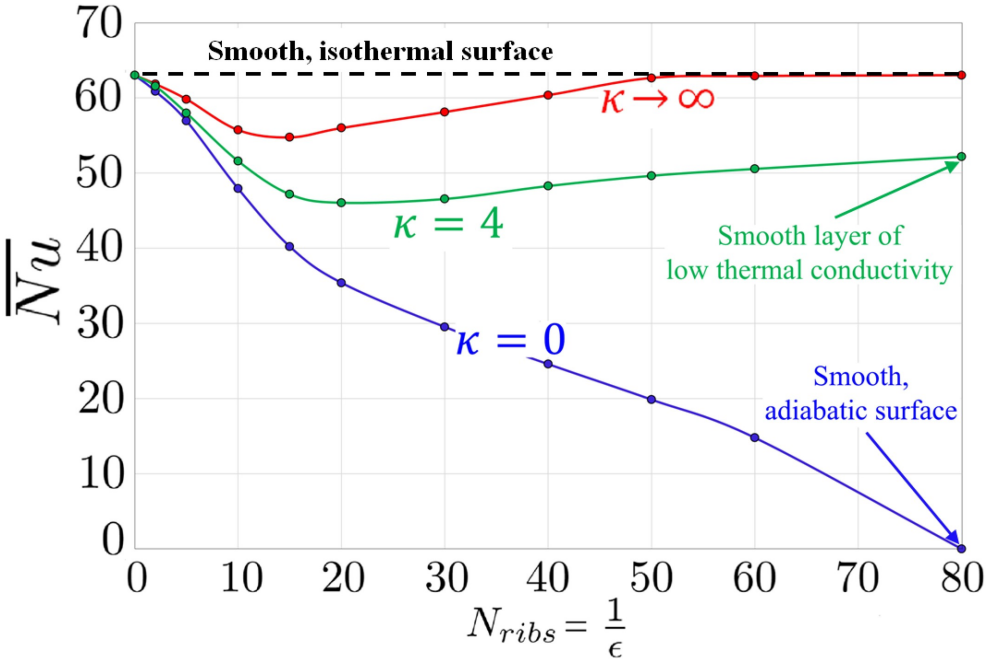

Figure 13: Effect of the number of ribs on the average Nusselt number, at a fixed rib height to plate length ratio ($\frac{e}{L} = \frac{1}{80}$). The values plotted are based on feature-resolving simulations, with three values of the rib-to-fluid thermal conductivity ratio: $\kappa = 0$ (adiabatic ribs), $\kappa = 4$, and $\kappa \to \infty$ (perfectly conducting, isothermal ribs). $Gr \approx 2.78 \times 10^8$ and $Pr \approx 0.712$.

Fig. 13 describes the behavior of the surface-averaged Nusselt number with the increase of N_{ribs} from 0 to 80. The case $N_{ribs} = 0$ obviously represents a smooth isothermal surface, for which $\overline{Nu} \approx 63.00$ as previously stated. At $N_{ribs} = 80$, the roughness elements are in direct contact and the inter-rib spaces vanish; the case of a smooth flat surface is therefore recovered again; however, the surface, which now consists of contiguous ribs, is either adiabatic (for $\kappa = 0$), isothermal (for $\kappa \to \infty$) or it resembles a smooth layer of low

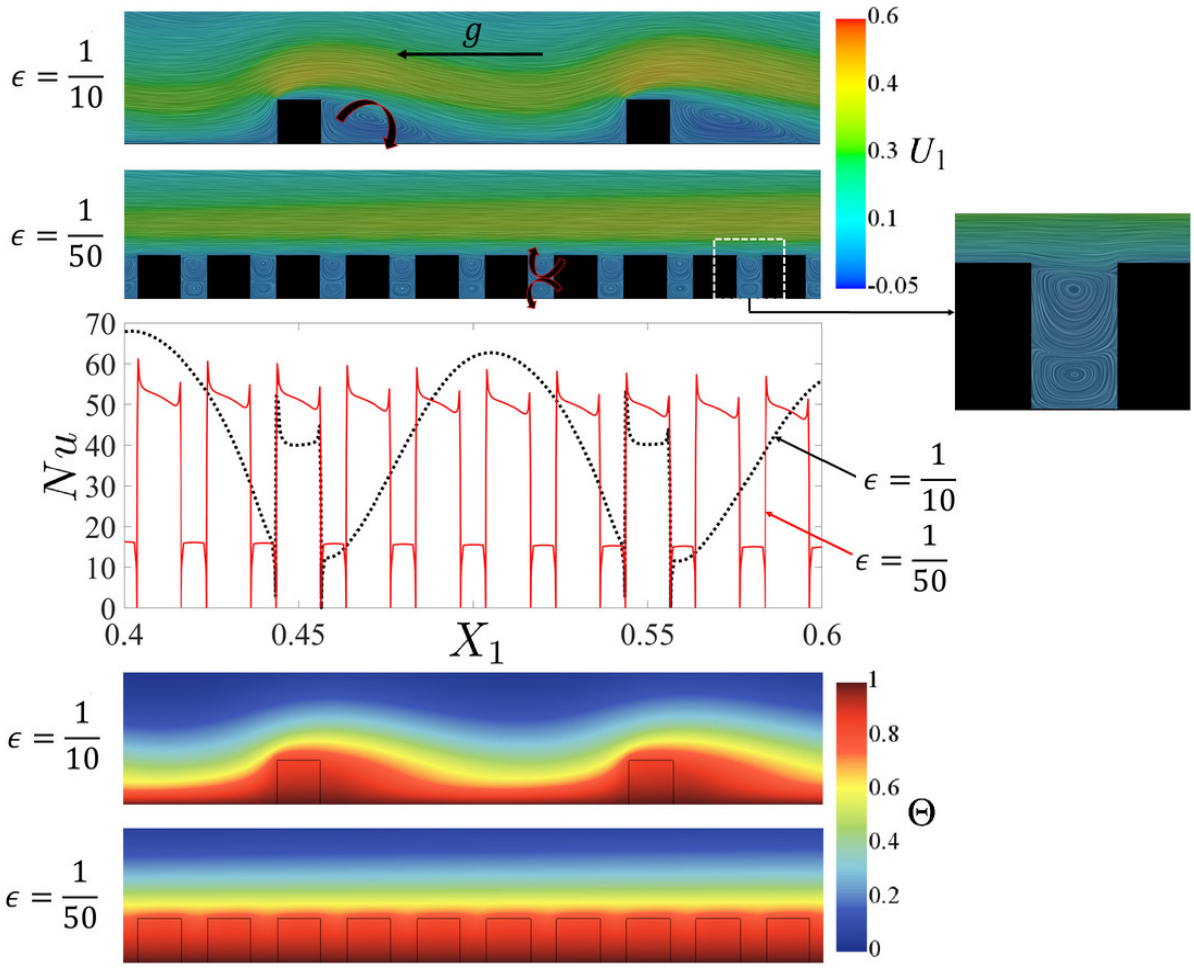

Figure 14: Contours of the fully-featured temperature and streamwise velocity fields next to the ribbed surface, for two different values of ϵ. Here, the conjugate heat transfer problems are considered at $\kappa = 4$ with $\frac{e}{L} = \frac{1}{80}$. The contours are displayed, and the behaviors of the local Nusselt number are plotted, over the region from $X_1 = 0.4$ to $X_1 = 0.6$.

thermal conductivity ($\kappa = 4$) overlying the isothermal baseplate. For the case of adiabatic ribs, the heat transfer performance monotonically deteriorates with the increase of N_{ribs} until the whole surface becomes thermally insulated ($\overline{Nu} = 0$ at $N_{ribs} = 80$). On the contrary, the behavior of the natural-convection heat transfer with the increase of N_{ribs} is complex when the ribs are thermally conducting, even if the thermal conductivity is small ($\kappa = 4$). For this case, two opposing effects mainly take place when the number of ribs increases: (i) the flow moves mostly above the ribs' outer rims, where local enhancement of the Nusselt number is expected (favorable effect); (ii) the inter-rib spaces become narrower, and the adverse effects of the hot dead recirculation zones between ribs on the local Nusselt number become therefore more pronounced. It is useful to interpret these phenomena using the illustrations in Fig. 14, which highlight the local enhancement of the heat transfer performance over the outer edges of the ribs, the early loss of mainstream reattachment to the baseplate when shifting to a denser roughness pattern ($\epsilon = \frac{1}{50}$) and

the consequent drop of the Nusselt number through these locations (compared to $\epsilon = \frac{1}{10}$), along with the local thickening of the thermal boundary layer. The two opposing effects discussed above justify the non-monotonic behavior of the average Nusselt number with the increase of the number of ribs for thermally-conducting ribs, displayed previously in Fig. 13.

4.4.2 *Validation of the model results*

For the cases initially studied with the feature-resolving approach (revisit the points plotted in Fig. 13), the homogenization-based model is further implemented and assessed. For each value of $N_{ribs} = \frac{1}{\epsilon}$, the rib size to pitch distance ratio is calculated as $\frac{e}{\ell} = \frac{e}{L} \times \frac{L}{\ell} = \frac{1}{80} \times N_{ribs}$. The value of $\frac{e}{\ell}$ is used to apply the compensation hypothesis given by eq. (19) and, together with each of the three considered values of κ, to evaluate the upscaled coefficients of the model; typical values of these coefficients are available in Fig. 3. Predictions for the average Nusselt number agree well with the reference results of the full simulations, as shown in Fig. 15, with deviations of the *corrected* model results always below 10% in magnitude.

5 CONCLUSIONS

The asymptotic homogenization technique was employed to upscale the steady conjugate heat transfer problem combining natural convection over a regularly micro-textured vertical surface and the thermal conduction through the roughness elements; the study of the effect of the ribs' thermal conductivity represents the novel contribution of the present work. The full domain was decomposed into two regions (microscopic/macroscopic), and two corresponding sub-problems were formulated. An asymptotic analysis was conducted in the near-wall, microscopic layer to eventually derive *effective* boundary conditions (eqs. (12-a to 12-d)), second-order accurate in terms of a small parameter $\epsilon = \frac{\text{rib pitch } (\ell)}{\text{plate height (L)}}$, for the velocity and temperature at a virtual plane interface of choice, where the two sub-problems are coupled. A significant difference from the model developed by Ahmed *et al.* (2022) is that the Robin-like temperature boundary condition includes a thermal-slip coefficient (λ_θ) which depends not only on the rib geometry but also on the rib-to-fluid thermal conductivity ratio, κ. The ability of the proposed conditions to mimic the effects of the surface microstructure on the macroscale flow behavior and heat transfer performance was assessed by validating the model against corresponding full feature-resolving simulations. Several case studies were investigated, for the particular case of spanwise-elongated square ribs, varying the number of elements attached to the surface and the thermal conductivity ratio. A correction of the model predictions for the Nusselt number was proposed over an initial distance of the surface, as per eq. (19), and was proved to

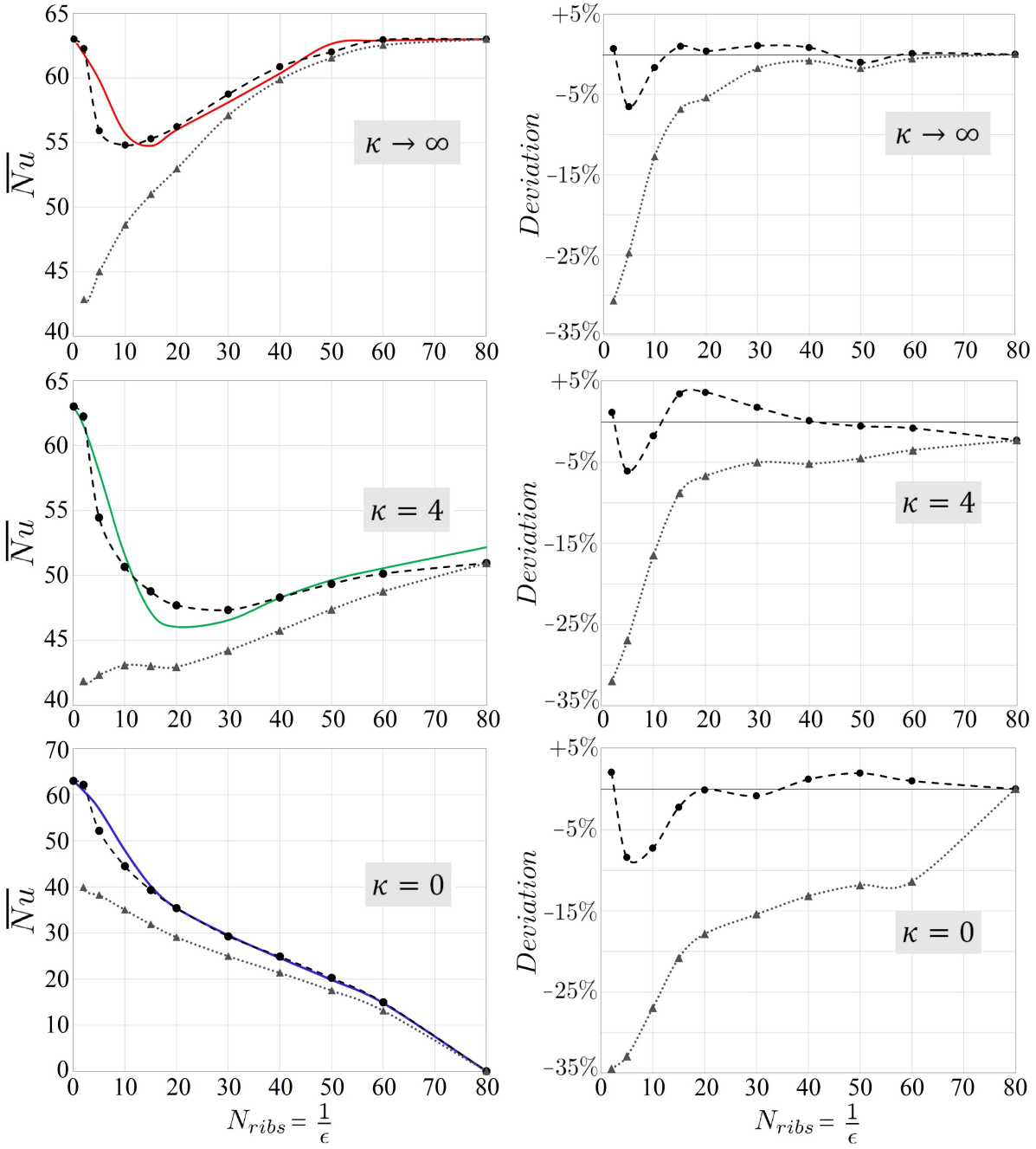

Figure 15: Effect of the number of ribs (N_{ribs}) on the average Nusselt number ($\overline{Nu}$), shown for: (top) isothermal ribs; (middle) a rib-to-fluid thermal conductivity ratio of 4; (bottom) adiabatic ribs. Results of the feature-resolving simulations (solid lines) are used as a reference to assess the accuracy of the *corrected* (dashed lines with filled circles) and the *uncorrected* (dotted lines with filled triangles) model predictions; percentage errors in the model results (*corrected* and *uncorrected*) are plotted in the right column. For all cases, it is $\frac{e}{L} = \frac{1}{80}$, $Gr \approx 2.78 \times 10^8$ and $Pr \approx 0.712$.

be efficient, especially at not-so-small values of ϵ when the scale separation assumption is gradually lost. Besides validation, the analysis of the numerical results revealed the following: (i) the presence of ribs has a negative effect on the heat transfer performance of the surface, compared with the smooth plate case, at least as long as the flow remains steady; (ii) the lower the thermal conductivity of the ribs, the more the overall convective heat transfer rate deteriorates, despite the local relative enhancements realized across the inter-rib regions of the baseplate; (iii) considering elements of low thermal conductivity as adiabatic ribs in the analysis may be critical, as we found that the performance of wooden ribs (for instance) is intermediate between the isothermal and the adiabatic limiting cases; (iv) as the number of perfectly conducting ribs increases, the average Nusselt number, $\overline{Nu}$, experiences a non-monotonic behavior, with an initial decrease and a subsequent increase up to the value of the isothermal flat surface, achieved when the ribs become contiguous; (v) as κ decreases, until reaching the case of adiabatic ribs, a monotonically negative effect of increasing the ribs' density is found.

This work aims to reveal the numerical advantages of the multiscale homogenization approach as a rapid and accurate tool for the analysis of complex phenomena amenable to separation of scales. The proposed model represents a more general/versatile version of the earlier ones by Ahmed *et al.* (2022) (valid exclusively for the case of perfectly-conducting ribs) and by Introïni *et al.* (2011) (where the buoyancy effect in the microscopic region was neglected). It is interesting to extend the present analytical procedure, along with numerical and experimental validation, to the case of three-dimensional patterns of wooden elements, for instance in-line/staggered arrangements of rib segments. This constitutes the main objective of ongoing research activity.

ACKNOWLEDGEMENTS

The authors would like to thank **Didier Lasseux** (University of Bordeaux, France) and **Francisco J. Valdés-Parada** (Universidad Autónoma Metropolitana-Iztapalapa, Mexico) for several interesting discussions on the subject of upscaling.

FUNDING

The financial support of the Italian Ministry of University and Research, program PRIN 2017, project 2017X7Z8S3 LUBRI-SMOOTH, is gratefully acknowledged.

REFERENCES

Ahmadi, M., Mostafavi, G. & Bahrami, M. 2014 Natural convection from rectangular interrupted fins. *Intl J. Therm. Sci.* **82**, 62–71.

Ahmed, E.N. 2023 Natural-convection heat transfer from regularly ribbed vertical surfaces: Homogenization-based simulations towards a correlation for the Nusselt number. *Numer. Heat Transfer A Appl.* **83** (9), 991–1013.

Ahmed, E.N., Bottaro, A. & Tanda, G. 2022 A homogenization approach for buoyancy-induced flows over micro-textured vertical surfaces. *J. Fluid Mech.* **941**, A53.

Bejan, A. 1993 *Heat Transfer*. New York, NY, USA: Wiley.

Bejan, A. & Lage, J.L. 1990 The Prandtl number effect on the transition in natural convection along a vertical surface. *ASME. J. Heat Transfer* **112** (3), 787–790.

Bhavnani, S.H. & Bergles, A.E. 1990 Effect of surface geometry and orientation on laminar natural convection heat transfer from a vertical flat plate with transverse roughness elements. *Intl J. Heat Mass Transfer* **33** (5), 965–981.

Cavazzuti, M. & Corticelli, M.A. 2008 Optimization of a buoyancy chimney with a heated ribbed wall. *Heat Mass Transfer* **44** (4), 421–435.

Churchill, S.W. & Chu, H.H.S. 1975 Correlating equations for laminar and turbulent free convection from a vertical plate. *Intl J. Heat Mass Transfer* **18** (11), 1323–1329.

El Ghandouri, I., El Maakoul, A., Saadeddine, S. & Meziane, M. 2020 Design and numerical investigations of natural convection heat transfer of a new rippling fin shape. *Appl. Therm. Eng.* **178**, 115670.

Guglielmini, G., Nannei, E. & Tanda, G. 1987 Natural convection and radiation heat transfer from staggered vertical fins. *Intl J. Heat Mass Transfer* **30** (9), 1941–1948.

Hærvig, J. & Sørensen, H. 2020 Natural convective flow and heat transfer on unconfined isothermal zigzag-shaped ribbed vertical surfaces. *Intl Commun. Heat Mass Transfer* **119**, 104982.

Introïni, C., Quintard, M. & Duval, F. 2011 Effective surface modeling for momentum and heat transfer over rough surfaces: Application to a natural convection problem. *Intl J. Heat Mass Transfer* **54** (15-16), 3622–3641.

Joshi, Y., Willson, T. & Hazard, S.J., III 1989 An experimental study of natural convection from an array of heated protrusions on a vertical surface in water. *ASME J. Electron. Packag.* **111** (2), 121–128.

Lienhard, J.H., IV & Lienhard, J.H., V 2019 *A Heat Transfer Textbook,* 5th ed. Cambridge, MA, USA: Phlogiston Press.

Nelson, L., Sekhon, K. & Fritz, J. 1978 Direct heat pipe cooling of semiconductor devices. In *the 3rd Int. Heat Pipe Conf.,* Palo Alto, California, USA. (doi: 10.2514/6.1978-450).

Nishikawa, M., Otomo, H., Yoshida, Y., Deguchi, J., Tsukamoto, M. & Yamamoto, T. 2020 The cooling mechanism of minuscule ribbed surfaces. *Sci. Rep.* **10** (1), 5635.

Peterson, G.P. & Ortega, A. 1990 Thermal control of electronic equipment and devices. *Adv. Heat Transfer* **20**, 181–314.

Tanda, G. 1997 Natural convection heat transfer in vertical channels with and without transverse square ribs. *Intl J. Heat Mass Transfer* **40** (9), 2173–2185.

Tanda, G. 2008 Natural convective heat transfer in vertical channels with low-thermal-conductivity ribs. *Intl J. Heat Fluid Flow* **29** (5), 1319–1325.

Tanda, G., Ahmed, E.N. & Bottaro, A. 2023 Natural convection heat transfer from a ribbed vertical plate: Effect of rib size, pitch, and truncation. *Exp. Therm. Fluid Sci.* **145**, 110898.

Tsuji, T. & Nagano, Y. 1988 Characteristics of a turbulent natural convection boundary layer along a vertical flat plate. *Intl J. Heat Mass Transfer* **31** (8), 1723–1734.

Van Leer, B. 1979 Towards the ultimate conservative difference scheme. V. A second-order sequel to Godunov's method. *J. Comput. Phys.* **32** (1), 101–136.

Van Leer, B. & Nishikawa, H. 2021 Towards the ultimate understanding of MUSCL: Pitfalls in achieving third-order accuracy. *J. Comput. Phys.* **446**, 110640.

Venkatakrishnan, V. 1993 On the accuracy of limiters and convergence to steady state solutions. In *the 31st Aerospace Sci. Meet.,* Reno, Nevada, USA. (doi: 10.2514/6.1993-880).

Yao, L.-S. 2006 Natural convection along a vertical complex wavy surface. *Intl J. Heat Mass Transfer* **49** (1-2), 281–286.

Zhang, K., Li, M.-J., Wang, F.-L. & He, Y.-L. 2020 Experimental and numerical investigation of natural convection heat transfer of W-type fin arrays. *Intl J. Heat Mass Transfer* **152**, 119315.

Zhou, Z., Tkachenko, S., Bahl, P., Tavener, D., de Silva, C., Timchenko, V., Jiang, J.Y., Keevers, M. & Green, M. 2022 Passive PV module cooling under free convection through vortex generators. *Renew. Energ.* **190**, 319–329.

SUPPLEMENTARY MATERIAL

This part includes supplementary data related to the main article "Conjugate natural convection along regularly ribbed vertical surfaces: A homogenization-based study" by **Essam Nabil Ahmed**, **Alessandro Bottaro** and **Giovanni Tanda.**

The numerical results obtained by solving sample auxiliary systems through a representative x_1-periodic unit cell in the microscopic domain are presented and discussed for the case of two-dimensional, transverse square ribs, with the outer boundary located at $x_2 = y_\infty = 5$.

For the Stokes problem forced by the outer shear stress in the streamwise direction (S_{12}), i.e. eqs. (6) in the main article (with the index k set to 1), the results of $\breve{u}_{11}$ near the rib are shown in Fig. S1, varying the rib size to pitch distance ratio ($\frac{e}{\ell}$). It is interesting to realize how the complexity of the pattern within the inter-rib region becomes more pronounced with the increase of ($\frac{e}{\ell}$), in analogy to the Stokes lid-driven cavity flow.

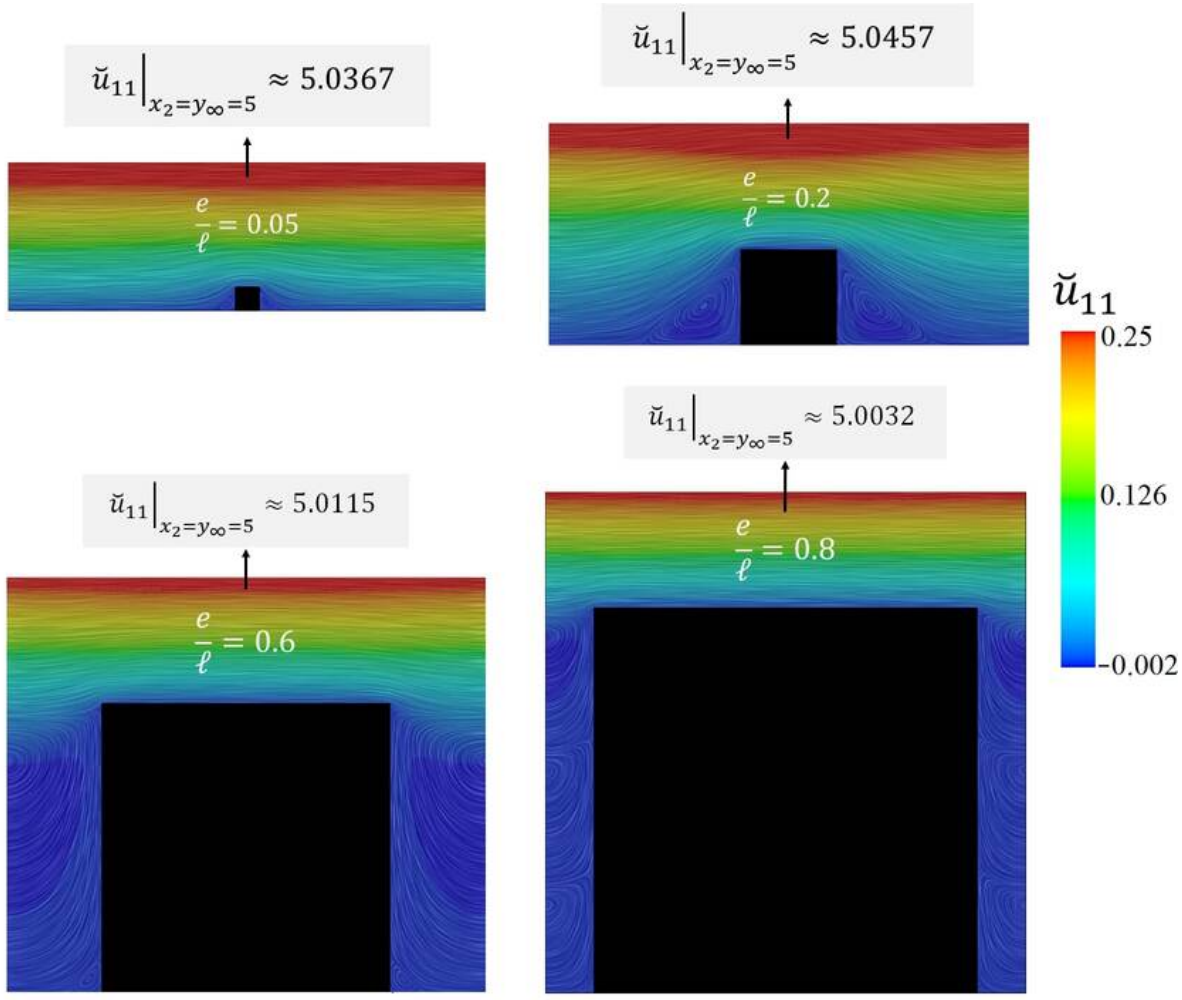

Figure S1: Numerical results of $\breve{u}_{11}$ in the vicinity of the ribbed wall, for different values of the rib size to pitch distance ratio ($\frac{e}{\ell}$). The values of $\breve{u}_{11}$ at the outer boundary ($y_\infty = 5$) are given. The superimposed lines are tangent to the vector $\breve{u}_{i1}$.

The numerical solution of the thermally-coupled Laplace system governing $\tilde{\theta}$ and

$\tilde{\phi}$, i.e. eqs. (9) in the main article, are displayed in Fig. S2 at two values of $(\frac{e}{\ell})$ for three different choices of the rib-to-fluid thermal conductivity ratio (κ). For the case of adiabatic ribs ($\kappa = 0$), it is sufficient to solve the problem in the fluid phase only, imposing zero normal gradient of $\tilde{\theta}$ at $\mathcal{I}_{rf}$. If the ribs are isothermal ($\kappa \to \infty$), a uniform value of $\tilde{\theta} = 0$ is set at $\mathcal{I}_{rf}$. This is based on the fact that isothermal ribs have by definition a uniform $\tilde{\phi}$ field so that the value of $\tilde{\phi}$ at $\mathcal{I}_{rf}$ is identical to its value at $\mathcal{I}_{br}$. Finally, for a finite value of κ (for instance, $\kappa \approx 4$), the solid/fluid coupled problem is solved. The isotherms near the boundary have a significantly different behavior as κ is varied; for example, for adiabatic ribs the values of $\tilde{\theta}$ are significantly larger than for thermally conducting ribs, especially at large $(\frac{e}{\ell})$.

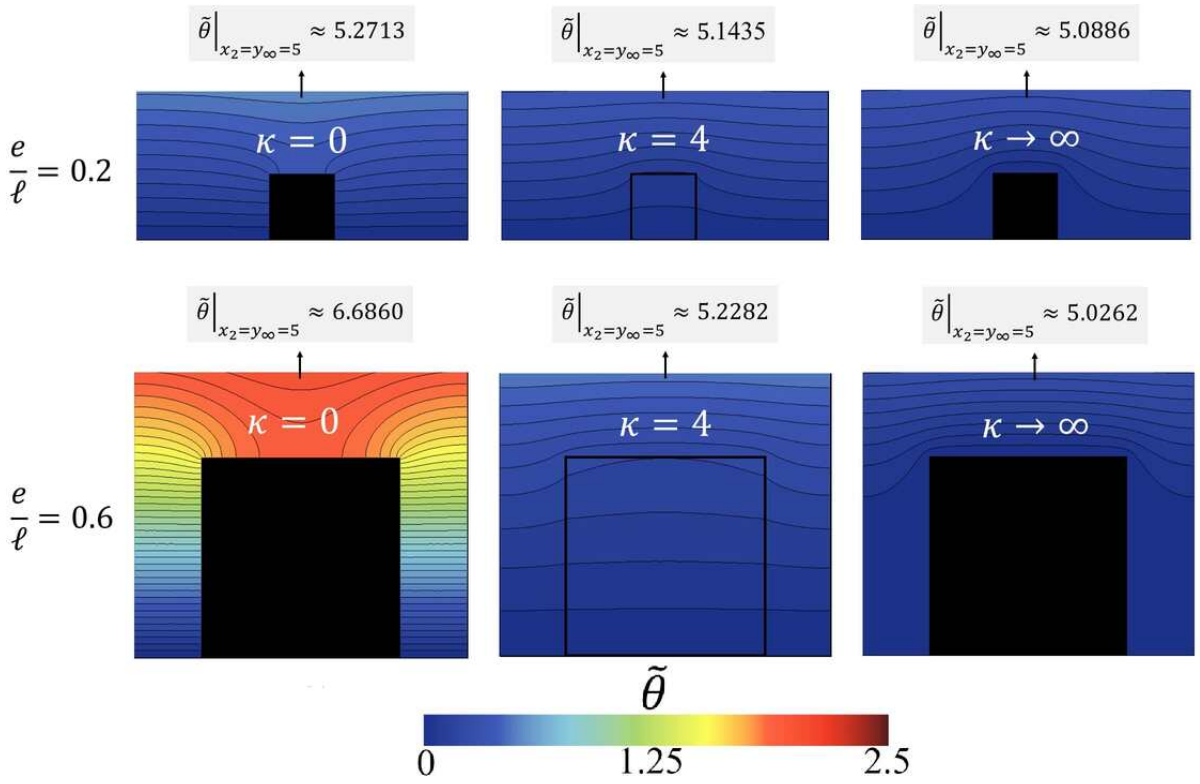

Figure S2: Contours of $\tilde{\theta}$ close to the ribbed wall at (top) $\frac{e}{\ell} = 0.2$ and (bottom) $\frac{e}{\ell} = 0.6$, for three values of the thermal conductivity ratio representing: (left) adiabatic ribs; (middle) conjugate heat transfer at $\kappa = 4$; (right) isothermal ribs. The contours of $\tilde{\phi}$ through the rib are also shown when $\kappa = 4$.

PAPER B4

Natural convection heat transfer from a ribbed vertical plate: Effect of rib size, pitch, and truncation [1]

Giovanni Tanda[a] , **Essam Nabil Ahmed**[b] and **Alessandro Bottaro**[b]

[a] *DIME, Università di Genova, via Montallegro 1, Genova, 16145, Italy*
[b] *DICCA, Università di Genova, via Montallegro 1, Genova, 16145, Italy*

Buoyancy-induced flows over ribbed vertical surfaces involve complex thermal and dynamic interactions between the mainstream and the surface texture, yielding contrasting effects on the heat transfer performance of the heated plate; proper analysis of the overall effect on the heat transfer rate is essential for efficient operation and optimization purposes. The present work pursues an insight into the different factors controlling this problem. Natural convection heat transfer from a vertical plate of 0.5 m height, regularly roughened with wooden transverse square ribs, is experimentally investigated. The surface temperature of the baseplate is varied so that a range of the plate Rayleigh number (Ra) from 3.4×10^8 to 4.9×10^8 is covered. The density of the roughness pattern and the rib pitch-to-height ratio (P/e) are varied by changing the number of ribs attached to the surface (from 10 to 40 rib rows) and using three different square cross-sections (of side lengths 2, 3, or 5 mm). The experimental work relies on the schlieren optical technique, through which the thermal boundary layer is visualized and the Nusselt number distribution is acquired. Analysis of the results reveals that enhancement of the local Nusselt number, relative to a corresponding smooth surface, may be attained only at the central part of the inter-rib region; this occurs exclusively for relatively large values of P/e. At a later stage, the effectiveness of rib truncation in enhancing the heat transfer from the baseplate is explored. Three staggered arrangements are considered, by varying the number of rib segments per row, and heat transfer enhancement, sensitive to the number of rib segments per row, is found. This paper also provides insight into the role of thermal-field disturbances close to turbulent transition, and sheds light on the potential of truncated ribs to amplify such perturbations.

[1] The Version of Record of this manuscript has been published and is available in: *Experimental Thermal and Fluid Science* **145** (2023) 110898. https://doi.org/10.1016/j.expthermflusci.2023.110898

1 INTRODUCTION

Natural convection heat transfer is a simple and reliable mechanism that does not require active devices such as fans or pumps to promote fluid motion. The effectiveness of natural convection is limited by the lower heat transfer coefficients (relative to forced convection) associated with the low buoyancy-induced flow rates. Strategies to enhance the heat transfer rate from a vertical surface include the addition of fins (which basically increase the heat transfer surface area) or large-scale roughness elements such as surface protrusions (with the purpose of increasing the heat transfer coefficient). In some applications (electronic equipment, building facades) protrusions exist naturally. Roughness elements affect the heat transfer effectiveness due to the surface alteration and the possible premature transition to turbulence. Fujii *et al.* (1973) were among the first to investigate the influence of various surface roughness elements on natural convection. Their experiments, conducted for water and oil flowing along a vertical cylinder, revealed little variations in heat transfer coefficient compared with the smooth surface (with slight reductions for water and slight increases for oil) and no effect of roughness on the upper limit of the laminar region. Bhavnani & Bergles (1990) studied the effect of repeated square ribs (of low and high thermal conductivity) and steps on natural convection heat transfer from a vertical isothermal surface. They found a substantial reduction of heat transfer performance associated with ribs due to the stagnation zone induced downstream and upstream of each rib (especially when the ribs have high thermal conductivity) and an increase in the heat transfer rate of up to 23% (as compared with a plain surface of equal projected area) for properly sized stepped surfaces. A few years later, Tanda (1997) found that repeated, high-thermal-conductivity, square ribs reduce heat transfer performance in asymmetrically heated vertical channels (both in terms of average heat transfer coefficient and heat transfer rate), particularly when the channel is narrow. The use of low-thermal-conductivity ribs yielded local heat transfer coefficients higher than that for a smooth surface, at the same elevation, just downstream of the ribs (where the main flow reattachment to the wall occurs), while, on average, the heat transfer performance even with low-thermal-conductivity ribs was degraded (Tanda, 2008). Studies documented in Refs. (Bhavnani & Bergles, 1990; Tanda, 1997, 2008) were conducted experimentally, using air as the working fluid at a relatively low Rayleigh number (of the order of 10^7), well within the laminar regime. More recently, Hærvig & Sørensen (2020) numerically studied the effect of zigzag-shaped ribs, finding, again for air in the laminar regime, an increase in average heat transfer coefficient by more than 4% (compared to the flat surface) and more than 11% when accounting for the increase in heat transfer area. Nghana *et al.* (2022) performed numerical simulations of turbulent natural convection in vertical and inclined channels with repeated square, triangular, and semi-circular ribs; they found significant heat transfer enhancements compared with the smooth channel, with the triangle-shaped ribs giving the best heat transfer performance. Based on the available studies of natural convection heat transfer in vertical channels or along unbounded vertical surfaces, the presence of repeated protrusions negatively affects the heat transfer performance (square ribs) or leads to little enhancements (steps and zigzag-shaped ribs) within the laminar regime, while they are more effective in the turbulent regime.

Even though some literature studies (e.g., Refs. (Bhavnani & Bergles, 1991; Yao, 2006)) suggest that large-scale roughness elements can trigger an early transition to turbulence, to the authors' best knowledge no systematic studies on natural convection heat transfer from vertical surfaces with repeated ribs addressed this issue, and few experimental and numerical results (for a limited number of geometries) are available either in the laminar or in the fully turbulent flow regime. This means that there is no evidence, in the literature, of premature transition to turbulence induced by repeated ribs or by macro-roughness elements of different shape and size.

A common practice to promote turbulence and heat transfer enhancement in forced convection is to use broken ribs, periodically deployed on the heat transfer surface. Broken ribs perform better than continuous ribs due to the higher turbulence levels induced (see, for instance, (Cavallero & Tanda, 2002)). However, the fluid motion under free convection conditions is not externally imposed but derives from a balance between buoyancy and viscous forces; therefore, turbulence promoters, which have proved to be effective in forced convection, may induce a weak buoyant flow in free convection and fail to yield premature transition to turbulence. Onbasioglu & Onbaşıoğlu (2004) considered the effect of two truncated ribs of lengths equal to 67% of the surface width and placed staggered on the baseplate. Experiments were performed by varying the height and the inclination angle of the ribs. Imbriale *et al.* (2012) experimentally investigated the effect of single or two staggered rows of ribs inclined at different angles and single or two staggered rows of V-shaped ribs. Both studies (Onbasioglu & Onbaşıoğlu, 2004; Imbriale *et al.*, 2012) indicated that ribs provide significant improvements in local and average heat transfer coefficient (compared with the flat vertical surface), even though the flow regime was laminar. Being able to favourably redirect the flow, interrupted roughness elements yield a favourable flow pattern, reducing the impact of inactive heat transfer regions typically occurring immediately upstream and downstream of continuous rib. Smirnov *et al.* (2018) numerically found that a couple of short and aligned ribs were able to trigger transitional processes in the free convection boundary layer.

Based on the above discussion of the literature, some issues remain unresolved. For instance, the survey of the literature did not reveal any systematic analysis concerning the effects of the main geometric parameters of ribs on heat transfer from a vertical plate. At the same time, the potential of triggering an early transition of the boundary layer has been previously unaccounted for, and the practice of interrupting the ribs to pursue the enhancement of the heat transfer performance has not been unveiled until now. To address these issues, in this work experiments have been performed to investigate natural convection heat transfer from an isothermal vertical plate with continuous square ribs having different size (from 2 to 5 mm) and pitch (from 12.5 to 50 mm), varying the wall-to-ambient temperature difference to achieve thermal conditions not far, for the smooth plate, from the upper threshold of the laminar flow regime. For the intermediate values of the rib size (3 mm) and rib pitch (25 mm), continuous ribs have been replaced by truncated ribs, having 3, 6, or 12 segments per row and attached in a staggered arrangement. A schlieren optical apparatus was employed to gain qualitative and quantitative information on heat transfer characteristics; the optical field encompassed the top 15 cm

of the heated plate (out of the 50 cm overall height), where the onset of transition to turbulence, if any, is likely to be observed.

2 EXPERIMENTAL SETUP AND PROCEDURE

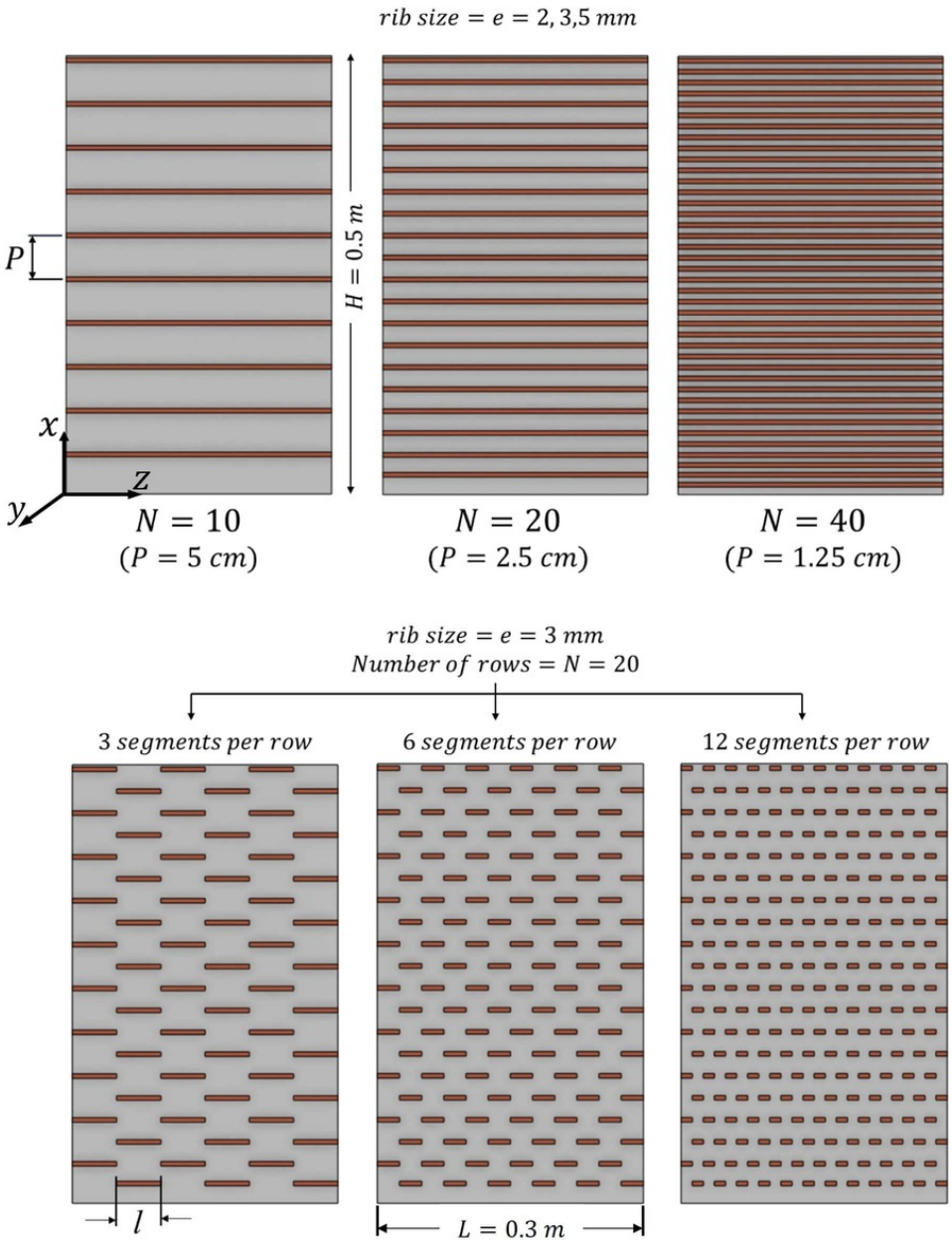

Figure 1: Sketch of the heated plate (frontal view): continuous ribs at different pitch P, with N representing the number of rib rows (top), truncated ribs of different length ℓ and different number of segments per row (bottom). H is the vertical plate height, L is the spanwise length of the plate, and e is the size of the square ribs.

Table 1: Description of rib configurations and main geometric parameters.

Rib type	Number of rib rows N	e (mm)	P (mm)	ℓ (mm)	Number of truncated ribs per row	P/e	e/H	ℓ/L
continuous	10	2	50	-	-	25	0.004	-
continuous	20	2	25	-	-	12.5	0.004	-
continuous	40	2	12.5	-	-	6.25	0.004	-
continuous	10	3	50	-	-	16.67	0.006	-
continuous	20	3	25	-	-	8.33	0.006	-
continuous	40	3	12.5	-	-	4.17	0.006	-
continuous	10	5	50	-	-	10	0.01	-
continuous	20	5	25	-	-	5	0.01	-
continuous	40	5	12.5	-	-	2.5	0.01	-
truncated	20	3	25	50	3	8.33	0.006	0.1667
truncated	20	3	25	25	6	8.33	0.006	0.0833
truncated	20	3	25	12.5	12	8.33	0.006	0.0417

The test surface was an aluminium plate, 0.5 m high, 0.3 m large, and 0.005 m thick, connected to a plane electrical heater. Since the high thermal conductivity of aluminium and the relatively large plate thickness promote an efficient redistribution of heat by conduction within the plate, the plate material was expected to be virtually isothermal. The heater-plate assembly, suspended at about 1.5 m from the floor, was insulated on one side in order to convey as much heat flux as possible towards the side exposed to the ambient air. To avoid significant sidewise air entrainment and minimize disturbances from the environment, the heated plate was bounded on both sides by two glasses (10 cm long and 50 cm high), and shrouded by a frontal polystyrene wall, placed at a distance from the heated plate approximately equal to half of the plate height. In such a way, the buoyant airflow, at ambient temperature, is mainly allowed to enter the test section from the bottom side and exit from the upper side after having flowed along the heated surface. The plate temperature was evaluated as the average among the readings given by several 0.5 mm-dia thermocouples (calibrated to ± 0.1 K) embedded at different plate elevations through small holes drilled into the material. The ambient air temperature was calculated by averaging the readings of three thermocouples situated below the heated plate.

Repeated ribs, of square cross-section, were attached to the heated plate in order to evaluate their effect on heat transfer performance. Prior experiments performed by Tanda (1997, 2017) for rib-roughened vertical plates, with air or water as convective fluid, considered metallic ribs integral to the baseplate to guarantee the absence of thermal contact resistance. However, the fabrication of such test sections is very expensive and does

not permit a systematic study of the effect of the main geometric parameters. For this reason, ribs were made of wood, due to the low cost and the ease of cutting and application. Three different rib sizes were considered, specifically $e = 2$, 3, and 5 mm, where e is the side length of the ribs. Regardless of the rib size, a different number of rib rows ($N = 10$, 20, or 40) were regularly deployed along the plate surface height. The majority of experiments were conducted with continuous ribs. Additional tests were subsequently performed with truncated ribs; i.e., rows of three, six, or twelve segments periodically arranged in a staggered arrangement. Details of rib configurations are reported in Table 1 and Fig. 1.

A schlieren optical system was used to visualize the thermal boundary layer and to evaluate the local, natural convection heat transfer coefficient. Optical methods are extremely versatile tools for making quantitative measurements of thermal phenomena because they allow a real-time, non-intrusive analysis over the whole optical field (Hauf & Grigull, 1970; Merzkirch, 1974). A large variety of optical techniques are currently employed in experimental heat transfer and fluid flow, such as the index-of-refraction optical methods. In this category of methods, among which interferometry and schlieren, the index of refraction (or its spatial derivative) of a medium is measured, and from this the temperature distribution through the medium is determined. Some applicative examples of these techniques, even in parallel, for gases and liquids, are provided in Refs. (Kleine *et al.*, 2006; Ambrosini & Tanda, 2006; Hargather & Settles, 2012; Raffel, 2015; Jain *et al.*, 2016; Settles, 2018; Vyas *et al.*, 2018; Schulz *et al.*, 2020). An exhaustive description of the schlieren apparatus employed is given in Refs. (Tanda, 1997, 2008, 2017, 1993; Devia *et al.*, 1994; Tanda & Devia, 1998; Tanda *et al.*, 2014). Basically, it consists of a white light beam (composed of parallel rays) crossing the test section, a concave mirror (i.e., the schlieren mirror), which focuses the light onto its focal plane (i.e., the cut-off plane), a filter, and a camera to acquire a real image of the test section. As shown in Fig. 2, when a focal filament (for instance, a thin dark strip or wire) is used as a filter, and no thermal gradients are present in the air crossed by the light beam, all light rays are intercepted by the filter when it is placed on the focus of mirror (and the image formed on the camera will be uniformly dark). In this work, the filter has been obtained by photographing a violet strip using a slide film. The slide produced in this manner, consisting of a 370 μm-wide, transparent, violet band, was directly used as focal filament filter. When thermal gradients (in the y-direction of Fig. 2) are present, individual light rays undergo angular deflections whose extent is related to the magnitude of the gradient; consequently, the corresponding spots appear bright in the camera, permitting a reliable visualization of the thermal boundary layer (more precisely of all air particles with a non-zero thermal gradient). The angular deflection α_y of a given light ray (i.e., passing through a given point of coordinates x, y) can be measured by moving the filter (connected to a micrometer) along the focal plane of the schlieren mirror until the point of interest appears coloured by the same colour adopted for the filter (violet). It can be demonstrated (Goldstein, 1976) that the angular deflection α_y is given by the ratio between the filter displacement and the focal length of the mirror (since the angular deviation is small, $\tan(\alpha_y) \approx \alpha_y$).

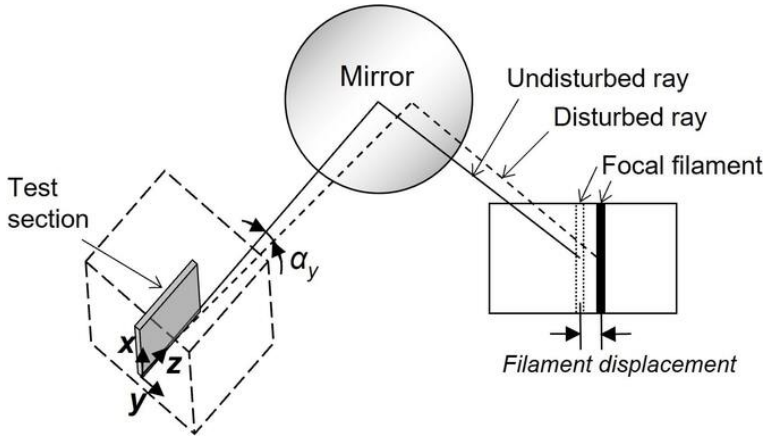

Figure 2: Quantitative schlieren (focal filament method): the angular deflection of perturbed light rays is detected by shifting the focal filament filter in the focal plane of the schlieren concave mirror.

The local heat transfer coefficient is now introduced as follows:

$$h = -k_{air,w} \frac{(\partial T/\partial y)_w}{T_w - T_{air}}, \tag{1}$$

where T_w and T_{air} are the plate and the ambient air temperatures, respectively, $(\partial T/\partial y)_w$ is the air temperature gradient, in the direction y normal to the heated plate, evaluated at the wall, and $k_{air,w}$ is the air thermal conductivity evaluated at the wall temperature. Due to the relation between angular deflection of light and thermal gradient of the crossed fluid, the heat transfer coefficient h can be directly calculated by measuring the deflection of light passing in the vicinity of the wall at the desired location, using the following formula (see, for instance, Ref. (Tanda, 1997)):

$$h = \frac{k_{air,w}\, \alpha_{y,w}\, T_w^2}{K(T_w - T_{air})}, \tag{2}$$

where $\alpha_{y,w}$ is the angular deflection, along the y-direction, of the light ray passing in the vicinity of the wall (i.e., at $y = 0$), and K is a constant (equal to about 0.024 mK in these experiments), which depends on some air properties (Gladstone-Dale and ideal gas constants, index of refraction, pressure) and the length of the plate in the direction of light beam propagation (z-coordinate of Fig. 2). Eq. (2) provides the heat transfer coefficient for a vertical surface, which depends of the thermal gradients in the y-direction. In principle, since the focal filament is mounted on a holder able to rotate through an arbitrary angle on the focal plane of the schlieren mirror, the technique allows light deflections along any direction (on a plane normal to the light beam propagation) to be detected. In this research, attention is focused on vertical inter-rib regions (and not, for instance, on horizontal sides of ribs); hence, the angular deviation along the y-direction is the only optical data on which the heat transfer coefficient depends.

Moreover, even though the schlieren technique may exploit, in some circumstances, a tomographic treatment of optical data to get local temperature or heat transfer coefficient

results for three-dimensional flows (Devia & Tanda, 2000), Eq. (2) assumes the thermal field to be two-dimensional, i.e., independent of the z-coordinate; otherwise, it is still valid but the calculated heat transfer coefficient corresponds to the value averaged along the plate spanwise length L, that is the plate dimension along the z-coordinate. This means that any three-dimensional feature of the flow emerging from the insertion of ribs can be observed only on a line-averaged basis. To partially overcome this issue, schlieren measurements were supplemented by the detection of air temperature fluctuations in the boundary layer by using a miniature thermocouple with an exposed junction, able to travel along the direction normal to the plate surface and to be located at any arbitrary position along the vertical and spanwise coordinates. A National Instrument acquisition unit (NI PXIe-1078 equipped with a NI TB-4353 module) was used to acquire the air temperature measurements at a frequency of 50 Hz.

The uncertainty in the results (at the 95% confidence level) was evaluated based on the root-sum-square of the contributions made by the uncertainties in each of the individual measurements. The details of the procedure followed for the evaluation of the experimental uncertainty are provided in previous literature studies, for instance Refs. (Tanda, 1993, 1997; Devia *et al.*, 1994). The main source of error in the calculation of the local heat transfer coefficient h, according to Eq. (2), is associated with the light ray displacement readings (i.e., the filament displacement in Fig. 2). As reported by Tanda (1997), the accuracy of the measurement of the light ray displacement improves as its value increases. For the present experiments, the light displacement at the focal plane of the schlieren mirror was typically between 3.5 and 1.5 mm, with associated errors ranging from 9 to 14%, increasing with the reduction of the light ray displacement. As errors in the wall-to-fluid temperature difference are accounted for, the uncertainty in h (and in Nusselt number) values falls into the $\pm 10 - 15\%$ range, while the uncertainty in Rayleigh number is estimated to be $\pm 5\%$.

Tests were carried out by delivering electrical power to the heater through a DC power supply, adjusting the input voltage in order to achieve the desired wall-to-fluid temperature difference. The degree of temperature uniformity of the plate was typically within $\pm 3\%$ of the mean wall-to-ambient temperature difference. The plate surface exchanges heat with the environment by natural convection and radiation. For the surface regions not covered by ribs, the radiant component is expected to be low, due to the low thermal emittance of aluminium ($\epsilon \approx 0.1$). Moreover, the schlieren method detects the air thermal gradient in the vicinity of the wall, which is unaffected by radiation, whose measurement or calculation is not required for the evaluation of the convective heat transfer coefficient. The ribs glued to the aluminium plate have a low thermal conductivity ($k_{rib} \approx 0.1$ W/mK) but a high emittance ($\epsilon_{rib} \approx 0.9$); hence, the amount of heat dissipated, by convection and radiation, from the ribs' surfaces is not negligible. In fact, measurements of surface temperature $T_{rib,w}$ of rib tips, by an infrared camera, revealed values not far from the aluminium surface temperature T_w; in dimensionless terms, $(T_{rib,w} - T_{air})/(T_w - T_{air})$ ranged from 0.8 for the smaller ribs ($e = 2$ and 3 mm) to 0.7 for the larger ribs ($e = 5$ mm). Increasing the rib length leads to a reduction of the fin efficiency evaluated according to the one-dimensional fin model (and considering the

rib as a small fin) and thus to a larger base-to-tip temperature drop. Schlieren measurements targeted only the baseplate regions not covered by ribs, ignoring any heat transfer contribution arising from the ribs' surfaces.

After the initiation of each test, steady state was achieved in about $6-7$ hours. At the end of the test, air and wall temperatures were acquired and schlieren measurements were performed. Since the optical field encompassed a circular region having a diameter of about 20 cm, measurements of the angular deflection of light rays and visualization of the thermal boundary layer were limited to the top third of the heated plate, where transition to turbulence, if any, is more likely to occur. Measurements of air temperature inside the boundary layer were performed for a number of representative tests, over a time period of about 15 minutes, at different distances from the plate surface and locations along the vertical and spanwise directions.

The Rayleigh and Nusselt numbers, based on the plate height H or the local vertical position x, are determined from

$$Ra = \frac{\beta g (T_w - T_{air}) H^3}{\nu \alpha}, \tag{3}$$

$$Nu = \frac{h\,H}{k_{air}}, \tag{4}$$

$$Ra_x = \frac{\beta g (T_w - T_{air}) x^3}{\nu \alpha}, \tag{5}$$

$$Nu_x = \frac{h\,x}{k_{air}}, \tag{6}$$

where h is the local heat transfer coefficient, given by Eq. (2), g is the gravitational acceleration, and β, α, ν, and k_{air} denote the coefficient of thermal expansion, the thermal diffusivity, the kinematic viscosity, and the thermal conductivity of air, respectively. Air properties have been evaluated at the film temperature given by $(T_w + T_{air})/2$, except for β, evaluated at the ambient air temperature, as suggested in Refs. (Raithby & Hollands, 1985; Tsuji & Nagano, 1988).

For each rib configuration, the wall-to-fluid temperature was varied from 32 to 51 K in order to span the range of Ra from 3.4 to 4.9×10^8. Each test, at a given wall-to-fluid temperature difference, was repeated from 2 to 5 times and local heat transfer results were averaged among identical tests to reduce the random error.

3 RESULTS AND DISCUSSION

In this section, experimental results are presented, for the smooth plate and for each rib configuration considered. First, attention is focused on the effect of the rib size and the rib pitch on local heat transfer results. Second, the effect of rib truncation is investigated.

Third, the intensity of air temperature fluctuations in the boundary layer is presented and discussed, together with qualitative visualizations of the flow in the boundary layer.

3.1 Nusselt number result

3.1.1 *The smooth plate*

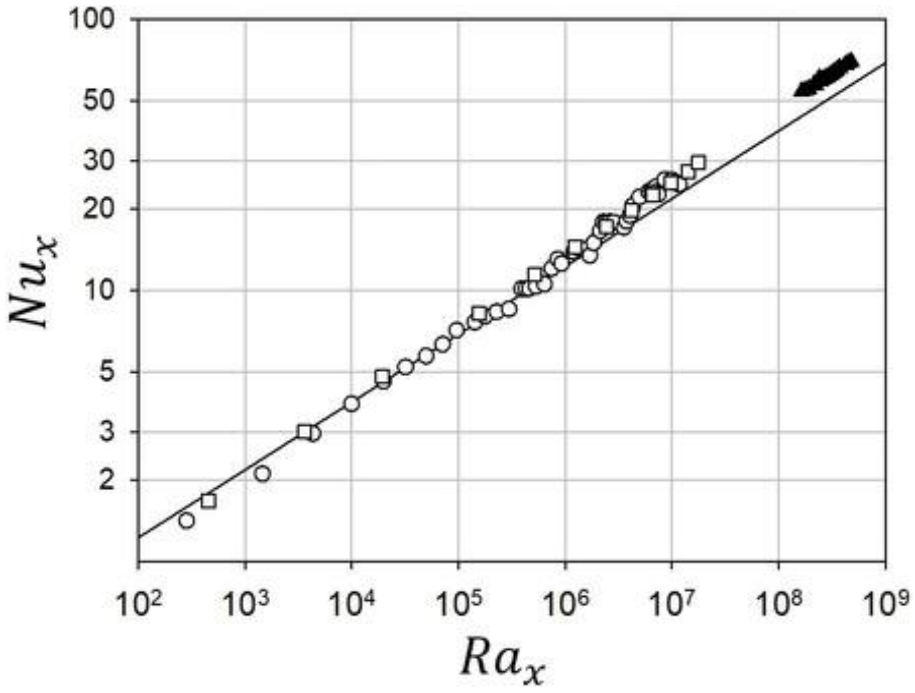

Figure 3: Local Nusselt number versus local Rayleigh number for a smooth, isothermal, vertical plate: comparison between Ostrach's solution ((Ostrach, 1953), solid line), literature results (empty circles (Bhavnani & Bergles, 1990), empty squares (Tanda, 1997)) and present results (filled triangles).

Heat transfer results for the smooth heated plate, in terms of the Rayleigh and the Nusselt numbers based on local elevation x, are summarized in Fig. 3. The same plot reports the analytical solution by Ostrach (1953) for a vertical isothermal flat plate and air as the convective fluid, as well as other experimental data extracted from Bhavnani & Bergles (1990) (by holographic interferometry) and Tanda (1997) (by schlieren technique, same apparatus as in the present contribution).

Ostrach's theoretical solution pertains to the laminar regime and therefore its application requires no evidence of transitional events. Interpretation of transition was provided Godaux & Gebhart (1974) who found a distinct thermal transition mechanism. The first signs of turbulent disturbances appear in the velocity boundary layer without

alteration of the temperature profile from the laminar form until reaching a point, further downstream, where the velocity disturbances become strong enough to change the temperature profile (the onset of thermal transition). The thermal transition region ends with the development of a completely turbulent boundary region where all flow variables fluctuate randomly. Nevertheless, no clear definition of the parameters ruling the transition of the buoyancy-driven flow over a vertical isothermal plate is apparent from the literature. Bejan & Lage (1990) showed that the Grashof number (and not the Rayleigh number = Grashof number × Prandtl number) marks the transition in all fluids, with a value of order 10^9 at the beginning of transition (i.e., Rayleigh number of 0.7×10^9 when air is the convective fluid). Cheesewright (1968), underlining the arbitrary nature of former attempts to specify beginning and end of transition, indicated a Grashof number of 2×10^9 as the condition at which significant fluctuations first appear in the boundary layer without significant changes in the mean temperature profiles or in the trend of heat transfer data; major changes in mean temperature profiles and heat transfer rates were found to appear at a Grashof number of 5×10^9 and up to 8×10^9; the amplitude of temperature fluctuations then decreased with the Grashof number from 8×10^9 to 2×10^{10}, while beyond the last threshold it remained approximately constant (meaning that the fully turbulent regime had been reached). It is worth noting that the large disagreements in the experimental evaluation of the critical Grashof number found in the literature suggest that results may depend on local conditions and the method of observation or that other quantities, instead of the Grashof number, can be more suitable to identify changes in flow regime, like, for instance, the total amount of thermal energy given to the boundary layer by the heated surface up to the current elevation, as suggested in Ref. (Godaux & Gebhart, 1974).

Inspection of Fig. 3 shows that the present experiments fall in the last decade (10^8 to 10^9) of the abscissa (Ra_x), not far from the onset of transitional regime for air (according to the general consensus emerging from the literature). A deviation of measured data, from Ostrach's solution, in the +20 to +30% range was found, even though experiments were performed in a large, isolated room, without windows and openings to the external environment, with good thermal stability and hosting only the experimental facility used for these experiments. This circumstance was observed also by other instrumentalists (e.g., Bhavnani & Bergles (1990); Cheesewright (1968)), especially towards large values of Ra_x, when the transition to turbulence was approached. According to Bhavnani & Bergles (1990), experimental uncertainty and external disturbances are possible causes of these discrepancies, while Cheesewright (1968) stated that uncontrolled thermal gradients in the laboratory room may trigger large-scale air currents, yielding increased heat transfer at large Rayleigh numbers. Ostrach (1953) attributed the unsatisfactory agreement between his laminar theory and experimental data from the literature to disturbances induced by the slight turbulence in the room air. Schaub *et al.* (2019) found that the Nusselt number (averaged from the leading edge to the current elevation) can be experimentally overestimated up to 29% (compared with Churchill and Chu correlation (Churchill & Chu, 1975)) just at the upper limit of the laminar regime, in line with the deviation resulting from the present experiments.

3.1.2 *Effect of rib size*

Figure 4 illustrates the local Nusselt number distributions along the inter-rib regions of the heated plate, for a normalized elevation x/H from 0.7 to 1.0. Each plot compares the Nusselt number (Nu) for three values of the rib size e at a given Rayleigh number and rib pitch (i.e., number of rib rows N). The corresponding results over the smooth surface are also plotted. Regardless of the rib size, the measurement points inside each inter-rib region (five for $N = 10$, four for $N = 20$, and three for $N = 40$) were taken at fixed locations, as it appears from inspection of the figure.

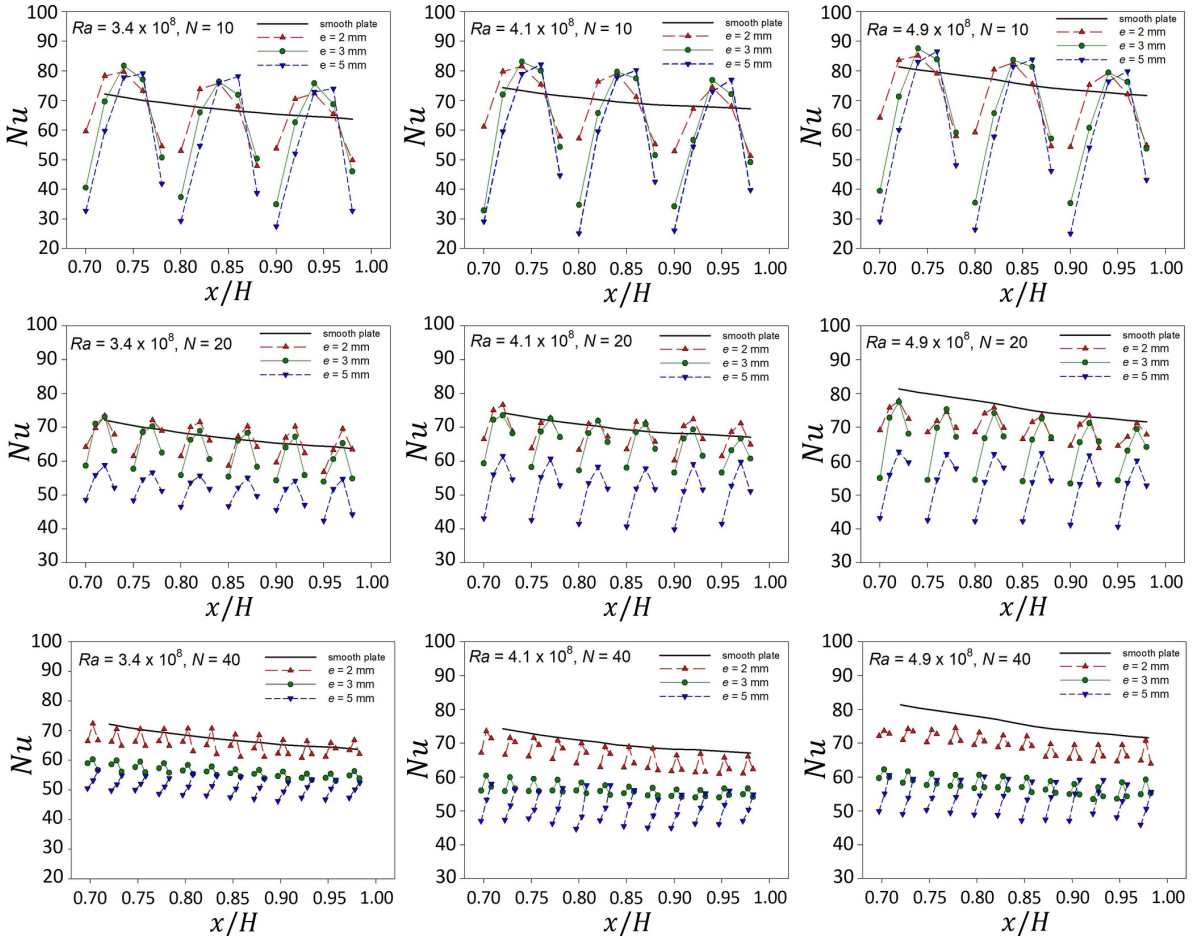

Figure 4: Nusselt number for ribbed (continuous ribs) and smooth plate: effect of the rib size.

When ribs are sparse ($N = 10$), heat transfer enhancement, relative to the smooth plate, is noticed in the central part of each inter-rib region, while marked reductions occur immediately downstream and upstream of each rib. As described in the literature (Bhavnani & Bergles, 1990; Tanda, 1997, 2008; Ahmed *et al.*, 2022), stagnation zones up- and downstream of the ribs are responsible for local heat transfer degradation while local enhancement is found where the main flow washes the inter-rib region. The primary effect of the increased size of the ribs is the extension of the stagnation zone downstream of

each rib; as a consequence, as the rib size e is increased from 2 to 5 mm, local Nu values downstream of each rib are markedly decreased and the relative maximum in the inter-rib region (whose value is poorly affected by the rib size) moves towards the downstream rib. Ribs of the lowest size ($e = 2$ mm) still perform better than others when they are more densely packed on the heated plate ($N = 20$ and 40); here the effect of the rib size is more evident, with heat transfer performance progressively degrading as the rib size is increased.

3.1.3 *Effect of rib pitch*

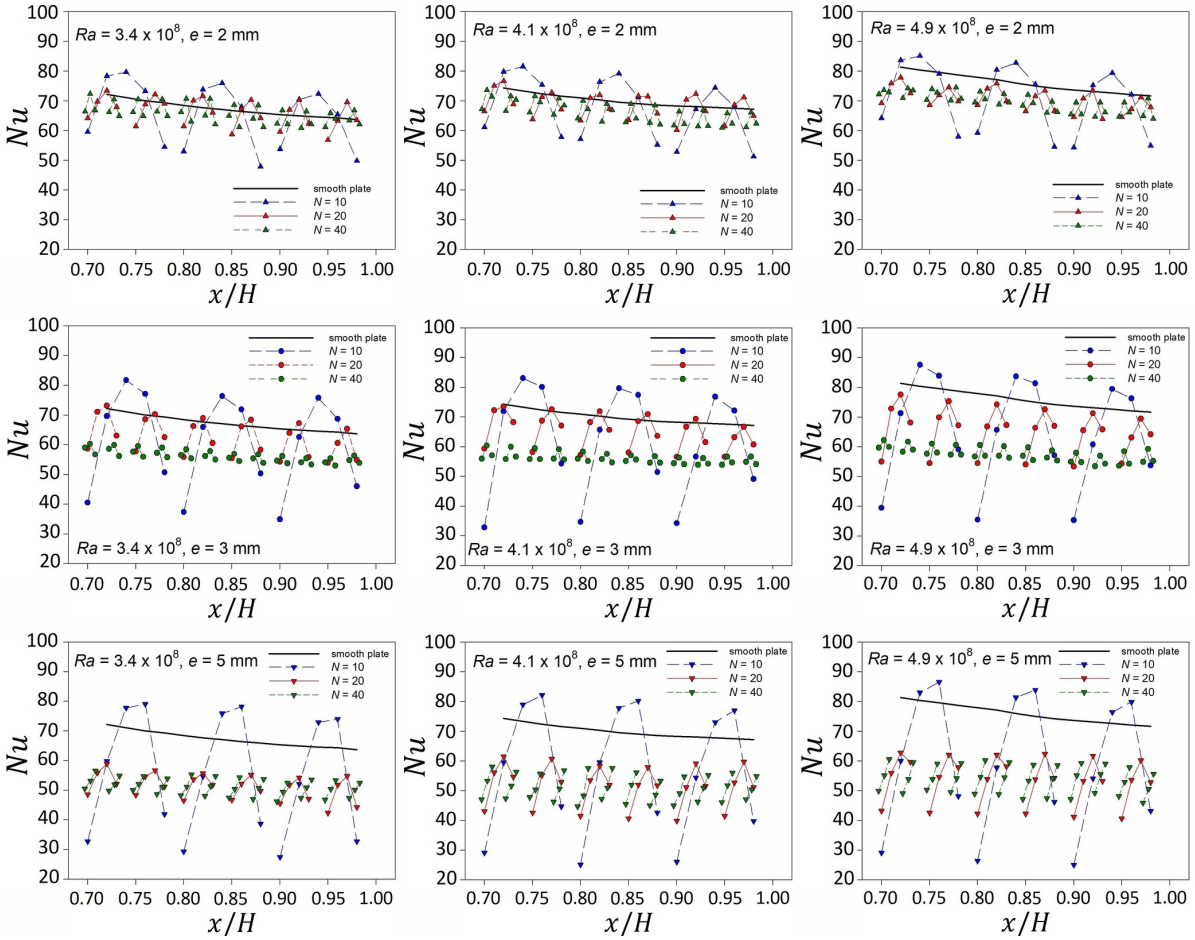

Figure 5: Nusselt number for ribbed (continuous ribs) and smooth plate: effect of the rib pitch (i.e., the number of rib rows).

Nusselt number data have been rearranged in Fig. 5 to highlight the effect of the rib pitch (i.e., the number of rib rows N). Inspection of the figure reveals that densely packing the ribs has a negative impact on the heat transfer performance, especially for the highest rib size ($e = 5$ mm). It is worth noting that, for $e = 5$ mm and $N = 40$, within the limits of the low number of measurement points in each inter-rib region, the ascending-descending

trend of local Nu values is not observed but Nu monotonically increases along each inter-rib region; it is conjectured that, due to the reduced space between ribs (only 7.5 mm), a single weak recirculating cell is trapped inside the inter-rib region.

With Table 1 in mind, the combination of rib size and rib number which leads to a local heat transfer enhancement, limited to the central part of the inter-rib region, corresponds roughly to a rib pitch-to-height ratio P/e larger than 10. A relatively low value of P/e (say ≤ 5), a parameter that captures the effect of rib size and pitch, negatively affects the heat transfer performance along the entire inter-rib surface.

3.1.4 *Effect of rib truncation*

Since the heat transfer enhancement, relative to the smooth plate, is the primary objective of this study, continuous ribs have been replaced by truncated ribs, seeking the potential favourable effects suggested in Refs. (Bhavnani & Bergles, 1991; Yao, 2006). Three, six, or twelve segments per row, displaced in a staggered arrangement, as sketched in Fig. 1, have been considered (ℓ = 50, 25, or 12.5 mm, respectively). Tests with truncated ribs were performed for the intermediate rib size only (e = 3 mm) and considering a fixed number of rows of rib segments (N = 20, corresponding to a rib pitch P = 25 mm). Figure 6 shows how Nu results are affected by the rib truncation at a given Ra number. Measured data refer to the inter-rib region only between rows since the free portions of the heated baseplate between the truncated pieces in each row are not optically accessible, as they are shadowed by rib segments.

Truncating the ribs generally increases the heat transfer performance throughout the majority (or the totality) of the inter-rib regions, as compared with the smooth plate geometry. An optimized number of segments per row is likely to exist; within the explored range of parameters for truncated ribs, the heat transfer rate from the surface is maximized with six rib segments per row (ℓ = 25 mm), which corresponds to a segment length to rib pitch ratio (ℓ/P) equal to 1.

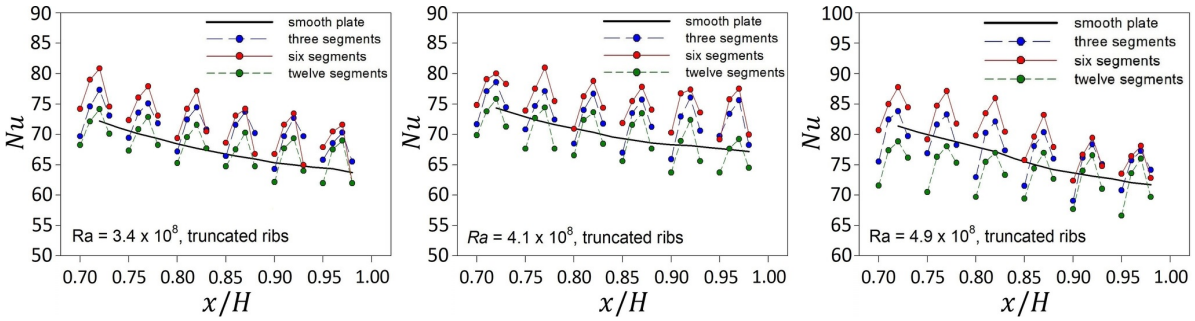

Figure 6: Nusselt number for ribbed (truncated ribs) and smooth plate: effect of the rib truncation.

3.1.5 *Module-averaged Nusselt number*

In order to quantify the relative merit (or demerit) of each rib configuration, local Nu values recorded within each inter-rib region have been averaged in order to obtain a module-averaged Nu. Even though the result may be biased by the limited number of measuring points (from 3 to 5 for each inter-rib region), the module-averaged data, plotted in Fig. 7 (where symbols corresponding to every module-averaged Nu have been conventionally located at the centre of the respective inter-rib region), reflect at a glance the increase or decrease in the heat transfer performance relative to the smooth plate case (solid line). Regardless of the Ra number, repeated continuous ribs having the largest size ($e = 5$ mm) and intermediate size ($e = 3$ mm) but with small pitch ($N = 40$) display the worst performances as compared with the smooth plate. Other continuous rib geometries perform better but always at a lower level than that observed for the smooth plate. A general trend towards a progressive attenuation of the decrease in the heat transfer performance is observed as the trailing edge of the plate is approached. As attention is turned to truncated ribs, an increased module-averaged value of Nu (as compared to the smooth plate case) occurs for two (out of three) truncated rib configurations, (namely those having three or six segments per row), even from a locally-averaged standpoint.

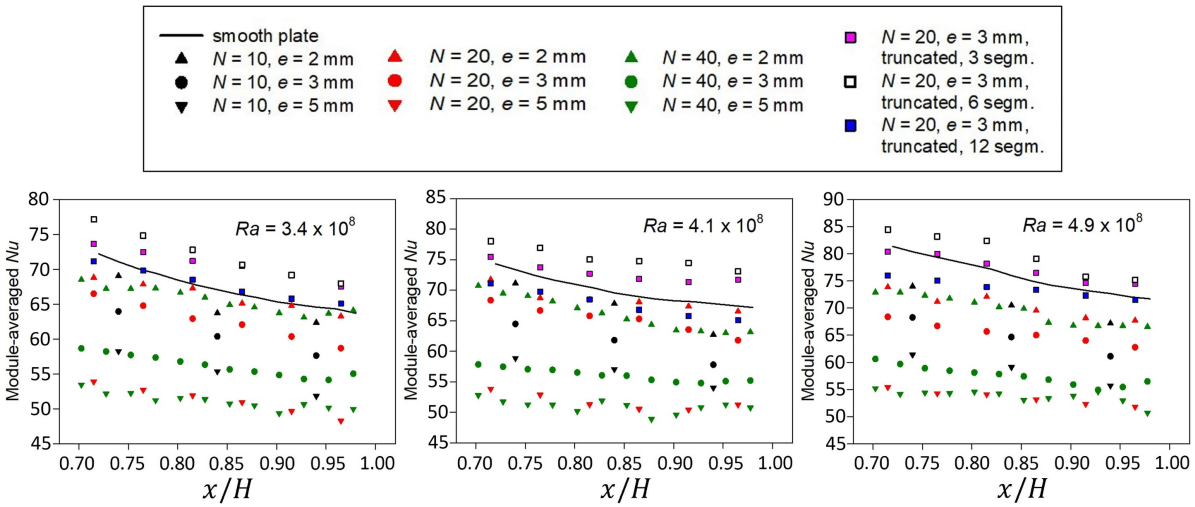

Figure 7: Module-averaged Nusselt number for ribbed and smooth plate.

Table 2 shows the deterioration or the enhancement (relative to the smooth plate) provided by continuous and truncated ribs for all the explored configurations; the table is indicative of values averaged (for both the smooth and ribbed plate) over the top 30% of the heated plate, as only this region was included in the field of view of the schlieren device. As it emerges from inspection of the table, continuous ribs have a negative impact on the heat transfer performance, with degradations of the average Nusselt number up to 30%, relative to the smooth plate case. Conversely, the truncated ribs, arranged in a staggered pattern, yield a mild improvement (up to +8%), especially when a proper number of segments per row is chosen: in fact, while no significant variations, with respect

to the smooth plate, are recorded for the truncated ribs with twelve segments per row, truncating the rib into three segments per row leads to a 2–5% Nu enhancement, which increases to 5–8% when six segments per row are considered.

Table 2: Ratio between average Nusselt numbers for the ribbed (only inter-rib regions) and the smooth plate. Only the top 30% of the heated plate is considered.

Rib type	Number of rib rows N	e (mm)	Number of truncated ribs per row	Nusselt number ratio (ribbed vs. smooth plate)		
				$Ra = 3.4 \times 10^8$	$Ra = 4.1 \times 10^8$	$Ra = 4.9 \times 10^8$
continuous	10	2	-	0.97	0.96	0.93
continuous	20	2	-	0.98	0.98	0.85
continuous	40	2	-	0.98	0.95	0.77
continuous	10	3	-	0.90	0.88	0.85
continuous	20	3	-	0.93	0.93	0.86
continuous	40	3	-	0.84	0.80	0.76
continuous	10	5	-	0.82	0.81	0.77
continuous	20	5	-	0.76	0.74	0.70
continuous	40	5	-	0.76	0.73	0.71
truncated	20	3	3	1.05	1.04	1.02
truncated	20	3	6	1.07	1.08	1.05
truncated	20	3	12	1.01	0.99	0.97

3.2 Boundary layer visualizations and air temperature fluctuations

The schlieren technique, based on a focal filament filter, allows a visualization of the boundary layer along the heated plate. In fact, when the filament is placed at the focus of the schlieren mirror, the points of the test section characterised by a non-zero thermal gradient (in the horizontal direction) appear bright in the schlieren image, while the undisturbed fluid region is coloured by the same colour of the filament (violet, as corresponding light rays are intercepted by the focal filament).

Figure 8 shows schlieren images of the boundary layers growing along the heated plate, without ribs and with continuous ribs having the same rib pitch (50 mm) and increasing rib size (2, 3, and 5 mm). All images refer to the largest Rayleigh number ($Ra = 4.9 \times 10^8$); a two-dimensional 1 cm × 1 cm grid has been superimposed to provide a dimensional reference (about the top 10 cm of the plate are framed in the images). Inspection of Fig. 8 reveals that the boundary layer, almost flat along the top region of the smooth plate, becomes wavy when ribs are arranged over the plate, and the waviness

amplitude is accentuated as the rib size increases. The effect of the ribs' density on the boundary layer is illustrated in Fig. 9, where 3-mm-ribs with pitches of 50, 25, and 12.5 mm are considered: schlieren images show that the boundary layer progressively returns to exhibit a flat profile as the density of ribs placed on the baseplate increases.

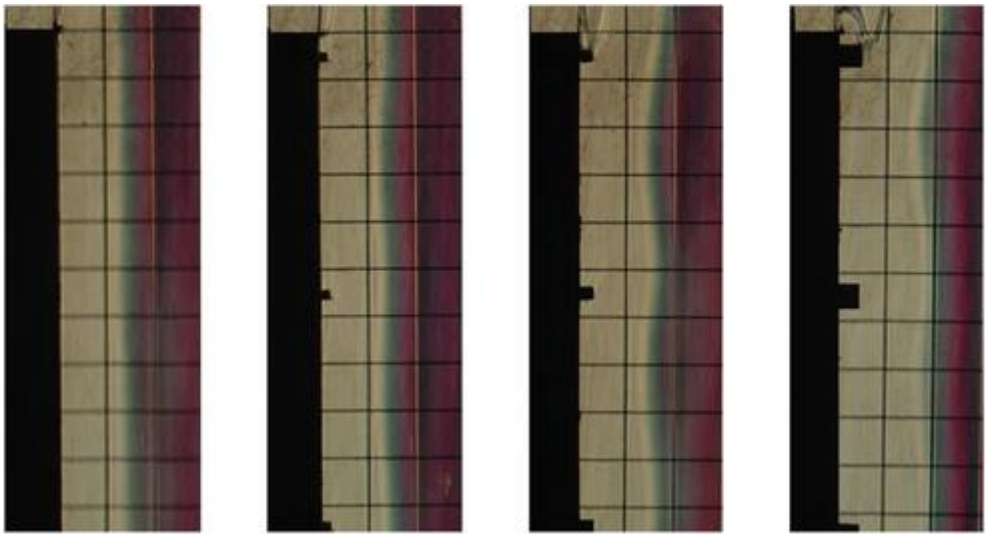

Figure 8: Schlieren images giving a qualitative representation of thermal boundary layer for the smooth plate and the ribbed plate (continuous ribs at different rib size).

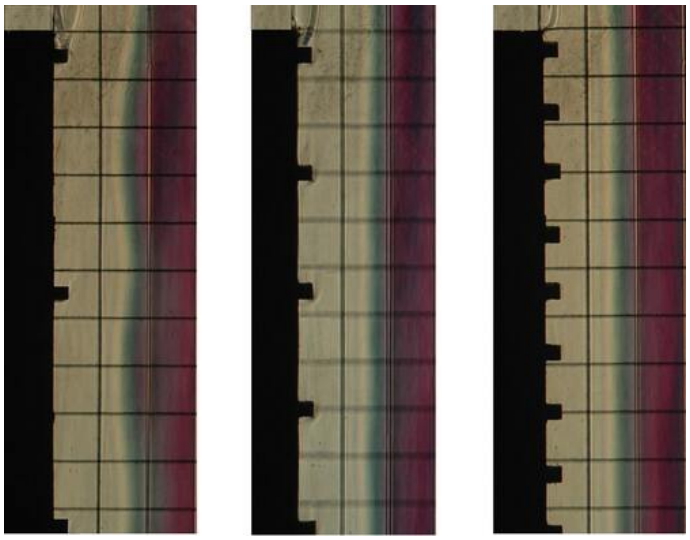

Figure 9: Schlieren images giving a qualitative representation of thermal boundary layer for the plate with continuous ribs at different rib pitch.

It is worth noting that the images shown in Figs. 8 and 9 were affected by low-frequency unsteady disturbances which are probably related to uncontrolled air currents in the laboratory room (the Rayleigh number was relatively large but not enough to

depart from the laminar regime, for the case of the smooth plate); these instabilities were more pronounced when truncated ribs (with six segments) were considered. Figure 10 shows three different schlieren images of the filament shadow (focal filament set at 0.35 mm from the focus) taken, on different time instants, for the truncated ribs (six segments per row): the line (filament shadow) projected on the camera, very close to the end of the boundary layer, has periodic disturbances at low frequency, with cycles of several seconds (left-hand and central picture), before recovering a quasi-steady behaviour (right-hand picture).

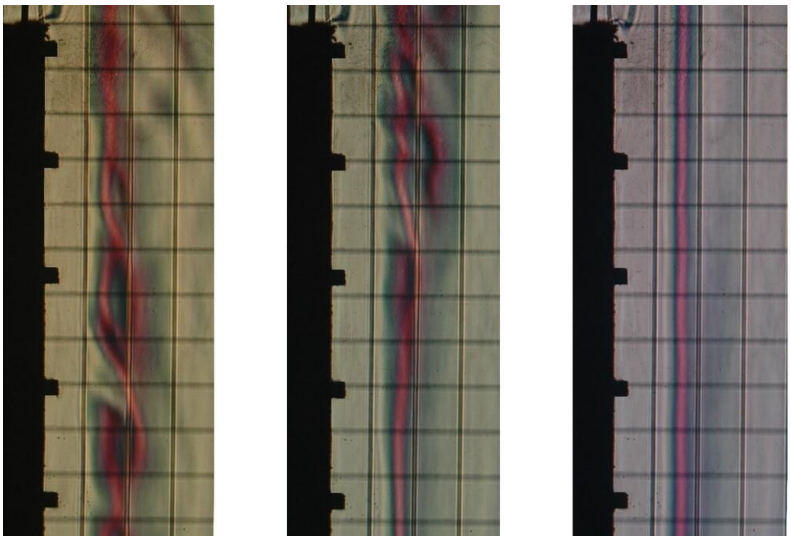

Figure 10: Examples of schlieren images showing the focal filament shadow (focal filament shifted by 0.35 mm from the focus) during low-frequency flow instabilities (truncated ribs, six segments per row).

Local air temperature measurements, performed at different elevations and distances from the heated plate, confirmed the schlieren observations. Figures 11 and 12 display the time history of the local to undisturbed air temperature difference and the root-mean-square of its fluctuations (normalized by the wall-to-ambient temperature difference) at various distances from the heated plate, respectively. Air temperature fluctuations shown in Fig. 11 were recorded at a 5 mm distance from the heated plate, approximately in the centre of the plate along the spanwise direction, and at different elevations, namely at 10 cm from the leading edge and at 8–10 cm to the trailing edge. For truncated ribs, the sensor was aligned to a row of rib segments and in the vicinity (within 1–2 mm) of the side face of a segment where the instabilities, if any, are likely to be induced. For continuous ribs, air temperature fluctuations were detected at elevations immediately downstream of the rib ($x = 0.405$) and in the inter-rib region ($x = 0.420$). Data refer to the highest Rayleigh number ($Ra = 4.9 \times 10^8$) and to ribs having a size of 3 mm. For the continuous ribs, the air temperature fluctuations were statistically confined within 2% of the wall-to-ambient temperature difference (with a larger attenuation in the stagnation zone, at $x = 0.405$ m), while temperature fluctuations registered for the truncated ribs with six segments, about at the same measurement elevation ($x = 0.397$ m) and same

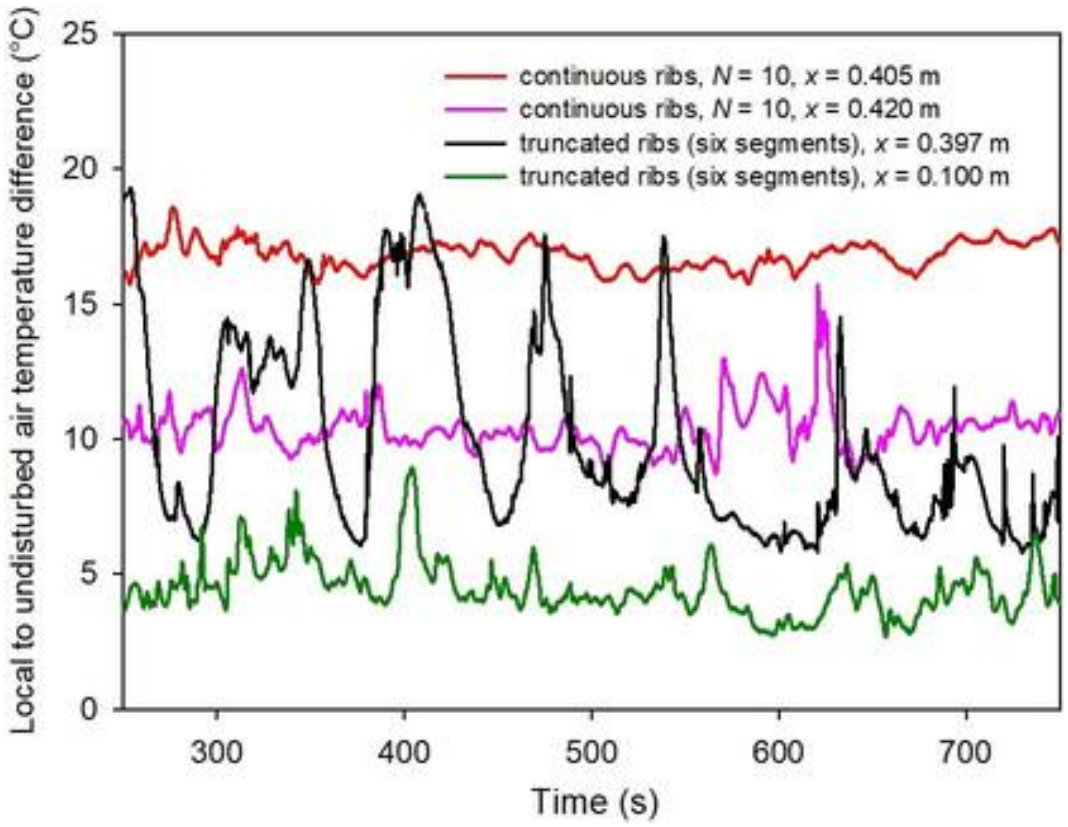

Figure 11: Traces of air temperature fluctuations, recorded at a 5 mm-distance from the heated plate and different elevations x, for the ribbed plate with continuous ribs ($e = 3$ mm, $N = 10$) and the ribbed plate with truncated ribs ($e = 3$ mm, $N = 20$ and six segments per row); $Ra = 4.9 \times 10^8$.

imposed wall-to-ambient temperature difference conditions, have a significantly larger magnitude. The amplification of disturbances was sensitive to the elevation (i.e., to the local Rayleigh number) as it was not observed close to the leading edge ($x = 0.1$ m). This circumstance is more evident from inspection of Fig. 12, where the distributions of the root-mean-square of the air temperature fluctuations (normalized by the wall-to-ambient temperature difference) along the coordinate normal to the heated plate, are reported for the smooth plate, continuous ribs, and truncated ribs with 3, 6, and 12 segments per row. Results show a peaked profile for truncated ribs with six segments, at the measurement station close to the trailing edge ($x = 0.397$ m) and in the vicinity of the segment side face, over the whole explored range of Ra based on plate height H (only points at the lowest and highest Ra are plotted), while fluctuations are markedly lower when detected again in the vicinity of the segment side face but close to the leading edge of the plate ($x = 0.100$ m). Measurements taken for truncated ribs with three and twelve segments per row, at the same vertical and spanwise coordinates, as well as those obtained for continuous ribs and the smooth plate, are characterised by markedly lower mean air temperature fluctuations at any distance from the heated plate. Even though air temperature fluctuation intensity (9% at the most), registered for truncated

ribs with six segments, remains below values that are typically experienced when the transitional and turbulent regimes take place (Tsuji & Nagano, 1988), it can be argued that the boundary layer growing along the truncated ribs (with six segments) interacts with, filters and amplifies the exogenous environmental disturbances sufficiently far away from the leading edge of the plate, thus yielding a possible explanation for the larger heat transfer coefficients measured, compared with those recorded for all other explored geometries.

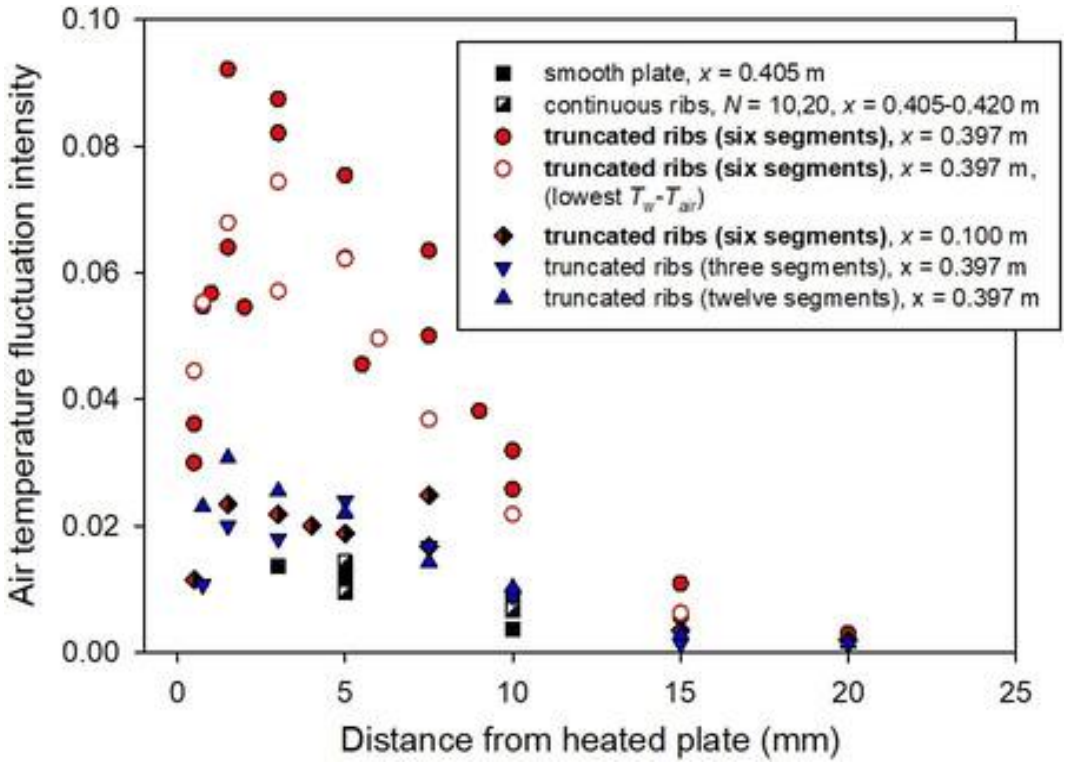

Figure 12: Intensity of air temperature fluctuations, at different distances from the heated plate and at different elevations x, for the smooth plate, the ribbed plate with continuous ribs ($e = 3$ mm, $N = 10$ and 20), and the ribbed plate with truncated ribs ($e = 3$ mm, $N = 20$ and 3, 6, and 12 segments per row). All data refer to the highest wall-to-ambient air temperature difference $T_w - T_{air}$ ($Ra = 4.9 \times 10^8$) except for data indicated with empty circles, recorded for the lowest $T_w - T_{air}$ ($Ra = 3.4 \times 10^8$).

4 CONCLUSIONS

The natural convection heat transfer from a ribbed vertical plate was experimentally investigated by varying the rib size and pitch and by considering the effect of rib truncation. The schlieren optical technique was employed as a diagnostic tool to estimate the heat transfer coefficient along the vertical plate. The main conclusions of this research are summarized below:

i. Compared to a smooth, isothermal, vertical surface, the presence of continuous ribs negatively affects the heat transfer performance within the range of variation of the parameters investigated, with degradations of the average Nusselt number up to 30%, relative to the smooth plate case. Only a local heat transfer enhancement in the inter-rib region was found for a relatively high rib pitch-to-height ratio (higher than 10), counterbalanced by a marked reduction immediately downstream and upstream of ribs due to the presence of stagnation regions.

ii. When continuous ribs are replaced by truncated ribs displaced in a staggered arrangement, significant heat transfer enhancements, relative to the smooth surface, were noticed throughout the majority, or the totality, of the inter-rib regions. To the authors' knowledge, this is the first time that this effect is documented. From the average point of view, the truncated ribs yield a mild improvement (up to +8%), with the best heat transfer performance obtained for a value of the number of segments per row (six) intermediate in the explored range (three to twelve), suggesting the presence of an optimal length of the rib segments, for given rib size and pitch, that maximizes the heat transfer enhancement.

iii. Supplementary air temperature measurements performed at short distances from the heated test plate showed that truncated ribs of a given value of the segment length (corresponding to the maximum heat transfer performance) induce fluctuations much larger than those occurring for the rest of the experimental campaign. The reason why the truncated rib arrangement yields enhanced heat transfer on the vertical smooth surface is likely related to either the more efficient redistribution of buoyant airflow within the laminar flow regime or to a premature transition to turbulence induced by rib truncation, as large-amplitude air temperature fluctuations suggest.

REFERENCES

Ahmed, E.N., Bottaro, A. & Tanda, G. 2022 A homogenization approach for buoyancy-induced flows over micro-textured vertical surfaces. *J. Fluid Mech.* **941**, A53.

Ambrosini, D. & Tanda, G. 2006 Comparative measurements of natural convection heat transfer in channels by holographic interferometry and schlieren. *Eur. J. Phys.* **27** (1), 159–172.

Bejan, A. & Lage, J.L. 1990 The Prandtl number effect on the transition in natural convection along a vertical surface. *ASME. J. Heat Transfer* **112** (3), 787–790.

Bhavnani, S.H. & Bergles, A.E. 1990 Effect of surface geometry and orientation on laminar natural convection heat transfer from a vertical flat plate with transverse roughness elements. *Intl J. Heat Mass Transfer* **33** (5), 965–981.

Bhavnani, S.H. & Bergles, A.E. 1991 Natural convection heat transfer from sinusoidal wavy surfaces. *Wärme-Stoffübertrag.* **26** (6), 341–349.

Cavallero, D. & Tanda, G. 2002 An experimental investigation of forced convection heat transfer in channels with rib turbulators by means of liquid crystal thermography. *Exp. Therm Fluid Sci.* **26** (2–4), 115–121.

Cheesewright, R. 1968 Turbulent natural convection from a vertical plane surface. *ASME J. Heat Transfer* **90** (1), 1–6.

Churchill, S.W. & Chu, H.H.S. 1975 Correlating equations for laminar and turbulent free convection from a vertical plate. *Intl J. Heat Mass Transfer* **18** (11), 1323–1329.

Devia, F., Milano, G. & Tanda, G. 1994 Evaluation of thermal field in buoyancy-induced flows by a schlieren method. *Exp. Therm. Fluid Sci.* **8** (1), 1–9.

Devia, F. & Tanda, G. 2000 Investigation of natural convection heat transfer from a horizontal isothermal plate by schlieren tomography. *Heat Technol.* **18** (1), 41–46.

Fujii, T., Fujii, M. & Takeuchi, M. 1973 Influence of various surface roughness on the natural convection. *Intl J. Heat Mass Transfer* **16** (3), 629–640.

Godaux, F. & Gebhart, B. 1974 An experimental study of the transition of natural convection flow adjacent to a vertical surface. *Intl J. Heat Mass Transfer* **17** (1), 93–107.

Goldstein, R.J. 1976 Optical techniques for temperature measurement, in: Eckert, E.R.G. & Goldstein, R.J. (Eds.), *Measurements in Heat Transfer*, 2nd ed. Washington, WA, USA: Hemisphere Publishing Corporation (Chapter 5) .

Hærvig, J. & Sørensen, H. 2020 Natural convective flow and heat transfer on unconfined isothermal zigzag-shaped ribbed vertical surfaces. *Intl Commun. Heat Mass Transfer* **119**, 104982.

Hargather, M.J. & Settles, G.S. 2012 A comparison of three quantitative schlieren techniques. *Opt. Lasers Eng.* **50** (1), 8–17.

Hauf, W. & Grigull, U. 1970 Optical methods in heat transfer, in: Hartnett, J.P. & Irvine, T.F. (Eds.), *Adavances in Heat Transfer*: Elsevier, **6,** pp. 133–366 .

Imbriale, M., Panelli, M. & Cardone, G. 2012 Heat transfer enhancement of natural convection with ribs. *Quant. InfraRed Thermogr. J.* **9** (1), 55–67.

Jain, D.S., Rao, S.S. & Srivastava, A. 2016 Rainbow schlieren deflectometry technique for nanofluid-based heat transfer measurements under natural convection regime. *Intl J. Heat Mass Transfer* **98**, 697–711.

Kleine, H., Grönig, H. & Takayama, K. 2006 Simultaneous shadow, schlieren and interferometric visualization of compressible flows. *Opt. Lasers Eng.* **44** (3–4), 170–189.

Merzkirch, W. 1974 *Flow Visualization*. Academic Press.

Nghana, B., Tariku, F. & Bitsuamlak, G. 2022 Numerical assessment of the impact of transverse roughness ribs on the turbulent natural convection in a BIPV air channel. *Build. Environ.* **217**, 109093.

Onbasioglu, S.U. & Onbaşioğlu, H. 2004 On enhancement of heat transfer with ribs. *Appl. Therm. Eng.* **24** (1), 43–57.

Ostrach, S. 1953 An analysis of laminar free-convection flow and heat transfer about a flat plate parallel to the direction of the generation body force. NACA Technical Report 1111 .

Raffel, M. 2015 Background-oriented schlieren (BOS) techniques. *Exp. Fluids* **56** (3), 60.

Raithby, G.D. & Hollands, K.G.T. 1985 Natural convection, in: Rohsenow, W.M., Hartnett, J.P. & Ganić, E.N. (Eds.), *Handbook of Heat Transfer Fundamentals*, 2nd ed. New York, NY, USA: McGraw Hill (Chapter 6). .

Schaub, M., Kriegel, M. & Brandt, S. 2019 Experimental investigation of heat transfer by unsteady natural convection at a vertical flat plate. *Intl J. Heat Mass Transfer* **136**, 1186–1198.

Schulz, J.M., Junne, H., Böhm, L. & Kraume, M. 2020 Measuring local heat transfer by application of Rainbow Schlieren Deflectometry in case of different symmetric conditions. *Exp. Therm. Fluid Sci.* **110**, 109887.

Settles, G.S. 2018 Smartphone schlieren and shadowgraph imaging. *Opt. Lasers Eng.* **104**, 9–21.

Smirnov, E.M., Abramov, A.G., Smirnovsky, A.A. & Smirnov, P.E. 2018 Numerical simulation of turbulence arising in the free convection boundary layer after a cross row of rectangular obstacles. *J. Phys.: Conf. Series* **1128**, 012090.

Tanda, G. 1993 Natural convection heat transfer from a staggered vertical plate array. *ASME J. Heat Transfer* **115** (4), 938–945.

Tanda, G. 1997 Natural convection heat transfer in vertical channels with and without transverse square ribs. *Intl J. Heat Mass Transfer* **40** (9), 2173–2185.

Tanda, G. 2008 Natural convective heat transfer in vertical channels with low-thermal-conductivity ribs. *Intl J. Heat Fluid Flow* **29** (5), 1319–1325.

Tanda, G. 2017 Experiments on natural convection in water-cooled ribbed channels with different aspect ratios. *Intl J. Heat Mass Transfer* **110**, 606–612.

Tanda, G. & Devia, F. 1998 Application of a schlieren technique to heat transfer measurements in free-convection. *Exp. Fluids* **24** (4), 285–290.

Tanda, G., Fossa, M. & Misale, M. 2014 Heat transfer measurements in water using a schlieren technique. *Intl J. Heat Mass Transfer* **71**, 451–458.

Tsuji, T. & Nagano, Y. 1988 Characteristics of a turbulent natural convection boundary layer along a vertical flat plate. *Intl J. Heat Mass Transfer* **31** (8), 1723–1734.

Vyas, A., Mishra, B., Agrawal, A. & Srivastava, A. 2018 Non-intrusive investigation of flow and heat transfer characteristics of a channel with a built-in circular cylinder. *Phys. Fluids* **30** (3), 033602.

Yao, L.-S. 2006 Natural convection along a vertical complex wavy surface. *Intl J. Heat Mass Transfer* **49** (1-2), 281–286.

PAPER B5

Experimental observations of the onset of unsteadiness for buoyant airflow along smooth and rough vertical isothermal walls [1,2]

Giovanni Tanda[a] , **Essam Nabil Ahmed**[b] and **Alessandro Bottaro**[b]

[a] *DIME, Università di Genova, via Montallegro 1, Genova, 16145, Italy*
[b] *DICCA, Università di Genova, via Montallegro 1, Genova, 16145, Italy*

The buoyant airflow along a vertical isothermal wall, under conditions close to transitional, is studied. The schlieren technique and miniature thermocouples are employed for qualitative (flow unsteadiness) and quantitative (heat transfer coefficient and local air temperature) observations. For the smooth surface, the phenomena are found to be sensitive to the enclosure configuration surrounding the plate. Roughening the heated surface with staggered rib segments of proper dimensions leads to increased heat transfer, ascribed to the onset of unsteadiness close to the segments' edges, together with a better redistribution of the flow thanks to a favorable hydrodynamic interaction between fluid and protrusions.

1 INTRODUCTION AND LITERATURE REVIEW

Transition phenomena in natural convective boundary layers have been studied extensively from the past century to today. Linear stability theory as well as numerical calculations of the growth and non-linear interaction of two-dimensional and transverse disturbances have been applied to study initial instability for a variety of natural convection flows and conditions (Dring & Gebhart, 1968; Gebhart, 1969; Audunson & Gebhart, 1976). Dring & Gebhart (1968) showed that as a disturbance in the flow adjacent to a vertical surface is convected downstream, disturbance components amplify selectively and in a very narrow band of frequencies; further downstream, non-linear and three-dimensional effects become important (Mahajan & Gebhart, 1979). Key aspects of the transition of an initially stable laminar natural convective flow to turbulence were clarified in Refs. (Jaluria & Gebhart, 1974; Godaux & Gebhart, 1974): the first signs of

[1] This paper is a revised version submitted to: *Experimental Heat Transfer* on April 10, 2024; the first version was submitted on March, 21, 2023.

[2] A Supplemental Video was submitted alongside this manuscript; it is available upon request from the corresponding author (*essameldin.abdo@edu.unige.it*).

turbulent disturbances were found to appear in the velocity boundary layer without alteration of the temperature profile from the laminar form until reaching a point, further downstream, where the velocity disturbances become strong enough to change the temperature profile (the onset of thermal transition). The thermal transition region ends with the development of a completely turbulent boundary region where all flow variables fluctuate randomly (fully turbulent region). Despite many research efforts, the pioneering experimental investigations of transitional effects, summarized in Refs. (Mahajan & Gebhart, 1979; Godaux & Gebhart, 1974) and obtained with different fluids, heating conditions, surface sizes and instrumentation (hot wire, thermocouples, interferometer), showed large disagreements concerning the characteristics of the beginning of transition adjacent to a vertical surface. Indeed, the assumption of the Grashof number criterion outlined by Bejan & Lage (1990) and still assumed in heat transfer books (Bejan, 1993) leads to a large spread of the critical values for the transition; a different correlator of the transition region location (beginning and end of the transition region), termed kinetic energy flux parameter, was proposed in (Godaux & Gebhart, 1974): it depends on the ratio between the Grashof number and the local elevation raised to a given exponent. Regardless of the parameter assumed to assess the end of the laminar regime for the buoyant flow, discrepancies among findings by various researchers when air is used as convective fluid may be also ascribed to the confinement configuration surrounding the heated plate or to poorly controlled thermal gradients or to slight turbulence of air in the laboratory room (Cheesewright, 1968; Warner & Arpaci, 1968; Tsuji & Nagano, 1988).

Despite the abundant literature dealing with the occurrence of transitional effects for a free-convective flow along a vertical wall, few and often contradictory research works have been devoted to the effect of macroscopic roughness elements on heat transfer from a vertical plate (Bhavnani & Bergles, 1990). Roughness elements alter the heat transfer from the plate due to the increased surface area, the more efficient redirection of the convective flow (caused by the surface alteration), and the possible premature transition to turbulence (caused by the occurrence of flow separation and instabilities).

The aim of this investigation is twofold. First, observations of the thermal field in a buoyant airflow, induced by a vertical, isothermal, and smooth plate were performed with focus on conditions close to the end of the laminar regime; second, the effect of the insertion of roughness elements (staggered rows of rib segments of finite length) glued onto the vertical plate was analyzed. The instrumentation employed includes the schlieren optical technique, useful to gain insights into the flow stability and heat transfer coefficient distribution at the wall (only for stable flows), and miniature thermocouples to detect the air temperature fluctuations at several stations in the boundary layer.

2 EXPERIMENTAL SETUP AND PROCEDURE

The test surface was an aluminum plate, 0.5 m high, 0.3 m large, and 0.005 m thick, connected to a plane electrical heater. The plate thickness was enough to ensure that

the condition of uniform wall temperature was attained fairly well. The height of the plate was specifically selected to promote, in conjunction with wall-to-air temperature differences of about 50 K, flow conditions not far from the end of the laminar regime (corresponding to a Grashof number of about 10^9, according to the general consensus (Bejan & Lage, 1990; Bejan, 1993)). The heater-plate assembly, suspended at about 1.5 m from the floor, was insulated on one side in order to convey as much heat flux as possible towards the side exposed to the ambient air. The plate temperature was evaluated as the average among the readings given by several 0.5 mm-dia thermocouples (calibrated to $\pm$ 0.1 K) embedded at different plate elevations through small holes drilled into the material. The ambient air temperature was calculated by averaging the readings of three thermocouples situated below the heated plate or aligned to the leading edge of the plate.

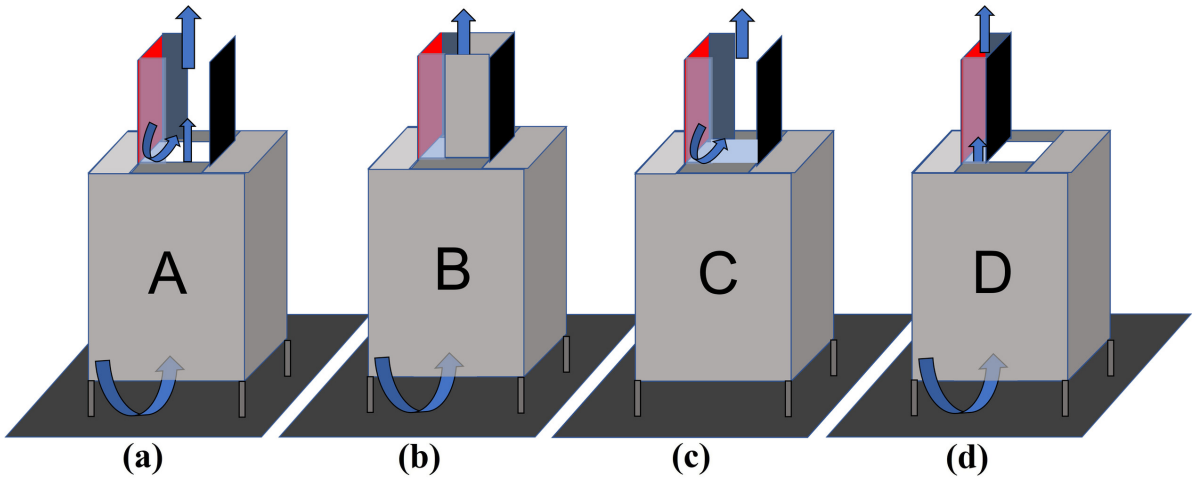

Figure 1: Natural convection experiments and configurations of confinement of the heated vertical plate (colored in red).

Even though in principle the experiment deals with the free convection from an unbounded vertical surface, the presence of confinement structures of the heated plate is necessary to prevent significant interaction with air movements in the laboratory room. Main body of experiments were performed by using a closed shield, below the heated plate, with openings in its bottom part to permit the buoyant air to enter and flow along the heated plate. To avoid significant sidewise air entrainment and minimize disturbances from the environment, the heated plate was then bounded on both sides by two glasses, 10 cm long and as high as the heated plate and shrouded by a frontal polystyrene wall, placed at a distance from the heated plate (25 cm) equal to half of the plate height. This configuration (A), schematically shown in Fig. 1(a), is similar to that used in previous literature studies (e.g., Refs. (Tanda, 1993; Schaub *et al.*, 2019)). A slightly different confinement of the plate (B) is represented in Fig. 1(b): here the lateral access of ambient air is completely inhibited, and air is constrained to flow only coming from the bottom (while in case A air comes from the bottom and, in part, from the side openings). A third example of confinement (C), similar to that used in experiments by Warner & Arpaci

(1968) and typically adopted for numerical simulations (e.g., (Hærvig & Sørensen, 2020)): the approaching flow is completely enclosed in a box (including a horizontal surface at short distance upstream of the leading edge of the heated plate) with ambient air entering the box through side slots and exiting through the top open surface, as shown in Fig. 1(c). The main difference between configurations A and C is the presence of the horizontal wall that forces the airflow to pass through the side openings, redirect toward the plate, and exit through the open top of the box. A fourth arrangement (D) is depicted in Fig. 1(d): the frontal polystyrene wall is here placed at 8 cm-distance from the heated plate; as compared to the configuration B, the shorter spacing between the two facing vertical walls (8 cm instead of 25 cm) is likely to induce a channel flow throughout the entire cross-sectional area of the confinement structure.

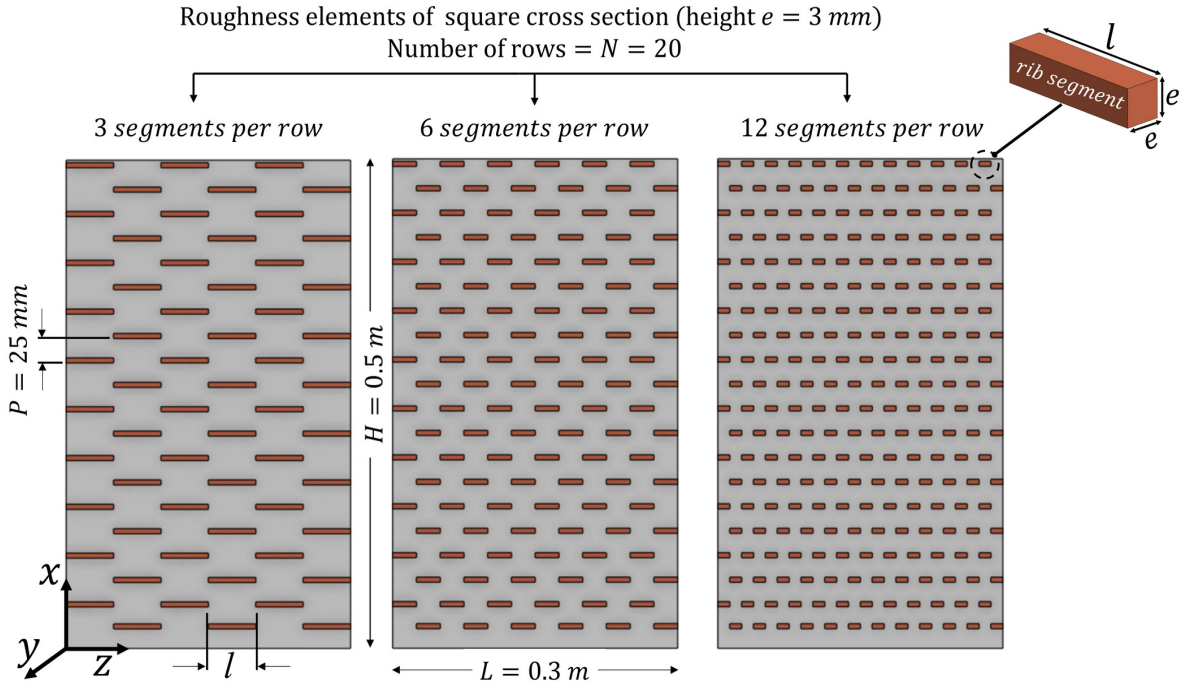

Figure 2: Sketch of the heated plate (frontal view) with roughness elements: segments are square in section with fixed height e, while the segment length l and the corresponding number of segments per row are varied from one experiment to another. H is the vertical plate height, L is the spanwise length of the plate, N is the number of rows, and P is the row pitch.

Table 1: Geometric details of the roughness pattern.

N	e (mm)	P (mm)	l (mm)	segments per row	P/e	e/H	l/L	l/P
20	3	25	50	3	8.33	6×10^{-3}	0.1667	2
20	3	25	25	6	8.33	6×10^{-3}	0.0833	1
20	3	25	12.5	12	8.33	6×10^{-3}	0.0417	0.5

Additional tests were subsequently performed adding macroscopic roughness elements, namely rows of three, six, or twelve rib segments periodically arranged in a staggered pattern. Details of roughness element geometry are reported in Fig. 2 and Table 1.

A schlieren optical system was used to visualize the thermal boundary layer and to evaluate the local, natural convective, heat transfer coefficient. An exhaustive description of the schlieren apparatus employed is given in Refs. (Devia *et al.*, 1994; Tanda & Devia, 1998; Tanda *et al.*, 2014). Basically, it consists of a white light beam (composed of parallel rays) crossing the test section, a concave mirror (i.e., the schlieren mirror), which focuses the light onto its focal plane (i.e., the cut-off plane), a filter, and a camera to acquire a real image of the test section. As shown in Fig. 3, when a focal filament (a thin dark strip) is used as a filter, and no thermal gradients are present in the air crossed by the light beam, all light rays are intercepted by the filter when it is placed on the focus of mirror (and the image formed on the camera will be uniformly dark). When thermal gradients (in the y-direction of Fig. 3) are present, individual light rays undergo angular deflections whose extent is related to the magnitude of the gradient; consequently, the corresponding spots appear bright in the camera, permitting a reliable visualization of the thermal boundary layer (more precisely of all air particles with a non-zero thermal gradient). The angular deflection α_y of a given light ray (i.e., passing through a given point of coordinates x, y) can be measured by moving the filter (connected to a micrometer) along the focal plane of the schlieren mirror until the point of interest becomes darkened by the filter. According to this procedure, a single iso-deflection line (line of points inducing the same deflection of light along the y-direction) inside the optical field of view can be visualized. The technique also permits to gain quantitative information: the heat transfer coefficient h can be directly calculated by measuring the deflection of light passing in the vicinity of the wall at the desired location, using the following formula:

$$h = \frac{k(T_w)\,\alpha_{y,w}\,T_w^2}{K(T_w - T_{air})}, \tag{1}$$

where T_w and T_{air} are plate wall and ambient air temperatures, respectively, $k(T_w)$ is the air thermal conductivity evaluated at the wall temperature, $\alpha_{y,w}$ is the angular deflection, along the y-direction, of the light ray passing in the vicinity of the wall (i.e., at $y = 0$), and K is a constant ($= 0.024$ m K in the present experiment) which depends on air properties (Gladstone-Dale and ideal gas constants, index of refraction, pressure) and on the length of the plate in the direction of light beam propagation (z-coordinate of Fig. 3). Equation (1) assumes the thermal field to be two-dimensional, i.e., independent of z-coordinate; otherwise, it is still valid but the calculated heat transfer coefficient corresponds to the value averaged along the plate length L, that is the plate dimension along the z-coordinate.

The uncertainty in the results (at the 95% confidence level) was evaluated based on the root-sum-square of the individual uncertainties in the measurements of each quantity. The main source of error in the calculation of the local heat transfer coefficient h is attributed to the measurement of angular deflection of light rays, whose accuracy improves

as its value increases (i.e., in the presence of large air temperature gradients). For the present experiments, errors in the light ray angular deflection were calculated to be in the range from 9 to 14%, increasing with the reduction of the recorded angular deflection. As errors in the wall-to-fluid temperature difference are also accounted for, the uncertainty in h (and in the Nusselt number) eventually falls into the ±10–15% range, while the uncertainty in the Rayleigh number is estimated to be ±5% (Tanda *et al.*, 2023).

Schlieren measurements were supplemented by the detection of air temperature fluctuations in the boundary layer by using a miniature thermocouple with an exposed, 100 μm-dia junction, able to travel along the direction normal to the plate surface, at an arbitrary position along the vertical and spanwise coordinates. A National Instrument acquisition unit (NI PXIe-1078 equipped with a NI TB-4353 module) was used to acquire the air temperature measurements at a frequency of 50 Hz.

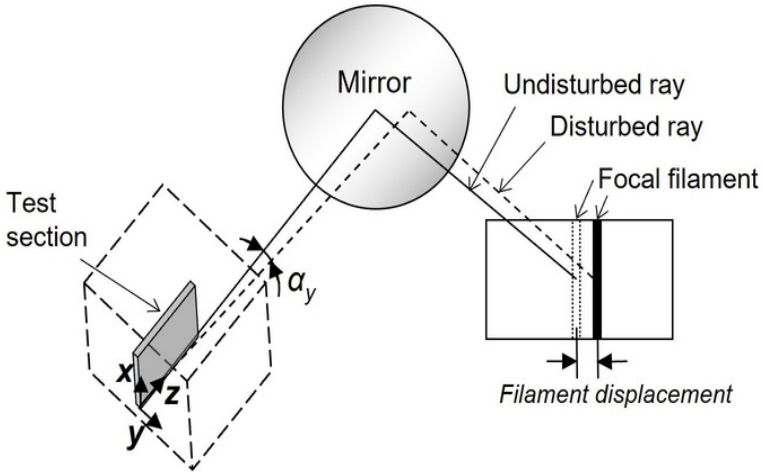

Figure 3: Focal filament schlieren method: the angular deflection of perturbed light rays is detected by shifting the focal filament filter in the focal plane of the schlieren concave mirror.

Tests were carried out by delivering electrical power to the heater through a DC power supply, adjusting the input voltage to achieve a temperature difference between the heated wall and the ambient air of about 50 K. An isothermal boundary condition was established due to the relatively high thickness of the plate and high thermal conductivity of aluminum. The degree of temperature uniformity of the plate was typically within ± 3% of the mean wall-to-ambient temperature difference. After the initiation of each test, steady state was achieved in about $6 - 7$ hours. At the end of the test, air and wall temperatures were acquired and schlieren measurements were performed. Measurements of air temperature inside the boundary layer were performed for a number of representative tests, over a time period of about 15 minutes, at different distances from the plate surface and locations along the vertical and spanwise directions.

The Rayleigh and Nusselt numbers, based on the plate height H or the local vertical

position x, were introduced as follows:

$$Ra = \frac{g\beta(T_w - T_{air})\,H^3}{\nu\alpha}, \tag{2}$$

$$Nu = \frac{h\,H}{k}, \tag{3}$$

$$Ra_x = \frac{g\beta(T_w - T_{air})\,x^3}{\nu\alpha}, \tag{4}$$

$$Nu_x = \frac{h\,x}{k}, \tag{5}$$

where h is the local heat transfer coefficient, given by eq. (1), g is the gravitational acceleration, and β, α, ν, k denote the coefficient of thermal expansion, the thermal diffusivity, the kinematic viscosity, and the thermal conductivity of air, respectively. Air properties have been evaluated at the film temperature given by $(T_w + T_{air})/2$, except for β, evaluated at the ambient air temperature.

Since the optical scope encompassed a circular region having a diameter of about 20 cm, not enough to frame the entire plate, measurements of the angular deflection of light rays (and the related quantities h and Nu_x) and visualization of the thermal boundary layer were limited to the top third of the heated plate, where the values of Ra_x are the largest.

3 RESULTS AND DISCUSSION

3.1 The smooth plate

Heat transfer results for the smooth heated plate, in terms of the Rayleigh and the Nusselt numbers based on local elevation x, are displayed in Fig. 4, together with the analytical solution by Ostrach (1953) for a vertical isothermal flat plate and air as the convective fluid. Rayleigh number ($= 0.71 \times Grashof\ number$) signaling, for air, the beginning of transition, according to different authors, are superimposed to the plot (solid line: Bejan & Lage (1990), dashed line: Warner & Arpaci (1968), dash-dotted line: Eckert & Soehngen (1951)). Results, plotted for three different configurations of the plate confinement depicted in Fig. 1, fall in a region astride the onset of transition. As mentioned before, experimental data were recorded in a region of the plate close to its trailing edge (last third of the plate height) and here values of Nu_x largely exceed (by $20-30$ percent) the theoretical predictions by Ostrach, valid in the laminar regime. Data obtained for configurations A and B were very close to each other while configuration D yielded further increases in local Nusselt number. No schlieren data were recorded for configuration C as the flow close to the wall was highly unstable. Figure 4b shows the dependence of Nu_x on Ra_x (experimentally obtained) for a shorter vertical plate (of height $H = 0.175$ m) with different confinement modes (same configurations as in Fig. 1) and

at three wall-to-fluid temperature differences corresponding to values of $Ra \approx 1.9 \times 10^7$, 1.5×10^7, and 8.6×10^6 (all well within the laminar regime). Unlike what had been found in the main experiments (Fig. 4a) concerning the plate of larger height ($H = 0.5$ m), the results for the shorter plate (Fig. 4b) were unaffected by the confinement arrangement; this was confirmed by schlieren-based observations of the thermal boundary layer over time (not presented here) which revealed that the flow is always stable.

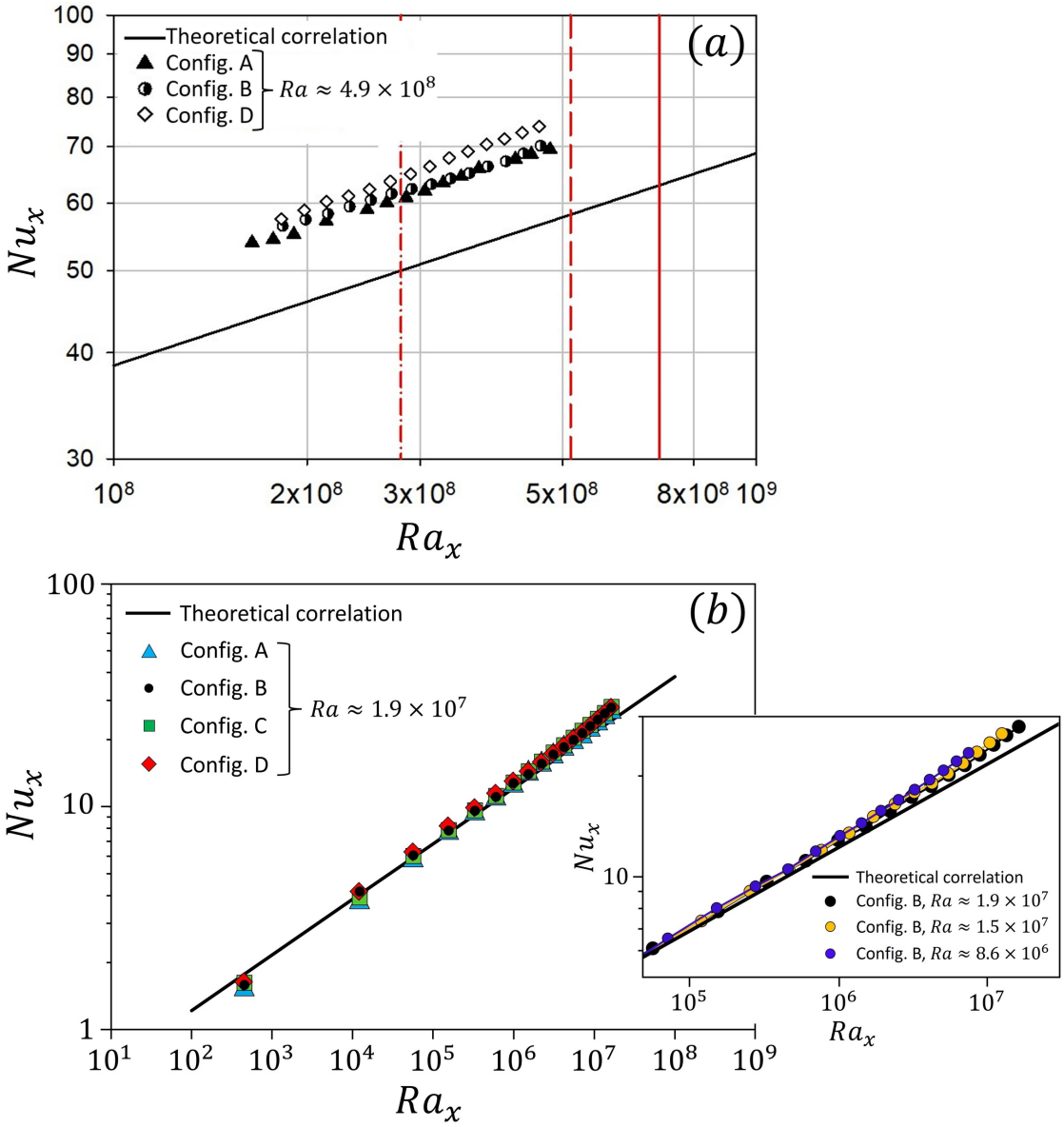

Figure 4: Local Nusselt number versus local Rayleigh number for a smooth, isothermal, vertical plate with different confinement configurations (A, B, C, and D). Results of the main experiments, conducted with the plate of height $H = 0.5$ m, are plotted in panel (a), with the red solid/dashed/dash-dotted lines indicating the transition onset according to different Authors Bejan & Lage (1990); Warner & Arpaci (1968); Eckert & Soehngen (1951). Panel (b) is dedicated to the results of additional experiments performed with a shorter plate ($H = 0.175$ m) to achieve lower values of Ra.

Moreover, the results satisfactorily agree with Ostrach's predictions, thus demonstrating the reliability of the experimental technique to capture accurate local heat transfer coefficient values. Even the deviations realized close to the trailing edge of the plate (highlighted in the inset of Fig. 4b) are justifiable, since, as pointed out by Ostrach Ostrach (1953) and found by Bhavnani and Bergles Bhavnani & Bergles (1990) in similar experimental circumstances, the slight turbulence in the laboratory room air probably affects the results near the top edge, leading to values in excess by 15% at the most. The effect of these exogenous disturbances is likely to be amplified at larger Ra_x, and the deviations from Ostrach correlation therefore become more pronounced, as seen in Fig. 4a.

A possible interpretation of results condensed in Fig. 4 can be inferred by schlieren observations (Fig. 5) and air temperature measurements over time (Fig. 6) in the boundary layer. Figure 5 shows schlieren images of the filament shadow (focal filament set at 0.35 mm from the focus) for the smooth heated plate and different confinements (A, B, C, and D; refer to Fig. 1): while for cases A and B the trace is stable (and it reacts to a perturbation damping it until a stable condition is attained), the case C leads to an unstable filament shadow (even in the vicinity of the wall, making unfeasible any heat transfer coefficient measurement) and the case D produces a slightly fluctuating trace, thus explaining the higher heat transfer coefficient recorded, relative to cases A and B; for a better view, the reader is referred to the *Supplemental Video* provided with this article. It is worth noting that, as the recorded schlieren image is a result of an integral of the light angular deflections along a line in the spanwise direction, even a small local instability can be hidden by the integration process and not detected by the schlieren observation. This means that the stability of the trace does not guarantee the absolute laminarity of flow; this is the reason why punctual air temperature measurements are required to provide further information about the stability of the flow.

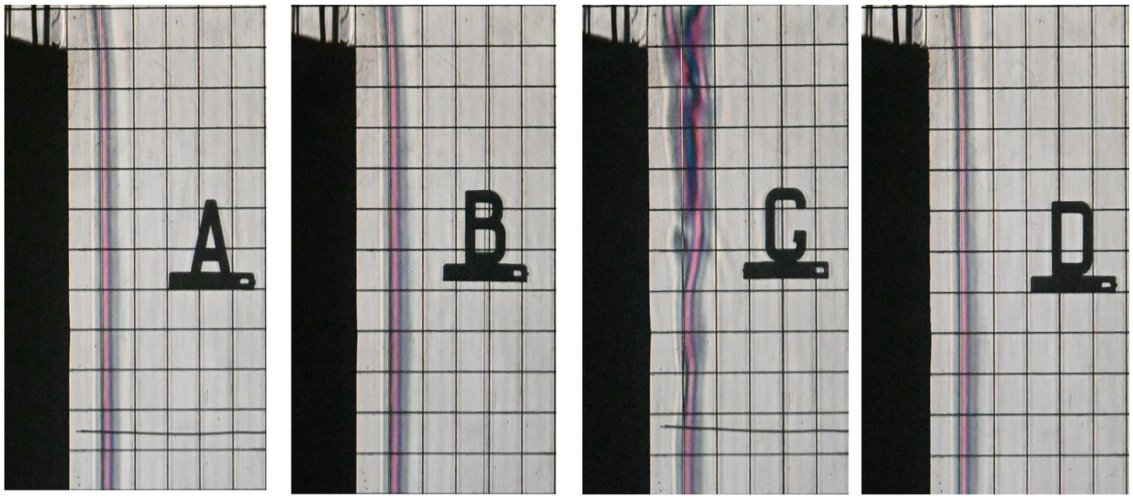

Figure 5: Schlieren images showing the focal filament shadow (focal filament shifted by 0.35 mm from the focus) for the smooth heated plate with different confinement arrangements. A two-dimensional $(x - y)$ grid consisting of 1 cm $\times$ 1 cm cells is superimposed; the top 11 cm of the plate are displayed here.

Inspection of Fig. 6 reveals that the air temperature, recorded at an elevation not far from the trailing edge ($x = 0.405$ m, corresponding to $Ra_x = 2.6 \times 10^8$) and at a short distance from the heated plate ($y = 0.005$ m, well inside the boundary layer), is not stable over time but is affected by low-frequency unsteady disturbances which are probably related to uncontrolled air currents in the laboratory room. These instabilities are much more pronounced when the heated plate is confined by a horizontal surface at the leading edge and the sensor is placed close to the plate side edge (case C), but still not related to intrinsic turbulence of the flow as the comparison with air temperature fluctuations recorded, by the same sensor and measurement chain, for a hot forced-air jet induced by a hair dryer seems to suggest. For case C remarkable differences between the time-averaged local temperature in the spanwise direction are also observed, denoting probably marked three-dimensional effect induced by the confinement of the heated plate. Air temperature fluctuations for cases A and B are qualitatively similar, while for case D, featured by a channel flow, the extent of fluctuations is higher, regardless of the spanwise coordinate. It may be concluded that the flow features, most importantly the recorded low-frequency instability, associated with the particular confinement arrangement adopted are likely to be responsible for the deviation of the local Nusselt number values from those calculated by Ostrach in the laminar flow regime.

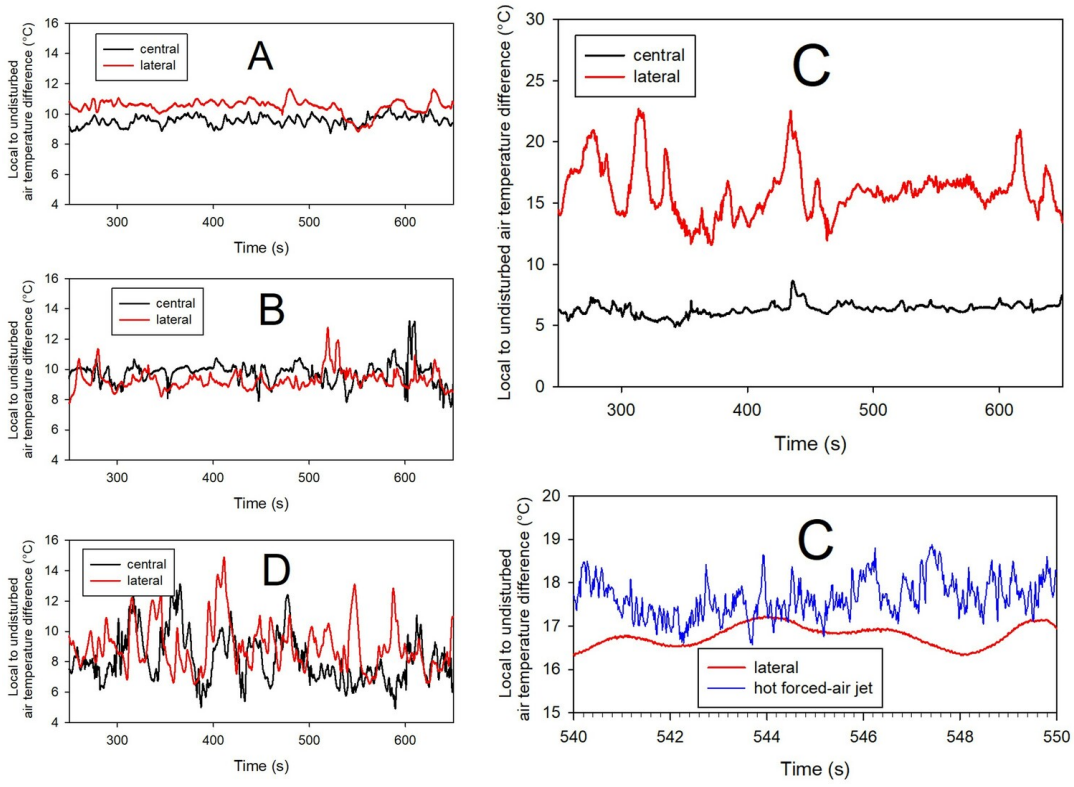

Figure 6: Traces of air temperature fluctuations, recorded at an elevation $x = 0.405$ m ($Ra_x = 2.6 \times 10^8$) and a distance from the heated plate $y = 0.005$ m. With respect to the spanwise coordinate, the sensor was placed at a central or lateral (4 cm from the edge) position. Comparison with fluctuations for a hot forced-air jet (a typical example of turbulence) is shown in the bottom-right frame.

3.2 The rough plate

The influence of roughening the vertical heated surface is investigated, exploiting the recent findings by the same group of authors (Tanda *et al.*, 2023) together with additional, complementary results and further analysis.

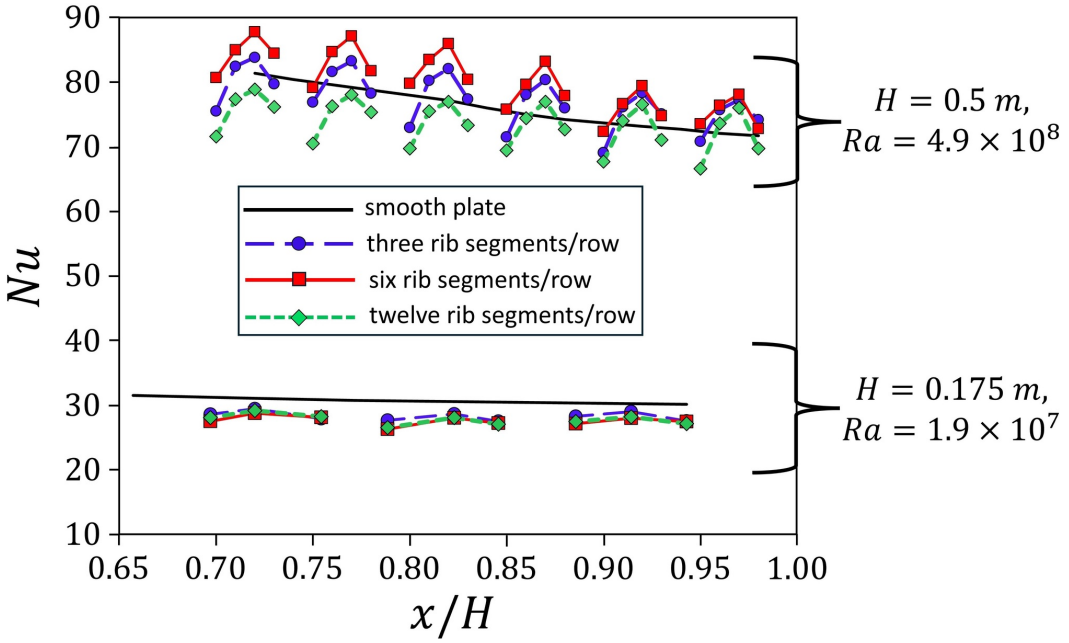

Figure 7: Nusselt number for the smooth and the rough plates: effect of the number of rib segments per row.

Wooden roughness elements (rib segments having a square section, $e \times e$, and a variable length, l) have been attached to the heated plate (refer to Fig. 2) in order to assess their impact on the heat transfer characteristics and the instability of the buoyant airflow. Figure 7 reports the spanwise-averaged Nusselt number recorded only over the last third of the plate (even though the whole heated plate, of height $H = 0.5$ m, was covered with 20 rows of roughness elements). The same wall-to-ambient air temperature difference (50 K) as the smooth plate case was considered, giving $Ra = 4.9 \times 10^8$, while the confinement configuration A of Fig. 1 was adopted. The presence of the roughness elements is found to generally increase the heat transfer performance throughout most of the regions between rows of segments, as compared with the smooth plate geometry, if the number of segments per row is properly selected. In fact, an optimized number of rib segments per row is likely to exist; within the explored range of parameters, the heat transfer rate from the surface is maximized with six rib segments per row ($l = 25$ mm), which corresponds to a segment length to rib pitch ratio (l/P) equal to 1. It is worth noting that the heat transfer coefficient over the surfaces of the rib segments and the increased surface area (per unit plate height) provided by ribs were not considered in the experimental analysis. Clearly, more pronounced heat transfer enhancements relative to the smooth plate (having the same frontal area) would be observed if the entire roughened

surface were considered. Besides, to demonstrate that the effect of perturbing the vertical heated surface is not merely intrinsic to the geometry of the rib segments, but it is also sensitive to the Rayleigh number, the corresponding distributions of Nu when the plate Rayleigh number is decreased by about one order of magnitude (i.e., $Ra = 1.9 \times 10^7$) are plotted in Figure 7. These results are obtained experimentally for a shorter plate ($H = 0.175$ m) roughened with rib segments (again, three, six, or twelve segments/row) having height $e = 2$ mm and pitch $P = 16$ mm, such that the rib pitch-to-height ratio ($P/e = 8$) is close to that for the plate of larger height (for which $P/e = 8.33$, as described in Table 1). It is evident from the figure that no heat transfer enhancement is attainable by roughening the shorter plate and that, at such a low Rayleigh number, the behavior of Nu is almost insensitive to the number of rib segments per row. In the discussions below, we provide insights on the recorded, selective heat transfer augmentation attainable exclusively at relatively large values of Ra, by considering only the plate of $H = 0.5$ m.

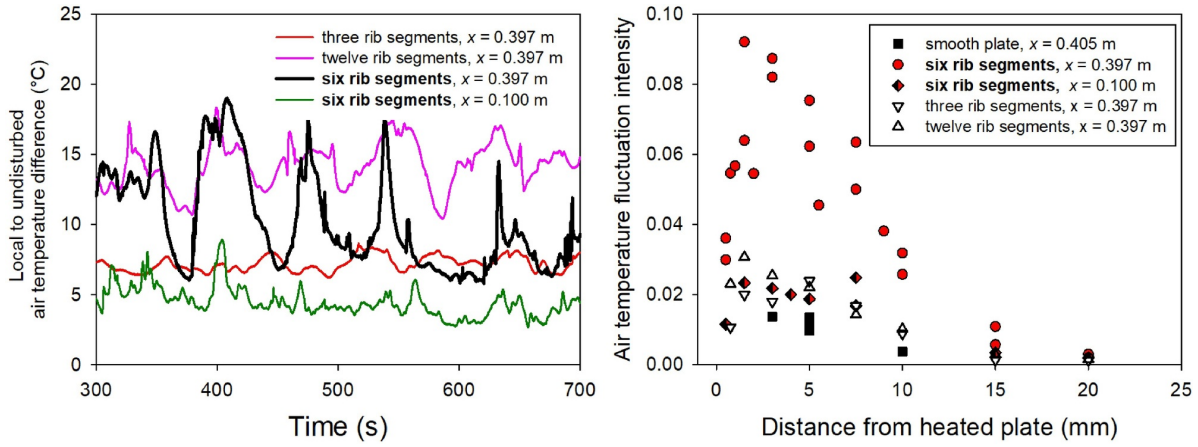

Figure 8: Traces of air temperature fluctuations, recorded at a 5 mm-distance from the plate (in y-direction) and different elevations x, for the rough plate (left) and intensity of air temperature fluctuations as a function of the wall-normal distance, at different elevations x, for the smooth and the rough plate (right).

Heat transfer coefficient measurements were again supplemented by local air temperature measurements (Fig. 8) and schlieren observations of the boundary layer (Fig. 9). The sensor for air temperature measurements was placed aligned to a row of rib segments and in the vicinity (within $1 - 2$ mm) of the side face of a segment where the instabilities, if any, are likely to be induced. As for the smooth plate, air temperature fluctuations at low frequency were recorded: while for three and twelve rib segments per row the air temperature fluctuations, shown in the left-hand side of Fig. 8, were statistically confined within 2% of the wall-to-ambient temperature difference, the temperature fluctuations registered for six segments per row at the same measurement elevation have a significantly larger magnitude. The amplification of disturbances was sensitive to the elevation (i.e., to the local Rayleigh number) as it was not observed close to the leading edge ($x = 0.1$ m). This circumstance is more evident from inspection of the right-hand side of Fig. 8, where the distributions of the root-mean-square of the air temperature

fluctuations (normalized by the wall-to-ambient temperature difference) along the coordinate normal to the heated plate, are reported for the smooth plate and for the rough plate with 3, 6, and 12 rib segments per row. Result shows a peaked profile for the rough plate with six segments per row, at the measurement station close to the trailing edge ($x = 0.397$ m) and in the vicinity of the segment side face, while the rms is markedly lower when detected again in the vicinity of the segment side face but close to the leading edge of the plate ($x = 0.100$ m). Measurements taken for the rough plate with three and twelve rib segments per row, at the same vertical and spanwise coordinates, as well as those obtained for the smooth plate, are featured by markedly lower mean air temperature fluctuations at any distance from the heated plate. Even though the air temperature fluctuation intensity (9% at the most) registered for the rough plate with six segments per row remains below values that are typically experienced when the transitional and turbulent regimes take place (Tsuji & Nagano, 1988), it can be argued that the boundary layer growing along the rough plate with six rib segments per row interacts with, filters and amplifies the exogenous environmental disturbances sufficiently far away from the leading edge of the plate, thus yielding a possible explanation for the larger heat transfer coefficients measured, compared with those recorded for all other geometries explored. Schlieren visualizations (Fig. 9) for the rough plate with six rib segments per row provide further evidence of the presence of local unsteadiness: three different schlieren images of the filament shadow (with the focal filament set at 0.35 mm from the focus), taken at different time instants, show that the trace of the filament shadow experiences periodic disturbances at low frequency, with cycles of several seconds (left and central pictures), before recovering a quasi-steady behavior (right picture), thus confirming the evidence of local unsteadiness reflected on the integral optical data recorded by the schlieren setup.

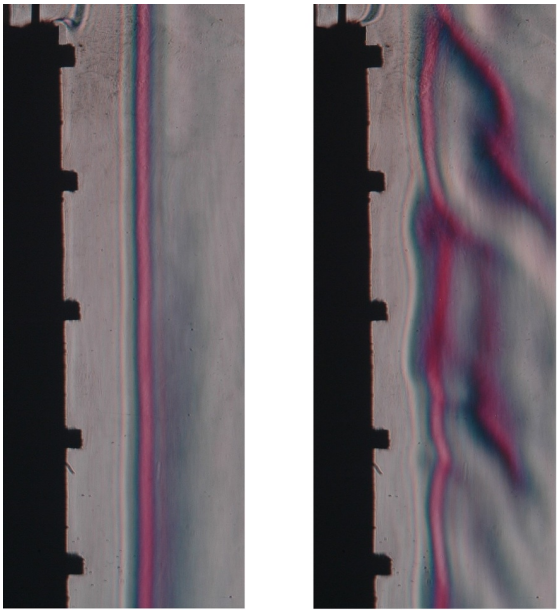

Figure 9: Schlieren images showing the focal filament shadow (focal filament shifted by 0.35 mm from the focus) during low-frequency flow unsteadiness for the rough plate. The pictures refer to the case of six rib segments per row, and the top five rows (out of 20) are framed here.

The experimental work was complemented by numerical simulations of the conjugate heat transfer problem, incorporating thermal conduction through the wooden ribs (of thermal conductivity ≈ 0.1 W/m K) and natural convection from the baseplate and the ribs' surfaces to air. The numerical analysis was carried out using Simcenter STAR-CCM+ 2021.1.1 software (version 16.02.009-R8) and imposing a stable buoyant airflow at the same Rayleigh number of the experiments ($Ra = 4.9 \times 10^8$). The crux here is to investigate whether the staggered arrangement of ribs with six segments per row can still optimize the convective heat transfer rate from the baseplate surface when the effect of flow instabilities/unsteadiness is excluded. Figure 10 shows at a glance the maps of the Nusselt number, Nu, for the rough surface (from left to right: 3, 6, and 12 rib segments per row) over the same plate elevation range ($x = 0.7\ H$ to $1.0\ H$) explored in the experiments; to facilitate the readability of the figure, only one-third of the plate span (along z-direction) is displayed. The results were analyzed and compared in terms of the spanwise-averaged value of the Nusselt number at each vertical position, x, in a manner similar to that followed in Fig. 7: superior heat transfer performance for the rough plate with six segments per row was detected even under stable flow conditions, which implies a better airflow redistribution, relative to the smooth plate case. Nonetheless, the numerical values of the spanwise-averaged Nu (for the different patterns of ribs and for the smooth surface) are, in general, lower than the experimental values reported in Fig. 7. These quantitative deviations are a clear sign of the heat-transfer-promoting effect of the boundary layer instabilities present in laboratory experiments and absent in numerical simulations.

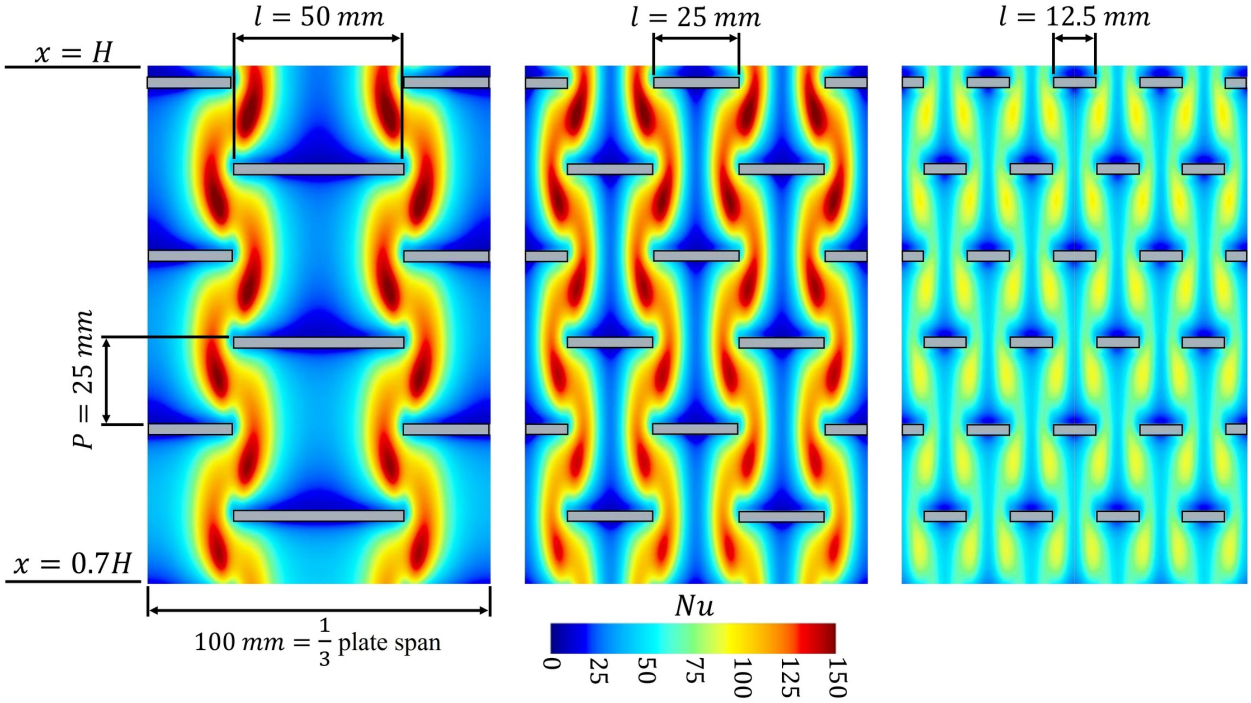

Figure 10: Contours of the Nusselt number, Nu, obtained by numerical simulations in the laminar regime: rib segments having three different lengths (50, 25 and 12.5 mm, corresponding to 3, 6, and 12 segments per row, respectively), $Ra = 4.9 \times 10^8$.

4 CONCLUSIONS

An experimental study on the buoyant airflow along a vertical surface with and without macro-roughness elements has been performed. Attention was directed to the upper part (top third) of the plate; since local conditions were close to transitional, heat transfer measurements were supplemented by local air temperature measurements in the boundary layer to detect possible unsteadiness in the flow, if any.

Main conclusions are summarized as follows:

i. natural convection heat transfer results for a smooth, isothermal, vertical plate were found to exceed by $20 - 30\%$ theoretical data from Ostrach, and low-frequency flow instabilities in the boundary layer, sensitive to the different configuration arrangements of the heated plate, were detected;

ii. adding roughness elements (rows of discrete rib segments arranged in a staggered pattern) led to an increase of heat transfer coefficient, relative to the smooth plate, especially if a proper size of the segment length is set;

iii. analysis of the air temperature fluctuations detected in the boundary layer and close to the segment side face revealed that they are strongly amplified when the optimal number of rib segments per row (six) was selected; these fluctuations are not regarded as intrinsic turbulence but the amplification of exogenous environmental disturbances present in the laboratory room;

iv. the heat transfer enhancement provided by the rough plate, with a proper size of rib segments, is likely to be due to the combined effect of the local unsteadiness originating over isolated spots (experimentally observed) and the better redistribution of flow remaining stable elsewhere (numerically deduced).

REFERENCES

Audunson, T. & Gebhart, B. 1976 Secondary mean motions arising in a buoyancy induced flow. *Intl J. Heat Mass Transfer* **19** (7), 737–750.

Bejan, A. 1993 *Heat Transfer*. New York, NY, USA: Wiley.

Bejan, A. & Lage, J.L. 1990 The Prandtl number effect on the transition in natural convection along a vertical surface. *ASME. J. Heat Transfer* **112** (3), 787–790.

Bhavnani, S.H. & Bergles, A.E. 1990 Effect of surface geometry and orientation on laminar natural convection heat transfer from a vertical flat plate with transverse roughness elements. *Intl J. Heat Mass Transfer* **33** (5), 965–981.

Cheesewright, R. 1968 Turbulent natural convection from a vertical plane surface. *ASME J. Heat Transfer* **90** (1), 1–6.

Devia, F., Milano, G. & Tanda, G. 1994 Evaluation of thermal field in buoyancy-induced flows by a schlieren method. *Exp. Therm. Fluid Sci.* **8** (1), 1–9.

Dring, R.P. & Gebhart, B. 1968 A theoretical investigation of disturbance amplification in external laminar natural convection. *J. Fluid Mech.* **34** (3), 551–564.

Eckert, E.R.G. & Soehngen, S.E. 1951 Interferometric studies on the stability and transition to turbulence of a free convection boundary layer. In *the Gen. Discuss. Heat Transfer,* London, pp. 321–323.

Gebhart, B. 1969 Natural convection flow, instability, and transition. *ASME J. Heat Transfer* **91** (3), 293–309.

Godaux, F. & Gebhart, B. 1974 An experimental study of the transition of natural convection flow adjacent to a vertical surface. *Intl J. Heat Mass Transfer* **17** (1), 93–107.

Hærvig, J. & Sørensen, H. 2020 Natural convective flow and heat transfer on unconfined isothermal zigzag-shaped ribbed vertical surfaces. *Intl Commun. Heat Mass Transfer* **119**, 104982.

Jaluria, Y. & Gebhart, B. 1974 On transition mechanisms in vertical natural convection flow. *J. Fluid Mech.* **66** (2), 309–337.

Mahajan, R.L. & Gebhart, B. 1979 An experimental determination of transition limits in a vertical natural convection flow adjacent to a surface. *J. Fluid Mech.* **91** (1), 131–154.

Ostrach, S. 1953 An analysis of laminar free-convection flow and heat transfer about a flat plate parallel to the direction of the generation body force. NACA Technical Report 1111 .

Schaub, M., Kriegel, M. & Brandt, S. 2019 Experimental investigation of heat transfer by unsteady natural convection at a vertical flat plate. *Intl J. Heat Mass Transfer* **136**, 1186–1198.

Tanda, G. 1993 Natural convection heat transfer from a staggered vertical plate array. *ASME J. Heat Transfer* **115** (4), 938–945.

Tanda, G., Ahmed, E.N. & Bottaro, A. 2023 Natural convection heat transfer from a ribbed vertical plate: Effect of rib size, pitch, and truncation. *Exp. Therm. Fluid Sci.* **145**, 110898.

Tanda, G. & Devia, F. 1998 Application of a schlieren technique to heat transfer measurements in free-convection. *Exp. Fluids* **24** (4), 285–290.

Tanda, G., Fossa, M. & Misale, M. 2014 Heat transfer measurements in water using a schlieren technique. *Intl J. Heat Mass Transfer* **71**, 451–458.

Tsuji, T. & Nagano, Y. 1988 Characteristics of a turbulent natural convection boundary layer along a vertical flat plate. *Intl J. Heat Mass Transfer* **31** (8), 1723–1734.

Warner, C.Y. & Arpaci, V.S. 1968 An experimental investigation of turbulent natural convection in air at low pressure along a vertical heated flat plate. *Intl J. Heat Mass Transfer* **11** (3), 397–406.

PAPER B6

An experimental and numerical study of laminar natural convection along vertical rib-roughened surfaces [1]

Essam Nabil Ahmed[a] and **Giovanni Tanda**[b]

[a] *DICCA, Università di Genova, via Montallegro 1, Genova, 16145, Italy*
[b] *DIME, Università di Genova, via Montallegro 1, Genova, 16145, Italy*

Air natural convection along a vertical surface periodically roughened with wooden ribs, square in section and either spanwise-elongated or truncated and arranged in a staggered pattern, is investigated at a Rayleigh number of 2×10^7, which corresponded to a stable buoyant air flow. The influence of roughness on local and overall convective heat transfer was analyzed experimentally via schlieren imaging and extensive energy balance calculations and numerically through both conventional and homogenization-based CFD (computational fluid dynamics) simulations. For the considered range of the rib pitch-to-height ratio (from 3.5 to 20), the continuous, transverse elements were generally found to degrade the local and overall convective heat transfer, with the deterioration becoming more pronounced when the ribs are densely packed on the surface. Furthermore, even staggered truncated ribs failed to provide any local/overall enhancement to convective heat transfer. The simulations performed via the homogenization-based treatment, which represents an easier alternative to the standard fine-grained numerical analysis, led to heat transfer trends in line with those obtained by fully resolving simulations and experiments. Both numerical approaches showed that the conjugate heat transfer problem must be tackled in the case of low-thermal-conductivity ribs since the solution, in terms of heat transfer characteristics, is intermediate between the cases of adiabatic and perfectly conducting elements.

1 INTRODUCTION

Natural convection heat transfer from vertical ribbed surfaces is relevant to a wide range of applications such as electronic equipment cooling (Incropera, 1988), photovoltaic and thermal solar systems (Nghana *et al.*, 2022), passive solar heating and ventilation of buildings (Bohn & Anderson, 1984; Gilani *et al.*, 2017), heat removal in nuclear technology (Tzanos *et al.*, 1991), and many others. There are situations where roughness or

[1] This manuscript was submitted to: *International Journal of Heat and Mass Transfer* on Dec 27, 2023 as a revised version, and is currently Under Review.

obstacles are present naturally (or to perform functions related to the specific application, without paying primary attention to their impact on heat transfer) and others in which they are added intentionally to alter the buoyant-flow behavior and the heat transfer characteristics, for instance by producing physical disturbances in the laminar boundary layer which may stimulate an earlier transition to turbulence and, therefore, lead to an enhancement of the heat transfer performance. The former may be the case of electronic circuit boards or even surfaces of buildings, while passive solar systems and photovoltaic modules are examples of the latter. In both cases, a proper understanding of the flow and thermal behavior of these systems is essential for their design.

As widely discussed in the literature, roughness elements over a vertical surface may induce marked modification to the buoyant flow and, at the same time, add an extra heat transfer area. Although the increase in surface area is clearly beneficial to the heat transfer rate exchanged with the convective fluid, the effectiveness of roughness elements in enhancing the heat transfer coefficient is intriguingly controversial, with some studies indicating a slight increase (relative to the smooth surface) in limited circumstances (e.g., zigzag-shaped surfaces (Hærvig & Sørensen, 2020), stepped surfaces (Bhavnani & Bergles, 1990), and truncated rib elements (Tanda *et al.*, 2023*a*)) and others finding a general reduction, as in the case of repeated spanwise-elongated ribs of square cross section (Bhavnani & Bergles, 1990; Tanda, 1997), due to the presence of stagnation zones just up- and downstream of the ribs, which result in local thickening of the thermal boundary layer. For some roughness geometries, the combined effect of the increase in surface area and the slight decrease of the heat transfer coefficient yields, eventually, an enhancement of the heat transfer rate (for example, complex wavy surfaces (Yao, 2006)).

Provided that in the laminar flow regime the surface roughness elements have a limited influence (negative in most cases) on the local heat transfer coefficient (as indicated, for instance, by Fujii *et al.* (1973)), a perspective of heat transfer enhancement may be related to the chance of triggering the transition to turbulence at lower Rayleigh numbers relative to the smooth surface case, as argued by Bhavnani & Bergles (1991) and Yao (2006). In recent experimental papers, Tanda *et al.* (2023*a*,*b*) found that the use of truncated ribs (in lieu of continuous ones), with a proper length of the rib segments and at a Rayleigh number close to that characterizing the upper threshold of the laminar regime over a corresponding smooth plate, was able to provide an increase in the heat transfer coefficient averaged over the inter-rib regions (the only portions along which the heat transfer coefficient was detected by the employed optical technique) of up to 8% relative to the smooth surface, with the peaks higher by 15% or more on a local basis. It is deemed that the relative enhancement would be markedly higher if the contribution of rib surfaces were accounted for. The investigation of the thermal boundary layer by means of schlieren visualization and miniature thermocouple measurements indicated the presence of local flow unsteadiness in isolated spots (in particular, close to the segment edges); this phenomenon, combined with a possibly favorable redistribution of the main buoyant flow due to the presence of rib protrusions, was conjectured to be responsible for the recorded enhancement of the heat transfer coefficient.

The present study is aimed at investigating, through a combined experimental-numerical framework, the same roughness geometries (continuous and truncated ribs) explored in Refs. (Tanda *et al.*, 2023*a*,*b*), yet under conditions, here, well within the laminar regime (by using a plate with a shorter vertical length and imposing an appropriate wall-to-fluid temperature difference). Since some optimized roughness geometries (e.g., truncated rib elements with a proper length) were found in Refs. (Tanda *et al.*, 2023*a*,*b*) beneficial for heat transfer coefficient enhancement when working close to the transitional regime, the crux of the present contribution is whether the imposition of a stable flow would guarantee, for the same geometries, superior heat transfer performance relative to the smooth plate. Besides the experimental survey in which the schlieren optical technique is employed together with energy balance calculations, carrying out the study under the laminar flow regime facilitates performing numerical simulations of the conjugate heat transfer problem (thermal conduction through ribs and natural convection from the ribs and the inter-rib portions of the baseplate to air) through conventional CFD tools as well as the homogenization-based treatment. The latter provides, via upscaling, a computationally cheaper alternative to the standard full feature-resolving simulation over regularly micro-structured vertical surfaces. The reader is referred to Refs. (Ahmed *et al.*, 2022, 2023; Ahmed, 2023) in which the homogenized model was formulated and implemented on relevant cases, at earlier stages of this research project.

The paper is structured as follows. In Section 2, the experimental procedure and the main quantities recorded (local and overall heat transfer coefficient) are outlined. Section 3 addresses features of the fine-grained CFD analysis and, then, describes the homogenization approach with focus on the definition of the effective boundary conditions to be imposed and the evaluation of the upscaled coefficients of interest. The results are presented and discussed in Section 4, while the main findings of the study are highlighted in Section 5.

2 EXPERIMENTAL SETUP AND PROCEDURE

The description of the experimental test section is facilitated by the sketches in Figs. 1 and 2, showing a three-dimensional view of a representative vertical plate equipped with transverse ribs and the geometric details of rib configurations, respectively. The plate (termed "heated plate") was made of two aluminum sheets with a plane heater sandwiched in between. The sandwich principle was adopted to provide, once the electric power has been supplied to the heater, a symmetrical heat transfer on both sides of the plate. The dimensions of the heated plate are: overall thickness $t = 12$ mm, height $H = 175$ mm, and spanwise length $L = 300$ mm. The length L was chosen such that it is much greater than the other two dimensions to favor a two-dimensional thermal field and to improve the resolution of the optical method employed to deduce local heat transfer characteristics, as described in Section 2.1. The thickness of each sheet was sufficient to ensure, combined with the high thermal conductivity of aluminum, an efficient redistribution of heat by conduction within the plate; for this reason, the plate material was

expected to be virtually isothermal. Six fine-gauge thermocouples, calibrated to ± 0.1 K, were embedded in the wall at different elevations, spanning the whole height of the heated plate, to verify temperature uniformity and to provide the mean value of the wall temperature, assumed to be the mean of the individual readings. For all the experimental runs, the temperature readings were uniform within $\pm 2\%$ of the mean plate-to-ambient temperature difference. Three additional thermocouples were located in the ambient air, sufficiently far from the heated plate, to provide a realistic measurement of the ambient air temperature and to detect any air thermal gradient in the vertical direction. Since the temperature difference among the air temperature readings provided by the three sensors was always less than 0.2 K, their average was assumed as representative of the ambient air temperature. Ambient air, at a temperature of 293 K (with a maximum variation of ± 1 K from one test to another), enters from the lower side of a shielding (cf. Fig. 1), whose function is to exclude possible air movements which are present in the laboratory room. For the same reason, at the top section of the shielding, the heated plate was delimited laterally by high-quality glasses (to permit optical access to the test section) and frontally by two smooth and unheated vertical walls, located at distances equal to half the plate height. According to the previous study by Tanda (1997), a relatively large channel spacing-to-height ratio ($= 0.5$) is expected to have almost no influence on the heat transfer behavior along the plate relative to the case of an unconfined, isothermal, vertical plate.

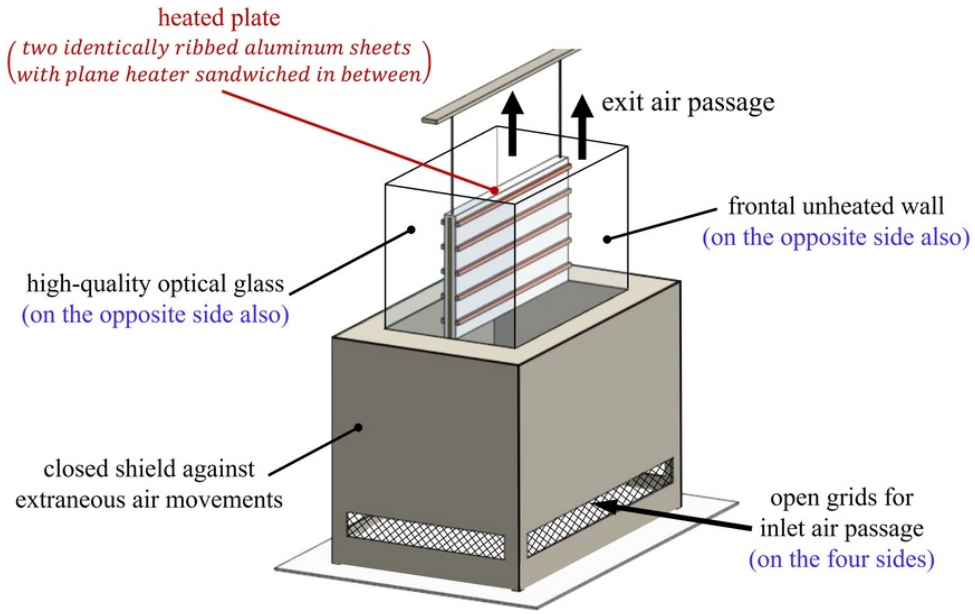

Figure 1: Schematic layout of the experimental test section.

Experiments were performed both in the absence and in the presence of the roughness elements on the heated plate surfaces. The ribs, made of wood, were square in section, with height e equal to 2 mm. Ribs, when present, were symmetrically attached on both sides of the heated plate at equal intervals, which were varied from one experiment to another such that a range of the ratio between the rib pitch ℓ and the rib height e

extending from 20 to 3.5 was covered; this corresponded to increasing the number of ribs on each side from 5 to 25. The majority of experiments considering the heated ribbed plate were conducted by using continuous, spanwise-elongated ribs. Additional experiments were carried out with truncated ribs, in order to investigate their potential to promote the heat transfer relative to the plate with continuous ribs and the smooth plate. A single value of the rib pitch-to-height ratio and three different values of the segment length, d, were considered for the truncated elements. Dimensional characteristics of the rib configurations are shown in Fig. 2 and summarized in Table 1.

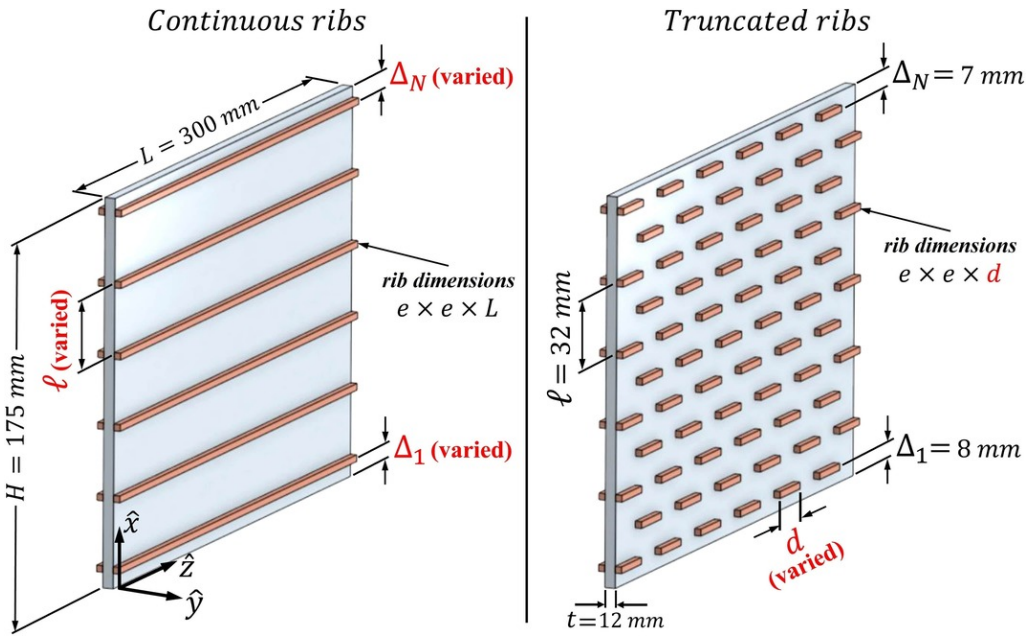

Figure 2: The tested heated plate with continuous and truncated ribs.

Table 1: Description of rib configurations and main geometric parameters.

Rib type	Config.	Number of rows	Number of truncated ribs per row	Δ_1 (mm)	Δ_N (mm)	ℓ (mm)	d (mm)	ℓ/e	d/ℓ	H/ℓ
continuous	A1	5	-	8	7	40	-	20	-	4.38
continuous	A2	9	-	8	7	20	-	10	-	8.75
continuous	A3	17	-	8	7	10	-	5	-	17.5
continuous	B1	6	-	8	7	32	-	16	-	5.47
continuous	B2	11	-	8	7	16	-	8	-	10.94
continuous	B3	21	-	8	7	8	-	4	-	21.88
continuous	C1	7	-	4	3	28	-	14	-	6.25
continuous	C2	13	-	4	3	14	-	7	-	12.5
continuous	C3	25	-	4	3	7	-	3.5	-	25
truncated	-	11	3	8	7	32	50	16	1.56	5.47
truncated	-	11	6	8	7	32	25	16	0.78	5.47
truncated	-	11	12	8	7	32	12.5	16	0.39	5.47

For each surface geometry, experimental runs were performed by adjusting the power input to the heater in order to maintain, when the steady state is attained, a mean plate-to-ambient temperature difference of 45 K, leading to a Rayleigh number Ra (based on the plate height H) equal to 2×10^7, where $Ra = g\beta(\hat{T}_w - \hat{T}_\infty)H^3/(\nu\alpha)$. In the previous expression, $\hat{T}_w$ and $\hat{T}_\infty$ are the baseplate wall and the ambient air temperatures, respectively, g is the gravitational acceleration, while β, α, and ν denote the thermal expansion coefficient, the thermal diffusivity, and the kinematic viscosity, respectively. Air properties were evaluated at the film temperature, that is $\hat{T}_{film} = (\hat{T}_w + \hat{T}_\infty)/2$, except for β, evaluated at the ambient air temperature. To ensure the repeatability of the experimental results, each test was repeated two or three times. Results, in terms of natural-convection, local and average heat transfer coefficients, were provided via two different approaches: local heat transfer coefficients along the surfaces (not covered by ribs) were deduced by the schlieren optical method, whereas average (overall) heat transfer coefficients along the entire rib-roughened surface (inclusive of ribs) were provided by exploitation of the energy balance based on the known input power and the calculated radiant heat exchange with the surroundings.

2.1 Local heat transfer measurements

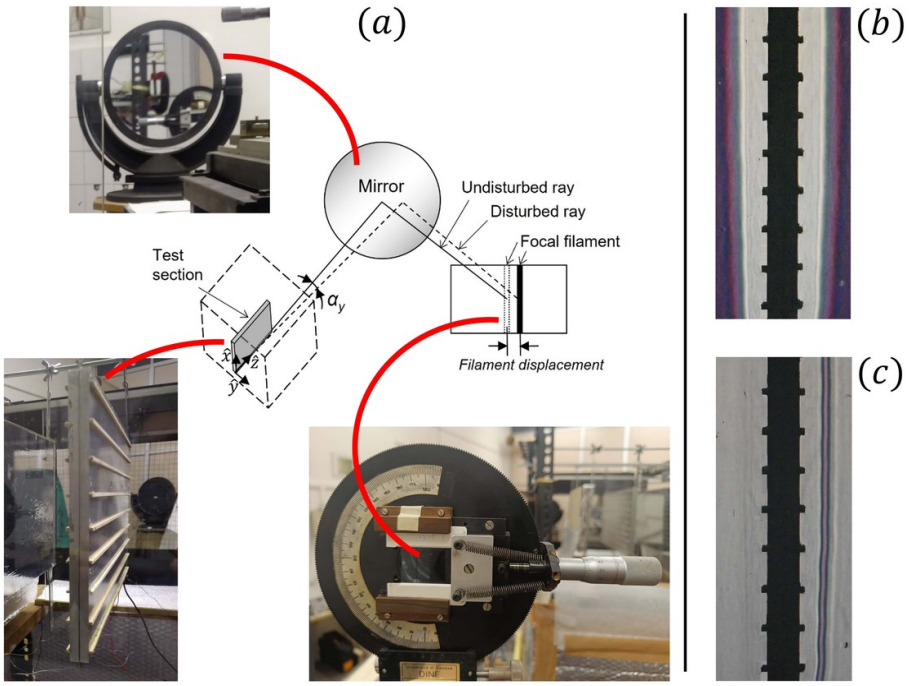

Figure 3: Illustration of the schlieren imaging method adopted. In panel (a), a simple sketch describing acquisition of light ray angular deflection is provided, besides typical photos of one of the test surfaces, the concave mirror, and the movable filter connected to a micrometer. The schlieren images presented show the optical field when the filament is positioned at the focus of schlieren mirror (frame b), and when it is displaced to intercept deflected light rays at a given angular deflection (frame c).

A schlieren optical system was used to visualize the thermal boundary layer and to evaluate the natural convection local heat transfer coefficient. An exhaustive description of the schlieren apparatus employed is given in Refs. (Tanda, 1993, 1997, 2008; Tanda & Devia, 1998). Basically, it consists of a white light beam (composed of parallel rays) crossing the test section, a concave mirror (i.e., the schlieren mirror), which focuses the light onto its focal plane (i.e., the cut-off plane), a filter, and a camera to acquire a real image of the test section. As shown in Fig. 3, when a focal filament (for instance, a thin dark strip or wire) is used as a filter, and no thermal gradients are present in the air crossed by the light beam, all light rays are intercepted by the filter when it is placed on the focus of mirror (and the image formed on the camera will be uniformly dark). When thermal gradients (in the $\hat{y}$-direction of Fig. 3) are present, individual light rays undergo angular deflections whose extent is related to the magnitude of the gradient; consequently, the corresponding spots appear bright in the camera, permitting a reliable visualization of the thermal boundary layer (more precisely of all air particles with a non-zero thermal gradient). The angular deflection α_y of a given light ray (i.e., passing through a given point of coordinates $\hat{x}$, $\hat{y}$) can be measured by moving the filter (connected to a micrometer) along the focal plane of the schlieren mirror until the point of interest appears colored by the same color adopted for the filter (violet). It can be demonstrated that the angular deflection α_y is given by the ratio between the filter displacement and the focal length of the mirror (since the angular deviation is small, $tan\,\alpha_y \approx \alpha_y$) (Goldstein, 1976).

The local heat transfer coefficient at a point on the vertical baseplate surface is introduced, conventionally, as follows:

$$h = -k_{air,w} \frac{(\partial \hat{T}/\partial \hat{y})_w}{\hat{T}_w - \hat{T}_\infty}, \tag{1}$$

where $(\partial \hat{T}/\partial \hat{y})_w$ is the air temperature gradient in the wall-normal direction, $\hat{y}$, evaluated at the point of interest on the baseplate, and $k_{air,w}$ is the air thermal conductivity evaluated at the wall temperature. Due to the relation between the angular deflection of light and the thermal gradient in the fluid crossed, the heat transfer coefficient, h, can be directly calculated by measuring the deflection of light passing in the vicinity of the wall, using the following formula (refer to, for instance, Ref. (Tanda, 1997)):

$$h = \frac{k_{air,w}\, \alpha_{y,w}\, \hat{T}_w^2}{K(\hat{T}_w - \hat{T}_\infty)}, \tag{2}$$

where $\alpha_{y,w}$ is the angular deflection, along the $\hat{y}$-direction, of the light ray passing in the vicinity of the wall at the desired location, and K is a constant (equal to about 0.024 mK in these experiments) which depends on some air properties (Gladstone-Dale and ideal gas constants, index of refraction, pressure) and the length of the plate in the direction of light beam propagation ($\hat{z}$-coordinate in Figs. 2 and 3). Equation (2) provides values of the local heat transfer coefficient for a vertical surface, which depend on the thermal gradients in the $\hat{y}$-direction (whose effect is implicitly included via the consequent angular deflections $\alpha_{y,w}$). In this research, attention is focused on the vertical inter-rib regions of

the plate; hence, the angular deviation along the $\hat{y}$-direction is the only optical data on which the heat transfer coefficient depends. Moreover, Equation (2) assumes the thermal field to be two-dimensional, i.e., independent of the $\hat{z}$-coordinate; otherwise, it is still valid, but the calculated heat transfer coefficient should, then, correspond to the value averaged along the plate spanwise length L. This implies that any three-dimensional feature of the flow emerging from the insertion of ribs can be visualized, via the current technique, only in a corresponding two-dimensional ($\hat{x}$-$\hat{y}$) domain with the results at each point averaged over a line extending in $\hat{z}$. Finally, in order to present the results in dimensionless form, the local Nusselt number was introduced as follows:

$$Nu = \frac{h\,H}{k_{air}}, \tag{3}$$

with k_{air} the thermal conductivity of air evaluated at the film temperature.

2.2 Overall heat transfer measurements (convection and radiation components)

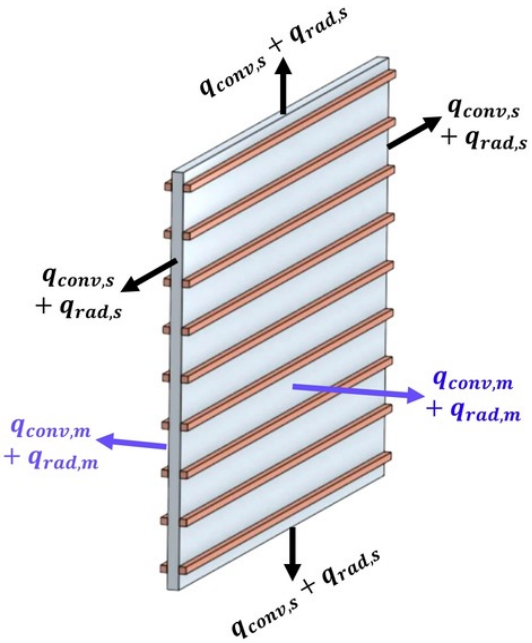

Figure 4: Sketch illustrating the convective (subscript conv) and radiant (subscript rad) heat transfer components from the main surfaces of the heated plate (subscript m) and from the sides generated by the plate thickness (subscript s).

The overall, combined-mode (convection and radiation) heat transfer rate was determined by an energy balance. With reference to Fig. 4, the surfaces of the heated plate exposed to the environment are those generated by the plate thickness (four surfaces having an overall area of $2 \times t\,(H + L)$ and performing always in the same manner, regardless of

the presence of ribs or not) and those washed by the main buoyant air flow (two surfaces having an overall area equal to $2 \times (HL)$ in the absence of ribs, while the area increases as a function of the number of continuous or truncated ribs when they are attached to the surfaces). To facilitate the description of the convective and radiant overall components, q_{conv} and q_{rad}, respectively, the subscripts m (main) and s (side) have been added based on whether the main surface area (where ribs are located) or the side area generated by the plate thickness is considered (see Fig. 4). Hence, at the steady state, the known electrically supplied power q_{el} is entirely dissipated into the environment according to the following equation:

$$q_{el} = q_{conv,m} + q_{rad,m} + q_{conv,s} + q_{rad,s}. \tag{4}$$

As the convective component from the main surfaces $q_{conv,m}$ is the quantity of major interest in this study, the remaining convection heat transfer rate $q_{conv,s}$ from the sides of the plate as well as the radiant components from all surfaces $(q_{rad,m} + q_{rad,s})$ must be calculated separately.

First, attention is given to heat transfer rate from the surfaces associated with the plate thickness: these surface areas are approximately 10% (or less in the presence of ribs) of the area ascribed to the main surfaces. For the radiant component, $q_{rad,s}$, the simple formula giving the radiation heat transfer between two gray surfaces (the thin side surface of the plate and a surrounding ideal surface taken at the ambient temperature) has been considered, with the thermal emittance of aluminum assumed to be equal to 0.12; cf. Ref. (Tanda, 1997). For the convective component $q_{conv,s}$, literature relationships for isothermal vertical and horizontal surfaces are expected to be unreliable due to the shape of the surfaces (with one side much larger than the other one) and their positioning (the vertical surfaces are facing the side glasses at a distance of few millimeters and not washed by an external buoyant flow): for these reasons, $q_{conv,s}$ was estimated from experiments conducted with the smooth heated plate simply by subtracting the overall radiation $q_{rad,m} + q_{rad,s}$ (straightforward to be estimated due to the simple geometry, and of limited amount due to the relatively low thermal emittance of aluminum) plus the convective component $q_{conv,m}$ (evaluated based on the integration of the local heat transfer coefficient distribution obtained by the schlieren method which can cover the entire surface when no ribs are attached) from the electrically supplied power. This procedure yielded for $q_{conv,s}$ a value of 1.8 W, which applies to all experiments (with and without ribs) conducted under the requirement of constant wall-to-ambient air temperature difference (45 K). This marginal heat transfer rate corresponds to about 5% of the overall power dissipated from the heated plate. Therefore, attention is directed mainly to the calculation of the radiant heat transfer rate for the ribbed surface, in order to extract the quantity $q_{conv,m}$ of primary interest.

Whereas the estimation of $q_{rad,s}$ is relatively straightforward (and the calculated quantity is almost negligible), the calculation of the radiant component for the main surfaces $(q_{rad,m})$ is an extremely complex undertaking when ribs are present, and the modeling task necessarily requires simplifying assumptions. An analytical scheme for determining the radiation heat transfer has been developed, using a diffuse, gray-body network, which includes interactions between the heated plate (i.e., each side of the

wooden ribs and the inter-rib aluminum surfaces) and the surrounding (i.e., the frontal unheated walls and the laboratory environment). As illustrated in Fig. 5, the plate surface with ribs comprises elements (assumed at uniform temperature, irradiance and radiosity within the respective areas and considered as gray and diffuse bodies) that behave differently from each other due to a different exposition and/or surface temperature and/or thermal emittance: the inter-rib surfaces of the baseplate directly exposed to the fluid (bf), the vertical sides of ribs (vs), and the horizontal sides of ribs (hs). The elements seen by the heated plate are the frontal unheated walls (ψ) and the ideal closing surfaces which delimit the enclosure from the top and the bottom. Configuration factor algebra (Siegel & Howell, 1992) was employed to calculate the configuration factors among the surfaces involved in the radiant heat exchange, making use of basic configuration factors such as a pair of parallel rectangles situated one above the other, or a pair of perpendicular rectangles sharing a common edge. Further assumptions are listed as follows: (i) the third (spanwise) dimension is assumed to be infinite to simplify the calculation of configuration factors; (ii) the wall temperature of each inter-rib aluminum surface is equal to the experimentally evaluated mean wall temperature $\hat{T}_w$; (iii) temperature of the surrounding surfaces is equal to the experimentally evaluated ambient air temperature $\hat{T}_\infty$; (iv) mean temperature of the rib surfaces $\hat{T}_{rib}$ is given by the empirical relationship $\hat{T}_{rib} = \hat{T}_\infty + \Theta\,(\hat{T}_w - \hat{T}_\infty)$, where Θ was set to 0.85, according to detailed infrared thermography measurements performed at the steady state; (v) values of the thermal emittance of aluminum surfaces (0.12), wooden rib surfaces (0.9), and unheated wall surfaces facing the heated plate (0.25) were taken from the literature (Bejan, 1993; Tanda, 1997), while the radiosity of the laboratory room surfaces was imposed to be $\sigma\hat{T}_\infty^4$, where σ is the Stefan-Boltzmann constant and with the ambient air temperature expressed here in K.

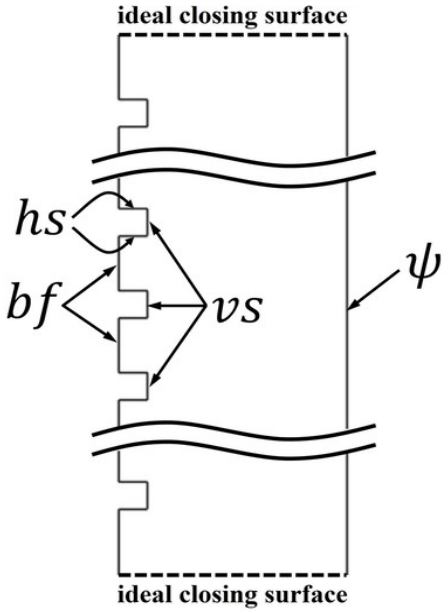

Figure 5: Sketch of the calculation domain for the radiant heat transfer component from the main surface, $q_{rad,m}$.

Once the convective and radiant components $q_{conv,s}$, $q_{rad,s}$, and $q_{rad,m}$ were calculated, the convective heat transfer rate from the main sides of the heated plate, $q_{conv,m}$, was directly obtained from Eq. (4). The average convective Nusselt number, $\overline{Nu}$, is expressed as

$$\overline{Nu} = \frac{q_{conv,m}}{2HL\,(\hat{T}_w - \hat{T}_\infty)} \times \frac{H}{k_{air}}. \tag{5}$$

Since the nominal area chosen in the aforementioned expression ($= 2HL$) is fixed regardless of the actual heat transfer area which depends on the number of ribs attached, the comparison of results based on $\overline{Nu}$ directly reflects the trends of $q_{conv,m}$ for the different configurations tested (see Table 1), which includes, by definition, the effect of surface area increase due to the presence of ribs.

To permit quantification of the impact of the radiant component $q_{rad,m}$ relative to the convective one, the average radiant Nusselt number was introduced as

$$\overline{Nu}_{rad} = \frac{q_{rad,m}}{2HL\,(\hat{T}_w - \hat{T}_\infty)} \times \frac{H}{k_{air}}. \tag{6}$$

The comparison between $\overline{Nu}_{rad}$ and $\overline{Nu}$ permits us to infer the role exerted by the two mechanisms. The radiant component is expected to be very little when ribs are absent or largely spaced; conversely, convective and radiant components tend to equalize when more ribs are densely fitted on the heated plate, as discussed later in Section 4.

2.3 Experimental uncertainty

The calculation of uncertainty in results of the main quantities (at the 95% confidence level) was performed according to the procedure outlined in Ref. Moffat (1988). In principle, the uncertainty in the local heat transfer coefficient h (deduced by the schlieren method), and consequently in the local Nusselt number Nu, is related to accuracy of the measurements of the angular deflection of light rays passing in the vicinity of the plate surface and of the wall absolute temperature and the wall-to-ambient temperature difference, as can be inferred from Eq. (2). According to the root-sum square combination of the effects of each of the individual uncertainties (Moffat, 1988), the dominant role is played by the uncertainty associated with the optical measurement, much larger than those related to the wall temperature and the wall-to-ambient temperature difference. In particular, the larger the recorded angular deflection, the smaller the error in the associated heat transfer coefficient. Based on the range of detected angular deflections, the uncertainty in h values was estimated to fall into the $\pm$ 9–12% range. The uncertainty in the average convective Nusselt number was calculated to be only $\pm$ 4% for the smooth surface, while, for the ribbed surface, it can be considerably affected by the error in the calculation of radiation heat transfer from ribs. The latter accounts for the uncertainty in the emittance of materials (aluminum, wooden ribs, frontal and lateral shrouding walls) and the approximation errors introduced by the methodology for the radiant component evaluation. The calculated uncertainty for the radiant component (i.e., the average

radiant Nusselt number) was $\pm 14\%$; since the contribution of radiation is expected to equalize, in the worst case, the convective one, the uncertainty in the average (convective) Nusselt number ranged from $\pm 4\%$ (for the smooth surface case) to $\pm 14\%$ (with the densest roughness pattern). Finally, the uncertainty associated with the Rayleigh number, mainly dependent on errors in the wall-to-ambient temperature difference, was estimated to be $\pm 2.5\%$.

3 NUMERICAL MODELING AND HOMOGENIZATION PROCEDURE

3.1 The feature-resolving simulations

The computational domains for the two- and the three-dimensional fine-grained simulations, those involving full resolution of the fields near and within the typical corrugations of the ribbed surface, are sketched in Fig. 6(a, b). Steady conjugate natural convection is considered a long the vertical plate since (i) the analysis takes place after balance is reached between the heat supplied to the baseplate and the heat dissipated to air, and (ii) the flow is assumed laminar (at $Ra \approx 2 \times 10^7$), which has been confirmed qualitatively by the schlieren observations of the thermal field. Under a uniform, time-independent baseplate wall temperature $\hat{T}_w \approx 338$ K and with the ambient temperature $\hat{T}_\infty \approx 293$ K (values imposed in conformity with experiments), the value of the criterion $\beta(\hat{T}_w - \hat{T}_\infty)$ is around 0.15 (β is the thermal expansion coefficient), much smaller than 1. The Boussinesq approximation is therefore assumed to be valid (Hærvig & Sørensen, 2020); it is applied here employing a linear temperature-density relationship. The conservation equations governing the spatial distribution of the velocity vector, $\hat{u}_i$, and the temperature, $\hat{T}$, in the fluid domain are

$$\frac{\partial \hat{u}_i}{\partial \hat{x}_i} = 0, \tag{7}$$

$$\rho\, \hat{u}_j \frac{\partial \hat{u}_i}{\partial \hat{x}_j} = -\frac{\partial (\hat{P} - \hat{P}_\infty)}{\partial \hat{x}_i} + \mu \frac{\partial^2 \hat{u}_i}{\partial \hat{x}_j^2} + \rho\beta(\hat{T} - \hat{T}_\infty) g\, \delta_{i1}, \tag{8}$$

$$\hat{u}_j \frac{\partial \hat{T}}{\partial \hat{x}_j} = \alpha \frac{\partial^2 \hat{T}}{\partial \hat{x}_j^2}, \tag{9}$$

where $\hat{P}_\infty$, g, and δ_{ij} are, respectively, the pressure in the stagnant region sufficiently far away from the wall, the magnitude of the gravitational acceleration, and the Kronecker delta function. To facilitate the reading of governing equations, $\hat{x}$, $\hat{y}$ and $\hat{z}$ coordinates were indicated in this section as $\hat{x}_1$, $\hat{x}_2$ and $\hat{x}_3$, respectively. Again, as in Section 2, the air density (ρ), dynamic viscosity (μ), thermal conductivity (k_{air}), and thermal diffusivity (α) are evaluated at the film temperature, while the volumetric thermal expansion coefficient (β) is evaluated at the ambient temperature. Steady thermal conduction takes

place through the roughness elements; the temperature distribution in the ribs, $\hat{\mathcal{T}}(\hat{x}_i)$, is governed by the Laplace's equation

$$\frac{\partial^2 \hat{\mathcal{T}}}{\partial \hat{x}_j^2} = 0. \tag{10}$$

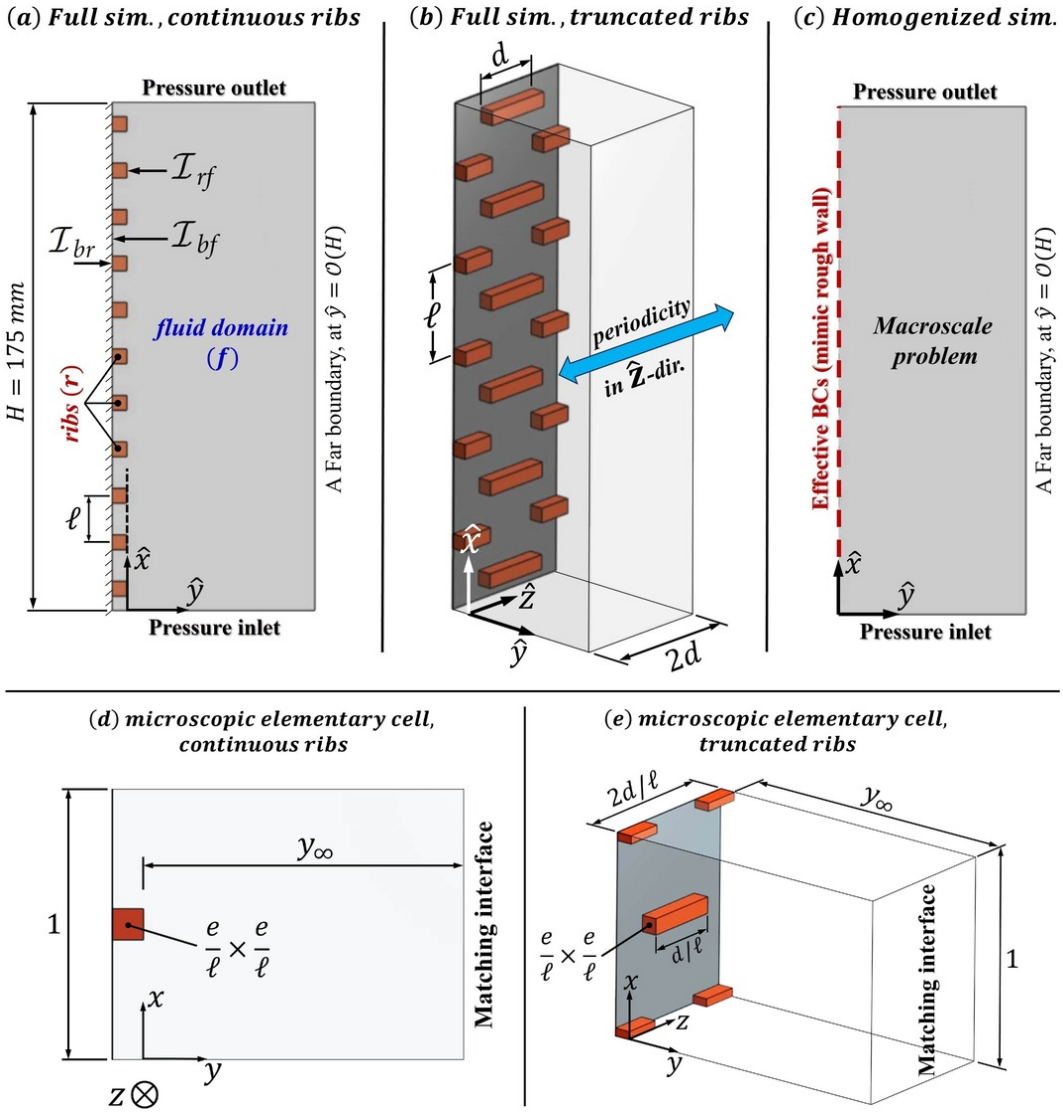

Figure 6: Sketches of the computational domains considered for different numerical simulations: (a) case of spanwise-elongated ribs, a two-dim. problem; (b) case of of truncated ribs, a three-dim. problem; (c) homogenized simulation. An elementary cell of the microscopic subdomain near the continuous ribs is presented in panel (d), while that for truncated ribs is shown in panel (e), both sketched in the dimensionless coordinates $x_i = \hat{x}_i/\ell$.

The temperature boundary conditions at the base-fluid interface ($\mathcal{I}_{bf}$), the base-rib

interface ($\mathcal{I}_{br}$), and rib-fluid interface ($\mathcal{I}_{rf}$) are

$$\begin{cases} \hat{T} = \hat{T}_w & \text{at } \mathcal{I}_{bf}, \\ \hat{\mathcal{T}} = \hat{T}_w & \text{at } \mathcal{I}_{br}, \\ \hat{T} = \hat{\mathcal{T}}, \ \frac{\partial \hat{T}}{\partial \hat{n}} = \kappa \frac{\partial \hat{\mathcal{T}}}{\partial \hat{n}} & \text{at } \mathcal{I}_{rf}, \end{cases} \tag{11}$$

with $\kappa = \dfrac{k_{rib}}{k_{air}} \approx 3.7$ the rib-to-fluid (wood-to-air) thermal conductivity ratio and $\hat{n}$ the dimensional distance in the direction normal to $\mathcal{I}_{rf}$ at any point. No-slip velocity boundary condition are imposed at $\mathcal{I}_{rf}$ and $\mathcal{I}_{bf}$. In addition, uniform pressure boundary conditions are defined at the inlet ($\hat{x}_1 = 0$) and the outlet ($\hat{x}_1 = H$), satisfying an equilibrium with the hydrostatic pressure head, for the flow to be driven purely by the buoyant force. At the far boundary (located at $\hat{y} = \mathcal{O}(H)$), the boundary conditions $\dfrac{\partial \hat{T}}{\partial \hat{x}_2} = \dfrac{\partial \hat{u}_1}{\partial \hat{x}_2} = 0$ and $\hat{u}_2 = 0$ are smoothly attained.

All the simulations were run using Simcenter STAR-CCM+ 2302 software (version 18.02.008-R8). The numerical procedure is similar to that adopted in Ref. (Ahmed *et al.*, 2023), at an earlier stage of this project. The surface-averaged Nusselt number, $\overline{Nu}$, was used as a criterion for convergence of the solution. At any point on the ribs or on the inter-rib regions of the baseplate, the local Nusselt number, Nu, is evaluated as follows:

$$Nu = \frac{-H}{\hat{T}_w - \hat{T}_\infty} \times \left. \frac{\partial \hat{T}}{\partial \hat{n}} \right|_{wall}. \tag{12}$$

The average Nusselt number is calculated, throughout this article, by integrating Nu over the area of the surfaces exposed to natural convection, i.e. the interfaces $\mathcal{I}_{bf}$ and $\mathcal{I}_{rf}$, while using the baseplate area ($\hat{\mathcal{A}}_{base}$), which is the same for all configurations including the smooth surface case, as a weight:

$$\overline{Nu} = \frac{1}{\hat{\mathcal{A}}_{base}} \int_{\mathcal{I}_{bf}+\mathcal{I}_{rf}} Nu \; d\hat{S}, \tag{13}$$

where $d\hat{S}$ is, ideally, an infinitesimal surface area. Since the computational domains considered for the different patterns of truncated ribs are three dimensional with periodicity of the fields in the spanwise direction over a distance equal to $2 \times d$, as shown in Fig. 6(b), Equation (13) reads

$$\left. \overline{Nu} \right|_{3D\,patterns} = \frac{1}{2d \times H} \int_{\mathcal{I}_{bf}+\mathcal{I}_{rf}} Nu \; d\hat{S}, \tag{14}$$

while two-dimensional ($\hat{x}$–$\hat{y}$) computational domains are considered for surfaces roughened with continuous ($\hat{z}$-elongated) ribs, and the definition of $\overline{Nu}$ thus reduces to

$$\left. \overline{Nu} \right|_{2D\,patterns} = \frac{1}{H} \int_{\mathcal{I}_{bf}+\mathcal{I}_{rf}} Nu \; d\hat{s}, \tag{15}$$

with $\hat{s}$ a distance that goes along the base-fluid and the rib-fluid interfaces.

Finally, to enhance reproducibility of the numerical results, we indicate that extra mesh refinement close to the leading edge of the vertical plate (where thickness of the thermal boundary layer is significantly small) was avoided by calculating the average Nusselt number over the region $0 \leq \hat{x}_1/H \leq 0.01$ of the baseplate surface (i.e., up to $\hat{x}_1 = 1.75$ mm) based on the correlation proposed by Churchill & Chu (1975) (the one proved to be valid over the full laminar flow range including when the corresponding Rayleigh number tends to *zero*, i.e., in the neighborhood of the leading edge) instead of evaluating it from the simulations; the reader is referred to the relevant implementation in Ref. (Ahmed *et al.*, 2023).

3.2 The homogenization-based simulations

The homogenization-based simulations are concerned with the macroscale behavior of the fluid flow over the ribbed vertical wall, by evaluating the macroscopic fields $(\ddot{u}_i, \ddot{T}, \ddot{P})$ rather than the fully-featured ones $(\hat{u}_i, \hat{T}, \hat{P})$ which are resolved in the fine-grained simulations. Taking the case of a wall roughened with truncated ribs of pitch distances $\ell_x = \ell$ and $\ell_z = 2d$ (refer to Fig. 6(b)) as an example, one can define the upscaled fields at a point $\Phi : (\hat{x}_\phi, \hat{y}_\phi, \hat{z}_\phi)$, located in the fluid domain beyond the roughness layer (i.e., $\hat{y}_\phi > 0$), by averaging the corresponding fully featured fields over a rectangular $\hat{x} - \hat{z}$ region whose dimensions are $\ell_x \times \ell_z$ and whose center is the point Φ, that is

$$\ddot{T}(\hat{x}_\phi, \hat{y}_\phi, \hat{z}_\phi) = \frac{1}{\ell_x \times \ell_z} \int_{\hat{x}_\phi - \ell_x/2}^{\hat{x}_\phi + \ell_z/2} \int_{\hat{z}_\phi - \ell_z/2}^{\hat{z}_\phi + \ell_z/2} \hat{T}(\hat{x}, \hat{y}_\phi, \hat{z})\, d\hat{z}\, d\hat{x}, \tag{16}$$

and likewise for $\ddot{u}_i$ and $\ddot{P}$. Although interaction between the buoyancy-driven flow and the truncated elements under study is clearly three-dimensional, the phenomena encountered are two-dimensional when analyzed from a macroscopic perspective; they are the variation of the velocity and temperature in the wall-normal direction, $\hat{y}$, and the developing of the boundary layers in the vertical direction, $\hat{x}$. Furthermore, the spanwise velocity component vanishes upon averaging, i.e. $\ddot{u}_3 = 0$. The homogenized simulations are, therefore, run over an $\hat{x} - \hat{y}$ fluid domain, as sketched in Fig. 6(c), where the spatial variations of $\ddot{u}_1$, $\ddot{u}_2$, and $\ddot{T}$ are governed by

$$\frac{\partial \ddot{u}_i}{\partial \hat{x}_i} = 0, \tag{17}$$

$$\rho\, \ddot{u}_j \frac{\partial \ddot{u}_i}{\partial \hat{x}_j} = -\frac{\partial (\ddot{P} - \hat{P}_\infty)}{\partial \hat{x}_i} + \mu\, \frac{\partial^2 \ddot{u}_i}{\partial \hat{x}_j^2} + \rho\beta(\ddot{T} - \hat{T}_\infty) g\, \delta_{i1}, \tag{18}$$

$$\ddot{u}_j \frac{\partial \ddot{T}}{\partial \hat{x}_j} = \alpha \frac{\partial^2 \ddot{T}}{\partial \hat{x}_j^2}, \tag{19}$$

subject to *effective* boundary conditions of the velocity and temperature over the fictitious plane interface at $\hat{y} = 0$, which are to mimic the influence of the rough layer (located at

$\hat{y} < 0$ and not resolved in the homogenized simulation) on the macroscale flow problem. These conditions are available from application of the asymptotic homogenization theory as per the detailed derivation given in Ref. (Ahmed *et al.*, 2023), and they are valid provided that the microscopic and the macroscopic length scales are well-separated, that is $\epsilon = \ell/H << 1$. Up to first-order in terms of ϵ, the effective boundary conditions read

$$\ddot{u}_1\Big|_{\hat{x}_2=0} \approx \Lambda_x \frac{\partial \ddot{u}_1}{\partial \hat{x}_2}\Big|_{\hat{x}_2=0} + M_{12}\frac{\rho g\beta\,(\hat{T}_w - \hat{T}_\infty)}{\mu}, \qquad \ddot{u}_2\Big|_{\hat{x}_2=0} = 0, \tag{20}$$

$$\ddot{T}\Big|_{\hat{x}_2=0} \approx \hat{T}_w + \Lambda_\theta \frac{\partial \ddot{T}}{\partial \hat{x}_2}\Big|_{\hat{x}_2=0}, \tag{21}$$

with Λ_x, Λ_θ, and M_{12} the dimensional Navier-slip, thermal-slip, and interface permeability coefficients, respectively. These upscaled parameters can be related to their dimensionless counterparts (λ_x, λ_θ, and m_{12}) as follows:

$$\Lambda_x = \lambda_x\, l, \quad \Lambda_\theta = \lambda_\theta\, l, \quad M_{12} = m_{12}\, l^2, \tag{22}$$

The macroscopic coefficients λ_x and m_{12} are dependent merely on the geometric characteristics of the roughness pattern, i.e. the rib height-to-pitch ratio (e/ℓ) besides the segment length-to-pitch ratio (d/ℓ) when truncated ribs are considered, while the thermal-slip coefficient, λ_θ, also depends on the rib-to-fluid thermal conductivity ratio, κ. To evaluate these coefficients, it is sufficient to solve a Stokes-like and a Laplace-like closure problems governing the distributions of the auxiliary variables ($\breve{u}_{i1}$, $\breve{p}_1$) and ($\tilde{\theta}$, $\tilde{\phi}$) in an elementary cell of the microscopic domain (refer to Fig. 6(d,e)) with the dimensions/coordinates normalized by the pitch distance ($x_i = \hat{x}_i/\ell$); such *ad hoc* problems can be written, respectively, as follows:

$$\begin{cases} \partial_i \breve{u}_{i1} = 0, \\ -\partial_i \breve{p}_1 + \partial_j^2 \breve{u}_{i1} = 0, \\ \breve{u}_{i1} = 0 \qquad \text{at } \mathcal{I}_{bf} \text{ and } \mathcal{I}_{rf}, \\ -\breve{p}_1\delta_{i2} + \partial_2 \breve{u}_{i1} + \partial_i \breve{u}_{21} = \delta_{i1} \qquad \text{at } y = y_\infty, \end{cases} \tag{23}$$

and

$$\begin{cases} \partial_i^2 \tilde{\theta} = 0 \qquad \text{in the fluid domain}, \\ \partial_i^2 \tilde{\phi} = 0 \qquad \text{in the ribs}, \\ \tilde{\theta} = 0 \qquad \text{at } \mathcal{I}_{bf}, \\ \tilde{\phi} = 0 \qquad \text{at } \mathcal{I}_{br}, \\ \tilde{\theta} = \tilde{\phi}, \;\; \frac{\partial \tilde{\theta}}{\partial n} = \kappa \frac{\partial \tilde{\phi}}{\partial n} \qquad \text{at } \mathcal{I}_{rf}, \\ \partial_2 \tilde{\theta} = 1 \qquad \text{at } y = y_\infty, \end{cases} \tag{24}$$

plus periodicity of all the dependent variables in the x and z directions. Note that $\partial_i = \dfrac{\partial}{\partial x_i}$ and $\partial_i^2 = \dfrac{\partial^2}{\partial x_i^2}$.

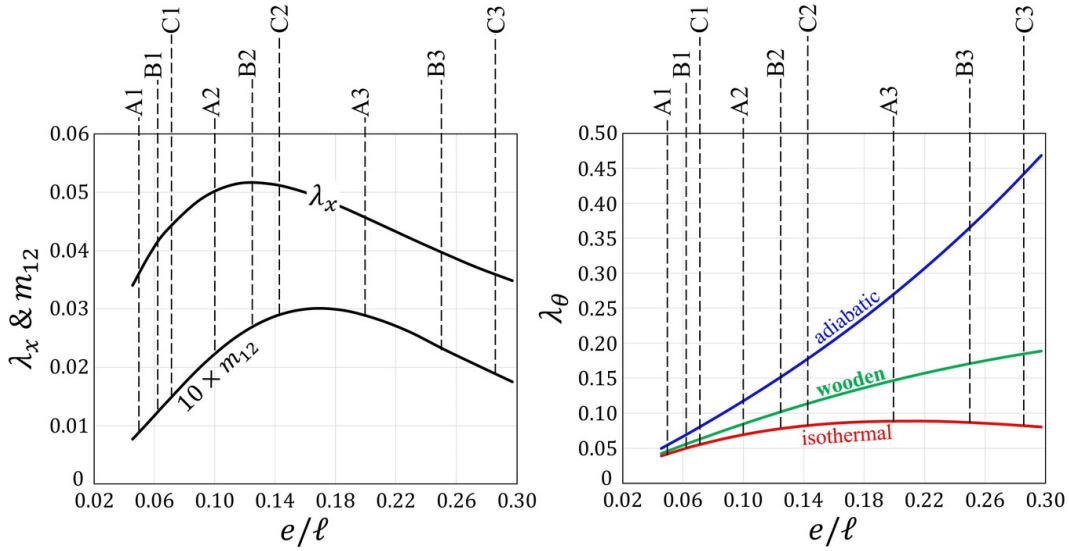

Figure 7: Upscaled coefficients for a surface roughened with transverse square elements of a rib height-to-pitch ratio e/ℓ. Behavior of λ_θ with variations in e/ℓ is plotted for $\kappa = 0$ (adiabatic ribs), $\kappa \to \infty$ (isothermal ribs), and $\kappa \approx 3.66$ (wooden ribs). The typical configurations of continuous ribs described in Table 1 are indicated with dashed lines.

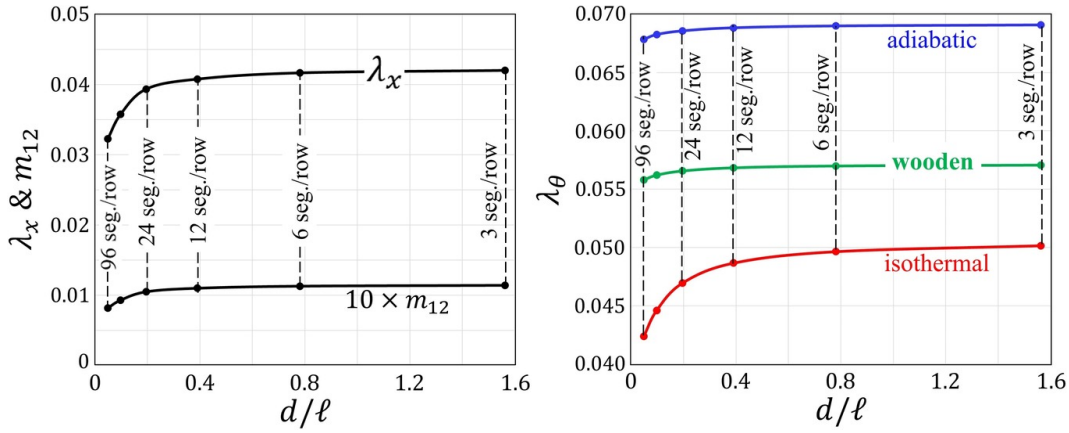

Figure 8: Model coefficients for a surface roughened with a staggered pattern of truncated elements having a rib height-to-pitch ratio of 0.0625, and a segment length-to-pitch ratio d/ℓ. The dependence of λ_θ on d/ℓ is shown for $\kappa = 0$ (adiabatic ribs), $\kappa \to \infty$ (isothermal ribs), and $\kappa \approx 3.66$ (wooden ribs). Dashed lines indicate the typical configurations of truncated ribs described in Table 1, and additional two with larger number of seg./row.

Once the closure variables $\breve{u}_{11}$ and $\tilde{\theta}$ are available by conducting numerical simulations with the matching interface, at $y = y_\infty$, set sufficiently far from the wall ($y_\infty \approx 5$ is commonly used), the macroscopic coefficients for a matching interface of choice at $y_\infty = 0$, i.e. the plane passing through the outer edges of the ribs, can be estimated

directly from the following averaging relations:

$$\lambda_x = \frac{1}{\mathcal{A}_{xz}} \int_{\mathcal{S}_0} \breve{u}_{11}\, dA, \quad m_{12} = \frac{1}{\mathcal{A}_{xz}} \int_{\mathcal{V}_0} \breve{u}_{11}\, dV, \quad \lambda_\theta = \frac{1}{\mathcal{A}_{xz}} \int_{\mathcal{S}_0} \tilde{\theta}\, dA, \tag{25}$$

with $\mathcal{S}_0$ and $\mathcal{V}_0$ the virtual surface at and the fluid volume below the plane $y = 0$, respectively, and $\mathcal{A}_{xz}$ the area of an $x - z$ cross section of the elementary cell (normalized by ℓ^2); $\mathcal{A}_{xz} = 1 \times \frac{2d}{\ell}$ for the case of truncated ribs. A parametric study of the dependence of the model coefficients on the characteristics of the roughness pattern has been performed, and the results for continuous and truncated ribs are presented in Figs. 7 and 8, respectively.

The homogenization-based numerical simulations were conducted with focus on the evaluation of the surface-averaged Nusselt number, to be validated against the corresponding results of the full fine-grained simulations. Since the virtual interface chosen at $\hat{x}_2 = 0$ is smooth and impermeable, the average Nusselt number can be simply calculated from the following relation:

$$\overline{Nu}\Big|_{homog.} = \frac{1}{H} \int_{\hat{x}_1=0}^{\hat{x}_1=H} Nu\Big|_{homog.}\, d\hat{x}_1, \tag{26}$$

with the Nusselt number $Nu\Big|_{homog.}$ defined locally at any point on the virtual interface as follows:

$$Nu\Big|_{homog.} = \frac{-H}{\hat{T}_w - \hat{T}_\infty} \times \frac{\partial \ddot{T}}{\partial \hat{x}_2}\Big|_{\hat{x}_2=0}. \tag{27}$$

It was explained in Ref. (Ahmed *et al.*, 2023) that the predictions of the homogenized model for the Nusselt number can deviate significantly from the accurate values close to the leading edge of the vertical plate; here, we follow the same technique adopted and validated by Ahmed *et al.* (2023) to alleviate this problem. Accordingly, the results of $Nu\Big|_{homog.}$ over an initial distance of the virtual interface, indicated here as the correction distance ($\hat{x}_{corr.}$), are replaced by the corresponding values of Nu over an isothermal flat surface when calculating $\overline{Nu}\Big|_{homog.}$ from Eq. (26). Such a distance was chosen in Ref. (Ahmed *et al.*, 2023) as

$$\hat{x}_{corr.} = 2\ell \left(1 - \frac{3}{\ell/e + 2}\right). \tag{28}$$

4 RESULTS AND DISCUSSION

Results for the local and the average Nusselt numbers over the heated vertical surface, based on the experiments carried out with different roughness patterns (continuous/truncated ribs; cf. Table 1) and the full feature-resolving CFD simulations, are

presented, discussed, and compared in this section, together with predictions of the homogenization-based numerical simulations.

4.1 Local heat transfer: experimental and numerical results

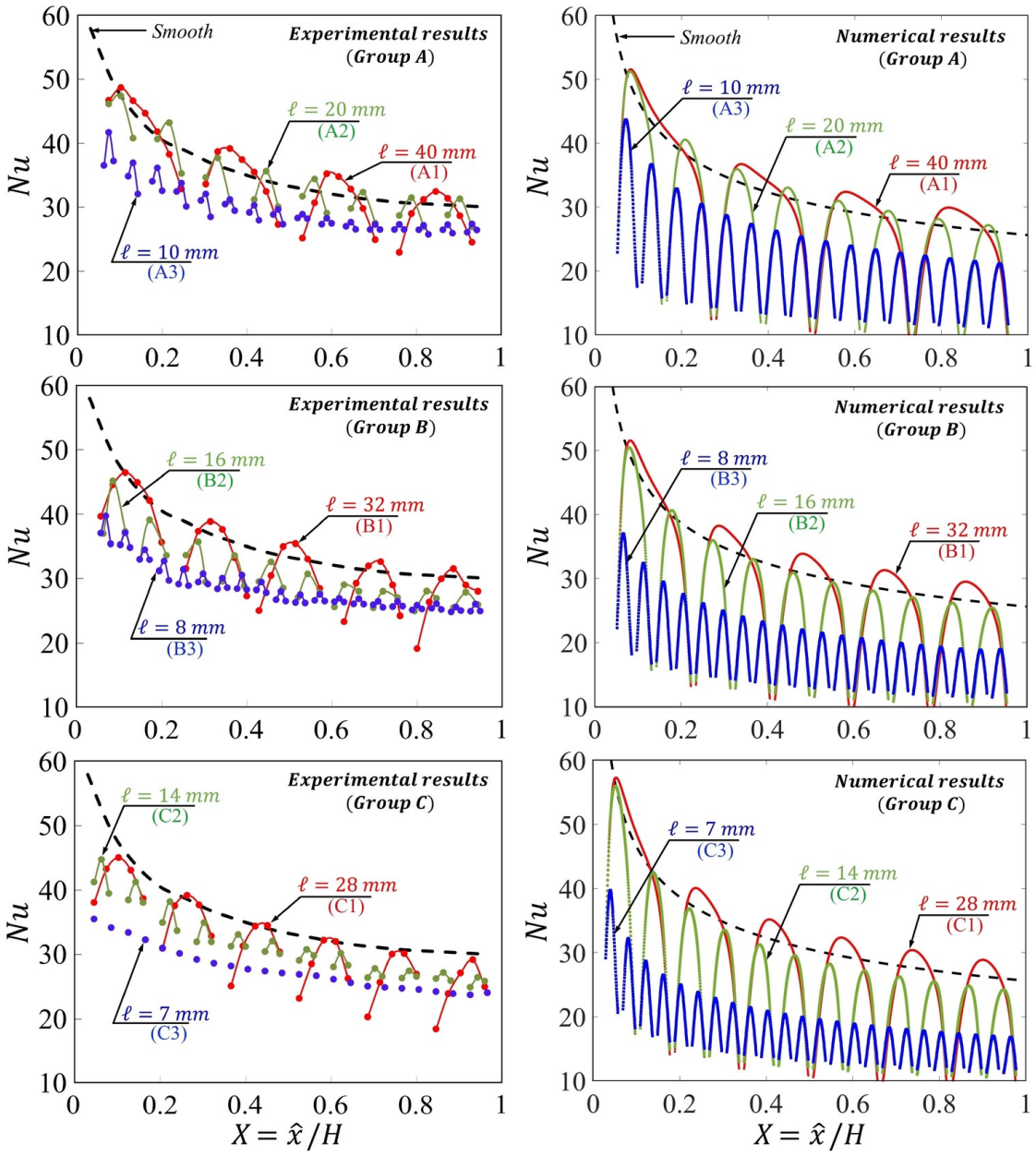

Figure 9: Local Nusselt number distributions along the vertical heated plate when continuous (spanwise-elongated) ribs are attached to the surface; typical geometric characteristics of the different configurations considered are available in Table 1.

Experimental results of the local Nu over the heated surface (on which spanwise-elongated ribs are arranged) are plotted versus the normalized vertical coordinate $X = \hat{x}/H$ in Fig. 9(left), while the corresponding trends obtained from the fine-grained simulations are displayed in Fig. 9(right). To facilitate the readability of the figure, the experiments with continuous ribs are grouped into Groups A, B, and C, each of which encompasses three different ribbed configurations, for instance, A1, A2, and A3 (and likewise for B and C); configuration no. 2 (respectively 3) is obtained simply by introducing an additional rib between each two adjacent ribs in configuration no. 1 (respectively 2) of the same group (see Table 1). The measured/calculated values of Nu are related only to the inter-rib regions of the baseplate surface. While results of the CFD simulations indicate marked reductions of Nu over the baseplate zones located immediately upstream and downstream of ribs (due to the separation eddies which cause local thickening of the thermal boundary layer; cf. the visualizations/comments in Refs. (Ahmed *et al.*, 2022, 2023; Ahmed, 2023)), experiments were unable to capture such effects due to some limitations on the optical accessibility to these regions. Despite this, the agreement between measured and calculated results is satisfactory; the outcomes of both approaches show that attaching continuous ribs to the heated surface has, in general, a negative impact on the convective heat transfer from the inter-rib spaces, except for specific spots located in the central regions of the inter-rib spaces, where the heat transfer performance may improve locally provided that the rib density over the heated plate is relatively low (i.e., for values of ℓ/e larger than about 10). These findings are consistent, at least from a qualitative point of view, with the local Nusselt number behaviors observed in Ref. (Tanda *et al.*, 2023*a*).

The experimental-numerical comparison for local Nu distributions in the presence of truncated ribs is presented in Fig. 10, where the results are provided only over the free baseplate spaces between rib rows. Spanwise-averaged values of Nu (i.e. averaged over a line extending in $\hat{z}$) are reported at each vertical position, $X = \hat{x}/H$. In previous activities carried out at relatively higher Rayleigh numbers (of order 10^8) (Tanda *et al.*, 2023*a*,*b*), attaching staggered truncated ribs to a heated vertical surface was found capable of enhancing the heat transfer performance throughout the majority of the inter-row spaces; it was conjectured that this favorable effect is due to the ability of truncated ribs to induce local instabilities close to the edges of each segment (first signs of transition to turbulence) when the Rayleigh number is close to (but hasn't reached yet) the transitional one for a corresponding smooth surface. In contrast, the present experimental and numerical activity is conducted at flow conditions ($Ra \approx 2 \times 10^7$) well within the laminar regime even when the ribs are introduced, as inferred based on numerous schlieren visualizations. This may justify why the corresponding experimental and numerical results in Fig. 10 (again in substantial agreement with each other) do not reveal any advantage in terms of the values of Nu along each inter-rib region, relative to the smooth plate case.

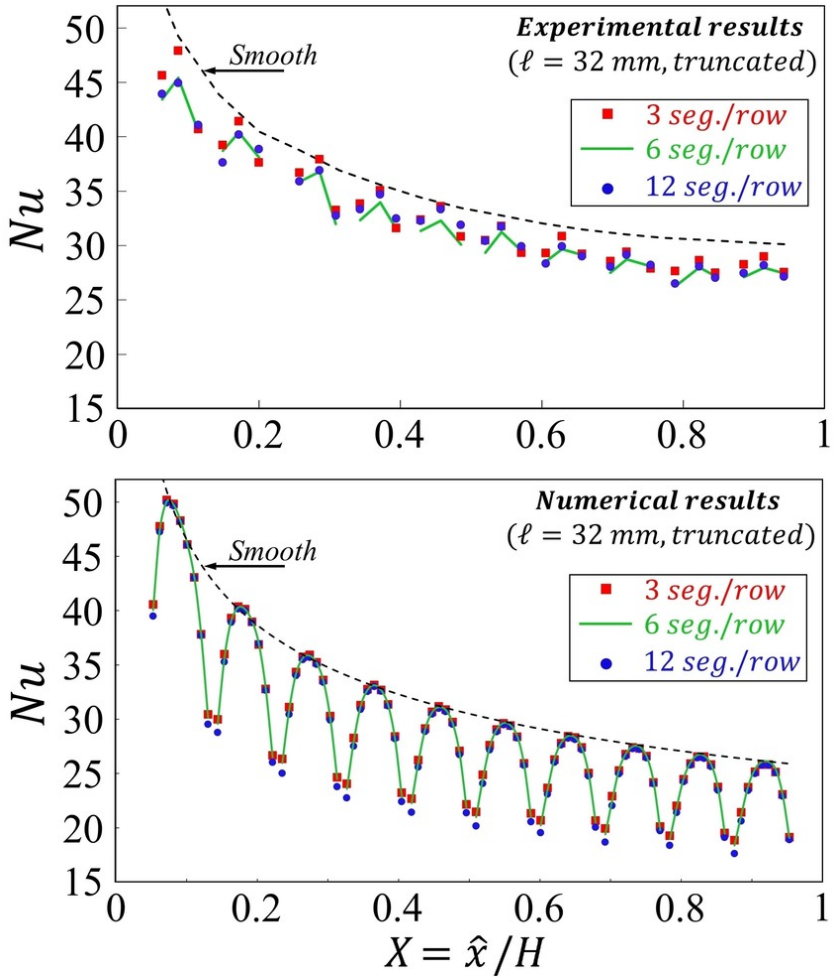

Figure 10: Experimental results (top) and numerical predictions (bottom) for the local Nusselt number along the vertical heated plate when truncated ribs are attached to the surface.

While the fully featured distributions of the local Nusselt number over the plate surface, including variations in the spanwise direction $\hat{z}$, are not obtainable via the imaging technique employed in the experiments, they are available from the fine-grained CFD simulations; these results can provide better insight into the influence of truncated ribs on the convective heat transfer from the baseplate surface. In Fig. 11, contours of the Nusselt number are displayed in the presence of the three different configurations considered for truncated ribs (i.e. by varying the element length), and, for more elaboration, plots of Nu along vertical lines passing either through the middle of the segments or close to their side surfaces. From inspection of the figure, it is evident that heat transfer from the baseplate peaks below some flow regions where the fluid stream is redirected (significantly deflected in the spanwise direction) due to the effect of rib truncation on the velocity field (cf. plots along lines II and IV); in addition, a local peak of Nu is observed in the central spot between each two ribs belonging to successive similar rows (cf. plots along lines I and III). An in-depth look at the contours of Nu reveals that, when the segment length is larger (i.e., with smaller number of segments per row), the following

effects are encountered: the regions of local heat transfer maximization due to deflection of the fluid stream are fewer (adverse effect), yet the levels of Nu in these regions, and also in the central spots between ribs of each two successive similar rows, are higher (favorable effect) compared with the case of the shortest segments. The aforementioned opposing effects, and others that may arise from the complex dynamic and thermal interaction between the flowing fluid and the protrusions, can justify the similarity between the Nusselt number trends over the different surfaces when the analysis is conducted on a line average basis (as in Fig. 10) or when the surface-averaged values are compared (as presented in the following subsection).

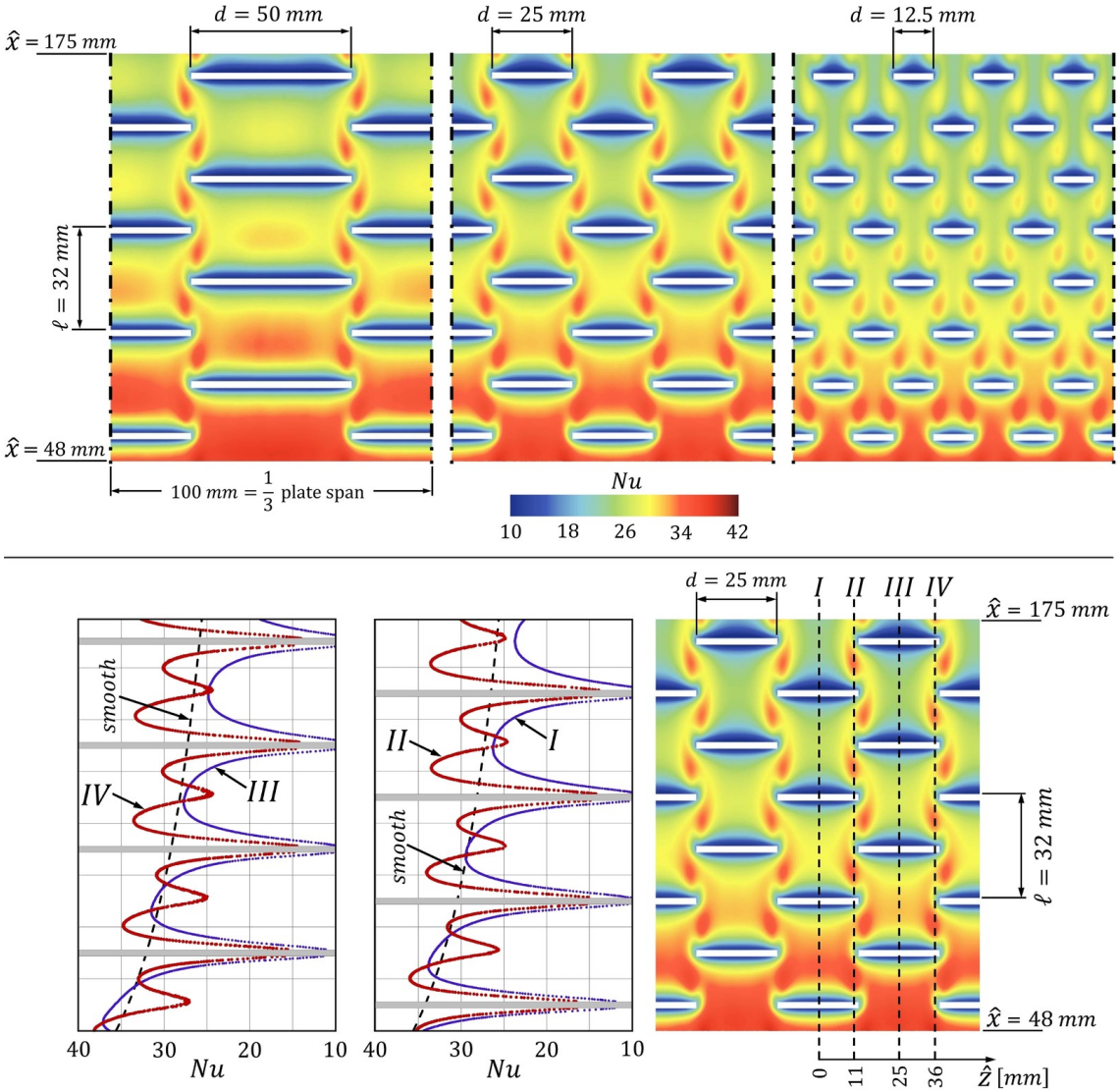

Figure 11: Numerical predictions for the fully featured results of Nu, displayed over an upper portion of the baseplate surface when truncated ribs are attached. The regions shown have spanwise lengths equal to one-third of that of the plate; hence, overall, the roughness patterns consist of (from top left to top right) 3, 6, and 12 segments/row, as presented in Table 1.

4.2 Overall heat transfer: experimental and numerical results

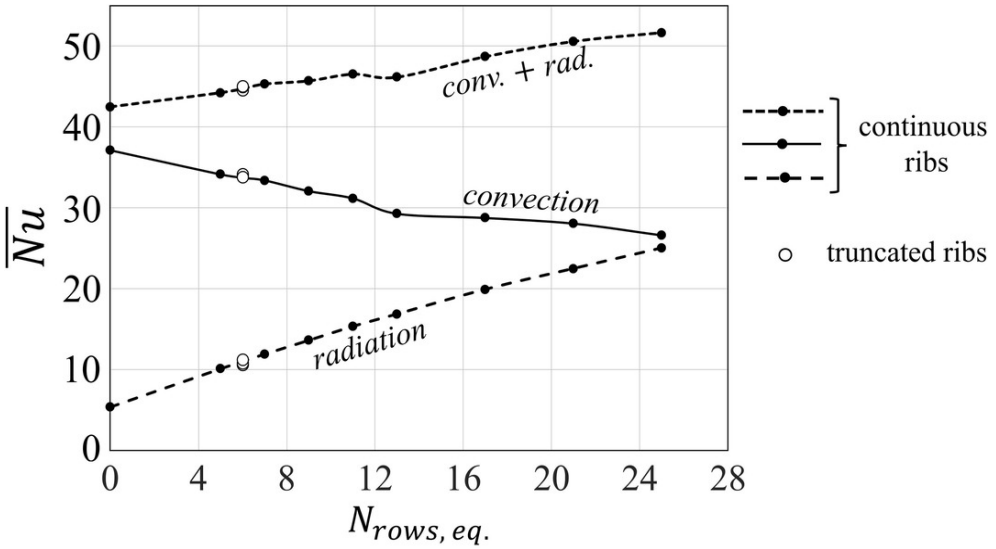

Figure 12: Experimental results for the convective and the radiant average Nusselt numbers (and their summation) over the vertical surface, plotted against the equivalent number of rib rows ($N_{rows,\,eq.}$) for the different configurations under study.

Trends of the average convective and radiant Nusselt numbers, defined respectively by Eqs. (5) and (6) with the corresponding heat transfer rates evaluated via experimental energy balance estimations and analytical analysis of radiation (refer to Section 2.2), are plotted in Fig. 12 as functions of the equivalent number of rib rows ($N_{rows,\,eq.}$) for the different configurations under study, that is, the typical number of rows ($= N_{rows}$, from 5 to 25) in the case of continuous ribs and approximately half the number of rows in the case of truncated ones ($\approx N_{rows}/2$, equal to 6). The following behaviors can be observed from the figure:

(i) The convective heat transfer rate decreases monotonically with the increase of the number of continuous ribs attached to the heated plate. In particular, the average convective Nusselt number drops from about 37.1 (in the absence of ribs) to almost 26.6 (when 25 ribs are present), thus deteriorating by more than 28%. This result is in line not only with the local heat transfer measurements in Fig. 9 but also with previous literature works reporting a general convective heat transfer degradation by adding the continuous ribs notwithstanding the associated increase in the heat transfer area (Bhavnani & Bergles, 1990; Tanda, 1997; Tanda *et al.*, 2023*a*).

(ii) The estimated radiant component dramatically increases (by up to about 400%) with the ribs becoming densely packed on the heated vertical plate due to increased surface area at relatively large thermal emittance (0.9 for wooden ribs' surfaces against 0.12 for aluminum baseplate surface).

(iii) The overall heat transfer rate (convection plus radiation) increases by up to 22% as the number of rib rows increases, thanks to the significant enhancement in the radiant component which outweighs the decline in the convective one.

(iv) The convective, the radiant, and thus the overall heat transfer rates in the presence of truncated ribs are the same as in the case of continuous ribs having the same number of equivalent rows ($N_{rows,eq.}$), and thus almost half the typical number of rows (N_{rows}). For more clarity, the heat transfer performance with 11 rows of truncated ribs (regardless of the number of segments per row) was found comparable to that with 6 continuous ribs, taking into account that the extra surface area introduced by ribs is almost the same in both cases.

The present findings draw attention to applications in which rib-like components are fixed on a heated surface to perform specific functions related to the operation of interest (for instance, electronic devices on a chip). In such situations, if the attached components are, for instance, of low emittance, and thus natural convection remains the only heat transfer regime of significance, the heat dissipation from the system is expected to degrade; therefore, the maximum allowable power supply is to be reduced, otherwise the operating temperature can exceed its permissible limit.

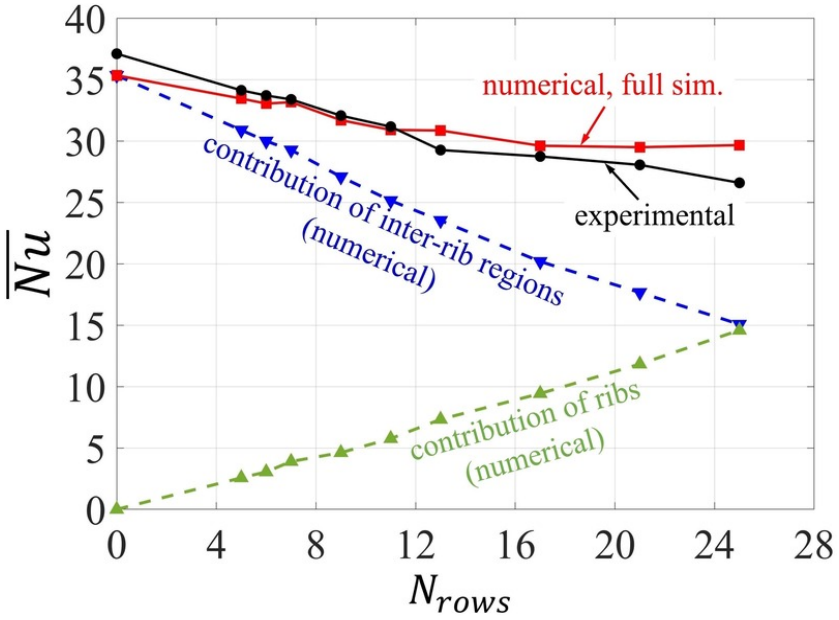

Figure 13: comparison between experimental and numerical results for the average convective Nusselt number with changes in the number of continuous ribs attached to the vertical surface.

Now, the focus shifts to the comparison between the experimentally obtained values of the average convective Nusselt number (see Eq. (5)) and the predictions of the feature-resolving CFD simulations (see Eqs. (13) to (15)) to validate the latter. Figure 13 shows that, for the different configurations of continuous ribs, experimental and numerical

results of $\overline{Nu}$ are in reasonable agreement, where deviations between the corresponding values are in general within $\pm 5\%$, with a maximum of about 12% observed for the densest roughness pattern (i.e. $N_{rows} = 25$), possibly due to experimental uncertainty in estimation of $\overline{Nu}$ which is more significant ($\pm 14\%$) for such a large number of ribs, as elaborated earlier in Section 2.3. The separate roles (numerically calculated) played by convection from the inter-rib portions of the baseplate and from the ribs' surfaces (by using either of the two heat transfer rates to define a corresponding Nusselt number as per Eq. (5)) are shown in the figure, with the latter equalizing the former when the largest number of ribs, here explored, is approached. Furthermore, the numerical results for truncated ribs were evaluated (not plotted in the figure) and were validated against the experimental ones. Both approaches indicate minor variations in $\overline{Nu}$ among the three patterns considered (as the number of segments/row changes): the average convective Nusselt number ranges from 33.30 to 33.42, according to the simulations, and from 33.76 to 34.13, based on the experiments.

4.3 Homogenization-based calculated results

The homogenization-based approach that aims to macroscopically mimic the effect of ribs on the buoyant flow and on the overall convective heat transfer from the heated surface, employing the effective boundary conditions elaborated in Section 3.2, is validated here against the fine-grained simulations.

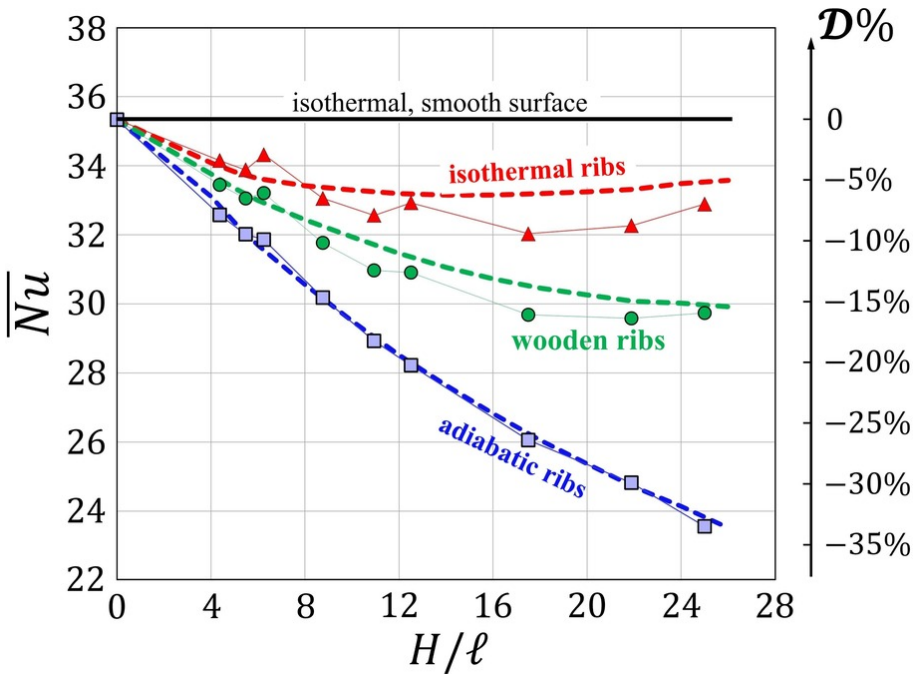

Figure 14: Comparison between predictions of the homogenized simulations (dashed lines) and of the reference fine-grained ones (thin solid lines with symbols) for $\overline{Nu}$ over the vertical heated surface in the presence of continuous ribs.

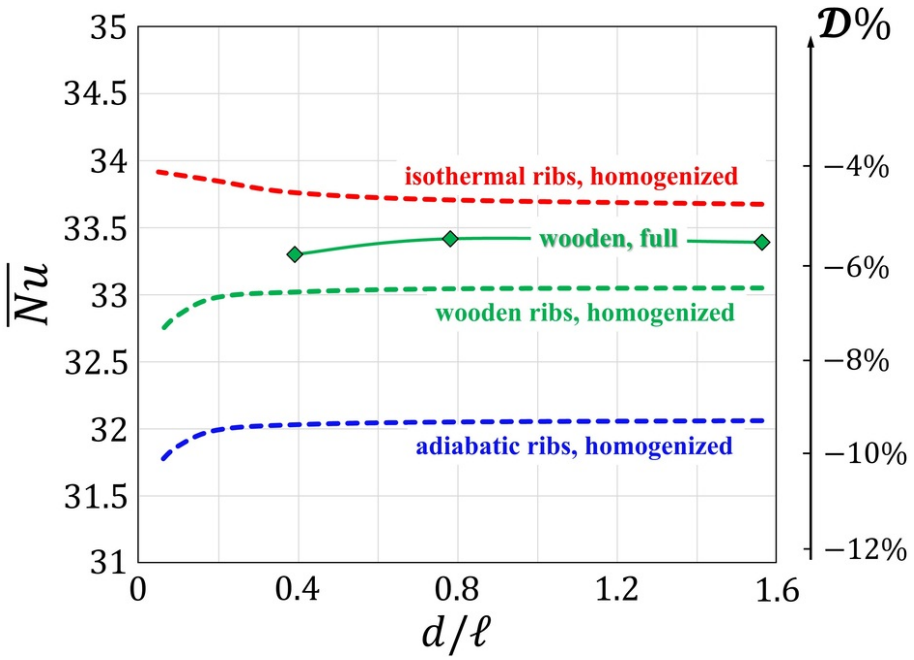

Figure 15: Homogenization-based predictions (dashed lines) for $\overline{Nu}$ in the presence of truncated ribs, plotted against the rib length-to-pitch ratio. Results of the full fine-grained simulations for the three patterns of truncated wooden ribs described in Table 1 are also presented.

Spanwise-elongated ribs are considered in Fig. 14, where the model predictions for the average convective Nusselt number, $\overline{Nu}$, and the consequent percentage change in the convective heat transfer rate (relative to the smooth surface case), $\mathcal{D}\%$, are validated against results of the reference feature-resolving simulations of the nine continuous-rib patterns described in Table 1. Since the plate height ($H = 175$ mm) and the rib height ($e = 2$ mm) are fixed, the rib pitch (ℓ) and the rib height-to-pitch ratio (e/ℓ) corresponding to each value of H/ℓ (the horizontal axis of Fig. 14) can be easily calculated. In addition, while all the laboratory experiments on the roughened surface were performed with wooden ribs ($\kappa = \dfrac{k_{rib}}{k_{air}} \approx 3.66$), the homogenized and the full simulations were run also for perfectly adiabatic/conducting ribs ($\kappa = 0$ and $\kappa \to \infty$, respectively) as the two limiting situations of the rib-to-fluid thermal conductivity ratio. The model coefficients ($\lambda_x, \lambda_\theta, m_{12}$) contributing to the effective boundary conditions (20) and (21), and thus necessary for the homogenized simulations, were evaluated for the different values of e/ℓ and κ according to the trends plotted in Fig. 7. From inspection of Fig. 14, the following observations are drawn:

(i) Model predictions for $\overline{Nu}$ agree well with results of the full numerical simulations for adiabatic, wooden, and perfectly conducting ribs, and over the whole range of H/ℓ here explored.

(ii) Although the thermal conductivity of wood ($k_{rib} \approx 0.1\,\mathrm{Wm^{-1}K^{-1}}$) is relatively low, the convective heat transfer rate with wooden ribs (of small size by definition)

is intermediate between the cases of adiabatic and perfectly conducting elements having the same geometry and pitch; this is consistent with the findings in Ref. (Ahmed *et al.*, 2023).

(iii) Simplifying the fine-grained simulations by assuming that low-thermal-conductivity ribs behave like adiabatic (or isothermal) ones, in order to avoid solving the conduction problem within the ribs and thus to reduce the mesh requirements, may lead to questionable results.

Predictions of the homogenized model for $\overline{Nu}$ in the case of truncated ribs (adiabatic, wooden, or isothermal) are presented in Fig. 15, with the role of the segment length-to-pitch ratio (d/ℓ) examined. The model coefficients ($\lambda_x, \lambda_\theta, m_{12}$) were estimated for the different values of d/ℓ and κ based on the behaviors shown in Fig. 8; note that the pitch distance ℓ is equal to 32 mm for all the truncated-rib patterns. When truncated wooden ribs are present, values of the average convective Nusselt number based on the model are found to be close to those obtained through the full simulations, with absolute deviations of less than 2%.

5 CONCLUSIONS

An experimental and numerical investigation of natural convection heat transfer from vertical rib-roughened surfaces under laminar regime is reported. The aim of the study was to determine whether transverse roughness elements can result in a heat transfer enhancement (relative to the smooth plate) in the laminar buoyant-flow regime. The major findings of the study are as follows:

(i) The presence of transverse continuous ribs, regularly spaced on the heated plate at a rib pitch-to-height ratio ranging from 3.5 to 20, resulted in a convective heat transfer degradation, from both local (for the plate regions not occupied by ribs) and overall average (from baseplate and ribs) perspectives; local heat transfer was found to be higher than the corresponding one for the smooth plate only for some spots located in the central region of the inter-rib space, exclusively when the rib pitch-to-height ratio is larger than about 10.

(ii) Truncating the ribs into segments arranged in a staggered pattern on the vertical surface, a practice found beneficial to heat transfer enhancement, relative to the smooth plate, in previous investigations (Tanda *et al.*, 2023*a*,*b*) conducted at a relatively high Rayleigh number (of order 10^8), did not provide any advantage in the present study where the Rayleigh number is relatively low (of order 10^7, ensuring stable flow). From an average point of view, they performed as a continuous rib configuration having a pitch double that of the truncated one.

(iii) All the circumstances above were confirmed via both conventional fine-grained CFD simulations of the conjugate heat transfer problem (conduction through ribs and convection from ribs' surfaces and inter-rib baseplate portions to air) and homogenization-based ones which exploit effective boundary conditions to macroscopically mimic the phenomena, thus simplifying the numerical work by bypassing resolution of the fields through/between/in close vicinity of the ribs.

(iv) Results of the numerical simulations showed that the heat transfer rate from surfaces roughened with wooden ribs ($k_{rib} \approx 0.1\,\mathrm{Wm^{-1}K^{-1}}$) may differ significantly from those roughened with perfectly adiabatic ones, especially when the ribs are densely packed on the wall. In particular, their performance was found intermediate between the cases of adiabatic and perfectly conducting elements, which implies that adopting the latter simplifications may lead to questionable results.

REFERENCES

Ahmed, E.N. 2023 Natural-convection heat transfer from regularly ribbed vertical surfaces: Homogenization-based simulations towards a correlation for the Nusselt number. *Numer. Heat Transfer A Appl.* **83** (9), 991–1013.

Ahmed, E.N., Bottaro, A. & Tanda, G. 2022 A homogenization approach for buoyancy-induced flows over micro-textured vertical surfaces. *J. Fluid Mech.* **941**, A53.

Ahmed, E.N., Bottaro, A. & Tanda, G. 2023 Conjugate natural convection along regularly ribbed vertical surfaces: A homogenization-based study. *Numer. Heat Transfer A Appl.* (doi: 10.1080/10407782.2023.2202347).

Bejan, A. 1993 *Heat Transfer*. New York, NY, USA: Wiley.

Bhavnani, S.H. & Bergles, A.E. 1990 Effect of surface geometry and orientation on laminar natural convection heat transfer from a vertical flat plate with transverse roughness elements. *Intl J. Heat Mass Transfer* **33** (5), 965–981.

Bhavnani, S.H. & Bergles, A.E. 1991 Natural convection heat transfer from sinusoidal wavy surfaces. *Wärme-Stoffübertrag.* **26** (6), 341–349.

Bohn, M. & Anderson, R. 1984 Heat-transfer enhancement in natural convection enclosure flow. *Solar Energy Research Institute,* Golden, CO, USA, Report No. SERI/TR–252-2103 .

Churchill, S.W. & Chu, H.H.S. 1975 Correlating equations for laminar and turbulent free convection from a vertical plate. *Intl J. Heat Mass Transfer* **18** (11), 1323–1329.

Fujii, T., Fujii, M. & Takeuchi, M. 1973 Influence of various surface roughness on the natural convection. *Intl J. Heat Mass Transfer* **16** (3), 629–636.

Gilani, S.E., Al-Kayiem, H.H., Woldemicheal, D.E. & Gilani, S.I. 2017 Performance enhancement of free convective solar air heater by pin protrusions on the absorber. *Sol. Energy* **151**, 173–185.

Goldstein, R.J. 1976 Optical techniques for temperature measurement, in: Eckert, E.R.G. & Goldstein, R.J. (Eds.), *Measurements in Heat Transfer*, 2nd ed. Washington, WA, USA: Hemisphere Publishing Corporation (Chapter 5) .

Hærvig, J. & Sørensen, H. 2020 Natural convective flow and heat transfer on unconfined isothermal zigzag-shaped ribbed vertical surfaces. *Intl Commun. Heat Mass Transfer* **119**, 104982.

Incropera, F.P. 1988 Convection heat transfer in electronic equipment cooling. *ASME J. Heat Transfer* **110** (4b), 1097–1111.

Moffat, R.J. 1988 Describing the uncertainties in experimental results. *Exp. Therm. Fluid Sci.* **1** (1), 3–17.

Nghana, B., Tariku, F. & Bitsuamlak, G. 2022 Numerical assessment of the impact of transverse roughness ribs on the turbulent natural convection in a BIPV air channel. *Build. Environ.* **217**, 109093.

Siegel, R. & Howell, J.R. 1992 *Thermal Radiation Heat Transfer,* 3rd ed. New York, NY, USA: Hemisphere Publishing Corporation.

Tanda, G. 1993 Natural convection heat transfer from a staggered vertical plate array. *ASME J. Heat Transfer* **115** (4), 938–945.

Tanda, G. 1997 Natural convection heat transfer in vertical channels with and without transverse square ribs. *Intl J. Heat Mass Transfer* **40** (9), 2173–2185.

Tanda, G. 2008 Natural convective heat transfer in vertical channels with low-thermal-conductivity ribs. *Intl J. Heat Fluid Flow* **29** (5), 1319–1325.

Tanda, G., Ahmed, E.N. & Bottaro, A. 2023*a* Natural convection heat transfer from a ribbed vertical plate: Effect of rib size, pitch, and truncation. *Exp. Therm. Fluid Sci.* **145**, 110898.

Tanda, G., Ahmed, E.N. & Bottaro, A. Submitted in 2023*b* Experimental observations of the onset of unsteadiness for buoyant airflow along smooth and rough vertical isothermal walls. *Exp. Heat Transfer* .

Tanda, G. & Devia, F. 1998 Application of a schlieren technique to heat transfer measurements in free-convection. *Exp. Fluids* **24** (4), 285–290.

Tzanos, C.P., Tessier, J.H. & Pedersen, D.R. 1991 An optimization study for the reactor vessel auxiliary cooling system of a pool liquid-metal reactor. *Nucl. Technol.* **94** (1), 68–79.

Yao, L.-S. 2006 Natural convection along a vertical complex wavy surface. *Intl J. Heat Mass Transfer* **49** (1-2), 281–286.

PAPER F1

Laminar flow in a channel bounded by porous/rough walls: revisiting Beavers-Joseph-Saffman [1]

Essam Nabil Ahmed and **Alessandro Bottaro**

DICCA, Università di Genova, via Montallegro 1, Genova, 16145, Italy

The fully developed, steady, incompressible, laminar flow in a channel delimited by rough and/or permeable walls is considered. The influence of the micro-structured bounding surfaces on the channel flow behavior is mimicked by imposing high-order effective boundary conditions which stem from homogenization theory and do not contain empirical parameters. A closed-form solution of the Navier-Stokes equations is found for the flow in the channel, with conditions at each virtual boundary linking the slip velocities to shear stress and streamwise pressure gradient. The boundary condition for the longitudinal velocity coincides with a little-noticed extension of the so-called Beavers-Joseph condition, first derived by P. G. Saffman (*Stud. Appl. Math.* **50**, 1971); it applies to both permeable and rough surfaces, including the case of separated flow (Couette-Poiseuille motion with adverse pressure gradient). The analytical solution obtained for the velocity distribution in the channel is validated against full feature-resolving simulations of the flow for either highly ordered or random textures, highlighting the accuracy and the applicability range of the model. The Stokes-based model used to identify slip and interface permeability coefficients in the effective boundary conditions is found to be reliable and accurate up to $\epsilon Re_\tau \approx 10$, with ϵ ratio of microscopic to macroscopic length scales and Re_τ the shear-velocity Reynolds number. Above this threshold, the coefficients must account for advective effects: a new upscaling procedure, based on an *Oseen's approximation*, is thus proposed and validated, extending considerably beyond the Stokes regime.

1 INTRODUCTION

The low-Reynolds-number motion of an incompressible fluid in a plane channel bounded by a porous wall which borders the duct in $\hat{y} = 0$ has been a classical problem since the seminal experimental work by Beavers & Joseph (1967). They observed that the flow rate in the channel was larger in the presence of the porous layer than with a no-slip wall

[1]The Version of Record of this manuscript has been published and is available in: *European Journal of Mechanics - B/Fluids* **103** (2024) 269–283. https://doi.org/10.1016/j.euromechflu.2023.10.012

and hypothesized that the fluid could slip at some *Stokes–Darcy interface* with velocity

$$\hat{u}_{slip} = \frac{\sqrt{\hat{\mathcal{K}}}}{\alpha} \frac{\partial \hat{u}}{\partial \hat{y}}\bigg|_{\hat{y}\to 0^+} + \frac{\hat{\mathcal{K}}}{\mu}\,\mathcal{M}, \tag{1}$$

with the second term on the r.h.s. of Eq. (1) corresponding to Darcy's velocity; $\hat{\mathcal{K}}$ is a scalar measure of the permeability of the porous medium in its bulk, μ is the dynamic viscosity, and $\mathcal{M} = |\partial\hat{p}/\partial\hat{x}|$ denotes the magnitude of the macroscopic, streamwise pressure gradient. The dimensionless constant α was later observed to depend on the properties and the geometry of the permeable material near the dividing surface, on the local direction of the flow, on the Reynolds number and on the possible presence of structural non-uniformities at the surface of the porous medium, where the porosity is locally larger (Larson & Higdon, 1986; Sahraoui & Kaviany, 1992). Such non-uniformities are hardly avoidable in practice since solid inclusions cannot pack as tightly near the porous/free-fluid interface as they do in the bulk of the porous medium (Nield, 2009).

Saffman (1971) gave a theoretical justification of the empirical condition by Beavers & Joseph (1967) by first applying ensemble averaging to the Stokes equation across the porous/free-fluid domain and then performing asymptotic matching at the two edges of the interface layer. A closer look at Saffman's development reveals that, upon retaining terms up to second order in the small parameter $\sqrt{\hat{\mathcal{K}}}$, the slip velocity is the same as in Eq. (1) except for Darcy's term, which was found to be corrected by an order one dimensionless factor B, to become $(B\hat{\mathcal{K}}/\mu)\,\mathcal{M}$. The literature is rich of studies that sought to revisit/extend/generalize the Beavers-Joseph-Saffman (BJS) condition and/or investigate its limitations and deficiencies, e.g. Refs. (Neale & Nader, 1974; Vafai & Kim, 1990; Auriault, 2010; Eggenweiler & Rybak, 2020, 2021; Strohbeck *et al.*, 2023).

Some of the papers that followed the works by Beavers, Joseph and Saffman used upscaling theories to close the problem and identify the constant α (and, rarely, also B). Among the major contributors, extensively cited in the recent review by Bottaro (2019), we count Mikelić and colleagues (using asymptotic homogenization) and Whitaker and colleagues (using volume averaging). Recent papers are those by Lācis & Bagheri (2017), Lācis *et al.* (2020), Sudhakar *et al.* (2021), and Naqvi & Bottaro (2021), where homogenization theory was brought to second order in terms of a small parameter, ratio of microscopic to macroscopic length scales, for the BJS condition to read (for the channel flow case):

$$\hat{u}_{slip} = \hat{\lambda}\,\frac{\partial \hat{u}}{\partial \hat{y}}\bigg|_{\hat{y}\to 0^+} + \frac{\hat{\mathcal{K}}^{itf}}{\mu}\,\mathcal{M}; \tag{2}$$

the coefficients $\hat{\lambda}$, a *Navier slip length*, and $\hat{\mathcal{K}}^{itf}$, the *interface permeability*, are not simply proportional to $\sqrt{\hat{\mathcal{K}}}$ and $\hat{\mathcal{K}}$, and can be found by solving microscopic (*auxiliary*) problems in a representative unit cell, for any regular microscopic pattern. It should be highlighted that: (*i*) the BJS condition (2) is valid for both permeable and rough, impermeable layers (in the latter case $\hat{\mathcal{K}}$ vanishes, whilst $\hat{\lambda}$ and $\hat{\mathcal{K}}^{itf}$ do not); (*ii*) computed values of $\hat{\lambda}$ and $\hat{\mathcal{K}}^{itf}$ are available in the literature for many rough (Lācis *et al.*, 2020; Bottaro

& Naqvi, 2020; Sudhakar *et al.*, 2021; Ahmed *et al.*, 2022*a*; Ahmed, 2023) and porous (Lācis *et al.*, 2020; Sudhakar *et al.*, 2021; Naqvi & Bottaro, 2021; Ahmed *et al.*, 2022*b*) wall microstructures; (*iii*) the theory is not limited to the simple case of plane channels; several examples with complex geometries are provided in the references given above. In the general case, Eq. (2) must be coupled to a zero-net mass flux condition for the wall-normal speed $\hat{v}$ at the virtual interface (Lācis *et al.*, 2020). Such transpiration becomes crucial when the flow is turbulent (Bottaro, 2019; Lācis *et al.*, 2020), but is of no concern in the present fully developed flow setting, as shown later.

In view of the aforementioned contributions, the authors believe that a comprehensive investigation that addresses and systematically pursues answers to the following critical questions regarding the boundary condition (2) is still needed:

i. How versatile is it for different wall patterns/textures?

ii. How does it perform when the microscopic and macroscopic length scales are comparable?

iii. Is accuracy enhanced when we advance in the order of the asymptotic approximation?

iv. Is it accurate in the presence of near-wall backflow?

v. Is the condition still valid beyond the Stokes flow regime?

vi. Can it be further improved, in the presence of sizeable near-wall advective effects, such that its applicability range is extended?

The purpose of this article is to highlight the extent of the validity of the BJS condition (2) when rough and/or permeable layers, of either isotropic or transversely isotropic microstructure in the $(\hat{x}-\hat{z})$ plane, delimit the flow, including the case of positive pressure gradient with flow separation; we further aim to show the effectiveness of homogenization theory to evaluate the macroscopic coefficients, $\hat{\lambda}$ and $\hat{\mathcal{K}}^{itf}$, for a wide range of surface/substrate microstructures. The goals above are accomplished by finding the analytical solutions of the Navier-Stokes equation for the Poiseuille and the combined Couette-Poiseuille problems in the channel, subject to slip boundary conditions, and comparing them to numerical simulations of the flow in both the channel and the porous/rough layer, with full resolution of the small-scale flow features within the pores and/or the textured surface(s). Moreover, a procedure is outlined to treat the case in which near-wall advection becomes relevant, illustrating how slip and surface permeability coefficients vary.

The basic homogenization approach is presented in Section 2 and the macroscopic coefficients are evaluated for a collection of surface patterns. In Section 3, the analytical solutions are derived and validated. Finally, a novel version of the homogenization approach, accounting for advection via an Oseen-based approach, is described and its advantages over the Stokes-based model are thoroughly discussed. Concluding remarks are provided in Section 4.

2 THE HOMOGENIZATION MODEL

2.1 Upscaling procedure and effective boundary conditions

The incompressible, isothermal, steady, laminar flow in a channel of height $2H$ bounded from the bottom and the top sides (subscripts b and t respectively) by rough/permeable walls, i.e. at $\hat{y}_b = 0$ and $\hat{y}_t = 0$, is analyzed; cf. Fig. 1(a). The dimensional mass and momentum conservation equations governing the distribution of the velocity vector (whose components are denoted as $\hat{u}_1 = \hat{u}$, $\hat{u}_2 = \hat{v}$, $\hat{u}_3 = \hat{w}$) and the modified pressure $\hat{p}$ over space ($\hat{x}_{1,b(t)} = \hat{x}_{b(t)}$, $\hat{x}_{2,b(t)} = \hat{y}_{b(t)}$, $\hat{x}_{3,b(t)} = \hat{z}_{b(t)}$) are

$$\frac{\partial \hat{u}_i}{\partial \hat{x}_i} = 0, \quad \rho \hat{u}_j \frac{\partial \hat{u}_i}{\partial \hat{x}_j} = -\frac{\partial \hat{p}}{\partial \hat{x}_i} + \mu \frac{\partial^2 \hat{u}_i}{\partial \hat{x}_j^2}, \tag{3}$$

based on either of the two coordinate systems; ρ is the fluid density and μ is the dynamic viscosity. The channel flow is influenced by the presence of the micro-structured boundaries where a complex, generally three-dimensional interaction takes place as the fluid passes near/within the surface corrugations. The presence of well-separated length scales, i.e. the microscopic scales ℓ_b and ℓ_t characterizing the bottom and top surfaces/substrates, respectively, and the macroscopic length scale (chosen here as H, half the channel height), renders the problem amenable to upscaling via the multiscale homogenization approach; *effective* boundary conditions of the velocity can be derived at fictitious plane interfaces, next to the physical rough/porous boundaries, to mimic the effects of small surface inhomogeneities on the macroscopic channel flow.

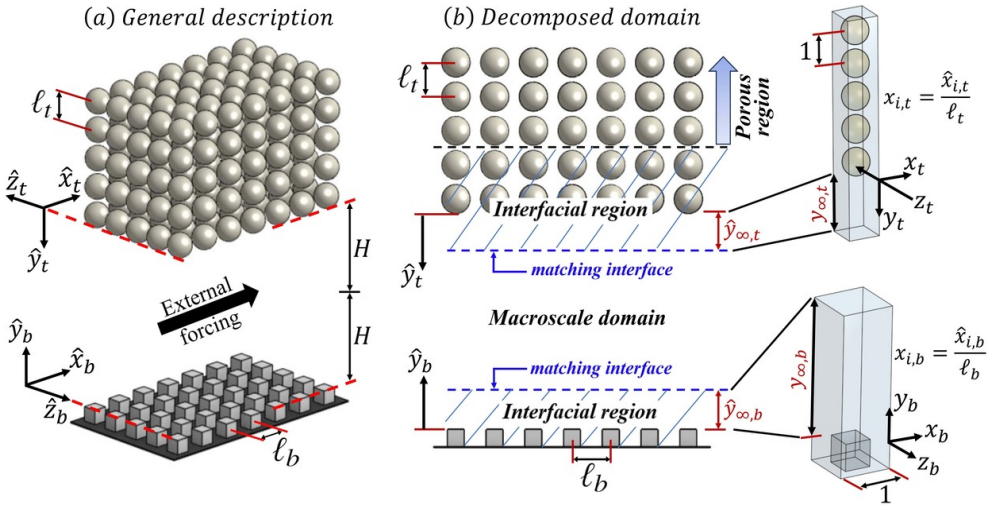

Figure 1: Sketch of the hierarchical flow problem under analysis, with indication of the microscopic/macroscopic length scales. The domain decomposition is illustrated in panel (b), and doubly periodic elementary cells (periodicity here is in the x and z directions) of the top and bottom microscopic domains are shown in the right frame, with their dimensions described in the dimensionless coordinates $x_{i,b(t)}$.

The homogenization approach adopted here proceeds along the same lines of Naqvi & Bottaro (2021) and Ahmed *et al.* (2022*b*). The whole flow domain is first decomposed into macroscopic and microscopic sub-domains, and virtual matching interfaces (at $\hat{y}_b = \hat{y}_{\infty,b}$ and $\hat{y}_t = \hat{y}_{\infty,t}$; cf. Fig. 1(*b*)) are defined where continuity of velocity and traction vectors is applied. An asymptotic analysis is then conducted on the microscopic problems (bottom/top), which are accordingly reconstructed at different orders of the small parameters $\epsilon_{b(t)} = \ell_{b(t)}/H$. At each order, a generic solution of the problem considered is assumed, in which auxiliary, newly introduced, purely microscopic variables appear; systems of partial differential equations permit to numerically evaluate these variables (discussed in more detail in Section 2.2) and to define, via an averaging procedure, the upscaled coefficients which enter directly the effective boundary conditions at the matching interface(s). In particular, it is convenient to eventually set $\hat{y}_{\infty,b(t)}$ to 0 and, hence, to evaluate the macroscopic coefficients for matching interface(s) passing by the tips/crests/outer rims of the ribs (or the first row of inclusions); cf. Fig. 1. The homogenized boundary conditions, valid up to second-order in terms of $\epsilon_{b(t)}$, can be formally expressed in the following dimensional form:

$$\hat{u}|_0 \approx \underbrace{\hat{\lambda}_x \left(\frac{\partial \hat{u}}{\partial \hat{y}} + \frac{\partial \hat{v}}{\partial \hat{x}} \right)\bigg|_0}_{\text{First order}} + \underbrace{\frac{\hat{\mathcal{K}}^{itf}_{xy}}{\mu} \frac{\partial}{\partial \hat{x}} \left(-\hat{p} + 2\mu \frac{\partial \hat{v}}{\partial \hat{y}} \right)\bigg|_0}_{\text{Second order}}, \tag{4}$$

$$\hat{v}|_0 \approx \underbrace{\frac{\hat{\mathcal{K}}_{yy}}{\mu} \left(-\frac{\partial \hat{p}}{\partial \hat{y}} + 2\mu \frac{\partial^2 \hat{v}}{\partial \hat{y}^2} \right)\bigg|_0 - \hat{\mathcal{K}}^{itf}_{xy} \frac{\partial}{\partial \hat{x}} \left(\frac{\partial \hat{u}}{\partial \hat{y}} + \frac{\partial \hat{v}}{\partial \hat{x}} \right)\bigg|_0 - \hat{\mathcal{K}}^{itf}_{zy} \frac{\partial}{\partial \hat{z}} \left(\frac{\partial \hat{w}}{\partial \hat{y}} + \frac{\partial \hat{v}}{\partial \hat{z}} \right)\bigg|_0}_{\text{Second order}}, \tag{5}$$

$$\hat{w}|_0 \approx \underbrace{\hat{\lambda}_z \left(\frac{\partial \hat{w}}{\partial \hat{y}} + \frac{\partial \hat{v}}{\partial \hat{z}} \right)\bigg|_0}_{\text{First order}} + \underbrace{\frac{\hat{\mathcal{K}}^{itf}_{zy}}{\mu} \frac{\partial}{\partial \hat{z}} \left(-\hat{p} + 2\mu \frac{\partial \hat{v}}{\partial \hat{y}} \right)\bigg|_0}_{\text{Second order}}, \tag{6}$$

evaluated at the boundary of interest (either $\hat{y}_b = 0$ or $\hat{y}_t = 0$).

An in-depth look at these expressions reveals that the no-slip boundary conditions for the streamwise and the spanwise velocity components (respectively, $\hat{u}$ and $\hat{w}$) are corrected at first order by the classical Navier-slip conditions and at second order by the gradients of the normal stress, while a transpiration velocity, $\hat{v}$, at the fictitious wall in $\hat{y}_{b(t)} = 0$ appears only at second order. The dimensional groups of coefficients, i.e. the Navier-slip lengths in the streamwise and the spanwise directions ($\hat{\lambda}_{x,b(t)}$, $\hat{\lambda}_{z,b(t)}$), and the interface and intrinsic permeability coefficients ($\hat{\mathcal{K}}^{itf}_{xy,b(t)}$, $\hat{\mathcal{K}}^{itf}_{zy,b(t)}$, $\hat{\mathcal{K}}_{yy,b(t)}$) are homogeneous to, respectively, a length and a surface area, and correspond to the product of their dimensionless counterparts times, respectively, $l_{b(t)}$ and $l^2_{b(t)}$, that is

$$\hat{\lambda}_x = \lambda_x \, l, \quad \hat{\lambda}_z = \lambda_z \, l, \tag{7}$$

$$\hat{\mathcal{K}}^{itf}_{xy} = \mathcal{K}^{itf}_{xy} \, l^2, \quad \hat{\mathcal{K}}^{itf}_{zy} = \mathcal{K}^{itf}_{zy} \, l^2, \quad \hat{\mathcal{K}}_{yy} = \mathcal{K}_{yy} \, l^2. \tag{8}$$

The dimensionless macroscopic coefficients are dependent only on the micro-structural details of the corresponding surface/substrate, for instance the protrusion size-to-pitch ratio and the porosity[2] (θ) for, respectively, the rough surface and the permeable bed sketched in Fig. 1. In other words, these coefficients are intrinsic to the geometric characteristics of the boundary and do not depend on the Reynolds number; the effective boundary conditions up to second-order accuracy in terms of ϵ requires considering the reconstructed microscopic problems at $\mathcal{O}(\epsilon^0)$ and $\mathcal{O}(\epsilon^1)$ (Ahmed *et al.*, 2022*b*) where the inertial terms are not yet present. For this reason, the closure problems required to evaluate the model parameters are all Stokes-like (as presented in Section 2.2). We anticipate at this stage that an alternative, modified approach in which the upscaled coefficients are sensitive to near-wall advection will be introduced in Section 3.2. Finally, it is noteworthy that the effective boundary conditions (Eqs. (4)–(6)) were formulated in Refs. (Naqvi & Bottaro, 2021; Ahmed *et al.*, 2022*b*) considering the simple case of a surface/substrate for which the coordinates $(\hat{x}, \hat{y}, \hat{z})$ are the principal axes of the Navier-slip tensor.

2.2 Evaluation of the macroscopic coefficients

In order to evaluate the dimensionless macroscopic coefficients for different surface textures, the closure problems derived in Refs. (Naqvi & Bottaro, 2021; Ahmed *et al.*, 2022*b*) are employed here, and the Stokes-based approach proposed for the calculation of the model parameters is adopted. The closure problems are solved over an elementary cell, representative of the microscopic domain of interest, with the dimensions normalized by the microscopic length scale ℓ; the dimensionless coordinates $x_i = \hat{x}_i/\ell$ used to describe the closure fields are shown in the right frame of Fig. 1.

For the Navier-slip (λ_x, λ_z) and interface permeability ($\mathcal{K}^{itf}_{xy}$, $\mathcal{K}^{itf}_{zy}$) coefficients, it is sufficient to solve two Stokes-like systems governing the auxiliary variables ($u^\dagger_{11}$, $u^\dagger_{21}$, $u^\dagger_{31}$, $p^\dagger_1$) and ($u^\dagger_{13}$, $u^\dagger_{23}$, $u^\dagger_{33}$, $p^\dagger_3$), which stem from the homogenization procedure, over the microscopic elementary cell, subject to periodicity of all the dependent variables in the x and z directions; the two systems are defined, respectively, as follows:

$$\begin{cases} \partial_i u^\dagger_{i1} = 0, \\ -\partial_i p^\dagger_1 + \partial^2_k u^\dagger_{i1} = 0, \\ u^\dagger_{i1} = 0 \qquad \text{at } \mathcal{I}_{\beta\sigma}, \\ -p^\dagger_1 \delta_{i2} + \partial_2 u^\dagger_{i1} + \partial_i u^\dagger_{21} = \delta_{i1} \qquad \text{at } y = y_\infty, \end{cases} \tag{9}$$

and

$$\begin{cases} \partial_i u^\dagger_{i3} = 0, \\ -\partial_i p^\dagger_3 + \partial^2_k u^\dagger_{i3} = 0, \\ u^\dagger_{i3} = 0 \qquad \text{at } \mathcal{I}_{\beta\sigma}, \\ -p^\dagger_3 \delta_{i2} + \partial_2 u^\dagger_{i3} + \partial_i u^\dagger_{23} = \delta_{i3} \qquad \text{at } y = y_\infty, \end{cases} \tag{10}$$

[2]The porosity θ of a permeable medium is defined as the ratio of the volume occupied by the pores to the total volume of the medium.

with the operators $\partial_i = \dfrac{\partial}{\partial x_i}$ and $\partial_i^2 = \dfrac{\partial^2}{\partial x_i^2}$, and δ_{ij} the Kronecker delta function. $\mathcal{I}_{\beta\sigma}$ refers to the physical interface between the fluid phase (β) and the ribs/grains/solid walls (σ). Systems (9) and (10) must be solved for a sufficiently large value of $y_\infty = \hat{y}_\infty/\ell$ so that the microscopic fields are homogeneous in x and z near the matching interface. Once the closure fields are available by performing simple numerical simulations with y_∞ set, for instance, to 5 (which is common practice), the macroscopic coefficients for a matching interface of particular interest at $y_\infty = 0$ can be directly evaluated, without having to rerun the simulations; they can be calculated as follows (Bottaro & Naqvi, 2020; Naqvi & Bottaro, 2021; Ahmed *et al.*, 2022*a*):

$$\lambda_x = \frac{1}{\mathcal{A}} \int_{\mathcal{S}_0} u_{11}^\dagger \, dA, \quad \lambda_z = \frac{1}{\mathcal{A}} \int_{\mathcal{S}_0} u_{33}^\dagger \, dA, \tag{11}$$

$$\mathcal{K}_{xy}^{itf} = \frac{1}{\mathcal{A}} \int_{\mathcal{V}_0} u_{11}^\dagger \, dV, \quad \mathcal{K}_{zy}^{itf} = \frac{1}{\mathcal{A}} \int_{\mathcal{V}_0} u_{33}^\dagger \, dV, \tag{12}$$

where $\mathcal{S}_0$ and $\mathcal{V}_0$ are the virtual surface at and the fluid volume below the plane $y = 0$, respectively, and $\mathcal{A}$ is the area of an $x - z$ cross section of the elementary cell (if the surface texture has a fixed dimensional pitch, ℓ, in both $\hat{x}$ and $\hat{z}$, then $\mathcal{A} = 1 \times 1$).

For the medium permeability component $\mathcal{K}_{yy}$, a triply periodic unit cell of the porous region is considered, and the following closure system is solved over it, with the free index j set to 2:

$$\begin{cases} \partial_i \breve{u}_{ij} = 0, \\ -\partial_i \breve{p}_j + \partial_k^2 \breve{u}_{ij} = -\delta_{ij}, \\ \breve{u}_{ij} = 0 \qquad \text{at } \mathcal{I}_{\beta\sigma}, \end{cases} \tag{13}$$

subject to periodicity of $\breve{u}_{ij}$ and $\breve{p}_j$ in x, y and z. The $\breve{u}_{22}$ field is then superficially averaged over the volume of the unit cell to evaluate the coefficient $\mathcal{K}_{yy}$. Should the medium permeability components $\mathcal{K}_{xx}$ or $\mathcal{K}_{zz}$ be needed (although they do not contribute to the effective boundary conditions), system 13 is to be solved for j equal to 1 or 3, respectively, and the superficial averaging is to be applied considering, respectively, $\breve{u}_{11}$ or $\breve{u}_{33}$. For the case of a corrugated, impermeable boundary, it is clear that $\mathcal{K}_{ii}$ vanishes identically, while the interface permeability coefficients do not.

Numerical values of the macroscopic coefficients entering the effective boundary conditions at the virtual interface for selected configurations of porous or rough layers are listed, respectively, in Tables 1 and 2; their behaviors with variations in the porosity (θ) for the different permeable beds and in the rib size-to-pitch ratio (e/ℓ) for the rough surfaces are correspondingly plotted in Figs. 2 and 3. The values reported are either evaluated through this work (for spherical grains, longitudinal/transverse ribs of semicircular cross sections, and cubic roughness elements) or gathered from the literature (for streamwise/spanwise cylinders (Ahmed *et al.*, 2022*b*) and ribs of square cross sections (Ahmed *et al.*, 2022*a*)).

Table 1: Dependence of the macroscopic coefficients (Navier-slip, λ_x, interface permeability, $\mathcal{K}_{xy}^{itf}$, and medium permeability, $\mathcal{K}_{xx}$) on porosity, θ, for substrates consisting of inline (i) longitudinal, X-elongated cylinders (LC), (ii) transverse, Z-elongated cylinders (TC), and (iii) spheres (SP).

Porosity	λ_x $(\times 10^{-2})$			$\mathcal{K}_{xy}^{itf}$ $(\times 10^{-2})$			$\mathcal{K}_{xx}$ $(\times 10^{-2})$		
(θ)	LC	TC	SP	LC	TC	SP	LC	TC	SP
0.215	5.88	4.10	-	0.38	0.18	-	0.12	0	-
0.5	6.88	4.51	10.49	0.56	0.22	0.88	0.70	0.18	0.30
0.6	7.40	4.71	10.72	0.67	0.24	0.97	1.21	0.43	0.55
0.7	8.17	4.99	11.70	0.90	0.27	1.16	2.22	0.96	1.06
0.8	9.35	5.39	12.81	1.41	0.30	1.49	4.18	1.99	2.16
0.9	11.30	6.01	14.84	2.64	0.41	2.44	8.03	3.97	5.08

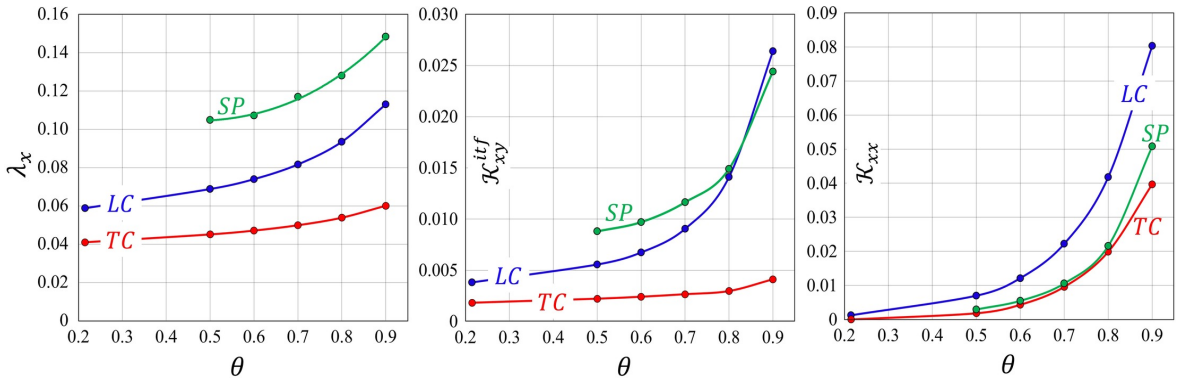

Figure 2: Graphical representation of the results in Table 1.

For the case of longitudinal (respectively transverse) solid inclusions/ribs, values of the coefficients λ_z, $\mathcal{K}_{zy}^{itf}$ and $\mathcal{K}_{zz}$ can be inferred, although they are not explicitly given in the tables, since they are equal to λ_x, $\mathcal{K}_{xy}^{itf}$ and $\mathcal{K}_{xx}$ of the transverse (respectively longitudinal) case at the same value of θ or e/ℓ. When the cylindrical inclusions are elongated in the spanwise (z) or in the streamwise (x) direction, the medium permeability component $\mathcal{K}_{yy}$ is the same (for given porosity) and is equal to $\mathcal{K}_{xx}$ for the case of transverse cylinders (which coincides with $\mathcal{K}_{zz}$ for longitudinal ones). For isotropic patterns such as porous substrates made of ordered spherical grains, it is clear that $\lambda_x = \lambda_z$, $\mathcal{K}_{xy}^{itf} = \mathcal{K}_{zy}^{itf}$, and $\mathcal{K}_{xx} = \mathcal{K}_{yy} = \mathcal{K}_{zz}$. Although the medium permeability component $\mathcal{K}_{xx}$ (and $\mathcal{K}_{zz}$) does not contribute to the homogenized, effective boundary conditions, its values are presented for permeable beds in Table 1 to highlight the difference with respect to the corresponding interface permeability $\mathcal{K}_{xy}^{itf}$ (also $\mathcal{K}_{zy}^{itf}$). For the rough walls considered, the macroscopic coefficients of interest exhibit non-monotonic relationships with the rib size-to-pitch ratio (Fig. 3), where they all peak within the range $0.1 \lesssim e/\ell \lesssim 0.3$. This behavior is not unexpected, since the model coefficients vanish for cubic or longitudinal/transverse square ribs as e/ℓ tends to 0 or 1, when the smooth surface case is recovered.

Table 2: Values of the macroscopic coefficients for surfaces roughened with (i) longitudinal square ribs (LSQ), (ii) transverse square ribs (TSQ), (iii) longitudinal semicircular elements (LSC), (iv) transverse semicircular elements (TSC), and (v) inline array of cubic elements (CU), at different values of the rib height-to-pitch ratio, e/ℓ.

e/ℓ	λ_x $(\times 10^{-2})$					$\mathcal{K}_{xy}^{itf}$ $(\times 10^{-2})$				
	LSQ	TSQ	LSC	TSC	CU	LSQ	TSQ	LSC	TSC	CU
0.05	4.22	3.67	4.22	3.79	4.90	0.10	0.09	0.10	0.09	0.12
0.10	6.95	5.06	6.96	5.50	9.09	0.34	0.23	0.32	0.24	0.45
0.15	8.40	5.09	8.42	5.86	12.02	0.60	0.30	0.56	0.33	0.87
0.20	8.86	4.57	8.90	5.65	13.29	0.82	0.29	0.72	0.34	1.26
0.25	8.61	3.98	8.72	5.33	13.34	0.96	0.23	0.79	0.31	1.49
0.30	7.92	3.46	8.17	5.02	12.46	1.00	0.17	0.76	0.28	1.57
0.40	6.02	2.59	6.88	4.53	9.50	0.86	0.08	0.55	0.22	1.28
0.50	4.16	1.78	5.88	4.10	6.47	0.58	0.04	0.38	0.18	0.83

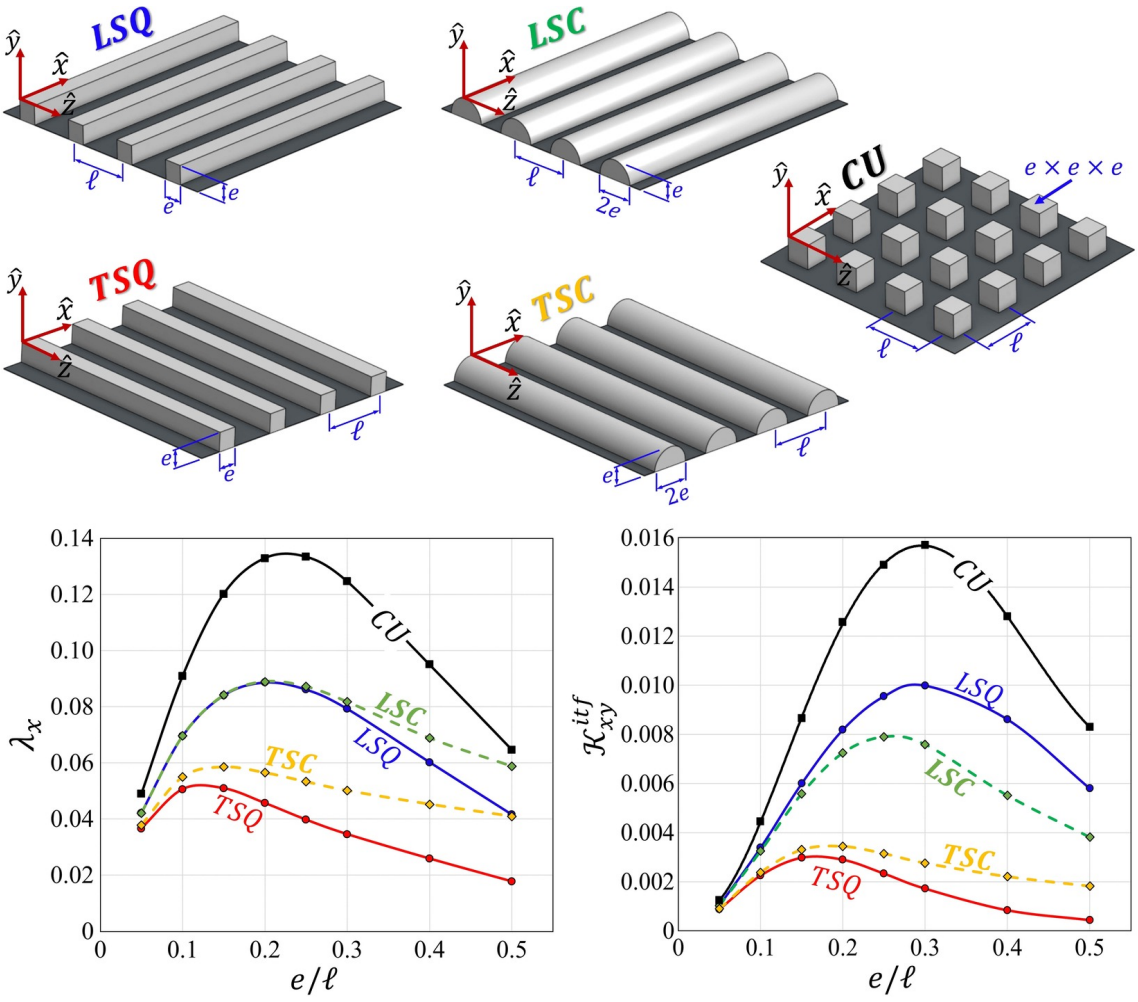

Figure 3: Graphical representation of the geometries and results in Table 2.

3 THE MACROSCALE PROBLEM: CASE STUDIES, VALIDATION AND DISCUSSION

3.1 Laminar Poiseuille flow in rough/permeable channels

3.1.1 *A generalized analytical solution*

The problem of laminar, pressure-driven flow in a channel that is bounded by stationary rough/permeable layers at $\hat{y} < 0$ and $\hat{y} > 2H$ is studied here in pursuit of a generalized analytical solution for the macroscopic velocity profile across the free-fluid region (cf. Fig. 4).

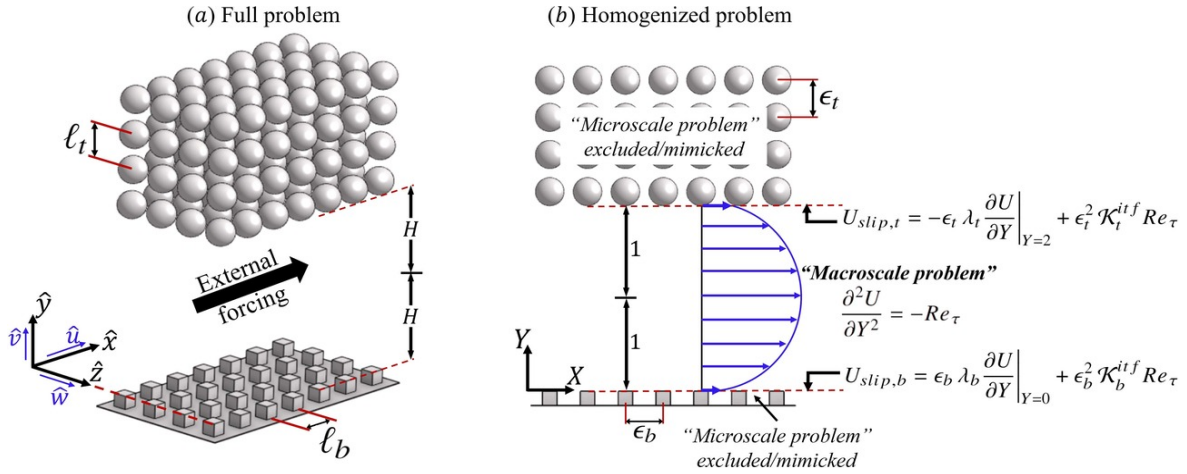

Figure 4: Description of the generalized Poiseuille flow problem, with examples of the rough/permeable walls: (*a*) sketch of the full problem in dimensional coordinates; (*b*) sketch of the homogenized problem in dimensionless macroscopic coordinates, with the governing equation and the effective boundary conditions explicitly indicated.

First, we seek dimensionless expressions of the governing equations (3) pertinent to the macroscale problem. With $\mathcal{M}$ the magnitude of the pressure gradient forcing the channel flow in the streamwise direction, a bulk stress/pressure scale may be defined as $\tau^{\mathcal{M}} = \mathcal{M} H$. The velocity scale is chosen as $u_\tau = \sqrt{\tau^{\mathcal{M}}/\rho}$, corresponding to a shear velocity. The dimensionless macroscopic variables are introduced as follows:

$$X_i = \frac{\hat{x}_i}{H}, \quad U_i = \frac{\hat{u}_i}{u_\tau}, \quad P = \frac{\hat{p}}{\mathcal{M} H}, \tag{14}$$

for the normalized pressure gradient to become $\partial P/\partial X = -1$. The $X - Z$ planform of the near-wall micro-patterns is assumed to be either isotropic or elongated in the spanwise or streamwise direction; in this case, there are no near-wall transverse velocity components (Stone *et al.*, 2004) and the fully developed flow is oriented only along X,

i.e. $U = U(Y)$ and $V = W = 0$. Substituting (14) into (3) we obtain the following dimensionless conservation equation governing the macroscale behavior of the flow:

$$\frac{\partial^2 U}{\partial Y^2} = -Re_\tau, \tag{15}$$

where $Re_\tau = \dfrac{\rho u_\tau H}{\mu}$ corresponds to a shear-velocity Reynolds number. A general solution of Eq. (15) is

$$U(Y) = Re_\tau \left[-\frac{Y^2}{2} + (1 - A)Y + B \right], \tag{16}$$

with A and B integration constants. Unlike the case of classical plane Poiseuille flow, A and B do not vanish and can be found from application of the effective boundary conditions which read:

$$U_{slip,b} = U\big|_{Y=0} = \epsilon_b \, \lambda_b \left.\frac{\partial U}{\partial Y}\right|_{Y=0} + \epsilon_b^2 \, \mathcal{K}_b^{itf} \, Re_\tau, \tag{17}$$

$$U_{slip,t} = U\big|_{Y=2} = -\epsilon_t \, \lambda_t \left.\frac{\partial U}{\partial Y}\right|_{Y=2} + \epsilon_t^2 \, \mathcal{K}_t^{itf} \, Re_\tau. \tag{18}$$

Notice that a single coordinate system has been used here, with $X = X_b$ and likewise for Y and Z. The constants A and B are found to be:

$$A = \frac{\Lambda_b \, (1 + \phi_b) - \Lambda_t \, (1 + \phi_t)}{2 + \Lambda_b + \Lambda_t}, \quad B = \Lambda_b \, \frac{\Lambda_t \, (1 + \phi_t) + (2 + \Lambda_t)(1 + \phi_b)}{2 + \Lambda_b + \Lambda_t}, \tag{19}$$

with the definitions $\Lambda_{b(t)} = \epsilon_{b(t)} \, \lambda_{b(t)}$ and $\phi_{b(t)} = \epsilon_{b(t)} \, \dfrac{\mathcal{K}_{b(t)}^{itf}}{\lambda_{b(t)}}$. The slip velocities at the virtual interfaces are

$$U_{slip,b} = B \, Re_\tau, \quad U_{slip,t} = (B - 2A) \, Re_\tau. \tag{20}$$

Equations (20) show that the slip speed at each boundary is sensitive to the macroscopic coefficients of both walls. Equation (16) can now be recast in the following form:

$$U(Y) = -\frac{Re_\tau}{2} \, Y^2 + \left(Re_\tau + \frac{U_{slip,t} - U_{slip,b}}{2} \right) Y + U_{slip,b}. \tag{21}$$

The position Y_m where the speed is the largest, and the corresponding value of the velocity, $U_{max} = U(Y = Y_m)$, are, respectively,

$$Y_m = 1 + \frac{U_{slip,t} - U_{slip,b}}{2Re_\tau}, \quad U_{max} = \frac{Re_\tau}{2} \left(1 + \frac{U_{slip,t} - U_{slip,b}}{2Re_\tau} \right)^2 + U_{slip,b}, \tag{22}$$

which means that for the *generalized Poiseuille* flow the plane $Y = Y_m$ shifts from the middle section ($Y = 1$) towards the boundary of larger slip, and the maximum velocity, U_{max}, is always larger than the corresponding value in a smooth channel by

$$\Delta U_{max} = \frac{U_{slip,t} + U_{slip,b}}{2} + \frac{1}{8Re_\tau} \left(U_{slip,t} - U_{slip,b} \right)^2. \tag{23}$$

In addition, the bulk, channel-averaged velocity, U_{ch}, deviates from the value for a classical Poiseuille flow by an amount directly proportional to the average of the two slip velocities; such a deviation and its percentage can be expressed as follows:

$$\Delta U_{ch} = \frac{U_{slip,b} + U_{slip,t}}{2}, \quad \Delta U_{ch}\% = 3\left(\frac{U_{slip,b} + U_{slip,t}}{2\,Re_\tau}\right) \times 100\%. \tag{24}$$

Finally, if the boundary conditions (17) and (18) were only first-order accurate, all the relations derived would hold, except for setting ϕ_b and ϕ_t to 0 in (19).

3.1.2 *Sample validation*

Focus shifts now on validating the analytical solution, assessing its applicability range and highlighting its practical relevance. We define the bulk Reynolds number as $Re = \rho \hat{u}_{ch} H/\mu$, with $\hat{u}_{ch}$ the dimensional channel-averaged velocity. Since $\hat{u}_{ch} = u_\tau U_{ch}$ as per the normalization adopted, the bulk Reynolds number is also $Re = U_{ch}\, Re_\tau$. For a smooth, impermeable channel, it is $U_{ch} = Re_\tau/3$, hence $Re_\tau = \sqrt{3\,Re}$. With a transitional Re of order 1000 for the classical plane Poiseuille flow (Schmid & Henningson, 2001; Sano & Tamai, 2016), the flow is expected to remain laminar until Re_τ of order 50. For all the cases discussed in this section, Re_τ is well below this threshold, typically $Re_\tau \leq 10$. The performance of the rough/permeable channels and the smooth ones are compared at a fixed Re_τ, i.e. at a fixed applied pressure gradient. Validation of the model requires conducting full Navier-Stokes simulations in a channel of length L_X, with all fields near and within the corrugations/pores of the surfaces/substrates well resolved. The length of the channel was progressively increased and dependency of the computed X-Z-averaged streamwise velocity on it was monitored; for the configurations/conditions considered here, it was proven that a single geometrically periodic cell of the channel is sufficient to apply periodicity of the fields and, thus, to fully describe the channel flow, which implies the absence of any flow instabilities such as vortex shedding in the vicinity of the roughness elements/grains (the reader is encouraged to refer to Ref. (Agnaou *et al.*, 2016) for a relevant description). Then, the velocity profile across the channel, constructed by evaluating the plane-averaged value of the streamwise velocity U at each wall-normal distance Y, was compared to the analytical solution (Eq. (21)). All simulations were run using Simcenter STAR-CCM+ finite-volume-based software (versions 16.02.009-R8 and 18.02.008-R8).

Three types of bounding walls are involved in the validation step. First, smooth, impermeable surfaces (SM) having $\lambda = \mathcal{K}^{itf} = 0$. Second, surfaces roughened by transverse, Z-elongated, square elements of a rib size-to-pitch ratio $e/\ell = 0.25$ ($\lambda = 0.03975$ and $\mathcal{K}^{itf} = 0.00233$; cf. Table 2), with $\epsilon = \ell/H = 0.4$ or 0.8. Such surfaces are indicated as $SQ_\epsilon^{e/\ell}$, i.e., $SQ_{0.4}^{0.25}$ and $SQ_{0.8}^{0.25}$. Third, fluid-saturated porous substrates formed by transverse cylindrical inclusions, with porosity $\theta = 0.8$ ($\lambda = 0.05385$ and $\mathcal{K}^{itf} = 0.00297$; cf. Table 1), with $\epsilon = \ell/H = 0.4$ or 0.8. These substrates are referred to as TC_ϵ^θ, i.e., $TC_{0.4}^{0.8}$ and $TC_{0.8}^{0.8}$. To provide extensive validation of the model predictions, six combinations of the aforementioned walls were selected, as illustrated in Fig. 5 with indication of

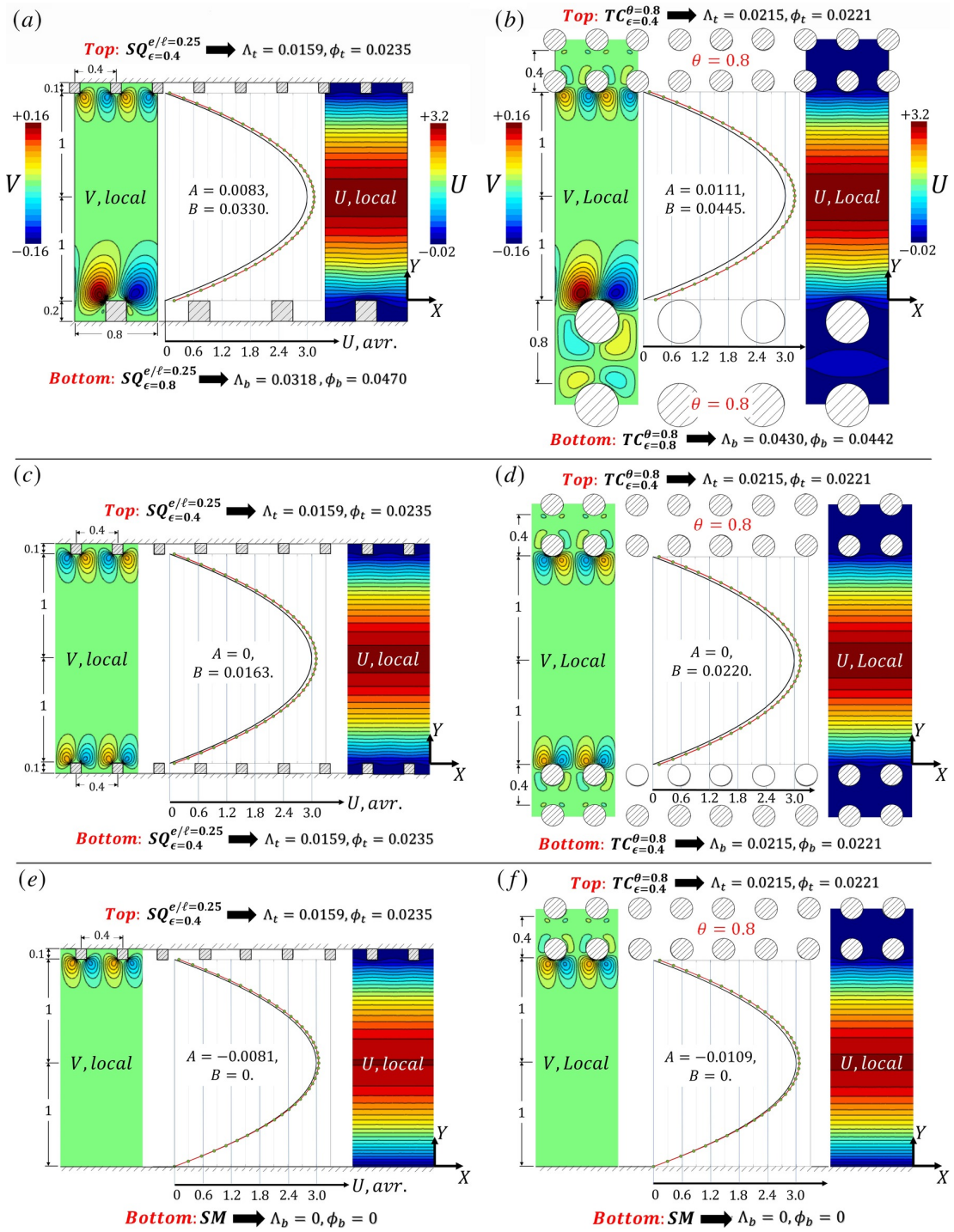

Figure 5: Laminar flow ($Re_\tau = 6$) in asymmetric rough (a) or permeable (b) channels, symmetric rough (c) or permeable (d) channels, and channels bounded by a smooth surface from one side and a rough surface (e) or a porous substrate (f) from the other side. The analytical results (second-order) for the velocity profiles (red lines) are validated by plane-averaged values from the full simulations (green-filled circles); the black profiles refer to Poiseuille flow in a smooth, impermeable channel, for which $A = B = 0$.

the values of Λ and ϕ for each boundary and the integration constants A and B for each channel. The macroscopic velocity profiles, based on Eq. (16), are in perfect agreement with results of the full simulations. The errors in the model predictions for the slip velocities, ΔU_{max} and ΔU_{ch} (cf. Eqs. (20), (23) and (24), respectively) are within about $\pm 3\%$. Since results of the first- and the second-order models are indistinguishable from one another to graphical accuracy, only the predictions of the latter are plotted in the figure.

3.1.3 *Considerations on model accuracy*

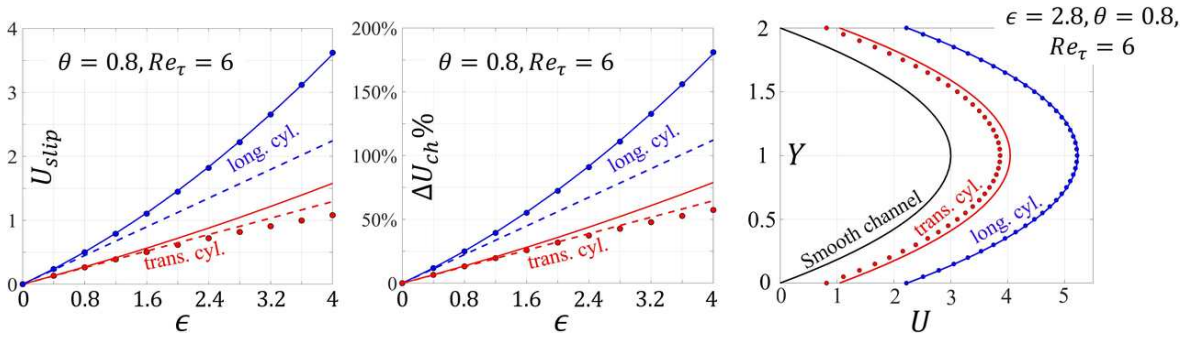

Figure 6: Laminar flow ($Re_\tau = 6$) in symmetric channels bounded by porous substrates consisting of either transverse or longitudinal cylinders, with porosity $\theta = 0.8$. The analytical results (dashed lines: first-order; solid lines: second-order) are compared with results of the full simulations (filled circles).

The applicability of the effective boundary conditions depends on the separation of scales between the microscopic and the macroscopic problems, with the accuracy of the model expected to degrade at large values of the ratios ϵ_b and ϵ_t. This may be associated with enhanced near-wall advection as the streamlines deflect due to the dynamic interaction of the fluid with surface protrusions; such inertial effects cannot be predicted by the Stokes-like systems underlying the homogenization procedure. Porous substrates ($\theta = 0.8$) formed by either spanwise- or streamwise-elongated cylinders are chosen here as representative examples, to highlight how errors in the model predictions increase with ϵ, as shown in Fig. 6. It is clear that even the second-order accurate interface condition does not guarantee high accuracy for the case of transverse cylinders when ϵ is sufficiently large (*cf.* Fig. 6, right). By contrast, if the cylinders are aligned along X, interaction with the bulk channel flow is simply in the form of a skin-friction force, with negligible inertial effects; this justifies the perfect agreement in Fig. 6 between the second-order macroscopic solution and the results of the full simulations. It is noteworthy that the slip and the bulk velocities are larger for the case of longitudinal cylinders since the macroscopic coefficients ($\lambda = 0.09347$ and $\mathcal{K}^{itf} = 0.01410$) are larger than for the transverse cylinders configuration at the same porosity ($\lambda = 0.05385$ and $\mathcal{K}^{itf} = 0.00297$; cf. Table 1).

3.1.4 *Random media*

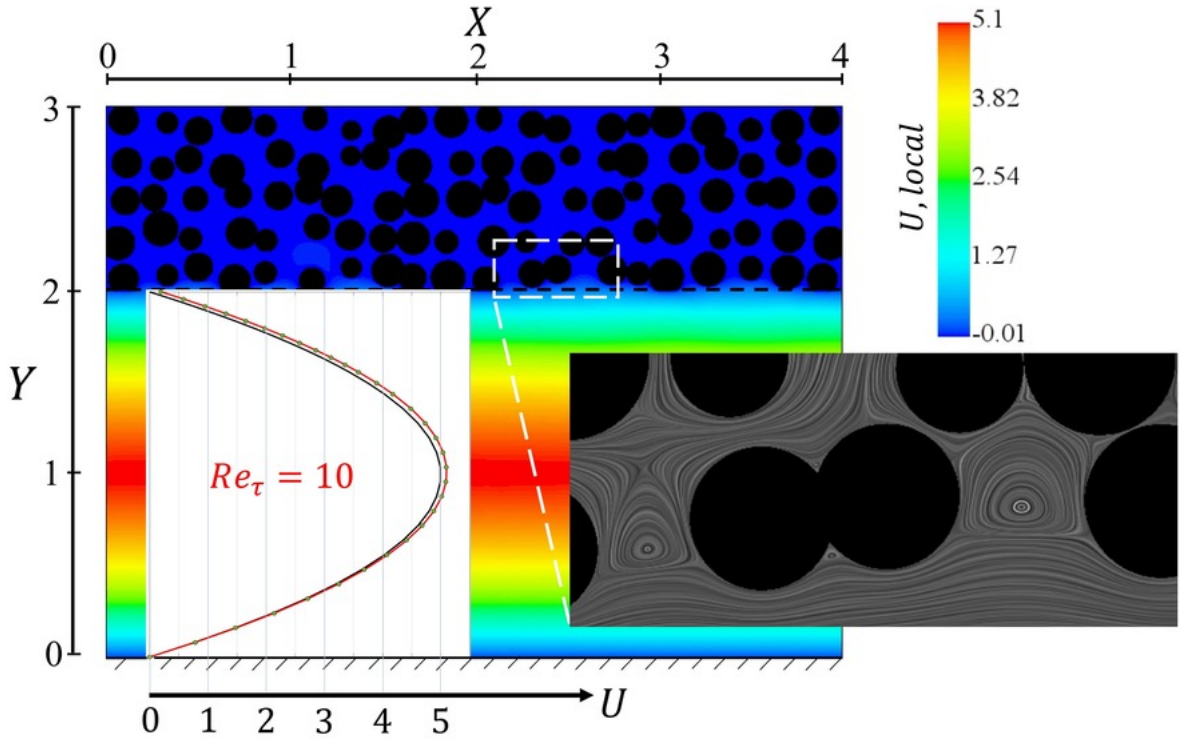

Figure 7: Laminar flow ($Re_\tau = 10$) in a channel bounded from the top by a porous layer consisting of randomly arranged, spanwise-aligned inclusions, with the average porosity equal to 0.5. A close-up of the velocity vector field near the interface (visualized via the line integral convolution method) is displayed in the gray frame. Analytical solution for the upscaled velocity profile is validated against the full simulation; symbols are identical to those in Fig. 5.

Channels delimited by porous substrates/structured surfaces formed by random patterns of inclusions/roughness elements represent a more practical situation. The homogenization approach applies to such configurations provided that a sufficiently large microscopic elementary volume is chosen to represent the features of the whole media/surface. An example is shown in Fig. 7; the permeable bed, bounding the flow from the upper side, consists of 100 Z-elongated inclusions, randomly displaced in the $X - Y$ plane, with overlapping allowed among neighboring grains. On average, there are 20 grains along X and 5 grains in Y; the diameters of the inclusions are varied, for the porosity to fluctuate locally between 0.25 and 0.75, yielding an average porosity $\theta_{avr} \approx 0.5$. The microscopic length scale, ℓ_t, was chosen as $L_X/20$, with $L_X = 4\,H$ the length of the periodic domain selected; hence, it can be concluded that $\epsilon_t = \ell_t/H = 0.2$. The microscale problem was approached in the same manner as that followed by Naqvi & Bottaro (2021) for a random medium, and the coefficients were evaluated to be $\lambda_t = 0.1012$ and $\mathcal{K}_t^{itf} = 0.0112$ ($\Lambda_t = 0.0202$ and $\phi_t = 0.0221$). The macroscopic velocity profile, based on the analytical solution (16), matches well the streamwise-averaged results from the full simulation, cf. Fig. 7.

3.1.5 *Three-dimensional patterns*

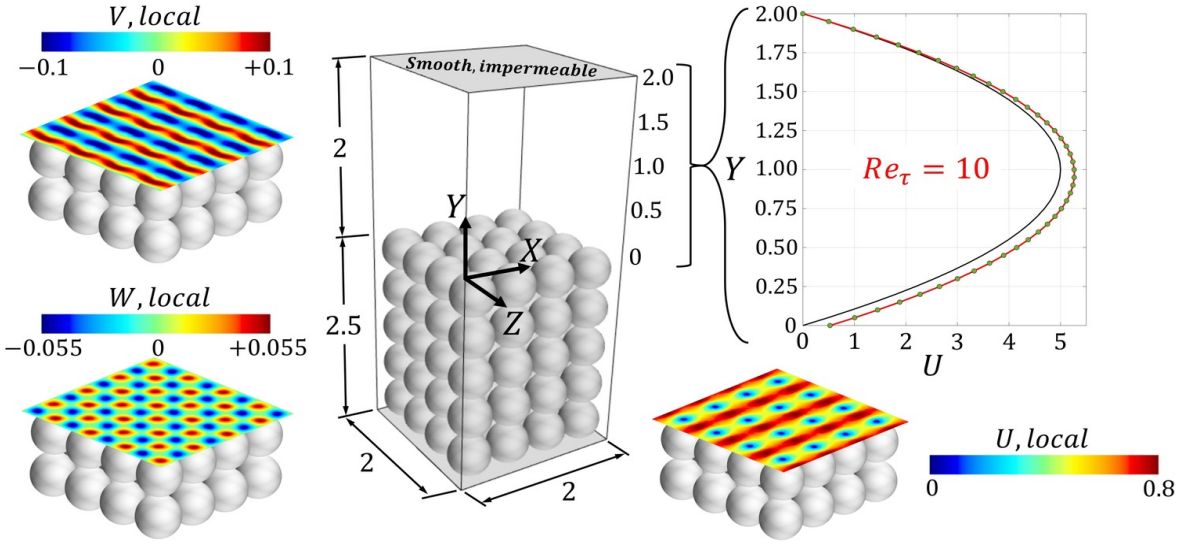

Figure 8: Laminar flow ($Re_\tau = 10$) in a channel bounded on the lower side by a porous bed consisting of inline spheres, with $\theta = 0.5$ ($\lambda_b = 0.1049$ and $\mathcal{K}_b^{itf} = 0.0088$; cf. Table 1) and $\epsilon = 0.5$. On the top right image, the analytical solution for U is plotted together with results from the full simulation, using the same symbols as in Fig. 5.

Until this point, validation of the model has been sought only for two-dimensional configurations of rough/porous walls. However, as mentioned in Section 3.1.1, a macroscopically one-directional flow is also expected over three-dimensional patterns provided that the external forcing (here in X) is aligned with one of the principal axes of the Navier-slip tensor. An example is illustrated in Fig. 8, where channel flow over a porous substrate consisting of aligned spherical grains is analyzed. Distributions of the three velocity components at the virtual interface ($Y = 0$) are displayed to confirm that, consistently with the aforementioned condition, the plane-averaged values of wall-normal and spanwise velocity components vanish; the analytical prediction of the streamwise velocity agrees very well with the X-Z-averaged result from the three-dimensional, feature-resolving simulation.

3.1.6 *Small roughness/grains amplitudes*

A simplified version of the *generalized Poiseuille* solution is proposed for laminar flows in channels bounded by walls of small roughness amplitude or by permeable layers with reduced dimensions of grains and pores. In these cases, ϵ is sufficiently small and we expect the hierarchy $\epsilon^2\mathcal{K}^{itf} << \epsilon\lambda << 1$ to hold. This permits not only to safely reduce the model to first order (by neglecting ϕ in (19)) but also to use the approximation

$1 + \Lambda \approx 1$ when evaluating the different parameters of interest; for instance, we obtain

$$U_{slip,b(t)} = Re_\tau \, \Lambda_{b(t)}, \quad \Delta U_{max} = Re_\tau \frac{\Lambda_b + \Lambda_t}{2}, \quad \Delta U_{ch}\% = 3 \, \frac{\Lambda_b + \Lambda_t}{2} \times 100\%. \tag{25}$$

The simplified solution is validated in Fig. 9 for the flow in a channel bounded on the top by a porous substrate of porosity equal to 0.5, for ϵ ranging from 0 to 0.8. For all types of porous inclusions considered, a linear behavior of $U_{slip,t}$, U_{max} and $\Delta U_{ch}\%$ is found versus ϵ, and the first-order boundary condition yields excellent predictions.

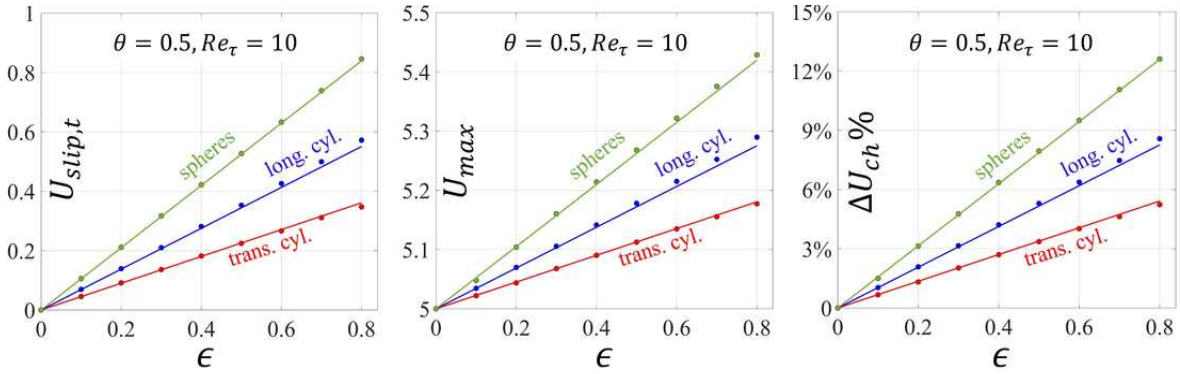

Figure 9: Laminar flow ($Re_\tau = 10$) in a channel bounded on one side by a smooth wall and on the other side by a porous substrate ($\theta = 0.5$) consisting of either spheres ($\lambda = 0.1049$), longitudinal cylinders ($\lambda = 0.0688$), or transverse cylinders ($\lambda = 0.0451$). The simplified solution (lines) is validated against full simulations (filled circles).

3.2 A crash introduction to the near-wall advection modeling

In the original structure of the homogenization model, described in Section 2 and validated in Section 3.1, inertial effects are absent from the problems at the two leading orders in ϵ, and the microscopic systems of equations are Stokes-like. Nevertheless, as anticipated in Section 3.1.3, near-wall advection may contribute significantly to the problem at relatively large values of ϵ, limiting the validity range of the upscaling model adopted. In this section, we propose (and then validate) an adjustment to the homogenization procedure such that effects of near-wall advection on the macroscale behavior of the laminar channel flow can be mimicked efficiently.

In the recent study by Ahmed & Bottaro (2023), the problem of seepage in porous media beyond the Stokes flow conditions has been treated, and it was proved that the same upscaled governing equation (Darcy's law in that case) still applies, but with the permeability appropriately modified to be dependent on the Reynolds number, deviating from the intrinsic permeability of the medium, which is merely geometry-dependent. The problem under study here is different since flow over, and not through, porous substrates is analyzed. However, an analogous procedure is adopted so that the effective boundary conditions (Eqs. (17) and (18)) and, hence, the generalized solution for the velocity

profile across the channel and all the relevant relationships derived in Section 3.1.1, hold at considerably large values of ϵ and/or Re_τ. The auxiliary systems used to evaluate the Navier-slip and the interface-permeability coefficients (respectively, $\lambda_{b(t)}$ and $\mathcal{K}^{itf}_{b(t)}$) are reformulated to properly model the sensitivity of the microscopic fields, and therefore the model coefficients, to near-wall inertia. The general procedure outlined by Buda (2021) is followed, with some adjustment, to yield a reliable homogenization framework aimed at genuinely capturing the role of near-interface advection in the *generalized Poiseuille* problem under laminar flow conditions. Extensive validation of the proposed model is subsequently performed for different geometric and flow conditions.

3.2.1 *Adjustment of the homogenization model*

An Oseen-like linearization was proposed by Buda (2021) to try to include the effects of near-interface advection in the homogenization scheme. Accordingly, the convective acceleration terms in the momentum conservation equation governing the microscopic problem were linearized, by defining a constant, spatially invariant, dimensional velocity $\hat{u}_{\phi,i} = (\hat{u}_\phi, 0, 0)$ representative of the velocity level near the physical wall where the inertial effects may be significant as the fluid interacts with the protrusions/grains. Hence, the microscale problem is now governed by the following conservation equations:

$$\frac{\partial \hat{u}_i}{\partial \hat{x}_i} = 0, \quad \rho \hat{u}_{\phi,j} \frac{\partial \hat{u}_i}{\partial \hat{x}_j} = -\frac{\partial \hat{p}}{\partial \hat{x}_i} + \mu \frac{\partial^2 \hat{u}_i}{\partial \hat{x}_j^2}. \tag{26}$$

The microscopic Reynolds number, defined as $Re_\phi = \rho\, \hat{u}_\phi\, \ell/\mu$, is now assumed to be of $\mathcal{O}(1)$. By introducing the dimensionless velocity $U_\phi = \dfrac{\hat{u}_\phi}{u_\tau}$, one may write

$$Re_\phi = \frac{\rho\, \hat{u}_\phi\, \ell}{\mu} = \frac{\ell}{H} \frac{\rho\, u_\tau H}{\mu} \frac{\hat{u}_\phi}{u_\tau} = \epsilon Re_\tau\, U_\phi. \tag{27}$$

A homogenization procedure similar, in principle, to that described in Section 2.1 was then followed by Buda (2021); the same effective boundary conditions (Eqs. (4)–(6)) were eventually attained, yet the closure problems based on which the macroscopic coefficients are calculated differ from those presented in Section 2.2 and read

$$\begin{cases} \partial_i u^\dagger_{i1} = 0, \\ -\partial_i p^\dagger_1 + \partial^2_k u^\dagger_{i1} = Re_\phi\, \partial_1 u^\dagger_{i1}, \\ u^\dagger_{i1} = 0 \qquad \text{at } \mathcal{I}_{\beta\sigma}, \\ -p^\dagger_1 \delta_{i2} + \partial_2 u^\dagger_{i1} + \partial_i u^\dagger_{21} = \delta_{i1} \qquad \text{at } y = y_\infty. \end{cases} \tag{28}$$

As before, the coefficients λ_x and $\mathcal{K}^{itf}_{xy}$ can be calculated based on the closure variable $u^\dagger_{11}$ as follows:

$$\lambda_x = \frac{1}{\mathcal{A}} \int_{\mathcal{S}_0} u^\dagger_{11}\, dA, \quad \mathcal{K}^{itf}_{xy} = \frac{1}{\mathcal{A}} \int_{\mathcal{V}_0} u^\dagger_{11}\, dV, \tag{29}$$

with the same definitions of $\mathcal{A}$, $\mathcal{S}_0$, $\mathcal{V}_0$ given in Section 2.2.

Attention is now drawn to the choice of the characteristic velocity U_ϕ, required for the definition of Re_ϕ which controls the auxiliary system (28). In Ref. (Buda, 2021), the simple assumption $\hat{u}_\phi = u_\tau$ was adopted, and thus $U_\phi = 1$ and $Re_\phi = \epsilon Re_\tau$. Here, a different approach is followed seeking a better approximation for U_ϕ. The velocity level at some normal distance, $\hat{y}_\phi$, away from the effective boundary, located in $\hat{y}_{b(t)} = 0$, is assumed to reasonably characterize near-wall advection; we hypothesize that this distance is proportional to the Navier-slip length $\hat{\lambda}_x$, or simply $\hat{y}_\phi = \hat{\lambda}_x$. In addition, the velocity profile near the boundary is assumed to follow the classical linear relationship

$$U = Y^+ + U_{slip}, \tag{30}$$

with $U = \dfrac{\hat{u}}{u_\tau}$, $Y^+ = \dfrac{\rho u_\tau \hat{y}}{\mu} = \dfrac{\hat{y}}{H} Re_\tau$, and $U_{slip} = \epsilon Re_\tau \, \lambda_x$ (as per the approximation in Eq. (25)). At $\hat{y} = \hat{\lambda}_x = \ell \lambda_x$, we obtain

$$U_\phi = \frac{\ell}{H} \lambda_x Re_\tau + \epsilon Re_\tau \, \lambda_x = 2 \epsilon Re_\tau \, \lambda_x, \tag{31}$$

and, therefore, $Re_\phi = 2\epsilon^2 Re_\tau^2 \, \lambda_x$. With the definition of λ_x in Eq. 29, the final form of the closure problem is

$$\begin{cases} \partial_i u_{i1}^\dagger = 0, \\ -\partial_i p_1^\dagger + \partial_k^2 u_{i1}^\dagger = 2 \, \epsilon^2 Re_\tau^2 \left[\dfrac{1}{\mathcal{A}} \displaystyle\int_{\mathcal{S}_0} u_{11}^\dagger \, dA \right] \partial_1 u_{i1}^\dagger, \\ u_{i1}^\dagger = 0 \qquad \text{at } \mathcal{I}_{\beta\sigma}, \\ -p_1^\dagger \delta_{i2} + \partial_2 u_{i1}^\dagger + \partial_i u_{21}^\dagger = \delta_{i1} \qquad \text{at } y = y_\infty, \end{cases} \tag{32}$$

a well-posed system to be solved over a representative elementary cell of the microscopic domain with all the dependent variables periodic in the x and z directions. This system renders the macroscopic parameters λ_x and $\mathcal{K}_{xy}^{itf}$ dependent not only on the geometry of the structured wall/substrate but also on the control parameter ϵRe_τ. The coefficients calculated based on this approach are indicated here as the *"Oseen-based"* coefficients, while those evaluated based on the original, advection-free system (9) are termed as the *"Stokes-based"* coefficients. Clearly, the Oseen-based system reduces to the Stokes' at $\epsilon Re_\tau = 0$ for any surface texture. However, they are also identical at finite values of ϵRe_τ for the special case of streamwise, x-elongated inclusions/ribs since all the closure variables in the auxiliary system (32) become x_1-invariant, and therefore $\partial_1 u_{i1}^\dagger$ vanishes; for this reason, the second-order accurate homogenization model with the Stokes-based coefficients exhibited good accuracy in the case of porous substrates constructed of streamwise-elongated cylinders even at large values of ϵ (in Section 3.1.3), unlike the case of transverse, spanwise-elongated cylinders for which the accuracy deterioration was obvious, and the Oseen-based coefficients should have been used instead, as will be confirmed in Section 3.2.2. In preparation for the upcoming validation step, the configuration of regularly arranged, transversely aligned cylinders with $\theta = 0.8$ was considered for the solution of the closure problem; this provides values of λ_x and $\mathcal{K}_{xy}^{itf}$ for ϵRe_τ ranging from 0 to 32, as presented in Fig. 10. It is worth noticing how advection (with the increase of ϵRe_τ) distorts the profiles of $u_{21}^\dagger$ and reduces the values of λ_x and $\mathcal{K}_{xy}^{itf}$; for example, at $\epsilon Re_\tau = 32$ these two coefficients are lower than their Stokes-based counterparts by about 35% and 62%, respectively (cf. frames (d) and (e)).

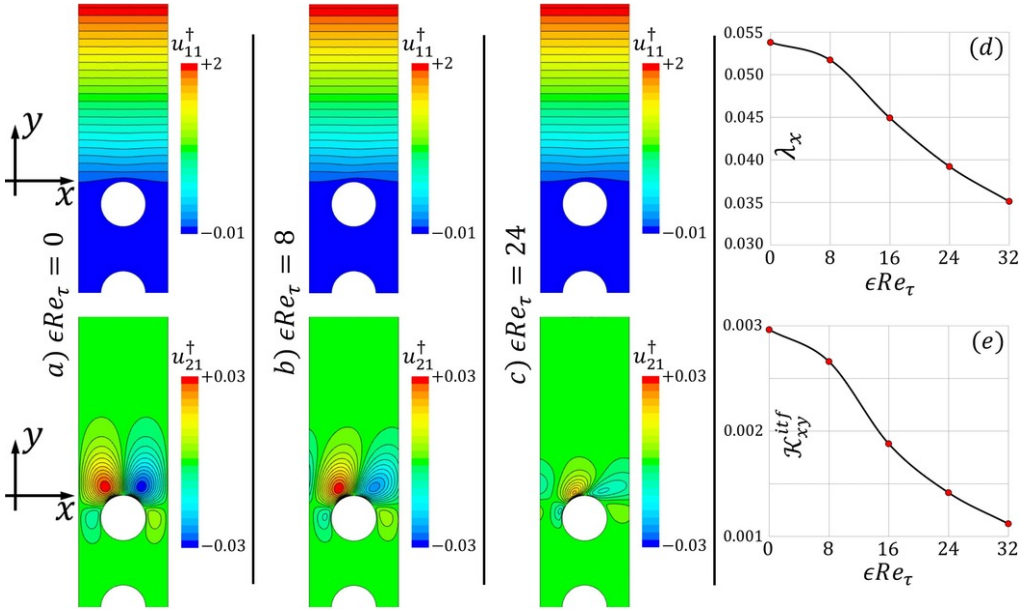

Figure 10: Contours of the microscopic variables $u_{11}^\dagger$ and $u_{21}^\dagger$ at three values of ϵRe_τ, shown over an $x-y$ plane for the case of spanwise-elongated cylinders of porosity $\theta = 0.8$ (panels a–c). Here, close-ups of the contours near the fluid-porous interface are presented, while in the typical simulations the porous bed ($y < 0$) consists of five rows of cylinders. The Oseen-based macroscopic coefficients λ_x and $\mathcal{K}_{xy}^{itf}$ are plotted in frames (d) and (e) against ϵRe_τ.

3.2.2 *Validation and accuracy improvement*

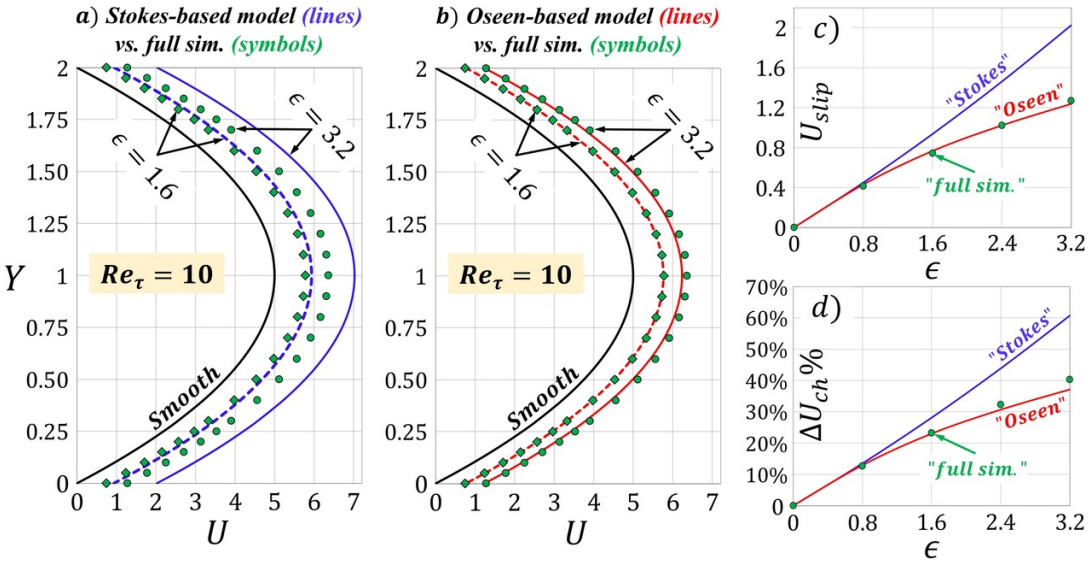

Figure 11: Poiseuille flow ($Re_\tau = 10$) in a channel bounded by two identical porous substrates consisting of inline patterns of spanwise-elongated cylinders ($\theta = 0.8$). Model predictions for the velocity profiles with (a) Stokes-based and (b) Oseen-based macroscopic coefficients are compared against results of the full simulations for two values of ϵ. Corresponding behaviors of (c) U_{slip} and (d) $\Delta U_{ch}\%$ are plotted for ϵ ranging from 0 to 3.2.

Validation of the Oseen-based homogenization approach, described in Section 3.2.1, is performed first on the laminar Poiseuille flow in symmetric channels bounded by permeable beds (porosity $\theta = 0.8$) made of spanwise-elongated cylindrical inclusions in an inline arrangement with equal pitch distances ℓ in the $\hat{x}$ and $\hat{y}$ directions. This configuration has been considered earlier, in Section 3.1.3, with the Stokes-based macroscopic coefficients, and deterioration of the model accuracy when proceeding to large values of $\epsilon = \ell/H$, at $Re_\tau = 6$, was highlighted and justified. Here, we monitor the improvement in the accuracy of the analytical model when the adjusted coefficients, dependent on the value of ϵRe_τ as plotted in Fig. 10, are plugged into the definition of the constants A and B (Eq. (19)) which control the velocity profile (Eq. 16). Full, fine-grained simulations were run for values of ϵRe_τ between 0 (Stokes') and 32, either by increasing ϵ from 0 to 3.2 with $Re_\tau = 10$ (presented in Fig. 11) or by increasing Re_τ from 0 to 40 with $\epsilon = 0.8$ (presented in Fig. 12), to provide reference results for validation. From inspection of Figs. 11 and 12, it is evident that predictions of the advection-capturing analytical solution agree very well with results of the feature-resolving simulations. The Stokes-based model overestimates the slip velocity, U_{slip}, at $\epsilon = 3.2$ and $Re_\tau = 10$ by about 60%, while the proposed adjustment is capable of reducing the absolute deviation from the result of the full simulation to less than 3%; cf. Fig. 11(c). This is reflected in more accurate predictions for the percentage change in the channel-averaged velocity due to the presence of the porous substrates, as shown in Fig. 11(d). Similar improvements can be observed in Fig. 12(b) and Fig. 12(c), respectively, as Re_τ increases.

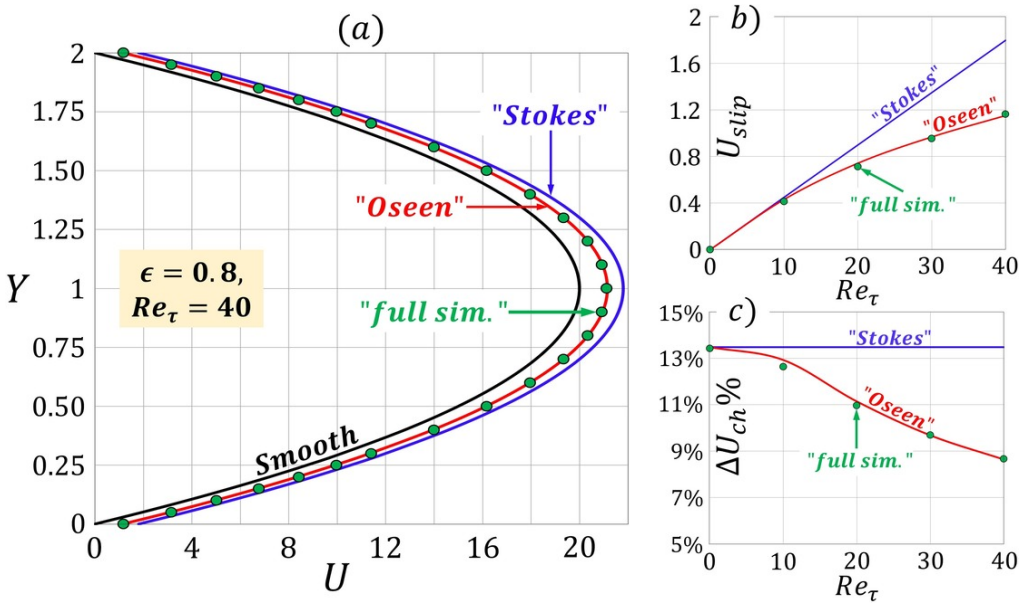

Figure 12: Poiseuille flow in a channel bounded by two identical porous substrates consisting of inline patterns of spanwise cylinders with $\theta = 0.8$ and $\epsilon = 0.8$. In panel (a), model predictions for the velocity profile using either Stokes-based or Oseen-based macroscopic coefficients are compared against result of the full simulation for $Re_\tau = 40$. Corresponding behaviors of (b) U_{slip} and (c) $\Delta U_{ch}\%$ are plotted with Re_τ varied from 0 to 40.

Furthermore, the robustness of the new model has been tested by validating its results for the laminar Poiseuille flow (at $Re_\tau = 12$) in symmetric channels bounded by rough surfaces of different textures. In particular, the boundaries considered are ribbed with transverse elements having square, rectangular, triangular (isosceles), or semicircular cross sections, where $\epsilon = \ell/H = 2$ for all configurations. The geometric characteristics of these patterns (denoted from I to IV), the values of the macroscopic coefficients and the corresponding Stokes- and Oseen-based predictions for the velocity profiles are presented in Fig. 13; the advantage of the Oseen-based approach in enhancing the accuracy of the homogenized model under significant near-wall advection is consistently confirmed.

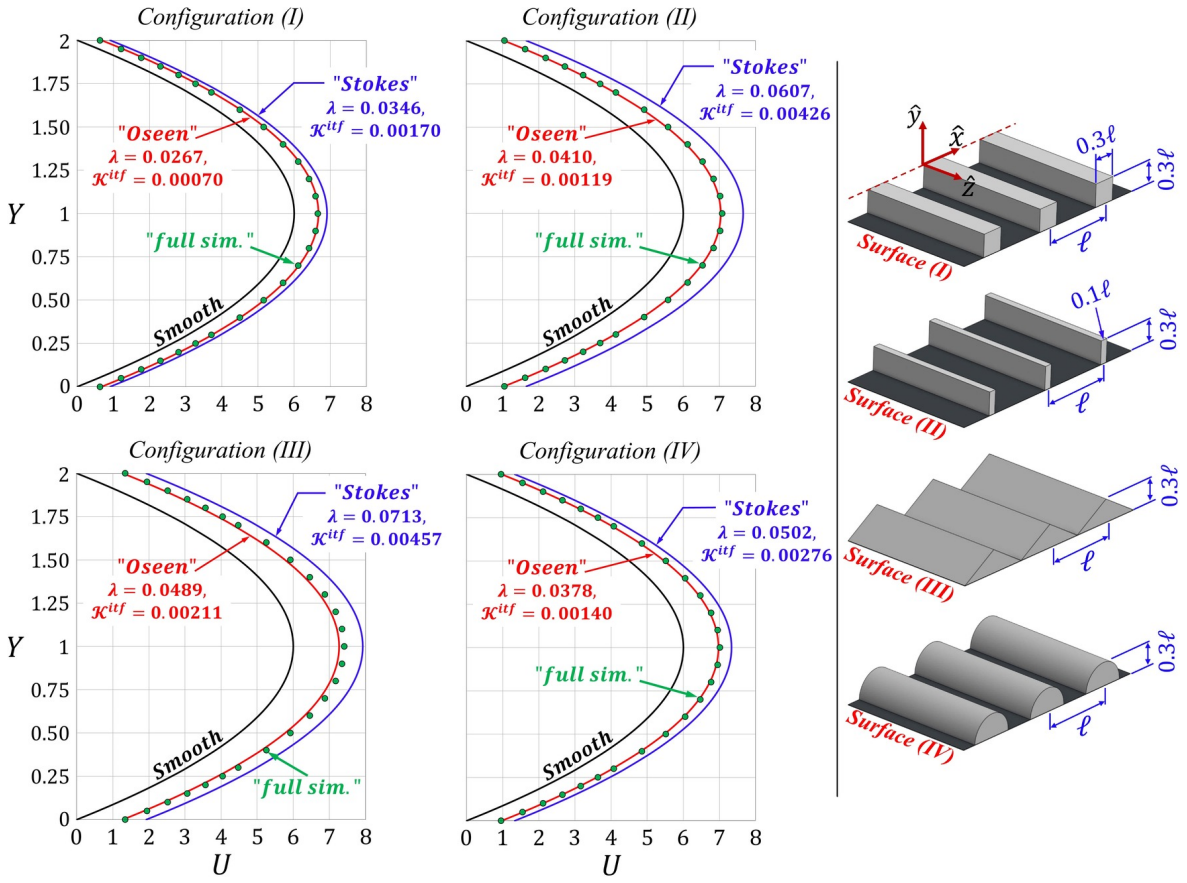

Figure 13: Poiseuille flow ($Re_\tau = 12$) in symmetric channels bounded by surfaces roughened with spanwise-elongated elements. Four different microstructures of the rough surfaces are considered (cf. the right frame) with $\epsilon = \ell/H = 2$. Model predictions for the velocity profiles (Stokes/Oseen) are compared against results of the full simulations.

To facilitate the use of the proposed Oseen-based model in further validation/optimization work, the case of flow over a surface roughened with spanwise-elongated ribs having a square cross section of side length e is considered for a parametric study investigating how the dependence of the Navier-slip and the interface permeability coefficients on the rib size-to-pitch ratio is sensitive to the value of ϵRe_τ, gradually departing from the Stokes flow conditions tested in Ref. (Ahmed *et al.*, 2022*a*). Figure 14 shows that λ_x and $\mathcal{K}^{itf}_{xy}$

decrease monotonically as ϵRe_τ increases, for all values of e/ℓ, with the coefficients more sensitive to ϵRe_τ within the range $0.1 \leq e/\ell \leq 0.3$.

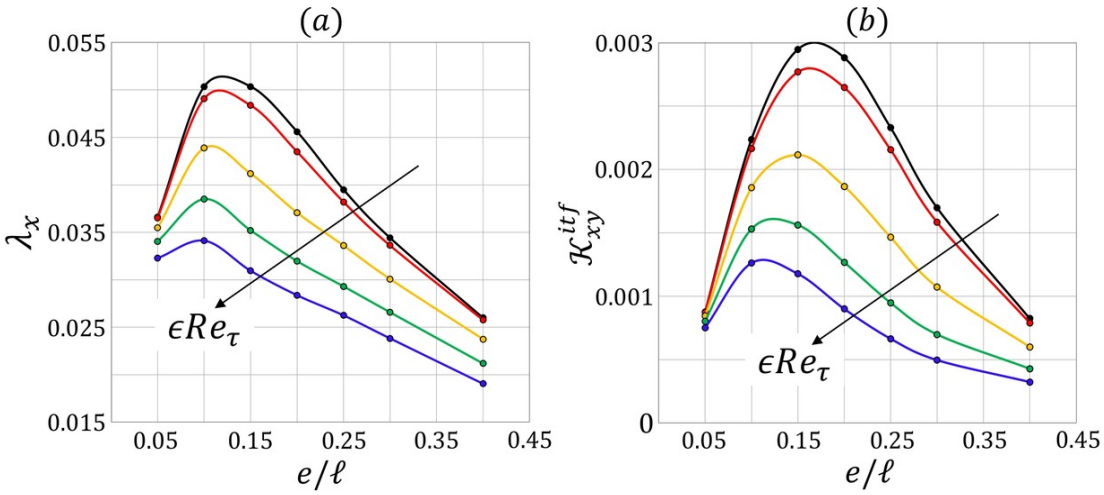

Figure 14: Surface roughened with transverse square ribs: dependence of λ_x and $\mathcal{K}_{xy}^{itf}$ on the rib size-to-pitch ratio, for ϵRe_τ ranging from 0 (black) to 32 (blue) in steps of 8.

Finally, it can be concluded from the trends of the macroscopic coefficients, presented in Figs. 10 and 14, and the results for the channel flow, plotted in Figs. 11 and 12, that the Stokes' model is reliable below the threshold $\epsilon Re_\tau \approx 10$, whereas a more versatile homogenization model, which accounts for advection, must be used beyond this limit; the proposed Oseen's linearization is an effective approach to capture this effect.

3.3 What about flow separation?

To investigate the accuracy of the adopted effective boundary conditions in predicting flow separation at the fluid-porous interface, we now consider the combined Couette-Poiseuille laminar flow in a channel bounded from the top (at $\hat{y} = 2H$) by a smooth, impermeable plate moving at a prescribed velocity $\hat{u}_m$ and from the bottom ($\hat{y} < 0$) by a stationary textured wall/substrate, where a fictitious plane interface between the rough/porous layer and the overlying channel flow of interest is chosen at $\hat{y} = 0$; the lower boundary is characterized by dimensionless Navier-slip and interface permeability coefficients, λ and $\mathcal{K}^{itf}$. Besides the motion of the upper plate, a macroscopic pressure gradient $\partial\hat{p}/\partial\hat{x}$ is applied, either favorably or adversely affecting the motion. We define the following dimensionless variables and control parameters:

$$Y = \frac{\hat{y}}{H}, \quad \mathcal{U} = \frac{\hat{u}}{\hat{u}_m}, \quad \mathcal{R} = \frac{H^2}{\mu\,\hat{u}_m}\frac{\partial\hat{p}}{\partial\hat{x}}, \quad \Lambda = \epsilon\,\lambda, \quad \phi = \epsilon\,\frac{\mathcal{K}^{itf}}{\lambda}, \tag{33}$$

where $\mathcal{R} = 0$ characterizes pure Couette flow and $+/-ve$ finite values of $\mathcal{R}$ indicate adverse/favorable pressure gradients, respectively. Under steady, fully developed flow

conditions, the following momentum conservation equation governs the problem:

$$\frac{\partial^2 \mathcal{U}}{\partial Y^2} = \mathcal{R}, \tag{34}$$

neglecting advective terms, controlled by the dimensionless parameter $\tilde{\mathcal{R}} = \dfrac{\rho\, \hat{u}_m H}{\mu}$. Equation (34) is subject to the boundary conditions

$$\mathcal{U}\big|_{Y=0} = \Lambda \left.\frac{\partial \mathcal{U}}{\partial Y}\right|_{Y=0} - \Lambda\phi\,\mathcal{R}, \qquad \mathcal{U}\big|_{Y=2} = 1. \tag{35}$$

The solution of such a *generalized Couette-Poiseuille* problem takes the form

$$\mathcal{U} = \frac{\mathcal{R}Y^2}{2} + \phi\mathcal{R}\,Y + (Y+\Lambda)\left[\frac{1-2\mathcal{R}(1+\phi)}{2+\Lambda}\right]. \tag{36}$$

Consequently, the slip velocity at the bottom boundary, $\mathcal{U}_{slip}$, and the bulk, channel-averaged velocity, $\mathcal{U}_{ch}$, read

$$\mathcal{U}_{slip} = \frac{\Lambda}{2+\Lambda}\big[1-2\mathcal{R}(1+\phi)\big], \quad \mathcal{U}_{ch} = \left(\frac{2}{3}+\phi\right)\mathcal{R} + \frac{1+\Lambda}{2+\Lambda}\big[1-2\mathcal{R}(1+\phi)\big]. \tag{37}$$

As before, if the boundary condition (35) were first-order accurate, the relations (36) and (37) would hold, with the parameter ϕ set to zero.

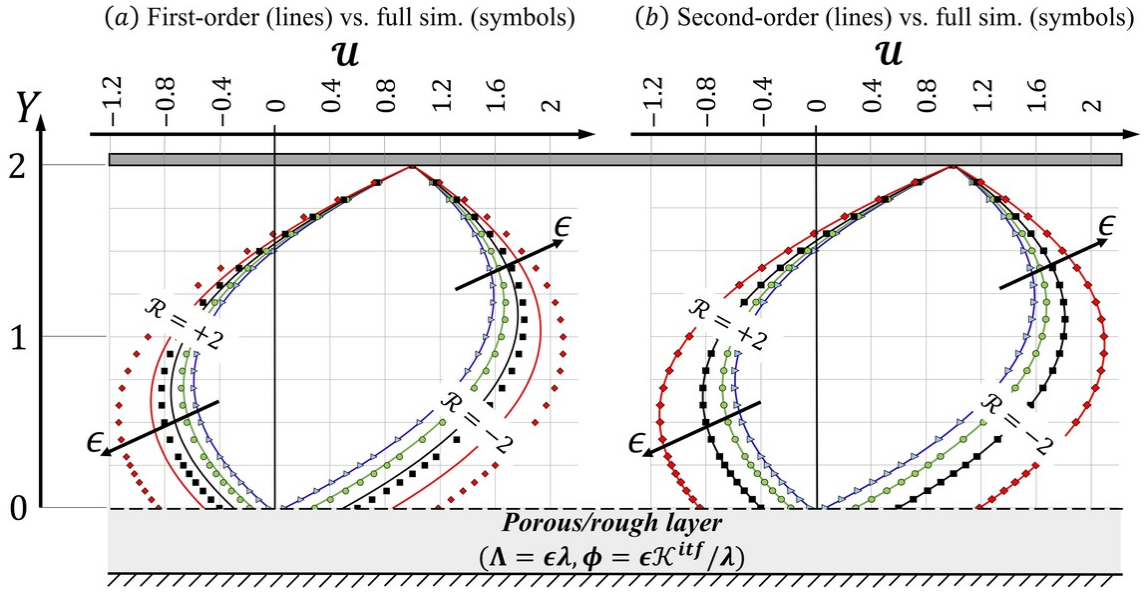

Figure 15: *Generalized Couette-Poiseuille* flow ($\mathcal{R} = \pm 2$) in a channel bounded from the bottom by a porous substrate consisting of an inline pattern of longitudinal cylinders with porosity $\theta = 0.5$ ($\lambda = 0.0688$, $\mathcal{K}^{itf} = 0.0056$). Four values of ϵ are tested, i.e. $\epsilon = 0.4$, 1.6, 3.2, and 6. Results of the full simulations (symbols) are used to validate the analytical solution for $\mathcal{U}$ (lines), based on either the first-order (a) or the second-order (b) model.

The analytical solution for the macroscopic velocity profile (Eq. (36)) is validated in Fig. 15 for the case of a combined Couette-Poiseuille flow subjected to either favorable ($\mathcal{R} = -2$) or adverse ($\mathcal{R} = +2$) pressure gradient, with the channel bounded from the bottom by a permeable layer constructed of streamwise-elongated cylindrical inclusions ($\theta = 0.5$). To assess sensitivity of the model accuracy to the value of $\epsilon = \ell/H$, departing from the case of perfect separation of length scales (at $\epsilon \to 0$), four configurations of the porous bed are considered with ϵ increased from 0.4 to 6. Interestingly, both the first and the second-order solutions are able to predict the flow separation at the permeable boundary for $R = +2$, yet it is clear that upgrading the effective boundary conditions to second order (by including effects of the interface permeability) significantly improves accuracy of the model predictions at the larger values of ϵ; this is consistent with the previous discussion in Section 3.1.3 for the corresponding case of Poiseuille flow.

We now elaborate a bit further on the predictions of the first-order accurate analytical solution, which has been proven to describe fairly well the macroscopic velocity profile at relatively low values of ϵ. The Couette-Poiseuille flow is now assumed to be controlled only by the parameters $\mathcal{R}$ and $\Lambda = \epsilon\lambda$. In Fig. 16, analytical predictions for the profile $\mathcal{U} = \mathcal{U}(Y)$, corresponding to different values of $\mathcal{R}$, are plotted for four values of the slip coefficient Λ, gradually deviating from the case of a smooth, impermeable boundary ($\Lambda = 0$). It is clear that the slip velocity at the permeable/rough boundary and the bulk, channel-averaged velocity increase with Λ for the case of no pressure-gradient or favorable pressure gradient (Figures 16(a) and (b)); the same effect of Λ, progressively less pronounced, is observed in the case of adverse pressure gradient, provided that the value of $\mathcal{R}$ is sufficiently small for backflow not to appear. At $\mathcal{R} = \mathcal{R}_{cr} = 0.5$, all profiles coincide regardless of the value of Λ, with vanishing slip velocity and velocity gradient at the bottom boundary; this is the critical threshold for separation (Fig. 16(d)). Larger values of $\mathcal{R}$ lead to progressively larger portion of the channel interested by backflow, and the larger the parameter Λ is, the more amplified the backflow becomes (cf. Fig. 16(e)). A summary of the first-order results obtained, in terms of $\mathcal{U}_{slip}$ and $\mathcal{U}_{ch}$, are shown in Fig. 16(f) and (g), for the values of Λ considered.

The conclusions to be inferred from Fig. 16 would be modified to some extent in case the parameters of the problem were such that upscaling were needed up to order two in ϵ, or consideration of near-wall nonlinear effects were necessary. This is, however, a trivial task to pursue, since Eqs. (36) and (37) remain valid, and one has simply to employ the appropriate values of Λ and ϕ, possibly via an Oseen-based approximation. For example, if second-order accurate effective boundary condition had been used, it is trivial to find that the critical limit of the dimensionless pressure gradient would be anticipated, i.e. $\mathcal{R}_{cr} = 0.5/(1+\phi)$; thus, for instance, if $\phi \approx 0.5$ (as for the pattern considered in Fig. 15 with $\epsilon = 6$), it would be $\mathcal{R}_{cr} \approx 0.34$.

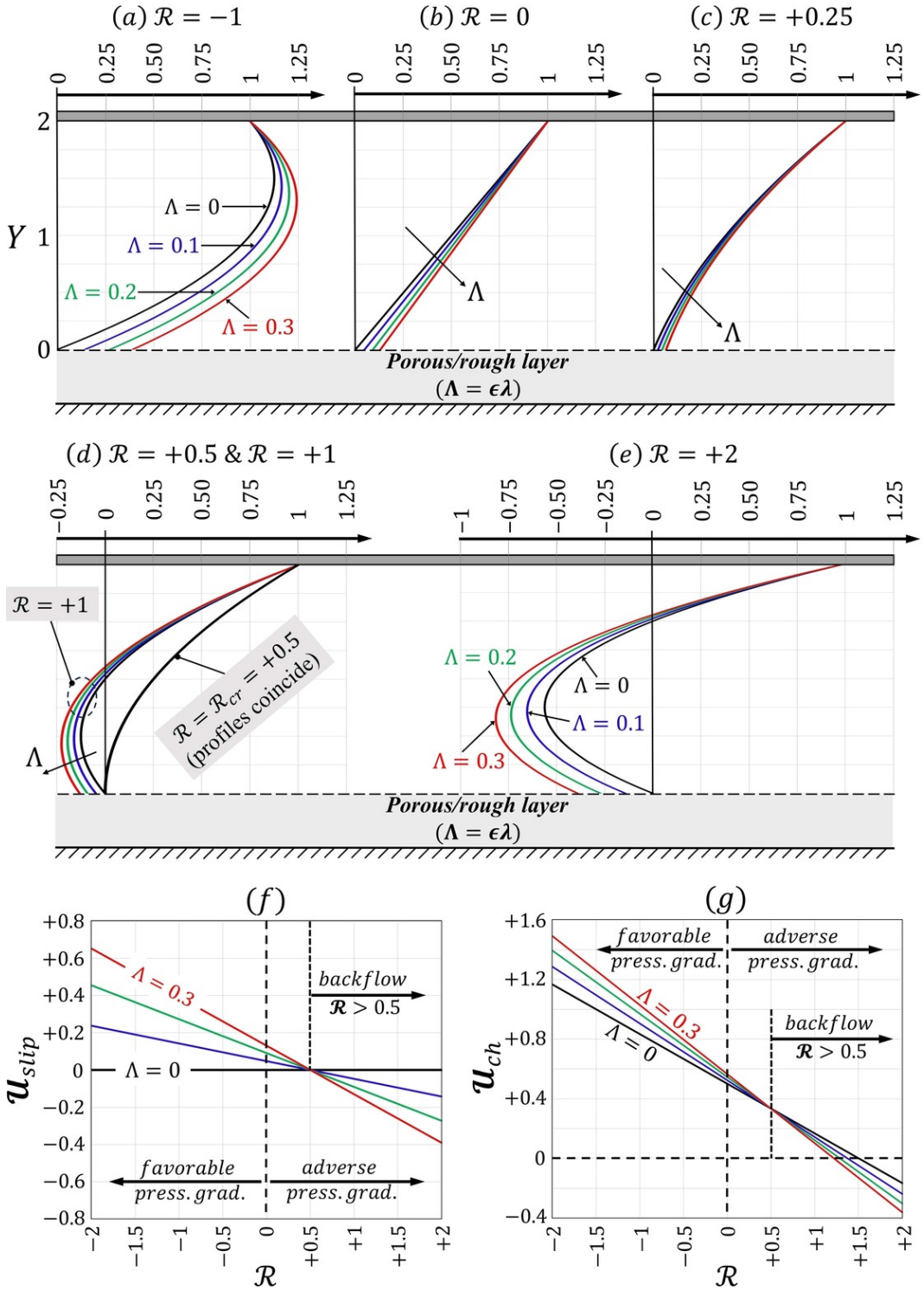

Figure 16: Predictions of the first-order analytical solution ($\phi = 0$) for the behavior of the *generalized Couette-Poiseuille* flow, with the parameter $\Lambda = \epsilon\lambda$ characterizing the bottom boundary of the channel varied between 0 (smooth, impermeable) and 0.3. The macroscopic velocity profiles are plotted in panels (a–e) for different values of $\mathcal{R}$, and the trends of the slip and the channel-averaged velocities are displayed in frames (f) and (g).

4 CONCLUSIONS

The laminar flow in a channel is crucially sensitive to the small-scale features of the rough/porous bounding walls; this is assessed here for the steady, incompressible, fully developed flow driven by a constant pressure gradient and/or by motion of a wall at a prescribed constant speed (i.e., pure Poiseuille, pure Couette, and combined Couette-Poiseuille flows). The microscopic pattern of the rough/permeable wall is assumed not to have a preferential orientation at an angle different from 0 or 90 degrees from the direction of the pressure gradient since, should that be the case, a near-wall transverse velocity component would appear (Stone *et al.*, 2004). In other words, the wall/substrate must be such that the Navier slip tensor has components only along the principal axes of the flow. These are quite general hypothesis, satisfied by many natural/engineered wall textures (Bottaro, 2019). Analytical solutions of the Navier-Stokes equation governing the one-directional flows, $\hat{u} = \hat{u}(\hat{y})$, exist, subject to BJS-like conditions which apply at a *virtual planar interface* in $\hat{y} = 0$ and/or $\hat{y} = 2H$, next to the physical boundaries. The classical upscaling approach is tenable as long as the parameter ϵ, ratio of the microscopic length scale to half the channel height, remains sufficiently small and the flow regime in close vicinity of the walls is Stokes-like. As a rule of thumb, the approach is found to be reliable until $\epsilon Re_\tau \approx 10$. Under these conditions, the *generalized Poiseuille* solution is very accurate when compared against feature-resolving simulations of the flow in channels with different combinations of wall textures. The *generalized combined Couette-Poiseuille* solution was tested under favorable/adverse pressure gradients, and its accuracy in predicting possible backflow next to the fluid-porous interface was highlighted.

One of the most important issues addressed in this article is how to efficiently incorporate the effects of near-wall advection into the homogenization procedure when ϵRe_τ is larger than about 10. For this purpose, an *Oseen's approximation* was employed to linearize the convective acceleration terms in the momentum conservation equations governing the microscale problem. Numerical solutions of the closure problems revealed a decreasing trend of the model coefficients, for any given tested microstructure, as inertial effects became significant. It was confirmed, via extensive validation, that the adjusted approach can widen the applicability range of the homogenized solution considerably. Nonetheless, should flow instabilities be present in the domain (e.g., at relatively high Reynolds numbers) in the form of vortex shedding next to the protrusions/grains or, eventually, transition to turbulence, homogenization would become a more complex undertaking. For instance, tackling near-wall advection with Oseen's linearization in the presence of such instabilities may be questionable, and a fully nonlinear model is probably needed; this could be achieved by the use of adjoint homogenization (Bottaro, 2019). In addition, when near-wall transient effects are significant, they should be considered in the upscaling framework, and sufficiently large *representative elementary cells* of the microscopic domain (possibly larger than a single geometric unit cell) must be identified (Agnaou *et al.*, 2016). Further, under turbulent flow conditions it is necessary to define a three-directional effective velocity at the fictitious wall, even if the mean flow is one-directional. This is important since turbulent fluctuations along directions both tangent

and normal to the fictitious interface considerably affect the behavior of the turbulent boundary layer and, therefore, the skin-friction drag (Orlandi *et al.*, 2006; Orlandi & Leonardi, 2006, 2008; Bottaro, 2019; Lācis *et al.*, 2020; Ahmed *et al.*, 2022*b*).

The analysis conducted attests to the effectiveness of multiscale homogenization and provides a low-cost framework for understanding the large-scale features of laminar flows over rough/permeable surfaces. One advantage of the approach is that the effective boundary conditions adopted are free of empirical parameters; the macroscopic coefficients involved are available from well-defined closure problems to be solved in a microscopic elementary cell, and can be evaluated systematically for walls characterized by different types of non-uniformity, including the effects of porosity, roughness, superhydrophobicity, compliance, etc. Several results for λ and $\mathcal{K}^{itf}$ have been recently computed (e.g. Refs. (Lācis *et al.*, 2020; Bottaro & Naqvi, 2020; Sudhakar *et al.*, 2021; Naqvi & Bottaro, 2021; Ahmed *et al.*, 2022*a*,*b*; Ahmed, 2023)) and can be used to assess the effect of a variety of rough/porous micro-structured media. These results (and others that might easily be obtained for different microscopic geometries) may serve for the inverse design of wall patterns, to satisfy specific constraints, or for the validation of newly developed computational fluid dynamics codes.

FUNDING

The financial support of the Italian Ministry of University and Research, program PRIN 2017, project 2017X7Z8S3 LUBRI-SMOOTH, is gratefully acknowledged.

REFERENCES

Agnaou, M., Lasseux, D. & Ahmadi, A. 2016 From steady to unsteady laminar flow in model porous structures: An investigation of the first Hopf bifurcation. *Comput. Fluids* **136**, 67–82.

Ahmed, E.N. 2023 Natural-convection heat transfer from regularly ribbed vertical surfaces: Homogenization-based simulations towards a correlation for the Nusselt number. *Numer. Heat Transfer A Appl.* **83** (9), 991–1013.

Ahmed, E.N. & Bottaro, A. 2023 Flow through porous metamaterials formed by TPMS-based unit cells: Effects of advection. *Eur. J. Mech. B/Fluids* **100**, 202–207.

Ahmed, E.N., Bottaro, A. & Tanda, G. 2022*a* A homogenization approach for buoyancy-induced flows over micro-textured vertical surfaces. *J. Fluid Mech.* **941**, A53.

Ahmed, E.N., Naqvi, S.B., Buda, L. & Bottaro, A. 2022*b* A homogenization approach for turbulent channel flows over porous substrates: Formulation and implementation of effective boundary conditions. *Fluids* **7** (5), 178.

Auriault, J.-L. 2010 About the Beavers and Joseph boundary condition. *Transp. Porous Med.* **83** (2), 257–266.

Beavers, G.S. & Joseph, D.D. 1967 Boundary conditions at a naturally permeable wall. *J. Fluid Mech.* **30** (1), 197–207.

Bottaro, A. 2019 Flow over natural or engineered surfaces: an adjoint homogenization perspective. *J. Fluid Mech.* **877**, P1.

Bottaro, A. & Naqvi, S.B. 2020 Effective boundary conditions at a rough wall: a high-order homogenization approach. *Meccanica* **55** (9), 1781–1800.

Buda, L. 2021 Drag reduction over rough permeable surfaces: A homogenized-based approach. Master's Thesis in Physics, University of Genoa, Italy. Available at http://www.dicat.unige.it/bottaro/Presentation%20group/Thesis_Buda.pdf.

Eggenweiler, E. & Rybak, I. 2020 Unsuitability of the Beavers–Joseph interface condition for filtration problems. *J. Fluid Mech.* **892**, A10.

Eggenweiler, E. & Rybak, I. 2021 Effective coupling conditions for arbitrary flows in Stokes–Darcy systems. *Multiscale Model. Simul.* **19** (2), 731–757.

Lācis, U. & Bagheri, S. 2017 A framework for computing effective boundary conditions at the interface between free fluid and a porous medium. *J. Fluid Mech.* **812**, 866–889.

Lācis, U., Sudhakar, Y., Pasche, S. & Bagheri, S. 2020 Transfer of mass and momentum at rough and porous surfaces. *J. Fluid Mech.* **884**, A21.

Larson, R.E. & Higdon, J.J.L. 1986 Microscopic flow near the surface of two-dimensional porous media. Part 1. Axial flow. *J. Fluid Mech.* **166**, 449–472.

Naqvi, S.B. & Bottaro, A. 2021 Interfacial conditions between a free-fluid region and a porous medium. *Intl J. Multiph. Flow* **141**, 103585.

Neale, G. & Nader, W. 1974 Practical significance of Brinkman's extension of Darcy's law: Coupled parallel flows within a channel and a bounding porous medium. *Can. J. Chem. Eng.* **52** (4), 475–478.

Nield, D.A. 2009 The Beavers–Joseph boundary condition and related matters: A historical and critical note. *Transp. Porous Med.* **78** (3), 537–540.

Orlandi, P. & Leonardi, S. 2006 DNS of turbulent channel flows with two- and three-dimensional roughness. *Journal of Turbulence* **7**, N73.

Orlandi, P. & Leonardi, S. 2008 Direct numerical simulation of three-dimensional turbulent rough channels: parameterization and flow physics. *Journal of Fluid Mechanics* **606**, 399–415.

Orlandi, P., Leonardi, S. & Antonia, R.A. 2006 Turbulent channel flow with either transverse or longitudinal roughness elements on one wall. *Journal of Fluid Mechanics* **561**, 279–305.

Saffman, P.G. 1971 On the boundary condition at the surface of a porous medium. *Stud. Appl. Math.* **50** (2), 93–101.

Sahraoui, M. & Kaviany, M. 1992 Slip and no-slip velocity boundary conditions at interface of porous, plain media. *Intl J. Heat Mass Transfer* **35** (4), 927–943.

Sano, M. & Tamai, K. 2016 A universal transition to turbulence in channel flow. *Nature Phys.* **12** (3), 249–253.

Schmid, P.J. & Henningson, D.S. 2001 *Stability and Transition in Shear Flows*. New York, NY, USA: Springer.

Stone, H.A., Stroock, A.D. & Ajdari, A. 2004 Engineering flows in small devices: Microfluidics towards a lab-on-a-chip. *Annu. Rev. Fluid Mech.* **36**, 381–411.

Strohbeck, P., Eggenweiler, E. & Rybak, I. 2023 A modification of the Beavers-Joseph condition for arbitrary flows to the fluid-porous interface. *Transp. Porous Med.* **147** (3), 605–628.

Sudhakar, Y., Lācis, U., Pasche, S. & Bagheri, S. 2021 Higher-order homogenized boundary conditions for flows over rough and porous surfaces. *Transp. Porous Med.* **136** (1), 1–42.

Vafai, K. & Kim, S.J. 1990 Fluid mechanics of the interface region between a porous medium and a fluid layer—an exact solution. *Intl J. Heat Fluid Flow* **11** (3), 254–256.

PAPER F2

A homogenization approach for turbulent channel flows over porous substrates: Formulation and implementation of *effective* boundary conditions [1]

Essam Nabil Ahmed[a], **Sahrish Batool Naqvi**[b], **Lorenzo Buda**[c] and **Alessandro Bottaro**[a]

[a] *DICCA, Università di Genova, via Montallegro 1, Genova, 16145, Italy*
[b] *DIME, Università di Genova, via Montallegro 1, Genova, 16145, Italy*
[c] *DIFI, Università di Genova, via Dodecaneso 33, Genova, 16146, Italy*

The turbulent flow through a plane channel bounded by a single permeable wall is considered; this is a problem of interest since a carefully chosen distribution of grains and voids in the porous medium can result in skin friction reduction for the flow in the channel. In the homogenization approach followed here, the flow is not resolved in the porous layer, but an *effective* velocity boundary condition is developed (and later enforced) at a virtual interface between the porous bed and the channel flow. The condition is valid up to order two in terms of a small gauge factor, the ratio of microscopic to macroscopic length scales; it contains slip coefficients, plus surface and bulk permeability coefficients, which arise from the solution of microscale problems solved in a representative elementary volume. Using the effective boundary conditions, free of empirical parameters, direct numerical simulations are then performed in the channel, considering a few different porous substrates. The results, examined in terms of mean values and turbulence statistics, demonstrate the drag-reducing effects of porous substrates with streamwise-preferential alignment of the solid grains.

1 INTRODUCTION

The large skin-friction drag characterizing wall-bounded turbulent flows, as compared to laminar ones, represents a major challenge in engineering applications where efficiency and running costs of fluid transport systems are of interest. This has motivated several experimental and numerical studies aimed at a better understanding of the phenomenon of turbulence production and generation of Reynolds shear stress in such flows (Mansour *et al.*, 1988; Bernard *et al.*, 1993; Orlandi & Jiménez, 1994; Vreman & Kuerten, 2014);

[1] The Version of Record of this manuscript has been published and is available in: *Fluids* **7** (5) (2022) 178. https://doi.org/10.3390/fluids7050178

the coherent structures in the inner region of the wall layer and the *bursting* (ejection) and *sweep* (inrush) events related to such structures have been the object of intense research activities (Kline *et al.*, 1967; Cantwell, 1981; Jeong *et al.*, 1997; Guo *et al.*, 2010). The design of active or passive techniques for turbulent drag reduction requires in-depth understanding of the interacting mechanisms which contribute to near-wall turbulence, in order for its effective control. The near-wall flow is characterized by a self-sustaining cycle responsible for the regeneration of turbulent fluctuations, owing to the dynamic interaction between longitudinal velocity streaks and quasi-streamwise vortices; this cycle is independent of the nature of the outer flow (Jiménez & Pinelli, 1999). Attenuating (or suppressing) any of the processes involved in this autonomous cycle can lead to a less disturbed flow field (or even to relaminarization) (Jiménez & Pinelli, 1999), a clear advantage when the objective of the control is skin-friction drag.

Many investigations have been conducted to optimize and assess the effectiveness and feasibility of active and passive drag reduction techniques, to favorably alter the structure of the turbulent boundary layer. Active techniques, involving energy input, have proved to yield significant drag reduction in wall-bounded turbulent flows. For instance, optimized uniform blowing of the fluid through a spanwise slot can produce a local drag reduction of 80% downstream of the slot (Kim *et al.*, 2003), while sufficiently high suction rates through a short porous flush-mounted strip can allow for local relaminarization of the turbulent boundary layer, resulting in a drag reduction of more than 50% (Antonia *et al.*, 1995). Counter-rotating large-scale streamwise vortices, externally initiated by a transverse array of longitudinal plasma actuators, can stabilize the streaks in the near-wall flow and attenuate the coherent structures, interrupting the turbulence regeneration cycle; a drag reduction of more than 25% can be achieved (Mahfoze & Laizet, 2017; Cheng *et al.*, 2021). Other studies focused on forcing wall-normal fluctuations (Kang & Choi, 2000) or in-plane wall oscillations (Choi, 2002; Wise & Ricco, 2014). Passive drag reduction techniques have also been investigated extensively, along with remarkable advances in bio-inspired designs. Riblets (longitudinal surface grooves) have proved to mitigate the velocity fluctuations near the wall, resulting in a more uniform flow field (Bechert & Bartenwerfer, 1989); studies on different configurations of riblets revealed that an optimized drag reduction of almost 10% can be achieved (Bechert *et al.*, 1997). Super-hydrophobic surfaces can reduce drag up to approximately 80% under optimal conditions, mainly due to the large effective slip of aqueous solutions on the walls (Rastegari & Akhavan, 2015). The ability of anisotropic permeable substrates to reduce skin-friction drag in turbulent channel flows has recently attracted much interest; this constitutes the main objective of the present study.

Porous substrates are encountered in various natural and engineering applications, and have been a source of inspiration for many studies in which the influence of wall permeability has been assessed on the behavior of the overlying turbulent boundary layer and ensuing drag alteration. Several configurations of the porous substrate have been investigated, with different values of the porosity (θ) and at different flow conditions. The main parameters tested in previous studies are the diagonal components of the permeability tensor of the porous medium ($\mathcal{K}_{xx}$, $\mathcal{K}_{yy}$, $\mathcal{K}_{zz}$) and the Navier-slip coefficients

(λ_x, λ_z) at the dividing surface between the free-fluid region in the channel and the permeable layer. In the following, x, y and z denote, respectively, the streamwise, wall-normal and spanwise directions. The numerical work by Rosti *et al.* (2015) on turbulent channel flows over isotropic porous substrates ($\mathcal{K}_{xx} = \mathcal{K}_{yy} = \mathcal{K}_{zz}$) has shown that even small values of the medium permeability can affect the response of the adjacent turbulent boundary layer: the disturbances were found to be intensified and the Reynolds stresses enhanced, with a consequent increase in skin-friction drag. This is in general agreement with the findings of earlier studies (Beavers *et al.*, 1970; Tilton & Cortelezzi, 2006, 2008). A similar behavior of disturbance intensification is observed when the porous substrates have preferential spanwise permeability. Wang *et al.* (2021) investigated the dynamic interaction between a turbulent channel flow and a porous bed made of spanwise-aligned cylinders, for which $\mathcal{K}_{zz} > \mathcal{K}_{xx} = \mathcal{K}_{yy}$. The structure of the *blowing* (upwelling) and *suction* (downwelling) events through the pores has been analyzed, particularly in terms of their role on the onset of the Kelvin-Helmholtz instability near the permeable wall. Other studies have focused on permeable walls potentially capable to yield turbulent drag reduction. Rosti *et al.* (2018) studied the turbulent flow over anisotropic porous beds characterized by equal values of the permeability in the streamwise and the spanwise directions, i.e., $\mathcal{K}_{xx} = \mathcal{K}_{zz} \neq \mathcal{K}_{yy}$. They showed that a drag reduction of up to 20% can be achieved from walls of high in-plane permeability ($\mathcal{K}_{xx} = \mathcal{K}_{zz} >> \mathcal{K}_{yy}$), whereas the skin-friction drag may increase by the same amount for substrates of preferential wall-normal permeability. Among the different configurations considered in the literature, the use of porous substrates of preferential permeability along the streamwise direction, consisting, e.g., of longitudinal cylinders with $\mathcal{K}_{xx} >> \mathcal{K}_{zz} = \mathcal{K}_{yy}$, appears to provide the best results in terms of turbulent drag reduction. The drag reduction curves for this configuration are similar to those of riblets (Gómez-de Segura & García-Mayoral, 2019), and the theory behind the ability of such substrates to reduce skin-friction drag has been elaborated by Abderrahaman-Elena & García-Mayoral (2017). Conceptually, the drag reduction (DR) is proportional to the difference between the slip lengths along the streamwise and the spanwise directions, that is, $DR \approx \mu_0(\lambda_x^+ - \lambda_z^+)$ (Luchini *et al.*, 1991; Jiménez, 1994), which has been approximated by $\mu_0\,\xi\left(\sqrt{\mathcal{K}_{xx}^+} - \sqrt{\mathcal{K}_{zz}^+}\right)$ (Abderrahaman-Elena & García-Mayoral, 2017). All the macroscopic parameters are measured in wall units and this is indicated by the superscript '+'; the coefficient μ_0 is a function of the Reynolds number (Garcia-Mayoral & Jiménez, 2011), while the parameter ξ characterizes the inter-connectivity of the flow between the pores (Abderrahaman-Elena & García-Mayoral, 2017). The relation above in terms of the square root of the permeability components holds for substrates of relatively low wall-normal permeability; if $\mathcal{K}_{yy}^+$ exceeds some critical threshold, Kelvin-Helmholtz-like rollers are developed near the interface, and the drag reduction mechanism is adversely affected (Gómez-de Segura *et al.*, 2018).

With the significant progress in manufacturing and fabrication techniques, the study of the interaction between the microscale features of the surface (such as roughness, porosity, irregularity, compliance, etc.) and the adjacent fluid flow has become more important for several applications. The numerical complexity of fully resolving the micro-details of the surface in Direct Numerical Simulations (DNS) or even in Large Eddy Simulations (LES) of turbulence represents a challenge, especially if optimization of the surface is

the ultimate goal. The multiscale homogenization approach adopted in this paper is a mathematical framework through which the rapidly varying properties of the surface (the porous substrate in the present case) can be replaced by upscaled properties such as slip, interface permeability, etc. (Babuška, 1976; Bottaro, 2019), which contribute to the definition of *effective* boundary conditions at a virtual plane surface. The macroscale behavior of, for instance, the turbulent channel flow is then targeted, bypassing the need to fully resolve the motion within the permeable substrate; the mesh requirements of the numerical simulations are therefore significantly alleviated. Multiscale homogenization has been known and used by applied mathematicians for a long time. In more recent years, it has been rediscovered and applied to a variety of physically relevant cases. Although the classical first-order slip condition over a generic solid surface, proposed by Navier (1823), was based on empirical considerations concerning the near-wall flow behavior, recent studies adopting the homogenization technique have provided a robust mathematical framework for the estimation of Navier's slip length, λ, without the need for any *ad hoc* correlation (Jiménez Bolaños & Vernescu, 2017). A tensorial generalization of the first-order Navier's slip condition over a micro-textured surface was given by Zampogna *et al.* (2019*a*), via the definition of a third-order slip tensor which depends on the geometry of the roughness pattern. The homogenized model was later extended to study the fluid motion over deformable riblets, to assess the potential drag reduction (Zampogna *et al.*, 2019*b*). The so-called *transpiration-resistance* model by Lācis *et al.* (2020) shed light on the role of the wall-normal velocity at the fictitious interface in improving the predictions of the homogenization-based direct simulations for turbulent flows over micro-patterned surfaces. The homogenization model for the flow over a rough surface was later pushed to third-order in terms of a small parameter, ratio of microscopic to macroscopic length scales, by Bottaro & Naqvi (2020). Most recently, the asymptotic homogenization theory has been employed by Ahmed *et al.* (2022) to study buoyancy-driven flows over vertical rough surfaces, by deriving and implementing upscaled velocity and temperature boundary conditions at a smooth virtual surface. Effective boundary conditions at the interface between a porous bed and an unconfined flow region have been explored by Sudhakar *et al.* (2021) and by Naqvi & Bottaro (2021).

In this work, asymptotic homogenization is used to derive second-order accurate *effective* boundary conditions for the three velocity components at a fictitious interface, chosen tangent to the porous material, to macroscopically mimic the effects of the small-scale features of an anisotropic porous layer on a turbulent boundary layer. The technique relies on reconstructing the microscale problem via asymptotic expansions of the microscopic dependent variables (velocity components and pressure) in powers of a small parameter ϵ, which represents the ratio between two well-separated scales, for instance the periodicity of the porous pattern (microscopic length scale) and half the channel height (macroscopic length scale). The problem is then solved up to any order in ϵ via numerical solution of *ad hoc* auxiliary systems which hold in a doubly periodic *representative elementary volume*. The equations governing the physical problem, the domain decomposition, and the chosen scales for each sub-domain are outlined in Section 2, with detailed explanation of the adopted asymptotic approach and with illustration of the numerical solutions for the auxiliary problems that arise. Different configurations

of the porous substrate are considered for the evaluation of the macroscopic coefficients of the model, in particular, spanwise- and streamwise-aligned elements of two different shapes.The macroscopic problem is addressed in Section 3. A direct numerical simulation was first conducted for a turbulent flow through a channel with smooth, impermeable walls at $Re_\tau \approx 190$, to validate the numerical code, the domain size, etc. The wall-bounded turbulent flow over a porous substrate is then considered. Standard turbulence statistics are compared for different porous substrates, and consequent skin-friction drag increase/reduction is indicated. The main findings of the study are highlighted in the concluding section.

2 THE HOMOGENIZATION MODEL

This section is dedicated to providing the details to derive *effective* boundary conditions at the fictitious interface between a channel flow and a porous substrate underneath. The procedure represents an extension of the model by Naqvi & Bottaro (2021), in which only isotropic or two-dimensional porous media were analyzed; in the present work, a three-dimensional, transversely isotropic, permeable bed is considered.

2.1 Governing equations and domain decomposition

Let us consider, for instance, a porous substrate made of regularly arranged, streamwise-aligned solid inclusions with given periodicity in the spanwise and wall-normal directions, cf. Figure 1. It is possible to identify two characteristic length scales, a microscopic one related to the porous medium, l (the periodicity of the configuration), and a macroscopic one related to the large-scale motion in the channel, H (half the channel thickness). The mass and momentum conservation equations governing the flow of a viscous, incompressible, Newtonian fluid can be expressed in terms of the dimensional variables $\hat{\bullet}$ as follows:

$$\frac{\partial \hat{u}_i}{\partial \hat{x}_i} = 0, \quad \rho\left(\frac{\partial \hat{u}_i}{\partial \hat{t}} + \hat{u}_j \frac{\partial \hat{u}_i}{\partial \hat{x}_j}\right) = -\frac{\partial \hat{p}}{\partial \hat{x}_i} + \mu \frac{\partial^2 \hat{u}_i}{\partial \hat{x}_j^2}, \tag{1}$$

with ρ the fluid density, μ the dynamic viscosity, $\hat{p}$ the pressure, $\hat{u}_i$ the velocity components ($\hat{u}_1 = \hat{u}$, $\hat{u}_2 = \hat{v}$, $\hat{u}_3 = \hat{w}$), $\hat{x}_i$ the space coordinates ($\hat{x}_1 = \hat{x}$, $\hat{x}_2 = \hat{y}$, $\hat{x}_3 = \hat{z}$), and $\hat{t}$ time. The streamwise direction ($\hat{x}_1$), the wall-normal direction ($\hat{x}_2$), and the spanwise direction ($\hat{x}_3$) are indicated in Figure 1.

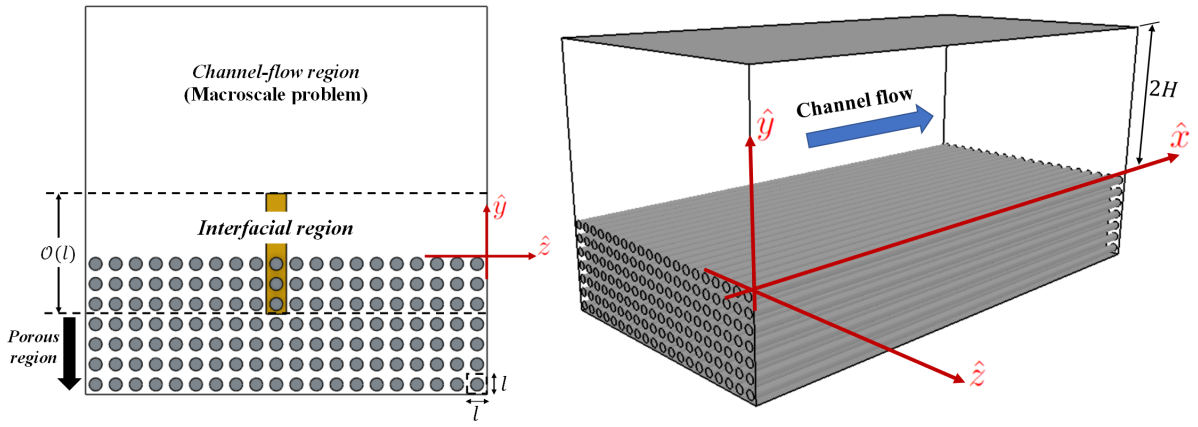

Figure 1: Sketch of the full domain for the case of streamwise-aligned cylindrical inclusions. The left frame illustrates in a constant $\hat{x}$-section the decomposition of the domain into three distinct sub-regions; the brown volume represents the doubly periodic elementary cell of the microscopic problem.

Provided that $l \ll H$, the microscopic problem is amenable to a multiple-scale expansion in terms of a small parameter $\epsilon = l/H \ll 1$. The full domain is decomposed into three sub-domains: a channel-flow region away from the interface (superscript "$\mathcal{C}$"), an interface region (superscript "$\mathcal{I}$") and a region within the porous layer away from boundaries, governed by Darcy's law (superscript "$\mathcal{P}$"). The normalized variables in the three regions are introduced as follows:

Channel-flow region $^{\mathcal{C}}$*:*

$$X_i = \hat{x}_i/H, \quad P^{\mathcal{C}} = \hat{p}/(\rho\mathcal{U}^2), \quad U_i^{\mathcal{C}} = \hat{u}/\mathcal{U}. \tag{2-a}$$

Interface region $^{\mathcal{I}}$*:*

$$x_i = \hat{x}_i/\ell, \quad P^{\mathcal{I}} = \hat{p}/(\mu\mathcal{U}/H), \quad U_i^{\mathcal{I}} = \epsilon^{-1}\hat{u}/\mathcal{U}. \tag{2-b}$$

Porous region $^{\mathcal{P}}$*:*

$$x_i = \hat{x}_i/\ell, \quad P^{\mathcal{P}} = \hat{p}/(\mu\mathcal{U}/H), \quad U_i^{\mathcal{P}} = \epsilon^{-2}\hat{u}/\mathcal{U}, \tag{2-c}$$

with $\mathcal{U}$ a suitable macroscopic velocity scale, for instance the bulk velocity in $0 \le \hat{y} \le 2H$. The normalization above leads to the following dimensionless systems in the $\bullet^{\mathcal{C}}$, $\bullet^{\mathcal{I}}$, and $\bullet^{\mathcal{P}}$ regions, respectively;

$$\frac{\partial U_i^{\mathcal{C}}}{\partial X_i} = 0, \quad \frac{\partial U_i^{\mathcal{C}}}{\partial t} + U_j^{\mathcal{C}}\frac{\partial U_i^{\mathcal{C}}}{\partial X_j} = -\frac{\partial P^{\mathcal{C}}}{\partial X_i} + \frac{1}{Re}\frac{\partial^2 U_i^{\mathcal{C}}}{\partial X_j^2}, \tag{3-a}$$

$$\frac{\partial U_i^{\mathcal{I}}}{\partial x_i} = 0, \quad \epsilon^2 Re\left(\frac{\partial U_i^{\mathcal{I}}}{\partial t} + U_j^{\mathcal{I}}\frac{\partial U_i^{\mathcal{I}}}{\partial x_j}\right) = -\frac{\partial P^{\mathcal{I}}}{\partial x_i} + \frac{\partial^2 U_i^{\mathcal{I}}}{\partial x_j^2}, \tag{3-b}$$

$$\epsilon \frac{\partial U_i^{\mathcal{P}}}{\partial x_i} = 0, \quad \epsilon^4 Re\, U_j^{\mathcal{P}} \frac{\partial U_i^{\mathcal{P}}}{\partial x_j} = -\frac{\partial P^{\mathcal{P}}}{\partial x_i} + \epsilon \frac{\partial^2 U_i^{\mathcal{P}}}{\partial x_j^2}, \tag{3-c}$$

with $Re = \dfrac{\rho \mathcal{U} H}{\mu}$. In the channel-flow region, the dependent variables are function of the macroscopic coordinates X_i only, whereas, in the intermediate and porous regions, the dependent variables depend on both microscopic and macroscopic coordinates (x_i, X_i respectively). The continuity of the fields across the interface between the $\bullet^{\mathcal{C}}$ and $\bullet^{\mathcal{I}}$ regions is represented by matching the velocity and the traction vectors at a dividing surface. If $x_2 = y = y_\infty$ is taken to be the microscopic vertical coordinate of this interface, and $Y = \mathcal{Y} = \epsilon y_\infty$ is the macroscopic vertical position at which the effective conditions are enforced, the matching conditions may be written as follows:

$$\lim_{y \to y_\infty} U_i^{\mathcal{I}} = \frac{1}{\epsilon} \lim_{Y \to \mathcal{Y}} U_i^{\mathcal{C}}, \tag{4-a}$$

$$\lim_{y \to y_\infty} -P^{\mathcal{I}} \delta_{i2} + \frac{\partial V^{\mathcal{I}}}{\partial x_i} + \frac{\partial U_i^{\mathcal{I}}}{\partial y} = \lim_{Y \to \mathcal{Y}} -Re\, P^{\mathcal{C}} \delta_{i2} + \frac{\partial V^{\mathcal{C}}}{\partial X_i} + \frac{\partial U_i^{\mathcal{C}}}{\partial Y}, \tag{4-b}$$

with δ_{ij} the Kronecker index. The conditions above are acceptable provided y_∞ is sufficiently large for the $\bullet^{\mathcal{I}}$ variables to become independent of x and z there. Should this not be the case, integration of the interface variables along the x and z direction must be done before matching velocity and traction components.

2.2 Asymptotic analysis of the microscale problem

The velocity and pressure fields in porous and interface regions are asymptotically expanded in terms of ϵ, for instance $U_i^I = u_i^{(0)} + \epsilon u_i^{(1)} + \epsilon^2 u_i^{(2)} + ...$, and the gradients are recast based on the chain rule ($\dfrac{\partial}{\partial x_i} \rightarrow \dfrac{\partial}{\partial x_i} + \epsilon \dfrac{\partial}{\partial X_i}$). The asymptotic expressions are plugged into the microscale governing equations and read:

$$\begin{cases} \partial_i u_i = -\epsilon\, \partial_i' u_i^{(0)} + \mathcal{O}\left(\epsilon^2\right), \\ -\partial_i p + \partial_j^2 u_i = \epsilon \left[\partial_i' p^{(0)} - 2\, \partial_j \partial_j' u_i^{(0)}\right] + \mathcal{O}\left(\epsilon^2\right), \end{cases} \tag{5}$$

with the microscopic and macroscopic derivatives indicated, respectively, by

$$\partial_i = \frac{\partial}{\partial x_i}, \quad \partial_i' = \frac{\partial}{\partial X_i}.$$

The microscale problem can be reconstructed at different orders of ϵ. The leading-order problem reads:

$$\mathcal{O}(1) : \begin{cases} \partial_i u_i^{(0)} = 0, \\ -\partial_i p^{(0)} + \partial_j^2 {u_i}^{(0)} = 0, \\ -p^{(0)} \delta_{i_2} + \partial_2 u_i^{(0)} + \partial_i u_2^{(0)} \Big|_{y_\infty} = S_{i2}^{\mathcal{C}}. \end{cases} \tag{6}$$

At next order we obtain:

$$\mathcal{O}(\epsilon):\begin{cases}\partial_i u_i^{(1)} = -\partial'_i u_i^{(0)},\\ -\partial_i p^{(1)} + \partial_j^2 u_i^{(1)} = \partial'_i p^{(0)} - 2\partial_j\partial'_j u_i^{(0)},\\ -p^{(1)}\delta_{i_2} + \partial_2 u_i^{(1)} + \partial_i u_2^{(1)}\Big|_{y_\infty} = -\partial'_2 u_i^{(0)} + \partial'_i u_2^{(0)}\Big|_{y_\infty},\end{cases} \tag{7}$$

where $S_{i2}^{\mathcal{C}}$ is the macroscopic traction vector evaluated at $Y = \mathcal{Y}$, i.e.

$$S_{i2}^{\mathcal{C}} = \boldsymbol{\sigma}^{\boldsymbol{\mathcal{C}}}\cdot\boldsymbol{e}_2|_{Y=\mathcal{Y}} = \left(\frac{\partial U^{\mathcal{C}}}{\partial Y} + \frac{\partial V^{\mathcal{C}}}{\partial X}, -ReP^{\mathcal{C}} + 2\frac{\partial V^{\mathcal{C}}}{\partial Y}, \frac{\partial W^{\mathcal{C}}}{\partial Y} + \frac{\partial V^{\mathcal{C}}}{\partial Z}\right)\Big|_{Y=\mathcal{Y}}, \tag{8}$$

with $\boldsymbol{\sigma}^{\mathcal{C}}$ the stress tensor. From now on, the superscript $\bullet^{\mathcal{C}}$ is omitted when referring to outer flow dependent variables.

Owing to the linearity of equations (6, 7)), generic forms of the solutions can be assumed. For the leading-order problem the dependent variables can be expressed as

$$\begin{cases} u_i^{(0)} = u_{ij}^{\dagger} S_{j2},\\ p^{(0)} = p_j^{\dagger} S_{j2},\end{cases} \tag{9}$$

with the new parameters, $u_{ij}^{\dagger}$ and $p_j^{\dagger}$ functions of only x_i. Three decoupled systems of equations, the so-called *auxiliary* problems, arise from substituting the preceding expressions into equations (6); they can be summarized as follows:

$$\begin{cases}\partial_i u_{ij}^{\dagger} = 0,\\ -\partial_i p_j^{\dagger} + \partial_l^2 u_{ij}^{\dagger} = 0,\\ \left(-p_j^{\dagger}\delta_{i2} + \partial_2 u_{ij}^{\dagger} + \partial_i u_{2j}^{\dagger}\right)\Big|_{y_\infty} = \delta_{ij},\end{cases} \tag{10}$$

where the three microscopic problems corresponds to $j = 1, 2, 3$. For $j = 2$, one finds the simple analytical solution:

$$u_{i2}^{\dagger} = 0, \quad p_2^{\dagger} = -1.$$

These results will directly enter, and simplify, the $\mathcal{O}(\epsilon)$ problems.

At $\mathcal{O}(\epsilon)$, the following generic forms hold:

$$\begin{cases} u_i^{(1)} = u_{ijk}^{\ddagger}\,\partial'_k S_{j2},\\ p^{(1)} = p_{jk}^{\ddagger}\,\partial'_k S_{j2}.\end{cases} \tag{11}$$

This leads to

$$\begin{cases} -\partial_i\partial_i u_{ijk}^{\ddagger} = -u_{kj}^{\dagger},\\ p_{jk}^{\ddagger} - p_j^{\dagger}\delta_{ki} + \partial_l^2 u_{ijk}^{\ddagger} + 2\partial_k u_{ij}^{\dagger} = 0,\\ \left(-p_{jk}^{\ddagger}\delta_{i2} + \partial_2 u_{ijk}^{\ddagger} + \partial_i u_{2jk}^{\ddagger}\right)\Big|_{y_\infty} = -\left(u_{ij}^{\dagger}\delta_{k2} + u_{2j}^{\dagger}\delta_{ik}\right)\Big|_{y_\infty},\end{cases} \tag{12}$$

which are nine decoupled problems to be solved in the microscopic cell, for $j, k = 1, 2, 3$. All these problems are subject to periodicity along x and z (for streamwise-aligned solid inclusions) and to the no-slip condition on the solid grains of the porous medium.

Numerical results are sought, in particular, at $y = y_\infty$, since $u^\dagger_{ij}\Big|_{y_\infty}$ and $u^\ddagger_{ijk}\Big|_{y_\infty}$ are eventually the numerical coefficients needed to close the macroscopic effective conditions. These conditions arise from matching the velocity vector at the specified interface (cf. equation (4-a)); finally, the second-order accurate upscaled conditions at the dividing surface are:

$$U_i|_{Y=\epsilon y_\infty} = \epsilon \left(u_i^{(0)}\Big|_{y_\infty} + \epsilon\, u_i^{(1)}\Big|_{y_\infty} \right) + \mathcal{O}(\epsilon^3) = \epsilon\, \tilde{u}_{ij}|_{y_\infty}\, S_{j2} + \epsilon^2\, u^\ddagger_{ijk}\Big|_{y_\infty} \frac{\partial S_{j2}}{\partial X_k} + \mathcal{O}(\epsilon^3). \quad (13)$$

2.3 Numerical solutions of the auxiliary systems

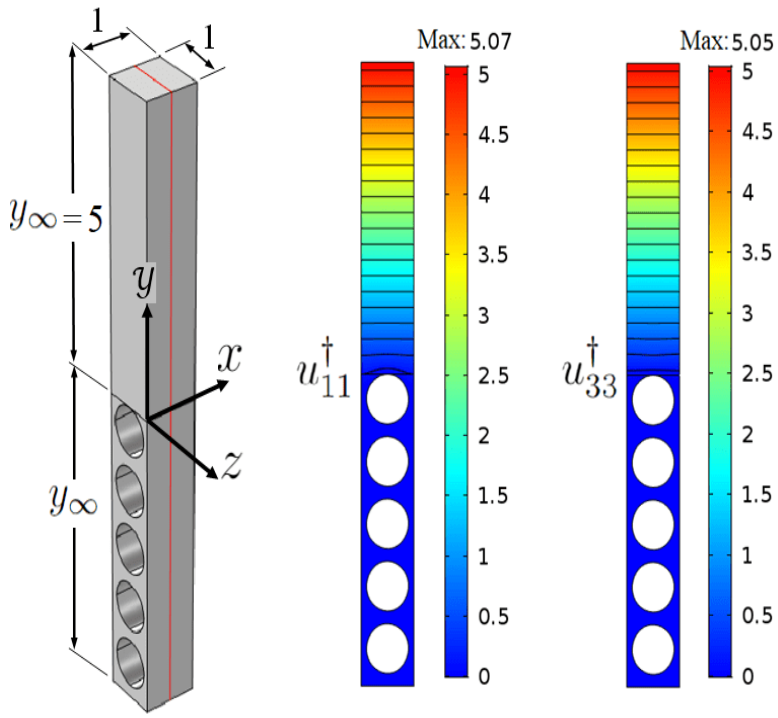

Figure 2: A full microscopic domain (in grey) with two-dimensional $zy-$plane (in red) over which contours of $u^\dagger_{11}$ and $u^\dagger_{33}$ are shown, for $\theta = 0.5$

With the aid of the Comsol Multiphysics® software, the auxiliary systems formulated in Section 2.2 are solved on a microscopic elongated domain, considering streamwise-aligned cylindrical inclusions. Specifically, the domain consists of a xyz box of sides $[1, 2y_\infty, 1]$; cf. Figure 2. The value of y_∞ is specified such that the microscopic fields are homogeneous

in x and z near $y = y_\infty$. It was numerically confirmed that $y_\infty = 5$ is sufficient to satisfy the preceding condition. The dividing surface is set at $y = 0$, the surface tangent to the uppermost cylinder, so that half of the domain ($0 < y \leq y_\infty$) is above it and the other half ($-y_\infty \leq y < 0$) is below it. For $-y_\infty \leq y < 0$, identical longitudinal cylinders are present, regularly spaced of one unit of length along y. The diameter of the cylinders was changed to study the effects of varying the porosity of the substrate, defined as $\theta = \mathcal{V}_{fluid}/\mathcal{V}_{tot}$, with $\mathcal{V}_{fluid}$ and $\mathcal{V}_{tot}$ the fluid's volume in a cubic unit cell within the porous domain and the total volume of the unit cell, respectively.

The numerical solutions of the auxiliary sub-systems related to the $\mathcal{O}(1)$ problem, i.e., equations (10), reveal that $u^\dagger_{11}$ and $u^\dagger_{33}$ are the only variables which do not vanish at the matching surface ($y = y_\infty = 5$). The contours of the two parameters throughout the microscopic domain are displayed in Figure 2; for brevity, fields of the other variables are not presented. Subsequently, the effect of varying the location of the matching interface was considered, by gradually increasing the value of y_∞ and monitoring the behaviors of $u^\dagger_{11}$ and $u^\dagger_{33}$. Linear trends have been detected, in the same manner as for the case of the fluid motion over a rough surface (Bottaro & Naqvi, 2020), i.e.

$$u^\dagger_{11}\Big|_{y_\infty} = y_\infty + \lambda_x, \quad u^\dagger_{33}\Big|_{y_\infty} = y_\infty + \lambda_z, \tag{14}$$

with λ_x and λ_z the dimensionless Navier-slip coefficients in the streamwise and the spanwise directions, respectively.

Solutions of the higher-order systems were then sought. The following trends of the microscopic parameters, with non-zero magnitudes at the matching interface, are obtained (the reader is referred to (Bottaro & Naqvi, 2020) and (Naqvi & Bottaro, 2021) for more details about the procedure):

$$\begin{aligned} -\,u^\ddagger_{211}\Big|_{y_\infty} &= u^\ddagger_{121}\Big|_{y_\infty} = 0.5\,y_\infty^2 + \lambda_x\,y_\infty + \mathcal{K}^{itf}_{xy}, \\ -\,u^\ddagger_{233}\Big|_{y_\infty} &= u^\ddagger_{323}\Big|_{y_\infty} = 0.5\,y_\infty^2 + \lambda_z\,y_\infty + \mathcal{K}^{itf}_{zy}, \\ u^\ddagger_{222}\Big|_{y_\infty} &= \mathcal{K}_{yy}, \end{aligned} \tag{15}$$

where $\mathcal{K}_{yy}$ is a *medium* permeability component, while $\mathcal{K}^{itf}_{xy}$ and $\mathcal{K}^{itf}_{zy}$ are interface permeabilities.

At this point, it is advantageous to extrapolate the solutions of the parameters of interest to a matching interface located at $y = 0$. This can be achieved simply by setting $y_\infty = 0$ in the fitting relations (equations (14, 15)). Thus, the values of the coefficients $\lambda_x, \lambda_z, \mathcal{K}^{itf}_{xy}, \mathcal{K}^{itf}_{zy}$ and $\mathcal{K}_{yy}$ are sufficient to describe the presence of the permeable interface up to second order in terms of ϵ, by enforcing effective boundary conditions on the plane $y = 0$. These coefficients characterize the microstructure of the porous substrate; for instance, they are dependent on the shape of the inclusions, their orientation and the porosity θ.

Simple methods can also be adopted to calculate the coefficients of interest, based on previous findings (Bottaro & Naqvi, 2020; Naqvi & Bottaro, 2021). The Navier-slip coefficients (λ_x, λ_z) can be computed by averaging the fields of $u^{\dagger}_{11}$ and $u^{\dagger}_{33}$ (those shown in Figure 2), respectively, over the plane $y = 0$. The numerical values of $\mathcal{K}^{itf}_{xy}$ and $\mathcal{K}^{itf}_{zy}$ can be recovered by taking the following volume integrals:

$$\begin{aligned} \mathcal{K}^{itf}_{xy} &= \int_{\mathcal{V}_{f\,Por}} u^{\dagger}_{11}\,\mathrm{d}V, \\ \mathcal{K}^{itf}_{zy} &= \int_{\mathcal{V}_{f\,Por}} u^{\dagger}_{33}\,\mathrm{d}V, \end{aligned} \tag{16}$$

where $\mathcal{V}_{f\,Por}$ denotes the whole fluid volume in the elementary cell below the interface. This method is particularly convenient since it means that interface permeabilities are already available from the $\mathcal{O}(1)$ problems, i.e. there is no need to solve the $\mathcal{O}(\epsilon)$ ones to compute them. Finally, as far as $\mathcal{K}_{yy}$ is concerned, one can compute it by simulating the $\mathcal{O}(\epsilon)$ system governing $u^{\ddagger}_{222}$ in a fully periodic unit cell (cf. Figure 3) and evaluating the integral:

$$\mathcal{K}_{yy} = \int_{\mathcal{V}_{fluid}} u^{\ddagger}_{222}\,\mathrm{d}V. \tag{17}$$

Should they be needed, the other diagonal components of the medium permeability tensor can be retrieved in the following way:

$$\begin{aligned} \mathcal{K}_{xx} &= \int_{\mathcal{V}_{fluid}} u^{\ddagger}_{121}\,\mathrm{d}V, \\ \mathcal{K}_{zz} &= \int_{\mathcal{V}_{fluid}} u^{\ddagger}_{323}\,\mathrm{d}V. \end{aligned} \tag{18}$$

We remark that, in this case, $\mathcal{K}_{xx}$ and $\mathcal{K}_{zz}$ do not correspond to any value of $u^{\ddagger}_{ijk}\big|_{y_\infty=0}$, and do not contribute to the interface conditions. Eventually, the following values of the macroscopic coefficients were attained for the case of longitudinal cylindrical inclusions with porosity $\theta = 0.5$:

$$\begin{gathered} \lambda_x = 0.06883, \quad \lambda_z = 0.04513, \quad \mathcal{K}^{itf}_{xy} = 0.005561, \quad \mathcal{K}^{itf}_{zy} = 0.002220, \\ \mathcal{K}_{xx} = 0.006966, \quad \mathcal{K}_{yy} = 0.001828, \quad \mathcal{K}_{zz} = 0.001828. \end{gathered} \tag{19}$$

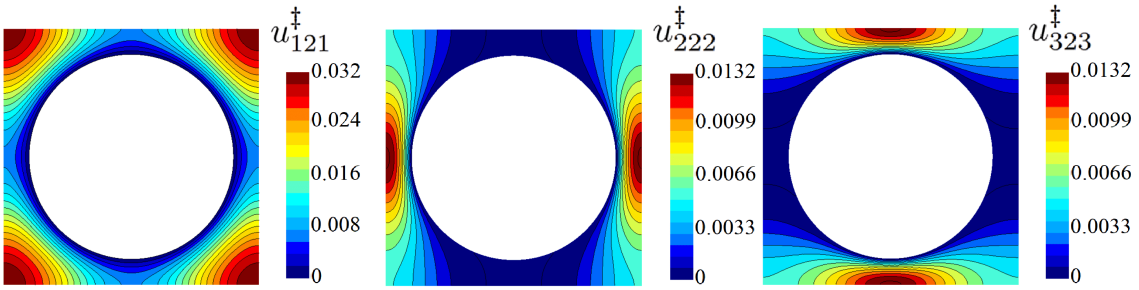

Figure 3: A fully periodic unit cell over which fields of $u^{\ddagger}_{121}$, $u^{\ddagger}_{222}$ and $u^{\ddagger}_{323}$ are shown for $\theta = 0.5$.

2.4 Formal expressions of the effective boundary conditions

The *effective* boundary conditions are

$$U|_{Y=0} = \epsilon\lambda_x S_{12}|_{Y=0} + \epsilon^2 \mathcal{K}_{xy}^{itf} \left.\frac{\partial S_{22}}{\partial X}\right|_{Y=0} + \mathcal{O}\left(\epsilon^3\right), \tag{20-a}$$

$$V|_{Y=0} = -\epsilon^2 \mathcal{K}_{xy}^{itf} \left.\frac{\partial S_{12}}{\partial X}\right|_{Y=0} - \epsilon^2 \mathcal{K}_{zy}^{itf} \left.\frac{\partial S_{32}}{\partial Z}\right|_{Y=0} + \epsilon^2 \mathcal{K}_{yy} \left.\frac{\partial S_{22}}{\partial Y}\right|_{Y=0} + \mathcal{O}\left(\epsilon^3\right), \tag{20-b}$$

$$W|_{Y=0} = \epsilon\lambda_z S_{32}|_{Y=0} + \epsilon^2 \mathcal{K}_{zy}^{itf} \left.\frac{\partial S_{22}}{\partial Z}\right|_{Y=0} + \mathcal{O}\left(\epsilon^3\right), \tag{20-c}$$

with the stresses S_{i2} defined by Eq. (8). Alternatively, the effective conditions, valid up to second order in ϵ, may be written in the following dimensional form:

$$\hat{u}|_0 \approx \hat{\lambda}_x \left.\left(\frac{\partial \hat{u}}{\partial \hat{y}} + \frac{\partial \hat{v}}{\partial \hat{x}}\right)\right|_0 + \left.\frac{\hat{\mathcal{K}}_{xy}^{itf}}{\mu} \frac{\partial}{\partial \hat{x}} \left(-\hat{p} + 2\mu \frac{\partial \hat{v}}{\partial \hat{y}}\right)\right|_0, \tag{21-a}$$

$$\hat{v}|_0 \approx \left.\frac{\hat{\mathcal{K}}_{yy}}{\mu} \frac{\partial}{\partial \hat{y}} \left(-\hat{p} + 2\mu \frac{\partial \hat{v}}{\partial \hat{y}}\right)\right|_0 - \left.\hat{\mathcal{K}}_{xy}^{itf} \frac{\partial}{\partial \hat{x}} \left(\frac{\partial \hat{u}}{\partial \hat{y}} + \frac{\partial \hat{v}}{\partial \hat{x}}\right)\right|_0 - \left.\hat{\mathcal{K}}_{zy}^{itf} \frac{\partial}{\partial \hat{z}} \left(\frac{\partial \hat{w}}{\partial \hat{y}} + \frac{\partial \hat{v}}{\partial \hat{z}}\right)\right|_0, \tag{21-b}$$

$$\hat{w}|_0 \approx \hat{\lambda}_z \left.\left(\frac{\partial \hat{w}}{\partial \hat{y}} + \frac{\partial \hat{v}}{\partial \hat{z}}\right)\right|_0 + \left.\frac{\hat{\mathcal{K}}_{zy}^{itf}}{\mu} \frac{\partial}{\partial \hat{z}} \left(-\hat{p} + 2\mu \frac{\partial \hat{v}}{\partial \hat{y}}\right)\right|_0, \tag{21-c}$$

where the dimensional model coefficients are defined by introducing the length microscale $l = \epsilon H$, as follows:

$$\hat{\lambda}_{x,\,z} = \lambda_{x,\,z}\, l, \quad \hat{\mathcal{K}}_{xy,\,zy}^{itf} = \mathcal{K}_{xy,\,zy}^{itf}\, l^2, \quad \hat{\mathcal{K}}_{yy} = \mathcal{K}_{yy}\, l^2. \tag{22}$$

2.5 The role of the porosity: parametric study

The values of the model coefficients have already been stated in (19) for the specific case of streamwise-aligned cylinders with a porosity of 0.5. However, it is practically advantageous to generate a database of these geometry-dependent parameters to cover a wide range of θ, so that the model can be directly implemented in optimization studies at a future stage. A range of $0.215 \leq \theta \leq 0.99$ is considered in the parametric analysis. The values of the upscaled coefficients have been estimated, following the numerical procedure described earlier in Section 2.3. The results are listed in Table 1, and are graphically presented in Figure 4. The minimum possible value of the porosity ($\theta = 0.215$) is related to a cylinder diameter equal to one; for this configuration, the physical interface between the channel flow and the porous substrate becomes impermeable in the wall-normal direction ($\mathcal{K}_{yy} = 0$), and the case of flow over semi-circular riblets (instead of a porous substrate) is retrieved. It can be realized from Figure 4 that all coefficients

monotonically increase with θ. It should be observed that high values of θ are not representative of typical porous media, aside from perhaps the case of sparse canopies.

Table 1: Numerical values of the macroscopic coefficients at different values of the porosity, for the case of longitudinal cylindrical inclusions.

θ	λ_x	λ_z	$\mathcal{K}_{yy} = \mathcal{K}_{zz}$	$\mathcal{K}_{xx}$	$\mathcal{K}_{xy}^{itf}$	$\mathcal{K}_{zy}^{itf}$
0.215	5.883E − 02	4.103E − 02	0	1.217E − 03	3.814E − 03	1.823E − 03
0.500	6.883E − 02	4.513E − 02	1.828E − 03	6.966E − 03	5.561E − 03	2.220E − 03
0.600	7.398E − 02	4.713E − 02	4.331E − 03	1.212E − 02	6.737E − 03	2.410E − 03
0.700	8.167E − 02	4.992E − 02	9.587E − 03	2.222E − 02	9.042E − 03	2.657E − 03
0.800	9.347E − 02	5.385E − 02	1.990E − 02	4.179E − 02	1.410E − 02	2.965E − 03
0.900	1.130E − 01	6.010E − 02	3.970E − 02	8.031E − 02	2.638E − 02	4.113E − 03
0.990	1.953E − 01	8.912E − 02	1.255E − 01	2.534E − 01	1.075E − 01	2.960E − 02

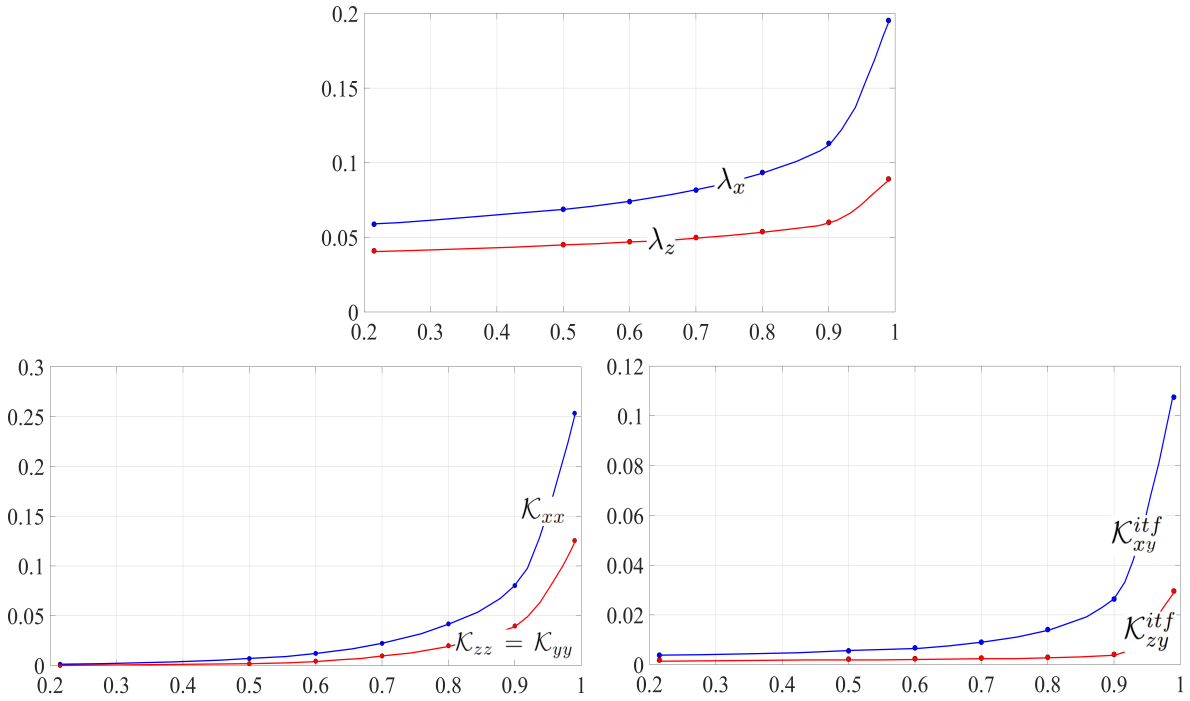

Figure 4: Variation of the model coefficients (Table 1) against porosity (θ).

3 THE MACROSCALE PROBLEM: SETUP, RESULTS AND DISCUSSION

This section is mainly dedicated to the macroscale problem concerning the turbulent channel flow over a porous substrate; the effective boundary conditions at the substrate/channel virtual interface, obtained in Section 2, are employed, with the macroscale

coefficients corresponding to different configurations of the porous bed, for detecting, comparing and analyzing the skin-friction drag increase/reduction. The direct numerical simulation of the turbulent flow through a smooth, impermeable channel is conducted first (Section 3.1). The main objectives of this preliminary step are to (i) assess the accuracy of the CFD code, (ii) confirm the adequacy of the domain size and the grid by means of extensive validation using the rich literature on smooth channel flow, and (iii) provide baseline results to which the main statistics of channel flows over permeable walls are later compared (Section 3.2).

3.1 Channel flow with smooth, impermeable walls

3.1.1 *Simulation definition and numerical schemes*

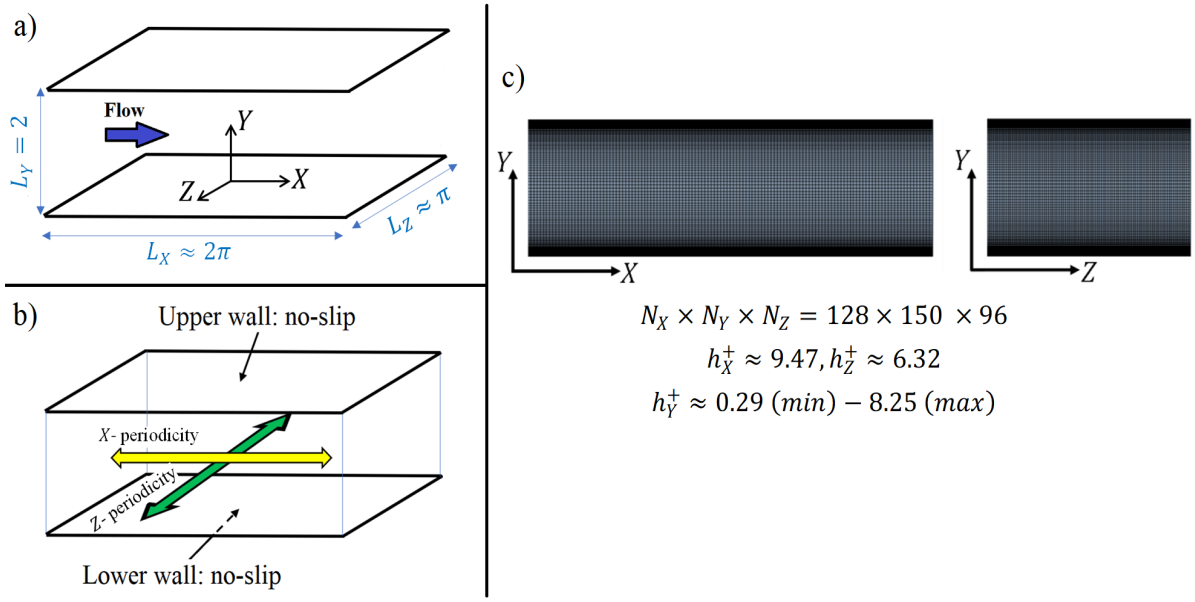

Figure 5: Simulation setup for smooth, impermeable channel case: a) dimensions of the computational domain; b) boundary conditions; c) grid structure and specifications.

The computational domain is sketched in Figure 5-a. The dimensions in the streamwise direction (L_X), the wall-normal direction (L_Y) and the spanwise direction (L_Z) are normalized with half the channel height (H); $L_Y = 2$ by definition, while the values $L_X \approx 2\pi$ and $L_Z \approx \pi$ are chosen. The no-slip/no-transpiration boundary condition are enforced at the upper and lower walls ($U = V = W = 0$). Since the flow is fully developed, periodic boundary conditions of the velocity vector and the pressure are used along the streamwise and spanwise directions (cf. Figure 5-b). The flow is forced by a uniform volumetric momentum source term in the $X-$direction, with a value $M = 1$; therefore, a wall shear stress τ_w of 1 (at lower and upper walls) is expected as the bulk balance between forces is reached. If the value of the fluid density in equation (1) is $\rho = 1$ and

the dynamic viscosity is $\mu \approx 1/190$, the shear velocity ($u_\tau = \sqrt{\tau_w/\rho}$) is equal to 1 so that the friction Reynolds number ($Re_\tau = \rho\, u_\tau\, H/\mu$) is approximately 190.

The governing equations are discretized with the finite volume method, as by the implementation of the Simcenter STAR-CCM+ multiphysics software (version 16.02.009-R8). The hybrid MUSCL 3rd-order/central-differencing scheme was employed for spatial discretization. The scheme combines boundedness and accuracy; under smooth local flow conditions, it is formulated as a linear blend between a MUSCL 3rd-order upwind scheme and a 3rd-order central-differencing scheme, with an upwind blending factor equal to 0.1. The reader is referred to (West & Caraeni, 2015) for details on the MUSCL/CD approach. A structured three-dimensional grid was generated (Figure 5-c). The mesh is uniform in streamwise and spanwise directions, where the respective spacings of the grid (in wall units) are $h_X^+ \approx 9.47$ and $h_Z^+ \approx 6.32$. The grid is gradually stretched in the wall-normal direction to obtain thinner elements near the walls ($h_Y^+ \approx 0.29$) and thicker near the centerline ($h_Y^+ \approx 8.25$). A second-order implicit scheme was used for temporal discretization. To maintain the maximum Courant number below 1, a time step of 0.0015 was applied (the time scale is $\dfrac{H}{u_\tau}$). The SIMPLE algorithm was used for pressure-velocity coupling.

Two critical points should be highlighted. First, the size of the computational domain is, in general, smaller than that used in some previous numerical studies. For instance, the dimensions $L_X = 4\pi$ and $L_Z = \frac{4}{3}\pi$ were chosen in (Vreman & Kuerten, 2014), while the dimensions $L_X = 4\pi$ and $L_Z = 2\pi$ were used in (Kim *et al.*, 1987), compared to $L_X = 2\pi$ and $L_Z = \pi$ in the present study. Second, the finite volume method used in this work is not the standard discretization approach followed in the literature dealing with the direct simulation of turbulent channel flow. The majority of previous studies adopted either a fully-spectral Fourier-Chebyshev spatial discretization method (Kim *et al.*, 1987; Moser *et al.*, 1999; Vreman & Kuerten, 2014) or a staggered high-order finite difference method (Abe *et al.*, 2001; Kozuka *et al.*, 2009; Vreman & Kuerten, 2014). The points above indicate that a comprehensive validation of the present setup is recommended.

3.1.2 *Results and validation*

First, the simulation was run for about 130 time units to establish the turbulence perturbations and go beyond the initial transient of the flow field. The statistics were then averaged over almost 35 time units. The main convergence criterion is the bulk velocity $\overline{U}_b$, that is, the volume-averaged mean streamwise velocity over the channel (normalized by u_τ). The bulk velocity $\overline{U}_b$ eventually converged to a value of 15.688 (meaning that the bulk Reynolds number is $Re \approx 2981$), compared to $\overline{U}_b = 15.70$ in (Vreman & Kuerten, 2014) and $\overline{U}_b = 15.73$ in (Abe *et al.*, 2001). The corresponding values of the skin-friction drag coefficient (C_f), based on $\overline{U}_b$, are: 0.00813 (present), 0.00811 (Vreman & Kuerten, 2014), and 0.00808 (Abe *et al.*, 2001). The statistics given below at any distance Y from the wall have been evaluated via spatial averaging over the corresponding $X - Z$ plane.

- Mean velocity profile:

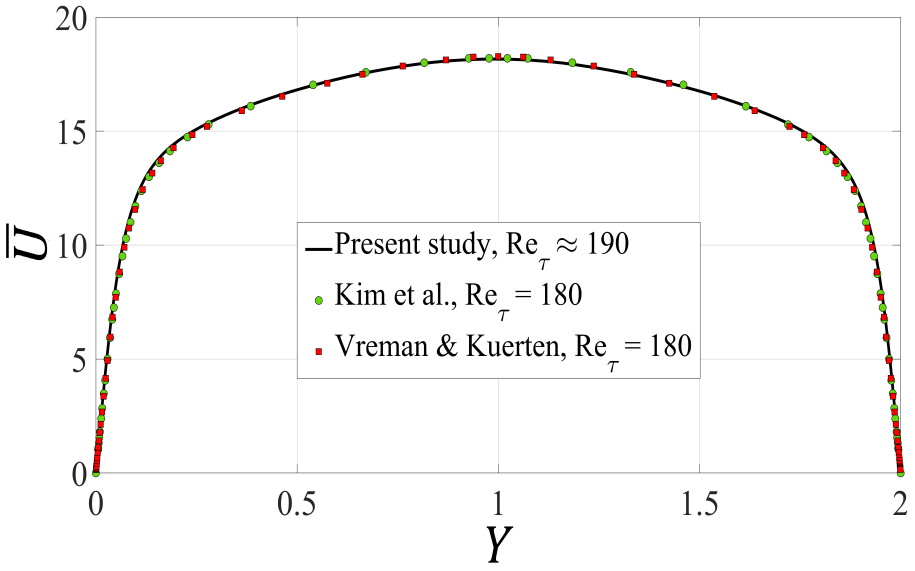

Figure 6: Mean velocity profile in global coordinates for the smooth channel case.

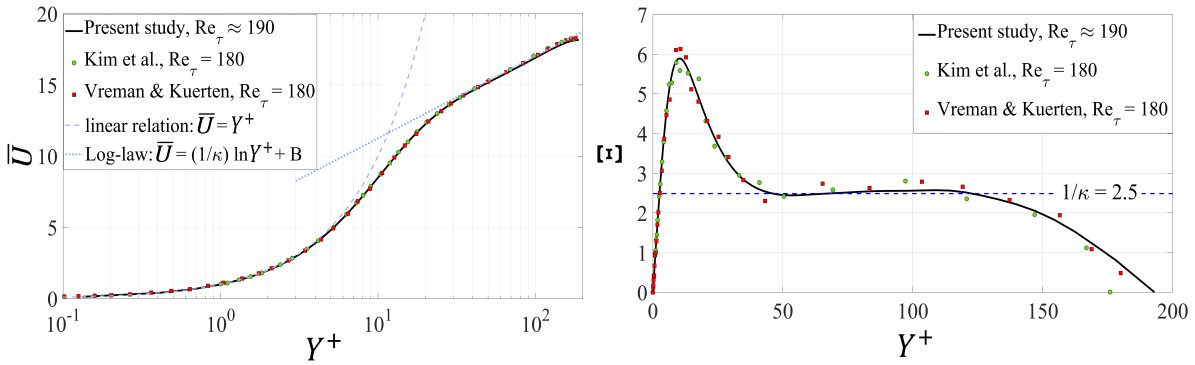

Figure 7: Behavior of the mean streamwise velocity, $\overline{U}$, in different regions of the turbulent boundary layer: (left) mean velocity profile in wall coordinates; (right) the log-law diagnose function, Ξ. Results are only displayed over the lower half of the smooth channel.

The distribution of the mean streamwise velocity ($\overline{U}$) is displayed in Figure 6 as a function of the normal distance (Y) from the lower wall. It is clear that the present numerical results for $\overline{U}$ agree well with the reference results by Vreman & Kuerten (2014) and Kim *et al.* (1987). For instance, the value of the centerline velocity $\overline{U}_c$ is equal to 18.3, compared to approximately 18.28 in (Vreman & Kuerten, 2014) and 18.18 in (Kim *et al.*, 1987). The velocity profile is plotted in wall coordinates in Figure 7-left; $Y^+ = Y\,Re_\tau$. The behavior fits well with the linear relation $\overline{U} = Y^+$ in the viscous sublayer (up to $Y^+ \approx 5$), while the log law, $\overline{U} = (1/\kappa)\,lnY^+ + B$, is satisfied for $Y^+ \gtrapprox 40$. Here, the von Kármán constant (κ) is 0.4, while a value of 5.5 was chosen for the intercept of

the logarithmic profile (B) to take into account the low Reynolds number effect (Kim *et al.*, 1987). The behavior of the log-law diagnose function, defined as $\Xi = Y^+ \dfrac{\partial \overline{U}}{\partial Y^+}$, is shown in Figure 7-right. The constancy of Ξ indicates, by definition, a typical logarithmic behavior of $\overline{U}$, where the constant value $\Xi \approx 2.5$ corresponds to the coefficient $1/\kappa$. It is clear that the upper validity limit of the log-law is $Y^+ \approx 125$.

- Turbulence statistics:

It is useful for both validation and physical interpretation purposes to analyze the primary fluctuations (U', V', W'), representing the instantaneous deviations of the velocity components from their time-averaged values; for example, $U' = U - \overline{U}$. The intensity of the fluctuations can be described by the root-mean-square (rms) values $(U_{rms}, V_{rms}, W_{rms})$, where $U_{rms} = \overline{U'U'}^{1/2}$, for example. Another measure is the intensity of the fluctuations $(I_u = \dfrac{U_{rms}}{\overline{U}}, I_v = \dfrac{V_{rms}}{\overline{U}}, I_w = \dfrac{W_{rms}}{\overline{U}})$. The behaviors of both estimates (rms, I) are show in wall coordinates in Figure 8, together with reference data from (Vreman & Kuerten, 2014; Kim *et al.*, 1987); the accuracy of the present results is confirmed.

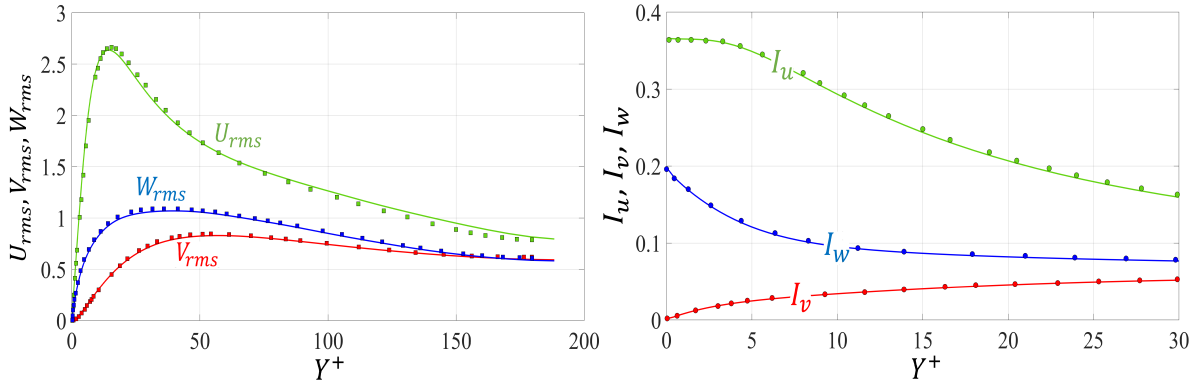

Figure 8: Estimates of the primary fluctuations for the smooth channel case: (left) root-mean-squares of the turbulent fluctuations in velocity components; (right) turbulence intensities. The reference results of the rms fluctuations by Vreman & Kuerten (2014) (square markers) and the values of the turbulence intensities by Kim *et al.* (1987) (filled circles) are also plotted for comparison.

The turbulent kinetic energy (TKE) is defined as $k = \dfrac{1}{2}(\overline{U'U'} + \overline{V'V'} + \overline{W'W'})$. The dissipation terms in the transport equations of $\overline{U'U'}, \overline{V'V'}, \overline{W'W'}$ are plotted in wall coordinates in Figure 9-left. They are defined, in dimensionless forms, as follows:

$$(\epsilon_u, \epsilon_v, \epsilon_w) = \frac{2}{Re_\tau^2}\left(\overline{|\nabla U'|^2}, \overline{|\nabla V'|^2}, \overline{|\nabla W'|^2}\right), \tag{23}$$

with the gradients of the primary fluctuations calculated using the dimensionless space variables (X, Y, Z). The total dissipation and production rates of TKE are approximately balanced within the log-law region, as can be realized from Figure 9-right. They are defined in dimensionless forms as:

$$\epsilon_T = \frac{1}{2}(\epsilon_u + \epsilon_v + \epsilon_w), \tag{24-a}$$

$$P_T = -\frac{1}{Re_\tau}\,\overline{U_i' U_j'}\,\frac{\partial \overline{U_i}}{\partial X_j}. \tag{24-b}$$

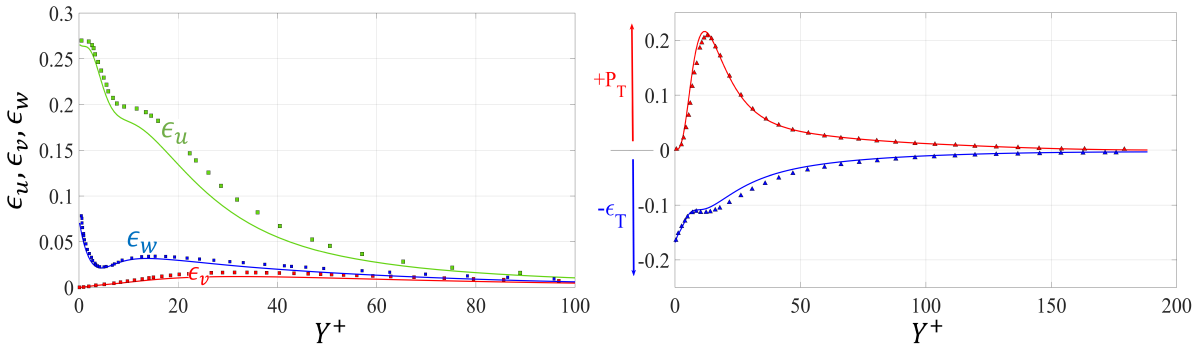

Figure 9: Components of turbulent dissipation (left) and production and dissipation rates of TKE (right). Present trends are plotted with solid lines. Reference results by Vreman & Kuerten (2014) and by Mansour *et al.* (1988) are used for validation in the left and right frames, respectively.

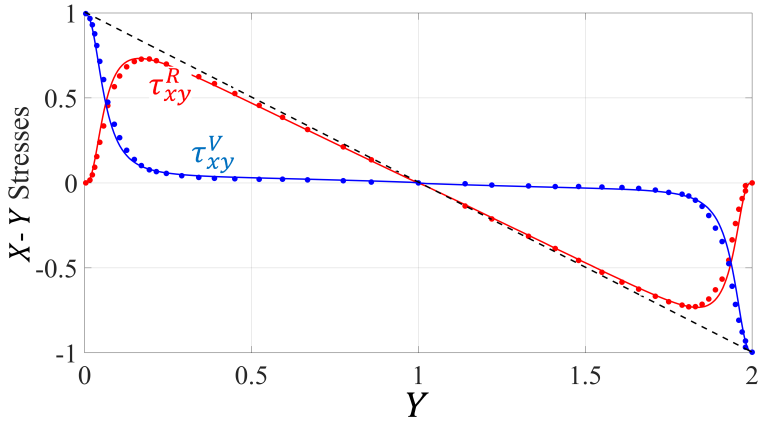

Figure 10: Distributions of $X - Y$ shear stresses over the full height of the smooth channel: (blue) viscous stress; (red) Reynolds stress; (black) total stress. The present results are shown with solid/dashed lines, while reference results by Kim *et al.* (1987) are plotted with filled circles.

One of the observables most focused upon in wall turbulence is the Reynolds stress tensor, $\boldsymbol{\tau}^{\boldsymbol{R}}$, and in particular the component τ^R_{xy} is the most relevant to skin-friction

drag. The total stress is defined as the sum of viscous and Reynolds stresses, that is, $\tau_{xy} = \tau^V_{xy} + \tau^R_{xy}$. With ρu_τ^2 as scale, the dimensionless stresses are given by $\tau^V_{xy} = \dfrac{1}{Re_\tau}\dfrac{\partial \overline{U}}{\partial Y}$ and $\tau^R_{xy} = -\overline{U'V'}$. The good agreement between the present results and those by Kim (1983), shown in Figure 10, further attests to the validity of the finite volume model employed here, and the suitability of the numerical setup.

3.2 Turbulent flow over porous substrates

3.2.1 *Basic definitions and implementation of the effective conditions*

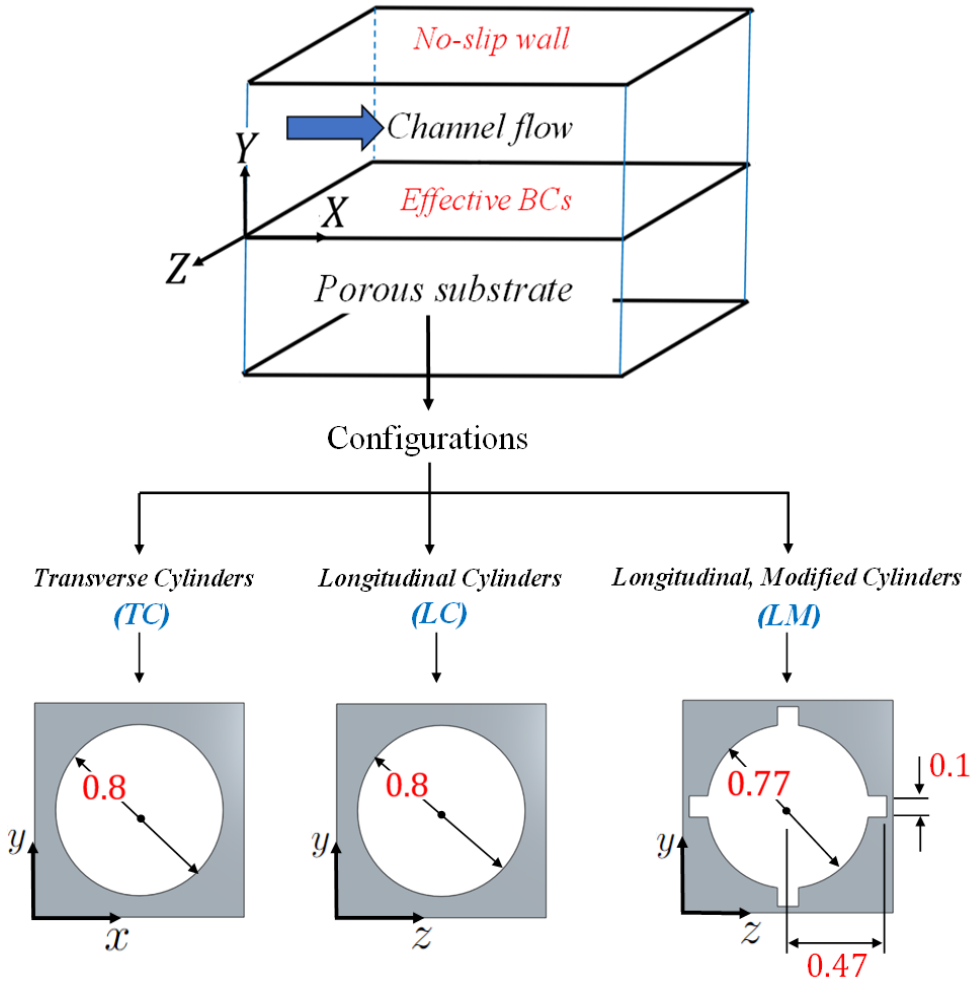

Figure 11: Sketch of the macroscale problems. The computational domain is displayed in the top panel, with the effective velocity boundary conditions imposed at the plane $Y = 0$. The usage of the effective conditions permits to not solve for the flow in the porous substrate. In the bottom frame, the configurations of the porous media under study are indicated, with the dimensions shown on a 1×1 unit cell. The dimensions of the inclusions yield a porosity $\theta = 0.5$.

The turbulent channel flow over porous substrates of different microstructures is macroscopically analyzed in this section, with the aid of the homogenization model described in Section 2. The numerical procedure, including the spatial and the temporal discretization schemes and the $X-$momentum forcing term, is identical to the setup of the smooth channel case, described in Section 3.1.1. The only modification is that the lower boundary (at $Y = 0$) now mimics a slip, permeable wall. This can be done by implementing the effective boundary conditions for the three velocity components given in equations (20-a) to (20-c), with model coefficients corresponding to the specific topology and orientation of the solid inclusions sketched in Figure 11. Focus is on the evaluation and the further interpretation of the favorable/adverse changes in the skin-friction drag, related to the presence of different anisotropic permeable substrates. It is important to highlight that the geometries of the inclusions described in Figure 11 are intentionally chosen to meet this objective. The inclusions considered are: (i) transverse, Z-aligned, cylinders (configuration: TC); (ii) longitudinal, X-aligned, cylinders (configuration: LC); (iii) longitudinal cylindrical elements modified with four longitudinal protrusions in the shape of parallelepipeds, equally-spaced along the circumference (configuration: LM). The dimensions of the solid inclusion within the unit cell are chosen to yield the same porosity, $\theta = 0.5$. The model coefficients for substrate LC have been estimated earlier; they are given in (19). The coefficients for the case of spanwise-aligned cylinders (TC) are directly available from the LC case, by simply switching the streamwise and spanwise coordinates, i.e.

$$\lambda_x = 0.04513, \quad \lambda_z = 0.06883, \quad \mathcal{K}_{xy}^{itf} = 0.002220, \quad \mathcal{K}_{zy}^{itf} = 0.005561, \\ \mathcal{K}_{xx} = 0.001828, \quad \mathcal{K}_{yy} = 0.001828, \quad \mathcal{K}_{zz} = 0.006966. \tag{25}$$

Conversely, configuration LM requires the numerical solution of the *ad hoc* problems given in Section 2.2 for this specific geometry: the dimensionless upscaled coefficients are found to be

$$\lambda_x = 0.1130, \quad \lambda_z = 0.0590, \quad \mathcal{K}_{xy}^{itf} = 0.01213, \quad \mathcal{K}_{zy}^{itf} = 0.00411, \\ \mathcal{K}_{xx} = 0.00762, \quad \mathcal{K}_{yy} = 0.000121, \quad \mathcal{K}_{zz} = 0.000121. \tag{26}$$

It should be noted that by modifying the longitudinal geometry with the addition of four thin fins we have been able to increase the difference between λ_x and λ_z; in light of literature results (presented in Section 1) this is expected to improve the drag-reducing effect of the porous layer.

The last parameter which needs to be set is $\epsilon = l/H$. Two values were tested: (i) $\epsilon = 0.05$, with the substrates indicated as TC_5, LC_5, LM_5; (ii) $\epsilon = 0.10$, with the substrates denoted by $TC_{10}, LC_{10}, LM_{10}$. For later discussion, it is also useful to define the model coefficients in wall units, with the slip coefficients (λ) multiplied by (ϵRe_τ) and the permeabilities ($\mathcal{K}^{inf}, \mathcal{K}$) multiplied by $(\epsilon Re_\tau)^2$; the numerical values of these parameters are given in Table 2, for all the substrates defined.

Table 2: Values of the macroscopic coefficients for the different configurations of the porous substrate, given in wall units with $Re_\tau \approx 190$.

Macroscopic parameters	Configurations					
	TC_5	LC_5	LM_5	TC_{10}	LC_{10}	LM_{10}
λ_x^+	0.4287	0.6539	1.0735	0.8574	1.3078	2.1470
λ_z^+	0.6539	0.4287	0.5605	1.3078	0.8574	1.1210
$\mathcal{K}_{xy}^{inf,+}$	0.2004	0.5018	1.0947	0.8016	2.0072	4.3788
$\mathcal{K}_{zy}^{inf,+}$	0.5018	0.2004	0.3709	2.0072	0.8016	1.4836
$\mathcal{K}_{xx}^{+}$	0.1650	0.6287	0.6877	0.6600	2.5148	2.7508
$\mathcal{K}_{yy}^{+}$	0.1650	0.1650	0.0109	0.6600	0.6600	0.0436
$\mathcal{K}_{zz}^{+}$	0.6287	0.1650	0.0109	2.5148	0.6600	0.0436

Numerically enforcing the effective boundary conditions (20-a)-(20-c) is a delicate task for several reasons. First, the pressure-gradient term $\left.\dfrac{\partial P}{\partial X}\right|_{Y=0}$, present at second order in ϵ in the definition of the streamwise slip velocity, may be decomposed into a mean term and a fluctuating part. The mean pressure gradient $\left.\dfrac{\partial \overline{P}}{\partial X}\right|_{Y=0}$ corresponds to the $X-$momentum volumetric source term ($M = 1$) which forces fluid motion through the channel. Second, imposing a wall-normal, transpiration, velocity component may induce numerical instabilities, associated with an imbalance between blowing and suction at the $Y = 0$ dividing surface. Hence, it is useful to define an *ad hoc* function, as part of the numerical code, to impose that the surface-averaged transpiration velocity at $Y = 0$ vanishes at each time step. Furthermore, we have found it to be advantageous to seek an explicit expression of the transpiration-velocity condition (equation (20-b), by writing

$$\left.\frac{\partial S_{12}}{\partial X}\right|_{Y=0} = \frac{1}{\epsilon\lambda_x}\left.\frac{\partial U}{\partial X}\right|_{Y=0} + \mathcal{O}(\epsilon), \qquad \left.\frac{\partial S_{32}}{\partial Z}\right|_{Y=0} = \frac{1}{\epsilon\lambda_z}\left.\frac{\partial W}{\partial Z}\right|_{Y=0} + \mathcal{O}(\epsilon). \tag{27}$$

The expressions above are immediately available from equations (20-a) and (20-c). Finally, mass conservation can be used to replace $\left(\dfrac{\partial V}{\partial Y}\right)$ by $\left(-\dfrac{\partial U}{\partial X} - \dfrac{\partial W}{\partial Z}\right)$ in the definition of the outer-stress component S_{22} in Eq. (20-b).

3.2.2 *Results for* $\epsilon = 0.05$

Detailed results for the substrates TC_5, LC_5 and LM_5 are considered here; they will provide insight into the main parameters which control skin-friction drag.

The quantities which we intend to discuss in detail are first defined and summarized here. The flow under study is bounded by a lower permeable wall (at $Y = 0$) and an

upper smooth wall (at $Y = 2$); hence, two different values of the total shear stress may be defined, i.e., τ_0 and τ_2, respectively. The ratio between the two stresses is $S_R = \frac{\tau_0}{\tau_2}$. The total shear stresses at the walls are linked to the $X-$momentum source term, M, on account of the balance of forces in the $X-$direction; that is, $\tau_0 + \tau_2 = 2\,M$. Here, a major parameter in the following discussions is defined, the source-term-based stress: $\tau_M = M = \frac{\tau_0 + \tau_2}{2}$. In the present case it is $\tau_M = 1$ for all simulations and the friction Reynolds number, based on τ_M, is equal to 190, as in the smooth channel case.

The drag coefficient is also based on τ_M and the bulk velocity $\overline{U}_b$, as follows:

$$C_f = \frac{2\,\tau_M}{\rho\,\overline{U}_b^2}. \tag{28}$$

The percentage deviation of the drag coefficient from the reference value of the smooth channel is defined as:

$$\Delta C_f\% = \frac{C_{f,porous} - C_{f,\,smooth}}{C_{f,\,smooth}} \times 100(\%), \tag{29}$$

with a negative value of $\Delta C_f\%$ which indicates drag reduction (implying an increase in the flow rate), and vice versa when $\Delta C_f\%$ is positive.

The numerical values of S_R and $\Delta C_f\%$, for the different configurations, are presented in Table 3. The results show that drag reduction is achieved by the configurations LC_5 and LM_5, which are characterized by preferential orientation of the solid inclusions in the streamwise direction, with $\mathcal{K}_{xx}^{+} > \mathcal{K}_{zz}^{+}$, $\lambda_x^{+} > \lambda_z^{+}$ and $\mathcal{K}_{xy}^{inf,+} > \mathcal{K}_{zy}^{inf,+}$ (cf. Table 2). This concept is well established in the literature of drag reduction by small surface manipulations (Gómez-de Segura & García-Mayoral, 2019; Gómez-de Segura *et al.*, 2018; Abderrahaman-Elena & García-Mayoral, 2017), in particular for porous substrates wall-normal permeability $\mathcal{K}_{yy}^{+}$ too small to initiate a Kelvin-Helmholtz instability in the turbulent boundary layer. The drag reduction is more pronounced for the substrate LM_5, a fact probably correlated to the accrued difference between λ_x^{+} and λ_z^{+}, as anticipated. It is also clear that drag reduction is associated with values of S_R lower than 1, which means that the total shear stress at the permeable wall ($Y = 0$) is smaller than its value at the upper smooth surface.

Table 3: Values of the total shear stress ratio between the lower and the upper walls ($S_R = \frac{\tau_0}{\tau_2}$) and of the percentage change in the skin-friction drag coefficient ($\Delta C_f\%$).

Quantities	Configurations			
	Smooth	TC_5	LC_5	LM_5
S_R	1	1.036	0.976	0.961
$\Delta C_f\%$	0	+2.423%	-2.157%	-3.681%

A summary of interfacial and peak values of a few observables is provided in Table 4 for all configurations considered so far. These results will be later referred to while discussing and comparing the behaviors of the different flow cases.

Table 4: Interfacial and peak values of the mean velocity and of turbulence-characterizing parameters for different configurations of the porous medium ($\theta = 0.5$ and $\epsilon = 0.05$). The peak values are those closer to the permeable surface. For reference, also the results for a smooth channel are given.

Quantity	Interfacial values ($Y = 0$)				Peak values			
	Smooth	TC_5	LC_5	LM_5	Smooth	TC_5	LC_5	LM_5
$\overline{U}$	0	0.4439	0.6605	1.0719	18.164	17.959	18.397	18.446
U_{rms}	0	0.1829	0.2388	0.3643	2.6359	2.6377	2.6102	2.5668
V_{rms}	0	0.0135	0.0078	0.0082	0.8292	0.8427	0.8184	0.8097
W_{rms}	0	0.1462	0.0876	0.1152	1.0692	1.0879	1.0529	1.0598
τ^R_{xy}	0	0.00081	0.00046	0.00064	0.7231	0.7521	0.7069	0.7023
I_u	0.3660	0.4120	0.3615	0.3399	0.3660	0.4120	0.3615	0.3399
I_w	0.2000	0.3293	0.1326	0.1075	0.2000	0.3293	0.1485	0.1297
ϵ_T	0.1680	0.2055	0.1567	0.1393	0.1680	0.2055	0.1567	0.1393

- Mean velocity profiles

The profiles of the mean streamwise velocity ($\overline{U}$) across the channel are displayed in Figure 12. The behavior of the slip velocity at the fictitious $Y = 0$ wall is highlighted in the lower frame of the figure, and compared to the solution obtained by enforcing no-slip conditions at both surfaces. A preliminary estimation of the value of the slip velocity can be obtained from the first-order term in the effective boundary condition of U, equation (20-a), which may be recast in terms of the mean velocity ($\overline{U}$) and the wall distance in viscous units (Y^+) as follows:

$$\overline{U}\big|_{Y=0} \approx \lambda_x^+ \left.\frac{\partial \overline{U}}{\partial Y^+}\right|_{Y=0}. \tag{30}$$

With the velocity gradient $\left.\dfrac{\partial \overline{U}}{\partial Y^+}\right|_{Y=0}$ equal to 1, Eq. (30) simplifies to a Dirichlet boundary condition, i.e.

$$\overline{U}\big|_{Y=0} \approx \lambda_x^+. \tag{31}$$

A comparison between the interfacial values of $\overline{U}$, in Table 4, and the corresponding values of λ_x^+, in Table 2, confirms the approximate result of equation (31), with minor deviations which can be attributed to second-order terms and to the fact that the shear velocity used as scale is calculated based on the momentum source term (M) and not on τ_0 (cf. Section 3.2.2).

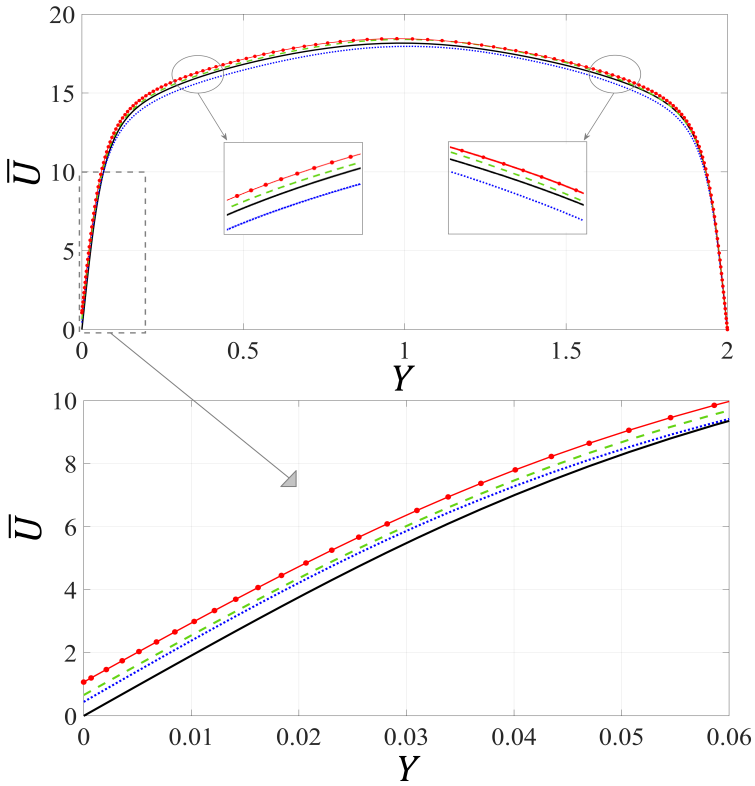

Figure 12: Mean streamwise velocity profiles plotted from the virtual interface between the channel flow and the porous bed ($Y = 0$) to the upper no-slip wall ($Y = 2$). The cases shown are: (solid black line) smooth channel; (dotted blue line) substrate TC_5; (dashed green line) substrate LC_5; (red line with markers) substrate LM_5.

The mean velocity profiles are plotted in wall coordinates in Figure 13, up to the centerline of the channel ($Y^+ = Re_\tau \approx 193$). A better vision of the boundary layer characteristics through the logarithmic region is available. The behavior of the velocity profiles follows the classical theory of near-wall turbulence, according to which the surface alterations only affect the intercept of the logarithmic profile, while the von Kármán constant ($\kappa \approx 0.4$) remains constant (Clauser, 1956; Abderrahaman-Elena & García-Mayoral, 2017). Hence, a general expression of the velocity distribution in the log-law region may be written as follows:

$$\overline{U} = \frac{1}{\kappa} lnY^+ + B + \Delta\overline{U}, \tag{32}$$

with B the intercept in the case of a smooth wall, and $\Delta\overline{U}$ the shift of the velocity profile from the corresponding smooth channel behavior. The variations in $\Delta\overline{U}$ across the boundary layers over different substrates are shown in the right frame of Figure 13. As expected, the logarithmic regions ($30 \leq Y^+ \leq 120$) are characterized by approximately constant values of $\Delta\overline{U}$ (corresponding to parallel profiles of $\overline{U}$); which can be directly linked to the deviations of the skin-friction drag coefficients from the smooth channel case; a positive value of $\Delta\overline{U}$ implies drag reduction (as for substrates LC_5 and LM_5), and vice versa for substrate TC_5.

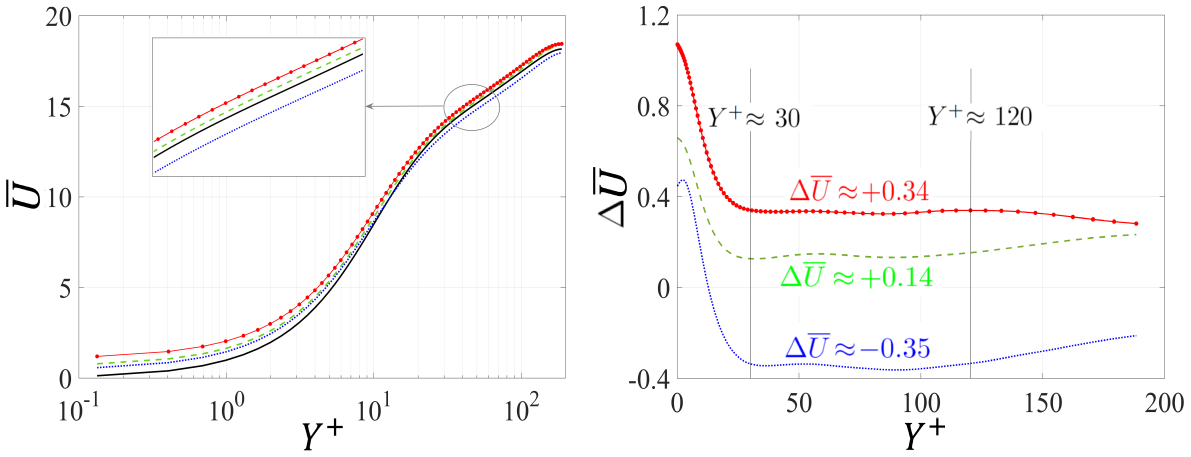

Figure 13: Mean velocity profiles next to the permeable walls: (left) velocity profiles in wall coordinates up to the centerline of the channel; (right) deviations of the mean velocity profiles over different substrates, from the corresponding smooth channel profile. The symbols are identical to those used in Figure 12.

- Turbulence statistics

A better understanding of the drag reduction mechanism is sought by the analysis of turbulence statistics near the permeable walls. The definitions of all the parameters under consideration here are the same as in Section 3.1.2.

The root-mean-squares of the velocity fluctuations are plotted in Figure 14 near the different permeable walls. A wall-normal range $0 \leq Y^+ \leq 75$ is used to display the distributions of U_{rms}, V_{rms} and W_{rms}, where significant features and deviations from the no-slip case are highlighted. In particular, the values of the rms fluctuations at the interface with the porous substrates deviate from zero, as quantified in Table 4, owing to the slip/transpiration boundary in $Y = 0$. The interfacial values of U_{rms} and W_{rms} appear to be directly correlated to λ_x^+ and λ_z^+, respectively (compare the corresponding values in Tables 4 and 2). Proceeding towards the logarithmic region, the deviation of U_{rms}, V_{rms} and W_{rms} from the smooth channel behavior yields some insight onto the ability of the substrates LC_5 and LM_5 to attenuate turbulence in the near-wall layer. This might explain the drag reduction caused by these longitudinal configurations, in comparison to the adverse effect of the spanwise-aligned inclusions, substrate TC_5. This can be confirmed by comparing the values of the percentage changes in skin-friction drag (Table 3) and the peak values of the rms velocity fluctuations (Table 4). The preceding concept applies also to the distributions of the Reynolds shear stress τ_{xy}^R; cf. Figure 15. An increase of the peak value of τ_{xy}^R by about 4% is realized for the substrate TC_5; this implies destabilization of the turbulent boundary layer overlying the transverse cylinders, which adversely affects skin-friction drag. Conversely, the production of Reynolds stresses in the logarithmic region is slightly mitigated by the configurations LC_5 and LM_5. It should be noted that the values of the Reynolds shear stress at the permeable walls (cf.

Table 4) are too small to be graphically captured; this may be ascribed to the low values of the wall-normal permeability, $\mathcal{K}_{yy}^{+}$.

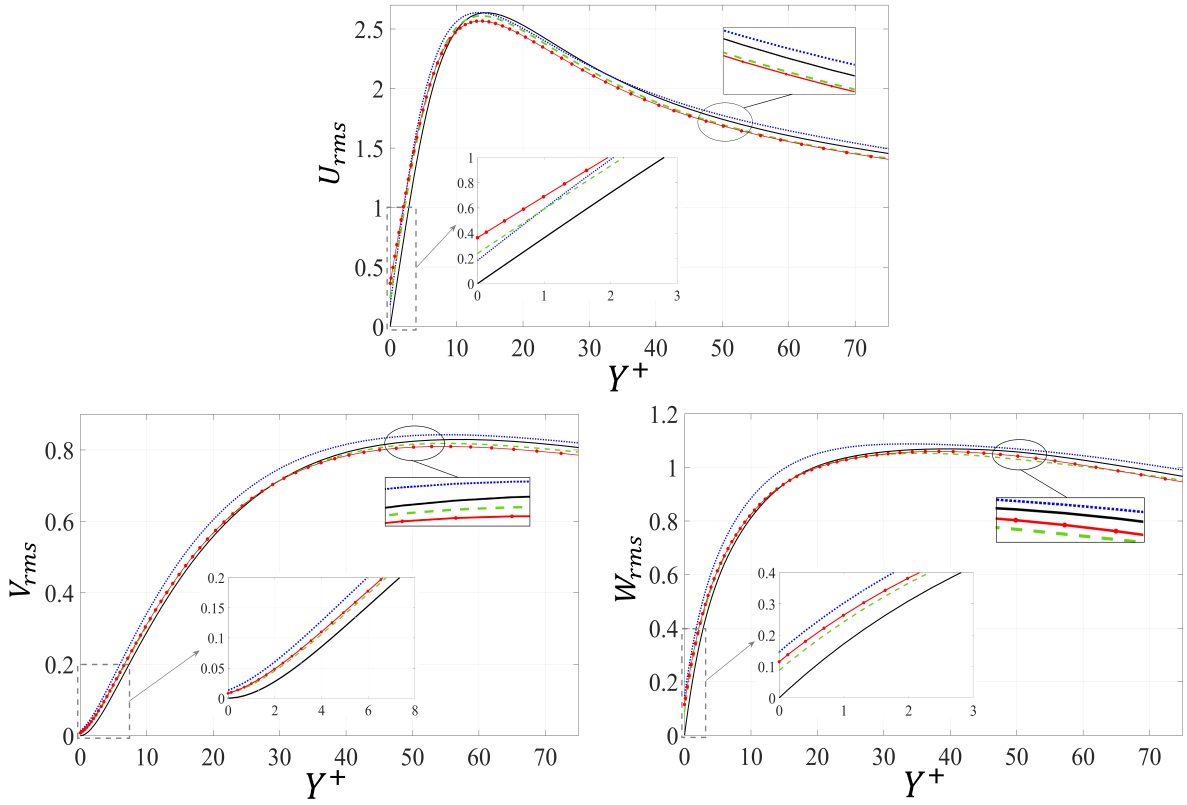

Figure 14: Root-mean-squares of the primary fluctuations over different permeable walls. Close-ups of the profiles in the neighborhood of the permeable wall and in the logarithmic layer are provided. The cases shown are: (solid black line) smooth channel; (dotted blue line) substrate TC_5; (dashed green line) substrate LC_5; (red line with markers) substrate LM_5.

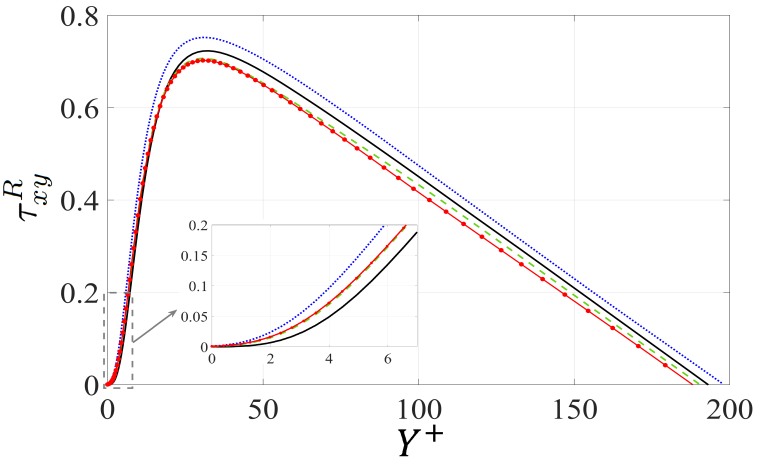

Figure 15: Distribution of the Reynolds stress, τ_{xy}^{R}, next to different permeable walls, plotted up to the centerline of the channel using the same symbols as in Figure 14.

The distributions of the turbulence intensities I_u and I_w are shown in Figure 16 in the neighborhood of the permeable walls, i.e. up to $Y^+ \approx 9$. Interestingly, the behaviors of these quantities, even at the permeable wall and within the adjacent viscous sublayer, are strongly linked to the corresponding changes in the skin-friction drag. The same concept applies to the turbulence dissipation (ϵ_T), displayed in Figure 17. For instance, the drag increase in the case of the substrate TC_5 is associated with increase in the interfacial values (at $Y = 0$) of I_u, I_w and ϵ_T by about 13%, 60% and 40%, respectively, whereas these parameters decrease by about 7%, 45% and 17% for the substrate LM_5. This should be compared to the rms of the velocity fluctuations, which proved to be representative of changes in the skin-friction drag coefficient only in the log-law region.

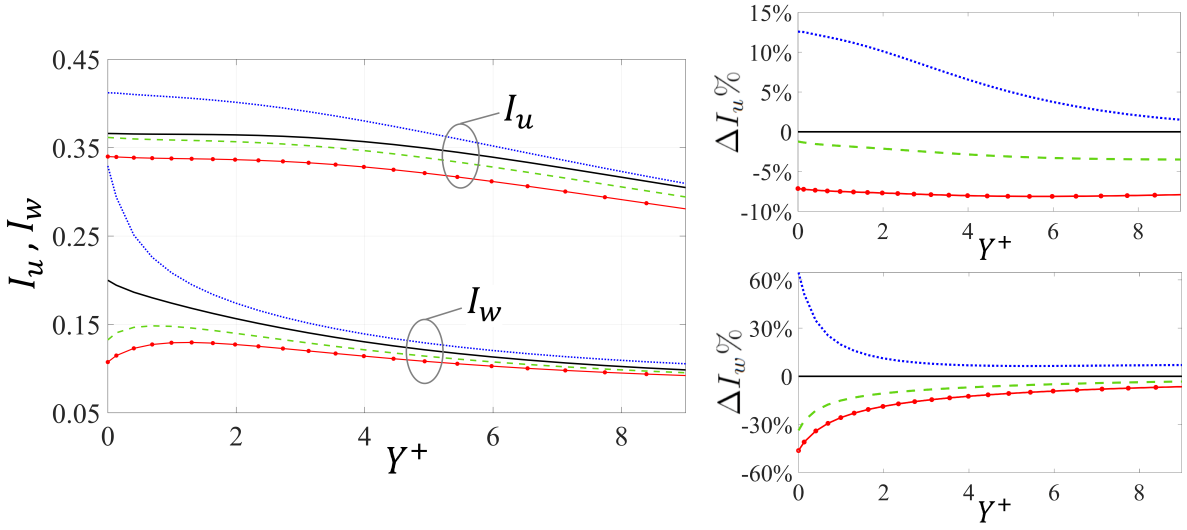

Figure 16: Turbulence intensities (I_u and I_w) near the permeable walls. In the right frames, the percentage deviations of the intensities from the reference smooth channel values are displayed. Symbols are identical to those in Figure 14.

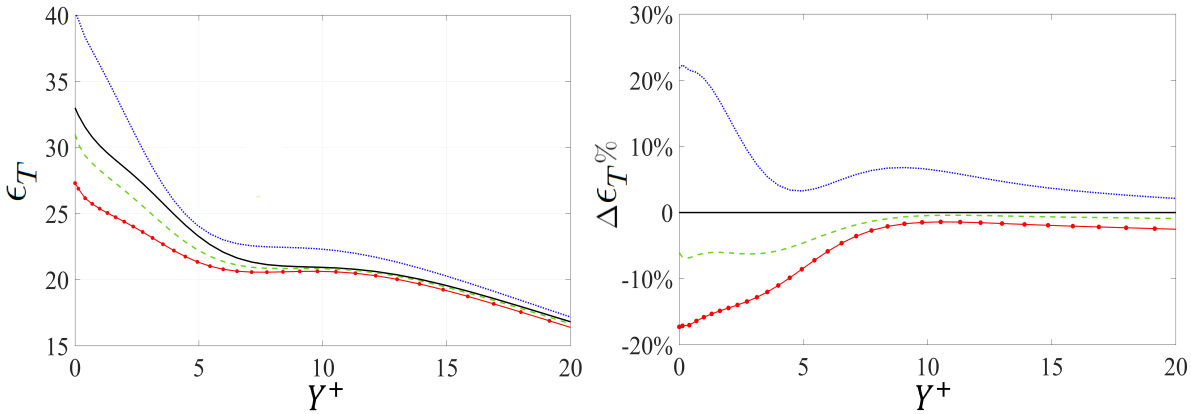

Figure 17: Distributions of the turbulent dissipation near the permeable wall for different configurations of the porous substrate, with the percentage deviations from the reference smooth surface case displayed in the right frame. Refer to Figure 14 for the definition of the symbols used.

3.2.3 *Results for* $\epsilon = 0.1$

The turbulent channel flow ($Re_\tau \approx 190$) over permeable walls of periodicity (ϵ) equal to 0.1 is analyzed in this section; the porous substrates TC_{10} and LM_{10} are specifically considered. In principle, by increasing the value of ϵ (with respect to the case $\epsilon = 0.05$ examined in Section 3.2.2), the differences between the slip lengths λ_x^+ and λ_z^+ are more significant (cf. Table 2), and the adverse/favorable changes in the skin-friction drag coefficient are expected to be more pronounced. This concept is confirmed by the homogenization-based numerical results of the percentage change in the drag coefficient ($\Delta C_f\%$), presented in Table 5. As can be realized, the substrate LM_{10}, with $\lambda_x^+ > \lambda_z^+$, allows for approximately 5% reduction in the skin-friction coefficient, whereas the drag coefficient increases by almost 9% in the case of the substrate TC_{10}, for which $\lambda_z^+ > \lambda_x^+$. The preceding values should be compared to a reduction by 3.68% and an increase by 2.42% with the substrates LM_5 and TC_5, respectively. It is clear that the increase in the skin-friction drag coefficient with substrate TC_{10} is associated to a significant increase in the shear stress ratio (S_R), in the sense that the total shear stress at the lower permeable wall (τ_0) is much larger than its value at the upper smooth wall (τ_2).

Table 5: Values of the total shear stress ratio between the lower and the upper walls ($S_R = \frac{\tau_0}{\tau_2}$) and the percentage change in the skin-friction drag coefficient ($\Delta C_f\%$), with the porous substrates characterized by $\epsilon = 0.1$.

Quantities	Configurations		
	Smooth	TC_{10}	LM_{10}
S_R	1	1.150	0.953
$\Delta C_f\%$	0	+8.976%	-4.934%

Table 6: Interfacial and peak values of the mean velocity and different turbulence-characterizing parameters, for two different configurations of the porous medium (with $\epsilon = 0.1$).

Quantity	Interfacial values ($Y = 0$)			Peak values		
	Smooth	TC_{10}	LM_{10}	Smooth	TC_{10}	LM_{10}
$\overline{U}$	0	0.9404	2.1573	18.164	17.5436	18.5930
U_{rms}	0	0.4615	0.7129	2.6359	2.6106	2.5090
V_{rms}	0	0.0589	0.0360	0.8292	0.8842	0.8044
W_{rms}	0	0.3563	0.2667	1.0692	1.1615	1.0688
τ_{xy}^R	0	0.0108	0.0053	0.7231	0.7960	0.7053
I_u	0.3660	0.4900	0.3303	0.3660	0.4900	0.3303
I_w	0.2000	0.3691	0.1238	0.2000	0.3691	0.1287
ϵ_T	0.1680	0.3168	0.1493	0.1680	0.3168	0.1493

The interfacial and the peak values of different quantities of interest over the substrates TC_{10} and LM_{10} are summarised in Table 6; they may be compared to the values of the same quantities with $\epsilon = 0.05$, given in Table 4. The correspondence between the values of the mean streamwise velocity ($\overline{U}$) at the interface ($Y = 0$) and the values of λ_x^+, given in Table 2, are still in line with the approximate relation (31), taking into account that, due to the increase in ϵ, the second-order terms in the effective boundary condition for U are now more pronounced. The effect of the $\mathcal{O}(\epsilon^2)$ terms is more apparent in the fluctuations of the transpiration velocity which is, by definition, a second-order effective boundary condition (cf. Eq. (20-b)); the values of V_{rms}, given in Table 6, are more than four times the corresponding values found at $\epsilon = 0.05$.

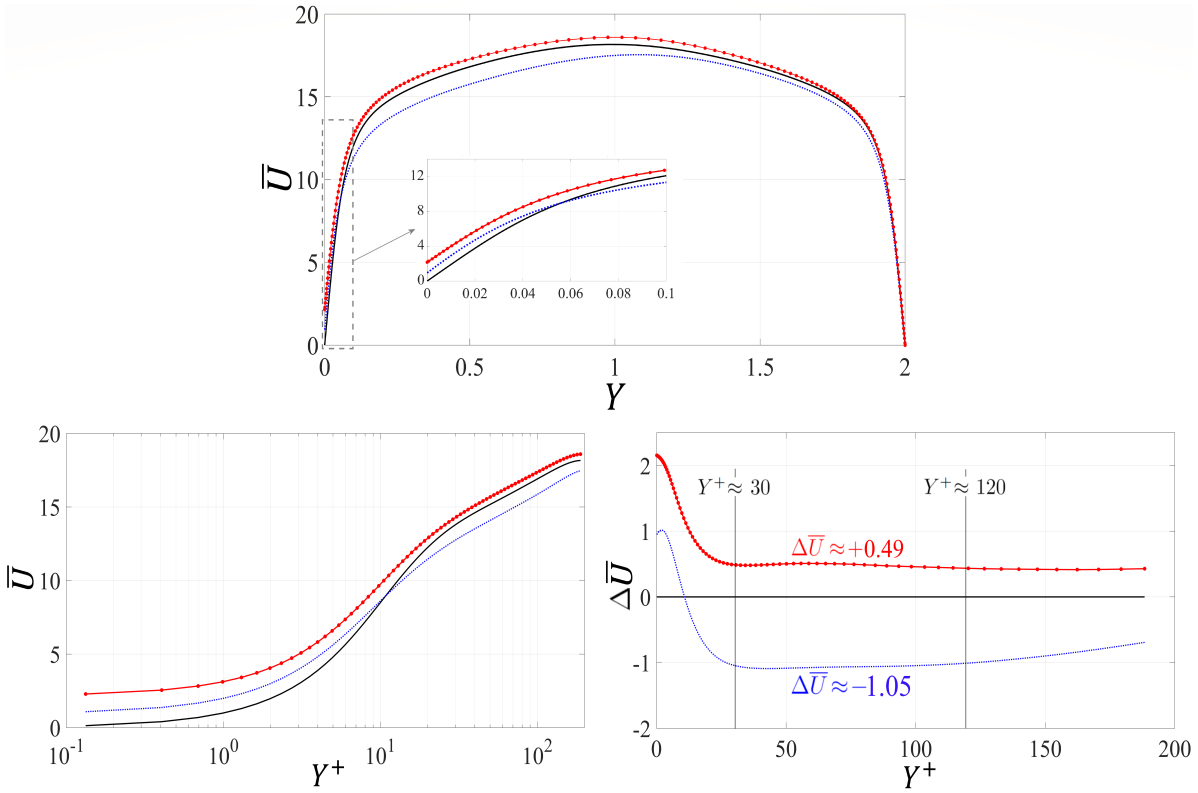

Figure 18: Mean streamwise velocity profiles plotted in global coordinates across the channel (top) and in wall coordinates over the permeable wall (bottom left), with the deviations from the smooth channel case plotted in the bottom right frame. The cases presented are: (solid black line) smooth channel; (dotted blue line) substrate TC_{10}; (red line with markers) substrate LM_{10}.

The profiles of the mean streamwise velocity ($\overline{U}$) over the permeable substrates TC_{10} and LM_{10} are displayed in Figure 18. It is clear that the positive/negative deviations ($\Delta\overline{U}$) in the intercept of the logarithmic profile (cf. equation (32)) are accentuated with respect to the corresponding cases with $\epsilon = 0.05$ (cf. Figure 13); this goes along with the larger changes in the drag coefficient at $\epsilon = 0.1$. In agreement with the previous discussion in Section 3.2.2, the turbulence intensities, presented in Figure 19, provide

a fair clarification of the levels of disturbances in the near-wall layer, which can justify the adverse/favorable changes in skin friction coefficient for substrates TC_{10} and LM_{10}, respectively.

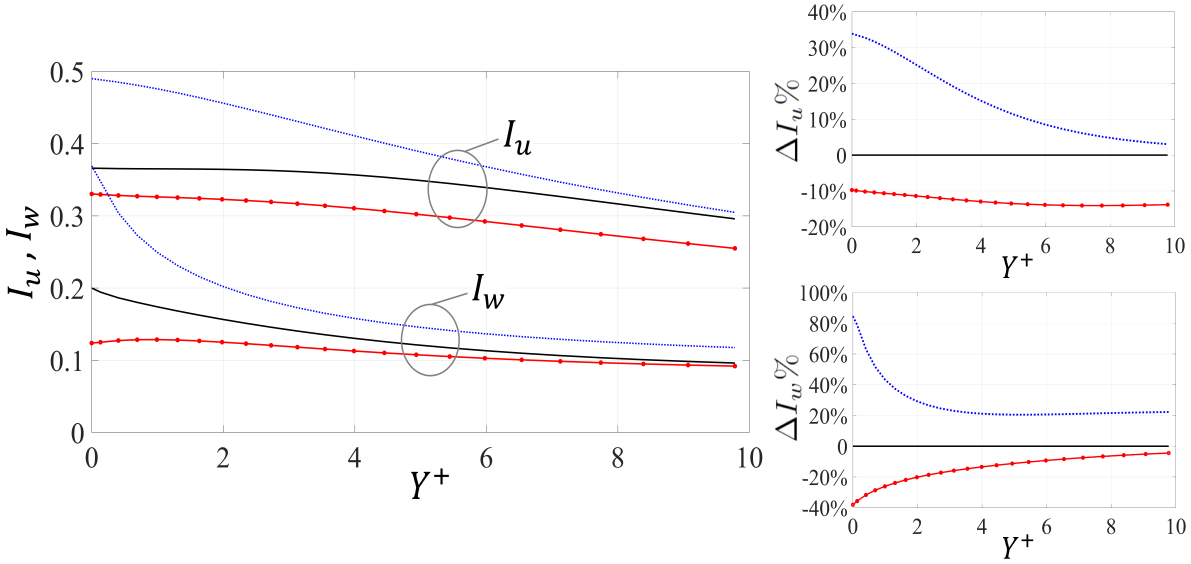

Figure 19: Turbulence intensities (I_u and I_w) near the permeable walls. The percentage deviations of the intensities from the reference smooth channel values are plotted in the right frames. Symbols are identical to those used in Figure 18.

4 CONCLUSIONS

The high skin-friction drag characterizing wall-bounded turbulent flows adversely affects the efficiency of fluid transportation systems. It is thus important to develop effective drag reduction strategies, e.g., properly engineered passive flow control surfaces/substrates. In the present work, turbulent channel flows over transversely isotropic permeable beds of different types were numerically studied, and the consequent favorable/adverse changes in the skin-friction drag coefficient were monitored and described by analyzing turbulence statistics.

A multiscale homogenization approach was introduced to avoid the numerical complexity and the expensive mesh requirements of a full resolution of the flow within the porous media. Expressions for the *effective* boundary conditions of the three velocity components were sought at a fictitious interface between the channel flow and the porous bed, up to second-order accuracy in terms of a small parameter $\epsilon = \dfrac{l\,(\text{porous pattern periodicity})}{H\,(\text{half channel height})}$. The upscaled coefficients appearing in the definition of the effective boundary conditions, i.e. the slip lengths (λ_x, λ_z), the medium permeability in the wall-normal direction $(\mathcal{K}_{yy})$ and the interfacial permeabilities $(\mathcal{K}_{xy}^{inf}, \mathcal{K}_{zy}^{inf})$, were numerically calculated for three microstructures of the porous substrate. In particular, the microstructures considered were:

(TC) transverse, Z-aligned, plain cylinders; (LC) longitudinal, X-aligned plain cylinders; (LM) longitudinal, X-aligned, cylinders modified by the addition of four fins on the circumference, especially designed to amplify the quantity $(\lambda_x - \lambda_z)$ while reducing the medium permeability, $\mathcal{K}_{yy}$.

Direct numerical simulations of the macroscale problem above the virtual interface with the different porous beds have been conducted, employing the finite volume method with the Hybrid MUSCL 3rd-order/central-differencing discretization scheme, initially validated on the flow through a smooth channel. A value of $\epsilon = 0.05$ was first employed, in order to focus on relatively small surface protrusions; the flow over the substrates TC_5, LC_5 and LM_5 was numerically studied, and the turbulence statistics were analyzed in detail. Secondly, the value of ϵ was increased to 0.10 for the substrates TC_{10}, LM_{10}, and the consequent changes in the skin-friction drag coefficient and other flow metrics of interest were examined. Clearly, the gauge factor ϵ cannot be increased too much for the asymptotic expansion to remain valid. The range of validity of the approach, in terms of acceptable values of ϵ, will be investigated in future work. The major findings of the present study are summarised below:

i. The permeable substrates with preferential slip in the streamwise direction ($\lambda_x^+ > \lambda_z^+$), i.e. those designed with longitudinal (either plain or modified) cylinders, are able to reduce skin-friction drag. This conclusion should hold up to some critical value of $\mathcal{K}_{yy}$ at which large-scale instabilities have their onset in the near-wall layer (Gómez-de Segura *et al.*, 2018).

ii. The adverse/favorable changes in the skin-friction drag coefficient are more pronounced for the substrates with $\epsilon = 0.1$. The drag coefficient increases by almost 9% with the substrate TC_{10}, while about 5% drag reduction is obtained with the substrate LM_{10}.

iii. The analysis of the turbulence intensities I_u and I_w provides a meaningful picture of the levels of disturbances in the neighborhood of the permeable walls; such intensities can be used, together with the streamwise slip velocity, to interpret changes in skin-friction drag.

iv. The implementation of the homogenization approach significantly reduces the numerical cost of direct numerical simulations over porous layers, since only the motion in the free-fluid region needs to be resolved. With the dimensions chosen for the domain, the total number of grid points is below 2×10^6, while the mesh requirements for a full feature-resolving simulation (including the porous substrate) may exceed 10^8 (cf. (Wang *et al.*, 2021)).

The present approximate framework needs to be properly validated against feature-resolving simulations which include the permeable medium, in order to provide full confidence in the model developed. This task is currently underway and preliminary results are encouraging. Once this validation phase is terminated, the homogenization model

developed will be employed in a large-scale optimization study: different microstructures of the porous substrate will be examined in pursuit of the *optimal* topology, size and arrangement of the solid grains, capable to yield the largest skin-friction reduction. It will also be of interest to compare the homogenized results for porous substrates with inline and staggered arrangements of grains; this is the case since the configuration of randomly arranged inclusions might be expected to lie in between these two limiting cases, as observed by Naqvi & Bottaro (2021).

REFERENCES

Abderrahaman-Elena, N. & García-Mayoral, R. 2017 Analysis of anisotropically permeable surfaces for turbulent drag reduction. *Phys. Rev. Fluids* **2** (11), 114609.

Abe, H., Kawamura, H. & Matsuo, Y. 2001 Direct numerical simulation of a fully developed turbulent channel flow with respect to the Reynolds number dependence. *ASME J. Fluids Eng.* **123** (2), 382–393.

Ahmed, E.N., Bottaro, A. & Tanda, G. 2022 A homogenization approach for buoyancy-induced flows over micro-textured vertical surfaces. *J. Fluid Mech.* **941**, A53.

Antonia, R.A., Zhu, Y. & Sokolov, M. 1995 Effect of concentrated wall suction on a turbulent boundary layer. *Phys. Fluids* **7** (10), 2465–2474.

Babuška, I. 1976 Homogenization and its application. Mathematical and computational problems, in: Hubbard, B. (Ed.), *Numerical Solution of Partial Differential Equations–III*, pp. 89–116. Academic Press .

Beavers, G.S., Sparrow, E.M. & Magnuson, R.A. 1970 Experiments on coupled parallel flows in a channel and a bounding porous medium. *J. Basic Eng.* **92** (4), 843–848.

Bechert, D.W. & Bartenwerfer, M. 1989 The viscous flow on surfaces with longitudinal ribs. *J. Fluid Mech.* **206**, 105–129.

Bechert, D.W., Bruse, M., Hage, W., Van der Hoeven, J.G.T. & Hoppe, G. 1997 Experiments on drag-reducing surfaces and their optimization with an adjustable geometry. *J. Fluid Mech.* **338**, 59–87.

Bernard, P.S., Thomas, J.M. & Handler, R.A. 1993 Vortex dynamics and the production of Reynolds stress. *J. Fluid Mech.* **253**, 385–419.

Bottaro, A. 2019 Flow over natural or engineered surfaces: an adjoint homogenization perspective. *J. Fluid Mech.* **877**, P1.

Bottaro, A. & Naqvi, S.B. 2020 Effective boundary conditions at a rough wall: a high-order homogenization approach. *Meccanica* **55** (9), 1781–1800.

Cantwell, B.J. 1981 Organized motion in turbulent flow. *Annu. Rev. Fluid Mech.* **13** (1), 457–515.

Cheng, X.Q., Wong, C.W., Hussain, F., Schröder, W. & Zhou, Y. 2021 Flat plate drag reduction using plasma-generated streamwise vortices. *J. Fluid Mech.* **918**.

Choi, K.S. 2002 Near-wall structure of turbulent boundary layer with spanwise-wall oscillation. *Phys. Fluids* **14** (7), 2530–2542.

Clauser, F.H. 1956 The turbulent boundary layer. *Adv. Appl. Mech.* **4**, 1–51.

Garcia-Mayoral, R. & Jiménez, J. 2011 Drag reduction by riblets. *Philos. Trans. Royal Soc. A* **369** (1940), 1412–1427.

Guo, H., Borodulin, V.I., Kachanov, Y.S., Pan, C., Wang, J.J., Lian, Q.X. & Wang, S.F. 2010 Nature of sweep and ejection events in transitional and turbulent boundary layers. *J. Turbul.* **11**, N34.

Jeong, J., Hussain, F., Schoppa, W. & Kim, J. 1997 Coherent structures near the wall in a turbulent channel flow. *J. Fluid Mech.* **332**, 185–214.

Jiménez, J. 1994 On the structure and control of near wall turbulence. *Phys. Fluids* **6** (2), 944–953.

Jiménez, J. & Pinelli, A. 1999 The autonomous cycle of near-wall turbulence. *J. Fluid Mech.* **389**, 335–359.

Jiménez Bolaños, S. & Vernescu, B. 2017 Derivation of the Navier slip and slip length for viscous flows over a rough boundary. *Phys. of Fluids* **29** (5), 057103.

Kang, S. & Choi, H. 2000 Active wall motions for skin-friction drag reduction. *Phys. Fluids* **12** (12), 3301–3304.

Kim, J. 1983 On the structure of wall-bounded turbulent flows. *Phys. Fluids* **26** (8), 2088–2097.

Kim, J., Kim, K. & Sung, H.J. 2003 Wall pressure fluctuations in a turbulent boundary layer after blowing or suction. *AIAA J.* **41** (9), 1697–1704.

Kim, J., Moin, P. & Moser, R. 1987 Turbulence statistics in fully developed channel flow at low Reynolds number. *J. Fluid Mech.* **177**, 133–166.

Kline, S.J., Reynolds, W.C., Schraub, F.A. & Runstadler, P.W. 1967 The structure of turbulent boundary layers. *J. Fluid Mech.* **30** (4), 741–773.

Kozuka, M., Seki, Y. & Kawamura, H. 2009 DNS of turbulent heat transfer in a channel flow with a high spatial resolution. *Intl J. Heat Fluid Flow* **30**, 514–524.

Lācis, U., Sudhakar, Y., Pasche, S. & Bagheri, S. 2020 Transfer of mass and momentum at rough and porous surfaces. *J. Fluid Mech.* **884**, A21.

Luchini, P., Manzo, F. & Pozzi, A. 1991 Resistance of a grooved surface to parallel flow and cross-flow. *J. Fluid Mech.* **228**, 87–109.

Mahfoze, O. & Laizet, S. 2017 Skin-friction drag reduction in a channel flow with streamwise-aligned plasma actuators. *Intl J. Heat Fluid Flow* **66**, 83–94.

Mansour, N.N., Kim, J. & Moin, P. 1988 Reynolds-stress and dissipation-rate budgets in a turbulent channel flow. *J. Fluid Mech.* **194**, 15–44.

Moser, R.D., Kim, J. & Mansour, N.N. 1999 Direct numerical simulation of turbulent channel flow up to Re_τ= 590. *Phys. Fluids* **11** (4), 943–945.

Naqvi, S.B. & Bottaro, A. 2021 Interfacial conditions between a free-fluid region and a porous medium. *Intl J. Multiph. Flow* **141**, 103585.

Navier, C. 1823 Mémoire sur les lois du mouvement des fluides. *Mém. Acad. R. Sci. Inst. France* **6**, 389–440.

Orlandi, P. & Jiménez, J. 1994 On the generation of turbulent wall friction. *Phys. Fluids* **6** (2), 634–641.

Rastegari, A. & Akhavan, R. 2015 On the mechanism of turbulent drag reduction with super-hydrophobic surfaces. *J. Fluid Mech.* **773**.

Rosti, M.E., Brandt, L. & Pinelli, A. 2018 Turbulent channel flow over an anisotropic porous wall–drag increase and reduction. *J. Fluid Mech.* **842**, 381–394.

Rosti, M.E., Cortelezzi, L. & Quadrio, M. 2015 Direct numerical simulation of turbulent channel flow over porous walls. *J. Fluid Mech.* **784**, 396–442.

Gómez-de Segura, G. & García-Mayoral, R. 2019 Turbulent drag reduction by anisotropic permeable substrates–analysis and direct numerical simulations. *J. Fluid Mech.* **875**, 124–172.

Gómez-de Segura, G., Sharma, A. & García-Mayoral, R. 2018 Turbulent drag reduction using anisotropic permeable substrates. *Flow Turbul. Combust.* **100** (4), 995–1014.

Sudhakar, Y., Lācis, U., Pasche, S. & Bagheri, S. 2021 Higher-order homogenized boundary conditions for flows over rough and porous surfaces. *Transp. Porous Med.* **136** (1), 1–42.

Tilton, N. & Cortelezzi, L. 2006 The destabilizing effects of wall permeability in channel flows: A linear stability analysis. *Phys. Fluids* **18** (5), 051702.

Tilton, N. & Cortelezzi, L. 2008 Linear stability analysis of pressure-driven flows in channels with porous walls. *J. Fluid Mech.* **604**, 411–445.

Vreman, A.W. & Kuerten, J.G.M. 2014 Comparison of direct numerical simulation databases of turbulent channel flow at Re_τ= 180. *Phys. Fluids* **26** (1), 015102.

Wang, W., Chu, X., Lozano-Durán, A., Helmig, R. & Weigand, B. 2021 Information transfer between turbulent boundary layers and porous media. *J. Fluid Mech.* **920**.

West, A. & Caraeni, M. 2015 Jet noise prediction using a permeable FW-H solver. In *the 21st AIAA/CEAS Aeroacoust. Conf.,* Dallas, TX, USA, p. 2371. (doi: 10.2514/6.2015-2371).

Wise, D.J. & Ricco, P. 2014 Turbulent drag reduction through oscillating discs. *J. Fluid Mech.* **746**, 536–564.

Zampogna, G.A., Magnaudet, J. & Bottaro, A. 2019*a* Generalized slip condition over rough surfaces. *J. Fluid Mech.* **858**, 407–436.

Zampogna, G.A., Naqvi, S.B., Magnaudet, J. & Bottaro, A. 2019*b* Compliant riblets: Problem formulation and effective macrostructural properties. *J. Fluids Struct.* **91**, 102708.

PAPER F3

Exploring the nexus among roughness function, apparent slip velocity and upscaling coefficients for turbulence over porous/textured walls [1]

Essam Nabil Ahmed and **Alessandro Bottaro**

DICCA, Università di Genova, via Montallegro 1, Genova, 16145, Italy

The interaction between a turbulent flow and a porous boundary is analyzed with focus on the sensitivity of the roughness function, ΔU^+, to the upscaled coefficients characterizing the wall. The study is aimed at (i) demonstrating that imposing *effective* velocity boundary conditions at a *virtual* plane boundary, next to the physical one, can efficiently simplify the direct numerical simulations (DNSs); and (ii) pursuing correlations to estimate ΔU^+ *a priori*, once the upscaled coefficients are calculated. The homogenization approach employed incorporates near-interface advection via an *Oseen*-like linearization, and the macroscopic coefficients thus depend on both the micro-structural details of the wall and a slip-velocity-based Reynolds number, Re_λ. A set of homogenization-simplified DNSs is run to study the channel flow over transversely isotropic porous beds, testing values of the grains' pitch within $0 < \ell^+ < 40$. Reduction of the skin-friction drag is attainable exclusively over streamwise-aligned inclusions for ℓ^+ values up to 20–30. The drag increase over spanwise-aligned inclusions (or streamwise-aligned ones at large ℓ^+) is accompanied by enhanced turbulence levels, including intensified sweep and ejection events. The r.m.s. fluctuations of the transpiration velocity at the virtual plane, $\tilde{V}_{rms}$, is a key control parameter of ΔU^+; our analysis shows that $\tilde{V}_{rms}$ is strongly correlated to a single macroscopic quantity, Ψ, which comprises the Navier-slip and interface/intrinsic permeability coefficients. Fitting relationships for ΔU^+ are proposed, and their applicability is confirmed against reference results for the turbulent flow over impermeable walls roughened with three-dimensional protrusions or different geometries of riblets.

1 INTRODUCTION

Turbulent channel flows are characterized by substantially large skin-friction drag, compared to laminar ones, and this can have severe consequences on the performance of fluid transport systems, in terms of efficiency, running costs, and the reduction of emissions. There is a vast literature on turbulence in smooth channels (Kim *et al.*, 1987; Mansour

[1] A draft prepared for submission to *J. Fluid Mech.*

et al., 1988; Bernard *et al.*, 1993; Jeong *et al.*, 1997; Jiménez & Pinelli, 1999; Vreman & Kuerten, 2014), which has focused, for instance, on the behaviors of the primary turbulent fluctuations and the higher-order statistics, on the role of *ejection* and *sweep* events in the generation of Reynolds stresses, on nonlinear recurrent patterns, or on the autonomous regeneration cycle responsible for maintaining near-wall turbulence. Since the seminal work by Nikuradse (1933), the study of turbulent flow in channels delimited by rough boundaries has become a major focus of research, whether the goal is (i) to explore how given surface topographies can alter the near-wall turbulence and the skin-friction drag (Orlandi *et al.*, 2006; Orlandi & Leonardi, 2006, 2008; Wang *et al.*, 2021; Hao & García-Mayoral, 2024), (ii) to propose and test simplified models for numerical analysis (Bottaro, 2019; Lācis *et al.*, 2020; Ahmed *et al.*, 2022*b*) or even predictive correlations (Forooghi *et al.*, 2017; Flack *et al.*, 2020), or (iii) to optimize and assess the feasibility of wall-based energy-saving control strategies of either active (Antonia *et al.*, 1995; Kang & Choi, 2000; Choi, 2002; Wise & Ricco, 2014; Cheng *et al.*, 2021) or passive nature (Walsh & Lindemann, 1984; Bechert *et al.*, 1997; Rastegari & Akhavan, 2015; Rosti *et al.*, 2018; Endrikat *et al.*, 2021*b*). This introductory section centers around these important aspects.

Passive drag reduction techniques (i.e., micro-textured surfaces, permeable substrates, etc. able, with no energy input, to favorably manipulate the turbulent boundary layer with a view to reducing the turbulent skin-friction drag compared to the smooth surface case) have been the subject of intense research activities. Properly designed superhydrophobic surfaces (SHS) and liquid-infused surfaces (LIS), permitting large effective slip thanks to air (or liquid lubricant, respectively) being trapped within grooves/cavities/micro-grates formed on them, can yield substantial drag reduction in turbulent channel flows (Park *et al.*, 2013; Rastegari & Akhavan, 2015; Fu *et al.*, 2017; Chang *et al.*, 2019). Riblets (longitudinal surface grooves) have proved to mitigate the velocity fluctuations near the wall, resulting in a more uniform flow field (Bechert & Bartenwerfer, 1989). The skin-friction drag over surfaces altered with riblets is crucially sensitive to their geometry and to the Reynolds number of the flow in their vicinity (characterized, for instance, by the lateral spacing of riblets measured in wall units, ℓ^+) as found by many investigators (Walsh & Lindemann, 1984; Bechert *et al.*, 1997; El-Samni *et al.*, 2007; Gatti *et al.*, 2020; Endrikat *et al.*, 2021*a*,*b*; von Deyn *et al.*, 2022). For example, the experiments by Bechert *et al.* (1997) on different configurations of riblets revealed that an optimized drag reduction of almost 10% can be attained, in particular with longitudinal blade ribs having depth and thickness equal to, respectively, 0.5 and 0.02 times the lateral rib spacing and with $\ell^+ \approx 17$. It should be noted that drag reduction ceases when ℓ^+ exceeds a value of about 30, and this is associated with the occurrence of inertial-flow mechanisms such as a Kelvin–Helmholtz instability (Garcia-Mayoral & Jimenez, 2011; Endrikat *et al.*, 2021*a*). Manipulating the turbulent boundary layer and achieving skin-friction reduction by means of properly engineered permeable substrates have recently caught the attention of many researchers. The porous medium permeability coefficients ($\hat{\mathcal{K}}_{ij}$) and the Navier slip lengths ($\hat{\lambda}_i$) are the main parameters whose role has been examined in a number of investigations, with different micro-structures of the substrate, sizes of the solid inclusions, porosities (θ), and flow conditions. Throughout this paper, $\hat{x}$, $\hat{y}$ and $\hat{z}$ refer to, respectively, the streamwise, wall-normal and spanwise directions. Among

the configurations studied, transversely isotropic porous beds of streamwise-preferential permeability $\hat{\mathcal{K}}_{xx} >> \hat{\mathcal{K}}_{yy} = \hat{\mathcal{K}}_{zz}$, for instance those constructed with cylindrical inclusions elongated in the direction of the mean flow, are repeatedly reported to potentially reduce drag in turbulent channel flows; the underpinning of their function has been explained by Abderrahaman-Elena & García-Mayoral (2017), Gómez-de Segura *et al.* (2018), and Gómez-de Segura & García-Mayoral (2019). The drag-reducing functioning of these structures is analogous to that of riblets. Gómez-de Segura *et al.* (2018) found that, at relatively large values of the wall-normal permeability, Kelvin-Helmholtz-like rollers are generated near the porous/free-fluid interface, and this adversely affects the drag-reducing mechanism. In addition to the contributions discussed above, several other studies of turbulence over porous substrates were conducted, either by experimental or numerical approaches. Among the most relevant ones, we cite those conducted by Suga's group (Suga *et al.*, 2013, 2018; Suga, 2016; Kuwata & Suga, 2017), and those by Breugem *et al.* (2006), Manes *et al.* (2011), Rosti *et al.* (2015, 2018), Wang *et al.* (2021, 2022), Esteban *et al.* (2022), Khorasani *et al.* (2024), and Hao & García-Mayoral (2024).

Investigating how the microscale features of the surface (e.g. roughness, porosity, superhydrophobicity, etc.) can alter the characteristics of the turbulent motion above it, and thus skin-friction drag or heat/mass transfer effectiveness, is important in several applications for both predictive and optimization purposes. The numerical complexity and the high computational cost associated with resolving turbulent fields near and across surface micro-details represent a challenge, because of the large variety of surface topographies encountered in practice, the computational costs required to carry out well-resolved direct numerical simulation (DNS) or large eddy simulations of the motion, and the uncertainties/errors related with the numerical representation of the rough surface or of the grain shape and distributions for the case of a porous bed. Despite the recent computational advances which have permitted numerical investigations with unprecedented levels of accuracy (Chung *et al.*, 2021), the aforementioned factors represent a major hurdle when optimization of the surface is the ultimate goal. In this respect, characterizing a surfaces by key parameters available *a priori* and exhibiting a strong relation with the roughness function, for example, can be very beneficial. However, this is a complex undertaking, and the quantities widely investigated throughout the literature are, in principle, available only *a posteriori* (i.e., after conducting the numerical/experimental study of the turbulent flow over the surface) and, hence, of limited use for prediction purposes. For example, we mention here (i) the equivalent sand-grain size, k_s, first introduced by Schlichting (1937) and later used as a classifier for rough surfaces in a large body of studies (refer to the limitations and drawbacks highlighted by Jiménez (2004) and Abderrahaman-Elena *et al.* (2019)); and (ii) the virtual origins of mean flow and turbulence (Luchini *et al.*, 1991; Jiménez, 1994; Luchini, 1996), with successive efforts devoted, in recent years, to the exploration of the statistical quantities whose near-wall behavior defines the virtual origin of turbulence (Orlandi *et al.*, 2006; Orlandi & Leonardi, 2006, 2008; Abderrahaman-Elena *et al.*, 2019; Ibrahim *et al.*, 2021; Khorasani *et al.*, 2022; Wong *et al.*, 2024). On the positive side, predictive models based on the aforementioned concepts, albeit not yet generalized, are beginning to emerge (Flack & Schultz, 2010; Yang & Meneveau, 2016; Yang *et al.*, 2016; Forooghi *et al.*, 2017; Flack *et al.*, 2020; Khorasani

et al., 2022).

The development of accurate macroscopic models for the fluid-wall interaction has become a very active field of research in the last decade or so. These are viable tools capable of simplifying the numerical analysis while maintaining an acceptable level of accuracy. The asymptotic, multiscale homogenization theory (Babuška, 1976; Mei & Vernescu, 2010) is a theoretical framework through which the rapidly varying properties characterizing a heterogeneous surface (irregular, rough, lubricant-infused, or porous, *inter alia*) can be replaced by homogeneous upscaled parameters such as the Navier's slip lengths or the interface permeability coefficients (Jiménez Bolaños & Vernescu, 2017; Lācis *et al.*, 2017; Bottaro, 2019; Zampogna *et al.*, 2019; Lācis *et al.*, 2020). The latter are necessary for the formulation of *effective* boundary conditions, free of empirical coefficients, to be imposed at a fictitious plane interface next to the physical textured boundary; the macroscale behavior of the channel flow is then studied numerically, eschewing the numerical resolution of flow details between/in close vicinity of the solid protrusions/grains and, consequently, alleviating mesh requirements and computational costs. The validity of the asymptotic homogenization approach is contingent on the presence of well-separated scales, for instance a microscopic length scale (ℓ) related to the periodicity of the surface texture and a macroscopic one ($\mathcal{L} >> \ell$) related to the large-scale flow structures in the channel, such that we are able to define the small parameter $\epsilon = \ell/\mathcal{L} << 1$ and seek a solution of the problem up to the required order of accuracy in terms of ϵ. Jiménez Bolaños & Vernescu (2017) provided a robust homogenization-based method for the evaluation of the slip coefficient, λ, contributing to the classical first-order slip condition over a generic solid surface, which was first proposed by Navier (1823) merely based on empirical considerations. High-order effective boundary conditions were derived by Bottaro & Naqvi (2020) and Ahmed *et al.* (2022*a*) for the flow over a rough surface and by Lācis *et al.* (2020), Sudhakar *et al.* (2021), Naqvi & Bottaro (2021) and Ahmed *et al.* (2022*b*) for the flow over a porous bed. Definitions of the three velocity components at the fictitious interface, valid up to second-order accuracy, are now available; this is crucial under turbulent flow conditions since turbulent fluctuations along directions both tangent and normal to the fictitious interface considerably affect the behavior of the turbulent boundary layer and, therefore, the skin-friction drag (Orlandi *et al.*, 2006; Orlandi & Leonardi, 2006, 2008; Bottaro, 2019; Lācis *et al.*, 2020). The near-wall advection was incorporated into the analysis by means of an Oseen's approximation in the studies by Buda (2021) and Ahmed & Bottaro (2024), and this was proven to widen the applicability range of the model considerably.

The present work is aimed at investigating the hydrodynamic interaction between a porous/rough boundary and a fluid under turbulent flow conditions, with the aid of a homogenization framework. The main focus is on exploring the relationship between the roughness function ΔU^+ (i.e., the shift in the intercept of the logarithmic velocity profile) and the macroscopic coefficients (i.e., the Navier-slip coefficients and the interface/intrinsic permeabilities) contributing to the effective boundary conditions at the wall. Throughout the work, it is assumed that the roughness elements do not protrude significantly into the free-fluid turbulent region, for outer layer similarity to hold (Townsend,

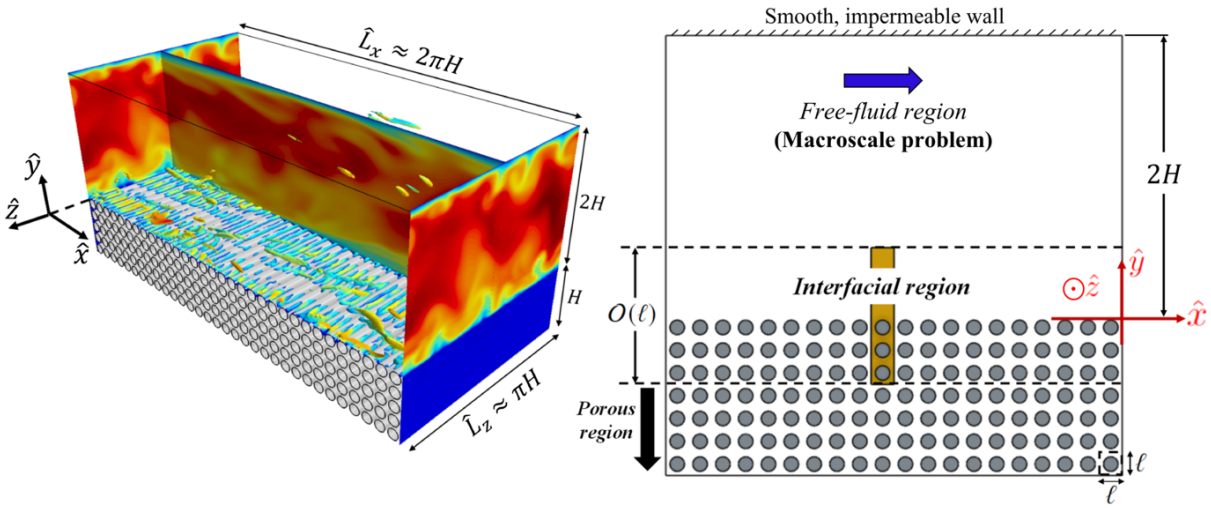

Figure 1: Sketch of the full domain for the case of a channel delimited from the top by a smooth, impermeable wall and from the bottom by a porous bed formed by spanwise-elongated cylindrical grains. The right frame illustrates in a constant $\hat{z}$-section the decomposition of the domain into three distinct sub-regions; the brown volume represents the horizontally periodic elementary cell of the microscopic problem.

1976). The study is twofold. First, turbulent channel flows over permeable boundaries of different geometries are considered, and high-order *effective* boundary conditions of the three velocity components, defined at a *fictitious* plane boundary tangent to the grains, are formulated (Section 2), validated (Section 3.1), and employed to simplify a set of direct numerical simulations (Section 3.2); the mean velocity profiles are obtained and the major turbulence statistics near the porous/free-fluid interface are analyzed to interpret the drag-reducing/increasing effects of the porous patterns. Second, in order to estimate the roughness function *a priori*, without the need for running direct numerical simulations, the available results are fitted to generate an explicit expression linking ΔU^+ to the upscaled coefficients of interest (Section 3.3); the generality of the fitting correlation(s) is confirmed via validation against results from the literature for the turbulent flow over rough, impermeable walls (Section 3.4). Concluding remarks are presented in Section 4.

2 PROBLEM STATEMENT AND UPSCALING APPROACH

2.1 Governing equations and domain decomposition

Let us consider the turbulent flow of a viscous, incompressible, Newtonian fluid in a channel delimited from one side (at $\hat{y} = 2H$) by a smooth, impermeable wall and from the other side (at $\hat{y} \leq 0$) by a permeable substrate constructed with spanwise-elongated ($\hat{z}$-aligned) solid inclusions, regularly arranged with given periodicity in the streamwise and wall-normal directions ($\hat{x}$ and $\hat{y}$, respectively); refer to figure 1. The velocity components

($\hat{u}_1 = \hat{u}$, $\hat{u}_2 = \hat{v}$, $\hat{u}_3 = \hat{w}$) and the pressure $\hat{p}$ are the dependent variables, to be evaluated over space ($\hat{x}_1 = \hat{x}$, $\hat{x}_2 = \hat{y}$, $\hat{x}_3 = \hat{z}$) and time $\hat{t}$. The conservation equations governing the flow can be expressed as follows:

$$\frac{\partial \hat{u}_i}{\partial \hat{x}_i} = 0, \quad \rho\left(\frac{\partial \hat{u}_i}{\partial \hat{t}} + \hat{u}_j \frac{\partial \hat{u}_i}{\partial \hat{x}_j}\right) = -\frac{\partial \hat{p}}{\partial \hat{x}_i} + \mu \frac{\partial^2 \hat{u}_i}{\partial \hat{x}_j^2}, \tag{2.1}$$

with ρ and μ the fluid density and dynamic viscosity, respectively.

We identify two characteristic length scales: a microscopic one, ℓ, characterizing the porous bed (particularly, the pitch distance of the inclusions), and a macroscopic one, $\mathcal{L}$, related to the large-scale motion in the channel. Provided that the two length scales are well-separated, i.e. $\ell \ll \mathcal{L}$, it is possible to manipulate the microscale problem by means of an asymptotic analysis in terms of a small parameter $\epsilon = \ell/\mathcal{L} \ll 1$. As illustrated in figure 1, the flow domain is decomposed into three distinct sub-domains: a channel-flow region away from the porous/free-fluid interface (superscript "$\mathcal{C}$"), an interfacial region (superscript "$\mathcal{I}$") and a region within the porous layer away from boundaries, governed by Darcy's law (superscript "$\mathcal{P}$"). Correspondingly, the following three sets of normalized variables are proposed:

$$X_i = \frac{\hat{x}_i}{\mathcal{L}}, \quad U_i^{\mathcal{C}} = \frac{\hat{u}}{\mathcal{U}}, \quad P^{\mathcal{C}} = \frac{\hat{p}}{\rho \mathcal{U}^2}, \tag{2.2a}$$

$$x_i = \frac{\hat{x}_i}{\ell}, \quad U_i^{\mathcal{I}} = \frac{\hat{u}}{\epsilon \mathcal{U}}, \quad P^{\mathcal{I}} = \frac{\hat{p}}{\mu \mathcal{U}/\mathcal{L}}, \tag{2.2b}$$

$$x_i = \frac{\hat{x}_i}{\ell}, \quad U_i^{\mathcal{P}} = \frac{\hat{u}}{\epsilon^2 \mathcal{U}}, \quad P^{\mathcal{P}} = \frac{\hat{p}}{\mu \mathcal{U}/\mathcal{L}}, \tag{2.2c}$$

where $\mathcal{U}$ is a suitable macroscopic velocity scale; a discussion on the proper selection of scales is provided later. Based on the normalization above, the governing equations (2.1) can be recast into the following dimensionless forms in the $\bullet^{\mathcal{C}}$, $\bullet^{\mathcal{I}}$, and $\bullet^{\mathcal{P}}$ regions, respectively;

$$\frac{\partial U_i^{\mathcal{C}}}{\partial X_i} = 0, \quad \frac{\partial U_i^{\mathcal{C}}}{\partial t} + U_j^{\mathcal{C}} \frac{\partial U_i^{\mathcal{C}}}{\partial X_j} = -\frac{\partial P^{\mathcal{C}}}{\partial X_i} + \frac{1}{Re} \frac{\partial^2 U_i^{\mathcal{C}}}{\partial X_j^2}, \tag{2.3a}$$

$$\frac{\partial U_i^{\mathcal{I}}}{\partial x_i} = 0, \quad \epsilon^2 Re\left(\frac{\partial U_i^{\mathcal{I}}}{\partial t} + U_j^{\mathcal{I}} \frac{\partial U_i^{\mathcal{I}}}{\partial x_j}\right) = -\frac{\partial P^{\mathcal{I}}}{\partial x_i} + \frac{\partial^2 U_i^{\mathcal{I}}}{\partial x_j^2}, \tag{2.3b}$$

$$\epsilon \frac{\partial U_i^{\mathcal{P}}}{\partial x_i} = 0, \quad \epsilon^4 Re\, U_j^{\mathcal{P}} \frac{\partial U_i^{\mathcal{P}}}{\partial x_j} = -\frac{\partial P^{\mathcal{P}}}{\partial x_i} + \epsilon \frac{\partial^2 U_i^{\mathcal{P}}}{\partial x_j^2}, \tag{2.3c}$$

with $Re = \rho \mathcal{U} \mathcal{L}/\mu$. Note that the time scale is the same in the interface and free-fluid region ($t = \hat{t}\mathcal{U}/\mathcal{L}$) and that in the bulk of the porous domain the motion is assumed steady. In the intermediate and porous regions, the dependent variables are function of both the fast (microscopic) and the slow (macroscopic) coordinates (x_i, X_i respectively), whilst in the channel-flow region, the dependent variables vary spatially with the macroscopic coordinates, X_i, only. A fictitious dividing surface between the channel-flow region and the interfacial layer is defined at $\hat{x}_2 = \hat{y}_\infty$, and continuity of the velocity and

the traction vectors is applied there. With $y_\infty = \hat{y}_\infty/\ell$ and $\mathcal{Y}_\infty = \hat{y}_\infty/\mathcal{L} = \epsilon y_\infty$ the microscopic and the macroscopic vertical coordinates of this interface, respectively, the matching conditions can be written as follows:

$$\lim_{x_2 \to y_\infty} U_i^{\mathcal{I}} = \frac{1}{\epsilon} \lim_{X_2 \to \mathcal{Y}_\infty} U_i^{\mathcal{C}}, \tag{2.4a}$$

$$\lim_{x_2 \to y_\infty} \left(-P^{\mathcal{I}} \delta_{i2} + \frac{\partial V^{\mathcal{I}}}{\partial x_i} + \frac{\partial U_i^{\mathcal{I}}}{\partial y} \right) = \lim_{X_2 \to \mathcal{Y}_\infty} \left(-Re\, P^{\mathcal{C}} \delta_{i2} + \frac{\partial V^{\mathcal{C}}}{\partial X_i} + \frac{\partial U_i^{\mathcal{C}}}{\partial Y} \right), \tag{2.4b}$$

with δ_{ij} the Kronecker index. For the conditions above to be valid, y_∞ is to be sufficiently large such that the $\bullet^{\mathcal{I}}$ variables become uniform in x and z at the virtual interface.

2.2 Asymptotic analysis of the microscale problem

The dependent variables in the interfacial and the porous sub-domains are asymptotically expanded in terms of ϵ as

$$U_i^{\mathcal{I}} = U_i^{\mathcal{I}(0)} + \epsilon U_i^{\mathcal{I}(1)} + \epsilon^2 U_i^{\mathcal{I}(2)} + ..., \quad P^{\mathcal{I}} = P^{\mathcal{I}(0)} + \epsilon P^{\mathcal{I}(1)} + \epsilon^2 P^{\mathcal{I}(2)} + ...,$$

$$U_i^{\mathcal{P}} = U_i^{\mathcal{P}(0)} + \epsilon U_i^{\mathcal{P}(1)} + \epsilon^2 U_i^{\mathcal{P}(2)} + ..., \quad P^{\mathcal{P}} = P^{\mathcal{P}(0)} + \epsilon P^{\mathcal{P}(1)} + \epsilon^2 P^{\mathcal{P}(2)} + ...$$

Furthermore, the gradients are recast using the chain rule ($\frac{\partial}{\partial x_i} \to \frac{\partial}{\partial x_i} + \epsilon \frac{\partial}{\partial X_i}$). The asymptotic expressions are substituted into the equations governing the flow in the microscopic regions, for the microscale problems to be reconstructed at different orders of ϵ. It has been shown (Naqvi & Bottaro, 2021) that the resulting systems of equations for the interfacial and the porous regions can be combined by defining a composite description of the asymptotic expansions, that is

$$u_i = u_i^{(0)} + \epsilon u_i^{(1)} + \mathcal{O}(\epsilon^2), \quad p = p^{(0)} + \epsilon p^{(1)} + \mathcal{O}(\epsilon^2), \tag{2.5a}$$

with

$$u_i^{(0)} = \begin{cases} U_i^{\mathcal{I}(0)}, & y \in \mathcal{I} \\ \epsilon U_i^{\mathcal{P}(0)}, & y \in \mathcal{P} \end{cases}, \quad u_i^{(1)} = \begin{cases} U_i^{\mathcal{I}(1)}, & y \in \mathcal{I} \\ \epsilon U_i^{\mathcal{P}(1)}, & y \in \mathcal{P} \end{cases}, \tag{2.5b}$$

and

$$p^{(0)} = \begin{cases} P^{\mathcal{I}(0)}, & y \in \mathcal{I} \\ P^{\mathcal{P}(0)} + \epsilon P^{\mathcal{P}(1)}, & y \in \mathcal{P} \end{cases}, \quad p^{(1)} = \begin{cases} P^{\mathcal{I}(1)}, & y \in \mathcal{I} \\ \epsilon P^{\mathcal{P}(2)}, & y \in \mathcal{P} \end{cases}. \tag{2.5c}$$

The following composite system, valid over the whole region below the dividing interface (i.e., $x_2 < y_\infty$), is thus obtained:

$$\begin{cases} \partial_i u_i = -\epsilon \partial_i' u_i^{(0)} + \mathcal{O}\left(\epsilon^2\right) \\ -\partial_i p + \partial_j^2 u_i = \mathcal{R}\, u_j \partial_j u_i + \epsilon \left[\partial_i' p^{(0)} - 2\partial_j \partial_j' u_i^{(0)} + \mathcal{R}\, u_j^{(0)} \partial_j' u_i^{(0)} \right] + \mathcal{O}\left(\epsilon^2\right) \end{cases} \tag{2.6}$$

with $\mathcal{R} = \epsilon^2 Re$ a microscopic Reynolds number and with derivatives indicated by $\partial_i = \frac{\partial}{\partial x_i}$ and $\partial_i' = \frac{\partial}{\partial X_i}$.

In order to treat the problem above, we first simplify it by linearising the convective terms applying an Oseen approximation. In particular, a constant value is assigned to the streamwise velocity component, u_1, near the interface, chosen as the surface-averaged slip velocity $u_{slip} = \dfrac{\hat{u}_{slip}}{\epsilon \mathcal{U}}$ (with $\hat{u}_{slip}$ the dimensional slip velocity at the plane $\hat{y} = 0$), i.e. $u_j^{(0)} \simeq (u_{slip}, 0, 0)$. Thus, the advection term in (2.6) simplifies as $\mathcal{R}\, u_{slip} \partial_1 u_i$, with

$$\mathcal{R}\, u_{slip} = \frac{\rho\, \hat{u}_{slip}\, \ell}{\mu} = Re_\lambda. \tag{2.7}$$

The quantity Re_λ is a slip-velocity Reynolds number, based on the microscopic length scale ℓ; as we will see later, its value is not necessarily small. The composite system (2.6) is now approximated as

$$\begin{cases} \partial_i u_i = -\epsilon \partial_i' u_i^{(0)} + \mathcal{O}\left(\epsilon^2\right) \\ -\partial_i p + \partial_j^2 u_i = Re_\lambda\, \partial_1 u_i + \epsilon \left[\partial_i' p^{(0)} - 2\partial_j \partial_j' u_i^{(0)} + Re_\lambda\, \partial_1' u_i^{(0)}\right] + \mathcal{O}\left(\epsilon^2\right) \end{cases} \tag{2.8}$$

The leading-order problem reads:

$$\mathcal{O}(1): \begin{cases} \partial_i u_i^{(0)} = 0, \\ -\partial_i p^{(0)} + \partial_j^2 {u_i}^{(0)} = Re_\lambda\, \partial_1 u_i^{(0)}, \\ \left(-p^{(0)}\delta_{i_2} + \partial_2 u_i^{(0)} + \partial_i u_2^{(0)}\right)_{x_2 = y_\infty} = S_{i2}^{\mathcal{C}}, \end{cases} \tag{2.9}$$

with $S_{i2}^{\mathcal{C}}$ the macroscopic traction vector evaluated at $X_2 = \mathcal{Y}_\infty$, i.e.

$$S_{i2}^{\mathcal{C}} = \boldsymbol{\sigma}^{\boldsymbol{\mathcal{C}}} \cdot \boldsymbol{e}_2|_{X_2 = \mathcal{Y}_\infty} = \left(\frac{\partial U^{\mathcal{C}}}{\partial Y} + \frac{\partial V^{\mathcal{C}}}{\partial X}, -ReP^{\mathcal{C}} + 2\frac{\partial V^{\mathcal{C}}}{\partial Y}, \frac{\partial W^{\mathcal{C}}}{\partial Y} + \frac{\partial V^{\mathcal{C}}}{\partial Z}\right)\Bigg|_{X_2 = \mathcal{Y}_\infty}, \tag{2.11}$$

where $\boldsymbol{\sigma}^{\mathcal{C}}$ is the stress tensor. From now on, the outer dependent variables are referred to without the superscript $\bullet^{\mathcal{C}}$.

At next order, we have

$$\mathcal{O}(\epsilon): \begin{cases} \partial_i u_i^{(1)} = -\partial_i' u_i^{(0)}, \\ -\partial_i p^{(1)} + \partial_j^2 u_i^{(1)} = Re_\lambda \left(\partial_1 u_i^{(1)} + \partial_1' u_i^{(0)}\right) + \partial_i' p^{(0)} - 2\partial_j \partial_j' u_i^{(0)}, \\ \left(-p^{(1)}\delta_{i_2} + \partial_2 u_i^{(1)} + \partial_i u_2^{(1)}\right)_{x_2 = y_\infty} = -\left(\partial_2' u_i^{(0)} + \partial_i' u_2^{(0)}\right)_{x_2 = y_\infty}. \end{cases} \tag{2.10}$$

The linearity of (2.9) and (2.10) permits us to assume generic solutions of the problems. For the leading-order problem, we express the dependent variables as

$$\begin{cases} u_i^{(0)} = u_{ij}^\dagger S_{j2}, \\ p^{(0)} = p_j^\dagger S_{j2}, \end{cases} \tag{2.12}$$

with the closure variables, $u^\dagger_{ij}$ and $p^\dagger_j$, dependent on only the microscopic coordinates, x_i. Decoupled *ad hoc* auxiliary systems arise from plugging the generic solutions into (2.9); they are

$$\begin{cases} \partial_i u^\dagger_{ij} = 0, \\ -\partial_i p^\dagger_j + \partial^2_l u^\dagger_{ij} = Re_\lambda\, \partial_1 u^\dagger_{ij}, \\ \left(-p^\dagger_j \delta_{i2} + \partial_2 u^\dagger_{ij} + \partial_i u^\dagger_{2j}\right)\Big|_{x_2=y_\infty} = \delta_{ij}, \end{cases} \tag{2.13}$$

where the microscopic problems correspond to $j = 1, 2, 3$. For the problem forced by S_{22} (i.e. with $j = 2$), the analytical solution $u^\dagger_{i2} = 0$, $p^\dagger_2 = -1$ is easily retrieved. At $\mathcal{O}(\epsilon)$ the following generic forms hold:

$$\begin{cases} u^{(1)}_i = u^\ddagger_{ijk}\, \partial'_k S_{j2}, \\ p^{(1)} = p^\ddagger_{jk}\, \partial'_k S_{j2}, \end{cases} \tag{2.14}$$

leading to

$$\begin{cases} \partial_i u^\ddagger_{ijk} = -u^\dagger_{kj}, \\ Re_\lambda \left(\partial_1 u^\ddagger_{ijk} + u^\dagger_{ij}\delta_{k1}\right) = -\partial_i p^\ddagger_{jk} - p^\dagger_j \delta_{ki} + \partial^2_l u^\ddagger_{ijk} + 2\partial_k u^\dagger_{ij}, \\ \left(-p^\ddagger_{jk}\delta_{i2} + \partial_2 u^\ddagger_{ijk} + \partial_i u^\ddagger_{2jk}\right)\Big|_{x_2=y_\infty} = -\left(u^\dagger_{ij}\delta_{k2} + u^\dagger_{2j}\delta_{ik}\right)\Big|_{x_2=y_\infty}; \end{cases} \tag{2.15}$$

these are nine decoupled systems, i.e. corresponding to $j, k = 1, 2, 3$. The closure problems (2.13) and (2.15) are to be solved in a representative unit cell of the microscopic region, subject to periodicity of all the dependent variables along x and z and to the boundary conditions $u^\dagger_{ij} = 0$ and $u^\ddagger_{ijk} = 0$ on the solid grains, which come from the no-slip condition.

2.3 Formal expressions of the effective boundary conditions

Numerical solutions are sought for systems (2.13) and (2.15), with focus on the values of the fields at $x_2 = y_\infty$ since $u^\dagger_{ij}\big|_{y_\infty}$ and $u^\ddagger_{ijk}\big|_{y_\infty}$ are eventually the necessary coefficients to close the macroscopic effective boundary conditions of the velocity; these conditions result from matching the velocity vector at the fictitious interface between the channel-flow and the interfacial regions, as per (2.4a). Finally, the upscaled conditions, second-order accurate in terms of ϵ, are expressed as:

$$U_i|_{\mathcal{Y}_\infty} = \epsilon \left(u^{(0)}_i\Big|_{y_\infty} + \epsilon\, u^{(1)}_i\Big|_{y_\infty} \right) + \mathcal{O}(\epsilon^3) = \epsilon\, u^\dagger_{ij}\Big|_{y_\infty} S_{j2} + \epsilon^2\, u^\ddagger_{ijk}\Big|_{y_\infty} \frac{\partial S_{j2}}{\partial X_k} + \mathcal{O}(\epsilon^3). \tag{2.16}$$

The numerical procedure to solve the closure problems is similar to that followed by Naqvi & Bottaro (2021) and Ahmed *et al.* (2022*b*) for porous media of either isotropic (such as spherical grains) or transversely isotropic microstructures in the $\hat{x} - \hat{z}$ plane (such as spanwise- or streamwise-elongated elements). We focus on the same parameters which

do not vanish at the matching interface found in these references:

$$\begin{aligned} & u^{\dagger}_{11}\Big|_{y_\infty} = y_\infty + \lambda_x, \quad u^{\dagger}_{33}\Big|_{y_\infty} = y_\infty + \lambda_z, \\ & -u^{\ddagger}_{211}\Big|_{y_\infty} = u^{\ddagger}_{121}\Big|_{y_\infty} = 0.5\, y_\infty^2 + \lambda_x\, y_\infty + \mathcal{K}^{itf}_{xy}, \\ & -u^{\ddagger}_{233}\Big|_{y_\infty} = u^{\ddagger}_{323}\Big|_{y_\infty} = 0.5\, y_\infty^2 + \lambda_z\, y_\infty + \mathcal{K}^{itf}_{zy}, \\ & u^{\ddagger}_{222}\Big|_{y_\infty} = \mathcal{K}_{yy}, \end{aligned} \tag{2.17}$$

with λ_x and λ_z the dimensionless Navier's slip coefficients in the streamwise and the spanwise directions, respectively, $\mathcal{K}^{itf}_{xy}$ and $\mathcal{K}^{itf}_{zy}$ the *interface permeability* coefficients, and $\mathcal{K}_{yy}$ an *intrinsic permeability* component. The novel contribution here is the incorporation of the effect of near-interface inertia on the microscale flow behavior, which renders the aforementioned parameters sensitive to the value of Re_λ.

It is convenient to set y_∞ to *zero* in the fitting relations (2.17) and, hence, to extrapolate the solutions of the model coefficients to a matching interface located at the upper boundary of the surface corrugation, that is the porous/free-fluid interface at $Y = 0$. Therefore, the values of the parameters $\lambda_x, \lambda_z, \mathcal{K}^{itf}_{xy}, \mathcal{K}^{itf}_{zy}$ and $\mathcal{K}_{yy}$ are sufficient to macroscopically mimic the presence of the permeable interface up to second-order accuracy, with the following effective boundary conditions on the $Y = 0$ plane:

$$U|_{Y=0} = \epsilon\lambda_x S_{12}|_{Y=0} + \epsilon^2 \mathcal{K}^{itf}_{xy} \frac{\partial S_{22}}{\partial X}\bigg|_{Y=0} + \mathcal{O}\left(\epsilon^3\right), \tag{2.18a}$$

$$V|_{Y=0} = -\epsilon^2 \mathcal{K}^{itf}_{xy} \frac{\partial S_{12}}{\partial X}\bigg|_{Y=0} - \epsilon^2 \mathcal{K}^{itf}_{zy} \frac{\partial S_{32}}{\partial Z}\bigg|_{Y=0} + \epsilon^2 \mathcal{K}_{yy} \frac{\partial S_{22}}{\partial Y}\bigg|_{Y=0} + \mathcal{O}\left(\epsilon^3\right), \tag{2.18b}$$

$$W|_{Y=0} = \epsilon\lambda_z S_{32}|_{Y=0} + \epsilon^2 \mathcal{K}^{itf}_{zy} \frac{\partial S_{22}}{\partial Z}\bigg|_{Y=0} + \mathcal{O}\left(\epsilon^3\right). \tag{2.18c}$$

At this point, something should be said about the macroscopic velocity and length scales (respectively, $\mathcal{U}$ and $\mathcal{L}$) used for normalization in the preceding equations. If the magnitude of the macroscopic pressure gradient driving the flow in the channel is $\mathcal{M} = \left|\Delta\hat{p}/\hat{L}_x\right|$, one may derive a stress $\tau_\mathcal{M} = \mathcal{M}\, H = (\tau_\mathcal{B} + \tau_\mathcal{T})/2$, with $\tau_\mathcal{B}$ and $\tau_\mathcal{T}$ the total shear stresses at $Y = 0$ (bottom) and $Y = 2$ (top), respectively. The corresponding shear velocity $u_{\tau(\mathcal{M})} = \sqrt{\tau_\mathcal{M}/\rho}$ is chosen here as the macroscopic velocity scale, i.e. $\mathcal{U} = u_{\tau(\mathcal{M})}$. A proper macroscopic length scale should be related to the turbulent motions in the free-fluid region; for this purpose, $\mathcal{L}$ can defined as $\mathcal{L} = \alpha \dfrac{\mu/\rho}{u_{\tau(\mathcal{M})}} = H \dfrac{\alpha}{Re_{\tau(\mathcal{M})}}$, with $Re_{\tau(\mathcal{M})} = \rho u_{\tau(\mathcal{M})} H/\mu$ the shear Reynolds number. The typical turbulent length scale is the mean spacing of adjacent streaks, which corresponds to α around 100; in the present settings, thus, the quantity $\alpha/Re_{\tau(\mathcal{M})}$ is of order one and, for practical purposes, it is convenient to take the macroscopic length scale $\mathcal{L}$ to coincide with H, the half-channel height.

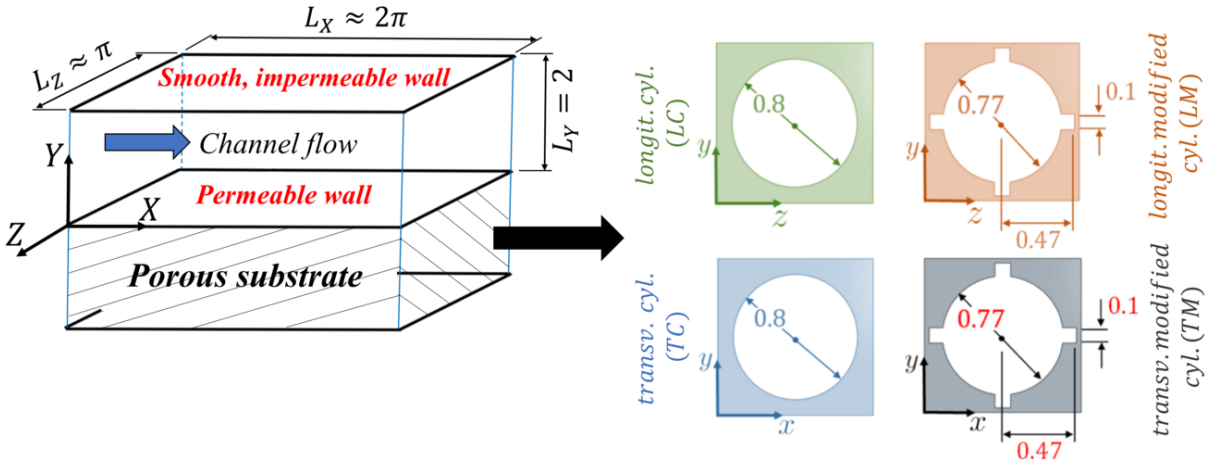

Figure 2: The problems under study. The computational domain is displayed in the left panel, with the dimensions indicated in the macroscopic coordinates (normalized by half the channel height). On the right, the bulk unit cell of the different porous media considered are drawn in microscopic dimensionless coordinates. All media have porosity $\theta = 0.5$.

In dimensional form, the effective conditions valid up to second order in ϵ, are

$$\hat{u}|_0 \approx \hat{\lambda}_x \left(\frac{\partial \hat{u}}{\partial \hat{y}} + \frac{\partial \hat{v}}{\partial \hat{x}} \right)\Big|_0 + \frac{\hat{\mathcal{K}}^{itf}_{xy}}{\mu} \frac{\partial}{\partial \hat{x}} \left(-\hat{p} + 2\mu \frac{\partial \hat{v}}{\partial \hat{y}} \right)\Big|_0 , \tag{2.19a}$$

$$\hat{v}|_0 \approx \frac{\hat{\mathcal{K}}_{yy}}{\mu} \frac{\partial}{\partial \hat{y}} \left(-\hat{p} + 2\mu \frac{\partial \hat{v}}{\partial \hat{y}} \right)\Big|_0 - \hat{\mathcal{K}}^{itf}_{xy} \frac{\partial}{\partial \hat{x}} \left(\frac{\partial \hat{u}}{\partial \hat{y}} + \frac{\partial \hat{v}}{\partial \hat{x}} \right)\Big|_0 - \hat{\mathcal{K}}^{itf}_{zy} \frac{\partial}{\partial \hat{z}} \left(\frac{\partial \hat{w}}{\partial \hat{y}} + \frac{\partial \hat{v}}{\partial \hat{z}} \right)\Big|_0 , \tag{2.19b}$$

$$\hat{w}|_0 \approx \hat{\lambda}_z \left(\frac{\partial \hat{w}}{\partial \hat{y}} + \frac{\partial \hat{v}}{\partial \hat{z}} \right)\Big|_0 + \frac{\hat{\mathcal{K}}^{itf}_{zy}}{\mu} \frac{\partial}{\partial \hat{z}} \left(-\hat{p} + 2\mu \frac{\partial \hat{v}}{\partial \hat{y}} \right)\Big|_0 , \tag{2.19c}$$

with the dimensional model coefficients defined as

$$\hat{\lambda}_{x,\,z} = \lambda_{x,\,z}\, l, \quad \hat{\mathcal{K}}^{itf}_{xy,\,zy} = \mathcal{K}^{itf}_{xy,\,zy}\, l^2, \quad \hat{\mathcal{K}}_{yy} = \mathcal{K}_{yy}\, l^2. \tag{2.20}$$

It is important to emphasize that these coefficients are not empirical, but arise from the solution of auxiliary systems of equations solved in the $\hat{x}$- or $\hat{z}$-periodic elementary cell of fig. 1. The two terms, $\hat{\mathcal{K}}^{itf}_{xy}$ and $\hat{\mathcal{K}}^{itf}_{zy}$, are defined as *interface permeabilities* since, in analogy to Darcy's law in the bulk of the porous domain, they multiply the streamwise and spanwise gradients of the pressure in the expressions of $\hat{u}|_0$ and $\hat{w}|_0$; however, they differ from the corresponding *intrinsic permeability* components since, near the porous/free-fluid interface, grains are not as closely packed as in the bulk.

2.4 Evaluation of the macroscopic coefficients for selected geometries

Typical geometries of the inclusions used to construct the porous media under study are illustrated in figure 2; they are aligned in either the streamwise direction (substrates LC and LM) or the spanwise direction (substrates TC and TM), all satisfying a porosity $\theta = 0.5$, where θ is defined by considering a cubic unit cell within the porous region and evaluating the ratio of the volume occupied by the fluid to the total volume of the cell.

A simple method, similar to that followed by Ahmed *et al.* (2022*b*), is used to numerically evaluate the macroscopic coefficients in the effective boundary conditions. First, the systems governing the microscale fields $u_{11}^{\dagger}$ and $u_{33}^{\dagger}$ are solved on a microscopic domain with a sufficiently large value of y_∞ (like, for instance, the domain sketched in the left frame of figure 3). Second, the Navier's slip coefficients (λ_x, λ_z) are estimated by averaging $u_{11}^{\dagger}$ and $u_{33}^{\dagger}$, respectively, over the plane $y = 0$. The numerical values of the interface permeability coefficients can be computed via the following volume integrals:

$$\begin{aligned} \mathcal{K}_{xy}^{itf} &= \textstyle\int_{\mathcal{V}_0} u_{11}^{\dagger}\, \mathrm{d}V, \\ \mathcal{K}_{zy}^{itf} &= \textstyle\int_{\mathcal{V}_0} u_{33}^{\dagger}\, \mathrm{d}V, \end{aligned} \tag{2.21}$$

where $\mathcal{V}_0$ denotes the whole fluid's volume in the elementary cell below the interface chosen at $y = 0$. This renders the dimensionless Navier-slip and the interface permeability coefficients dependent, in general, on the geometry of the inclusions and the slip-velocity Reynolds number, Re_λ, which appears in the microscopic auxiliary systems. On the other hand, the medium permeability $\mathcal{K}_{yy}$ is intrinsic to the geometry of the porous region, where the velocity level is much smaller than u_{slip} and the inertial effects are thus negligible; $\mathcal{K}_{yy}$ can be estimated by solving a Stokes system on a triply-periodic cell of the porous domain, imposing unit forcing along y, and evaluating the superficial average of the corresponding microscopic field over that cell (Mei & Vernescu, 2010).

Transverse ($\hat{z}$-elongated) and longitudinal ($\hat{x}$-elongated) inclusions allow for further simplification of the microscopic, auxiliary problems, by setting either $\partial/\partial x_3$ or $\partial/\partial x_1$ to zero, respectively, yielding two-dimensional systems of equations. For the case of spanwise-elongated inclusions, we get the following two systems of interest at the leading order:

$$\begin{cases} \partial_1 u_{11}^{\dagger} + \partial_2 u_{21}^{\dagger} = 0, \\ -\partial_1 p_1^{\dagger} + \partial_1^2 u_{11}^{\dagger} + \partial_2^2 u_{11}^{\dagger} = Re_\lambda\, \partial_1 u_{11}^{\dagger}, \\ -\partial_2 p_1^{\dagger} + \partial_1^2 u_{21}^{\dagger} + \partial_2^2 u_{21}^{\dagger} = Re_\lambda\, \partial_1 u_{21}^{\dagger}, \\ \left(\partial_2 u_{11}^{\dagger} + \partial_1 u_{21}^{\dagger}\right)\Big|_{x_2 = y_\infty} = 1, \\ \left(-p_1^{\dagger} + 2\partial_2 u_{21}^{\dagger}\right)\Big|_{x_2 = y_\infty} = 0, \end{cases} \tag{2.22}$$

and

$$\begin{cases} \partial_1^2 u_{33}^{\dagger} + \partial_2^2 u_{33}^{\dagger} = Re_\lambda\, \partial_1 u_{33}^{\dagger}, \\ \left(\partial_2 u_{33}^{\dagger}\right)\Big|_{x_2 = y_\infty} = 1. \end{cases} \tag{2.23}$$

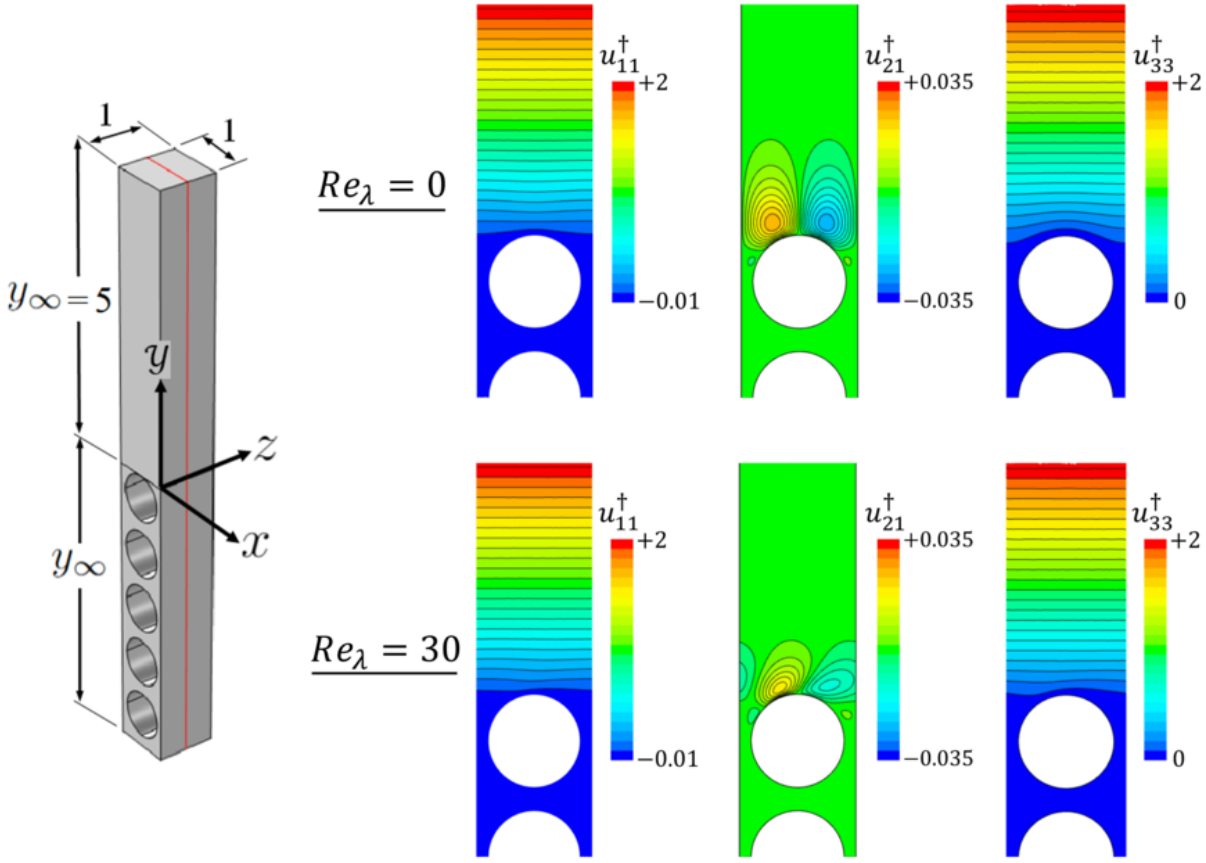

Figure 3: Contours of the microscopic variables $u_{11}^\dagger$, $u_{21}^\dagger$, and $u_{33}^\dagger$ at (top) $Re_\lambda = 0$ and (bottom) $Re_\lambda = 30$, shown over an $x - y$ plane for the case of spanwise-elongated cylinders of porosity $\theta = 0.5$. Close-ups of the contours near the fluid-porous interface are presented, while the typical domain considered in the simulations is shown in the left frame.

The numerical solutions of the previous systems under Stokes conditions and at $Re_\lambda = 30$ are shown in figure 3 for the case of transverse cylindrical inclusions, while the dependence of the macroscopic coefficients on Re_λ is displayed in figure 4(a) for the substrates TC and TM. A preliminary estimation of the value of the slip velocity can be obtained from the first-order term in the effective boundary condition of U, equation (2.18a), which may be recast in terms of the wall distance in viscous units ($Y^+ = YRe_{\tau(\mathcal{M})}$) and the mean velocity, already normalized by $u_{\tau(\mathcal{M})}$ and hence from now on indicated as $\overline{U}^+$, as follows:

$$\overline{U}^+\Big|_{Y=0} \approx \lambda_x^+ \frac{\partial \overline{U}^+}{\partial Y^+}\bigg|_{Y=0}, \tag{2.24}$$

where $\lambda_x^+ = \dfrac{\rho u_{\tau(\mathcal{M})} \hat{\lambda}_x}{\mu} = \epsilon Re_{\tau(\mathcal{M})} \lambda_x$. Provided the roughness maintains a sufficiently small amplitude so that the velocity gradient $\dfrac{\partial \overline{U}^+}{\partial Y^+}\Big|_{Y=0}$ at the virtual wall remains close

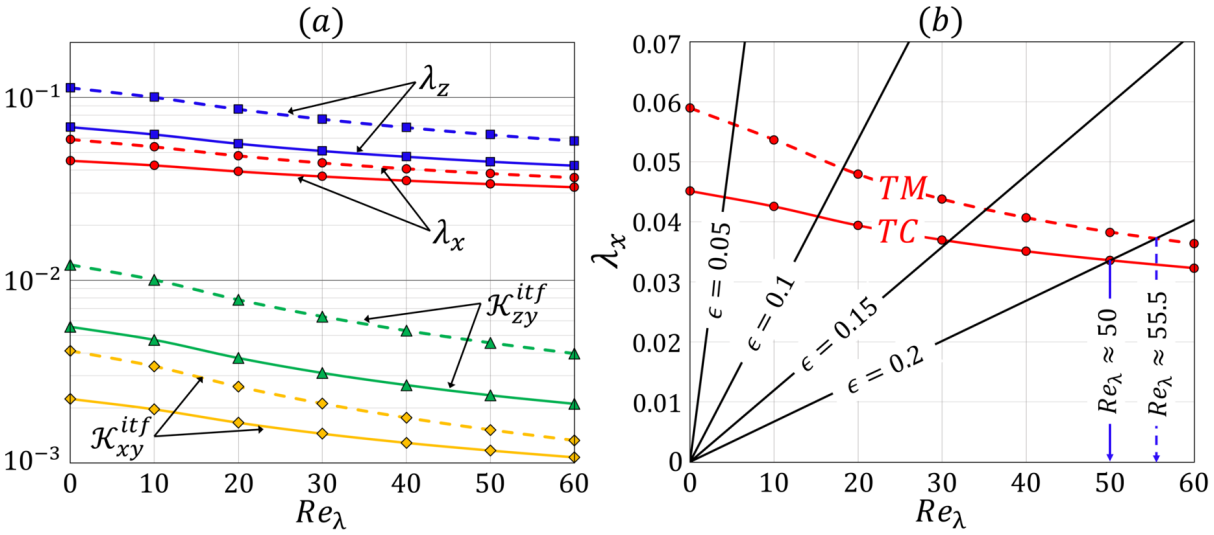

Figure 4: Behaviors of the homogenization model parameters. Frame (a) displays results of the closure problems for the Navier-slip and interface permeability coefficients as functions of Re_λ for the porous substrates TC (solid lines) and TM (dashed lines). In panel (b), the linear relation (2.26) between λ_x and Re_λ is plotted (black lines) for four values of ϵ, fixing $Re_{\tau(\mathcal{M})} = 193$, in order to evaluate Re_λ at the intersection points.

to 1, (2.24) simplifies to a Dirichlet boundary condition, i.e.

$$\overline{U}^+\Big|_{Y=0} = \frac{\hat{u}_{slip}}{u_{\tau(\mathcal{M})}} \approx \epsilon Re_{\tau(\mathcal{M})}\lambda_x, \tag{2.25}$$

which means that the slip-velocity Reynolds number can be written as

$$Re_\lambda = \frac{\rho \hat{u}_{slip}\ell}{\mu} = \frac{\rho u_{\tau(\mathcal{M})}\ell}{\mu}\epsilon Re_{\tau(\mathcal{M})}\lambda_x = \epsilon^2 Re^2_{\tau(\mathcal{M})}\,\lambda_x. \tag{2.26}$$

With $\lambda_x = \dfrac{Re_\lambda}{\epsilon^2 Re^2_{\tau(\mathcal{M})}}$, a linear relation between λ_x and Re_λ can be drawn for different values of ϵ, at the fixed value of the friction Reynolds number, $Re_{\tau(\mathcal{M})} = 193$; cf. figure 4(b). The value of Re_λ at the intersection point is evaluated as shown in figure 4(b), yielding as an immediate consequence all the macroscopic coefficients at this value; table 1 reports all coefficients for ϵ ranging from 0.05 (subscript 5) to 0.2 (subscript 20).

Streamwise-elongated inclusions (substrates LC and LM) represent a special case since inertial effects at the microscale level disappear as a consequence of setting $\partial/\partial x_1$ to zero in the auxiliary systems (Luchini *et al.*, 1991); as such, the macroscopic coefficients are independent of Re_λ. The coefficients for these substrates are directly available by revisiting the results for TC and TM, at $Re_\lambda = 0$, and simply switching the streamwise and spanwise coordinates.

Table 1: Values of the macroscopic coefficients for the sixteen porous substrates considered in the present study.

Substrate	Re_λ (intersection)	Dimensionless macroscopic coefficients				
		λ_x	λ_z	$\mathcal{K}_{xy}^{itf}$	$\mathcal{K}_{zy}^{itf}$	$\mathcal{K}_{yy}$
TC_5	4.1	0.0440	0.0663	0.0021	0.0052	0.0018
TC_{10}	15.2	0.0409	0.0591	0.0018	0.0042	0.0018
TC_{15}	30.9	0.0368	0.0506	0.0014	0.0031	0.0018
TC_{20}	50.0	0.0336	0.0445	0.0012	0.0023	0.0018
LC_{5-20}	Any	0.0688	0.0451	0.0056	0.0022	0.0018
TM_5	5.3	0.0562	0.1062	0.0037	0.0110	0.00012
TM_{10}	18.2	0.0489	0.0888	0.0028	0.0082	0.00012
TM_{15}	35.3	0.0421	0.0721	0.0019	0.0058	0.00012
TM_{20}	55.5	0.0372	0.0599	0.0014	0.0042	0.00012
LM_{5-20}	Any	0.1130	0.0590	0.0121	0.0041	0.00012

3 THE MACROSCALE PROBLEMS

For the direct numerical simulations of the macroscale problem, considering the turbulent channel flow over different porous substrates, the computational domain, the mesh/time step specifications, and the numerical scheme are the same as in Ahmed *et al.* (2022*b*). It is appropriate to provide further details on how the transpiration boundary condition (2.19b) is enforced in the numerical code; they are given in Appendix A.

3.1 Validation of the model

The applicability of the upscaling approach followed is assessed here by considering the turbulent flow ($Re_{\tau(\mathcal{M})} = 193$) in a channel delimited from the bottom ($Y \leq 0$) by the substrate TC_{20} (transverse cylinders, $\epsilon = 0.2$), and validating sample results of the homogenized simulation, based on the effective boundary conditions (2.18a–2.18c) with the macroscopic coefficients given in Table 1, against a classical fine-grained simulation. The mesh requirements, and thus the numerical cost, of the latter are much higher since it needs to resolve the seepage flow in the bulk of the porous domain and to account for the interactions occurring across the interfacial region, where significant ejection and sweep events take place (cf. figure 5).

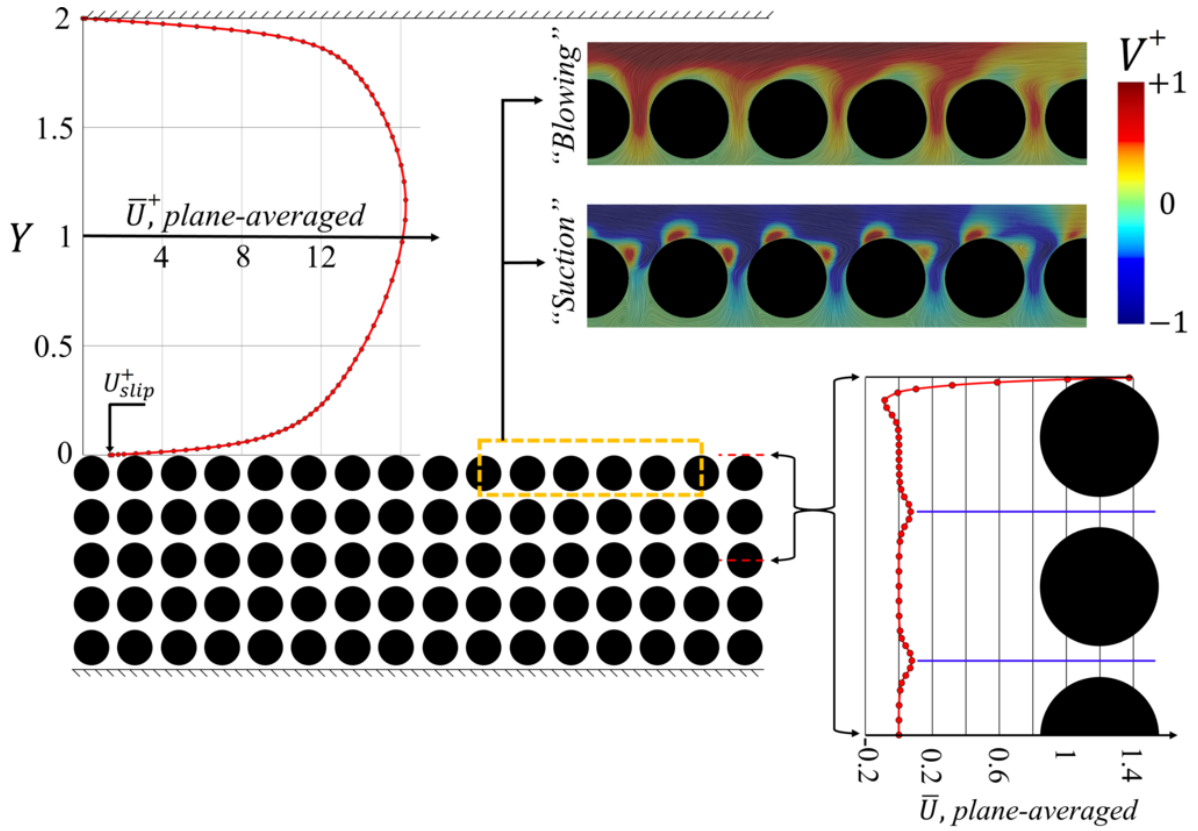

Figure 5: Full feature-resolving simulation of the coupled flow problem including the flow through and the turbulent flow over the porous substrate TC_{20} at $Re_{\tau(\mathcal{M})} = 193$: profiles of the X-Z-averaged mean velocity across the free-fluid region and closely below the fluid-porous interface are plotted. Instantaneous distributions (examples) of the interface-normal velocity component, V^+, captured during "*suction*" and "*blowing*" events are also presented.

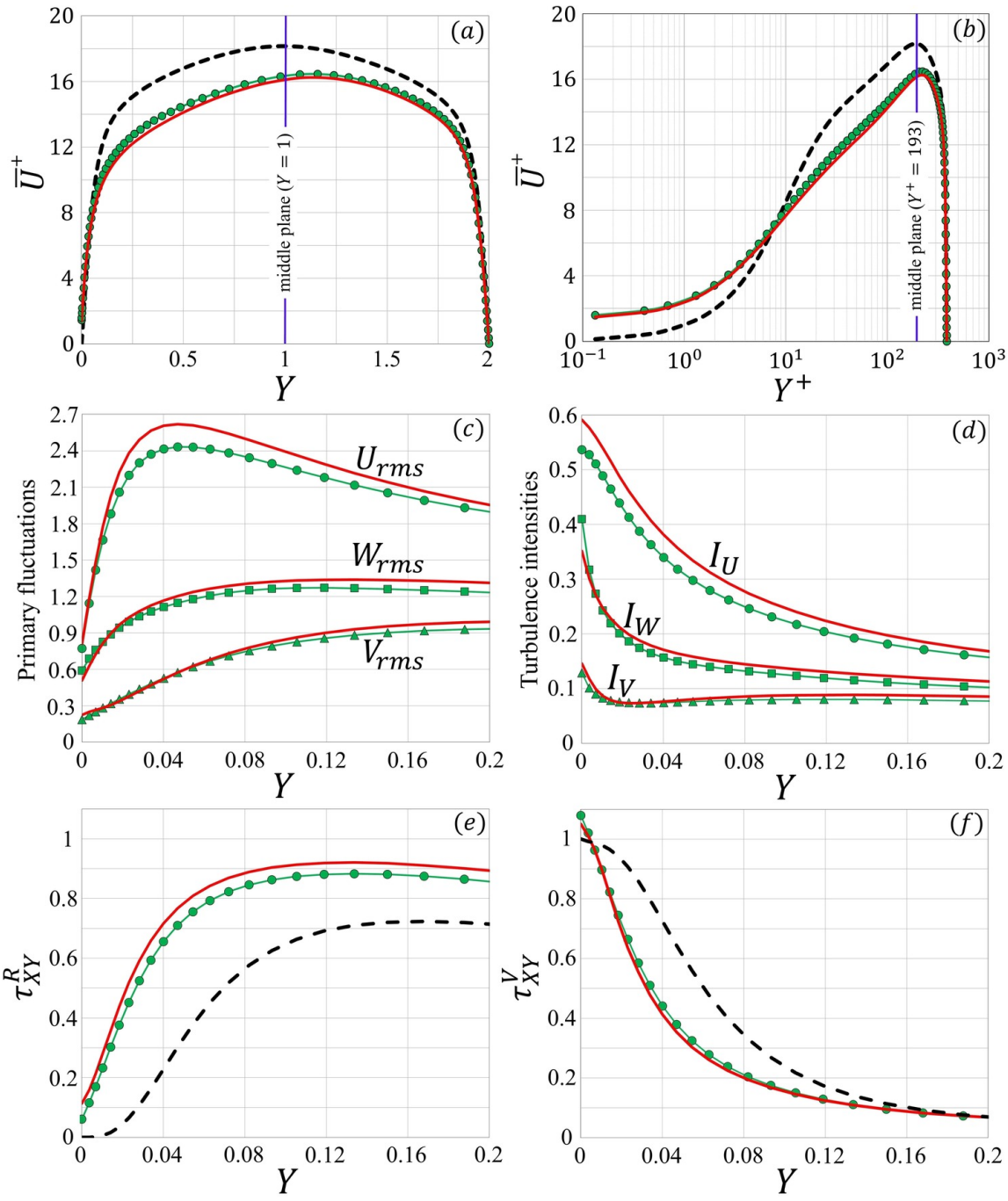

Figure 6: Turbulent channel flow ($Re_{\tau(\mathcal{M})} = 193$) over the porous substrate TC_{20}: predictions of the homogenized model, indicated by green lines with filled symbols, for (*a, b*) the mean velocity profile across the channel and for the near-interface distributions of (*c*) the root-mean-squares of the turbulent fluctuations in the three velocity components, (*d*) the turbulence intensities, and (*e, f*) the Reynolds/viscous shear stresses are validated against results of the full simulation (red lines). The dashed black profiles refer to the corresponding smooth, impermeable channel case.

The results in the free-fluid region are presented and compared (homogenization-based vs. fine-grained) in figures 6 and 7, in terms of the following dimensionless parameters: the mean velocity, $\overline{U}^+$; the root-mean-square values (r.m.s.) of the fluctuations in the velocity components, $(U_{rms}, V_{rms}, W_{rms}) = (\overline{U'U'}^{1/2}, \overline{V'V'}^{1/2}, \overline{W'W'}^{1/2})$ where the turbulent fluctuations are defined as $U_i' = U_i^+ - \overline{U}_i^+$; the intensity of the fluctuations, $(I_U, I_V, I_W) = (\frac{U_{rms}}{\overline{U}^+}, \frac{V_{rms}}{\overline{U}^+}, \frac{W_{rms}}{\overline{U}^+})$; the Reynolds shear stress, $\tau_{XY}^R = -\overline{U'V'}$; the viscous shear stress, $\tau_{XY}^V = \frac{1}{Re_{\tau(\mathcal{M})}}\frac{\partial \overline{U}^+}{\partial Y}$; and the production rate of the turbulent kinetic energy, $P_T = \frac{-1}{Re_{\tau(\mathcal{M})}}\overline{U_i'U_j'}\frac{\partial \overline{U}_i^+}{\partial X_j}$. While figure 6 focuses on the validation of the present model with the effective boundary conditions of the three velocity components imposed at $Y = 0$, figure 7 shows, in addition, the corresponding macroscopic results when the interface-normal velocity component is suppressed (i.e., $V\big|_{Y=0} = 0$) and only the in-plane slip velocities are applied; this is important since it highlights the need of accounting for transpiration at the virtual boundary (Bottaro, 2019; Lācis *et al.*, 2020).

From inspection of figure 6, it is clear that the model captures well the trends of the mean velocity and the turbulence statistics displayed. The velocity profile can be analyzed in terms of the slip velocity, $U_{slip}^+ = \overline{U}^+\big|_{Y=0}$; the shift in the intercept of the logarithmic velocity profile, ΔU^+ (taking the smooth channel case as a reference for the measurement and averaging the shift over the region $30 \lesssim Y^+ \lesssim 120$); the percentage change in the bulk (channel-averaged) velocity through the free-fluid region, $\Delta U_{ch}^+\%$ (taking the bulk velocity in a fully smooth channel, $U_{ch}^+ \approx 15.69$, as a reference); and the corresponding percentage change in skin-friction coefficient, $\Delta C_f\%$ (taking the smooth-channel value, $C_f = 2/(U_{ch}^+)^2 \approx 0.00813$, as a reference). The analysis performed here shows that, for the turbulent flow over the perturbed boundaries considered, the log-law is still valid (over $30 \lesssim Y^+ \lesssim 120$), yet it is shifted (relative to the one for a smooth wall) by ΔU^+ such that the logarithmic profile reads

$$\overline{U}^+ = \frac{1}{\kappa}\ln(Y^+) + B + \Delta U^+, \tag{3.1}$$

where κ is the von Kármán constant and B is the intercept of the logarithmic profile for the flow over a corresponding smooth wall. Based on (3.1), if $\Delta U^+ < 0$ (respectively $\Delta U^+ > 0$), the logarithmic profile is shifted downwards (upwards), and in general the skin-friction drag increases (decreases); this is consistent with the definition of the roughness function, ΔU^+ adopted by Gómez-de Segura & García-Mayoral (2019), Ibrahim *et al.* (2021), and Khorasani *et al.* (2022, 2024), which differs in sign from that originally introduced by Hama (1954) and Clauser (1954). According to (3.1), $\Delta U^+ < 0$ is generally accompanied by $\Delta U_{ch}^+\% < 0$ and $\Delta C_f\% > 0$. The full feature-resolving simulation for the case chosen for validation (TC_{20}) yields $(U_{slip}^+, \Delta U^+, \Delta U_{ch}^+\%, \Delta C_f\%) \approx (1.37, -2.76, -12.2\%, +29.6\%)$, while the values obtained from the complete homogenized simulation are respectively $(1.44, -2.33, -10.3\%, +24.4\%)$; a decrease in flow rate and, therefore, an increase in skin-friction coefficient is realized in both simulations. Moreover, the model predictions for the r.m.s. fluctuations of the velocity components at the

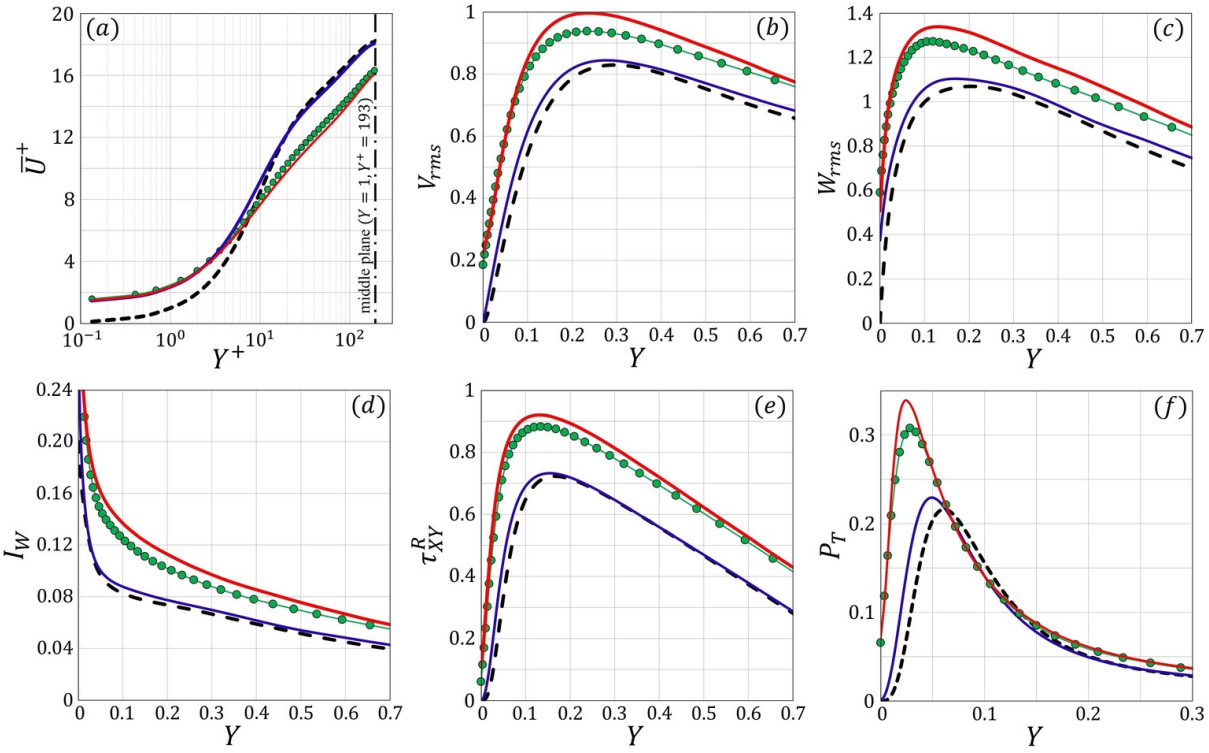

Figure 7: Distribution of the mean velocity (a) and behaviors of quantities of interest related to turbulence statistics $(b–f)$ over the porous substrate TC_{20}: predictions of the homogenized simulation when the effective boundary conditions of the three velocity components are imposed (green lines with filled circles) or when transpiration is neglected (blue lines) are validated against results of the fine-grained simulation (red lines), while the dashed profiles are related to the smooth, impermeable channel case.

fictitious interface ($Y = 0$) match well the results of the full simulation and deviate significantly from zero. In general, the accuracy of the macroscopic model is reasonable taking into account that the value of $\epsilon = 0.2$ ($\ell^+ \approx 40$) related to the porous substrate chosen for validation (TC_{20}) is rather large, meaning that microscopic and macroscopic length scales do not differ widely. On the other hand, it is obvious from figure 7 that the comparison with the fine-grained simulation is not satisfactory when the transpiration-free model is applied, where the mechanism of drag increase is idle, ΔU^+ is close to 0, and the trend of the turbulence statistics next to the fictitious boundary is similar to that of a smooth, impermeable channel.

3.2 Case studies: results and discussion

Numerical simulations were run for the channel flow over the different porous substrates (*TC*, *LC*, *TM*, *LM*), with four values of ϵ tested for each ($\epsilon = 0.05, 0.1, 0.15, 0.2$). The macroscopic model already validated was employed to study the sixteen problems under consideration, with the Oseen-based upscaled coefficients contributing to the effective boundary conditions available in table 1. The main results are presented and discussed below.

3.2.1 *Mean velocity and skin-friction drag*

In table 2, the pitch distance and the macroscopic coefficients for each porous pattern are expressed in wall units based on the velocity scale $u_{\tau(\mathcal{M})}$; they are defined by

$$\ell^+ = \frac{\rho\, u_{\tau(\mathcal{M})}\, \ell}{\mu} = \epsilon Re_{\tau(\mathcal{M})}, \tag{3.2a}$$

$$\lambda_x^+ = \frac{\rho\, u_{\tau(\mathcal{M})}\, \hat{\lambda}_x}{\mu} = \epsilon Re_{\tau(\mathcal{M})}\lambda_x, \quad \lambda_z^+ = \epsilon Re_{\tau(\mathcal{M})}\lambda_z, \tag{3.2b}$$

$$\mathcal{K}_{xy}^{itf,+} = \epsilon^2 Re_{\tau(\mathcal{M})}^2 \mathcal{K}_{xy}^{itf}, \quad \mathcal{K}_{zy}^{itf,+} = \epsilon^2 Re_{\tau(\mathcal{M})}^2 \mathcal{K}_{zy}^{itf}, \quad \mathcal{K}_{yy}^{+} = \epsilon^2 Re_{\tau(\mathcal{M})}^2 \mathcal{K}_{yy}. \tag{3.2c}$$

Values of the major quantities related to the behavior of mean velocity through the free-fluid region are also listed in the table (refer to the definitions in Section 3.1). The most significant finding is that reduction of the skin-friction drag coefficient (negative values of $\Delta C_f\%$, associated with positive ΔU^+ and $\Delta U_{ch}^+\%$) is attainable only by the porous substrates formed by longitudinal inclusions (*LC* and *LM*), those characterized by streamwise-preferential slip lengths and interface permeabilities ($\lambda_x^+ > \lambda_z^+$, $\mathcal{K}_{xy}^{itf,+} > \mathcal{K}_{zy}^{itf,+}$). Such a favorable influence (up to 5% reduction in C_f) takes place exclusively at relatively small values of ℓ^+, a behavior analogous to that exhibited by riblets (Bechert & Bartenwerfer, 1989; Garcia-Mayoral & Jiménez, 2011; Endrikat *et al.*, 2021*a*,*b*; Wong *et al.*, 2024). On the other hand, permeable beds consisting of transverse grains yield only drag increase, and this becomes more pronounced with ℓ^+. For comparison purposes, the

Table 2: Values of the macroscopic coefficients characterizing the different configurations considered for the porous substrate, estimated in wall units with $Re_{\tau(\mathcal{M})} = 193$ and ϵ varied from 0.05 (subscript 5) to 0.2 (subscript 20). Major results are presented, with the normalization based on $u_{\tau(\mathcal{M})}$.

Substrate	ℓ^+	**Model coefficients**					**Sample results**			
		λ_x^+	λ_z^+	$\mathcal{K}_{xy}^{itf,+}$	$\mathcal{K}_{zy}^{itf,+}$	$\mathcal{K}_{yy}^+$	U_{slip}^+	ΔU^+	$\Delta U_{ch}^+\%$	$\Delta C_f\%$
Smooth	0	0	0	0	0	0	0	0	0	0
TC_5	9.7	0.43	0.64	0.20	0.49	0.17	0.43	−0.33	−1.1%	+2.1%
TC_{10}	19.3	0.79	1.14	0.67	1.57	0.68	0.83	−0.77	−3.2%	+6.7%
TC_{15}	29.0	1.07	1.46	1.20	2.57	1.53	1.14	−1.55	−6.4%	+14.2%
TC_{20}	38.6	1.30	1.72	1.74	3.49	2.72	1.44	−2.33	−10.3%	+24.4%
LC_5	9.7	0.66	0.44	0.52	0.21	0.17	0.66	+0.15	+1.1%	−2.1%
LC_{10}	19.3	1.33	0.87	2.07	0.84	0.68	1.33	+0.08	+0.9%	−1.9%
LC_{15}	29.0	1.99	1.31	4.66	1.88	1.53	2.05	−0.54	−1.4%	+2.8%
LC_{20}	38.6	2.66	1.74	8.29	3.34	2.72	2.87	−1.63	−6.7%	+15.0%
TM_5	9.7	0.54	1.03	0.35	1.03	0.01	0.56	−0.61	−2.3%	+4.7%
TM_{10}	19.3	0.94	1.71	1.03	3.06	0.05	1.02	−1.38	−5.5%	+12.0%
TM_{15}	29.0	1.22	2.09	1.62	4.84	0.10	1.36	−2.09	−9.0%	+20.9%
TM_{20}	38.6	1.44	2.31	2.10	6.29	0.18	1.61	−2.56	−11.3%	+27.0%
LM_5	9.7	1.09	0.57	1.13	0.38	0.01	1.07	+0.33	+1.9%	−3.7%
LM_{10}	19.3	2.18	1.14	4.52	1.53	0.05	2.15	+0.45	+2.6%	−5.0%
LM_{15}	29.0	3.27	1.71	10.17	3.44	0.10	3.36	−0.33	−0.4%	+0.7%
LM_{20}	38.6	4.36	2.28	18.08	6.12	0.18	4.48	−0.94	−2.9%	+6.1%

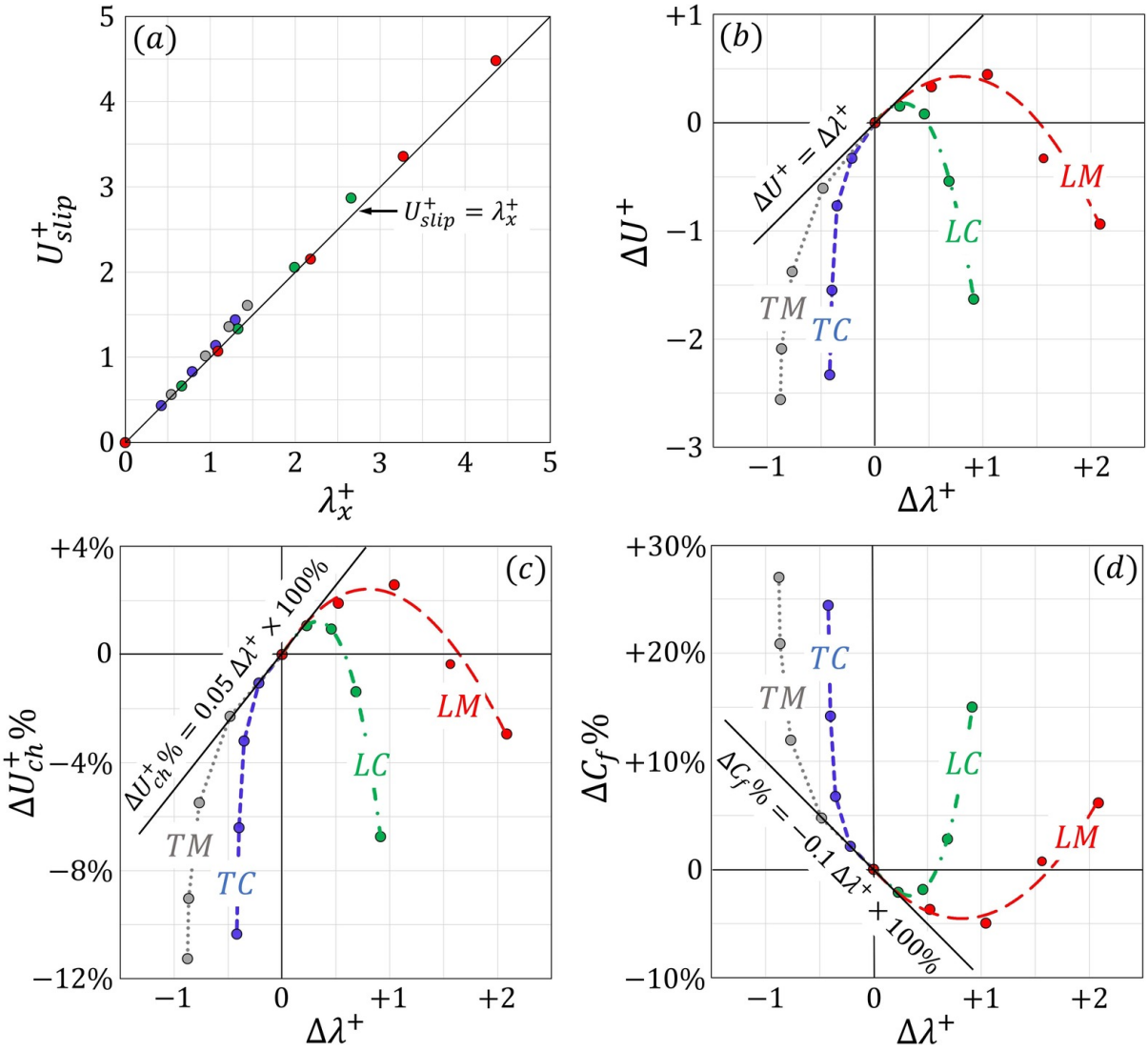

Figure 8: Dependence of (a) the slip velocity U^+_{slip} on λ^+_x and of (b) the shift of the logarithmic profile intercept ΔU^+, (c) the percentage change in the bulk mean velocity $\Delta U^+_{ch}\%$, and (d) the percentage change in the skin-friction coefficient $\Delta C_f\%$ on $\Delta\lambda^+ = \lambda^+_x - \lambda^+_z$, for turbulent channel flows ($Re_{\tau(\mathcal{M})} = 193$) over the four types of permeable beds under study; cf. table 2. Simple linear relations fitting the behavior of U^+_{slip} with λ^+_x and the performance of the other quantities at small values of $\Delta\lambda^+$ are presented.

results with the normalization based on the shear velocity of the bottom surface, $u_{\tau(\mathcal{B})}$, are given in Appendix B.

The behavior of the sample quantities reported on the right-hand side of table 2 for the four substrate configurations are graphically presented as function of the streamwise Navier-slip lengths in figure 8. It is important to highlight the following features with reference to the trends of the figure:

(i) As discussed in Section 2.4, the first-order term in the effective boundary condition of the streamwise velocity yields a slip velocity at the permeable interface $U^+_{slip} \approx \lambda^+_x \left.\dfrac{\partial \overline{U}^+}{\partial Y^+}\right|_{Y=0} \approx \lambda^+_x$. Figure 8($a$) shows that this linear dependence fits well with the results of the simulations, for the roughness amplitudes considered. Besides the omission of the higher-order term, the small percentage errors (up to $\approx 11\%$ in absolute value) may be attributed to the deviation of $\left.\dfrac{\partial \overline{U}^+}{\partial Y^+}\right|_{Y=0}$ from 1 because the parameters are expressed in wall units based on $u_{\tau(\mathcal{M})}$, and not the permeable-interface shear velocity $u_{\tau(\mathcal{B})}$. However, one can write $\left.\dfrac{\partial \overline{U}^+}{\partial Y^+}\right|_{Y=0} = \left.\dfrac{\partial \overline{U}^{+(\mathcal{B})}}{\partial Y^{+(\mathcal{B})}}\right|_{Y=0} \left[\dfrac{u_{\tau(\mathcal{B})}}{u_{\tau(\mathcal{M})}}\right]^2$, where $\left.\dfrac{\partial \overline{U}^{+(\mathcal{B})}}{\partial Y^{+(\mathcal{B})}}\right|_{Y=0} \approx 1$ (assuming that the Reynolds stress at $Y = 0$ is much smaller than the viscous stress), which results in the modified relation $U^+_{slip} \approx \left[\dfrac{u_{\tau(\mathcal{B})}}{u_{\tau(\mathcal{M})}}\right]^2 \lambda^+_x$. This expression enhances the predictions of the slip velocity (maximum error below 4%), yet it cannot be employed *a priori*, since the values of the shear-velocity ratio (table 3) are available only after numerical simulations have been conducted.

(ii) It has been found convenient to express the roughness function as the difference between the shifts of the virtual origins of mean and turbulent flows, i.e. $\Delta U^+ \approx \ell^+_U - \ell^+_{Turb.}$ (Wong *et al.*, 2024). For small protrusion heights, Luchini *et al.* (1991) have shown that ΔU^+ takes the form $\Delta U^+ = \lambda^+_x - \lambda^+_z = \Delta\lambda^+$; in the present settings, this assumption holds only up to $|\Delta\lambda^+| \lesssim 0.25$; cf. figure 8($b$).

(iii) To describe the trends of $\Delta C_f\% = \dfrac{C_f - C_{f,\,smooth}}{C_{f,\,smooth}} \times 100\%$, the classical relation $\Delta C_f\% = \dfrac{-\Delta U^+}{(2C_{f,\,smooth})^{-0.5} + (2\kappa)^{-1}} \times 100\%$ can be employed. With $\Delta U^+ = \Delta\lambda^+$, $C_{f,\,smooth} = 0.00813$, and the von Kármán constant $\kappa = 0.4$, the linear dependence $\Delta C_f\% \approx -0.1\,\Delta\lambda^+ \times 100\%$ is valid provided that $|\Delta\lambda^+|$ remains sufficiently small, as confirmed in figure 8(d). Under the same condition, it can be shown that $\Delta U^+_{ch}\% \approx -0.5\Delta C_f\% \approx +0.05\,\Delta\lambda^+ \times 100\%$, which matches well the results in figure 8(c).

(iv) It is notable that, at any fixed value of $\Delta\lambda^+$, the porous substrates LM and TM outperform the configurations LC and TC in terms of either maximizing the drag reduction or minimizing the drag increase. One possible justification is that the permeable beds constructed with modified cylinders (LM and TM) exhibit much smaller values of the medium permeability $\mathcal{K}_{yy}^+$ compared to those designed based on flat cylinders (LC and TC), as can be realized from table 2. This favorable feature enhances ΔU^+ by attenuating the transpiration velocity at the fictitious interface ($Y = 0$), an effect which can be perceived as a mitigation of the blowing and suction events. The influence of transpiration on ΔU^+ will be discussed in further detail in Section 3.3.

In figure 9, the different results are plotted against the pitch distance, ℓ^+. With regard to the slip velocity, assuming the simple linear relation $U_{slip}^+ \approx \lambda_x^+ = \ell^+\lambda_x$ and recalling the trends of λ_x from table 1, one can expect that U_{slip}^+ changes linearly with ℓ^+ for the porous beds LC and LM since λ_x is independent of ℓ^+ for these streamwise-elongated patterns, in contrast to the spanwise-elongated patterns TC and TM for which the coefficient λ_x decreases with the increase of ℓ^+. These expectations agree with the behaviors displayed in figure 9(a). For small ℓ^+ values, the quantities ΔU^+, $\Delta U_{ch}^+\%$, and $\Delta C_f\%$ are directly proportional to $\Delta\lambda^+ = \ell^+\Delta\lambda$, where $\Delta\lambda$ is equal to $\lambda_x - \lambda_z$. Table 1 implies that $\Delta\lambda\big|_{LM} > \Delta\lambda\big|_{LC} > \Delta\lambda\big|_{TC} > \Delta\lambda\big|_{TM}$ with the first two positive and the last two negative. For a small value of ℓ^+, one should therefore expect $\Delta U^+\big|_{LM} > \Delta U^+\big|_{LC} > \Delta U^+\big|_{TC} > \Delta U^+\big|_{TM}$ (and likewise for $\Delta U_{ch}^+\%$ and $-\Delta C_f\%$) with the substrate LM yielding the maximum drag reduction and TM resulting in the maximum drag increase; cf. figure 9(b–d). Departing from the viscous regime, it is found that the drag reduction attainable by LM and LC peaks at some value of ℓ^+ between 10 and 20. The performance of these porous substrates then degrades, yet drag reduction is still achievable until a threshold within $20 \lesssim \ell^+ \lesssim 30$ is reached, beyond which drag increase takes place. Gómez-de Segura *et al.* (2018) studied highly connected porous media with streamwise-preferential permeability and attributed the aforementioned behavior to the formation of drag-increasing spanwise-coherent rollers associated with a Kelvin-Helmholtz-like instability whose initiation is governed by the intrinsic permeability component $\mathcal{K}_{yy}^+$ of the medium.

3.2.2 *The mechanism of drag increase/reduction*

The influence of porous substrates on the near-interface turbulence is considered next. For sufficiently small values of ℓ^+, the wall texture alters the structure of turbulence merely by shifting down its virtual origin by a distance $\ell_{Turb.}^+ \approx \lambda_z^+$, whereas the effect is much more complicated beyond the viscous regime, especially with the increase in transpiration velocity. It is therefore useful to present and discuss some turbulence statistics of interest for the channel flow over selected porous beds of relatively large grain spacings/sizes (LM_{10}: longitudinal modified inclusions, $\ell^+ \approx 20$, the maximum drag re-

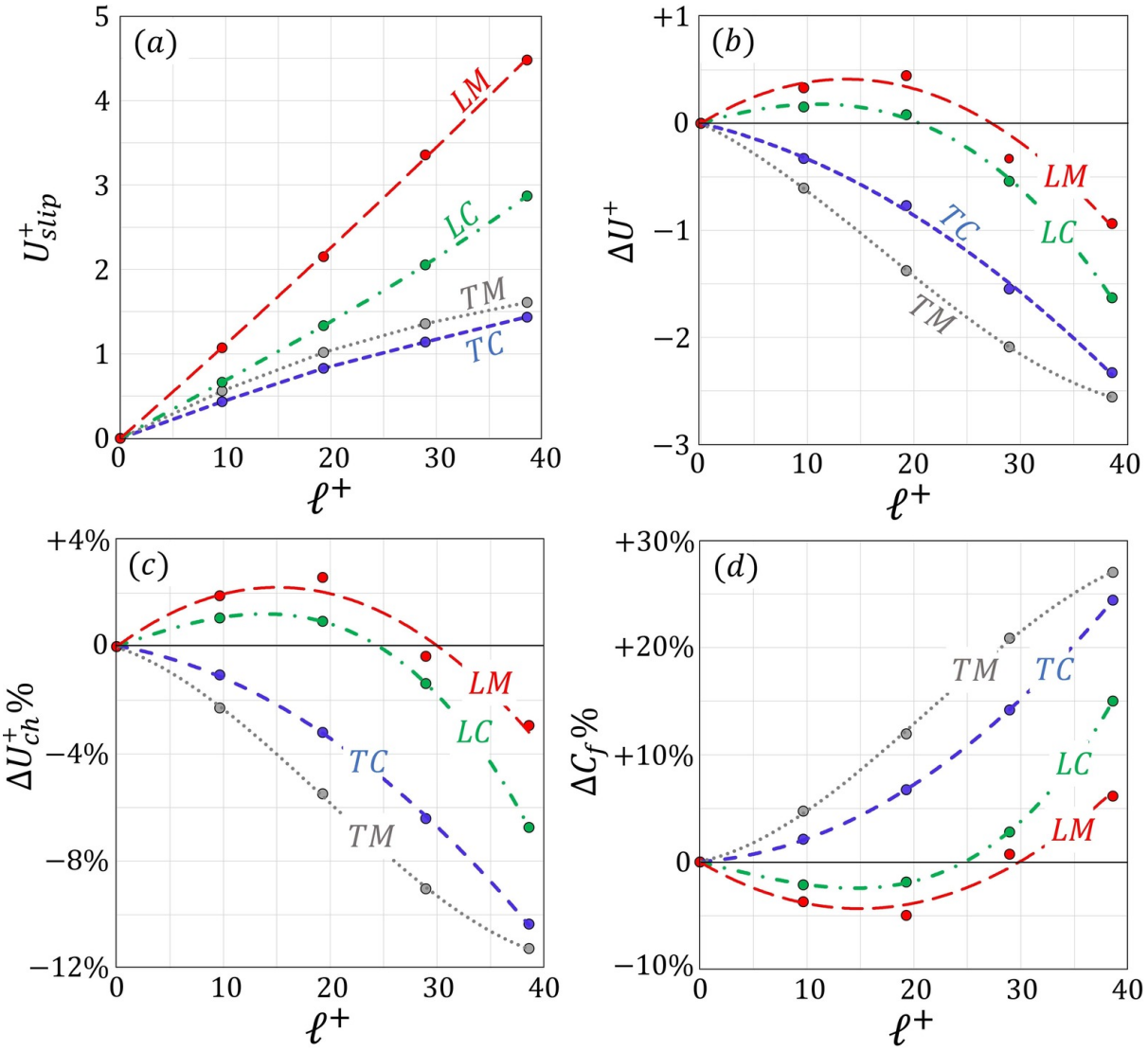

Figure 9: Dependence of major quantities characterizing the turbulent channel flow over the porous substrates under study on the pitch distance of the inclusions measured in wall units, $\ell^+ = \epsilon Re_{\tau(\mathcal{M})}$.

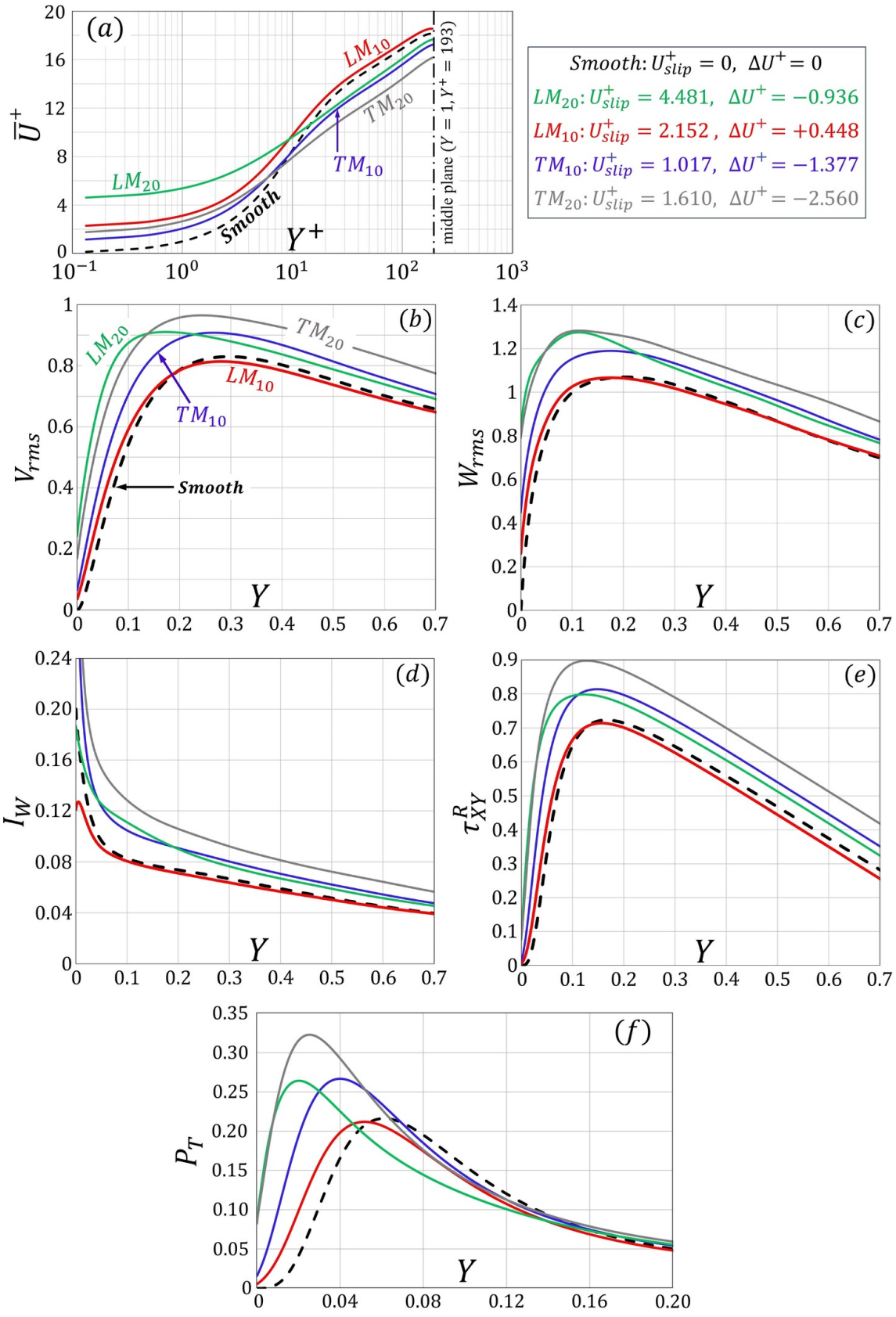

Figure 10: Predictions of the homogenization-based model for (a) the mean velocity profiles and (b–f) sample statistics for the channel flow ($Re_{\tau(\mathcal{M})} = 193$) over four different porous substrates.

duction reported; LM_{20}: longitudinal modified inclusions, $\ell^+ \approx 40$, drag increase; TM_{10}: transverse modified inclusions, $\ell^+ \approx 20$, drag increase; TM_{20}: transverse modified inclusions, $\ell^+ \approx 40$, the maximum drag increase reported). The velocity profiles are plotted in figure 10(a). The turbulence-characterizing quantities plotted in figure 10(b) are chosen since, as shown by Ahmed *et al.* (2022*b*), their behaviors near the porous/free-fluid interface can be linked to the favorable/adverse effects of the permeable boundaries on friction drag. With focus on the peak values of V_{rms}, W_{rms}, τ^R_{XY}, and P_T, and the distributions of I_W, it can be realized that the drag-reducing substrate (LM_{10}) yields results comparable to those in the reference case of turbulence over a smooth, impermeable wall; this applies also to the other drag-reducing patterns not considered in the figure, i.e. LM_5, LC_5, LC_{10}. Conversely, the drag-increasing ones result in intensified levels of these quantities. For instance, with TM_{20}, the peak values V_{rms}, τ^R_{XY}, and P_T are larger than the values in a smooth channel by about 16%, 24%, and 50%, respectively. The values of the quantities at the fictitious interface, $Y = 0$, are of particular interest in the present work and their correlations with ΔU^+ are explored in Section 3.3; it is evident from the figure that significant values of V_{rms} are obtained at the plane $Y = 0$, in particular when ℓ^+ is sufficiently large, an effect which would obviously be absent if transpiration were unaccounted for in the formulation of the model.

The quadrant analysis in figure 11 reveals details of the generation of the Reynolds stress, τ^R_{XY}, from the turbulent events taking place in the flow near the substrates LM_{10} and TM_{20}. In figure 11, the instantaneous distributions of (U', V') are displayed over the plane at $Y^+ \approx 1$, directly adjacent to the substrate-channel interface, and the plane at $Y^+ \approx 80$, well within the logarithmic layer. The phenomena can be classified into negative-production events (first and third quadrants, with $-U'V' < 0$) and positive-production ones (second and fourth quadrants, with $-U'V' > 0$). Eventually, the Reynolds stress generated from the sum of the positive contributions from the *ejection* (second quadrant, bursting of low-speed fluid) and the *sweep* (fourth quadrant, inrush of high-speed fluid) events at any Y^+ level is generally larger than that arising from the sum of the contributions of the other two quadrants. The production of turbulence is dominated by the sweep event in the close vicinity of the boundary (cf. figure 11(a, b)), while ejection is dominant away from the wall (cf. figure 11(c, d)). For a better understanding, the contributions from the four quadrants to the Reynolds shear stress at a given time instant, evaluated over different $X - Z$ planes up to $Y^+ \approx 80$, are plotted in figure 11(e, f); they are obtained by integrating the values of $-U'V'$ related to each of the quadrants, separately, over the area occupied by the specific event and using the overall area of the $X - Z$ plane ($= 2\pi \times \pi$) as a weight. It is notable that ejection becomes dominant beyond a threshold within $Y^+ = 12$–15. All the findings above agree qualitatively with the results by Kim *et al.* (1987) in a channel delimited by smooth, impermeable walls. From a quantitative perspective, the production of turbulence via both ejection and sweep is clearly intensified for case TM_{20} (the porous substrate of maximum drag increase) compared to the levels with LM_{10} (the substrate of largest drag reduction), at all the values of Y^+ considered, with the intensification exceeding 600% at the porous/free-fluid interface and ranging from 10–70% in the logarithmic region.

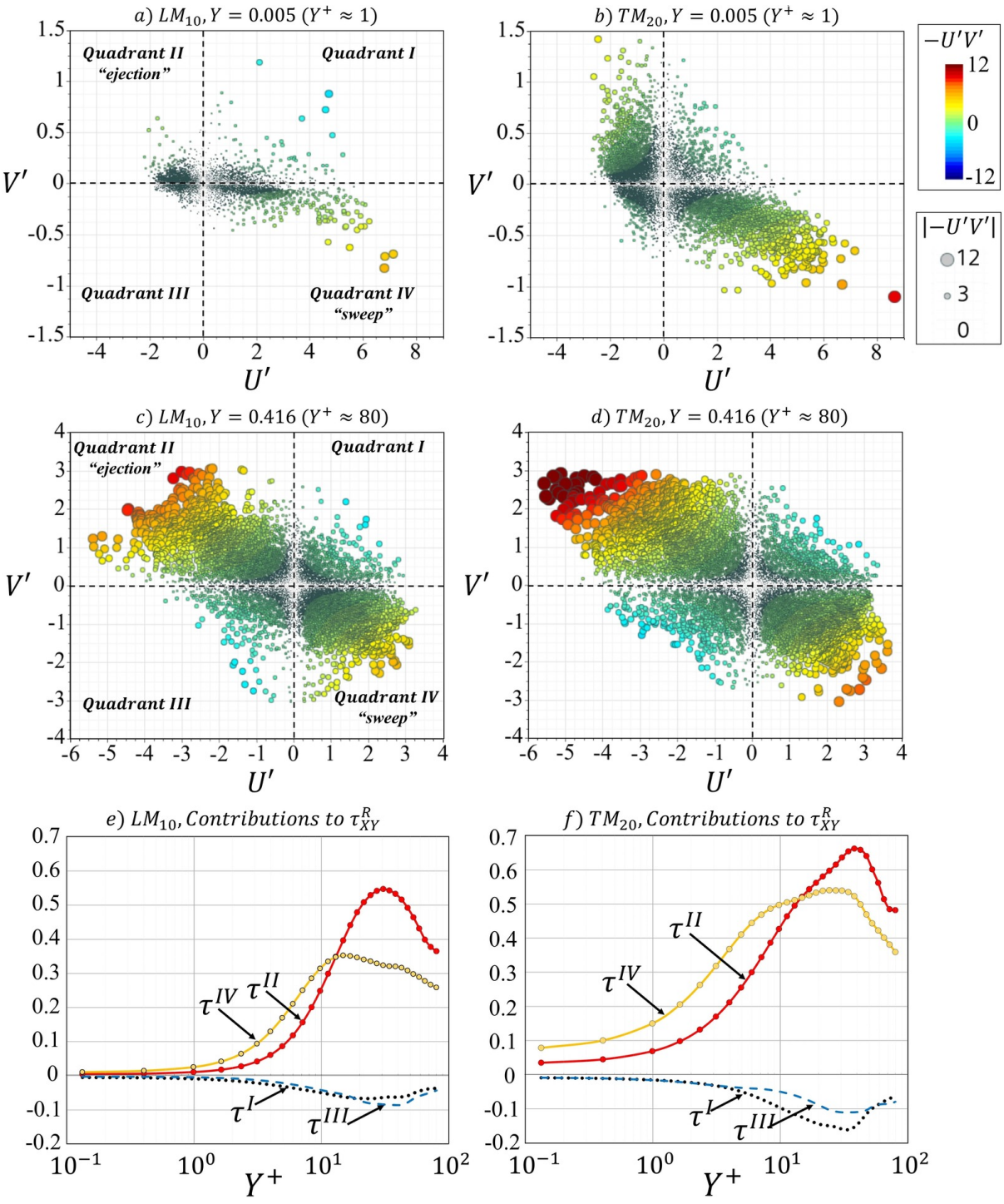

Figure 11: Quadrant analysis of the Reynolds shear stress, τ_{xy}^R, for turbulent channel flows ($Re_{\tau(\mathcal{M})} = 193$) over two different porous substrates (LM_{10} and TM_{20}). Instantaneous values of (U', V') throughout the planes at $Y = 0.005$ and $Y = 0.416$ (evaluated at all grid points) are shown in panels (a) to (d), while contributions to τ_{xy}^R from each quadrant are plotted in the bottom frames against $Y^+ = YRe_{\tau(\mathcal{M})}$ up to the centerline of the channel.

3.3 In pursuit of a correlation for ΔU^+ over porous/textured walls

We proceed from the earlier discussion on figure 10, concerning how the near-wall distributions of some turbulence-characterizing parameters can control the mechanism of drag reduction/increase over the permeable boundaries, to try here to explore the correlation between the roughness function ΔU^+ and the fictitious-interface values of quantities of particular interest: $\tilde{V}_{rms} = V_{rms}\big|_{Y=0}$, $\tilde{W}_{rms} = W_{rms}\big|_{Y=0}$, and $\tilde{\tau}^R_{XY} = \tau^R_{XY}\big|_{Y=0}$. Figure 12($a$–$c$) reveals that the dependence of ΔU^+ on $\tilde{V}_{rms}$ cannot be described by a universal function valid for all permeable boundaries; the same can be said for $\tilde{W}_{rms}$ and $\tilde{\tau}^R_{XY}$. Conversely, each configuration yields a unique relationship, and even the general trends differ when porous substrates of streamwise-preferential permeability (*LC* and *LM*, non-monotonic behavior) are compared with those consisting of spanwise-elongated grains (*TC* and *TM*, strictly monotonic decrease). To justify this, let us assume conditions corresponding to a small value of $\tilde{V}_{rms}$ fixed for the four patterns (e.g., $\tilde{V}_{rms} = 0.01$) and analyze the resulting ΔU^+. While a fixed value of $\tilde{V}_{rms}$ may imply that, for all the boundaries, the virtual origin of turbulence has the same shift from the $Y = 0$ plane (i.e., constant $\ell^+_{Turb.}$), the position of the virtual origin of the mean flow, $\ell^+_U \approx \lambda^+_x$, can significantly differ according to the value of the streamwise Navier-slip length, λ^+_x, for each wall, and, consequently, different values of the roughness function $\Delta U^+ = \ell^+_U - \ell^+_{Turb.}$ are obtained. In the search of a function displaying a universal behavior, we follow two separate paths.

The first path relies on analyzing the mean velocity profile, $\overline{U}^+(Y^+)$, over each of the permeable substrates to monitor the upward shifts of the velocity at matched Y^+ values, taking the profile over a smooth, impermeable wall as a reference (for instance, cf. figure 10(a)). Such a velocity shift is, by definition, equal to U^+_{slip} at $Y = 0$ and to ΔU^+ in the logarithmic region. Whether ΔU^+ is positive or negative, it is $U^+_{slip} > \Delta U^+$ for all textured boundaries (for $\ell^+ = 0$, the smooth, impermeable wall is retrieved, and the limit $U^+_{slip} = \Delta U^+ = 0$ is reached). The function $\mathcal{D} = U^+_{slip} - \Delta U^+ \geq 0$ can therefore be defined to indicate the depression in the velocity shift when moving from the wall to the logarithmic region; it is plotted against the turbulence parameters in figure 12(d–f). In the second path, we proceed from the fact that the approximation $\Delta U^+ = \Delta\lambda^+$ holds only for small surface roughness, while a further reduction in the value of the roughness function occurs with the increase of ℓ^+, i.e. $\Delta U^+ = \Delta\lambda^+ - \mathcal{F}$, with the newly defined function $\mathcal{F} \geq 0$. The behavior of $\mathcal{F}$ is shown in figure 12(g–i).

Both functions $\mathcal{D}$ and $\mathcal{F}$ increase monotonically with each of $\tilde{V}_{rms}$, $\tilde{W}_{rms}$, and $\tilde{\tau}^R_{XY}$, and it can be realized from figure 12(d–i) that, even from a quantitative point of view, general trends emerge. Eventually, the following fitting relationships can be proposed (together with their accuracy levels):

$$\mathcal{D} = 11.5 \times \left[\tilde{V}_{rms}\right]^{0.6}, \qquad NRMS_{error} \approx 11\%, \tag{3.3}$$

$$\mathcal{D} = 6 \times \tilde{W}_{rms}, \qquad NRMS_{error} \approx 13\%, \tag{3.4}$$

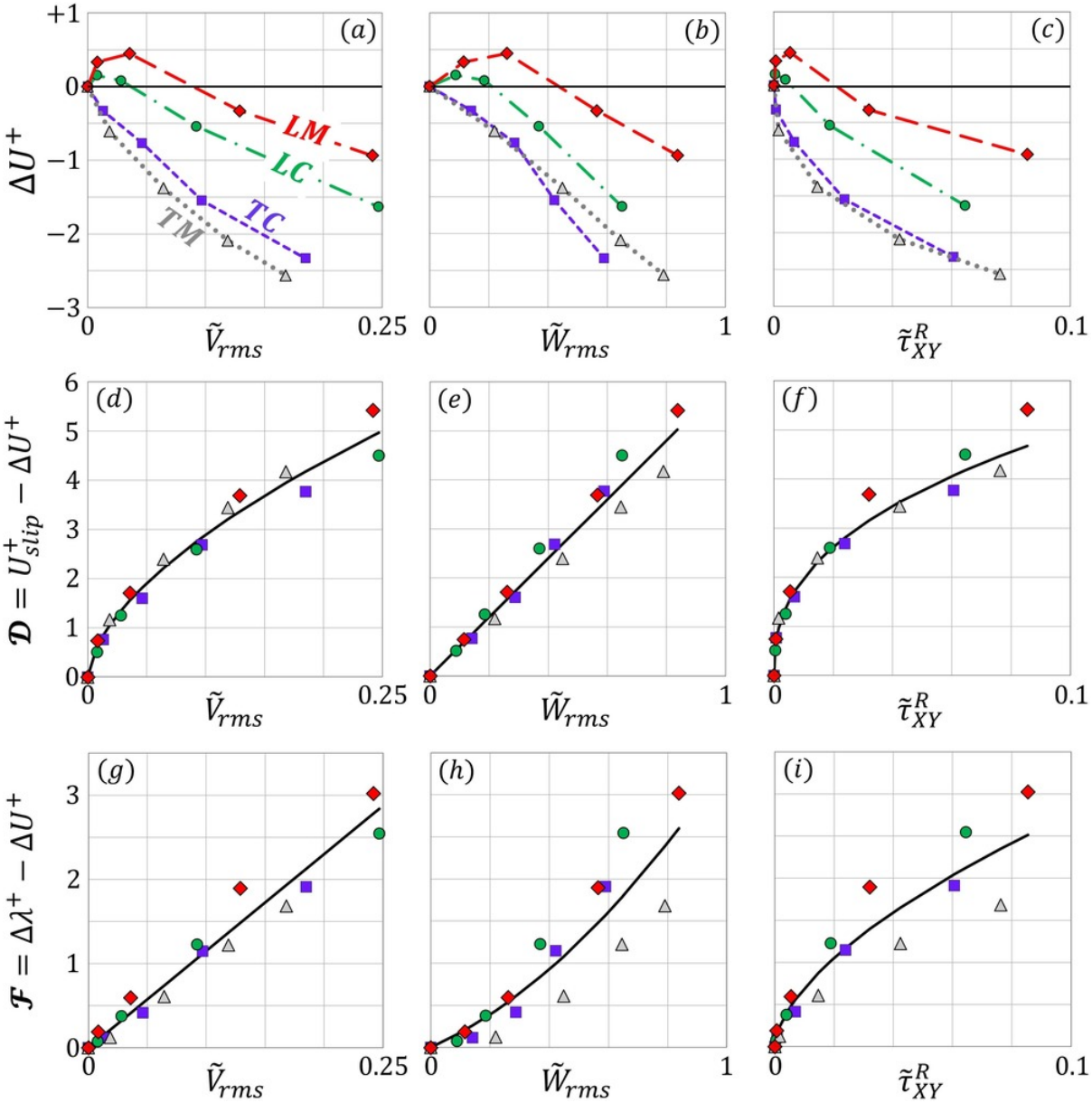

Figure 12: Dependence of ΔU^+ (top panels) and the related quantities $\mathcal{D}$ (middle panels) and $\mathcal{F}$ (bottom panels) on turbulence-characterizing parameters of interest measured at the fictitious interface (at $Y = 0$). The filled symbols indicate results of the homogenized simulations for turbulent flow over the four substrate configurations under study (cf. figure 2), with ℓ^+ varied for each pattern as described in Table 2, while the fitting relations (3.3–3.8) are plotted with solid lines in the middle and the bottom frames.

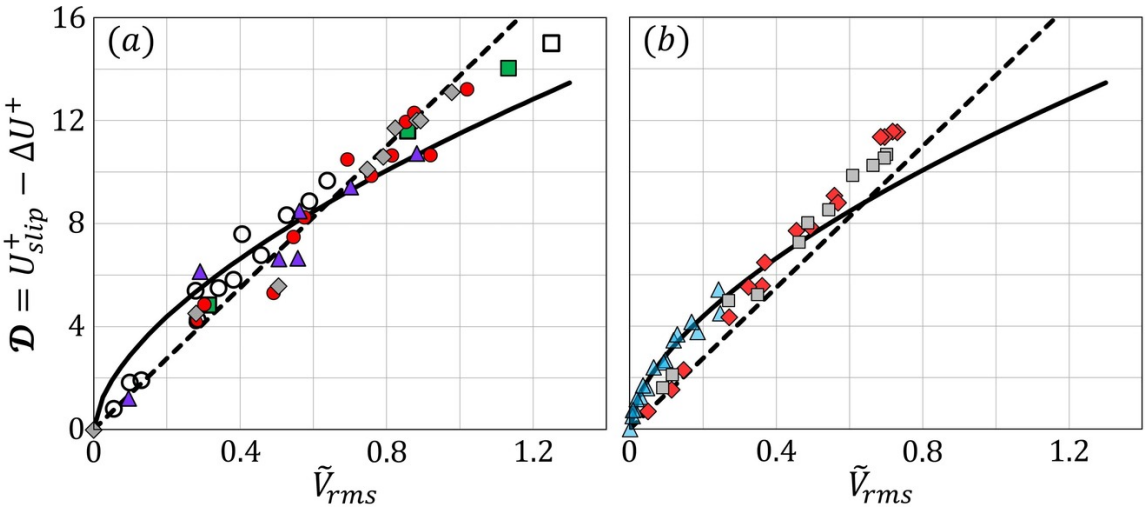

Figure 13: Values of the parameter $\mathcal{D}$ plotted against the r.m.s. of the turbulent fluctuations in the wall-normal velocity at the plane $Y = 0$. In panel (a), results from the literature for channels roughened with streamwise-elongated, spanwise-elongated, or three-dimensional elements are shown: blank square, Cheng & Castro (2002); red circles, Leonardi *et al.* (2003); purple triangles, Orlandi & Leonardi (2006); green squares, Burattini *et al.* (2008); gray diamonds, Orlandi & Leonardi (2008); blank circles, Hao & García-Mayoral (2024). In panel (b), the results of Hao & García-Mayoral (2024) for symmetric channels bounded by either deep (red diamonds) or shallow (gray squares) porous substrates are plotted, together with the values of the present homogenization-based simulations (light-blue triangles). Solid lines refer to correlation (3.3), while the linear relationship by Orlandi & Leonardi (2008) is plotted with dashed lines.

$$\mathcal{D} = 12.5 \times \left[\tilde{\tau}^R_{XY}\right]^{0.4}, \qquad NRMS_{error} \approx 11\%, \tag{3.5}$$

$$\mathcal{F} = 11.5 \times \tilde{V}_{rms}, \qquad NRMS_{error} \approx 18\%, \tag{3.6}$$

$$\mathcal{F} = 1.8 \times \left[\tilde{W}_{rms}\right]^2 + 1.6 \times \tilde{W}_{rms}, \qquad NRMS_{error} \approx 37\%, \tag{3.7}$$

$$\mathcal{F} = 11 \times \left[\tilde{\tau}^R_{XY}\right]^{0.6}, \qquad NRMS_{error} \approx 29\%, \tag{3.8}$$

where the normalized root-mean-square error, $NRMS_{error}$, is evaluated by dividing the conventional RMS_{error} by the mean value of either $\mathcal{D}$ or $\mathcal{F}$. The ranges of validity of the relations proposed are

$$0 \le \tilde{V}_{rms} \lesssim 0.25, \quad 0 \le \tilde{W}_{rms} \lesssim 0.85, \quad 0 \le \tilde{\tau}^R_{XY} \lesssim 0.085. \tag{3.9}$$

In the remainder of this section, we aim to demonstrate *(i)* that transpiration strongly controls the depression in the velocity shift over a wide range of textured boundaries and *(ii)* that correlating $\tilde{V}_{rms}$ to the macroscopic coefficients of the homogenization model permits the use of (3.3) and (3.6) for an *a priori* estimate of the roughness-function-related parameters $\mathcal{D}$ and $\mathcal{F}$.

Orlandi *et al.* (2003) demonstrated that the principal characteristics of the flow over a rough surface are closely related to the presence of wall-normal velocity distribution

at the interface between the protrusions and the overlying turbulent boundary layer. A more formal description of this dependence has been proposed by Orlandi *et al.* (2006) and Orlandi & Leonardi (2006) who found good correlation between the quantity $\mathcal{D} = U^+_{slip} - \Delta U^+$ and the r.m.s. fluctuations of the wall-normal velocity at the plane passing through the crests of the roughness elements. Later, Orlandi & Leonardi (2008) explored the relationship between $\mathcal{D}$ and $\tilde{V}_{rms}$ for walls with different textures, by collecting and plotting many results from the literature (Cheng & Castro, 2002; Leonardi *et al.*, 2003; Orlandi & Leonardi, 2006; Burattini *et al.*, 2008; Flores & Jiménez, 2006) together with new ones related to the flow over surfaces roughened with longitudinal/transverse bars or various three-dimensional patterns. They concluded their study proposing the correlation $\mathcal{D} = \dfrac{B}{\kappa}\,\tilde{V}_{rms}$, with B and κ as by (3.1). Most of the data considered by Orlandi & Leonardi (2008) in addition to the recent results by Hao & García-Mayoral (2024) are presented in figure 13(a); the strong correlation between $\mathcal{D}$ and $\tilde{V}_{rms}$ is evident, and the linear relationship by Orlandi & Leonardi (2008), plotted with $B = 5.5$ and $\kappa = 0.4$ is found to perform well, where $NRMS_{error}$ is below 12%. Interestingly, good correlation between $\mathcal{D}$ and $\tilde{V}_{rms}$ can also be realized in figure 13(b) for the turbulent flow over permeable boundaries, based on the values reported by Hao & García-Mayoral (2024) plotted next to the results of the present macroscopic DNSs; the $NRMS_{error}$ for Orlandi-Leonardi relationship is about 23%. With regard to the present correlation (3.3), the deviations are comparable to those reported above, with $NRMS_{error} \approx 14\%$ for the rough walls and $\approx 18\%$ for the porous boundaries, even for values of $\tilde{V}_{rms}$ much larger than the validity limit (3.9) of our simulations. Figure 13 thus confirms that $\tilde{V}_{rms}$ is a key parameter which controls the roughness function in the turbulent flow over rough/porous boundaries and that (3.3) performs well even for quite large values of $\tilde{V}_{rms}$. The major difficulty in putting (3.3), or Orlandi-Leonardi correlation, to practical use is that $\tilde{V}_{rms}$ is not available until a full simulation of the turbulent flow above a textured wall is conducted.

The crux of the matter is thus the search of a simplified expression for $\tilde{V}_{rms}$, as function of the macroscopic coefficients which permit to describe the near wall flow. After some efforts, we have found that the parameter Ψ defined as

$$\Psi = \left(\frac{\mathcal{K}^{itf,+}_{xy}}{\lambda^+_x} + \frac{\mathcal{K}^{itf,+}_{zy}}{\lambda^+_z} + \sqrt{\mathcal{K}^+_{yy}} \right) \left(\frac{\lambda^+_z}{\lambda^+_x} \right)^{0.25} \tag{3.10}$$

is well correlated to $\tilde{V}_{rms}$, as shown in figure 14. It is worth highlighting that (3.10) is inspired from the boundary condition for the transpiration velocity (2.19b): the parameters $\dfrac{\mathcal{K}^{itf,+}_{xy}}{\lambda^+_x}$ and $\dfrac{\mathcal{K}^{itf,+}_{zy}}{\lambda^+_z}$ appear when the streamwise/spanwise Navier-slip conditions $\left(\dfrac{\partial \hat{u}}{\partial \hat{y}} + \dfrac{\partial \hat{v}}{\partial \hat{x}}\right)\Big|_0 = \dfrac{\hat{u}|_0}{\hat{\lambda}_x}$ and $\left(\dfrac{\partial \hat{w}}{\partial \hat{y}} + \dfrac{\partial \hat{v}}{\partial \hat{z}}\right)\Big|_0 = \dfrac{\hat{w}|_0}{\hat{\lambda}_z}$ are substituted into the second and the third terms on the right hand side of (2.19b) and the equation is recast in wall units, while $\sqrt{\mathcal{K}^+_{yy}}$ quantifies the role of the intrinsic permeability for porous boundaries. The presence of $\dfrac{\lambda^+_z}{\lambda^+_x}$ in (3.10) permits to differentiate between walls of spanwise-preferential

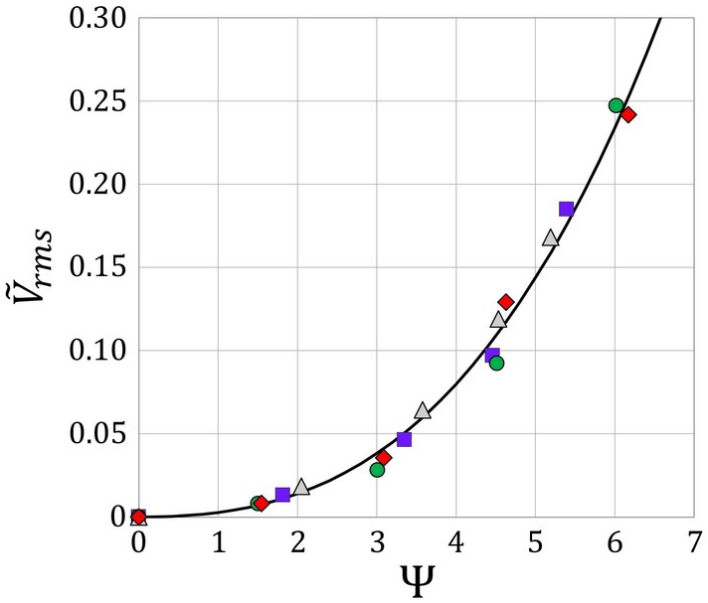

Figure 14: The r.m.s. of turbulent fluctuations in the transpiration velocity at $Y = 0$, plotted against the compound macroscopic parameter Ψ for the different porous patterns considered (same symbols as in figure 12). The solid line represents a third-order polynomial fitting.

slip ($\lambda_z^+ > \lambda_x^+$) and those exhibiting preferential streamwise slip ($\lambda_x^+ > \lambda_z^+$), and implies that, for the same values of $\dfrac{\mathcal{K}_{xy}^{itf,+}}{\lambda_x^+}$, $\dfrac{\mathcal{K}_{zy}^{itf,+}}{\lambda_z^+}$, and $\sqrt{\mathcal{K}_{yy}^+}$, relatively stronger transpiration is associated with the former wall patterns (e.g. substrates constructed with transverse inclusions). Based on the data plotted in figure 14, we propose the fitting equation

$$\tilde{V}_{rms} = 0.00075\,\Psi^3 + 0.002\,\Psi^2, \tag{3.11}$$

for which the $NRMS_{error}$ is less than 10%. Substituting (3.11) into (3.3) and (3.6), we finally obtain the following expressions for the roughness-function-related quantities:

$$\mathcal{D} = U_{slip}^+ - \Delta U^+ = 11.5 \times \left(0.00075\,\Psi^3 + 0.002\,\Psi^2\right)^{0.6}, \tag{3.12}$$

$$\mathcal{F} = \Delta\lambda^+ - \Delta U^+ = 11.5 \times \left(0.00075\,\Psi^3 + 0.002\,\Psi^2\right), \tag{3.13}$$

valid up to $\Psi \approx 6$. Estimates of $\mathcal{D}$ and $\mathcal{F}$ for the turbulent flow over a perturbed wall of given microstructure and given value of $\ell^+ = \epsilon Re_{\tau(\mathcal{M})}$ are thus available provided *(i)* ℓ^+ is lower than about 40, and *(ii)* outer layer similarity is maintained.

3.4 Can we make a-priori predictions?

It is useful to assess the accuracy of (3.12) and (3.13) for the turbulent flow over perturbed boundaries different from the porous ones based on which these correlations have been

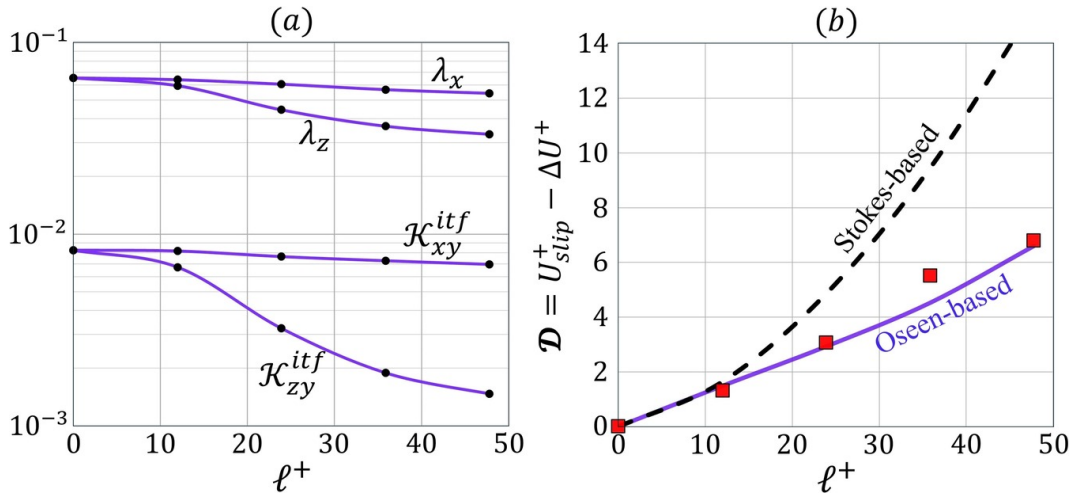

Figure 15: Turbulent flow ($Re_\tau \approx 180$) in a symmetric channel whose top/bottom boundaries are roughened with cubes (in-line arrangement) of size-to-pitch ratio $e/\ell = 0.5$, with the spacing in wall units, $\ell^+ = \epsilon Re_{\tau(\mathcal{M})}$, varied up to 50. Values of the macroscopic coefficients are plotted against ℓ^+ in panel (a). In panel (b), the behavior of the parameter $\mathcal{D}$ based on (3.12) is shown (blue curve), and is validated against the results by Hao & García-Mayoral (2024) obtained from full simulations (squares). The black dashed curve refers to the predictions of (3.12) when Ψ is evaluated with the Stokes-based upscaled coefficients, neglecting near-wall inertia; they are $\lambda_x = \lambda_z \approx 0.0653$ and $\mathcal{K}_{xy}^{itf} \approx \mathcal{K}_{zy}^{itf} = 0.0083$.

generated. In particular, we choose to check the generality of the relations above by validating them against existing numerical/experimental results for the motion over rough, impermeable walls ($\mathcal{K}_{yy} = 0$) with either two- or three-dimensional wall corrugations. The results in figure 15 are related to the turbulent flow $\left(Re_{\tau(\mathcal{M})} = 182.70\right)$ in a symmetric channel delimited by walls roughened with in-line patterns of cubical protrusions having side length e and pitch $\ell = 2e$. The Oseen-based upscaled coefficients, sensitive to the level of near-interface advection and hence to the value of ℓ^+, are evaluated for $\ell^+ = (0, 12, 23.9, 35.9, 47.8)$ and are plotted in figure 15(a). The corresponding values of Ψ are $(0, 2.84, 4.39, 5.78, 7.29)$, and are used to predict the behavior of the quantity $\mathcal{D}$ in figure 15(b). These predictions are compared against the numerical results of the feature-resolving simulations by Hao & García-Mayoral (2024), and good agreement is observed. To highlight the need of incorporating near-wall advection into the homogenization model, the calculations have been repeated by setting Re_λ equal to 0 in (2.22) and (2.23), and significant errors in the predictions of $\mathcal{D}$ are found when ℓ^+ exceeds 10. In fact, the Stokes-based results coincide with the Oseen-based ones for $\ell^+ \lesssim 10$, a threshold similar to that reported by Ahmed & Bottaro (2024) for laminar channel flows. Since $\Delta U^+ = U_{slip}^+ - \mathcal{D}$, the calculation of the roughness function based on the values obtained for $\mathcal{D}$ requires knowledge of the slip velocity, U_{slip}^+. It may be tempting to use the approximation $U_{slip}^+ = \lambda_x^+ \left.\dfrac{\partial \overline{U}^+}{\partial Y^+}\right|_{Y=0} \approx \lambda_x^+$, but care must be exerted, since significant errors appear in the predicted U_{slip}^+ as ℓ^+ becomes large, as a result of the large Reynolds stress

generated at the channel virtual boundary in $Y = 0$ (Hao & García-Mayoral, 2024). It is the approximation $\left.\frac{\partial \overline{U}^+}{\partial Y^+}\right|_{Y=0} = 1$ which eventually breaks down. In fact, based on the values of U^+_{slip} and λ^+_x reported by Hao & García-Mayoral (2024), we observe that the absolute deviations between the two quantities, for $\ell^+ = (12, 23.9, 35.9, 47.8)$, are respectively $(1\%, 4\%, 28\%, 53\%)$. If we substitute $U^+_{slip} = \lambda^+_x$ into (3.12), with the Oseen-based coefficients, we obtain $\Delta U^+ \approx (-0.73, -1.48, -2.49, -4.01)$, progressively deviating from the values computed by Hao & García-Mayoral (2024): $\Delta U^+ \approx (-0.50, -1.69, -3.77, -4.91)$. As a side remark, we observe that the present correlations have been generated by fitting data relative to the motion in an asymmetric channel, with one boundary perturbed and the other smooth and impermeable. This point can be critical since, on the one hand, the DNS by Hao & García-Mayoral (2024) are conducted in a symmetric channel and, on the other, we evaluate ℓ^+ and normalize the velocity profile based on the scale $u_{\tau(\mathcal{M})}$, and not on the shear velocity at the textured boundary, $u_{\tau(\mathcal{B})}$.

The next case examined is that of riblets. Rather than using the expression recalled earlier, $\Delta U^+ = \ell^+_U - \ell^+_{Turb.}$, which is not predictive, unless turbulent simulations are conducted for any shape of the riblets, we employ (3.13). Clearly, when Ψ is vanishingly small the relationship (3.13) yields the classical viscous approximation $\Delta U^+ = \Delta\lambda^+$ (Luchini, 1996; Garcia-Mayoral & Jiménez, 2011). Conversely, the behavior of the roughness function can deviate significantly from this linear equation as ℓ^+ increases and transpiration becomes more pronounced. Different ribleted surfaces are shown in figure 16. For each geometry, the macroscopic coefficients are calculated (Appendix C) and expressed in wall units by applying (3.2b) and (3.2c) for different spacings $\ell^+ = \epsilon Re_{\tau(\mathcal{M})}$ within the range considered ($0 \leq \ell^+ \leq 36$); the values of Ψ are accordingly between 0 and 7.4. The predictions in the form ΔU^+ versus ℓ^+ are validated against the DNS results by Wong *et al.* (2024) and the experimental findings by Bechert *et al.* (1997); a reasonably good agreement can be ascertained from the figure, including the deviation from the linear dependence departing from the viscous regime, the performance degradation when the pitch distance exceeds a threshold between 15 and 20, and eventually the drag increase for large riblets' periodicity. For larger values of ℓ^+, not considered in the figure, predictions of the correlation are questionable since the resulting values of Ψ are significantly beyond the applicability range of the present correlation. For instance, Gatti *et al.* (2020) studied the turbulent flow over trapezoidal riblets (similar to those in figure 16(d) but with angle of 53.5° and height equal to $0.476\,\ell$) and found that ΔU^+ tends to become almost constant for ℓ^+ larger than about 60, a behavior which cannot be captured by (3.13). Finally, it is important to note that some quantitative uncertainty is associated with the literature results reported in figure 16, related to the choice of the shear-velocity used for normalization and of the virtual origin of the turbulent velocity profile over the rough surface.

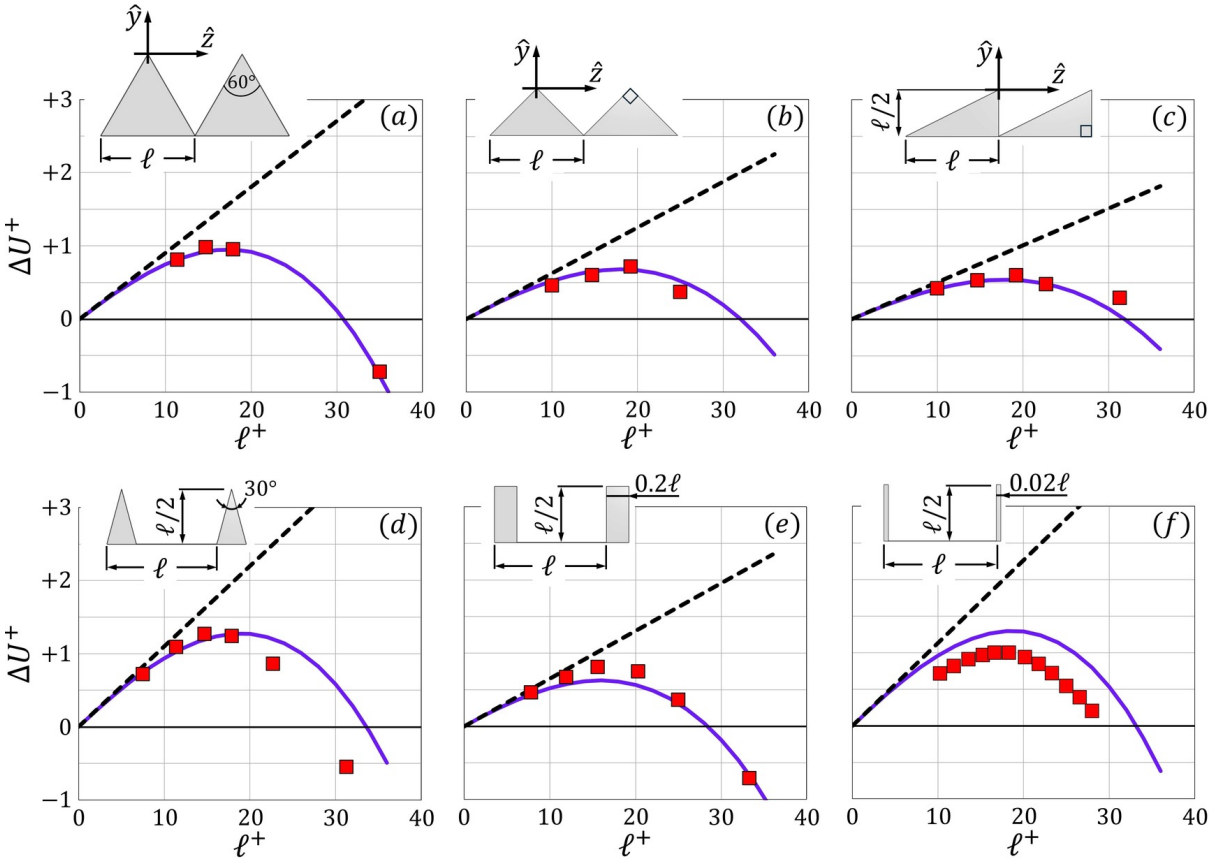

Figure 16: Behavior of ΔU^+ with the increase in ℓ^+, for the turbulent flow over surfaces with different shapes of riblets. The proposed correlation (blue solid lines) is validated against relevant results from the literature (red symbols), while the black dashed lines represent the simple linear dependence $\Delta U^+ = \lambda_x^+ - \lambda_z^+$. The literature results plotted are by (*a–e*) Wong *et al.* (2024) and (*f*) Bechert *et al.* (1997); the latter were reported originally in terms of $\frac{\Delta C_f}{C_{f,\,smooth}}$ and the corresponding values of ΔU^+ are obtained here employing the relation $\Delta U^+ = -\frac{\Delta C_f}{C_{f,\,smooth}} \times [(2C_{f,\,smooth})^{-0.5} + 1.25]$.

4 CONCLUSIONS

The features of the turbulent boundary layer over a permeable/textured wall are explored, with focus on the dependence of the roughness function, ΔU^+, on the macroscopic coefficients characterizing the perturbed boundary, i.e., the Navier-slip coefficients (λ_x, λ_z), the interface permeabilities ($\mathcal{K}_{xy}^{itf}$, $\mathcal{K}_{zy}^{itf}$), and the intrinsic medium permeability ($\mathcal{K}_{yy}$, nonzero for porous boundaries). These parameters are sensitive to the micro-structural details of the wall and, in general, to the level of advection in the vicinity of the interface. The asymptotic homogenization framework adopted incorporates the latter effect into the analysis of the microscale problem via an *Oseen-like* linearization, and a Reynolds number (Re_λ) defined based on the slip velocity ($\hat{u}_{slip}$) and the microscopic length scale (ℓ) hence appears in the closure problems used to evaluate the upscaled coefficients of the model, which contribute to the definition of high-order *effective* boundary conditions of the three velocity components (2.19a–2.19c) at a virtual plane boundary next to the physical porous/rough one.

First, the effective boundary conditions were employed to simplify a set of direct numerical simulations of the turbulent flow in a channel delimited from one side (at $Y = 2$) by a smooth, impermeable wall and from the other side (at $Y \leq 0$) by a transversely isotropic porous substrate having a porosity $\theta = 0.5$. Four patterns of the substrate were studied, two streamwise-elongated and two spanwise-elongated, and for each of them four values of the inclusions pitch, ℓ^+, were tested in the range $0 < \ell^+ < 40$. The model was validated, for one case (transverse cylinders with $\ell^+ \approx 40$) against a classical fine-grained DNS, and acceptable agreement was found. The mean velocity profiles and the turbulence statistics at, and next to, the permeable walls were analyzed to interpret the behavior of the roughness function and the ensuing increase/reduction in skin-friction drag, $\Delta C_f\%$. Drag reduction (here up to 5%) is achieved exclusively with substrates of streamwise-preferential permeability (where $\lambda_x^+ > \lambda_z^+$ and $\mathcal{K}_{xy}^{itf,+} > \mathcal{K}_{zy}^{itf,+}$), and is proportional, for small values of ℓ^+, to $\Delta\lambda^+ = \lambda_x^+ - \lambda_z^+$. For the turbulent flow over substrates of spanwise-preferential permeability (or even those elongated in the streamwise direction and characterized by excessive ℓ^+ values), an increase in the skin-friction drag is detected (here up to 27%) and is accompanied by large levels of r.m.s. fluctuations in wall-normal and spanwise velocity components, in the Reynolds stress, τ_{xy}^R, and in the rate of production of turbulent kinetic energy, P_T, near the substrate/channel interface.

Second, in view of the results extracted from the sixteen DNSs performed for the turbulent flow over permeable boundaries, special attention was directed to the dependence of the roughness function, ΔU^+, on $\tilde{V}_{rms}$, $\tilde{W}_{rms}$, and $\tilde{\tau}_{xy}^R$ (tildes are used to denote values at the porous/free-fluid interface, $Y = 0$). While the relation between ΔU^+ and each of these turbulence-characterizing quantities differs according to the geometry/configuration of the porous bed, the data are found to collapse quite well when specific roughness-function-related quantities are examined; they are $\mathcal{D} = U_{slip}^+ - \Delta U^+$ and $\mathcal{F} = \Delta\lambda^+ - \Delta U^+$, and they increase monotonically with $\tilde{V}_{rms}$, $\tilde{W}_{rms}$, and $\tilde{\tau}_{xy}^R$. Moreover, evidence of the significant role played by $\tilde{V}_{rms}$ as a control parameter in the turbulent

flow over not only permeable but also rough, impermeable boundaries was demonstrated, particularly thanks to the work by Leonardi, Orlandi and collaborators (Leonardi *et al.*, 2003; Orlandi & Leonardi, 2006, 2008). The quantities $\mathcal{D}$ and $\mathcal{F}$ were expressed as functions of $\tilde{V}_{rms}$ via the fitting correlations (3.3) and (3.6), respectively. To put these relationships to practical use in the *a priori* evaluation of the roughness function (i.e., without the need for running the direct numerical simulations) the dependence of $\tilde{V}_{rms}$ on the upscaled coefficients of the homogenization model was explored; based on the present results, a compound macroscopic quantity Ψ, defined by (3.10), is proposed as a single parameter correlated to $\tilde{V}_{rms}$. Eventually, the most significant result of the present study is the nexus found among the roughness function, the slip velocity, and the upscaled coefficients, i.e.

$$\Delta U^+ = U^+_{slip} - 11.5 \times \left(0.00075\,\Psi^3 + 0.002\,\Psi^2 \right)^{0.6}, \tag{4.1}$$

$$\Delta U^+ = \Delta\lambda^+ - 11.5 \times \left(0.00075\,\Psi^3 + 0.002\,\Psi^2 \right). \tag{4.2}$$

Although these equations are originally based on fitting the present results for the turbulent flow over porous substrates, they yield satisfactory agreement with simulation and experimental results for selected rough, impermeable boundaries (Hao & García-Mayoral, 2024; Wong *et al.*, 2024; Bechert *et al.*, 1997). One very interesting point is that the non-monotonic behavior of ΔU^+ with the increase in ℓ^+ for the case of riblets (linear/non-linear trends of drag reduction followed by performance degradation and eventually drag increase) can be captured by (4.2) up to ℓ^+ values of about 40.

The present analysis provides sufficient motivation to carry out further investigations for the purpose of either assessing the versatility of (4.1) and (4.2) for the turbulent flow over various textured boundaries or proposing more robust correlations. Once this is accomplished, the findings can be employed, for instance, to accelerate large-scale optimization studies of the wall micro-structure (topology/size/arrangement of the grains), avoiding direct or large eddy simulations at least in the preliminary stages of the work.

FUNDING

Activity funded by the European Union Next Generation EU, via PRIN PNRR 2022 grant, project code P2022CZ5KZ.

Appendices

A CONSIDERATIONS ON THE TRANSPIRATION VELOCITY BOUNDARY CONDITION

The following assumptions/simplifications related to the imposition of the boundary condition (2.19b) in the direct numerical simulations are adopted, mainly to guarantee the stability of the solution. Handling the pressure gradient $\dfrac{\partial \hat{p}}{\partial \hat{y}}$ at the fictitious plane $\hat{y} = 0$ is of much importance. If the physical wall were smooth and impermeable, one would write $\left.\dfrac{\partial \hat{p}}{\partial \hat{y}}\right|_0 = \mu \left.\dfrac{\partial^2 \hat{v}}{\partial \hat{y}^2}\right|_0$, which also applies to walls/substrates with small surface protrusions, e.g., vanishingly small values of ℓ^+. The present work includes the study of the turbulent flow over porous substrates having relatively large values of ℓ^+ (up to ≈ 40), and thus the aforementioned expression becomes questionable. To enhance the validity of the assumption, we incorporate the inertial effects associated with the transpiration velocity into the expression, to obtain $\left.\dfrac{\partial \hat{p}}{\partial \hat{y}}\right|_0 = \left.\left(\mu \dfrac{\partial^2 \hat{v}}{\partial \hat{y}^2} - \rho \hat{v} \dfrac{\partial \hat{v}}{\partial \hat{y}}\right)\right|_0$. The boundary condition (2.19b) now reads

$$\hat{v}|_0 \approx \frac{\hat{\mathcal{K}}_{yy}}{\mu} \left.\left(\rho \hat{v} \frac{\partial \hat{v}}{\partial \hat{y}} + \mu \frac{\partial^2 \hat{v}}{\partial \hat{y}^2}\right)\right|_0 - \hat{\mathcal{K}}^{itf}_{xy} \frac{\partial}{\partial \hat{x}} \left.\left(\frac{\partial \hat{u}}{\partial \hat{y}} + \frac{\partial \hat{v}}{\partial \hat{x}}\right)\right|_0 - \hat{\mathcal{K}}^{itf}_{zy} \frac{\partial}{\partial \hat{z}} \left.\left(\frac{\partial \hat{w}}{\partial \hat{y}} + \frac{\partial \hat{v}}{\partial \hat{z}}\right)\right|_0 . \tag{A1}$$

With the continuity equation in mind, we have

$$\left.\frac{\partial^2 \hat{v}}{\partial \hat{y}^2}\right|_0 = \left.\frac{\partial}{\partial \hat{y}} \left(\frac{\partial \hat{v}}{\partial \hat{y}}\right)\right|_0 = \left.\frac{\partial}{\partial \hat{y}} \left(-\frac{\partial \hat{u}}{\partial \hat{x}} - \frac{\partial \hat{w}}{\partial \hat{z}}\right)\right|_0 , \tag{A2}$$

and (A1) becomes

$$\hat{v}|_0 \approx \hat{\mathcal{K}}_{yy} \left.\left(\frac{\rho}{\mu} \hat{v} \frac{\partial \hat{v}}{\partial \hat{y}} - \frac{\partial}{\partial \hat{x}} \frac{\partial \hat{u}}{\partial \hat{y}} - \frac{\partial}{\partial \hat{z}} \frac{\partial \hat{w}}{\partial \hat{y}}\right)\right|_0 - \hat{\mathcal{K}}^{itf}_{xy} \frac{\partial}{\partial \hat{x}} \left.\left(\frac{\partial \hat{u}}{\partial \hat{y}} + \frac{\partial \hat{v}}{\partial \hat{x}}\right)\right|_0 - \hat{\mathcal{K}}^{itf}_{zy} \frac{\partial}{\partial \hat{z}} \left.\left(\frac{\partial \hat{w}}{\partial \hat{y}} + \frac{\partial \hat{v}}{\partial \hat{z}}\right)\right|_0 . \tag{A3}$$

Employing the Navier's slip conditions

$$\hat{u}|_0 \approx \hat{\lambda}_x \left.\left(\frac{\partial \hat{u}}{\partial \hat{y}} + \frac{\partial \hat{v}}{\partial \hat{x}}\right)\right|_0 \approx \hat{\lambda}_x \left.\frac{\partial \hat{u}}{\partial \hat{y}}\right|_0 , \quad \hat{w}|_0 \approx \hat{\lambda}_z \left.\left(\frac{\partial \hat{w}}{\partial \hat{y}} + \frac{\partial \hat{v}}{\partial \hat{z}}\right)\right|_0 \approx \hat{\lambda}_z \left.\frac{\partial \hat{w}}{\partial \hat{y}}\right|_0 , \tag{A4}$$

to further simplify the boundary condition for the transpiration velocity component, we eventually obtain the following expression:

$$\hat{v}|_0 \approx \frac{\rho \hat{\mathcal{K}}_{yy}}{\mu} \left.\left(\hat{v} \frac{\partial \hat{v}}{\partial \hat{y}}\right)\right|_0 - \frac{\hat{\mathcal{K}}^{itf}_{xy} + \hat{\mathcal{K}}_{yy}}{\hat{\lambda}_x} \left.\frac{\partial \hat{u}}{\partial \hat{x}}\right|_0 - \frac{\hat{\mathcal{K}}^{itf}_{zy} + \hat{\mathcal{K}}_{yy}}{\hat{\lambda}_z} \left.\frac{\partial \hat{w}}{\partial \hat{z}}\right|_0 . \tag{A5}$$

Note that we have neglected the two terms in (A3) where $\hat{v}$ appears derived with respect to either $\hat{x}$ or $\hat{z}$, since the vertical velocity at the wall is of order ϵ^2 (cf. 2.18b).

The following equation, which can be simply derived from (A5), is the expression of the transpiration velocity boundary condition implemented in the numerical code:

$$\hat{v}\big|_0 \approx \left(-\frac{\hat{\mathcal{K}}^{itf}_{xy} + \hat{\mathcal{K}}_{yy}}{\hat{\lambda}_x} \frac{\partial \hat{u}}{\partial \hat{x}}\bigg|_0 - \frac{\hat{\mathcal{K}}^{itf}_{zy} + \hat{\mathcal{K}}_{yy}}{\hat{\lambda}_z} \frac{\partial \hat{w}}{\partial \hat{z}}\bigg|_0 \right) \Bigg/ \left(1 - \frac{\rho \hat{\mathcal{K}}_{yy}}{\mu} \frac{\partial \hat{v}}{\partial \hat{y}}\bigg|_0 \right). \tag{A6}$$

Special attention is directed to the denominator of the right-hand-side term in (A6) since small values at one iteration may result in excessively large transpiration velocities, which can seriously disrupt the progress of the iterative process and the solution. For numerical calculations at a given time, $\hat{t}$, the value of the denominator is explicitly evaluated from the previous time instant, $\hat{t} - \Delta\hat{t}$. Clearly, for vanishingly small values of ℓ^+, the near-interface advection is negligible compared to the viscous effects, and hence $\dfrac{\rho \hat{\mathcal{K}}_{yy}}{\mu} \dfrac{\partial \hat{v}}{\partial \hat{y}}\bigg|_0$ approaches 0 so that the denominator in (A6) tends to 1. On the other hand, for porous substrates made of transverse/longitudinal cylindrical inclusions with the largest ℓ^+ studied here, the distributions of the value of the denominator over space ($\hat{x}$–$\hat{z}$) at different time instants are found to lie within a range extending from 0.25 to 2; values outside this range (recorded at less than 1% of the points on the virtual wall) are considered as outliers and are forced equal to the closest limit (either 0.25 or 2). Similarly, the value of the transpiration velocity $\hat{v}\big|_0$ is monitored and is bounded within $\pm 2\, u_{\tau(\mathcal{M})}$, again with outliers detected at less than 1% of the points. Finally, for conservation of mass to be satisfied over the whole computational domain, the plane-averaged value of $\hat{v}\big|_0$ must vanish. Small deviations associated with numerical error are found to undermine convergence; to overcome this, the plane-averaged value of $\hat{v}\big|_0$ is evaluated every 10 time steps and uniformly subtracted from the local values.

B NORMALIZATION BASED ON WALL SHEAR VELOCITY

The macroscopic-pressure-gradient-based velocity scale $u_{\tau(\mathcal{M})}$ has been used for normalization throughout the paper. To facilitate comparisons with previous studies we also provide the values of the major parameters related to the mean velocity profile when normalized by the permeable-interface shear velocity $u_{\tau(\mathcal{B})}$, and of the model coefficients when the $Re_{\tau(\mathcal{B})}$ is used in (3.2b) and (3.2c); these quantities are available in table 3. It is evident that the cases of skin-friction drag increase are characterized by shear-velocity ratios $\dfrac{u_{\tau(\mathcal{B})}}{u_{\tau(\mathcal{M})}}$, and therefore stress ratios $\dfrac{\tau_{\mathcal{B}}}{\tau_{\mathcal{M}}}$, larger than 1, which can be attributed to the fact that the total stress at the permeable boundary for each of these cases is larger than that at the top smooth wall. The opposite applies to the cases of drag reduction. Accordingly, the values of ΔU^+, $\Delta U^+_{ch}\%$, and $\Delta C_f\%$ in table 3 are all larger, in absolute value, than those in table 2.

Table 3: Macroscopic coefficients and major results defined/normalized based on the fictitious-interface (bottom) shear velocity $u_{\tau(\mathcal{B})}$.

Substrate	$\frac{u_{\tau(\mathcal{B})}}{u_{\tau(\mathcal{M})}}$	**Macroscopic coefficients**					**Sample results**		
		λ_x^+	λ_z^+	$\mathcal{K}_{xy}^{itf,+}$	$\mathcal{K}_{zy}^{itf,+}$	$\mathcal{K}_{yy}^+$	ΔU^+	$\Delta U_{ch}^+\%$	$\Delta C_f\%$
Smooth	1	0	0	0	0	0	0	0	0
TC_5	1.008	0.43	0.65	0.20	0.49	0.17	−0.45	−1.8%	+3.8%
TC_{10}	1.023	0.81	1.17	0.71	1.64	0.71	−1.12	−5.4%	+11.8%
TC_{15}	1.037	1.10	1.52	1.29	2.76	1.65	−2.06	−9.7%	+22.7%
TC_{20}	1.068	1.38	1.83	1.99	3.98	3.10	−3.19	−16.0%	+41.8%
LC_5	0.996	0.66	0.43	0.51	0.21	0.17	+0.22	+1.5%	−2.9%
LC_{10}	0.996	1.32	0.87	2.06	0.83	0.68	+0.14	+1.3%	−2.6%
LC_{15}	1.011	2.01	1.32	4.77	1.92	1.57	−0.71	−2.5%	+5.1%
LC_{20}	1.045	2.78	1.82	9.05	3.65	2.97	−2.25	−10.8%	+25.6%
TM_5	1.014	0.55	1.04	0.36	1.05	0.01	−0.82	−3.6%	+7.7%
TM_{10}	1.037	0.98	1.78	1.10	3.29	0.05	−1.90	−8.9%	+20.5%
TM_{15}	1.063	1.30	2.22	1.83	5.47	0.11	−2.91	−14.5%	+36.6%
TM_{20}	1.078	1.55	2.49	2.45	7.31	0.21	−3.53	−17.7%	+47.7%
LM_5	0.990	1.08	0.56	1.11	0.38	0.01	+0.50	+2.9%	−5.6%
LM_{10}	0.988	2.15	1.12	4.41	1.49	0.04	+0.65	+3.8%	−7.3%
LM_{15}	1.010	3.30	1.72	10.38	3.52	0.10	−0.49	−1.4%	+2.8%
LM_{20}	1.024	4.47	2.33	18.96	6.42	0.19	−1.29	−5.2%	+11.3%

C MACROSCOPIC COEFFICIENTS FOR SURFACES WITH RIBLETS

For the different ribleted surfaces sketched in figure 16, values of the upscaled coefficients contributing to the effective boundary conditions (2.18a–2.18c) are evaluated (table 4) for a virtual boundary at $\hat{y} = 0$, i.e. the plane passing through the tips/outer rims of the longitudinal protrusions. These walls are impermeable ($\mathcal{K}_{yy} = 0$), and they exhibit streamwise-preferential slip with $\lambda_x > \lambda_z$ and $\mathcal{K}_{xy}^{itf} > \mathcal{K}_{zy}^{itf}$. For each surface, the

Table 4: Macroscopic coefficients for surfaces altered with riblets.

Riblets' geometry	Dimensionless macroscopic coefficients			
	λ_x	λ_z	$\mathcal{K}_{xy}^{itf}$	$\mathcal{K}_{zy}^{itf}$
equilateral triangle	0.1708	0.0807	0.02821	0.00586
right triangle, symmetric	0.1397	0.0770	0.01683	0.00573
right triangle, asymmetric	0.1273	0.0768	0.01411	0.00502
trapezoidal	0.1915	0.0816	0.03484	0.00542
thick blade	0.1144	0.0491	0.02102	0.00213
thin blade	0.1915	0.0783	0.03788	0.00455

coefficients are calculated by solving the auxiliary systems (2.22) and (2.23) over a two-dimensional $(\hat{y}-\hat{z})$ elementary cell representative of the microscopic domain. The riblets are $\hat{x}$-elongated, which allows to set $\partial/\partial x_1$ to zero in the closure problems, thus rendering them advection-insensitive.

REFERENCES

Abderrahaman-Elena, N., Fairhall, C.T. & García-Mayoral, R. 2019 Modulation of near-wall turbulence in the transitionally rough regime. *J. Fluid Mech.* **865**, 1042–1071.

Abderrahaman-Elena, N. & García-Mayoral, R. 2017 Analysis of anisotropically permeable surfaces for turbulent drag reduction. *Phys. Rev. Fluids* **2** (11), 114609.

Ahmed, E.N. & Bottaro, A. 2024 Laminar flow in a channel bounded by porous/rough walls: Revisiting Beavers-Joseph-Saffman. *Eur. J. Mech. B Fluids* **103**, 269–283.

Ahmed, E.N., Bottaro, A. & Tanda, G. 2022*a* A homogenization approach for buoyancy-induced flows over micro-textured vertical surfaces. *J. Fluid Mech.* **941**, A53.

Ahmed, E.N., Naqvi, S.B., Buda, L. & Bottaro, A. 2022*b* A homogenization approach for turbulent channel flows over porous substrates: Formulation and implementation of effective boundary conditions. *Fluids* **7** (5), 178.

Antonia, R.A., Zhu, Y. & Sokolov, M. 1995 Effect of concentrated wall suction on a turbulent boundary layer. *Phys. Fluids* **7** (10), 2465–2474.

Babuška, I. 1976 Homogenization and its application. Mathematical and computational problems, in: Hubbard, B. (Ed.), *Numerical Solution of Partial Differential Equations–III*, pp. 89–116. Academic Press .

Bechert, D.W. & Bartenwerfer, M. 1989 The viscous flow on surfaces with longitudinal ribs. *J. Fluid Mech.* **206**, 105–129.

Bechert, D.W., Bruse, M., Hage, W., Van der Hoeven, J.G.T. & Hoppe, G. 1997 Experiments on drag-reducing surfaces and their optimization with an adjustable geometry. *J. Fluid Mech.* **338**, 59–87.

Bernard, P.S., Thomas, J.M. & Handler, R.A. 1993 Vortex dynamics and the production of Reynolds stress. *J. Fluid Mech.* **253**, 385–419.

Bottaro, A. 2019 Flow over natural or engineered surfaces: an adjoint homogenization perspective. *J. Fluid Mech.* **877**, P1.

Bottaro, A. & Naqvi, S.B. 2020 Effective boundary conditions at a rough wall: a high-order homogenization approach. *Meccanica* **55** (9), 1781–1800.

Breugem, W.P., Boersma, B.J. & Uittenbogaard, R.E. 2006 The influence of wall permeability on turbulent channel flow. *J. Fluid Mech.* **562**, 35–72.

Buda, L. 2021 Drag reduction over rough permeable surfaces: A homogenized-based approach. Master's Thesis in Physics, University of Genoa, Italy. Available at http://www.dicat.unige.it/bottaro/Presentation%20group/Thesis_Buda.pdf.

Burattini, P., Leonardi, S., Orlandi, P. & Antonia, R.A. 2008 Comparison between experiments and direct numerical simulations in a channel flow with roughness on one wall. *J. Fluid Mech.* **600**, 403–426.

Chang, J., Jung, T., Choi, H. & Kim, J. 2019 Predictions of the effective slip length and drag reduction with a lubricated micro-groove surface in a turbulent channel flow. *J. Fluid Mech.* **874**, 797–820.

Cheng, H. & Castro, I.P. 2002 Near wall flow over urban-like roughness. *Boundary-Layer Met.* **104**, 229–259.

Cheng, X.Q., Wong, C.W., Hussain, F., Schröder, W. & Zhou, Y. 2021 Flat plate drag reduction using plasma-generated streamwise vortices. *J. Fluid Mech.* **918**.

Choi, K.S. 2002 Near-wall structure of turbulent boundary layer with spanwise-wall oscillation. *Phys. Fluids* **14** (7), 2530–2542.

Chung, D., Hutchins, N., Schultz, M.P. & Flack, K.A. 2021 Predicting the drag of rough surfaces. *Annu. Rev. Fluid Mech.* **53**, 439–471.

Clauser, F.H. 1954 Turbulent boundary layers in adverse pressure gradients. *J. Aeronaut. Sci.* **21** (2), 91–108.

von Deyn, L.H., Gatti, D. & Frohnapfel, B. 2022 From drag-reducing riblets to drag-increasing ridges. *J. Fluid Mech.* **951**, A16.

El-Samni, O.A., Chun, H.H. & Yoon, H.S. 2007 Drag reduction of turbulent flow over thin rectangular riblets. *Intl. J. Eng. Sci.* **45** (2–8), 436–454.

Endrikat, S., Modesti, D., García-Mayoral, R., Hutchins, N. & Chung, D. 2021*a* Influence of riblet shapes on the occurrence of Kelvin–Helmholtz rollers. *J. Fluid Mech.* **913**, A37.

Endrikat, S., Modesti, D., MacDonald, M., García-Mayoral, R., Hutchins, N. & Chung, D. 2021*b* Direct numerical simulations of turbulent flow over various riblet shapes in minimal-span channels. *Flow Turbul. Combust.* **107** (1), 1–29.

Esteban, L.B., Rodríguez-López, E., Ferreira, M.A. & Ganapathisubramani, B. 2022 Mean flow of turbulent boundary layers over porous substrates. *Phys. Rev. Fluid* **7** (9), 094603.

Flack, K.A. & Schultz, M.P. 2010 Review of hydraulic roughness scales in the fully rough regime. *ASME. J. Fluids Eng.* **132** (4), 041203.

Flack, K.A., Schultz, M.P. & Barros, J.M. 2020 Skin friction measurements of systematically-varied roughness: Probing the role of roughness amplitude and skewness. *Flow Turbul. Combust.* **104** (2-3), 317–329.

Flores, O. & Jiménez, J. 2006 Effect of wall-boundary disturbances on turbulent channel flows. *J. Fluid Mech.* **566**, 357–376.

Forooghi, P., Stroh, A., Magagnato, F., Jakirlić, S. & B., Frohnapfel 2017 Toward a universal roughness correlation. *ASME. J. Fluids Eng.* **139** (12), 121201.

Fu, M.K., Arenas, I., Leonardi, S. & Hultmark, M. 2017 Liquid-infused surfaces as a passive method of turbulent drag reduction. *J. Fluid Mech.* **824**, 688–700.

Garcia-Mayoral, R. & Jiménez, J. 2011 Drag reduction by riblets. *Philos. Trans. Royal Soc. A* **369** (1940), 1412–1427.

Garcia-Mayoral, R. & Jimenez, J. 2011 Hydrodynamic stability and breakdown of the viscous regime over riblets. *J. Fluid Mech.* **678**, 317–347.

Gatti, D., von Deyn, L., Forooghi, P. & Frohnapfel, B. 2020 Do riblets exhibit fully rough behaviour? *Exp. Fluids* **61** (3), 81.

Hama, F.R. 1954 Boundary layer characteristics for smooth and rough surfaces. *Trans. Soc. Nav. Archit. Mar. Engrs* **62**, 333–358.

Hao, Z. & García-Mayoral, R. 2024 Turbulent flows over porous and rough substrates, arXiv: 2402.15244.

Ibrahim, J.I., Gómez-de Segura, G., Chung, D. & García-Mayoral, R. 2021 The smooth-wall-like behaviour of turbulence over drag-altering surfaces: a unifying virtual-origin framework. *J. Fluid Mech.* **915**, A56.

Jeong, J., Hussain, F., Schoppa, W. & Kim, J. 1997 Coherent structures near the wall in a turbulent channel flow. *J. Fluid Mech.* **332**, 185–214.

Jiménez, J. 1994 On the structure and control of near wall turbulence. *Phys. Fluids* **6** (2), 944–953.

Jiménez, J. 2004 Turbulent flows over rough walls. *Annu. Rev. Fluid Mech.* **36**, 173–196.

Jiménez, J. & Pinelli, A. 1999 The autonomous cycle of near-wall turbulence. *J. Fluid Mech.* **389**, 335–359.

Jiménez Bolaños, S. & Vernescu, B. 2017 Derivation of the Navier slip and slip length for viscous flows over a rough boundary. *Phys. of Fluids* **29** (5), 057103.

Kang, S. & Choi, H. 2000 Active wall motions for skin-friction drag reduction. *Phys. Fluids* **12** (12), 3301–3304.

Khorasani, S.M.H., Luhar, M. & Bagheri, S. 2024 Turbulent flows over porous lattices: alteration of near-wall turbulence and pore-flow amplitude modulation. *J. Fluid Mech.* **984**, A63.

Khorasani, S.M.H., Lācis, U., Pasche, S., Rosti, M.E. & Bagheri, S. 2022 Near-wall turbulence alteration with the transpiration-resistance model. *J. Fluid Mech.* **942**, A45.

Kim, J., Moin, P. & R., Moser 1987 Turbulence statistics in fully developed channel flow at low reynolds number. *J. Fluid Mech.* **177**, 133–166.

Kuwata, Y. & Suga, K. 2017 Direct numerical simulation of turbulence over anisotropic porous media. *J. Fluid Mech.* **831**, 41–71.

Lācis, U., Sudhakar, Y., Pasche, S. & Bagheri, S. 2020 Transfer of mass and momentum at rough and porous surfaces. *J. Fluid Mech.* **884**, A21.

Lācis, U., Zampogna, G.A. & Bagheri, S. 2017 A computational continuum model of poroelastic beds. *Proc. R. Soc. A* **473**, 20160932.

Leonardi, S., Orlandi, P., Smalley, R.J., Djenidi, L. & Antonia, R.A. 2003 Direct numerical simulations of turbulent channel flow with transverse square bars on one wall. *J. Fluid Mech.* **491**, 229–238.

Luchini, P. 1996 Reducing the turbulent skin friction. In *Computational Methods in Applied Sciences '96* (ed. J.A. Désidéri et al.), pp. 466–470.

Luchini, P., Manzo, F. & Pozzi, A. 1991 Resistance of a grooved surface to parallel flow and cross-flow. *J. Fluid Mech.* **228**, 87–109.

Manes, C., Poggi, D. & Ridolfi, L. 2011 Turbulent boundary layers over permeable walls: scaling and near-wall structure. *J. Fluid Mech.* **687**, 141–170.

Mansour, N.N., Kim, J. & Moin, P. 1988 Reynolds-stress and dissipation-rate budgets in a turbulent channel flow. *J. Fluid Mech.* **194**, 15–44.

Mei, C.C. & Vernescu, B. 2010 *Homogeneization Methods for Multiscale Mechanics*. World Sci.

Naqvi, S.B. & Bottaro, A. 2021 Interfacial conditions between a free-fluid region and a porous medium. *Int. J. Multiph. Flow* **141**, 103585.

Navier, C. 1823 Mémoire sur les lois du mouvement des fluides. *Mém. Acad. R. Sci. Inst. France* **6**, 389–440.

Nikuradse, J. 1933 Laws of flow in rough pipes. *Tech. Memo. 1292* .

Orlandi, P. & Leonardi, S. 2006 DNS of turbulent channel flows with two- and three-dimensional roughness. *J. Turbul.* **7**, N73.

Orlandi, P. & Leonardi, S. 2008 Direct numerical simulation of three-dimensional turbulent rough channels: parameterization and flow physics. *J. Fluid Mech.* **606**, 399–415.

Orlandi, P., Leonardi, S. & Antonia, R.A. 2006 Turbulent channel flow with either transverse or longitudinal roughness elements on one wall. *J. Fluid Mech.* **561**, 279–305.

Orlandi, P., Leonardi, S., Tuzi, R. & Antonia, R.A. 2003 Direct numerical simulation of turbulent channel flow with wall velocity disturbances. *Phys. Fluids* **15** (12), 3587–3601.

Park, H., Park, H. & Kim, J. 2013 A numerical study of the effects of superhydrophobic surface on skin-friction drag in turbulent channel flow. *Phys. Fluids* **25** (11), 110815.

Rastegari, A. & Akhavan, R. 2015 On the mechanism of turbulent drag reduction with super-hydrophobic surfaces. *J. Fluid Mech.* **773**.

Rosti, M.E., Brandt, L. & Pinelli, A. 2018 Turbulent channel flow over an anisotropic porous wall–drag increase and reduction. *J. Fluid Mech.* **842**, 381–394.

Rosti, M.E., Cortelezzi, L. & Quadrio, M. 2015 Direct numerical simulation of turbulent channel flow over porous walls. *J. Fluid Mech.* **784**, 396–442.

Schlichting, H. 1937 Experimental investigation of the problem of surface roughness. *Tech. Memo. 823, Natl. Adv. Comm. Aeronaut.,Washington, DC* .

Gómez-de Segura, G. & García-Mayoral, R. 2019 Turbulent drag reduction by anisotropic permeable substrates–analysis and direct numerical simulations. *J. Fluid Mech.* **875**, 124–172.

Gómez-de Segura, G., Sharma, A. & García-Mayoral, R. 2018 Turbulent drag reduction using anisotropic permeable substrates. *Flow Turbul. Combust.* **100** (4), 995–1014.

Sudhakar, Y., Lācis, U., Pasche, S. & Bagheri, S. 2021 Higher-order homogenized boundary conditions for flows over rough and porous surfaces. *Transp. Porous Med.* **136** (1), 1–42.

Suga, K. 2016 Understanding and modelling turbulence over and inside porous media. *Flow Turbul. Combust.* **96** (3), 717–756.

Suga, K., Okazaki, Y., Ho, U. & Kuwata, Y. 2018 Anisotropic wall permeability effects on turbulent channel flows. *J. Fluid Mech.* **855**, 983–1016.

Suga, K., Tominaga, S., Mori, M. & Kaneda, M. 2013 Turbulence characteristics in flows over solid and porous square ribs mounted on porous walls. *Flow Turbul. Combust.* **91** (1), 19–40.

Townsend, A.A. 1976 *The Structure of Turbulent Shear Flow, 2nd edn.*. Cambridge University Press.

Vreman, A.W. & Kuerten, J.G.M. 2014 Comparison of direct numerical simulation databases of turbulent channel flow at Re_τ= 180. *Phys. Fluids* **26** (1), 015102.

Walsh, M. & Lindemann, A. 1984 Optimization and application of riblets for turbulent drag reduction. In *the 22nd Aerosp. Sci. Meet.,* Reno, NV, USA. (doi: 10.2514/6.1984-347).

Wang, W., Chu, X., Lozano-Durán, A., Helmig, R. & Weigand, B. 2021 Information transfer between turbulent boundary layers and porous media. *J. Fluid Mech.* **920**, A21.

Wang, W., Lozano-Durán, A., Helmig, R. & Chu, X. 2022 Spatial and spectral characteristics of information flux between turbulent boundary layers and porous media. *J. Fluid Mech.* **949**, A16.

Wise, D.J. & Ricco, P. 2014 Turbulent drag reduction through oscillating discs. *J. Fluid Mech.* **746**, 536–564.

Wong, J., Camobreco, C.J., García-Mayoral, R., Hutchins, N. & D., Chung 2024 A viscous vortex model for predicting the drag reduction of riblet surfaces. *J. Fluid Mech.* **978**, A18.

Yang, X.I.A. & Meneveau, C. 2016 Large eddy simulations and parameterisation of roughness element orientation and flow direction effects in rough wall boundary layers. *J. Turbul.* **17** (11), 1072–1085.

Yang, X.I.A., Sadique, J., Mittal, R. & Meneveau, C. 2016 Exponential roughness layer and analytical model for turbulent boundary layer flow over rectangular-prism roughness elements. *J. Fluid Mech.* **789**, 127–165.

Zampogna, G.A., Magnaudet, J. & Bottaro, A. 2019 Generalized slip condition over rough surfaces. *J. Fluid Mech.* **858**, 407–436.

PAPER F4

Flow through porous metamaterials formed by TPMS-based unit cells: Effects of advection [1]

Essam Nabil Ahmed and **Alessandro Bottaro**

DICCA, Università di Genova, via Montallegro 1, Genova, 16145, Italy

The design of metamaterials based on triply periodic minimal surfaces (TPMS) is currently a very active field of research. An upscaling approach is used here to study the flow in TPMS-based porous media, with focus on the effects of advection. The *effective* medium permeability, function of the Reynolds number Re of the flow through the pores, is numerically evaluated for varying porosity θ, for six types of TPMS-based structures, namely *Gyroid*, *I-WP*, *Schwarz P*, *Split P*, *Fischer-Koch S*, and *Neovius*. Inertial effects are found to be significant; for instance, the permeability is reduced by $15-50\%$ (according to the surface type) as Re increases from 0 to 50000, when $\theta = 0.98$.

1 INTRODUCTION

Metamaterials are artificially engineered media, designed and fabricated to attain unique properties (electromagnetic, acoustic, mechanical, etc.) allowing them to offer novel functionalities, often unachievable by conventional materials (Chohan & Singh, 2022; Govindaraman *et al.*, 2022). Recent advances in material science and manufacturing techniques have opened up avenues for research on the development of customized metamaterials for applications such as energy harvesting (Govindaraman *et al.*, 2022), manipulation of sound waves (Arjunan *et al.*, 2022), or thermal cloaking (Imran *et al.*, 2020). The use of triply periodic minimal surfaces (TPMS), i.e. periodic structures which locally minimize their area subject to specific boundary constraints, to form metamaterials, exemplifies the integration between mathematics, applied physics, and manufacturing technology. TPMS-based structures are self-standing, highly interconnected, possibly of high porosity, lightweight, and manufacturable by 3D printing (Feng *et al.*, 2019; Asbai-Ghoudan *et al.*, 2021); the unique topological, acoustic, hydrodynamic, and mechanical features they may exhibit render them multifunctional and promising for applications ranging from architectural structures (Feng *et al.*, 2019) to biomedical engineering (Bobbert *et al.*, 2017; Ali *et al.*, 2020) and to sound absorption (Yang *et al.*, 2020).

[1]The Version of Record of this manuscript has been published and is available in: *European Journal of Mechanics - B/Fluids* **100** (2023) 202–207. https://doi.org/10.1016/j.euromechflu.2023.04.002

In recent years, many researchers focused on the hydrodynamics in porous structures consisting of TPMS-based cells; *Schoen Gyroid* (Asbai-Ghoudan *et al.*, 2021; Zeng & Wang, 2022; Zou *et al.*, 2022; Rathore *et al.*, 2023), *Schoen I-WP* (Zeng & Wang, 2022; Rathore *et al.*, 2023), *Schwarz P* (Asbai-Ghoudan *et al.*, 2021; Zeng & Wang, 2022; Rathore *et al.*, 2023), *Schwarz D* (Zou *et al.*, 2022; Rathore *et al.*, 2023), and *Fischer-Koch S* (Asbai-Ghoudan *et al.*, 2021; Zou *et al.*, 2022) are examples of minimal surfaces examined. Despite the analytical, numerical and experimental studies already conducted on these patterns, a systematic analysis is still needed, especially beyond the linear, Stokes-flow regime. In this work, seepage in TPMS-based porous materials is targeted for upscaling, with advection included in the analysis; the flow rate is eventually linked to the macroscopic pressure gradient via a Darcy-like equation where an *effective* permeability tensor is introduced. The upscaling procedure and the geometries considered are described in the next section. In Sec. 3, dependence of the permeability on the porosity and the Reynolds number is investigated for six types of TPMS, and the significance of inertial effects is highlighted. Summarizing remarks are presented in Sec. 4.

2 PROBLEM STATEMENT AND UPSCALING PROCEDURE

2.1 Problem description and preliminaries

Steady, isothermal, incompressible, Newtonian flow through a rigid, homogeneous porous medium formed by several TPMS-based unit cells is considered (cf. Fig. 1). The conservation equations governing the spatial variations of the velocity, $\hat{u}_i$, and the modified pressure (accounting also for conservative volume forces), $\hat{p}$, through the fluid domain are

$$\frac{\partial \hat{u}_i}{\partial \hat{x}_i} = 0, \tag{1}$$

$$\rho \hat{u}_j \frac{\partial \hat{u}_i}{\partial \hat{x}_j} = -\frac{\partial \hat{p}}{\partial \hat{x}_i} + \mu \frac{\partial^2 \hat{u}_i}{\partial \hat{x}_j^2}, \tag{2}$$

with ρ and μ the density and dynamic viscosity of the fluid, respectively. In addition, the no-slip boundary condition is defined at the interface $\mathcal{A}_{\beta\sigma}$ between the fluid domain (β) and the solid phase (σ):

$$\hat{u}_i = 0 \qquad \text{at } \mathcal{A}_{\beta\sigma}. \tag{3}$$

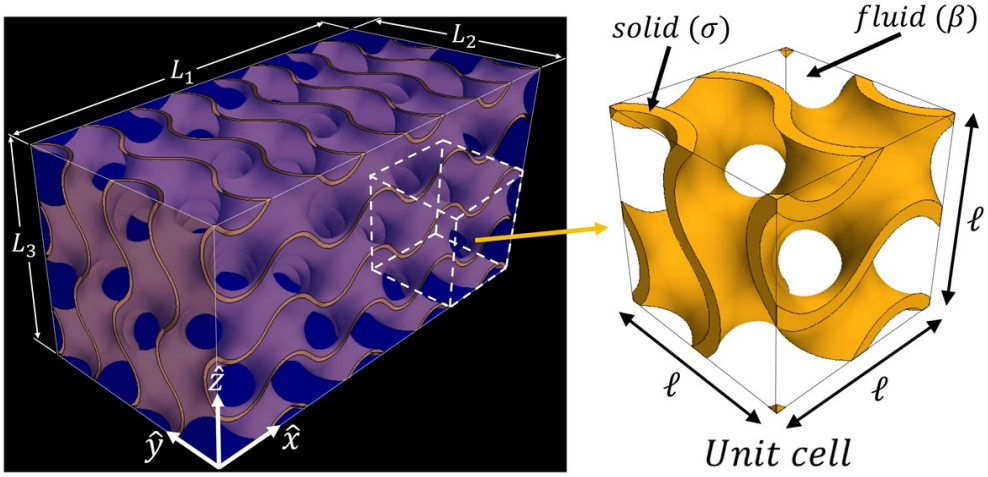

Figure 1: Sketch of the problem under study; right frame: gyroid-based unit cell.

The problem is amenable to upscaling provided that the microscopic length scale, e.g. the pattern periodicity ℓ, and the macroscopic length scale L, which characterizes large-scale processes, are well separated, i.e. $\epsilon = \ell/L \ll 1$. We can then define a *fast*, dimensionless spatial variable $x_i = \hat{x}_i/\ell$, related to field variations occurring at the small-scale level, and a *slow* one, $X_i = \hat{x}_i/L = \epsilon\, x_i$. Given that the volume of the averaging domain is $V = V_\beta + V_\sigma$ (with the porosity $\theta = V_\beta/V$), the intrinsic average and the superficial average of any property ψ, defined over the fluid domain, are respectively defined as

$$< \psi >^\beta = \frac{1}{V_\beta} \int_{\mathcal{V}_\beta} \psi \, dV, \quad < \psi >= \frac{1}{V} \int_{\mathcal{V}_\beta} \psi \, dV = \theta \, < \psi >^\beta . \tag{4}$$

The microscopic velocity scale, v_{ref}, is related to the magnitude of the external force driving the flow through the porous medium. In the present framework, the macroscopic pressure gradient, $\hat{\mathbf{M}}$, its magnitude, $\mathcal{M}$, and a unit vector along its direction, $\mathbf{e}^M$, are defined as follows:

$$\hat{M}_i = \frac{1}{L} \frac{\partial < \hat{p} >^\beta}{\partial X_i}, \qquad \mathcal{M} = \left|\left|\hat{\mathbf{M}}\right|\right|, \qquad e_i^M = \frac{\hat{M}_i}{\mathcal{M}}. \tag{5}$$

If viscous forces within the pores balance the external forcing, i.e. $\mu \frac{v_{ref}}{\ell^2} \sim \mathcal{M}$, the microscopic Reynolds number might be defined as

$$Re = \frac{\rho \mathcal{M} \ell^3}{\mu^2}. \tag{6}$$

2.2 Upscaling procedure

We follow an upscaling approach similar to that developed and validated by Valdés-Parada & Lasseux (2021*a*,*b*); the problem here is simpler than theirs, since only the homogeneous porous region (far away from the external boundaries of the medium) is considered, and since the no-slip condition applies at $\mathcal{A}_{\beta\sigma}$. The reader is referred to the aforementioned references for details about the model construction. Eventually, the upscaled velocity vector can be expressed in terms of the macroscopic pressure gradient, $\hat{\mathbf{M}}$, and the *effective* (also termed *apparent*) permeability tensor, $\hat{\mathbf{H}}$, as follows:

$$< \hat{u}_i > = -\frac{\hat{H}_{ij}}{\mu}\,\hat{M}_j, \tag{7}$$

and a dimensionless effective permeability, $H_{ij} = \hat{H}_{ij}/\ell^2$, can be introduced as

$$H_{ij} = < \mathcal{H}_{ij} > . \tag{8}$$

where $\mathcal{H}$ is a purely microscopic tensor (dependent on x_i only), available from the numerical solution of one *ad hoc* auxiliary system of equations defined on a *representative elementary volume* (REV). Such an adjoint problem, governing the spatial variations of $\mathcal{H}_{ij}$ and h_j[2], is

$$\frac{\partial \mathcal{H}_{ij}}{\partial x_i} = 0 \qquad \text{in } \mathcal{V}_\beta, \tag{9}$$

$$-Re\,\mathcal{H}_{\ell q}\frac{\partial \mathcal{H}_{ij}}{\partial x_\ell}\,e_q^M = -\frac{\partial h_j}{\partial x_i} + \frac{\partial^2 \mathcal{H}_{ij}}{\partial x_\ell^2} + \delta_{ij} \qquad \text{in } \mathcal{V}_\beta, \tag{10}$$

subject to

$$\mathcal{H}_{ij} = 0 \qquad \text{at } \mathcal{A}_{\beta\sigma}, \tag{11}$$

together with periodicity of the microscopic fields along x_1, x_2, and x_3. Additionally, since h_j appears in the closure problem in terms of its gradient only, we impose $< h_j >^\beta = 0$ for the problem to be well-posed.

The closure problem renders the effective permeability, $\mathbf{H}$, dependent not only on the micro-structural details of the porous medium (including shape of solid inclusions and porosity) but also on the Reynolds number, Re, and on the direction of the applied external forcing, $\mathbf{e}^M$. This implies that Eq. (7) is a more general version of Darcy's equation. An extensive discussion on the effects of inertia is provided by Lasseux *et al.* (2011). In the limit $Re \to 0$, the effective permeability, $\mathbf{H}$, becomes identical to the *intrinsic* permeability of the medium, $\mathbf{K}$; then, the classical Darcy's law is retrieved.

[2]The vector $\mathbf{h}$, defined in the REV, plays the role of a Lagrange multiplier to ensure that $\mathcal{H}$ is divergence-free.

2.3 Typical porous structures under consideration

Six types of triply periodic minimal surfaces are chosen for the analysis; they are indicated and mathematically defined in Table 1, and sketched in Fig. 2(left). Given that these surfaces are triply-periodic over a dimensional distance ℓ, cf. Fig. 1, which is chosen here as the microscopic length scale, a $1\times1\times1$ unit cell is sufficient to describe each geometry in the microscopic coordinates ($x_i = \hat{x}_i/\ell$); in the absence of unsteadiness or flow instabilities at large Re, the same unit block could be selected as a periodic, representative cell for solving the closure problem governing the microscopic fields ($\mathcal{H}_{ij}, h_j$).

A range of porosities ($0.5 \leq \theta \leq 0.98$) is covered in this work; it is thus necessary to adjust the material thickness of the chosen solid surface to obtain the chosen values of θ, as shown in Fig. 2(middle). Geometries were modeled in MATLAB (Release 2021a) and exported in STL format (Rouhana, 2022, Sep. 4; Sven, 2023). The volumes occupied by the fluid were then extracted, by subtracting the solid inclusions from the cubic unit cells, as presented in Fig. 2(right), and were meshed using polyhedral cells, with sufficient refinement near $\mathcal{A}_{\beta\sigma}$. All simulations were performed using Simcenter STAR-CCM+ (16.02.009-R8).

Table 1: Mathematical definitions of the TPMS under study. $(x', y', z') = 2\pi\,(x, y, z)$.

Surface	Formula
Schoen Gyroid	$cosx'siny' + cosy'sinz' + cosz'sinx' = 0$
Schoen I-WP	$2\,(cosx'cosy' + cosy'cosz' + cosz'cosx')$ $-\,(cos2x' + cos2y' + cos2z') = 0$
Schwarz P	$cosx' + cosy' + cosz' = 0$
Split P	$1.1\,(sin2x'sinz'cosy' + sin2y'sinx'cosz'$ $+sin2z'siny'cosx') - 0.2\,(cos2x'cos2y'$ $+cos2y'cos2z' + cos2z'cos2x')$ $-0.4\,(cos2x' + cos2y' + cos2z') = 0$
Fischer-Koch S	$cos2x'siny'cosz' + cos2y'sinz'cosx'$ $+cos2z'sinx'cosy' = 0$
Neovius	$3\,(cosx' + cosy' + cosz') + 4\,cosx'cosy'cosz' = 0$

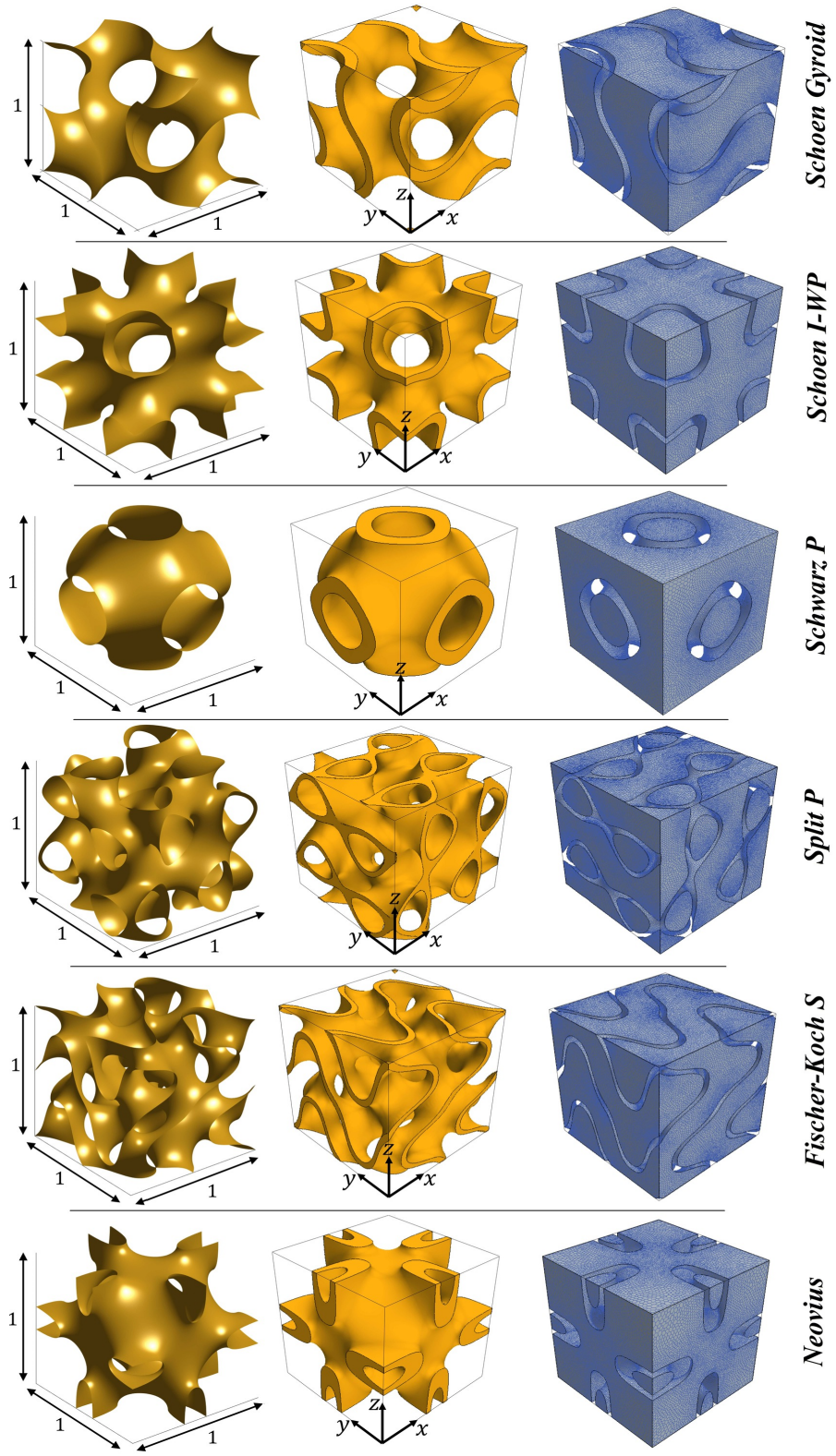

Figure 2: The TPMS-based unit cells examined. From left to right: triply-periodic minimal surface; solid frame of finite thickness ($\theta = 0.8$); volume occupied by the fluid.

3 NUMERICAL RESULTS AND DISCUSSIONS

We start by considering external forcing in the X_1-direction such that the macroscopic pressure gradient reads $\hat{M}_j = -\mathcal{M}\delta_{j1}$, and Eq. (7) simplifies to $< \hat{u}_i > = \dfrac{\hat{H}_{i1}}{\mu}\mathcal{M}$; this renders $\hat{H}_{i1} = \ell^2 H_{i1} = \ell^2 < \mathcal{H}_{i1} >$ the only components of interest in the permeability tensor. Since $\mathbf{e}^M$, the unit vector parallel to the direction of the macroscopic pressure gradient, may now be expressed as $(e_1^M, e_2^M, e_3^M) = (-1, 0, 0)$, Eq. (10) governing the microscopic fields can be written for $\mathcal{H}_{i1}$ as follows:

$$Re\,\mathcal{H}_{\ell 1}\frac{\partial \mathcal{H}_{i1}}{\partial x_\ell} = -\frac{\partial h_1}{\partial x_i} + \frac{\partial^2 \mathcal{H}_{i1}}{\partial x_\ell^2} + \delta_{i1} \qquad \text{in } \mathcal{V}_\beta. \tag{12}$$

Should the macroscopic pressure gradient be directed along $\mathbf{e}^M = (0, -1, 0)$, the permeability components of interest would be $\hat{H}_{i2} = \ell^2 H_{i2} = \ell^2 < \mathcal{H}_{i2} >$, and Eq. (10) would be recast for the fields $\mathcal{H}_{i2}$ as follows:

$$Re\,\mathcal{H}_{\ell 2}\frac{\partial \mathcal{H}_{i2}}{\partial x_\ell} = -\frac{\partial h_2}{\partial x_i} + \frac{\partial^2 \mathcal{H}_{i2}}{\partial x_\ell^2} + \delta_{i2} \qquad \text{in } \mathcal{V}_\beta. \tag{13}$$

and similarly in case the pressure forcing were oriented along X_3. Eventually, based on the numerical simulations conducted, it is found that the off-diagonal terms of $\mathbf{H} =< \mathcal{H} >$, originating from the aforementioned systems, vanish, and H_{11} (for X_1-forcing) $= H_{22}$ (for X_2-forcing) $= H_{33}$ (for X_3-forcing). Such components of interest of the effective permeability are, from now on, simply termed H. For $Re \to 0$ it is clearly $H = \mathcal{K}$, i.e. the intrinsic permeability of the isotropic medium is recovered.

Sample numerical results of $\mathcal{H}_{11}$ computed with Eq. (12) are presented in Fig. 3, showing the effects of changing the porosity from 0.7 to 0.98 at $Re = 0$ (left and middle columns), and how the field (at $\theta = 0.98$) is affected by the inclusion of inertia ($Re = 50000$, right column). Inspection of the figure, with attention directed to the levels defined on the color bars, reveals that values of $\mathcal{H}_{11}$ increase as the medium becomes more porous, while a decreasing trend for $\mathcal{H}_{11}$ is observed when Re goes from $Re = 0$ to $Re = 50000$, for all geometries studied.

The behavior of the effective permeability, H, with the porosity, θ, is presented in Fig. 4, under Stokes flow conditions ($Re = 0$; $H = \mathcal{K}$) and in the presence of inertia ($Re = 50000$). It is notable that: *(i)* H increases with the increase in θ, where second-degree polynomial functions (solid lines) perfectly fit the numerical results (symbols) for all the structures considered; *(ii)* the effective permeability consistently decreases with advection. These two findings are consistent with the earlier observations on Fig. 3, with reference to values of the microscopic constitutive field $\mathcal{H}_{11}$. From a quantitative perspective, *Schwarz P*-based structures exhibit the largest permeability (beyond $\theta = 0.7$) out of the patterns examined, with $\mathcal{K}$ at $\theta = 0.98$ equal to six times the value of the corresponding *Neovius*-based structure. At the largest porosity, all media are found to

be two orders of magnitude less permeable, at $Re = 0$, than the case of in-line spheres (Naqvi & Bottaro, 2021), for which $\mathcal{K} \approx 0.17$ at $\theta = 0.98$.

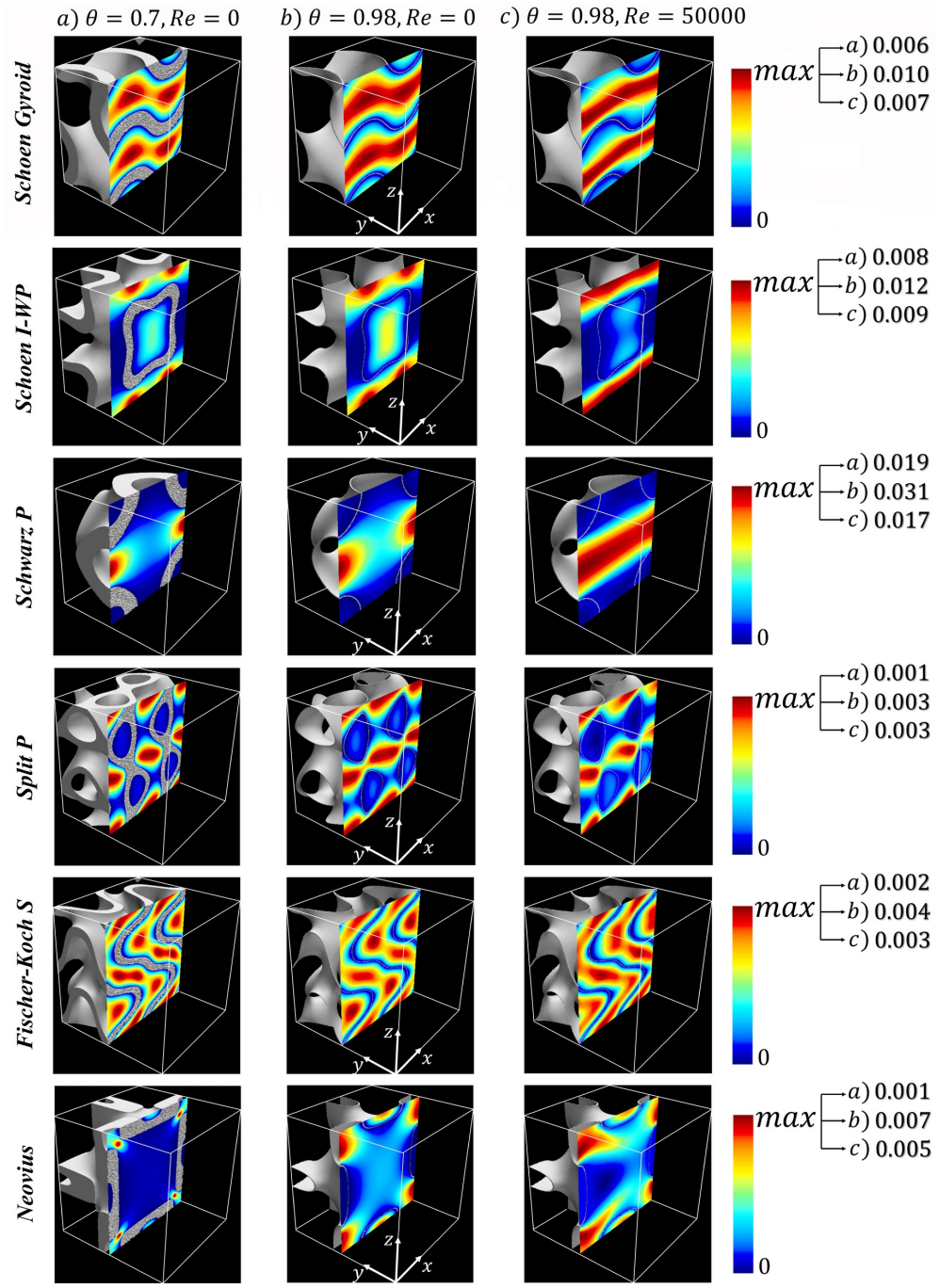

Figure 3: Contours of $\mathcal{H}_{11}$ on the $y = 0.5$ plane for different TPMS-based unit cells. Effect of porosity and Reynolds number.

To highlight the role played by advection, the effective-to-intrinsic permeability ratio, $H/\mathcal{K}$, is plotted in Fig. 5 as function of Re at different values of θ; the effective perme-

ability decreases monotonically with the increase of the Reynolds number and exhibits a stronger sensitivity to Re at larger values of θ.

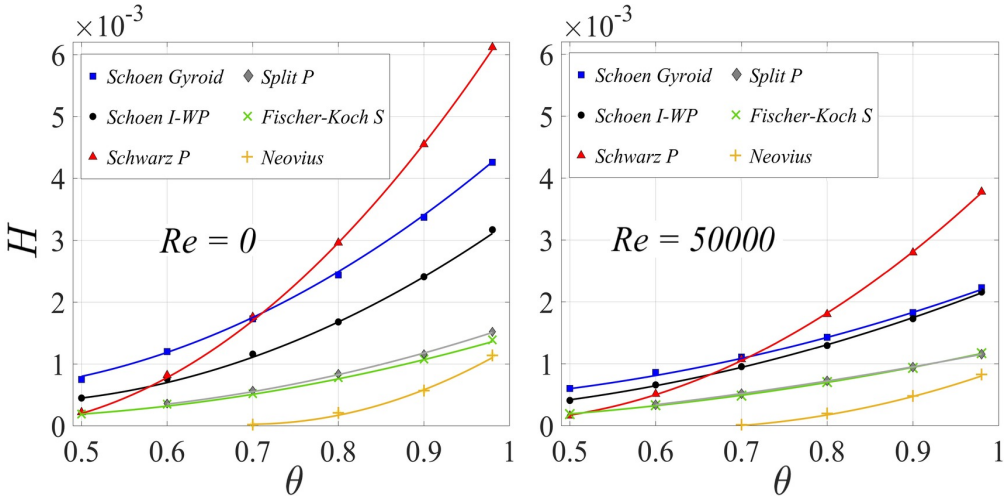

Figure 4: Effective permeability H as function of the porosity θ, for six types of TPMS-based porous structures, at two different values of Re.

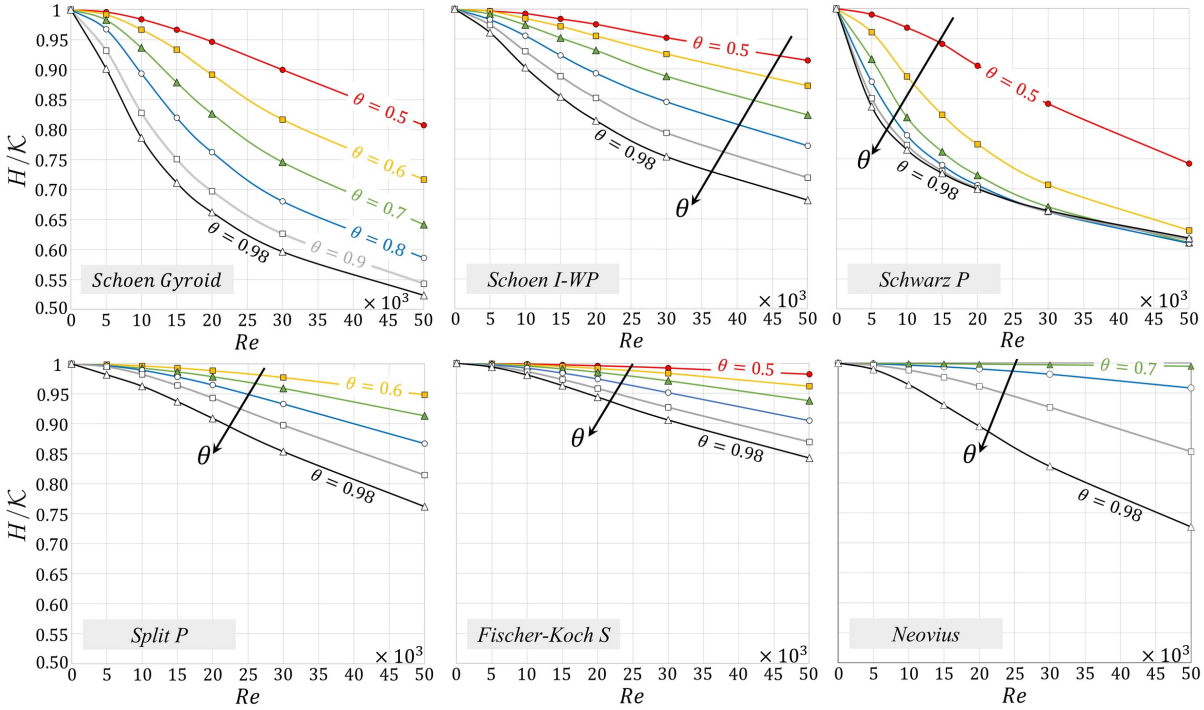

Figure 5: Effective-to-intrinsic permeability ratio for variable θ and $Re = 0 \rightarrow 50000$.

Finally, the model was validated against *full* simulations, in which the full Navier-Stokes equations (including transient terms) are solved in a domain consisting of 4 unit cells in $\hat{x}$ (direction of the external forcing) and 2 cells in both $\hat{y}$ and $\hat{z}$ (cf. Fig. 1). The

following parameters, yielding $Re = 50000$, are chosen: $\ell = 0.1\,m$, $\mu = 0.001\,Pa\,s$, $\rho = 1000\,kg\,m^{-3}$, inlet-to-outlet pressure drop equal to $0.02\,Pa$. Results of the volumetric flow rate are presented in Table 2 for sample structures; almost perfect agreement with Navier-Stokes solutions is obtained when the effective (instead of the intrinsic) permeability is used in Darcy's law (7), highlighting the validity of the model.

Table 2: Validation for $\theta = 0.9$; volumetric flow rate Q computed by "full" Navier-Stokes simulations (yielding steady solutions for all cases examined) against "model" results with Darcy's law (using either the intrinsic or the effective permeability).

Parameters of interest		Geometry		
		Gyroid	*I-WP*	*Schwarz P*
Permeability $[mm^2]$	$\hat{\mathcal{K}}$ $(Re = 0)$	34.12	24.34	44.96
	$\hat{H}$ $(Re = 50000)$	18.49	17.41	27.41
$Q\,[lit/min]$	"model", $Re = 0$	4.094	2.921	5.395
	"model", $Re = 50000$	2.219	2.089	3.289
	"full", $Re = 50000$	2.222	2.101	3.303

4 CONCLUSIONS

An upscaling procedure was used to study the flow through TPMS-based porous media, with conditions departing from Stokes'. Dependence of the average velocity on the macroscopic pressure gradient is properly described by a Darcy-like equation, with an *effective* permeability, H, strong function of the Reynolds number. A closure problem was numerically solved through a $1 \times 1 \times 1$ *representative elementary volume* (REV) to evaluate H for sample TPMS (Table 1), varying the parameters. Inertial effects play a significant role in the seepage, especially at large porosities. For instance, permeability of *Gyroid*-based structures is almost halved as Re goes from 0 to 50000 at $\theta = 0.98$. Nonetheless, a porous material formed by *Gyroid* cells is the most permeable at low porosities ($\theta < 0.7$), almost independently of Re, for all tested structures. Above $\theta = 0.7$ the largest permeability is displayed by a *Schwarz P*-based metamaterial. Finally, for highly porous media (i.e. beyond $\theta \approx 0.9$), the *Fischer-Koch S* pattern is affected the least, among all the shapes examined, by inertia.

For selected cases, the model was validated against Navier-Stokes simulations performed in a larger domain; the good agreement in terms of throughput attests the adequacy of the unit block as a REV, at least up to $Re = 50000$ (sufficiency of a single geometric unit cell was also checked at the closure problem level, for sample cases, and REV-independent results of H were obtained). Should transient and/or large-scale effects be present in the domain, larger REVs would be needed (Agnaou *et al.*, 2016).

REFERENCES

Agnaou, M., Lasseux, D. & Ahmadi, A. 2016 From steady to unsteady laminar flow in model porous structures: an investigation of the first Hopf bifurcation. *Comput. Fluids* **136**, 67–82.

Ali, D., Ozalp, M., Blanquer, S.B.G. & Onel, S. 2020 Permeability and fluid flow-induced wall shear stress in bone scaffolds with TPMS and lattice architectures: A CFD analysis. *Eur. J. Mech. B Fluids* **79**, 376–385.

Arjunan, A., Baroutaji, A. & Robinson, J. 2022 Advances in acoustic metamaterials. In *Encyclopedia of Smart Materials*, , vol. 3, pp. 1–10. Oxford: Elsevier.

Asbai-Ghoudan, R., Ruiz de Galarreta, S. & Rodriguez-Florez, N. 2021 Analytical model for the prediction of permeability of triply periodic minimal surfaces. *J. Mech. Behav. Biomed. Mater.* **124**, 104804.

Bobbert, F.S.L., Lietaert, K., Eftekhari, A.A., Pouran, B., Ahmadi, S.M., Weinans, H. & Zadpoor, A.A. 2017 Additively manufactured metallic porous biomaterials based on minimal surfaces: A unique combination of topological, mechanical, and mass transport properties. *Acta Biomater.* **53**, 572–584.

Chohan, J.S. & Singh, R. 2022 Thermosetting polymer application as meta materials. In *Encyclopedia of Materials: Plastics and Polymers*, , vol. 1, pp. 576–583. Oxford: Elsevier.

Feng, J., Fu, J., Shang, C., Lin, Z. & Li, B. 2019 Sandwich panel design and performance optimization based on triply periodic minimal surfaces. *Comput. Aided Des.* **115**, 307–322.

Govindaraman, L.T., Arjunan, A., Baroutaji, A., Robinson, J. & Olabi, A.-G. 2022 Metamaterials for energy harvesting. In *Encyclopedia of Smart Materials*, , vol. 2, pp. 522–534. Oxford: Elsevier.

Imran, M., Zhang, L. & Gain, A.K. 2020 Advanced thermal metamaterial design for temperature control at the cloaked region. *Sci. Rep.* **10**, 11763.

Lasseux, D., Abbasian Arani, A.A. & Ahmadi, A. 2011 On the stationary macroscopic inertial effects for one phase flow in ordered and disordered porous media. *Phys. Fluids* **23** (7), 073103.

Naqvi, S.B. & Bottaro, A. 2021 Interfacial conditions between a free-fluid region and a porous medium. *Intl J. Multiph. Flow* **141**, 103585.

Rathore, S.S., Mehta, B., Kumar, P. & Asfer, M. 2023 Flow characterization in triply periodic minimal surface (TPMS)-based porous geometries: Part 1– Hydrodynamics. *Transp. Porous Med.* **146** (3), 669–701.

Rouhana, R. 2022, Sep. 4 Generate gyroid structures using Matlab (Meshlab + FreeCAD conversion) [Video], YouTube. https://www.youtube.com/watch?v=uvCfVsFAcSw .

Sven 2023 stlwrite - write ASCII or Binary STL files. MATLAB Central File Exchange .

Valdés-Parada, F.J. & Lasseux, D. 2021*a* Flow near porous media boundaries including inertia and slip: A one-domain approach. *Phys. Fluids* **33** (7), 073612.

Valdés-Parada, F.J. & Lasseux, D. 2021*b* A novel one-domain approach for modeling flow in a fluid-porous system including inertia and slip effects. *Phys. Fluids* **33** (2), 022106.

Yang, W., An, J., Chua, C.K. & Zhou, K. 2020 Acoustic absorptions of multifunctional polymeric cellular structures based on triply periodic minimal surfaces fabricated by stereolithography. *Virtual Phys. Prototyp.* **15** (2), 242–249.

Zeng, C. & Wang, W. 2022 Modeling method for variable and isotropic permeability design of porous material based on TPMS lattices. *Tribol. Int.* **176**, 107913.

Zou, S., Mu, Y., Pan, B., Li, G., Shao, L., Du, J. & Jin, Y. 2022 Mechanical and biological properties of enhanced porous scaffolds based on triply periodic minimal surfaces. *Mater. Des.* **219**, 110803.